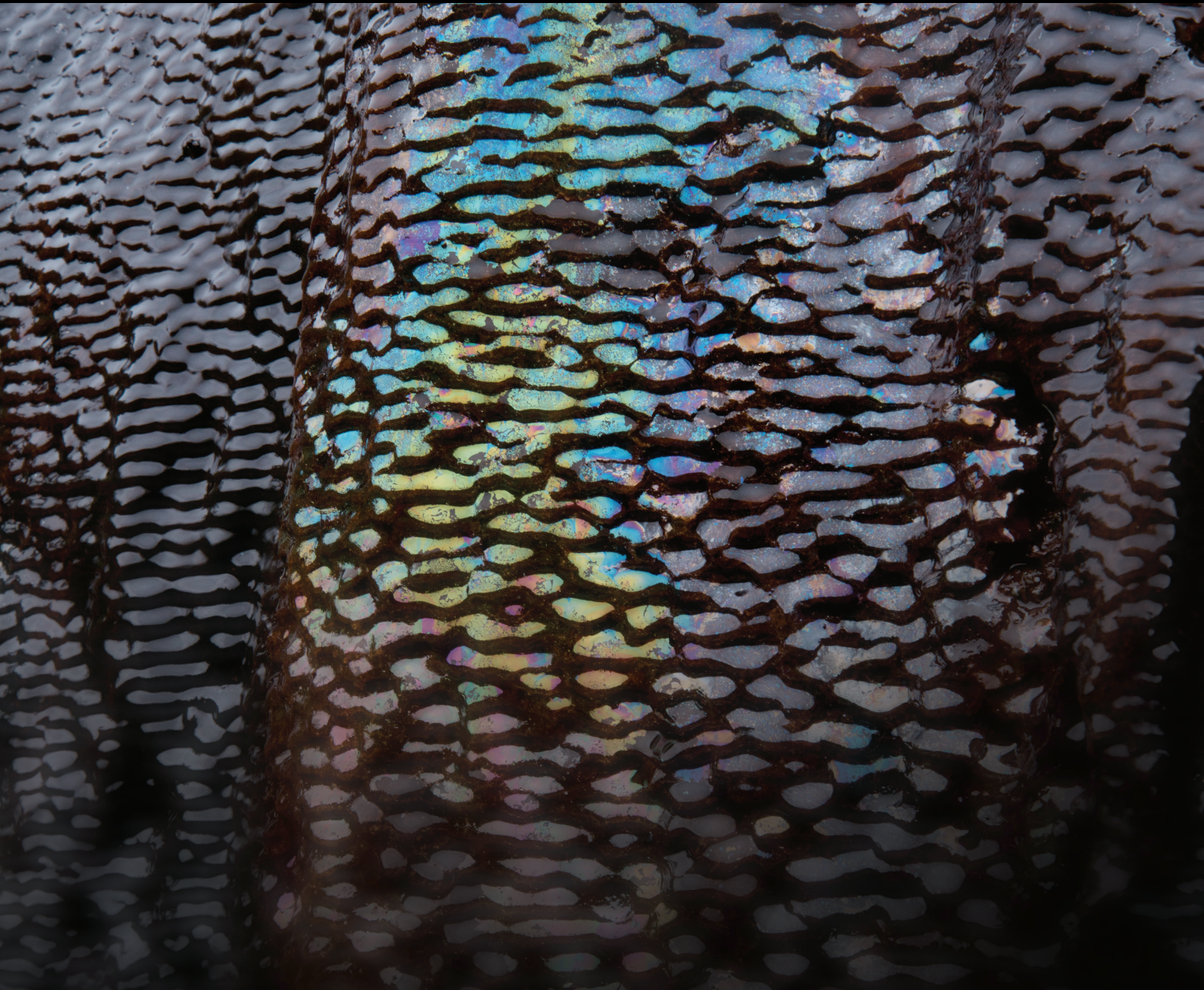


Geofluids

Geofluids and Energy for the XXI Century

Lead Guest Editor: Fabrizio Agosta

Guest Editors: Sergio Longhitano, Stefano Mazzoli, Giorgio Minelli,
and Emanuele Tondi





Geofluids and Energy for the XXI Century

Geofluids

Geofluids and Energy for the XXI Century

Lead Guest Editor: Fabrizio Agosta

Guest Editors: Sergio Longhitano, Stefano Mazzoli,
Giorgio Minelli, and Emanuele Tondi



Copyright © 2019 Hindawi. All rights reserved.

This is a special issue published in "Geofluids." All articles are open access articles distributed under the Creative Commons Attribution License, which permits unrestricted use, distribution, and reproduction in any medium, provided the original work is properly cited.

Editorial Board

Carmine Apollaro, Italy
Baojun Bai, USA
Maurizio Barbieri, Italy
Julien Bourdet, Australia
Andrea Brogi, Italy
David A. Butterfield, USA
Mauro Cacace, Germany
I. Chambeftort, New Zealand
Shengnan Nancy Chen, Canada
Paola Cianfarra, Italy
Daniele Cinti, Italy
Timothy S. Collett, USA
Nicoló Colombani, Italy
Mercè Corbella, Spain
Henrik Drake, Sweden
Lionel Esteban, Australia
Cinzia Federico, Italy
Paulo Fonseca, Portugal
Francesco Frondini, Italy
Paolo Fulignati, Italy
Paola Gattinoni, Italy
Mauro Giudici, Italy

Fausto Grassa, Italy
Salvatore Inguaggiato, Italy
Francesco Italiano, Italy
Jaewon Jang, Republic of Korea
Luchao Jin, USA
Shinsuke Kawagucci, Japan
Karsten Kroeger, New Zealand
Cornelius Langenbruch, USA
Huazhou Li, Canada
Liangping Li, USA
Marcello Liotta, Italy
Stefano Lo Russo, Italy
Constantinos Loupasakis, Greece
Lin Ma, USA
Paolo Madonia, Italy
Fabien Magri, Germany
Andrew H. Manning, USA
Micòl Mastrocicco, Italy
John A. Mavrogenes, Australia
Agnes Mazot, New Zealand
Yuan Mei, Australia
Jean-Luc Michelot, France

Ferenc Molnar, Finland
Julie K. Pearce, Australia
Daniele Pedretti, Italy
Marco Petitta, Italy
Christophe Renac, France
Reza Rezaee, Australia
Mohammad Sarmadivaleh, Australia
Christian Siebert, Germany
Ricardo L. Silva, Canada
Ondra Sracek, Czech Republic
Andri Stefansson, Iceland
Pietro Teatini, Italy
Svetlana G. Tessalina, Australia
Rene Therrien, Canada
Umberta Tinivella, Italy
Tivadar M. Tóth, Hungary
Zhenjiang You, Australia
Keni Zhang, China
Ye Zhang, USA
Ling-Li Zhou, Ireland

Contents

Geofluids and Energy for the XXI Century

Fabrizio Agosta , Sergio Giuseppe Longhitano, Stefano Mazzoli , Giorgio Minelli, and Emanuele Tondi
Editorial (3 pages), Article ID 7097252, Volume 2019 (2019)

How Can Temperature Logs Help Identify Permeable Fractures and Define a Conceptual Model of Fluid Circulation? An Example from Deep Geothermal Wells in the Upper Rhine Graben

Jeanne Vidal , Régis Hehn, Carole Glaas , and Albert Genter
Research Article (14 pages), Article ID 3978364, Volume 2019 (2019)

A Cause Analysis of the High-Content Nitrogen and Low-Content Hydrocarbon in Shale Gas: A Case Study of the Early Cambrian in Xiuwu Basin, Yangtze Region

Yizhou Huang , Kun Zhang , Zhenxue Jiang , Yan Song , Shu Jiang , Chengzao Jia, Weiwei Liu, Ming Wen , Xuelian Xie, Tianlin Liu, Xin Li, Xin Wang, Xiaoxue Liu, Ye Zhang, and Ling Tang
Research Article (13 pages), Article ID 1435892, Volume 2019 (2019)

Petrophysical Properties and Microstructural Analysis of Faulted Heterolithic Packages: A Case Study from Miocene Turbidite Successions, Italy

Hannah Riegel , Miller Zambrano , Fabrizio Balsamo , Luca Mattioni, and Emanuele Tondi
Research Article (23 pages), Article ID 9582359, Volume 2019 (2019)

Mechanical Properties and Statistical Damage Constitutive Model of Rock under a Coupled Chemical-Mechanical Condition

Yun Lin , Feng Gao , Keping Zhou, Rugao Gao , and Hongquan Guo
Research Article (17 pages), Article ID 7349584, Volume 2019 (2019)

Investigation of the Velocities of Coals of Diverse Rank under Water- or Gas-Saturated Conditions for Application in Coalbed Methane Recovery

Jizhao Xu, Cheng Zhai , Pathegama Gamage Ranjith, Yong Sun, Jisheng Guo, Zheng Ma, Huiteng Ma, and Lei Qin
Research Article (14 pages), Article ID 3729381, Volume 2019 (2019)

Structural and Mineralogical Characterization of a Fossil Hydrothermal System Located at the Outermost Front of the Southern Apennines Fold-and-Thrust Belt

Paolo Fulignati , Fabrizio Agosta , Claudia Belviso , Giacomo Prosser , Antonio Lettino , Angela Vita Petrullo , and Francesco Cavalcante 
Research Article (14 pages), Article ID 1840436, Volume 2019 (2019)

Analysis of Fracture Roughness Control on Permeability Using SfM and Fluid Flow Simulations: Implications for Carbonate Reservoir Characterization

Miller Zambrano , Alan D. Pitts, Ali Salama, Tiziano Volatili, Maurizio Giorgioni, and Emanuele Tondi
Research Article (19 pages), Article ID 4132386, Volume 2019 (2019)

History Matching of a Channelized Reservoir Using a Serial Denoising Autoencoder Integrated with ES-MDA

Sungil Kim, Baehyun Min , Seoyoon Kwon, and Min-gon Chu
Research Article (22 pages), Article ID 3280961, Volume 2019 (2019)

Recent Advance of Microbial Enhanced Oil Recovery (MEOR) in China

Haicheng She , Debin Kong , Yiqiang Li , Zaiqiang Hu, and Hu Guo 

Review Article (16 pages), Article ID 1871392, Volume 2019 (2019)

Variable Pore Structure and Gas Permeability of Coal Cores after Microwave Irradiation

Yi-du Hong, Bai-quan Lin, Hua Xiang, Chuan-jie Zhu, Zheng Wang, and Wen Nie 

Research Article (13 pages), Article ID 9240206, Volume 2018 (2019)

Editorial

Geofluids and Energy for the XXI Century

Fabrizio Agosta ¹, **Sergio Giuseppe Longhitano**,¹ **Stefano Mazzoli** ², **Giorgio Minelli**,³
and Emanuele Tondi⁴

¹*Dipartimento di Scienze, Università della Basilicata, Italy*

²*Dipartimento di Scienze della Terra, dell'Ambiente e del Mare, Università Federico II di Napoli, Italy*

³*Dipartimento di Fisica e Geologia, Università di Perugia, Italy*

⁴*Scuola di Scienze e Tecnologie, Università di Camerino, Italy*

Correspondence should be addressed to Fabrizio Agosta; fabrizio.agosta@unibas.it

Received 15 May 2019; Accepted 15 May 2019; Published 22 July 2019

Copyright © 2019 Fabrizio Agosta et al. This is an open access article distributed under the Creative Commons Attribution License, which permits unrestricted use, distribution, and reproduction in any medium, provided the original work is properly cited.

1. Motivations and Background

This special issue entitled “Geofluids and Energy for the XXI Century” focuses on cutting edge research findings in the fields of geology, rock physics, petrophysics, geomechanics, and numerical modelling. In particular, specific problems regarding the management of underground resources are tackled in terms of their exploration, production, and environmental vulnerability and sustainability. The present volume contains contributions following the scientific session entitled “Georesources and Energy for the XXI Century” held in 2018 during the annual meeting of the Italian Geological Society, which included 30 oral and poster communications [1]. The main topic covered by the presentations dealt with the great uncertainty associated with the assessment of the effective properties of subsurface reservoirs of geofluids, in particular to the complex distribution of the inner heterogeneities due to depositional [2–4], diagenetic [5, 6], and/or tectonic processes [7–11]. Along these lines, the present volume includes scientific articles dealing with three main topics including conventional hydrocarbons, unconventional hydrocarbons and methane recovery from coal beds, and geothermal systems.

2. Contents of the Special Issue

This special issue received 19 manuscripts, 10 of which were accepted for publication.

Most of them were based on the numerical simulations and experimental work on selected rock types, whereas others dealt with the geological characterization of exhumed fault zones. The first topic of conventional hydrocarbons includes five contributions. M. Zambrano et al. presented a research article entitled “Analysis of Fracture Roughness Control on Permeability Using SfM and Fluid Flow Simulations: Implications for Carbonate Reservoir Characterization,” wherein the authors tackled the control exerted by fracture roughness on the computed values of permeability. They presented a complete protocol for fracture surface mapping, roughness evaluation, fracture modelling, fluid flow simulation, and permeability estimation. This protocol included laboratory-based, high-resolution, structure-from-motion photogrammetry of selected fracture surfaces, power spectral density surface evaluation, synthetic fracture modelling, and fluid flow simulation using the Lattice-Boltzmann method. S. Kim et al. presented a research article entitled “History Matching of a Channelized Reservoir Using a Serial Denoising Autoencoder Integrated with ES-MDA.” There, the authors report the results of analyses conducted by means of a serial denoising autoencoder composed of two neural network filters, which utilized the machine-learning algorithm for relieving noise effects in the process of ensemble smoother-multiple data assimilation (ES-MDA) improving the overall history-matching performance. H. She et al. presented a review article entitled “Recent Advance of Microbial Enhanced Oil Recovery (MEOR) in

China,” in which the authors summarize the recent progress in laboratory studies and microbial flooding recovery field tests. Biotechnology was employed to investigate microbial flooding recovery mechanisms on a molecular level. Particular, attention was paid by the authors on both emulsification and wettability alternation due to microbial effects. Y. Lin et al. presented a research article entitled “Mechanical Properties and Statistical Damage Constitutive Model of Rock under a Coupled Chemical-Mechanical Condition.” The authors focused on the chemical corrosion that might affect the mechanical properties of rocks by investigating selected sandstone samples subjected to coupled chemical-mechanical conditions. In particular, they discussed the results of conventional triaxial compressive tests performed on specimens under the effect of chemical corrosion to improve a pre-existing statistical damage constitutive model, which was established by using the Drucker-Prager strength criterion. H. Riegel et al. presented a research article entitled “Petrophysical Properties and Microstructural Analysis of Faulted Heterolithic Packages: A Case Study from Miocene Turbidite Successions, Italy.” The authors focused on the results of field survey, optical microscopy, petrophysical analysis, and X-ray microtomography of hand specimens collected along fault zones cropping out in peninsular Italy. The studied fault zones crosscut turbidite deposits of Miocene age, which underwent similar tectonic evolutions and burial histories. Results of this multidisciplinary work highlighted the role exerted by the amount of clay and their distribution throughout the sedimentary successions on the cross-fault fluid flow properties of natural fault zones.

The second topic of unconventional hydrocarbons and methane production from coal beds includes three contributions. Y. Huang et al. presented a research article entitled “A Cause Analysis of the High-Content Nitrogen and Low-Content Hydrocarbon in Shale Gas: A Case Study of the Early Cambrian in Xiuwu Basin, Yangtze Region.” The authors focused on the study of nitrogen concentration in shale gas of the Yangtze Region, China. By integrating gas component analysis, stable nitrogen isotope analysis, and permeability tests with core description, field surveys, and seismic interpretation, they showed that the nitrogen present in the lower Cambrian shale in Xiuwu Basin derived from the atmosphere and the deep crust-upper mantle. Due to bedding planes and deep faults, which formed pathways for shale gas migration and diffusion, the authors documented a mechanism that led to a significant exchange between shale gas and the atmosphere. Results were therefore discussed in light of well-known models of shale gas diffusion in complex tectonic areas. J. Xu et al. presented a research article entitled “Investigation of the Velocities of Coals of Diverse Rank under Water- or Gas-Saturated Conditions for Application in Coalbed Methane Recovery.” The authors analyzed samples of lignite, bituminite, and anthracite prepared under both water and gas saturation conditions to investigate the residual water and gas in open cracks. For both water- and gas-saturated cores, the diverse velocity distributions were investigated Both longitudinal and transverse ultrasonic

pulse velocities were considered to assess both dimension and geometry of opening-mode fractures and primary pores in coal samples. Y. Hong et al. presented a research article entitled “Variable Pore Structure and Gas Permeability of Coal Cores after Microwave Irradiation.” The authors investigated the effect of microwave energy on pore structure and gas permeability of coal samples analyzing them by means of nuclear magnetic resonance. Results showed that the amount of water saturation significantly influenced the transverse relaxation time distribution only after a microwave energy treatment. In fact, the measured coal permeability increased after microwave energy irradiation, which was hence proposed as a tool to increase the degassing of coal seams.

The third topic of geothermal systems includes two contributions. P. Fulignati et al. presented a research article entitled “Structural and Mineralogical Characterization of a Fossil Hydrothermal System Located at the Outermost Front of the Southern Apennines Fold-and-Thrust Belt.” The authors investigated the structural setting, mineral assemblage, and fluid inclusions of fossil hydrothermal systems cropping out along the outermost edge of the southern Apennines belt, Italy, specifically along the eastern flank of the inactive Vulture Volcano. There, the authors recognized three main stages of hydrothermal activity, which took place during the Middle Pleistocene-to-present day times. The first stage was due to the circulation of low pH ($\text{pH} \approx 3-4$) fluids with a relatively high SO_4 -activity, which determined the formation of alunite group minerals, jarosite in particular. These hydrothermal fluids were likely characterized by temperatures of ca. $200^\circ\text{-}210^\circ\text{C}$. The second stage of hydrothermal circulation was recorded by opal A-rich veins, which precipitated from fluids characterized by lower temperature conditions with respect to the former ones. The third stage is currently taking place all along the study area flanking the Vulture Volcano, with goethite mineralization from groundwater-derived fluids at near surface temperatures. J. Vidal et al. presented a research article entitled “How Can Temperature Logs Help Identify Permeable Fractures and Define a Conceptual Model of Fluid Circulation? An Example from Deep Geothermal Wells in the Upper Rhine Graben.” The authors focused on permeable fault zones crosscutting a granitic basement penetrated by deep geothermal wells. By considering the temperature log datasets acquired from these wells during production and at equilibrium, along with the associated flow logs, they were able to investigate the fluid circulation at borehole scales. Geothermal fluids localize within the fault-related open fractures. At thermal equilibrium, the water temperature was estimated with respect to the temperature of the surrounding host rock. Accordingly, the peaks of high temperature were associated with the dilated fault zones and hence used to estimate reliable models of geothermal fluid flow in the study area of the Upper Rhine Graben.

Conflicts of Interest

The editors declare that they have no conflicts of interest regarding the publication of this special issue.

Acknowledgments

The guest editors would like to thank all the reviewers, who generously spent their valuable time in providing high-quality reviews for the submitted manuscripts. The special issue is part of the activities promoted by the “Georesources and Energy” Section of the Italian Geological Society.

Fabrizio Agosta
Sergio Giuseppe Longhitano
Stefano Mazzoli
Giorgio Minelli
Emanuele Tondi

References

- [1] M. F. Petti, B. Carmina, R. Cirrincione, and C. Monaco, “Geosciences for the environment, natural hazards, and culture heritage,” in *Abstract Book of the Italian Geological Society*, pp. 238–268, Italian Geological Society, 2018.
- [2] J. H. Barwis, J. G. McPherson, and J. R. J. Studlick, “Sandstone petroleum reservoirs,” in *Casebooks in Earth Sciences*, R. N. Ginsburg, Ed., p. 555, Springer-Verlag, 1990.
- [3] J. Lucia, *Carbonate reservoir characterization, an integrated approach*, Springer-Verlag Berlin Heidelberg, 2007.
- [4] S. G. Longhitano, L. Sabato, M. Tropeano et al., “Outcrop reservoir analogous and porosity changes in continental deposits from an extensional basin: the case study of the upper Oligocene Sardinia Graben System, Italy,” *Marine and Petroleum Geology*, vol. 67, pp. 439–459, 2015.
- [5] E. Parker and B. W. Sellwood, “Quantitative diagenesis: recent developments and applications to reservoir geology,” in *NATO ASI Series*, p. 287, Springer, 1994.
- [6] A. Rustichelli, E. Tondi, F. Agosta, C. Di Celma, and M. Giorgioni, “Sedimentologic and diagenetic controls on pore-network characteristics of Oligocene–Miocene ramp carbonates (Majella Mountain, Central Italy),” *American Association of Petroleum Geologists Bulletin*, vol. 97, no. 3, pp. 487–524, 2013.
- [7] E. Tondi, A. Cilona, F. Agosta et al., “Growth processes, dimensional parameters and scaling relationships of two conjugate sets of compactive shear bands in porous carbonate grainstones, Favignana Island, Italy,” *Journal of Structural Geology*, vol. 37, pp. 53–64, 2012.
- [8] S. Mazzoli, L. Aldega, S. Corrado, C. Invernizzi, and M. Zattin, “Pliocene-Quaternary thrusting, syn-orogenic extension and tectonic exhumation in the Southern Apennines (Italy): insights from the Monte Alpi area,” in *Styles of Continental Contraction*, S. Mazzoli and R. W. H. Butler, Eds., pp. 55–77, Geological Society of America, 2006.
- [9] G. Lena, M. R. Barchi, W. Alvarez, F. Felici, and G. Minelli, “Mesostructural analysis of S-C fabrics in a shallow shear zone of the Umbria–Marche Apennines (Central Italy),” *Geological Society, London, Special Publications*, vol. 409, no. 1, pp. 149–166, 2015.
- [10] M. D. Zoback, *Reservoir Geomechanics*, Cambridge University Press, 2007.
- [11] R. A. Nelson, *Geologic Analysis of Naturally Fractured Reservoirs*, Gulf Professional Publishing, 2001.

Research Article

How Can Temperature Logs Help Identify Permeable Fractures and Define a Conceptual Model of Fluid Circulation? An Example from Deep Geothermal Wells in the Upper Rhine Graben

Jeanne Vidal , Régis Hehn, Carole Glaas , and Albert Genter

ES-Géothermie, Bat Le Belem 5 rue de Lisbonne, 67300 Schiltigheim, France

Correspondence should be addressed to Jeanne Vidal; jeannevidal@ing.uchile.cl

Received 7 November 2018; Revised 25 January 2019; Accepted 19 February 2019; Published 10 July 2019

Guest Editor: Fabrizio Agosta

Copyright © 2019 Jeanne Vidal et al. This is an open access article distributed under the Creative Commons Attribution License, which permits unrestricted use, distribution, and reproduction in any medium, provided the original work is properly cited.

Identifying fluid circulation in fracture zones (FZs) is a key challenge in the extraction of deep geothermal heat from natural reservoirs in the Upper Rhine Graben. This study focuses on permeable FZs present within the granitic basement penetrated by deep geothermal well GPK-1 at Soultz and GRT-1 and GRT-2 at Rittershoffen (France). The various temperature (T) log datasets acquired from these wells during production and at equilibrium, with the associated flow logs, allow for the unique opportunity to interpret fluid circulation at the borehole scale. All permeable FZs identified by permeability indicators measured during drilling operations and from image logs spatially coincide with positive or negative T anomalies observed in the T logs during production and/or at equilibrium. However, within the FZs, partially open fractures act as narrower paths for circulation at different temperatures. These temperatures can even be estimated with confidence if the associated flow log is available. The polarity of the T anomalies correlates with the state of equilibrium of the well and thus can change over the well history. During production, the temperature of the water inflow through the fractures can be estimated relative to the mixture of water circulating below the fractures. At thermal equilibrium, the water temperature is estimated with respect to the temperature of the surrounding rock formation. Because temperature fluxes and geothermal fluids are intimately linked, T logs are a useful, reliable, and very sensitive tool to localize the inflow of geothermal water through FZs.

1. Introduction

In the Upper Rhine Graben (URG), the underground temperature distribution is spatially heterogeneous, and a series of local anomalies with temperatures above 140°C at a 2 km depth are observed at the regional scale [1–4]. These temperature anomalies are interpreted as convective cells circulating along vertical local faults (Figure 1) [2, 5, 6]. Hot upwellings are mainly concentrated around N-S-striking local faults on the western side of the URG. These N-S-striking local faults, which originate in the Paleozoic granitic basement and extend through the sedimentary cover, channelize these deep fluids. Over more than 30 years, 18 deep geothermal wells have targeted these faults in Germany (Landau, Insheim, Bruchsal, and Brühl) and France (Soultz-sous-Forêts, Rittershoffen and, most recently, Illkirch and Vendenheim) (Figure 1) [7–12]. Temperature (T) logs obtained from these

wells confirm the presence of hydrothermal convection and assert the roles of faults and fracture zones (FZs) as preferential pathways for geothermal brine [12–15]. The top of the granitic basement, which is highly fractured and affected by hydrothermal alteration, presents a low geothermal gradient associated with the vertical flow of brine and is locally affected by temperature anomalies interpreted as the thermal signatures of the FZs (Figures 2–4) [14–16].

Thus, the characterization of permeable fracture zones that act as primary potential paths for fluid flow is a key challenge for the development of geothermal reservoirs in granitic rocks. Experience shows that the characterization of permeable FZs by flow logs (obtained with a spinner tool) is difficult because flow logs are hard to obtain and interpret in these reservoirs. In contrast, T logs are cheap and easily acquired. T anomalies are interpreted as the thermal expressions of permeable FZs in several deep wells in geothermal

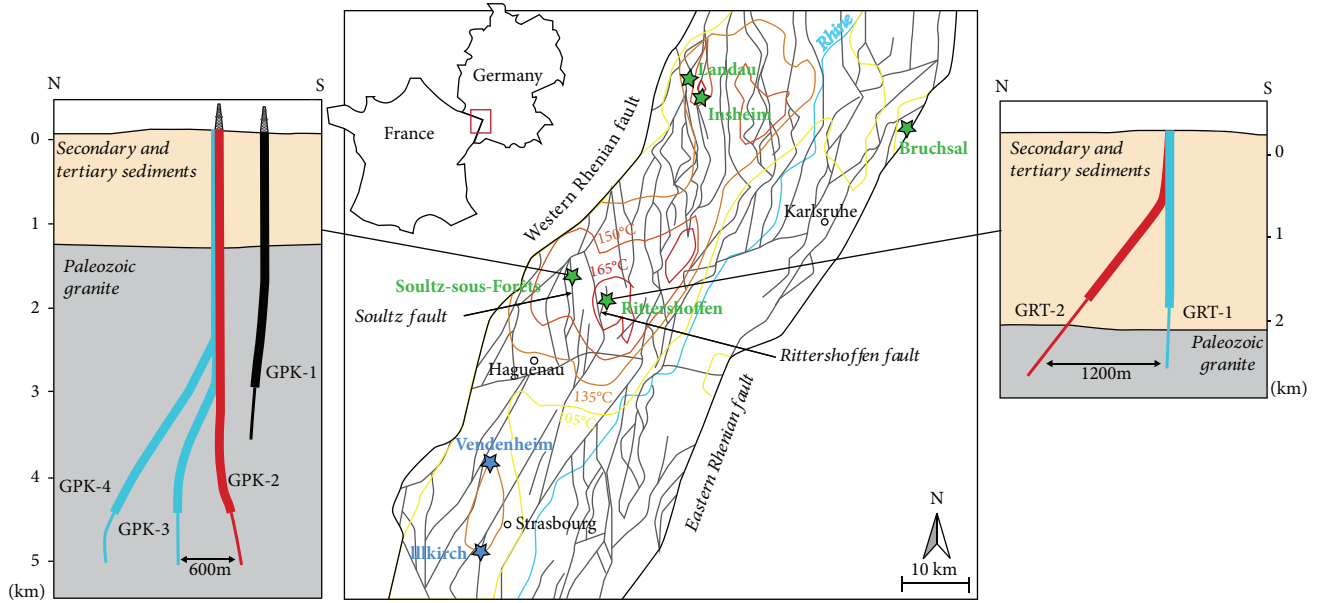


FIGURE 1: Structural map of the center of the Upper Rhine Graben with isotherms at a 2 km depth from the geoportal GeORG [55]. The geothermal anomaly in the Strasbourg area is from the dataset of Baillieux et al. [1]. Geothermal power plants in operation are represented by green stars, and the geothermal projects under drilling operations are represented by blue stars. On the left: N-S section through the geothermal wells of the Soultz-sous-Forêts power plant with a simplified geology. On the right: N-S section through the geothermal wells of the Rittershoffen power plant with a simplified geology. The thick line represents the casing section of the well, whereas the thin one represents the open hole. Production wells are in red, and injection wells are in blue. The GPK-1 well is represented in black because it is now used as an observation well.

systems worldwide [13, 14, 17–19]. However, in this paper, the datasets of the T logs acquired from wells at equilibrium and during production, combined with flow logs when they are available, offer a unique chance to further interpret T logs at the borehole scale. The reinterpretation of T logs at equilibrium and during production and their comparison with the permeability indicators and structural data from the FZs in well GPK-1 at Soultz and wells GRT-1 and GRT-2 at Rittershoffen provide a new perspective to better understand brine circulation through FZs in the granitic basement.

After a structural analysis of the main permeable fracture network that has channelized geothermal brines at the first order, the attention is focused on a comparison of T logs obtained at equilibrium and during production with flow logs if they are available from the wells. Finally, a conceptual model of fluid circulations through the FZs and the associated T anomalies is proposed at the borehole scale.

2. Soultz and Rittershoffen Geothermal Sites

Both projects exploit the hot upwelling of geothermal brine concentrated around the Soultz and the Rittershoffen faults (Figure 1). Extensive studies have identified convection associated with these hot upwellings; these studies have used numerical models on both the regional scale [4, 20] and local scale [21]. The role of faults as preferential fluid pathways is evident in other geothermal systems [22–25].

The pilot project of Soultz-sous-Forêts was initiated in the late 1980s. The target of the project was the development, hydraulic testing, and modeling of two Enhanced Geothermal System (EGS) heat exchangers within the granitic

basement at depths of 3.5 and 5 km [15, 26, 27]. In 1987, exploration well GPK-1 was drilled to a depth of 2 km and extended to a depth of 3.6 km in 1992 after hydraulic stimulation (Figure 1). At Soultz, geothermal water was pumped from the production well (GPK-2) and reinjected at a lower temperature into the injection wells (GPK-3 and GPK-4) after delivering geothermal energy through a heat exchanger to a binary power plant [10].

The geothermal project in Rittershoffen was initiated in 2008 and advised by lessons learned in Soultz. It is located less than 10 km east of Soultz (Figure 1). Injection well GRT-1 was drilled to a depth of 2.5 km in 2012 and thermally, chemically, and hydraulically stimulated in 2013. Production well GRT-2 was drilled to a depth of 2.5 km and is highly deviated accordingly to the geometry of the Rittershoffen fault (Figure 1). Well GRT-2 was not stimulated and thus, is defined as a hydrothermal well. The geothermal reservoir is mainly located in the granitic basement.

Geochemical studies indicate that the same brine is circulating within the large-scale fractured reservoir between Soultz and Rittershoffen [28, 29]. The reservoir was thoroughly investigated with a large amount of data (obtained from core samples, image logs, geophysical logs, microseismic data, vertical seismic profile, seismic reflection, etc.); these data were used to develop structural models of the multiscale fracture network associated with the Soultz and Rittershoffen faults [13, 30–33] as well as models of hydraulic circulation [34].

At the borehole scale, structural information from the granitic basement indicates that the highest density of fractures occurs in the first hundred meters of the

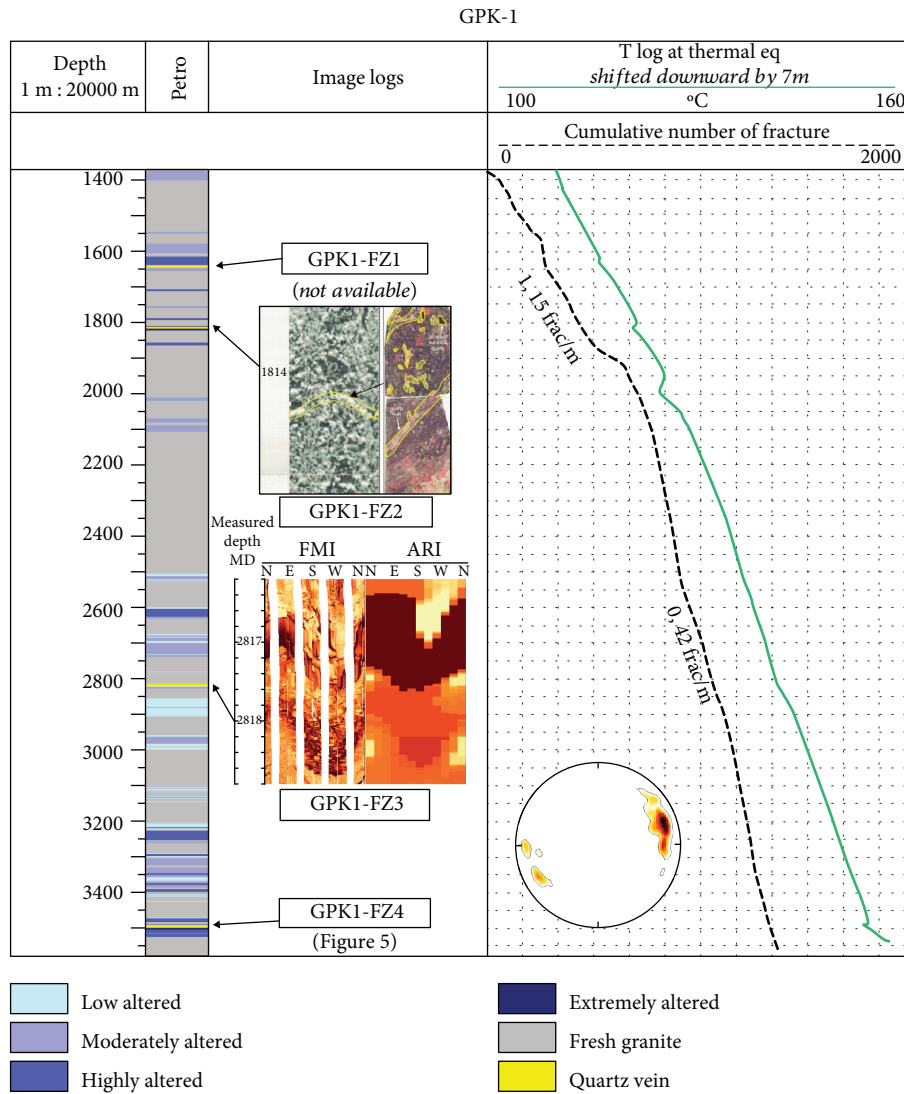


FIGURE 2: T logs from the granitic basement at thermal equilibrium in GPK-1 (Mar 1993, five months after the last hydraulic tests). T anomalies are associated with the permeable FZs observed in the image logs. The structural data of these FZs are presented in Table 1. Depth is expressed in Measured Depth (MD). T logs and flow logs were shifted manually to fit the anomalies with the fracture zones. Petrographic results are from Genter and Traineau [38]. Schmidt diagrams (lower hemisphere) and the cumulative number of fractures in the granitic basement are from Genter et al. [35].

hydrothermally altered granite. Data from acoustic image logs indicate values of 1,15 frac/m in GPK-1 in the first 500 m (data from a BoreHole TeleViewer, [35]) (Figure 2), 1,15 frac/m in GRT-1 in the first 200 m (Figure 3), and 0,75 frac/m in the deviated well GRT-2 (data from ultrasonic borehole images, [36]) (Figure 4). The fractures are mainly oriented NNW-SSE, with a steep dip mainly westward in GPK-1 (data from BHTV, [35]). In well GRT-1, the fractures strike mainly N10°E and dip approximately 60°W, whereas they are more scattered in GRT-2, with the main set oriented N160° to N-S and dipping 60°W (data from UBI, [36]). Hydraulic tests in GPK-1 indicate that 95% of the fluid flow enters the rock mass at only 10 discrete flow points [14]. These tests are consistent with cores from the permeable FZ, where a high density of partially open fractures promotes fluid circulation. These partially open fractures are

centimeters thick and are mainly filled by geodic quartz [37, 38]. An investigation of a quartz vein in the exploration borehole EPS-1 revealed at least seven generations of quartz, indicating a pulsed system of circulation [39]. Surrounding the core is a damage zone, with a width that ranges from centimeters to tens of meters. In this altered and porous zone, primary minerals are partly dissolved, and illite precipitation dominates the granite matrix [38, 40]. The degrees of alteration in the granite were determined based on the observations of the illitization amount in the core samples or cuttings [37, 41–43].

These permeable FZs mainly intersected in the granitic section, which is dominated by low temperature gradients associated with convection. The T gradients are approximately 20°C/km in GPK-1, nearly in GRT-1, and 18°C/km in GRT-2 (Figures 2–4). All permeable FZs have T anomalies

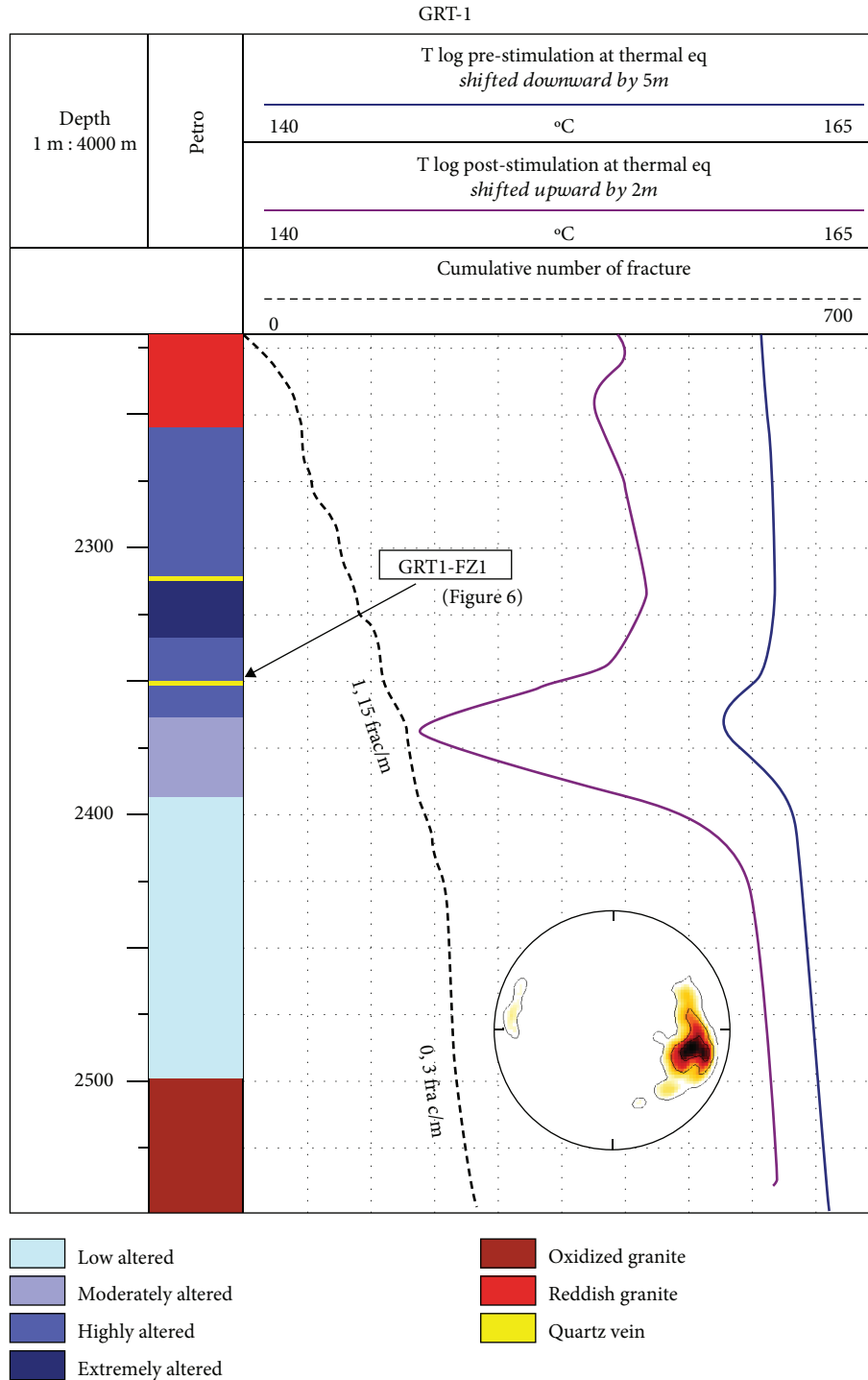


FIGURE 3: T logs from the granitic basement at thermal equilibrium in GRT-1 prestimulation (Apr 2013, four months after hydraulic tests) and poststimulation (Dec 2013, five months after hydraulic stimulation). T anomalies are associated with the permeable FZs observed in the image logs. The structural data of these FZs are presented in Table 1. Depth is expressed in Measured Depth (MD). T logs and flow logs were shifted manually to fit the anomalies with the fracture zones. Petrographic results are from Vidal et al. [44] and Glaas et al. [41]. Schmidt diagrams (lower hemisphere) and the cumulative number of fractures in the granitic basement are from Vidal et al. [36].

that spatially correlate with null observations in the T logs (Figures 2–4) [13–16]. Negative T anomalies are interpreted as the remnant cooling of porous damage zones after mud invasions during drilling operations and water injection

during stimulation operations [15]. However, is this interpretation still true several months after drilling operations and hydraulic tests, when the well is at thermal equilibrium? Could we propose another interpretation based on the

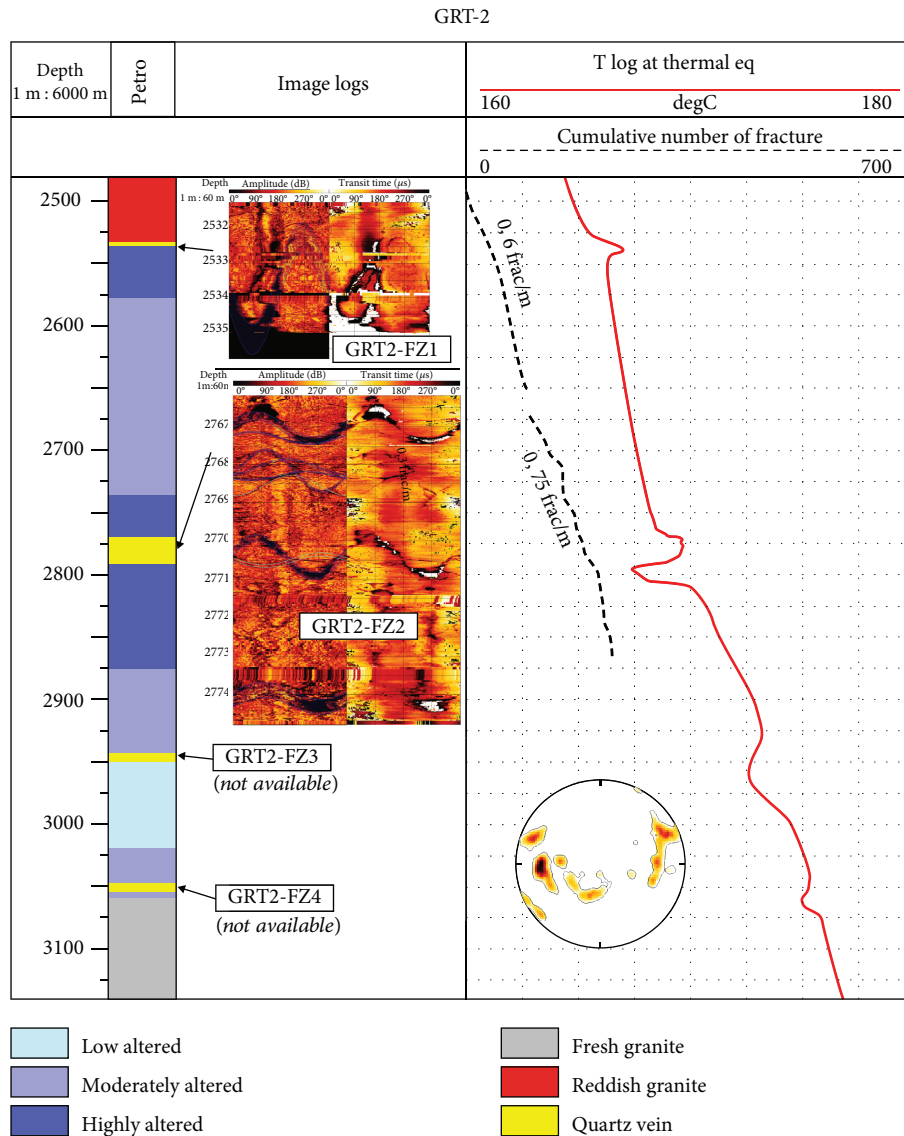


FIGURE 4: T logs from the granitic basement at thermal equilibrium in GRT-2 (September 2014, one month after drilling). T anomalies are associated with the permeable FZs observed in the image logs. The structural data of these FZs are presented in Table 1. Depth is expressed in Measured Depth (MD). T logs and flow logs were shifted manually to fit the anomalies with the fracture zones. Petrographic results are from Vidal et al. [44] and Glaas et al. [41]. Schmidt diagrams (lower hemisphere) and the cumulative number of fractures in the granitic basement are from Vidal et al. [36].

internal organization of the FZs? Is the intensity of the anomaly linked with the degree of permeability of the FZs? How could we explain the polarity and variations in the intensity of T anomalies over time?

3. Materials and Methods

3.1. *Permeable FZs from Mud Logs and Image Logs.* FZs that correspond to clusters of fractures partially open at the borehole scale and surrounded by a halo of hydrothermal alteration were identified in previous studies in Soultz and Rittershoffen [16, 44]. The core of the FZ is composed of opened fractures and quartz veins, and the damage zone is composed of illitic minerals [38]. Other secondary

minerals could be present (carbonates, sulfates, sulfides, and Fe-oxides).

Permeable FZs were identified using permeability indicators from several mud logs as follows:

- (i) Drilling mud losses and brine outflow are linked to permeable FZs [13–15, 33, 38, 45, 46]
- (ii) The occurrence of alkanes, as well as other gases such as helium, CO₂, and radon, indicates permeable fracture zones [47, 48]
- (iii) The mineralogical investigation of rock cuttings or core samples, when available, is an efficient method for identifying hydrothermally altered zones in the

granite [13, 49]. Brine circulation through a permeable fracture zone leads to partial sealing by secondary geodic quartz and clay mineral deposits, which are easily detectable in cuttings by visual inspection and in the laboratory by XRD [39, 40, 43, 50]. When cuttings are not available or reliable, gamma ray (GR) logging, which measures natural radioactivity, is a good indicator of hydrothermal alteration [42]. In GR, the occurrence of geodic quartz is associated with sharp localized negative anomalies, whereas clay minerals, which are K-bearing minerals, are associated with positive anomalies that can extend several meters

Finally, once the permeability indicators are identified, acoustic image logs allow for the identification of the geometry of the FZs and the acoustic aperture of the fractures at the borehole scale.

3.2. T Logs and Flow Logs. The T anomalies observed in a temperature profile are considered the most reliable of the permeability indicators [14, 16, 18, 24]. T logs can be acquired at thermal equilibrium, i.e., after several weeks without well operations, or during production. When T logs are acquired during production, a flow log can also be acquired, and the flow is measured based on the speed of the rotation of the helix (spinner tool). T logs acquired at equilibrium are acquired downward; T logs and flow logs acquired during production are acquired upward. T logs acquired during production allow for temperature estimation of the water circulating into the fracture zone with the following equation (assuming a first-order approximation) (Figure 5):

$$T_r \times Q_r + T_f \times Q_f = T_m \times Q_m, \quad (1)$$

where T_r is the temperature of the water coming from below the fracture, Q_r is the flowrate of the water coming from below the fracture, T_f is the temperature of the water coming from the fracture, Q_f is the flowrate of the water coming from the fracture, T_m is the temperature of the mix of water above the fracture, and Q_m is the flowrate of the mix of water above the fracture.

At equilibrium, T anomalies were identified primarily with T logs acquired before stimulation (Figures 2–4). Thermal equilibrium must not be influenced by cold mud or cold water stored in fractures after drilling and hydraulic operations. Poststimulation T logs were compared to prestimulation T logs. It is possible to observe some vertical depth shifts between T anomalies and fracture zones from core samples and image logs. These shifts could have several explanations. All logs were not acquired at the same time, and the process of depth matching among all logs is complicated. Moreover, temperature variations led to cable elongations that were not corrected for the well-logging data. The logs were shifted downward or upward based on the depths of the main open fractures observed in the acoustic logs.

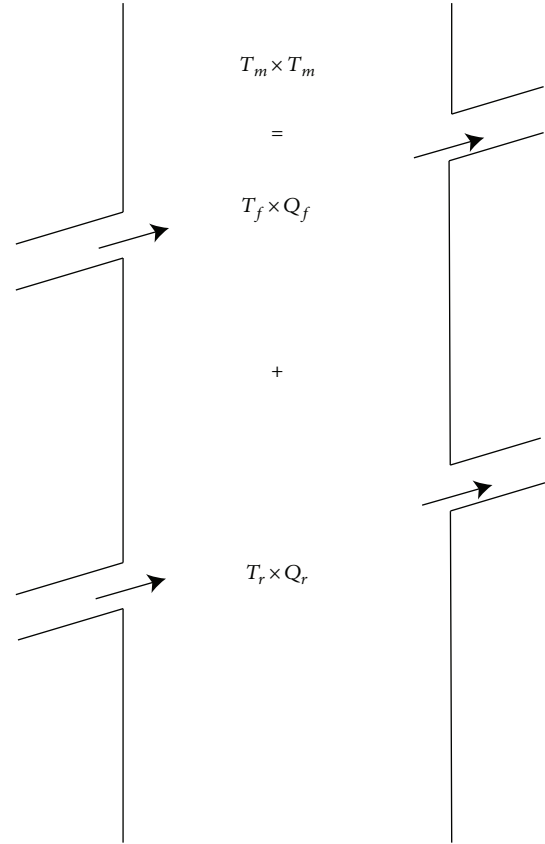


FIGURE 5: Scheme of the mixture of fluids coming from fractures into a permeable FZ.

4. Results

4.1. Permeable FZs from T Logs at Thermal Equilibrium. Four permeable FZs are identified in GPK-1, and they are all associated with negative thermal anomalies at thermal equilibrium (Table 1 and Figure 2). The borehole images of GPK1-FZ2 and GPK1-FZ3 are available in Vidal et al. [16, 43, 44]. Another negative anomaly is visible at a depth of 2100 m, but based on hydraulic tests, the FZ was identified as permeable after stimulation [51].

In GRT-1, one FZ was identified as permeable after stimulation and is associated with a negative anomaly at thermal equilibrium (Table 1 and Figure 3). GRT1-FZ1 includes the two permeable fractures observed in the granitic basement, as described in Vidal et al. [16]. A poststimulation anomaly is observed in the T log at 2236 m MD, but it is not spatially correlated with permeability indicators obtained before stimulation. Four permeable FZs are identified in GRT-2; two are associated with positive anomalies (GRT2-FZ1 and GRT2-FZ2), and two are associated with negative anomalies (GRT2-FZ3 and GRT2-FZ4) (Figure 4). GRT2-FZ1 includes the two uppermost permeable fractures observed in the table 1 of Vidal et al. [16], and GRT2-FZ2 includes the five deepest fractures. The borehole images of GRT-1 and GRT-2 are available in Vidal et al. [16].

Permeable fractures are mainly oriented N170°E and dip westward (Figure 6). Fractures that dip westward are associated with positive or negative T anomalies. Fractures that dip

TABLE 1: Temperature anomalies in well GPK-1 in Soultz and GRT-1 and GRT-2 in Rittershoffen. Structural data from the main open fractures in the FZs, as well as the polarity and depth of the anomalies, are presented. Structural data in italics indicate that acoustic images are not available. For GRT-2, values are calculated from oriented calipers [41].

Name	Main open fracture			Temperature anomaly	
	MD m	Strike Deg	Dip Def	MD m	Signal
GPK1-FZ1	1645	N155°E	76°W	1623	-
GPK1-FZ2	1814	N120°E	47°E	1815	-
GPK1-FZ3	2817	N150°E	75°W	2818	-
	2818.5	N140°E	70°X		
GPK1-FZ4	3489	N160°E	60°W	3495	-
	3496	N170°E	70°W		
GRT1-FZ1	2328	N20°E	50°W	2380	-
	2368	N170°E	55°W		
GRT2-FZ1	2534	N00°E	80°E	2537	+
	2540	N10°E	72°E		
	2767	N154°E	83°W		
GRT2-FZ2	2770.5	N160°E	87°W	2775	+
	2774	N170°E	64°W		
	2787	N45°E	57°E		
GRT2-FZ3	2788	N00°E	55°W	2970	-
	2950	<i>N170°E</i>	<i>90°E</i>		
GRT2-FZ4	3050	<i>N00°E</i>	<i>70°W</i>	3060	-

eastward are also associated with T anomalies that are positive or negative. The polarity of T anomalies is not directly linked to the fracture orientation or the dip direction. Thus, it is not possible to anticipate the polarity of the anomalies with respect to the fracture geometry.

4.2. Fluid Circulation from T Logs during Production

4.2.1. GPK-1. The permeable FZ in GPK1-FZ4 is presented in Figure 7. In September 1996, during production at 10.8 L/s, a flow log and a T log were acquired. The first inflow of water into the well was observed at 3496 m MD, with a measured flow of 1.5 L/s. This inflow depth corresponds with a negative T anomaly (148°C) in the T logs acquired during production. These anomalies are spatially correlated with an open fracture, which is visible in the acoustic image log, striking N170°E and dipping westward 70° at 3496 m MD. Then, several small positive anomalies are observed and associated with a flow increase at the same depth as the open fracture, striking N160°E and dipping 60°W at 3489 m MD. All of these small anomalies are assumed to originate from the same fracture. Above this, the flow is 2.7 L/s, and the measured temperature is 149°C. Following the equation described in Section 3.2, the temperature of the water that arrives in this major fracture is approximately 150°C:

$$\frac{149 \times 2.7 - 148 \times 1.5}{(2.7 - 1.5)} = 150.2. \quad (2)$$

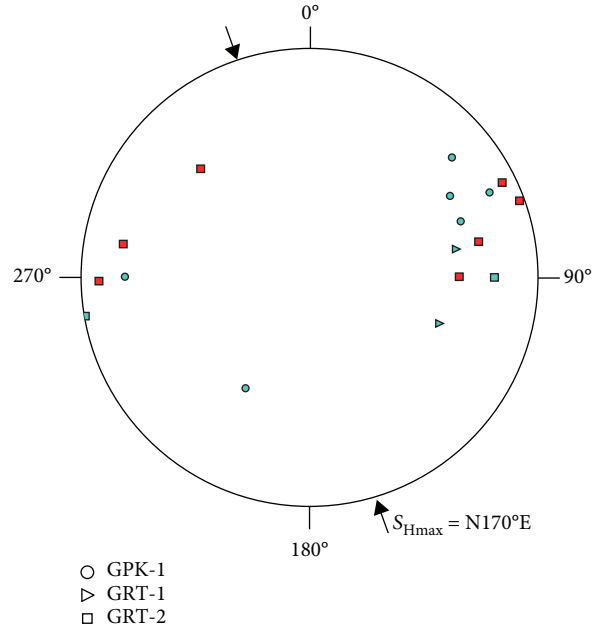


FIGURE 6: Stereoplot of the permeable fractures identified in acoustic image logs from GPK-1 (circle), GRT-1 (triangle), and GRT-2 (square). Blue symbols indicate fractures associated with negative anomalies, and red symbols indicate positive anomalies. Orientations and dips are detailed in Table 1. The maximum horizontal stress is from [56] for Soultz and from [57] for Rittershoffen.

At equilibrium (five months after the hydraulic tests), the water inflow through GPK1-FZ4 is associated with a negative anomaly in the T log acquired in March 1993.

The subsequent T logs acquired from well GPK-1 during production are more affected by hydraulic circulation than the other wells and thus are less reliable.

4.2.2. GRT-1. In GRT-1, during hydraulic tests in January 2013, a T log and a flow log were acquired during airlift production at 12,3 L/s. However, the flow log is not entirely useful; anomalies are observed but are barely quantifiable. T logs at equilibrium were acquired pre- and poststimulation in April and December of 2013, respectively (Figure 8).

In the production T log, a small negative anomaly is observed at 2233 m MD, which is not correlated with the flow anomaly (Figure 8(a)). This T anomaly is not observed in the prestimulation T log at thermal equilibrium. However, a T anomaly is observed in the poststimulation T log at 2235.5 m MD. This anomaly corresponds with an open fracture striking N180°E and dipping 60° westward at 2236.5 m MD.

The main permeable FZ of GRT1-FZ1 extends from 2325 to 2368 m MD. Two major open fractures associated with mud losses were also identified. The first one, which is found at the top of the FZ, strikes N20°E and dips 50° westward and is located at 2326 m MD [16]. Although mud losses were observed during drilling operations, no T anomaly was observed during production at this depth. A small negative anomaly is observed in the poststimulation T log (Figure 3).

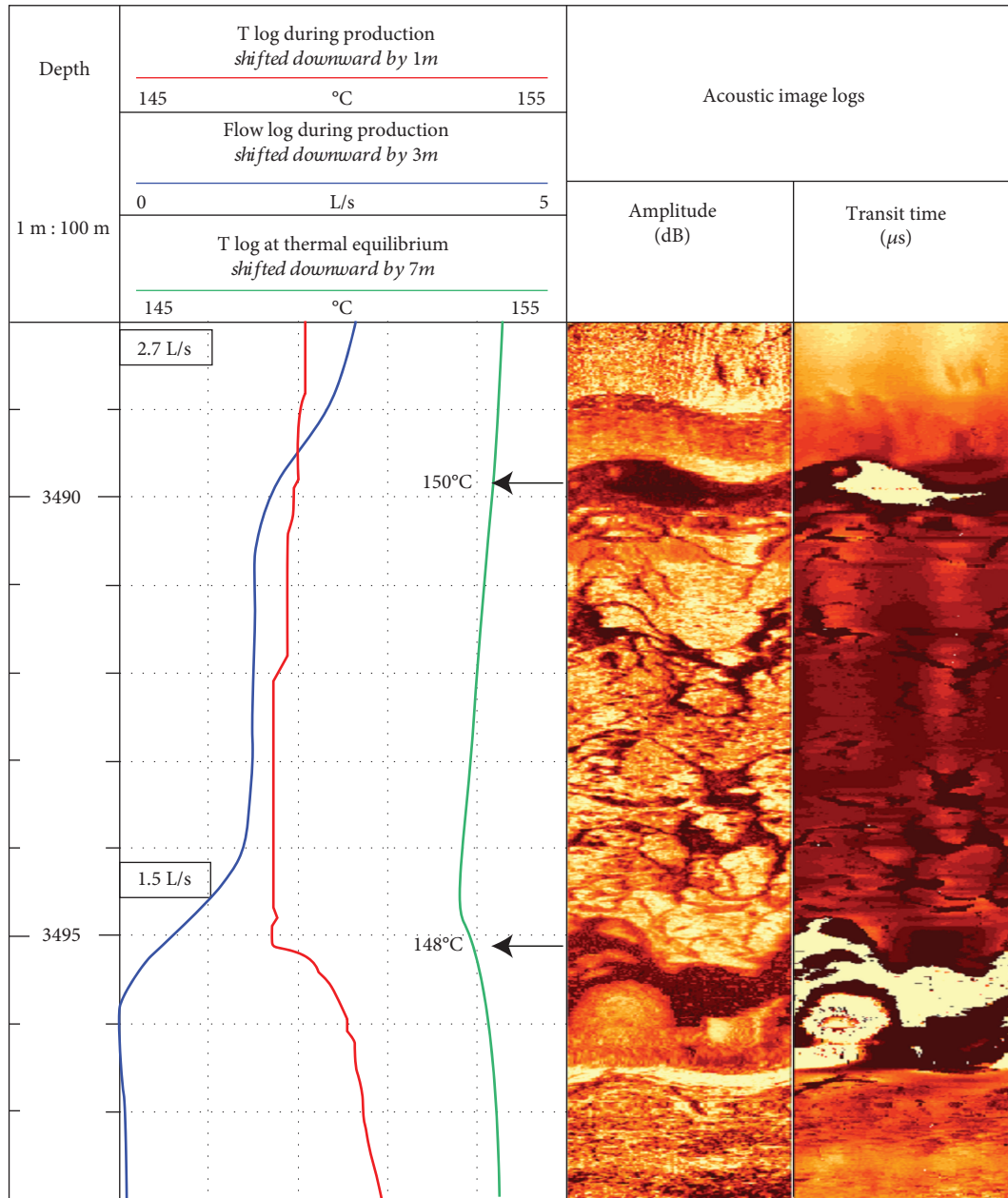
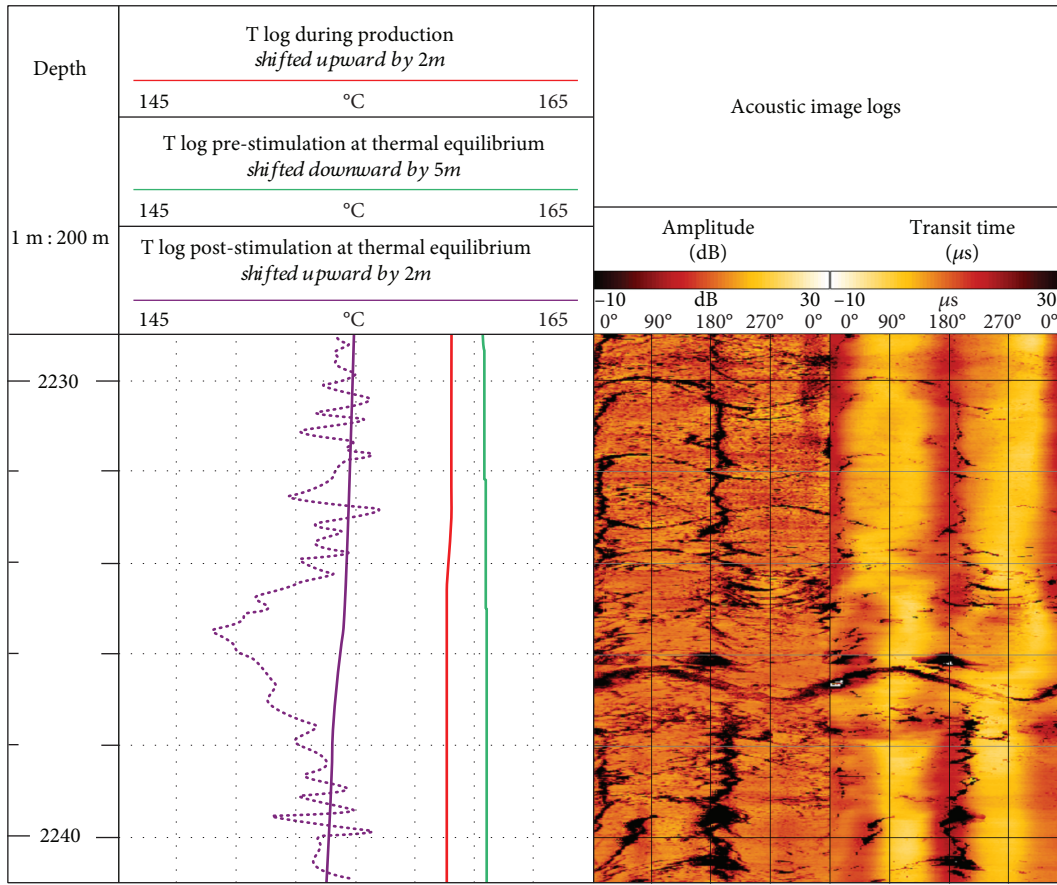


FIGURE 7: T logs from well GPK-1 at thermal equilibrium (Mar 1993, five months after the last hydraulic tests) and during production, with the corresponding flow log (Sept 1996, production test at 11 L/s). T and flow anomalies are associated with the open fractures observed in the acoustic image logs at 3490 and 3495 m MD, respectively. Arrows indicate inflows of geothermal water through the fractures. Depth is expressed in MD. The T logs and flow logs were shifted manually to fit the anomalies with fracture zones in all wells.

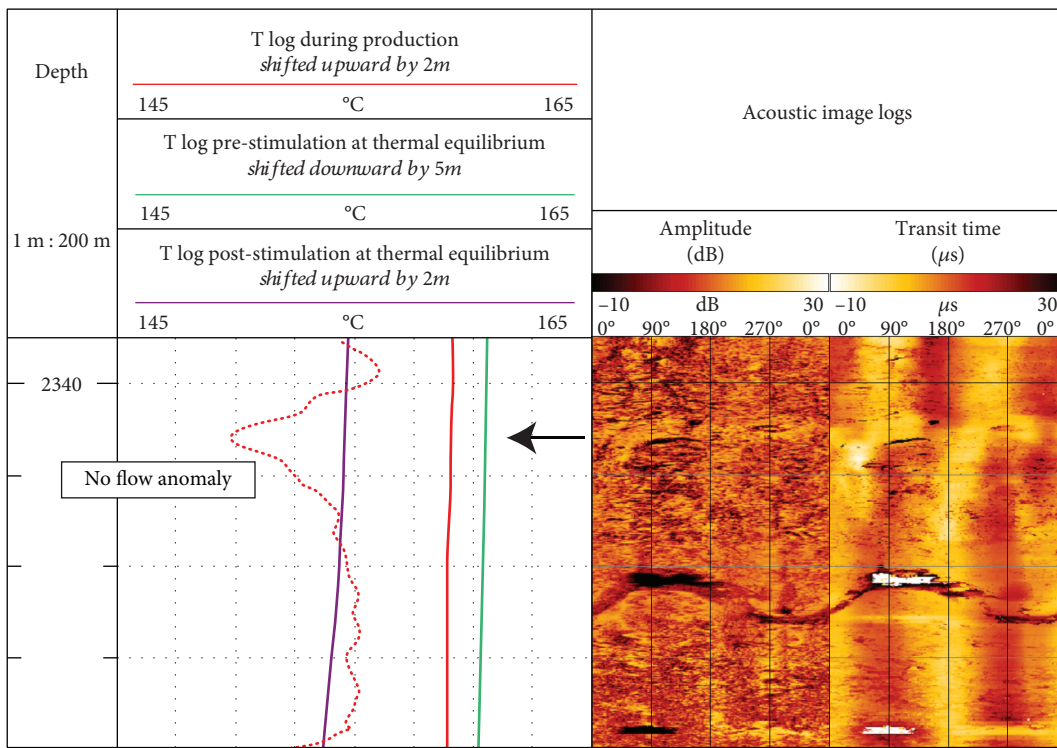
In the production T log, a small negative anomaly is observed at 2341 m MD that is not correlated with a flow anomaly (Figure 8(b)). This T anomaly is incorporated into a larger anomaly evident in the prestimulation T log at thermal equilibrium and in the poststimulation T log (Figure 3). These anomalies correlate with an open fracture striking N25°E and dipping 60° westward at 2345 m MD (Figure 8(b)).

The second open fracture of GRT1-FZ1 is associated with mud losses and is located at 2368 m MD. It is striking N175°E and dipping 65° westward. This fracture controls 2/3 of the total flowrate and is at the interface between highly altered

and fractured granite above and low altered granite below [16]. Thus, this fracture permits the first inflow of water into the well. Surprisingly, the flow log is not consistent with this observation and is thus considered unreliable for the evaluation of the absolute flow associated with the fractures in the well. The flow anomaly is associated with a T anomaly (+3°C) at 2364 m MD (Figure 8(c)). A second T anomaly (+5°C) at 2350 m MD is observed. This positive T anomaly is not clearly associated with an open fracture but is associated with a cluster of thin fractures. However, the calculation of the water temperature at this depth is not possible because the flow log is not reliable. At equilibrium,

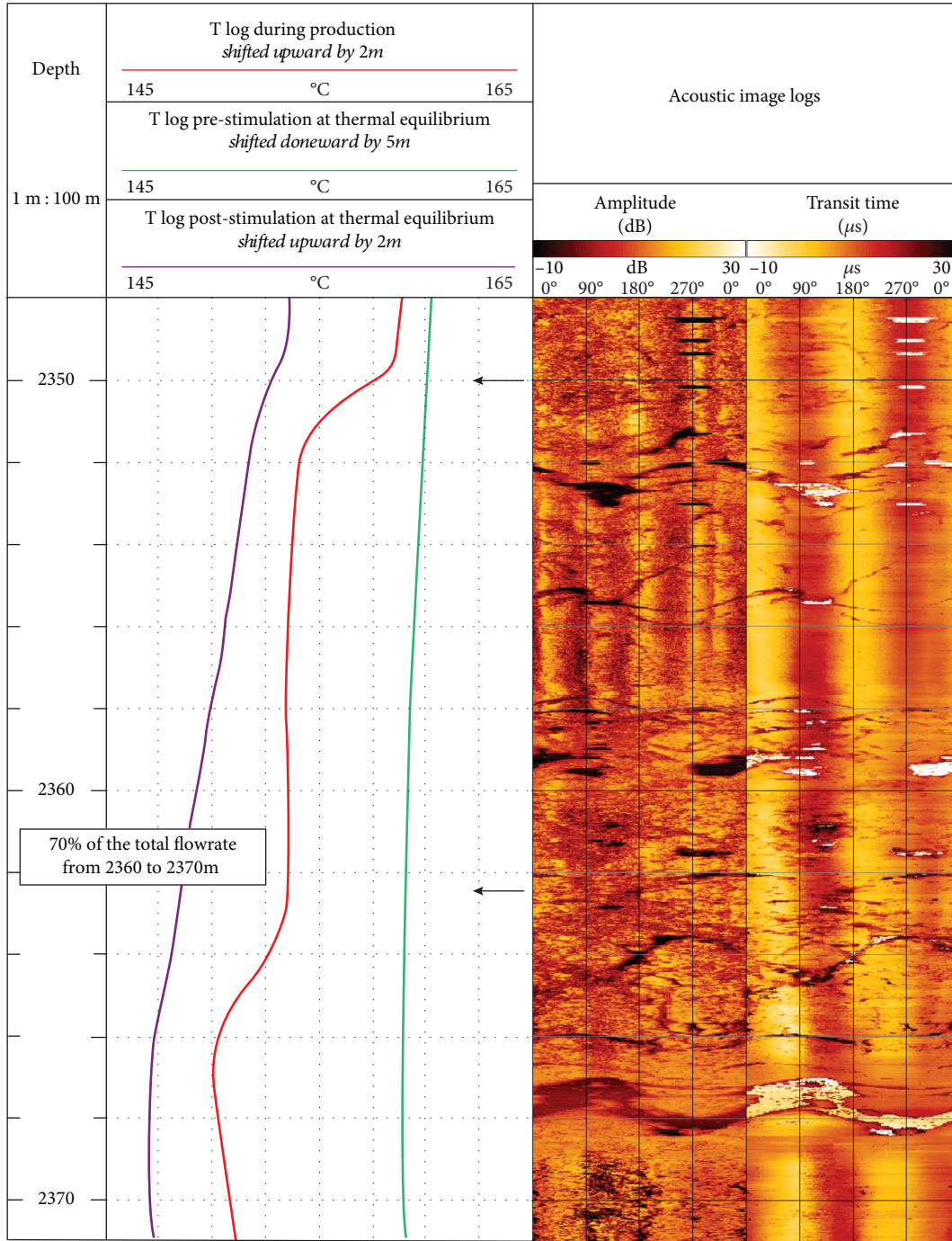


(a)



(b)

FIGURE 8: Continued.



(c)

FIGURE 8: T logs obtained from well GRT-1 during production (Jan 2013, airlift production), at thermal equilibrium prestimulation (Apr 2013, four months after hydraulic tests) and poststimulation (Dec 2013, five months after hydraulic stimulation). Dotted lines indicate the gradient of the T logs during production (red) and poststimulation (purple). T anomalies are associated with open fractures observed in acoustic image logs at (a) 2236 m MD, (b) 2345 m MD, and (c) 2368 m MD. Arrows indicate inflows of geothermal water through fractures. Depth is expressed in MD. T logs and flow logs were shifted manually to match anomalies with fracture zones.

the prestimulation log indicates a large negative T anomaly, whereas the poststimulation T log indicates two negative anomalies that correspond with those observed during production (Figure 3).

4.2.3. GRT-2. Only one temperature log at thermal equilibrium was acquired in this well in September 2014. Two positive T anomalies are observed for GRT2-FZ1 and GRT2-FZ2 (Figure 4). These anomalies are the only positive

ones observed in the well, but as they are observed at thermal equilibrium, without previous injection into the well, they are considered reliable. They indicate water inflows hotter than the surrounding rock formation. Unfortunately, the temperature of this water cannot be precisely calculated because flow logs and T logs acquired during production are not available. Both anomalies are associated with open fractures at the borehole scale, which mainly strike N170°E and dip westward [16].

5. Discussion

5.1. Thermal Signature of Permeable FZs. GPK1-FZ4 corresponds to the first inflow of water into the well and thus marks the beginning of thermal convection. The first inflow of water into the well is at 148°C through a fracture at 3496 m MD (Figure 7). The negative anomaly in the production T log is explained by an inflow of water colder than the deeper reservoir during production. The positive anomaly described above is interpreted as the inflow of water from a fracture at 3489 m MD, which is hotter (150°C) than water from the fracture at 3496 m MD (148°C). At thermal equilibrium, GPK1-FZ4 is associated with a negative anomaly because the water inflows have temperatures of 148°C and 150°C and are probably colder than the temperature of the deep granite at equilibrium (Figure 2).

GRT1-FZ1 also corresponds to the first inflow of water into the well and thus to the beginning of thermal convection. Positive T anomalies are observed in the bottom part of the FZ at 2365 and 2350 m MD because geothermal water that comes from the fractures is hotter than the water coming from the underlying reservoir (Figure 8(c)). At thermal equilibrium, these hot water inflows are no longer observed, but the negative T anomaly does not suggest that hot water does not circulate. This means that the circulating water is probably colder than the reservoir at equilibrium. These fractures correlate with a flow anomaly. However, T anomalies during production at 2341 m MD and 2235 m MD indicate inflows of water colder than the mix of water below, a trend not seen in the flow log (Figures 8(a) and 8(b)). The T anomaly at 2231 m MD is associated with an FZ enhanced after stimulation at 2236 m MD because it is associated with a negative T anomaly in the poststimulation T log (Figure 8(a)).

GRT2-FZ1 and GRT2-FZ2 exhibit the only two positive T anomalies at equilibrium observed in the wells of Rittershoffen. Positive T anomalies are probably less common than negative T anomalies at equilibrium because the reservoir at equilibrium is generally hotter than the circulating water. Fractures are direct paths for cold mud or water during drilling and hydraulic operations and thus cool faster than the rest of the rock formation. The greater the quantity of cold water that is injected, the fewer positive anomalies visible. Because well GRT-2 was not stimulated, positive anomalies are probably more common in that well than in the stimulated well GRT-1 and GPK-1.

As observed by Evans et al. [14], temperature flux and geothermal fluid flow are intimately linked. T logs are better tools than flow logs for examining water circulation because T logs are more sensitive to small water inflows than flow

logs, which require massive water inflow to produce an observable modification in the rotation speed of the helix. However, the estimation of the absolute water temperature circulating in a fracture requires a reliable associated flow log, which is often not available.

5.2. Water Circulation through Permeable FZs. Based on T and flow logs, most of the water circulation in the wells occurs in the first hundreds of meters of the granitic basement, where a high density of permeable FZs is observed: in the first 500 meters of the Soultz basement (1400 to 2100 m MD in GPK-1) and in the first 200 meters of the Rittershoffen basement (2200 to 2400 m MD in GRT-1 and 2500 to 2800 m MD (i.e., 2200 to 2400 m TVD) in the deviated well GRT-2) (Figures 2–4). The partially open fractures are several centimeters wide inside the FZs and are probably interconnected to each other over short distances, leading to a rather complex 3D organization that has channelized the water circulation [45, 46]. Inside a permeable FZ, geothermal water can circulate at different temperatures through different partially open fractures, representing multichannel pathways for geothermal fluids, as observed in GPK-1, where the water coming from the upper fracture is hotter (Figure 7). In this case, water coming from fractures less than 10 m apart circulates at different temperatures, which is surprising because circulations coming from narrow fractures should reach a state of equilibrium and a homogeneous temperature. Water may circulate through the FZs too fast to reach equilibrium. From the dataset presented in this article, the velocity and direction of these circulations cannot be determined.

The orientations and dips of the fractures cannot be linked to the polarity of the T anomalies at equilibrium (Figure 6). Negative T anomalies at equilibrium are observed more often than positive ones in the Soultz and Rittershoffen wells, but the negative anomalies are linked to the contrast between the temperature of the fluid circulating through the FZs and the temperature of the reservoir at equilibrium, which is generally hotter than the circulating water. During production, a positive T anomaly indicates an inflow of water hotter than the mix of water circulating below (Figure 9). At equilibrium, this anomaly could be positive if the geothermal water coming from the fracture is hotter than the surrounding rock formation or negative if the geothermal water is colder than the surrounding rock formation. T logs acquired during production are representative of the mix of water present during circulation, whereas T logs at thermal equilibrium reflect the temperature of the water leaching through the FZs relative to the temperature of the surrounding rock formations.

Contrary to the interpretation proposed by Genter et al. [15], the negative T anomalies in T logs at equilibrium are not a result of cooling of the FZs but only indicate that the circulation of water is colder than the surrounding formation. However, equilibrium could be difficult to identify depending on the volume of cold water previously injected and the time since the last injection.

The recurrence of negative anomalies could also be influenced by hydrothermal alteration (Figure 9). As modeled by Gentier et al. [52], during cold injection, thermal

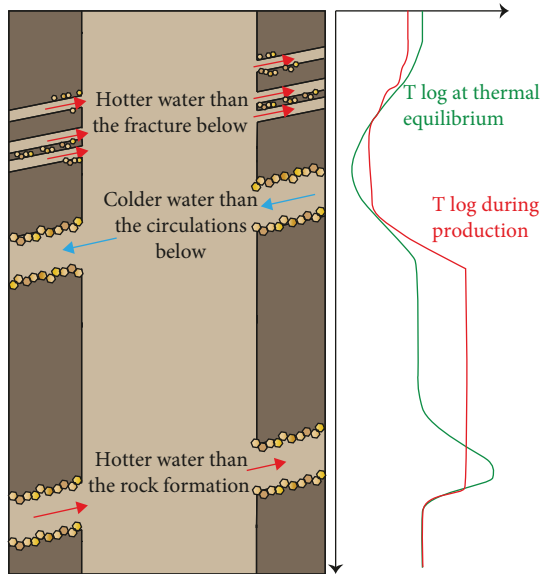


FIGURE 9: Conceptual model of fluid circulation in an FZ partly plugged with quartz and illite and the associated T anomalies measured during production and at thermal equilibrium.

microcracking of quartz within the FZ is observed, which creates preferential flow paths and thus leads to preferential cooling in these fractures. All permeable fractures are associated with quartz veins, which could enhance the thermal effect of cold reinjection through the FZs (Figures 2–4). Moreover, Tung et al. [53] and Alevizos et al. [54] suggested that occurrences of illite could enhance fault creeping, which can release fluid and trigger endothermic chemical reactions. In the case of GPK-1, Sausse et al. [33] identified the correlation between GPK1-FZ4 and the fault zone imaged in the reservoir. The influence of clay minerals, particularly illite, on the fault movements at Soultz was already proposed by Meller et al. [49]. In the case of GRT-1 and GRT-2, preliminary geometrical modeling suggests a possible correlation between GRT1-FZ1 and GRT2-FZ2 and a fault zone imaged in the reservoir [7, 16]. The influence of these endothermic reactions on permeable FZs and the associated T anomalies should be investigated in further studies.

6. Concluding Remarks

In this study, a network of permeable FZs was identified in well GPK-1 at Soultz and wells GRT-1 and GRT-2 at Rittershoffen based on the reinterpretation of T logs obtained during production and at thermal equilibrium; these T logs were correlated with permeability indicators measured during drilling operations, acoustic image logs, and flow logs obtained during hydraulic tests. All permeable FZs present similar characteristics as follows:

- (1) They are composed of cm thick fractures partly filled by quartz
- (2) They are associated with T anomalies during production and/or at thermal equilibrium

This study presents a unique dataset of T logs and associated flow logs (if available) acquired during production and at thermal equilibrium at different times in well histories. T logs are useful and inexpensive tools for the localization of permeable FZs because they are more sensitive to small water inflows into wells than flow logs. Moreover, the comparison of T logs acquired in production and at thermal equilibrium provides a new interpretation of temperature anomalies. Based on these data, the temperature of water coming from partially open fractures was estimated. The study shows that geothermal water could circulate at different temperatures and in different fractures a few meters apart within the same FZ, which suggests a new interpretation of T anomalies. At temperature equilibrium, T anomalies are positive or negative with respect to the temperature of the surrounding rock formations. Because the surrounding formations are often hotter than the fractures, which are direct paths for fluid and thus cool faster than the surrounding rocks, negative anomalies are more often observed than positive ones. The nature of secondary deposits could also enhance the cooling effect observed in the T logs. In contrast, during production, anomalies are positive or negative with respect to the mix of water circulating below the fracture and not with respect to the surrounding formation. Therefore, anomaly polarity could change over time depending on the equilibrium state.

Data Availability

Please contact ES-Géothermie for data requests at geothermie@es.fr.

Conflicts of Interest

The authors declare that there are no conflicts of interest regarding the publication of this paper.

Acknowledgments

This work received funding from the European Union's Horizon 2020 research and innovation programme under grant agreement no. 792037 (MEET project). The study was partly funded by ADEME (French Agency of Energy and Environment) in the framework of the DEEP-EM project. The authors acknowledge the GEIE EMC and ECOGI for providing the data. The authors appreciate the helpful and constructive remarks of the two anonymous reviewers and the lead guest editor of this special issue, Dr Fabrizio Agosta.

References

- [1] P. Baillieux, E. Schill, J.-B. Edel, and G. Mauri, "Localization of temperature anomalies in the Upper Rhine Graben: insights from geophysics and neotectonic activity," *International Geology Review*, vol. 55, no. 14, pp. 1744–1762, 2013.
- [2] Y. Benderitter and P. Elsass, "Structural control of deep fluid circulation at the Soultz HDR site, France: a review, France," *Geothermal Science and Technology*, vol. 4, pp. 227–237, 1995.
- [3] D. Pribnow and C. Clauser, "Heat and fluid flow at the Soultz Hot Dry Rock system in the Rhine Graben," in *Proceedings of*

- World Geothermal Congress 2000*, Kyushu - Tohoku, Japan, 2000.
- [4] D. Pribnow and R. Schellschmidt, "Thermal tracking of upper crustal fluid flow in the Rhine Graben," *Geophysical Research Letters*, vol. 27, no. 13, pp. 1957–1960, 2000.
- [5] D. Bächler, T. Kohl, and L. Rybach, "Impact of graben-parallel faults on hydrothermal convection-Rhine Graben case study," *Physics and Chemistry of the Earth*, vol. 28, no. 9–11, pp. 431–441, 2003.
- [6] P. Baillieux, E. Schill, Y. Abdelfettah, and C. Dezayes, "Possible natural fluid pathways from gravity pseudo-tomography in the geothermal fields of northern Alsace (Upper Rhine Graben)," *Geothermal Energy*, vol. 2, no. 1, 2014.
- [7] C. Baujard, A. Genter, E. Dalmais et al., "Hydrothermal characterization of wells GRT-1 and GRT-2 in Rittershoffen, France: implications on the understanding of natural flow systems in the Rhine graben," *Geothermics*, vol. 65, pp. 255–268, 2017.
- [8] J. Baumgärtner and C. Lerch, "Geothermal 2.0: the Insheim geothermal power plant. The second generation of geothermal power plants in the Upper Rhine Graben," in *Proceedings of third European geothermal review*, Mainz, Germany, 2013.
- [9] J. Baumgärtner, D. Teza, T. Hettkamp, G. Homeier, R. Baria, and S. Michelet, "Electricity production from hot rocks," in *Proceedings of World Geothermal Congress 2005*, Antalya, Turkey, 2005.
- [10] A. Genter, C. Baujard, N. Cuenot et al., "Geology, geophysics and geochemistry in the Upper Rhine Graben: the frame for geothermal energy use," in *Proceedings of European Geothermal Congress 2016*, Strasbourg, France, 2016.
- [11] T. Hettkamp, J. Baumgärtner, D. Teza, and C. Lerch, "Experiences from 5 years operation in Landau," in *Proceedings of Third European Geothermal Review*, Mainz, Germany, 2013.
- [12] J. Vidal and A. Genter, "Overview of naturally permeable fractured reservoirs in the central and southern Upper Rhine Graben: insights from geothermal wells," *Geothermics*, vol. 74, pp. 57–73, 2018.
- [13] C. Dezayes, A. Genter, and B. Valley, "Structure of the low permeable naturally fractured geothermal reservoir at Soultz," *Comptes Rendus Geoscience*, vol. 342, no. 7–8, pp. 517–530, 2010.
- [14] K. F. Evans, A. Genter, and J. Sausse, "Permeability creation and damage due to massive fluid injections into granite at 3.5 km at Soultz: 1. Borehole observations," *Journal of Geophysical Research: Solid Earth*, vol. 110, no. B4, 2005.
- [15] A. Genter, K. Evans, N. Cuenot, D. Fritsch, and B. Sanjuan, "Contribution of the exploration of deep crystalline fractured reservoir of Soultz to the knowledge of enhanced geothermal systems (EGS)," *Comptes Rendus Geoscience*, vol. 342, no. 7–8, pp. 502–516, 2010.
- [16] J. Vidal, A. Genter, and F. Chopin, "Permeable fracture zones in the hard rocks of the geothermal reservoir at Rittershoffen, France," *Journal of Geophysical Research: Solid Earth*, vol. 122, no. 7, pp. 4864–4887, 2017.
- [17] C. A. Barton, M. D. Zoback, and D. Moos, "Fluid flow along potentially active faults in crystalline rock," *Geology*, vol. 23, no. 8, pp. 683–686, 1995.
- [18] J. Bradford, J. McLennan, J. Moore et al., "Recent developments at the Raft River geothermal field," in *Proceedings of Thirty-Eighth Workshop on Geothermal Reservoir Engineering*, Stanford University, California, USA, 2013.
- [19] A. Mas, D. Guisseau, P. Patrier Mas et al., "Clay minerals related to the hydrothermal activity of the Bouillante geothermal field (Guadeloupe)," *Journal of Volcanology and Geothermal Research*, vol. 158, no. 3–4, pp. 380–400, 2006.
- [20] C. Le Carlier, J.-J. Royer, and E. L. Flores, "Convective heat transfer at the Soultz-sous-Forêts geothermal site: implications for oil potential," *First Break*, vol. 12, no. 1285, 1994.
- [21] V. Magnenet, C. Fond, A. Genter, and J. Schmittbuhl, "Two-dimensional THM modelling of the large scale natural hydrothermal circulation at Soultz-sous-Forêts," *Geothermal Energy*, vol. 2, no. 1, 2014.
- [22] S. Bellani, A. Brogi, A. Lazzarotto, D. Liotta, and G. Ranalli, "Heat flow, deep temperatures and extensional structures in the Larderello geothermal field (Italy): constraints on geothermal fluid flow," *Journal of Volcanology and Geothermal Research*, vol. 132, no. 1, pp. 15–29, 2004.
- [23] D. Curewitz and J. A. Karson, "Structural settings of hydrothermal outflow: fracture permeability maintained by fault propagation and interaction," *Journal of Volcanology and Geothermal Research*, vol. 79, no. 3–4, pp. 149–168, 1997.
- [24] N. C. Davatzes and S. H. Hickman, "Controls on fault-hosted fluid flow; preliminary results from the Coso geothermal field, CA," in *Geothermal Resources Council Transactions*, pp. 343–348, Geothermal Resources Council, Davis, California, 2005.
- [25] J. E. Faulds and N. H. Hinz, "Favorable tectonic and structural settings of geothermal systems in the Great Basin region, Western USA: proxies for discovering blind geothermal systems," in *Proceedings of World Geothermal Congress 2015*, Melbourne, Australia, 2015.
- [26] C. Dezayes, A. Genter, and S. Gentier, *Deep geothermal energy in Western Europe: the Soultz Project - Final Report (open file no. BRGM/RP-54227-Fr)*, BRGM, Orléans, France, 2005.
- [27] A. Gérard, A. Genter, T. Kohl, P. Lutz, P. Rose, and F. Rummel, "The deep EGS (enhanced geothermal system) project at Soultz-sous-Forêts (Alsace, France)," *Geothermics*, vol. 35, no. 5–6, pp. 473–483, 2006.
- [28] B. Sanjuan, R. Millot, C. Dezayes, and M. Brach, "Main characteristics of the deep geothermal brine (5 km) at Soultz-sous-Forêts (France) determined using geochemical and tracer test data," *Comptes Rendus Geoscience*, vol. 342, no. 7–8, pp. 546–559, 2010.
- [29] B. Sanjuan, J. Scheiber, F. Gal, S. Touzelet, A. Genter, and G. Villadangos, "Interwell chemical tracer testing at the Rittershoffen site (Alsace, France)," in *Proceedings of European Geothermal Congress 2016*, Strasbourg, France, 2016.
- [30] A. Genter and H. Traineau, "Analysis of macroscopic fractures in granite in the HDR geothermal well EPS-1, Soultz-sous-Forêts, France," *Journal of Volcanology and Geothermal Research*, vol. 72, no. 1–2, pp. 121–141, 1996.
- [31] O. Lengliné, M. Boubacar, and J. Schmittbuhl, "Seismicity related to the hydraulic stimulation of GRT1, Rittershoffen, France," *Geophysical Journal International*, vol. 208, no. 3, pp. 1704–1715, 2017.
- [32] J. Place, M. Diraison, C. Naville, Y. Géraud, M. Schaming, and C. Dezayes, "Decoupling of deformation in the Upper Rhine Graben sediments. Seismic reflection and diffraction on 3-component vertical seismic profiling (Soultz-sous-Forêts area)," *Comptes Rendus Geoscience*, vol. 342, no. 7–8, pp. 575–586, 2010.

- [33] J. Sausse, C. Dezayes, L. Dorbath, A. Genter, and J. Place, “3D model of fracture zones at Soultz-sous-Forêts based on geological data, image logs, induced microseismicity and vertical seismic profiles,” *Comptes Rendus Geoscience*, vol. 342, no. 7-8, pp. 531–545, 2010.
- [34] S. Gentier, X. Rachez, T. D. T. Ngoc, M. Peter-Borie, and C. Souque, “3D flow modelling of the medium-term circulation test performed in the deep geothermal site of Soultz-sous-Forêts (France),” in *Proceedings of World Geothermal Congress 2010*, Kyushu - Tohoku, Japan, 2010.
- [35] A. Genter, C. Castaing, C. Dezayes, H. Tenzer, H. Traineau, and T. Villemin, “Comparative analysis of direct (core) and indirect (borehole imaging tools) collection of fracture data in the Hot Dry Rock Soultz reservoir (France),” *Journal of Geophysical Research*, vol. 102, no. B7, pp. 15419–15431, 1997.
- [36] J. Vidal, A. Genter, F. Chopin, and E. Dalmais, “Natural fractures and permeability at the geothermal site Rittershoffen, France,” in *Proceedings of European Geothermal Congress 2016*, Strasbourg, France, 2016.
- [37] H. Traineau, A. Genter, J.-P. Cautru, H. Fabriol, and P. Chèvremont, “Petrography of the granite massif from drill cutting analysis and well log interpretation in the geothermal HDR borehole GPK-1 (Soultz, Alsace, France),” in *Geothermal Energy in Europe—The Soultz Hot Dry Rock Project*, J. C. Bresee, Ed., pp. 1–29, Gordon and Breach Science Publishers S.A., Montreux, Switzerland, 1992.
- [38] A. Genter, H. Traineau, B. Ledésert, B. Bourguine, and S. Gentier, “Over 10 years of geological investigations within the HDR Soultz project, France,” in *Proceedings of World Geothermal Congress 2000*, Kyushu - Tohoku, Japan, 2000.
- [39] M. P. Smith, V. Savary, B. W. D. Yardley, J. W. Valley, J. J. Royer, and M. Dubois, “The evolution of the deep flow regime at Soultz-sous-Forêts, Rhine Graben, eastern France: evidence from a composite quartz vein,” *Journal of Geophysical Research: Solid Earth*, vol. 103, no. B11, pp. 27223–27237, 1998.
- [40] B. Ledésert, G. Berger, A. Meunier, A. Genter, and A. Bouchet, “Diagenetic-type reactions related to hydrothermal alteration in the Soultz-sous-Forêts Granite, France,” *European Journal of Mineralogy*, vol. 11, no. 4, pp. 731–742, 1999.
- [41] C. Glaas, A. Genter, J. F. Girard, P. Patrier, and J. Vidal, “How do the geological and geophysical signatures of permeable fractures in granitic basement evolve after long periods of natural circulation? Insights from the Rittershoffen geothermal wells (France),” *Geothermal Energy*, vol. 6, no. 1, p. 14, 2018.
- [42] G. R. Hooijkaas, A. Genter, and C. Dezayes, “Deep-seated geology of the granite intrusions at the Soultz EGS site based on data from 5 km-deep boreholes,” *Geothermics*, vol. 35, no. 5-6, pp. 484–506, 2006.
- [43] J. Vidal, P. Patrier, A. Genter et al., “Clay minerals related to the circulation of geothermal fluids in boreholes at Rittershoffen (Alsace, France),” *Journal of Volcanology and Geothermal Research*, vol. 349, pp. 192–204, 2018.
- [44] J. Vidal, A. Genter, C. Glaas, R. Hehn, N. Cuenot, and C. Baujard, *Temperature Signature of Permeable Fracture Zones in Geothermal Wells of Soultz-sous-Forêts in the Upper Rhine Graben*, GRC Transactions, Reno, Nevada, USA, 2018.
- [45] J. Sausse, C. Dezayes, A. Genter, and A. Bisset, “Characterization of fracture connectivity and fluid flow pathways derived from geological interpretation and 3D modelling of the deep seated EGS reservoir of Soultz (France),” in *Proceedings of Thirty-Third Workshop on Geothermal Reservoir Engineering*, Stanford University, California, USA, 2008.
- [46] J. Sausse, M. Fourar, and A. Genter, “Permeability and alteration within the Soultz granite inferred from geophysical and flow log analysis,” *Geothermics*, vol. 35, no. 5-6, pp. 544–560, 2006.
- [47] L. Aquilina, M. Brach, J. C. Foucher, A. De Las Heras, and G. Braibant, *Deepening of GPK-1 HDR Borehole 2000-3600 m (Soultz-sous-Forêts, France)*, *Geochemical Monitoring of Drilling Fluids (open file no. R36619)*, BRGM, Orléans, France, 1993.
- [48] F.-D. Vuataz, M. Brach, A. Criaud, and C. Fouillac, “Geochemical monitoring of drilling fluids: a powerful tool to forecast and detect formation waters,” *SPE Formation Evaluation*, vol. 5, no. 2, pp. 177–184, 1990.
- [49] C. Meller, A. Kontny, and T. Kohl, “Identification and characterization of hydrothermally altered zones in granite by combining synthetic clay content logs with magnetic mineralogical investigations of drilled rock cuttings,” *Geophysical Journal International*, vol. 199, no. 1, pp. 465–479, 2014.
- [50] M. Dubois, B. Ledésert, J. L. Potdevin, and S. Vançon, “Détermination des conditions de précipitation des carbonates dans une zone d’altération du granite de Soultz (soubassement du fossé Rhénan, France) : l’enregistrement des inclusions fluides,” *Comptes Rendus de l’Académie des Sciences - Series IIA - Earth and Planetary Science*, vol. 331, no. 4, pp. 303–309, 2000.
- [51] R. Jung, “Hydraulic fracturing and hydraulic testing in the granitic section of borehole GPK-1, Soultz-sous-Forêts,” in *Geothermal Energy in Europe - The Soultz Hot Dry Rock Project*, J. C. Bresee, Ed., pp. 149–198, Gordon and Breach Science Publishers S.A., Montreux, Switzerland, 1992.
- [52] S. Gentier, A. Hosni, C. Dezayes, and A. Genter, *Projet GEFRA: modélisation du comportement hydro-thermo-mécanique des milieux fracturés (module 1) (Open file report No. BRGM/RP-52702-FR)*, BRGM, 2004.
- [53] R. Tung, T. Poulet, M. Peters, M. Veveakis, and K. Regenauer-Lieb, “Explaining high permeability on localised fault zones through THMC feedbacks - a Soultz-sous-Forêts inspired approach,” in *Proceedings of 40th New Zealand Geothermal Workshop. Presented at the New Zealand Geothermal Workshop*, Taupo, New Zealand, 2018.
- [54] S. Alevizos, T. Poulet, and E. Veveakis, “Thermo-poro-mechanics of chemically active creeping faults. 1: theory and steady state considerations,” *Journal of Geophysical Research: Solid Earth*, vol. 119, no. 6, pp. 4558–4582, 2014.
- [55] GeORG Team, “EU-Projekt GeORG - Geoportail [WWW Document],” 2017, June 2017, <http://www.geopotenziale.org/home?lang=3>.
- [56] B. C. Valley and K. F. Evans, “Stress state at Soultz-sous-Forêts to 5 km depth from wellbore failure and hydraulic observations,” in *Proceedings of Thirty-Second Workshop on Geothermal Reservoir Engineering*, Stanford University, California, USA, 2007.
- [57] R. Hehn, A. Genter, J. Vidal, and C. Baujard, “Stress field rotation in the EGS well GRT-1 (Rittershoffen, France),” in *Proceedings of European Geothermal Congress 2016*, Strasbourg, France, 2016.

Research Article

A Cause Analysis of the High-Content Nitrogen and Low-Content Hydrocarbon in Shale Gas: A Case Study of the Early Cambrian in Xiuwu Basin, Yangtze Region

Yizhou Huang ^{1,2}, Kun Zhang ^{1,2,3,4,5}, Zhenxue Jiang ^{1,2}, Yan Song ^{1,2,4},
Shu Jiang ^{5,6,7}, Chengzao Jia,⁴ Weiwei Liu,⁸ Ming Wen ^{1,2}, Xuelian Xie,⁹ Tianlin Liu,^{1,2}
Xin Li,^{1,2,3} Xin Wang,^{1,2} Xiaoxue Liu,^{1,2} Ye Zhang,¹⁰ and Ling Tang^{1,2,3}

¹State Key Laboratory of Petroleum Resources and Prospecting, China University of Petroleum, Beijing 102249, China

²Unconventional Natural Gas Institute, China University of Petroleum, Beijing 102249, China

³Unconventional Petroleum Collaborative Innovation Center, China University of Petroleum, Beijing 102249, China

⁴Research Institute of Petroleum Exploration and Development, Beijing 100083, China

⁵Key Laboratory of Tectonics and Petroleum Resources of Ministry of Education, Faculty of Earth Resources, China University of Geosciences, Wuhan 430074, China

⁶Research Institute of Unconventional Oil & Gas and Renewable Energy, China University of Petroleum (East China), Qingdao 266580, China

⁷Energy and Geoscience Institute, University of Utah, Salt Lake City, Utah 84108, USA

⁸Jiangxi Provincial Natural Gas Company Ltd., Nanchang 330000, China

⁹Guangzhou Marine Geological Survey, Guangzhou 510760, China

¹⁰National and Local Joint Engineering Research Center of Shale Gas Exploration and Development, Chongqing Institute of Geology and Mineral Resources, Chongqing 400042, China

Correspondence should be addressed to Zhenxue Jiang; zhenxuejiangedu@126.com, Yan Song; yansongpetrochina@126.com, and Shu Jiang; jiangsu@cug.edu.cn

Yizhou Huang and Kun Zhang contributed equally to this work.

Received 29 November 2018; Accepted 27 January 2019; Published 12 June 2019

Guest Editor: Giorgio Minelli

Copyright © 2019 Yizhou Huang et al. This is an open access article distributed under the Creative Commons Attribution License, which permits unrestricted use, distribution, and reproduction in any medium, provided the original work is properly cited.

There are successes and failures in the exploration of marine shale gas in South China. In some shale gas plays with great basis for hydrocarbon generation, a phenomenon exists that gas loggings reflect low gas bearing in some of the wells and the gas is dominated by nitrogen rather than hydrocarbon gas. The study of nitrogen concentration in shale gas contributes to solve the question that how shale gas diffuses in complex tectonic areas, which helps to figure out the preservation requirements and accumulation mechanisms of shale gas and avoid exploration crisis. This study focused on the lower Cambrian shale in Xiuwu Basin, Lower Yangtze Region, with emphasis on the well Jiangye-1, using gas component analysis, stable nitrogen isotope analysis, overburden permeability tests in parallel and perpendicular directions, and FIB-HIM experiments, also combining with core description, outcrop observation, and seismic interpretation to explore the causes of the high-content nitrogen and low-content hydrocarbon in the lower Cambrian shale gas. The results show that the nitrogen of the lower Cambrian shale in Xiuwu Basin is derived from the atmosphere and the deep crust-upper mantle. The bedding planes and the detachment layer at the bottom of the lower Cambrian compose the lateral pathways, and the widespread deep faults are the vertical pathways for shale gas migration and diffusion. Combining these two, an effective pathway network was built, favorable to gas exchange between the shale gas interval and the atmosphere, partly leading to the concentration of nitrogen and the diffusion of

hydrocarbon gas. In the Jurassic, the magmatic activities occurred frequently in the surrounding areas, which not only brought nitrogen from the deep crust-upper mantle but also increased the value of paleo-heat flow even though the basin began to uplift, which promoted the graphitization of organic matter and the collapse of organic pores and accelerated the loss of shale gas. Based on the study above, an explanation model was summarized to expound the causes of high-content nitrogen and low-content hydrocarbon in shale gas plays near the plate-active region in Xiuwu Basin, Lower Yangtze Region.

1. Introduction

In recent years, because of the progress in geological theories and hydraulic fracturing technology, shale gas has drawn an increasing attention of exploration and development of oil and gas all over the world [1–3]. In China, since 2010, the well Wei-201 in Weiyuan Structure realized the industrialization of shale gas resources. Until 2018, shale gas plays like Weiyuan, Changning, Fushun-Yongchuan, Jiaoshiba, and Dingshan were continually established to achieve large-scale exploration and exploitation [4, 5]. Although successes are achieved, failures still exist that the gas content varies dramatically depends on plays [6, 7]. This makes further study on shale gas accumulation mechanism urgent to be carried out [8, 9]. Explorations on the accumulation mechanisms of shale gas have been carried out by previous works, including shale heterogeneity [10–12], shale pore connectivity [13–16], shale sedimentary environments [17], and structural styles [18, 19]. However, compared with North America, the Paleozoic marine shale in South China experienced a more complex, multistage tectonic and thermal evolution. Although the plays were equipped with similar materials basis, such as the similar total organic carbon (TOC) content and mineral composition, the gas-bearing properties are diverse under different preservation conditions. Thus, accurate selections of favorable intervals and areas are important for shale gas exploration [20].

Methods have been applied to previous studies about preservation conditions of shale gas. Cheng et al. [21] researched shale gas preservation conditions of the lower Cambrian Niutitang formation in the Enshi-Lichuan Play. From material basis, tectonic effects, and evolution history, they proposed a comprehensive evaluation index system of shale gas preservation. Guo et al. [22] put forward “accumulation controlling production” theory which considered preservation conditions crucial for shale gas accumulation. Quality roof and floor effectively prevent hydrocarbon from diffusing vertically and strand hydrocarbon right after its generation. The strength and duration of tectonic effects determine the preservation conditions, which are key geological factors in the theory. A shale reservoir, with quality gas-bearing properties, large porosity, and high formation pressure, is inclined to be a prolific area enriched by natural gas. Zhai et al. [23] demonstrated the main controlling factors of production of marine shale gas reservoir in South China which include quality organic-rich shale deposited in deep-water shelf (favorable for hydrocarbon generation) and appropriate tectonic uplift time and structural styles (keys of shale gas accumulation and preservation). They summarized three major types of shale gas structural styles: the complete, the residual, and the destructive styles. Also, overpressure is considered as a necessary prerequisite for high production.

Many shale gas plays of the lower Cambrian located outside the Sichuan Basin, represented by Xiuwu Basin, are blessed with great material basis but no considerable commercial discoveries, only slightly gas bore. Among the wells, a phenomenon is shown in common that the nitrogen content is distinguished, reflecting the complexity of the preservation conditions of shale gas in the lower Cambrian [24–29]. Since nitrogen is an indicator, directly reflecting the preservation conditions of oil and gas plays, the study of nitrogen in shale gas promotes the clarification of the preservation regulations and shale gas accumulation mechanism [30–33], which are important for accurately selecting favorable intervals and areas and avoiding crisis during the shale gas exploitation.

Therefore, based on the detailed components of the lower Cambrian shale gas, this paper combined stable nitrogen isotopes and previous works to determine the sources of nitrogen and then figured out the causes of high-content nitrogen and low-content hydrocarbon in the lower Cambrian shale gas by the comprehensive analysis of regional geological settings, tectonic characteristics, and thermal evolution history. Finally, a shale gas accumulation model was established to explain the causes, significant to the exploration and exploitation of shale gas in highly matured shale in complex tectonic zones.

2. Geological Settings

2.1. Tectonic and Sedimentary Characteristics. The study area is located in Xiuwu Basin, Lower Yangtze Region (Figure 1). Xiuwu Basin was a stable cratonic basin in the Cryogenian and then experienced a regression in the late Cryogenian, when the Piyuncun formation was deposited. A massive transgression occurred in the early Cambrian, leading to the deposition of the Wangyinpu formation in a deep-water basin (Figure 2), which is a set of black organic-rich siliceous shale of 45–60 m thick. Afterwards, the seawater was gradually shallower and the upper part of the Guanyintang formation formed in shallow-water shelf facies [34]. Subsequently, the sedimentary environments transformed from a clastic sedimentary system in early Cambrian to a carbonate system in the middle-late Cambrian and further to a detrital sedimentary system in the early-middle Ordovician [35]. In the late Ordovician-early Silurian, due to the plate collision, the study area changed to a deep-water basin when the Xinkailing-Lishuwo shale was deposited. Since the middle Silurian, the seawater became shallower and the study area began to uplift to ancient lands in the late Silurian [36, 37]. In the Devonian-Carboniferous, sedimentation and uplift interlaced with little deposition. The Permian and the early-middle Triassic welcomed another major sedimentary period. The late Triassic was affected by the collision

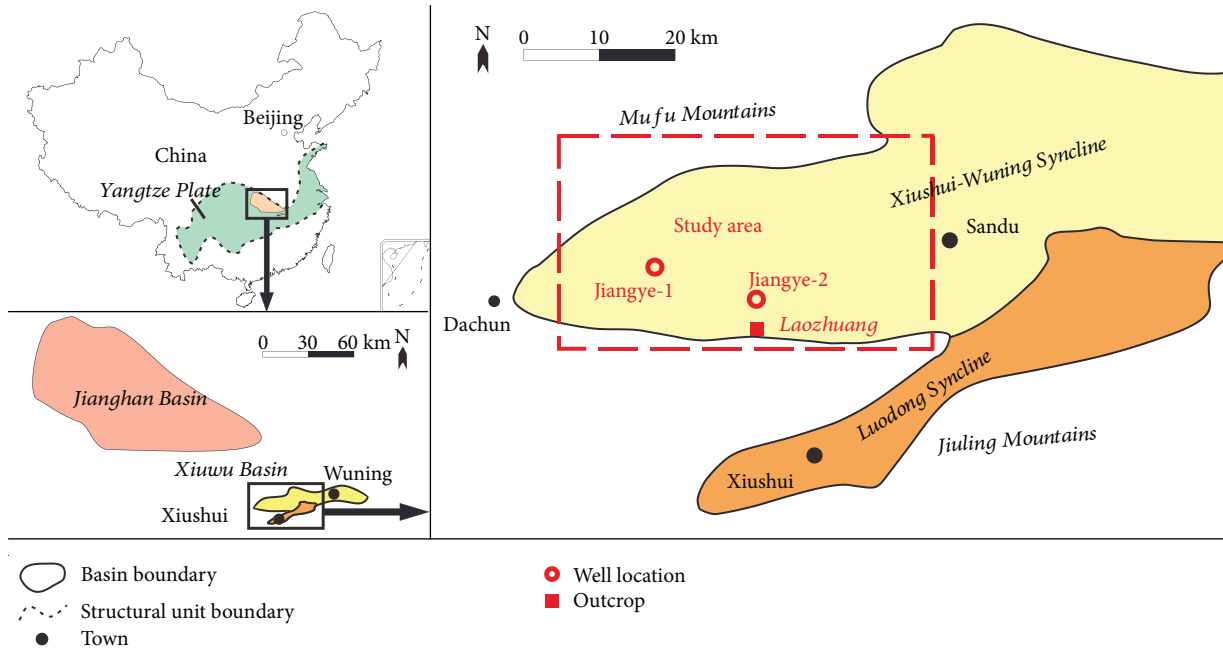


FIGURE 1: Locations of the study area and wells and outcrop mentioned.

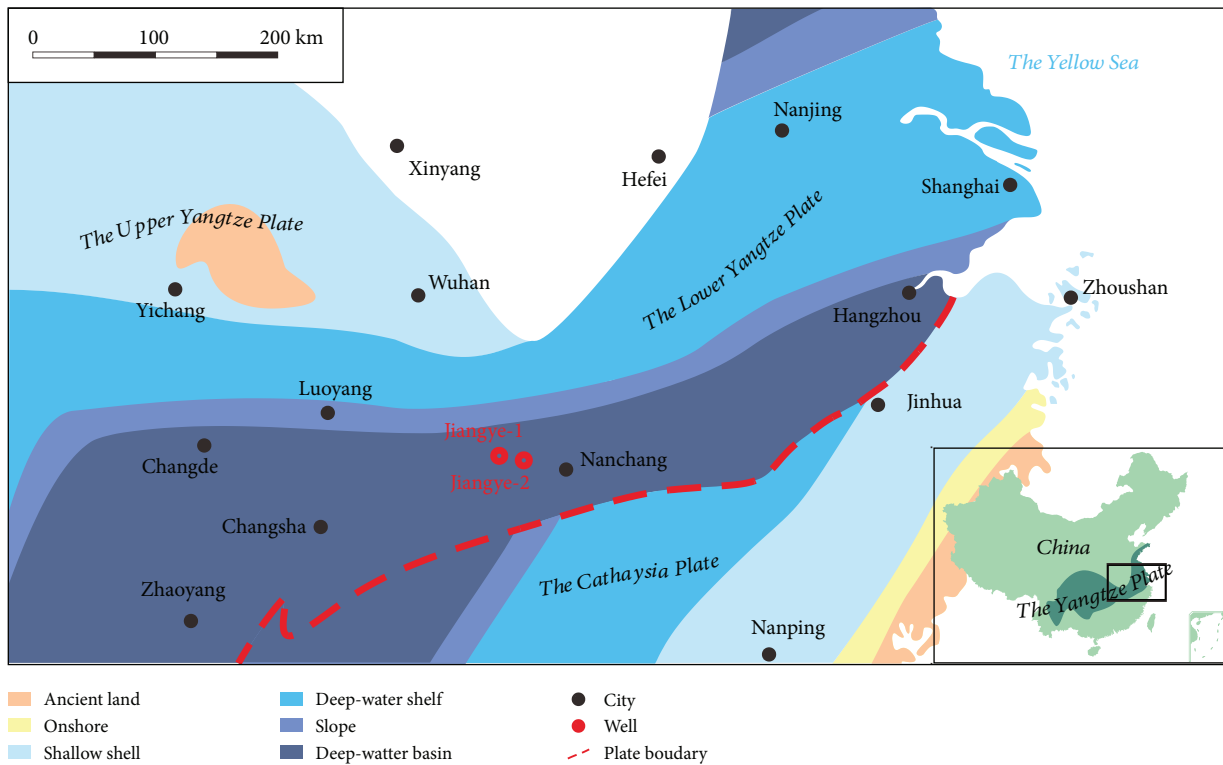


FIGURE 2: A map of the regional sedimentary characteristics of the lower Cambrian in the Lower Yangtze, South China.

between the North China and the Southern China plates; thus, the study area was uplifted [27, 38] and ended up a syncline with lots of thrust faults in the early-middle Jurassic by extrusion [39].

2.2. *Stratigraphic Characteristic.* The research target is the lower Cambrian Wangyinpu and Guanyintang formations. Wangyinpu formation is underlain by the late Ediacaran Piyuancun formation, which is dominated by gray siliceous

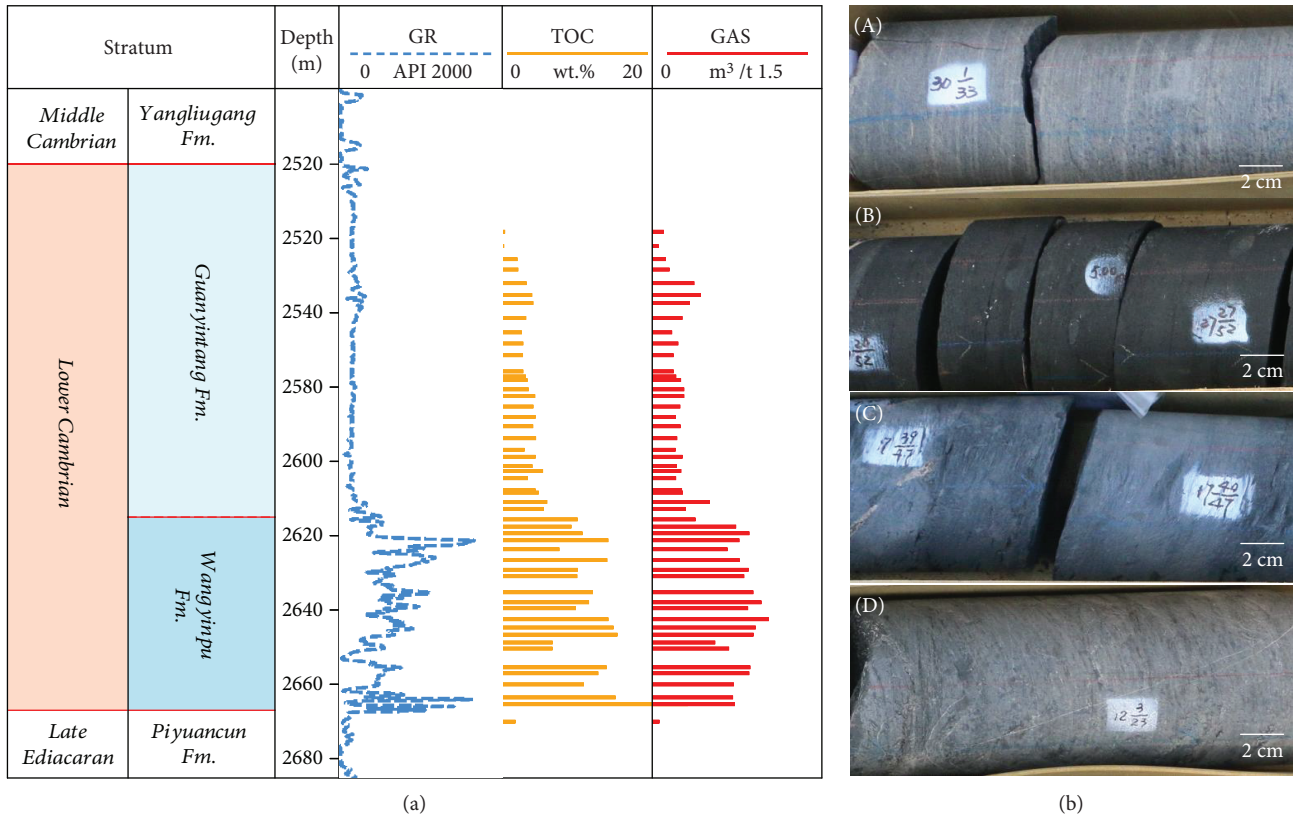


FIGURE 3: A stratigraphic column and core photos of the late Ediacaran and the lower-middle Cambrian of Jiangye-1. (A) The late Ediacaran Piyuancun formation (depth: 2675 m). (B) The lower Cambrian Wangyinpu formation (depth: 2638 m). (C) The lower Cambrian Guanyintang formation (depth: 2546 m). (D) The middle Cambrian Yangliugang formation (depth: 2511 m). The data of gamma ray log and total gas content were from Schlumberger. See Figure 1 for the well location. Fm. = formation; GR = gamma ray log; TOC = total organic carbon content; GAS = total gas content.

dolomite. The Wangyinpu formation is black siliceous shale, and Guanyintang formation is dark gray siliceous shale. Guanyintang formation is the middle Cambrian Yangliugang formation, a set of gray micrite limestone (Figure 3(b)). These strata are all conformably contacted.

2.3. Present Conditions of Exploration. According to the exploration history, there are two shale gas wells named Jiangye-1 and Jiangye-2 (Figure 1). The lower Cambrian shale of Jiangye-1 is around 58 m thick and equipped with sapropel-type kerogen. The TOC content is generally larger than 2 wt% (Figure 3(a)), and the average porosity is about 2.1%. Based on the previous study of storage potential, the theoretical gas content of the lower Cambrian shale is 2.29–5.73 m³/t. Therefore, it tells that the study area is theoretically favorable for hydrocarbon generation.

However, the gas logging of Jiangye-1 reflects a weak gas bearing with a decreasing downwards gas content of 0.01–1.23 m³/t (Figure 3(a)) and the adsorbed gas on field of Jiangye-2 is dominated by nitrogen. This contrast leads to the target problem of this paper why there is high-content nitrogen rather than hydrocarbon gas in the shale gas in an area theoretically favorable for hydrocarbon generation.

3. Methodology

3.1. TOC Content Test and Gas Content Test. From the lower Cambrian shale in Jiangye-1, fifty-one core samples were selected in total. Present-day TOC content tests were carried out by an OG-2000v analyzer and gas content tests were operated by LH-2 shale gas content analyzer.

3.2. Gas Component Analysis and Nitrogen Isotope Analysis. Using the AD-RJ-150-6-type shale gas field analytical instrument, there are sixteen gas samples of different depths collected from the cores of the lower Cambrian Guanyintang and Wangyinpu formations in Jiangye-1 (Table 1). The cores were taken on field. The gas samples underwent gas component analysis by the GC-2014C Gas Chromatograph and stable nitrogen isotope analysis by the EA IsoLink™ 253 Plus™ IRMS.

3.3. Overburden Permeability Test. From the lower Cambrian Wangyinpu formation in the Lower Yangtze, there were ten samples selected, among which 2 were from Jiangye-1 and the other 8 were from Jiangye-2 (Table 2). The overburden permeability analyzer PDP-200 was adopted in the tests in both directions of parallel (for lateral permeability) and perpendicular (for vertical permeability) to bedding planes. The

TABLE 1: Information of gas samples from Jiangye-1. See Figure 1 for the well location.

No.	Well	Depth (m)	Fm.
1	Jiangye-1	2540	Guanyintang
2	Jiangye-1	2545	Guanyintang
3	Jiangye-1	2562	Guanyintang
4	Jiangye-1	2568	Guanyintang
5	Jiangye-1	2574	Guanyintang
6	Jiangye-1	2580	Guanyintang
7	Jiangye-1	2585	Guanyintang
8	Jiangye-1	2590	Guanyintang
9	Jiangye-1	2595	Guanyintang
10	Jiangye-1	2602	Guanyintang
11	Jiangye-1	2612	Wangyinpu
12	Jiangye-1	2620	Wangyinpu
13	Jiangye-1	2635	Wangyinpu
14	Jiangye-1	2641	Wangyinpu
15	Jiangye-1	2655	Wangyinpu
16	Jiangye-1	2669	Wangyinpu

No. = sample number; Fm. = formation.

TABLE 2: Information of samples for permeability tests. See Figure 1 for the well locations.

No.	Well	Depth (m)	Fm.
1	Jiangye-1	2635	Wangyinpu
2	Jiangye-1	2641	Wangyinpu
3	Jiangye-2	3090	Wangyinpu
4	Jiangye-2	3095	Wangyinpu
5	Jiangye-2	3101	Wangyinpu
6	Jiangye-2	3108	Wangyinpu
7	Jiangye-2	3115	Wangyinpu
8	Jiangye-2	3122	Wangyinpu
9	Jiangye-2	3129	Wangyinpu
10	Jiangye-2	3135	Wangyinpu

No. = sample number; Fm. = formation.

pressure of the permeability test and the confining pressure was 1000 and 1500 psi, respectively.

3.4. FIB-HIM Experiment. FIB-HIM is suitable for shale micropore reorganization for its high resolution, which makes it possible to achieve a resolution of 0.5 nm under 45 kV. An ORION NanoFab microscope is used to identify organic pores. Additionally, grinding and Ar-ion polishing were involved in a sample preparation.

In this paper, samples were chosen from the organic-rich shale of the lower Cambrian Wangyinpu formation in Jiangye-1 at a depth of 2630 m. The data of the experimental results of the lower Silurian Longmaxi formation shale of the Jiaoye-1 in Sichuan Basin, South China, were from Wang et al. [13, 14, 40].

4. Results and Discussion

4.1. Gas Components. The results of gas components analysis are shown in Figure 4. It supposes that the shale gas is dominated by nitrogen and oxygen with the percentage of volume of 80% and 17%, respectively, which is close to the content in the air (78% and 21%, respectively). The average methane content is only 0.22%.

In comparison, the average nitrogen content in natural gas is about 3% in the United States and less than 8% in most plays of China [30]. The nitrogen content is 10%~30% in natural gas of the Tarim Basin, where nitrogen is highly concentrated [31, 33], less than 10% in Northeast Chongqing shale gas and almost 0 in Jiaoshiba shale gas play, Fuling [28, 30, 32]. The nitrogen content of the study area is far higher than average and reflects its unique accumulation characteristics.

4.2. Nitrogen Sources. From the tests of stable nitrogen isotope, the $\delta^{15}\text{N}$ of all the sixteen samples ranges from -0.8‰ to 0‰ (Figure 5). It is summarized from the previous researches that the content of stable nitrogen isotope depends on its sources, and based on Krooss et al. [41], Zeng [42], and Liu et al. [43], nitrogen sources, genesis mechanisms, and corresponding isotopic content are summarized in Table 3. The $\delta^{15}\text{N}$ of the study area falls in two sources. Therefore, it indicates the mixed origins of nitrogen, the atmosphere, and the deep crust-upper mantle.

4.3. Causes of Nitrogen Concentration

4.3.1. Effective Pathway Network to Atmosphere

(1) Lateral Pathway. In the overburden permeability tests, the lateral permeability and the vertical permeability were obtained by samples being tested in parallel and perpendicular, respectively, to the bedding planes. As Figure 6 shows, generally, the lateral is larger than the vertical and the ratio of these two reflects that the lateral permeability is more than 1~40 times higher than the vertical, indicating a dominant migration pathway along the bedding planes (Figure 7).

Cores were from the bottom of the lower Cambrian shale in Jiangye-1 and Jiangye-2. The observation revealed obvious characteristics of the bedding slip deformation (Figures 8(a) and 8(b)). Furthermore, apparent slippage and crinkle phenomenon (Figure 8(c)) are presented in the Laozhuang Outcrop. These obvious deformation structures are widely developed at the bottom of the Wangyinpu formation in the study area, reflecting the general existence of a detachment layer at the bottom of the lower Cambrian in Xiuwu Basin, which resulted from the relative slipping between the soft shales of the Wangyinpu formation and the hard siliceous dolomite of Piyuancun formation under the North-South extrusion influencing the whole basin. The gas content of the Wangyinpu formation decreased when it is near the bottom, from 0.93 m³/t in the lower part to 0.73 m³/t at the bottom of the formation. The detachment layer at the bottom of the lower Cambrian greatly accelerated the diffusion process of shale gas.

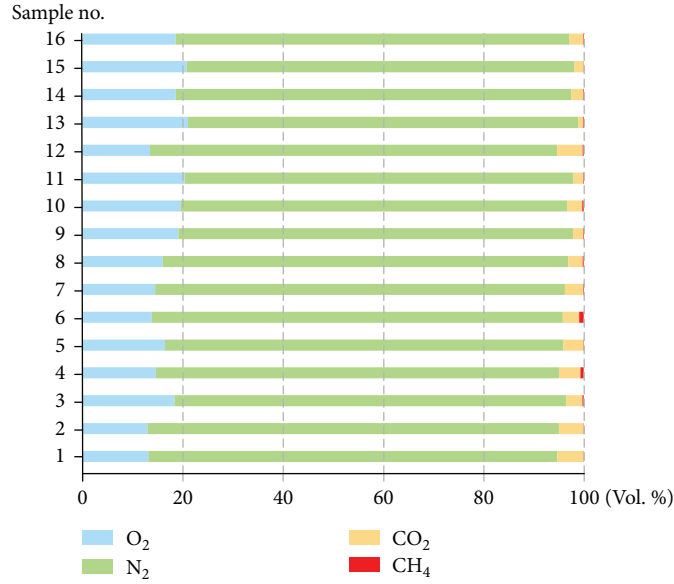


FIGURE 4: Gas components of the lower Cambrian Guanyintang and Wangyinpu formations of Jiangye-1. See Figure 1 for the location of the well location.

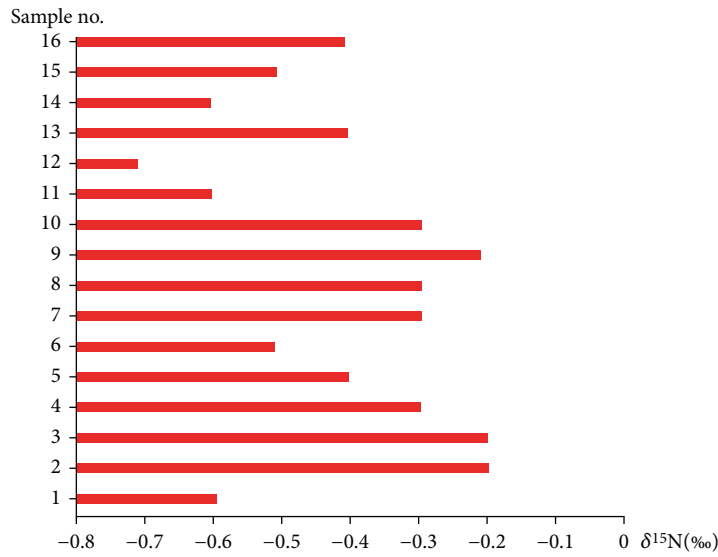


FIGURE 5: δ¹⁵N content of the lower Cambrian Guanyintang and Wangyinpu formation shale gas of Jiangye-1. See Figure 1 for the location of the well location.

TABLE 3: Summarized characteristics of stable nitrogen isotope of nitrogen in natural gas of different sources (modified from Zeng [42] and Liu et al. [43]).

Sources	Genesis mechanism		Nitrogen isotope (δ ¹⁵ N‰)	
Atmosphere	Carried by surface water, diffused underground		0‰	
Deep crust-upper mantle	Thermal reactions and radiation effects in the Earth's core		-2‰~+1‰	
	Metamorphism	High temperature metamorphism of nitrogenous minerals	+1‰~+3.5‰	
Sedimentation	Microbial denitrification	Generated by interactions between organisms and organic matter	-17‰~-10‰	
	Thermal evolution	Evolutionary stages of organic matter	Immature	<-10‰
			Mature-highly mature	-10‰~-1‰
Overmature			+5‰~+20‰	

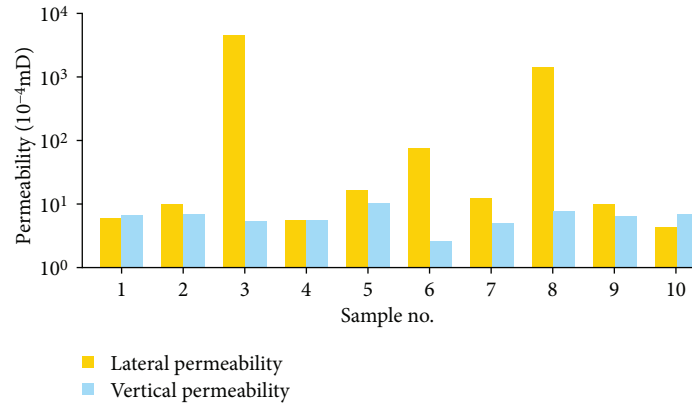


FIGURE 6: Lateral and vertical permeability of the lower Cambrian shale of Jiangye-1 and Jiangye-2. See Figure 1 for the well locations.

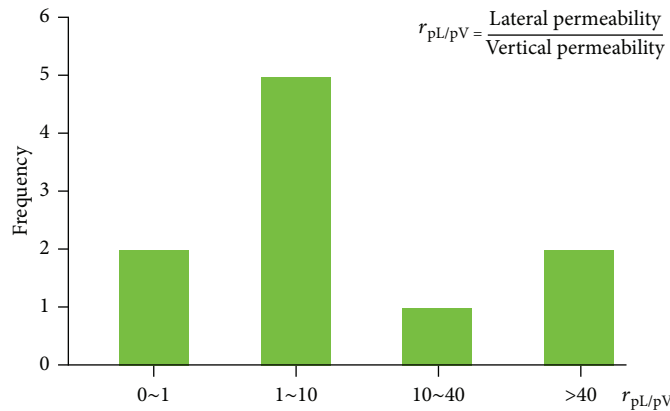


FIGURE 7: The ratio of lateral and vertical permeability of the lower Cambrian of Jiangye-1 and Jiangye-2. See Figure 1 for the well locations.

From the analysis above, the bedding surface and the detachment layer comprise the migration pathways in the lateral direction to communicate with the atmosphere, partly leading to the concentration of nitrogen and the diffusion of hydrocarbon gas.

(2) *Vertical Pathway*. Physical sealing is the main mechanism that roof and floor seal the natural gas within organic-rich shale in vertical direction. A quality seal on organic-rich shale requires a large thickness of roof and floor and a lower porosity than shale gas interval. The burial depth, the thickness of the organic-rich shale, and the average TOC content control the self-sealing property of the shale. As Table 4 tells, the roof of Guangyintang formation and the floor of Piyuancun formation are equipped with a large thickness and much lower porosity than the shale gas interval. In the meanwhile, the shale gas interval of Wangyinpu formation is buried at a moderate depth (2609.5~2672 m) with a large thickness of organic-rich shale (62.5 m). Its TOC content is higher than the roof and the floor reflecting a stronger adsorption capability of shale gas and a strong self-sealing property. Therefore, it reveals that the lower Cambrian shale should have a favorable physical sealing.

However, things changed when it comes to the tectonic evolution and seismic interpretation.

As mentioned in geological settings, tectonic evolution history shows that, influenced by the collision between the Southern China and the North China plates, study area was squeezed into a syncline with a large number of thrust faults in the early-middle Jurassic [39]. After that, in the Late Cretaceous to the Paleogene, the stress of the whole basin changed from extrusion to tension forcing the faults reopened due to the tension effects from the subduction of the Pacific Plate to the Eurasian Plate [44]. The stress did not change back to extrusion from tension until the Neogene [13, 14].

According to the seismic inter of the section through the study area, deep and large faults developed massively going through the roof, the shale gas interval, and even the floor (Figure 9). These faults destroyed the physical sealing in vertical direction, forming the vertical pathways, composing the pathway network with the lateral ones and made it more effective for gas exchange with the atmosphere. Furthermore, the reopening of the faults in Late Cretaceous to the Paleogene contributes to a large loss of shale gas.

4.3.2. *Frequent Magmatic Activities Brought Nitrogen*. According to the previous studies [45], the value of paleo-heat flow changed greatly since the early Cambrian. The value of paleo-heat flows increased slowly at first (the Cambrian to the Late Triassic: 543 Ma~205 Ma) and then

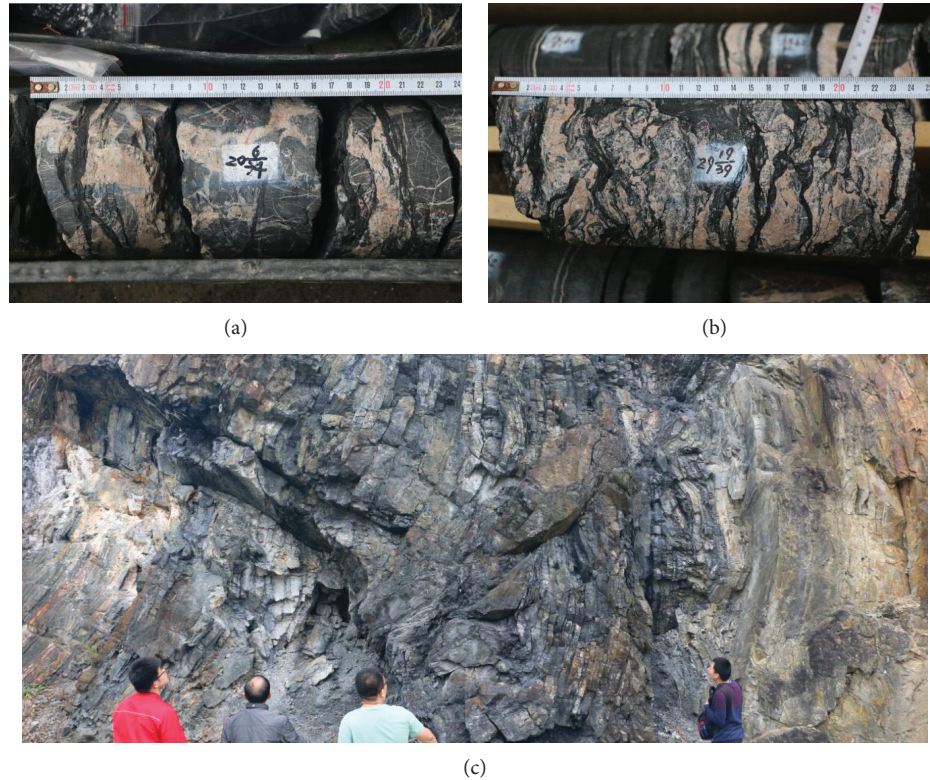


FIGURE 8: A detachment layer widely developed at the bottom of the lower Cambrian Wangyinpu formation shale in Xiuwu Basin. Core photos at the bottom of the lower Cambrian Wangyinpu formation: (a) in Jiangye-1 (depth: 2670 m) and (b) in Jiangye-2 (depth: 3135 m). (c) A photo of Laozhuang Outcrop at the bottom of the lower Cambrian Wangyinpu formation. See Figure 1 for the well locations.

TABLE 4: The sealing parameters of shale and its roof and floor in Jiangye-1 of the lower Cambrian Wangyinpu formation. The data of average TOC content and average porosity is referred to Liu et al. [24]. See Figure 1 for the well locations.

Part	Fm.	Lith.	Depth (m)	Avg. TOC (%)	Avg. porosity (%)	Thk. (m)
Roof	Guanyintang	Silty shale	2520~2609.5	2~4	1.2	89.5
Shale gas interval	Wangyinpu	Organic-rich siliceous shale	2609.5~2672	7~14	2.2	62.5
Floor	Piyuanchun	Silty shale	>2672	0.1~0.6	0.7	>50

Fm. = formation; Lith. = lithology; Avg. = average; TOC = total organic carbon; Thk. = thickness.

began a rapid increase since the Late Triassic (around 205 Ma). According to regional tectonic evolution, it was when the plates of the North China and the South China collided leading to frequent magmatic activities in surrounding areas. At the turn of the Jurassic and the Cretaceous (around 137 Ma), it reached a maximum. It gradually cooled down during the early Cretaceous (137 Ma~96 Ma). In the Late Cretaceous to the Paleogene (96 Ma~23.3 Ma), it reached another high point due to the tectonic movements (Figure 10). It slowly cooled down to the present value afterwards.

The frequent magmatic activities brought nitrogen from the deep crust and upper mantle to the basin basement. In the process of magma cooling, nitrogen was vaporized into the lower Cambrian shale reservoir.

4.3.3. Overmaturity Accelerated Diffusion. The thermal evolution of organic matter is mainly controlled by paleo-geotemperature, while paleo-geotemperature is related to buried depth and value of paleo-heat flows. According to

the previous researches [39, 45–48], Xiuwu Basin reached the maximum burial depth when the North China plate collided with the South China plate in the Triassic. As it can be told from the burial and thermal evolution history (Figure 11), even though it uplifted after reaching the maximum depth, the geotemperature continued to increase as the value of paleo-heat flows increased rapidly and reached 270°C at the turn of the Jurassic and the Cretaceous (137 Ma). The organic matter was consequently overcooked with the vitrinite reflection (R_o) of 3.8% and evolved into graphitization stage [45].

Generally, organic pores are more developed in moderate maturity (R_o : 2%~3%). The graphitization of organic matter may collapse the organic pores and lead to the decrease of the adsorption capacity of organic matter to natural gas, and, therefore, reducing of gas bearing potential of shale [49–54]. The low-mature Longmaxi shale and the overmature Wangyinpu shale were compared. Figures 12(a) and 12(b) are FIB-HIM photos of the Longmaxi shale in

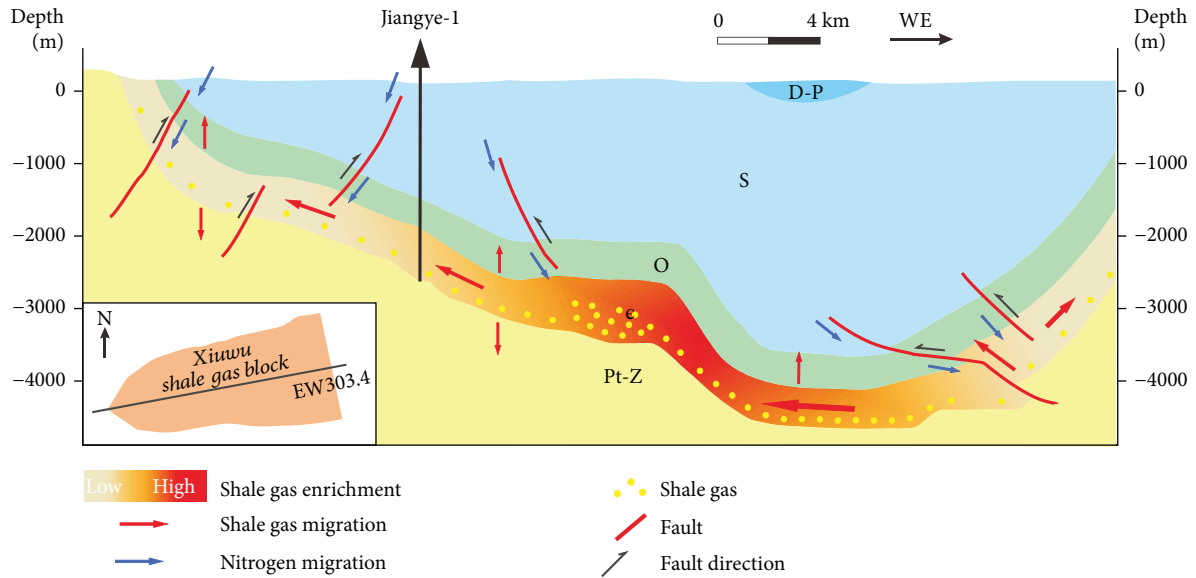


FIGURE 9: Hydrocarbon gas diffuses and nitrogen from atmosphere entrances through bedding planes, the detachment layer, and deep faults in section of EW303.4 through Xiuwu Basin. See Figure 1 for the well locations.

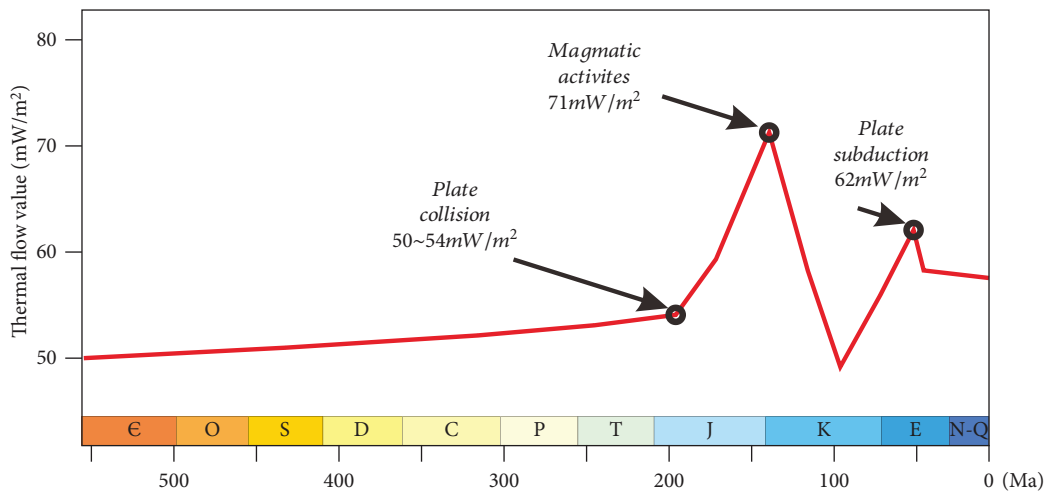


FIGURE 10: Value of the paleo-heat flows in Xiuwu Basin. Data is referred to Li et al. [45].

Jiaoye-1 and the Wangyinpu shale in Jiangye-1. It shows much fewer organic pores observed in the Wangyinpu shale. This resulted in the diminishment of storage ability of shale and promoted the loss of hydrocarbon gas and relatively increased the nitrogen content.

4.4. Explanation Model Summarization. After all the studies above, a model was summarized to explain the destruction of shale gas reservoirs and the causes of high-content nitrogen and low-content hydrocarbon in shale gas of the study area, which affected by active plate movements. As presented in Figure 13, the effective network of migration pathways made the gas exchange possible between the shale gas reservoir and the atmosphere. The network is composed of the lateral pathways including the bedding surface and the detachment layer and the vertical ones which are the trust faults. The magmatic activities not only brought the nitrogen

from the deep crust and upper mantle but also overcooked the organic matter and accelerated the loss of shale gas, which increased the relative content of nitrogen.

As a shale gas play, which was favorable for hydrocarbon generation but experienced complex tectonic evolution and affected by plate movements, the study area represents areas near the plate conjecture in the Lower Yangtze Region. The summarized model is applicable to explain the causes of the destruction of shale gas reservoirs and the widespread phenomenon where nitrogen concentrates and hydrocarbon diffuses in tectonic-complex areas in the Lower Yangtze Region and even in the some plate-active areas.

5. Conclusions

To solve the problem why a general phenomenon exists that nitrogen is highly concentrated and hydrocarbon diffuses in

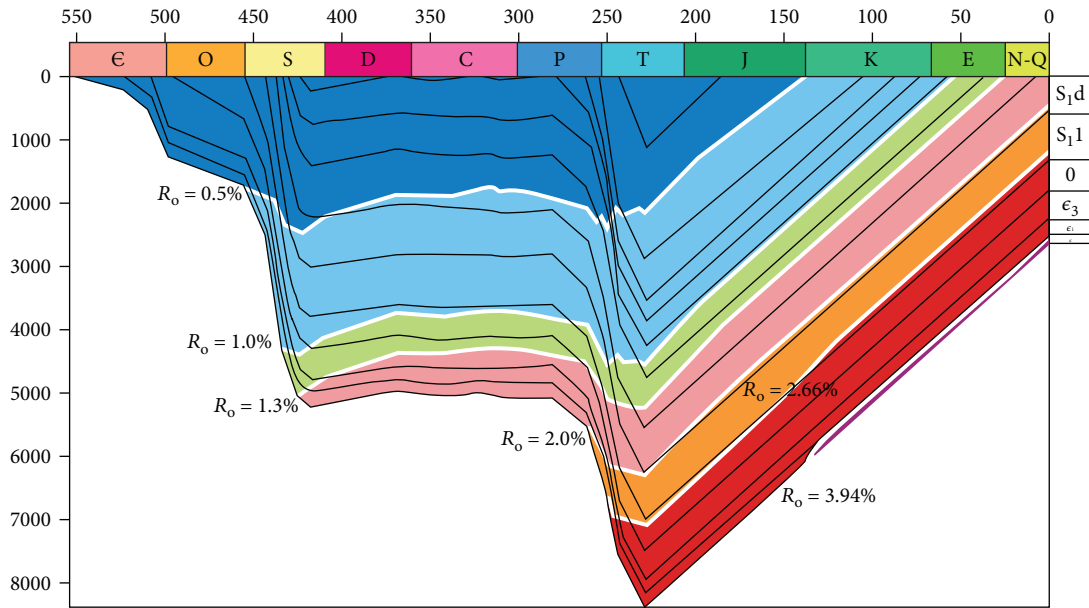


FIGURE 11: The burial history and the thermal evolution history of Jiangye-1 in Xiuwu Basin. See Figure 1 for the well location (modified from Li et al. [45]).

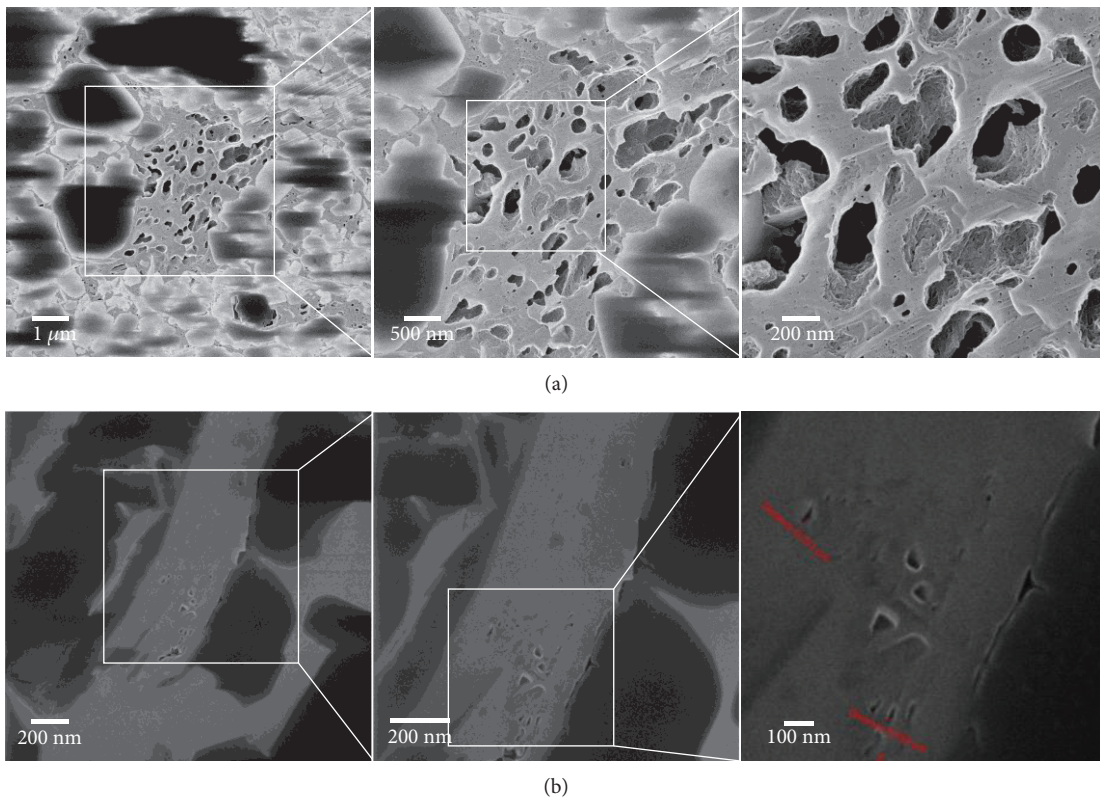


FIGURE 12: FIB-HIM photos of organic-rich shale: (a) the lower Silurian Longmaxi shale in Jiaoye-1, Jiaoshiba Play (depth: 2402 m, TOC: 4.44%, R_o : 2.58%) (from Wang et al. [13]) and (b) the lower Silurian Wangyinpu shale in Jiangye-1, Xiuwu Basin (depth: 2402 m, TOC: 11.27%, R_o : 3.8%). See Figure 1 for the well locations.

the lower Cambrian shale gas play in Xiuwu Basin, this paper takes two shale gas exploration wells, Jiangye-1 and Jiangye-2, as examples. After determining the detailed shale gas composition through the on-field gas component analysis, stable nitrogen isotopes were applied to identify the sources

of the nitrogen. Then the overburden permeability tests in different directions reflected the existence of migration pathways and the FIB-HIM photos revealed the negative impact of overmaturity on organic pores, which, combined with the comprehensive analysis of the geological settings, the

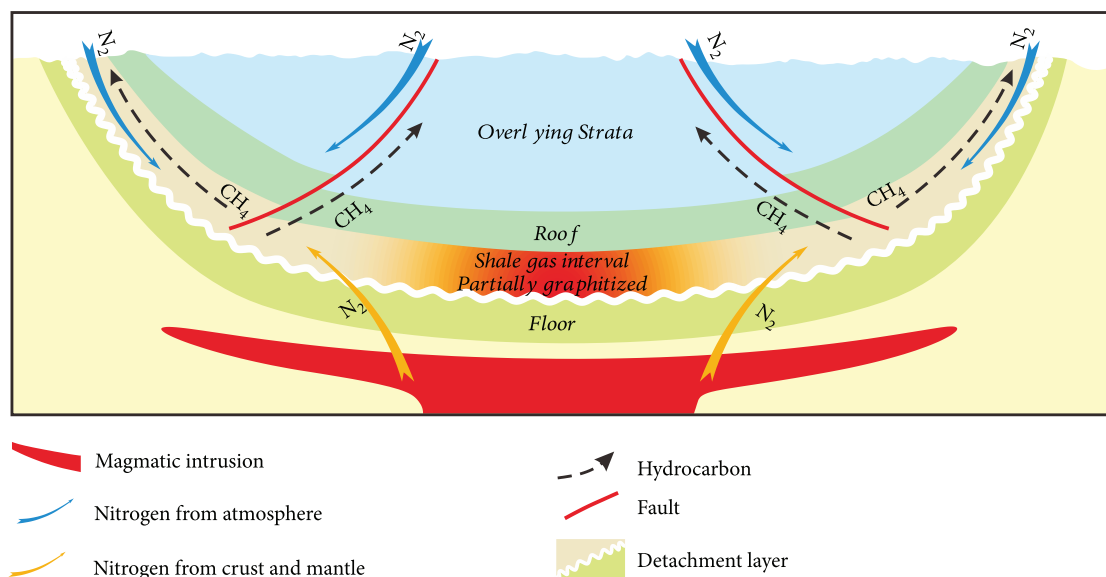


FIGURE 13: An explanation model for the destruction of shale gas reservoirs and the nitrogen concentration in the study area.

description of cores and outcrop, the interpretation of seismic section, and the history of thermal and tectonic evolution reveal the causes of the phenomenon which was the result of the effects of the effective pathway network, the magmatic activities, and the consequent overmaturity of organic matter. The explanation model of the destruction of shale gas reservoir in study area was summarized, and the conclusion was drawn as follows:

- (i) With the gas component analysis on the field, it revealed that the nitrogen accounts for 80 vol.% in the lower Cambrian shale gas. The value of $\delta^{15}\text{N}$ ranges from -0.8‰ to 0‰ , which reflects that the nitrogen is mainly from the atmosphere and the deep crust and upper mantle according to the summary of previous works
- (ii) Effective network of migration pathways partly led to the high content of nitrogen. The shale bedding surface and the detachment layer at the bottom of the lower Cambrian compose of the lateral pathways to atmosphere. In vertical, massively developed trust faults damaged the quality sealing, forming the pathway network with the lateral ones
- (iii) The frequent magmatic activities in the Jurassic brought nitrogen from deep crust and upper mantle and caused the organic matter highly overmatured to the graphitization stage, consequently reducing the storage capability and accelerating the methane loss, which increased the relative content of nitrogen in shale gas

Data Availability

Some of the data are contained in a published source cited in the References. All the data in this article is accessible to readers.

Disclosure

An earlier version of this study was presented as an abstract in GSA Annual Meeting in Indianapolis, Indiana, USA—2018.

Conflicts of Interest

There are no conflicts of interest with respect to the results of this paper.

Authors' Contributions

Yizhou Huang and Kun Zhang contributed equally to this work.

Acknowledgments

Thanks are due to all the financings supporting the research, which are the National Science and Technology Major Project, the Science Foundation of the Ministry of Land and Resources of China, the National Natural Science Foundation of China, the Performance Incentive and Guidance of Chongqing Scientific Research Institute, and the Sinopec Key Laboratory of Shale Oil/Gas Exploration and Production Technology. Also, thanks are due to all coauthors who worked with me through the whole research.

References

- [1] J. B. Curtis, "Fractured shale-gas systems," *AAPG Bulletin*, vol. 86, no. 11, pp. 1921–1938, 2002.
- [2] S. L. Montgomery, D. M. Jarvie, K. A. Bowker, and R. M. Pollastro, "Mississippian Barnett shale, Fort Worth basin, north-central Texas: gas-shale play with multi-trillion cubic foot potential," *AAPG Bulletin*, vol. 89, no. 2, pp. 155–175, 2005.

- [3] D. N. Warlick, "Gas shale and CBM development in North America," *Oil & Gas Financial Journal*, vol. 3, no. 11, pp. 1–5, 2006.
- [4] D. Dong, Y. Wang, X. Li et al., "Breakthrough and prospect of shale gas exploration and development in China," *Natural Gas Industry B*, vol. 3, no. 1, pp. 12–26, 2016.
- [5] T. Guo, "Key geological issues and main controls on accumulation and enrichment of Chinese shale gas," *Petroleum Exploration and Development*, vol. 43, no. 3, pp. 349–359, 2016.
- [6] H.-Y. Zhu, X. C. Jin, J. C. Guo, F. C. An, Y. H. Wang, and X. . Lai, "Coupled flow, stress and damage modelling of interactions between hydraulic fractures and natural fractures in shale gas reservoirs," *International Journal of Oil, Gas and Coal Technology*, vol. 13, no. 4, p. 359, 2016.
- [7] H. Zhu, J. Deng, X. Jin, L. Hu, and B. Luo, "Hydraulic fracture initiation and propagation from wellbore with oriented perforation," *Rock Mechanics and Rock Engineering*, vol. 48, no. 2, pp. 585–601, 2015.
- [8] G. Xusheng, H. Dongfeng, W. Zhihong, L. Yuping, and W. Xiangfeng, "Discovery and exploration of Fuling shale gas field," *China Petroleum Exploration*, vol. 21, no. 3, pp. 24–37, 2016.
- [9] W. Xiangfeng, Z. Zhengbao, W. Qingbo, L. Zhujiang, Z. Min, and Z. Hui, "Comprehensive evaluation on geological conditions of the shale gas in Upper Ordovician Wufeng Formation—Lower Silurian Longmaxi Formation in Dingshan area, Qijiang, Southeastern Sichuan," *Geological Review*, vol. 63, no. 1, pp. 153–164, 2017.
- [10] X. Tang, Z. Jiang, Z. Li et al., "The effect of the variation in material composition on the heterogeneous pore structure of high-maturity shale of the Silurian Longmaxi formation in the southeastern Sichuan Basin, China," *Journal of Natural Gas Science and Engineering*, vol. 23, pp. 464–473, 2015.
- [11] X. Tang, Z. Jiang, S. Jiang, P. Wang, and C. Xiang, "Effect of organic matter and maturity on pore size distribution and gas storage capacity in high-mature to post-mature shales," *Energy & Fuels*, vol. 30, no. 11, pp. 8985–8996, 2016.
- [12] X. Tang, Z. Jiang, S. Jiang, L. Cheng, and Y. Zhang, "Characteristics and origin of in-situ gas desorption of the Cambrian Shuijingtuo Formation shale gas reservoir in the Sichuan Basin, China," *Fuel*, vol. 187, pp. 285–295, 2017.
- [13] P. Wang, Z. Jiang, L. Chen et al., "Pore structure characterization for the Longmaxi and Niutitang shales in the Upper Yangtze Platform, South China: evidence from focused ion beam–He ion microscopy, nano-computerized tomography and gas adsorption analysis," *Marine and Petroleum Geology*, vol. 77, pp. 1323–1337, 2016.
- [14] P. Wang, Z. Jiang, W. Ji et al., "Heterogeneity of intergranular, intraparticle and organic pores in Longmaxi shale in Sichuan Basin, South China: evidence from SEM digital images and fractal and multifractal geometries," *Marine and Petroleum Geology*, vol. 72, pp. 122–138, 2016.
- [15] L. Chen, Z. Jiang, K. Liu, J. Tan, F. Gao, and P. Wang, "Pore structure characterization for organic-rich Lower Silurian shale in the Upper Yangtze Platform, South China: a possible mechanism for pore development," *Journal of Natural Gas Science and Engineering*, vol. 46, pp. 1–15, 2017.
- [16] L. Chen, Z. Jiang, K. Liu et al., "Effect of lithofacies on gas storage capacity of marine and continental shales in the Sichuan Basin, China," *Journal of Natural Gas Science and Engineering*, vol. 36, pp. 773–785, 2016.
- [17] K. Zhang, Z. Jiang, L. Yin et al., "Controlling functions of hydrothermal activity to shale gas content-taking lower Cambrian in Xiuwu Basin as an example," *Marine and Petroleum Geology*, vol. 85, pp. 177–193, 2017.
- [18] K. Zhang, Z. Jiang, X. Xie et al., "Lateral percolation and its effect on shale gas accumulation on the basis of complex tectonic background," *Geofluids*, vol. 2018, Article ID 5195469, 11 pages, 2018.
- [19] Q. Y. Liu, L. Tao, H. Y. Zhu, Z. D. Lei, S. Jiang, and J. D. McLennan, "Macroscale mechanical and microscale structural changes in Chinese Wufeng shale with supercritical carbon dioxide fracturing," *SPE Journal*, vol. 23, no. 3, pp. 691–703, 2018.
- [20] W. Zhao, J. Li, T. Yang, S. Wang, and J. Huang, "Geological difference and its significance of marine shale gases in South China," *Petroleum Exploration and Development*, vol. 43, no. 4, pp. 547–559, 2016.
- [21] L.-Y. Cheng, Z.-Q. Yong, T.-Y. Wang, N. Lan, J.-Y. Yu, and B. Den, "Evaluation index of shale gas preservation for Niutitang Formation in the strong transformation zone," *Natural Gas Geoscience*, vol. 26, no. 12, pp. 2408–2416, 2015.
- [22] X. Guo, D. Hu, Y. Li, Z. Wei, X. Wei, and Z. Liu, "Geological factors controlling shale gas enrichment and high production in Fuling shale gas field," *Petroleum Exploration and Development*, vol. 44, no. 4, pp. 513–523, 2017.
- [23] G. Zhai, Y. Wang, S. Bao et al., "Major factors controlling the accumulation and high productivity of marine shale gas and prospect forecast in southern China," *Earth Science*, vol. 42, no. 7, pp. 1057–1068, 2017.
- [24] W.-W. Liu, J.-C. Tian, X.-B. Lin, J.-N. Shi, C.-Y. Yang, and S.-F. Peng, "Characteristics and significance of mineral compositions in lower Cambrian black shale from Xiuwu Basin, Jiangxi, China," *Journal of Chengdu University of Technology (Science & Technology Edition)*, vol. 42, no. 1, pp. 90–97, 2015.
- [25] F. Pang, S. J. Bao, S. M. Ren, S. Li, C. Tong, and L. Zeng, "Shale gas accumulation conditions and favorable areas of the Lower Cambrian in Xiuwu Basin," *Journal of Northeast Petroleum University*, vol. 38, no. 5, pp. 23–30, 2014.
- [26] W. Qin, Q. Han, and J. Wang, "Shale gas reservoiring condition analysis in Xiuwu Basin," *Energy Research and Management*, vol. 3, no. 1, pp. 46–49, 2013.
- [27] G. Wang, Y. Ju, and K. Han, "Early Paleozoic shale properties and gas potential evaluation in Xiuwu Basin, western Lower Yangtze Platform," *Journal of Natural Gas Science and Engineering*, vol. 22, pp. 489–497, 2015.
- [28] W.-W. Jiao, S.-X. Wang, L.-J. Cheng, Q.-Y. Luo, and G.-J. Fang, "The reason of high nitrogen content and low hydrocarbon content of shale gas from the Lower Cambrian Niutitang Formation in southeast Chongqing," *Natural Gas Geoscience*, vol. 28, no. 12, pp. 1882–1890, 2017.
- [29] G. He, "Geological characteristics of Lower Cambrian Shale in Xiuwu Basin," in *Annual Meeting of Chinese Geoscience Union*, vol. 10, pp. 132–134, Beijing, China, 2014.
- [30] C. Anding, "Nitrogen as an index of oil-gas preservation conditions in marine strata," *Petroleum Geology & Experiment*, vol. 27, no. 1, pp. 85–89, 2005.
- [31] J. Chen and Y. Zhu, "The origin of molecular nitrogen in natural gas and geochemical characters of molecular nitrogen in natural gas from east part of Tarim Basin," *Natural Gas Geoscience*, vol. 14, no. 3, pp. 172–176, 2003.

- [32] J. He, W. Yan, and J. Cui, "Nitrogen gas source tracking and distinguishing in margin basins, northern South China Sea," *Marine Origin Petroleum Geology*, vol. 17, no. 3, pp. 85–89, 2012.
- [33] J. Li, Z. Li, D. Wang et al., "Geochemical characteristics and N₂ source of nitrogen riched natural gas in Tarim Basin," *Acta Petrolei Sinica*, vol. 34, no. S1, pp. 102–111, 2013.
- [34] K. H. Xiao, H. Chen, Y. J. Wo, Y. Zhou, and Y. X. Zhang, "Impact of tectonic evolution on Paleozoic and Mesozoic petroleum systems in Jiangnan plain," *Oil & Gas Geology*, vol. 26, no. 5, pp. 688–693, 2005.
- [35] F. F. Guo, J. Y. Kang, J. F. Sun, J. Z. Lu, and X. P. Wang, "Tectonic evolution and hydrocarbon accumulation model for marine strata in Jiangnan Basin," *Lithologic Reservoirs*, vol. 22, no. 1, pp. 23–29, 2010.
- [36] Z. Feng, Y. Peng, and Z. Jin, "Lithofacies paleogeography of the Cambrian in South China," *Journal of Palaeogeography*, vol. 3, no. 1, pp. 1–14, 2001.
- [37] J. M. Yang, F. Yi, and L. Hou, "Genesis and petro-geochemical characteristics of the lower cambrian black shale series in the southeast of chongqing and tts adjacent area," *Acta Mineralogica Sinica*, vol. 24, no. 3, pp. 286–291, 2004.
- [38] X. Qi, Q. Hu, and X. Yi, "Shale gas exploration prospect of lower Cambrian Wangyinpu formation in Xiuwu basin," *China Mining Magazine*, vol. 24, no. 10, pp. 102–107, 2015.
- [39] L. F. Mei, D. F. Deng, C. B. Shen, and Z. Q. Liu, "Tectonic dynamics and marine hydrocarbon accumulation of Jiangnan-Xuefeng uplift," *Geological Science and Technology Information*, vol. 31, no. 5, pp. 85–93, 2012.
- [40] P. Wang, Z. Jiang, B. Han et al., "Reservoir geological parameters for efficient exploration and development of Lower Cambrian Niutitang Formation shale gas in South China," *Acta Petrolei Sinica*, vol. 39, no. 2, pp. 152–162, 2018.
- [41] B. M. Krooss, R. Littke, B. Müller, J. Frielingsdorf, K. Schwochau, and E. F. Idiz, "Generation of nitrogen and methane from sedimentary organic matter: implications on the dynamics of natural gas accumulations," *Chemical Geology*, vol. 126, no. 3-4, pp. 291–318, 1995.
- [42] Z. Zeng, "Genetic type of nitrogen gas in sedimentary basins in China," *Natural Gas Geoscience*, vol. 13, no. 3/4, pp. 29–33, 2002.
- [43] Q. Liu, W. Liu, and B. M. Krooss, "Advances in nitrogen geochemistry of natural gas," *Natural Gas Geoscience*, vol. 17, no. 1, pp. 119–124, 2006.
- [44] Y. Wo, Y. Zhou, and K. Xiao, "The burial history and models for hydrocarbon generation and evolution in the marine strata in Southern China," *Sedimentary Geology and Tethyan Geology*, vol. 27, no. 3, pp. 94–100, 2007.
- [45] Y. Li, Z. Jiang, W. Liu et al., "The effect of the tectonic thermal evolution history to gas content of Lower Cambrian Shales at Xiuwu Basin," *Journal of Engineering Science and Technology Review*, vol. 16, no. 34, pp. 44–51, 2016.
- [46] H. Nie, S. Bao, B. Gao et al., "A study of shale gas preservation conditions for the Lower Paleozoic in Sichuan Basin and its periphery," *Earth Science Frontiers*, vol. 19, no. 3, pp. 280–294, 2012.
- [47] H. Nie, Z. Jin, R. Bian, and W. Du, "The "source-cap hydrocarbon-controlling" enrichment of shale gas in Upper Ordovician Wufeng Formation-Lower Silurian Longmaxi Formation of Sichuan Basin and its periphery," *Acta Petrolei Sinica*, vol. 37, no. 5, pp. 557–571, 2016.
- [48] F. Zhou, *Hydrocarbon Accumulation and Petroleum Formation in the Northern Margin of Jiangnan Uplift*, China University of Geosciences, 2006.
- [49] M. E. Curtis, B. J. Cardott, C. H. Sondergeld, and C. S. Rai, "Development of organic porosity in the Woodford Shale with increasing thermal maturity," *International Journal of Coal Geology*, vol. 103, pp. 26–31, 2012.
- [50] W. Ji, Y. Song, Z. Jiang et al., "Fractal characteristics of nano-pores in the Lower Silurian Longmaxi shales from the Upper Yangtze Platform, South China," *Marine and Petroleum Geology*, vol. 78, pp. 88–98, 2016.
- [51] W. Ji, Y. Song, Z. Jiang, X. Wang, Y. Bai, and J. Xing, "Geological controls and estimation algorithms of lacustrine shale gas adsorption capacity: a case study of the Triassic strata in the southeastern Ordos Basin, China," *International Journal of Coal Geology*, vol. 134-135, pp. 61–73, 2014.
- [52] S.-F. Wang, Z.-Y. Zhang, D.-Z. Dong et al., "Microscopic pore structure and reasons making reservoir property weaker of Lower Cambrian Qiongzhusi shale, Sichuan Basin, China," *Natural Gas Geoscience*, vol. 27, no. 9, pp. 1619–1628, 2016.
- [53] W. Zhao, T. Jing, X. Xiong, B. Wu, and Y. Zhou, "Graphitization characteristics of organic matter in marine-facies shale," *Geological Science and Technology Information*, vol. 37, no. 2, pp. 183–191, 2018.
- [54] Y. Wang, D. Dong, X. Cheng, J. Huang, S. Wang, and S. Wang, "Electric property evidences of carbonification of organic matters in marine shales and its geologic significance: a case study of the Lower Cambrian Qiongzhusi shale in the southern Sichuan Basin," *Natural Gas Industry B*, vol. 1, no. 2, pp. 129–136, 2014.

Research Article

Petrophysical Properties and Microstructural Analysis of Faulted Heterolithic Packages: A Case Study from Miocene Turbidite Successions, Italy

Hannah Riegel ^{1,2}, Miller Zambrano ^{1,2,3}, Fabrizio Balsamo ⁴, Luca Mattioni,⁵
and Emanuele Tondi^{1,2,3}

¹*School of Science and Technology-Geology Division, University of Camerino, Via Gentile III da Varano, 7, Camerino 62032, Italy*

²*Reservoir Characterization Project, Italy*

³*GeoMORE s.r.l, Via Gentile III da Varano, 7, Camerino 62032, Italy*

⁴*Department of Chemistry, Life Sciences, and Environmental Sustainability, Parma University, Campus Universitario, Parco Area delle Scienze 157/A, I-43124 Parma, Italy*

⁵*Neptune Energy International S.A. Faubourg de l'Arche, 1 Place Samuel de Champlain, La Défense, Paris 92930, France*

Correspondence should be addressed to Hannah Riegel; riegelhb@gmail.com

Received 30 November 2018; Revised 17 March 2019; Accepted 9 April 2019; Published 2 June 2019

Academic Editor: Ye Zhang

Copyright © 2019 Hannah Riegel et al. This is an open access article distributed under the Creative Commons Attribution License, which permits unrestricted use, distribution, and reproduction in any medium, provided the original work is properly cited.

Geofluid reservoirs located in heterolithic successions (e.g., turbidites) can be affected by vertical and lateral compartmentalization due to interbedded fine-grained facies (i.e., shale, siltstones) and the presence of faults, respectively. A fault can behave as a conduit or barrier to fluid flow depending on its architecture and the individual hydraulic behavior of its components (i.e., fault core, damage zone). The fault core, normally composed by fault rock or smeared clay material, commonly acts as a flow inhibitor across the fault. Fault-related fractures (macro- and microscopic) in the damage zone generally increase the permeability parallel to the fault, except when they are cemented or filled with gouge material. Although macrofractures (which define the fracture porosity) dominate fluid flow, the matrix porosity (including microfractures) begins to have a more important role in fluid flow as the aperture of macrofractures is occluded, particularly at greater depth. This study investigates the variation in matrix permeability in fault zones hosted in heterolithic successions due to fault architecture and stratigraphy of host rock (i.e., sand-rich turbidites). Two key areas of well-exposed, faulted Miocene turbidites located in central and southern Italy were selected. For this study, six separate fault zones of varying offset were chosen. Each impacts heterolithic successions that formed under similar tectonic conditions and burial depths. Across the selected fault zones, an extensive petrophysical analysis was done in the field and laboratory, through air permeameter measurements, thin section, and synchrotron analysis in both host rock, damage zone, and fault core. Results suggest that the amount and distribution of clay layers in a heterolithic sequence affects fluid flow across the fault, regardless of fault offset.

1. Introduction

Heterolithic successions (e.g., sand-rich turbidites) represent important deep-water targets for oil and gas exploration due to their considerable lateral continuity and high sand volume [1, 2]. Despite a high net-to-gross value, the production of hydrocarbon in these reservoirs can be affected by vertical and lateral compartmentalization due

to interbedded fine-grained facies (i.e., shale, siltstones) and faults, respectively [3, 4].

The control exerted by the fault on fluid flow is defined by three main elements: (1) juxtaposition, (2) fault rock, and (3) the surrounding damage zone [5–13]. The fault rock may often diminish the fluid flow perpendicular to the fault, depending on its mineral composition, grain size, and cementation (e.g., [7, 13]). In a heterolithic succession, the

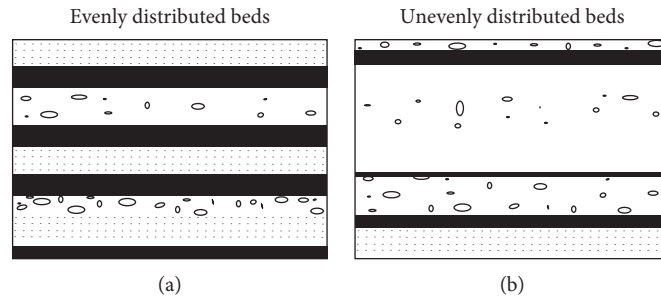


FIGURE 1: The two-types of packages found at the key sites: (a) evenly distributed beds contain a relatively even distribution of interbedded clay layers (in black) throughout the package; (b) unevenly distributed beds contain a sparse or random arrangement of clay beds relative to the other lithofacies (e.g., siltstone, sandstone, conglomerates) present.

presence of clay within the fault core may also contribute to the sealing behavior of the fault (clay smearing process) [14–17]. In these reservoirs, the stratigraphy may exert a primary control on the fracture intensity distribution in both host rock (diffuse deformation) and fault zones (localized deformation) [18–23]. In general, fractures within the damage zone are more abundant in comparison to the host rock as the distance to the fault core decreases [24–28]. The fractures in the damage zone may enhance the fluid flow parallel to the fault if they are opened (e.g., joints, partially cemented joints) and connected. However, they may inhibit the cross-flow when closed by secondary mineralization, fault gouge, or deformation banding [13, 29–33]. The permeability associated to fractures within the damage zone may change over time due to the interplay of coseismic fracturing, pressure variation, and sealing/healing [34–37].

Despite the fact that macrofractures (which define the fracture porosity) generally dominate fluid flow within the fault zone, the matrix porosity (including microfractures) may start to have a more important role to fluid flow as the aperture of macrofractures decreases, particularly at greater depths [37, 38]. Matrix porosity (and permeability) can be increased at low stress levels due to the development of microfractures, even though the regional stresses are below the fracture strength of the rock [39–41]. Like fracture porosity, matrix porosity can increase toward the main fault surface due to a higher density of fault-related microfractures [37, 42]. The control exerted by the stratigraphy (lithology and their relative thickness distribution) on matrix permeability distribution in fault zones hosted in heterolithic succession has been poorly investigated.

This study investigates the matrix permeability variation in fault zones hosted in heterolithic successions due to fault architecture and stratigraphy of host rock (i.e., even vs. unevenly distributed beds; Figure 1). The proposed methodology consists on combining in situ air permeameter measurements with thin section and X-ray computed microtomography (X-ray microCT) image analysis in host rock, damage zone, and fault core. The evaluation of fault zone architecture, fault slip, and lithofacies associations is completed at each outcrop. The study is focused in two key outcrop areas located in central and southern Italy, where the Macigno Formation and the Cilento Group are exposed (Figure 2). Despite the geographic distance, both sand-rich

turbidites formed under similar tectonic conditions and shared similar structural evolution.

2. Geological Setting

This study was developed in two different locations: (i) Livorno-Piombino (Figure 2(a)) and (ii) San Marco di Castellabate (Figure 2(b)). Despite the distance (~530 km), the heterolithic successions exposed in both areas were formed under similar tectonic conditions resulting in similar structural evolution [43–46].

2.1. Livorno–Piombino Area. The first study area is located within the Macigno Formation, which is made up of Late Oligocene to Miocene turbidite deposits [49]. Part of a diachronically migrating foredeep system, the Macigno Formation was laid down in a compressional setting, most likely a thrust-top basin [43, 44]. According to paleogeographic reconstructions, the Macigno Basin was 150–200 km wide and occupied a part of the present Ligurian and Tyrrhenian seas [43]. It was then deformed and organized into several thrust units in multiple tectonic events during the Miocene and the Pliocene [50, 51]. While the orogenic front and foredeep basin were migrating, the proximal turbidite facies of the transversal feeders (named as the “Macigno costiero”) were substituted by distal turbidite facies of the longitudinal basin feeders (named as the “Macigno appenninico”) [43, 44, 49]. Faults in the area are characterized as NW-SE-striking dip slip faults with minor WSW-ENE strike slip faults characterized by different degrees of maturity [52–54].

The Macigno costiero primarily crops out between the towns of Livorno and Piombino in central Italy (Figure 2(a)). It is a quartz- and feldspar-rich siliciclastic succession made up of Late Oligocene-Early Miocene foredeep-related sediments of thickness ranging from 0.5 to 3.0 km. It is dominated by turbiditic sandstones with minor shales and siltstones, rare conglomerates, and some detrital limestones [49]. These turbidites flowed transversely, with respect to the basin, and were deposited in a wide foredeep basin located close to the orogenic wedge where sedimentation first developed in the internal zones [53].

In coastal outcrops, the Macigno costiero contains fossils and carbonates due overall to proximal turbidite facies

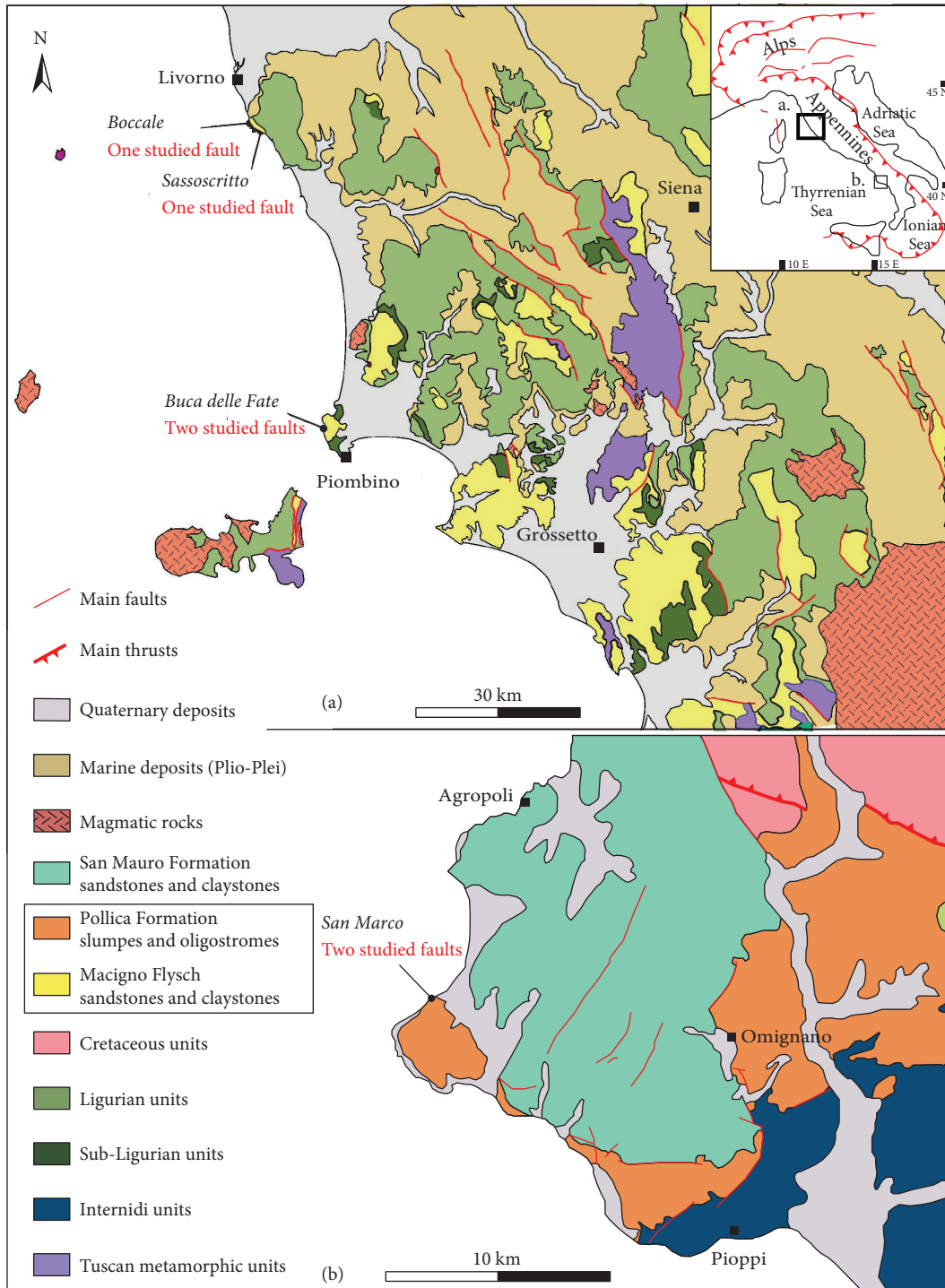


FIGURE 2: Locations of study areas along with key sites denoted in italics. The focused geologic formations are denoted inside the rectangle. (a) Livorno-Piombino area [47], (b) Agropoli-Pioppi area (San Marco di Castellabate) [48].

instead of distal [55, 56]. The Macigno costiero sandstone beds, from cm- to m-thick and gray-colored (ochre-weathering), are mainly made up of quartz and feldspar grains (plagioclase and k-feldspar), as well as white mica and chlorite grains, and crystalline lithics consisting of igneous and metamorphic rock fragments [55–57]. The cements of sandstones are mainly argillaceous-phylosilicates, calcite,

and to a lesser degree quartz [57]. At the Bay of Baratti (Buca delle Fate site; Figure 2(a)), carbonate lithics are present. Gneiss and quartz- and muscovite-rich schists are the most common metamorphic lithic grains [58]. The sandstones are classifiable as feldspathic litharenite [57]. In Calafuria (sites Boccale, Sassoscritto, and Scogli di Calafuria; Figure 2(a)), volcanic grains have an

intermediate composition [58]. Like Baratti, gneiss and quartz-muscovite schists are the prevalent metamorphic grains [58].

2.2. San Marco di Castellabate. The second study area is located in southern Italy between the towns of Agropoli and Pioppi, where the Cilento Group is exposed (Figure 2(b)). The Cilento Group was deposited in the Early Miocene (Late Burdigalian to Serravallian) and unconformably overlies the tectonized Ligurian accretionary complex [59–62]. These tectonized units represent the beginning of the Apennine mountain-building [45, 46].

Structurally, the area is characterized by left lateral wrench faults trending WNW-ESE [52]. The tectonized Ligurian units that are overlain by the Cilento Group are cut by a series of SE down-throwing listric faults [52, 63]. Shortening is also present, most noticeably in the sediments affected by the overthrusting of the Lagonegro Units onto the Cilento Group [52, 64].

The predominantly sandstone Cilento Group formed as a wedge-top basin succession [45, 46, 62, 64] and is sourced mainly from a siliciclastic Calabrian basement [65]. The Cilento Group contains a mix of heterogeneous strata including beds with fine-grained matrix with detached layers and pebble-boulder clasts, alternating clay layers, and sandstones, making up the oldest thrust-top syntectonic strata represented in the southern Apennines [60].

For this study, outcrops from the Pollica Formation, the oldest formation pertaining to the Cilento Group (Langhian), are studied. [66]. Deposited on an episutural basin of pre-Burdigalian strata [67, 68], both formations are primarily composed of siliciclastic arenites and marly siliciclastic arenitic turbidites [63]. The Pollica Formation ranges in thickness from 350 to 600 m and is made up of two members, (1) the Cannicchio Member and (2) the Pollica Sandstones [66]. The Cannicchio Member is primarily made up of mainly siliciclastic arenites with lesser clay facies dispersed throughout (sandstone/pelite ratio < 1) [66]. It is characterized by synsedimentary deformation and debris flows with a muddy matrix. The Pollica Sandstones Member is the thicker of the two, varying in thickness between 200 and 400 m. It is characterized by coarser-grained material (sandstone/pelite ratio > 1) in relation to the Cannicchio Member, with several cycles of coarsening up. Debris flows are also present [66].

3. Methods

3.1. Air Permeameter Measurements. Field-based direct permeability measurements (646 in total) were carried out in fault zones located in both study areas (Table 1). In the Livorno-Piombino area, 3 sites were analyzed: (i) Boccale and (ii) Sassoscritto, which represent channel fill facies, and (iii) Buca delle Fate which represents channel-levee facies. In San Marco di Castellabate, a succession composed of channel-levee environment and less turbulent environments associated with marl beds is exposed.

Permeability measurements were taken in vertical sections (cliffs) along transects of 2–3 m-long across six faults

(including host rock, damage zone, and fault core) crosscutting different lithofacies (i.e., sandstones, siltstones, and shale). Where possible, measurements were taken perpendicular to the fault plane as well. Measurements were performed using a TinyPerm II Portable Air Permeameter (manufactured by New England Research) which provides reliable values from 10^{-4} to 10 Darcy [30, 69–71]. To avoid bias due to surface irregularities and weathering, sampling sites were cleaned and cleared of detritus that would influence the measurements [30]. Macrofractures may influence permeability measurements and so were avoided. A silicon ring (5 mm of diameter) was used to avoid air leaking from the minipermeameter nozzle, which is far smaller than the width of fault cores sampled. In order to convert the TinyPerm II output value (T) to standard units of permeability (i.e., Darcy, D), we used the equation provided in the manual of the device [71]:

$$k = \frac{10^{(T-12.8737/-0.8206)}}{1000}, \quad (1)$$

where T is the output value (unitless) of the device, and k corresponds to the permeability in Darcy, (D).

3.2. Structural Analysis. Studied faults are divided into three different groups based on architecture, not offset (Figure 3; Table 1). Incipient faults are characterized by a single fault plane with minimal fault core (<3 cm, not including shale gouge). Well-developed faults are characterized by through-going slip surfaces associated with well-developed splays and fault core. Faults deemed “complex” are also found at the study sites. They characteristically have a well-developed fault core (often with cataclasite/clay smear) and an extensive, thick damage zone. Three or more fault planes are often present.

3.3. Lab-Based Analysis

3.3.1. Thin Section Observations, Density, and Porosity Analysis. Samples for thin section and laboratory analysis were collected at each location in order to study properties like microstructural features, mineralogy, and grain orientation that would impact permeability. Samples were taken from the host rock of shale, fine sandstone, medium sandstone, coarse sandstone, and microconglomerates (if applicable), damage zone, and fault core. Samples from the fault core were composed of cataclasite, crushed breccia, shale gouge, and protocataclasite. Thin sections were cut from the field samples and analyzed under petrographic microscope under cross-polarized view.

Density analysis was performed with a helium pycnometer UltraPyc 1200e (Quantachrome Instruments) on 11 samples from the Macigno and Cilento sites. Samples were first cleaned and then analyzed with a mercury-intrusion PoreMaster 33 porosimeter (Quantachrome Instruments) to measure total porosity and pore size distribution in the range of 0.0064 to 950 μm . Before measurements, samples were dried at 40°C for 24 hr, and then 2 g of material was analyzed in a sample cell of 1.0 \times 3.0 cm. The parameters used

TABLE 1: List of faults studied along with the associate formation, location, and characteristics.

Fault_ID	Location	Kinematics	Orientation	Offset	Fault core	Classification	Type of package
FIE	Boccale, Macigno Fm.	Dip slip (normal)	200°, 65°	0.4 m	Minimal in sandstone, shale gouge through clay	Incipient fault	Evenly thick
FIU	Buca delle fate, Macigno Fm	Oblique (normal, dextral)	211°, 35-56°	0.5 m	Cataclasite, shale gouge	Incipient fault	Unevenly thick
FWE	San Marco di Castellabate, San Mauro Fm.	Oblique (normal, sinistral)	296°, 86°	>30 m	Fault breccia, shale gouge	Well-developed fault	Evenly thick
FWU	Buca delle fate, Macigno Fm	Oblique (normal, sinistral)	256°, 12-51°	1.3 m	Protocataclasite, shale gouge	Well-developed fault	Unevenly thick
FCE	San Marco di Castellabate, San Mauro Fm.	Oblique (normal, sinistral)	304°, 86°	3.5 m	Cataclasite, shale gouge	Complex fault 3 fault planes	Evenly thick
FCU	Sassoscritto, Macigno Fm	Oblique (normal, sinistral)	225°, 80°	2.1 m	Cataclasite, shale gouge	Complex fault 3 fault planes	Unevenly thick

Note: all measurements done in right hand rule.

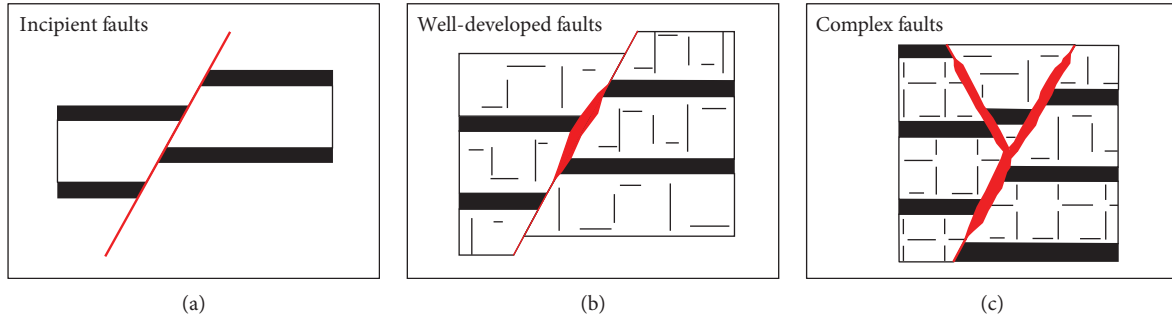


FIGURE 3: Faults were divided into groups based on the overall architecture. Black layers are representative of claystone, whereas the white beds represent a more competent layer, such as sandstone, limestone, and conglomerates. (a) Incipient faults are usually small in offset (<0.50 m) and are characterized by their lack of fault core; (b) well-developed faults are characterized by the presence of a fault core (in red); (c) complex faults contain two or more fault planes that contribute to an overall more mature fault core.

for porosity measurements are as follows: pressure range, 0.5–33000 psi; contact angle of mercury, 140 degrees; and surface tension of mercury, 0.48 N/m (480 dyn/cm). The obtained mercury intrusion curves approximate pore size distributions, being the applied hydraulic pressure, (P) related to the cross-sectional radius, and (R) of pore throats accessible by the pressured mercury [72].

3.3.2. X-Ray Micro-CT 3D Image Analysis. A total of eleven fault core samples (Table 2) were collected to be investigated using the synchrotron-based X-ray micro-CT imaging technique. In the laboratory, samples were carefully cut into thin cylinders (diameter ~ 3 mm, length 10–40 mm). The samples were targeted according to the sampling area: (i) Buca delle Fate (BDF_) and (ii) Sassoscritto (SS_). The pores sizes are smaller than 10 microns, and the grains may be characterized by highly variable mineral composition and mass density. In order to obtain an accurate assessment of the pore structure, work was done in phase-contrast mode with a high spatial resolution (ca. 2 microns).

The selected rock samples were scanned at the SYRMEP (SYnchrotron Radiation for MEDical Physics) beamline of Elettra Synchrotron (Trieste, Italy), following the methodology (including image processing and quantitative analysis) described by previous authors [73–75], which is suitable for many types of rocks (e.g., [76–80]). At the SYRMEP beamline, a bending magnetic source is located 23 m from the source, allowing a nearly parallel geometry and a high spatial coherence of the X-ray beam [81, 82], which takes full advantage of phase-contrast effects [83].

For the experiments, a white beam configuration mode [84] was used setting the X-ray energy to 22 keV and filtering the X-ray beam with 1.5 mm Si + 0.025 mm of Mo. The sample-to-detector distance was set at 150 mm and 200 mm. For each sample, 1800 projections were acquired over a total scan angle of 180° with exposure time/projection of 2 s, 2.5 s, or 3.0 s (depending on the sample and the quality output image). The detector consisted of a 16 bit, air-cooled, sCMOS camera (Hamamatsu C11440-22C) with a 2048×2048 -pixel chip. The effective pixel size of the detector varies from $1.25 \mu\text{m}$ to $1.80 \mu\text{m}$ (depending on the sample), yielding a view of approximately $2.5 \text{ mm} \times 2.5 \text{ mm}$.

The tomographic slice reconstruction of the synchrotron X-ray microCT images was performed using the SYRMEP Tomo Project software developed at Elettra [85] and powered by ASTRA tomography toolbox [86] and TomoPy [87]. To improve their liability of quantitative morphological analysis and enhance the contrast among the different mineralogical components of the solid phases and the porous phase, a single-distance phase-retrieval algorithm was applied to the white beam projections using Paganin’s algorithm [88] based on the Transport of Intensity Equation (TIE). After reconstruction, 3D images were filtered, segmented, and analyzed using the Pore3D software library, custom-developed at Elettra [89]. A 3D bilateral filter was applied to the reconstructed data for removing noise and preserving edges [90]. Considering the multiphase composition of the imaged rocks, an automatic multiphase k -means clustering [91] with four to five classes was used for segmenting suitable volumes of interests in two phases: (i) pores and (ii) grains (including material with different mineralogy and cement). Permeability is proportional to the square of the porosity and inversely proportional to the square of the specific surface area as in the Kozeny-Carman equation [92, 93]:

$$k = \frac{\phi}{\beta \times \tau^2 \times S_v^2}, \quad (2)$$

where β , the pore shape factor, is fixed to the common value of 5. The tortuosity, τ , defined as the ratio of the geodesic length (shortest path connecting two points in the pore space) and the Euclidean length (shortest distance between two points), which generally varies between 1.5 and 2.0 in rocks. However, the permeability should be also controlled by the connectivity, which may vary in function of the cementation degree.

The quantitative analysis consists of measuring the following parameters (sensu [73–75]):

- (i) Total porosity, ϕ_t (%): the volume of pores (connected and/or isolated) divided by the total rock volume

TABLE 2: Volumes of interest analyzed.

Name	Description	Voxel size (μm)	Size in voxels	Volume (mm^3)
BDF_1a	Well-developed fault; sandstone	1.37	$500 \times 500 \times 500$	0.32
BDF_1b	Well-developed fault; sandstone	1.37	$900 \times 900 \times 620$	1.29
BDF_2a	Incipient fault; sandstone	1.37	$1200 \times 1200 \times 620$	2.30
BDF_2b	Incipient fault; sandstone	1.37	$1200 \times 1200 \times 1100$	4.07
BDF_6a	Well-developed fault; silty sand	1.37	$1200 \times 1200 \times 620$	2.30
BDF_6b	Well-developed fault; silty sand	1.37	$1150 \times 1150 \times 620$	2.11
BDF_7a	Complex fault; sandstone	1.37	$1200 \times 1200 \times 620$	2.30
BDF_7b	Complex fault; sandstone	1.37	$1200 \times 1200 \times 620$	2.30
BDF_9a	Well-developed fault; sandstone	1.80	$1200 \times 1200 \times 620$	5.21
BDF_11a	Complex fault; sandstone	1.25	$1200 \times 1200 \times 680$	1.91
BDF_11b	Complex fault; sandstone	1.25	$680 \times 680 \times 680$	0.61
BDF_12a	Complex fault; silty gouge	1.80	$620 \times 620 \times 620$	1.39
BDF_12b	Complex fault; silty gouge	1.80	$620 \times 620 \times 620$	1.39
BDF_12c	Complex fault; silty gouge	1.80	$620 \times 620 \times 620$	1.39
SS_1a	Complex fault; sandstone	1.37	$1200 \times 1200 \times 620$	2.30
SS_1b	Complex fault; sandstone	1.37	$1200 \times 1200 \times 620$	2.30
SS_2a	Complex fault; sandstone	1.80	$620 \times 620 \times 620$	1.39
SS_2b	Complex fault; sandstone	1.80	$620 \times 620 \times 620$	1.39
SS_3a	Complex fault; shale gouge	1.37	$500 \times 500 \times 500$	0.32
SS_3b	Complex fault; shale gouge	1.37	$620 \times 620 \times 620$	0.61

- (ii) Specific surface area, S_v (mm^{-1}): the surface of pores divided by the total volume of pores
- (iii) Euler characteristic, Eu. Ch. (mm^{-3}): for the purpose of this paper, the Euler characteristic is a connectivity index for the 3D pore network [94]. The value of the Euler characteristic tends to be higher and positive when the number of the pores not connected to each other exceeds the number of connected pores. On the contrary, it tends to be lower and sometimes negative when the connectivity of the pore network increases

4. Results

4.1. Field-Based Permeability Measurements. Average permeability values in the host rock of different lithofacies varied according to values in Table 3. In clay beds, values range from 0.0046 to 0.0433 D. Silt beds and fine sandstone values vary over two orders of magnitude, the former at 0.0101 to 0.864 D and the latter 0.093 to 0.485 D. For the most part, sandstone beds vary over one order of magnitude. Medium sandstone varies from 0.366 to 3.088 D. Coarse sandstone varies from 0.738 to 2.268 D. Permeability values in conglomerates do not vary significantly from 2.085 to 3.088 D. Heterolithic packages derive values ranging from 0.101 to 1.849 D. This variability is most likely from the introduction of sand into the silt beds.

For a better visualization of the relative variation of permeability across the fault zone and the different lithologies, permeability values (normalized by the highest value

for each lithofacies) are represented in graphs versus the distance to the fault core and divided per lithofacies (Figures 4–6). The results are also divided by the fault architecture classified as follows: (i) incipient, (ii) well-developed, and (iii) complex faults.

4.1.1. Incipient Faults. In the two analyzed faults, a different behavior of the normalized permeability was observed. In the fault FIE (Figure 4(a)), characterized by a single plane and an evenly thick package distribution, the permeability in the damage zone tends to decrease towards the fault. All the lithofacies show similar results. However, it is less evident for the microconglomeratic facies. Whereas in the fault FIU (Figure 4(b)), characterized by different segments and unevenly thick package distribution, the permeability within the damage zone shows differing trends. In other words, the permeability could increase or decrease towards the fault. This trend seems related to the architecture of the fault, which means that increments of permeability are associated with the presence of linkage zones in the fault segments.

Regarding the fault core in fault FIE, fault core permeability values decrease. In the clay bed, permeability levels ranged from 0.005 to 0.015 D (Figure 4(e)). In coarse sandstone, values are an order to two orders of magnitude greater, spanning from 0.240 to 1.762 D. In the case of fault FIU, fault core permeability values are more variable. In heterolithic successions with a large influence of silt, values range from 0.001 to 0.036 D (Figure 4(f)). In the fault core associated with medium sandstone beds, values are highly variable,

TABLE 3: Table of average porosity, and pore size of the 7 main facies and 2 faults that produced different types of fault core along the same plane.

Sample	Lithology	Structural domain	Porosity (%)	Pore size (μm)	Average permeability (D)
BDF_1A	Siltstone/medium sandstone	<i>Host</i>	14.74	0.087	0.0162
BDF_1B	Siltstone/medium sandstone	<i>Host</i>	12.55	0.072	0.2925
BDF_1C	Fine sandstone	<i>Host</i>	5.62	0.26	0.0661
SM_A	Fine sandstone w/heavy lithics	<i>Host</i>	17.85	0.42	0.145
SM_L	Medium sandstone	<i>Host</i>	18.39	0.22	0.1126
SM_D	Medium sandstone	<i>Host</i>	8.99	0.21	0.1668
SM_F	Coarse sandstone	<i>Host</i>	10.14	1.22	0.0979
SSI_HBC	Fault breccia clast	<i>Fault</i>	14.89	0.55	0.0351
SSI_HBV	Vein inside fault breccia	<i>Mineralized breccia</i>	10.62	0.28	0.0024
SM1_2S	Shale gouge	<i>Fault</i>	4.46	0.033	0.0039
SM1_2	Sandy breccia	<i>Fault</i>	4.29	19.48	0.1577

ranging from 0.088 to 2.268 D. Coarse sandstone is relatively high and stable, ranging from 1.531 to 2.468 D.

4.1.2. Well-Developed Faults. When comparing permeability values across well-developed faults in evenly and unevenly thick layers, a stark contrast is apparent (Figures 5(a) and 5(b), respectively). In evenly thick layers, permeability values decrease at the fault core with respect to the damage zone (Figure 5(c)). In unevenly thick layers, permeability values increase (Figure 5(d)). In the fault core, the lowest values are found in the silt layers, from 0.008 D to 0.072 D (Figure 5(e)). In contrast, silt beds with a large percentage of silt (>45%) have up to 2 orders of magnitude larger values, 1.7133 to 4.834 D. The fault core associated with fine sand and coarse sand has about the same values, ranging from 0.642 to 1.408 D (Figures 5(e) and 5(b), respectively).

In evenly thick layers, relative fault core values were lower in respect to unevenly thick layers. In the fault core associated with clay beds, permeability values range from 0.004 to 0.0171 D (Figure 5(e)). In breccia, values remain relatively stable, from 2.085 to 4.705 D. In gouge associated with sand and silt beds, values are intermediate, from 0.157 to 0.955 D.

4.1.3. Complex Faults. Complex faults show a decrease in permeability across fault zones in evenly layered packages and an increase in across fault zones in unevenly thick layers (Figures 6(a) and 6(b), respectively). For faults cutting unevenly distributed layers, the fault core in silt with lithics ranges from 1.713 to 4.838 D, whereas in relatively pure silt, values are much lower at 0.008 to 0.072 D. In fine sand, values span an order of magnitude from 0.641 to 1.408 D (Figure 6(e)). Coarse sandstone is similar at 0.574 to 1.258 D (Figures 6(e) and 6(f), respectively).

In evenly thick packages, permeability values are overall much lower. The largest values are found in gouge associated with sand layers, with values from 0.048 to 1.369 D (Figure 6(f)). Intermediate values are found in gouge associated with heterolithic successions, as values range from 0.0900 to 0.1867 D. The lowest values are found in clay, with values ranging from 0.003 D to 0.017 D.

4.2. Laboratory-Based Porosity and Grain Size Distribution. Pore size ranges from averaged 0.080 μm for siltstones and 0.340 μm for fine sandstones. In medium sandstone, the values are quite different, from 8.99 to 18.39 μm . Coarse sandstone pore size is 10.14 μm . In faulted material, intermediate values are found in crushed breccia (0.55 μm). Pore size is smallest in shale gouge (0.033 μm) and largest in breccias associated with sandstone beds (19.48 μm). Details of the pore size distribution are in Figures 7 and 8.

Porosity values found in the host rock vary, even within the same grain size (Table 3, Figures 7 and 8). In host rock, fine sandstone with a high amount of lithics has a higher value of porosity (17.85%), in relation to relatively “clean” fine sandstone (5.62%). The porosity of medium sandstone beds varies greatly, from 18.39% to 8.99%. Coarse sandstone beds have a relatively intermediate porosity of 10.14%. In the fault core, fault breccias have the highest amount of porosity (14.89%) whereas the gouges had relatively similar values (4.46% and 4.29%).

4.3. Microstructural and Mineralogical Analysis of Host Rock. Thin section analysis revealed microstructures and mineralogy of sampled lithologies present (Figure 9). Claystones exhibit weak to moderate iso-orientation to bedding (Figure 9(a)) and are composed mainly of quartz and feldspar crystals and/or mica grains. Siltstone facies are generally moderately sorted, subangular to subrounded (Figure 9(b)). They are composed of a mosaic of very closely packed quartz and feldspar detrital grains and authigenic crystals. White mica is common. Brownish to gray limonite groundmass fills the intercrystalline space and occurs as sparse nodules and as rust red or brownish impregnations/coatings on quartz and feldspar crystals. Numerous tiny limonite veins occur as well, surrounded by limonite halos that fill the host rock. Thin sections taken from fine sandstone consist mostly of detrital quartz (Figure 9(c)). Grains are generally subangular to subrounded and closely packed. Sorting is moderate. Several white mica flakes occur, and their iso-orientation forms a subtle layering. Brownish limonite groundmass fills the intergranular space. Medium sandstones in the studied areas

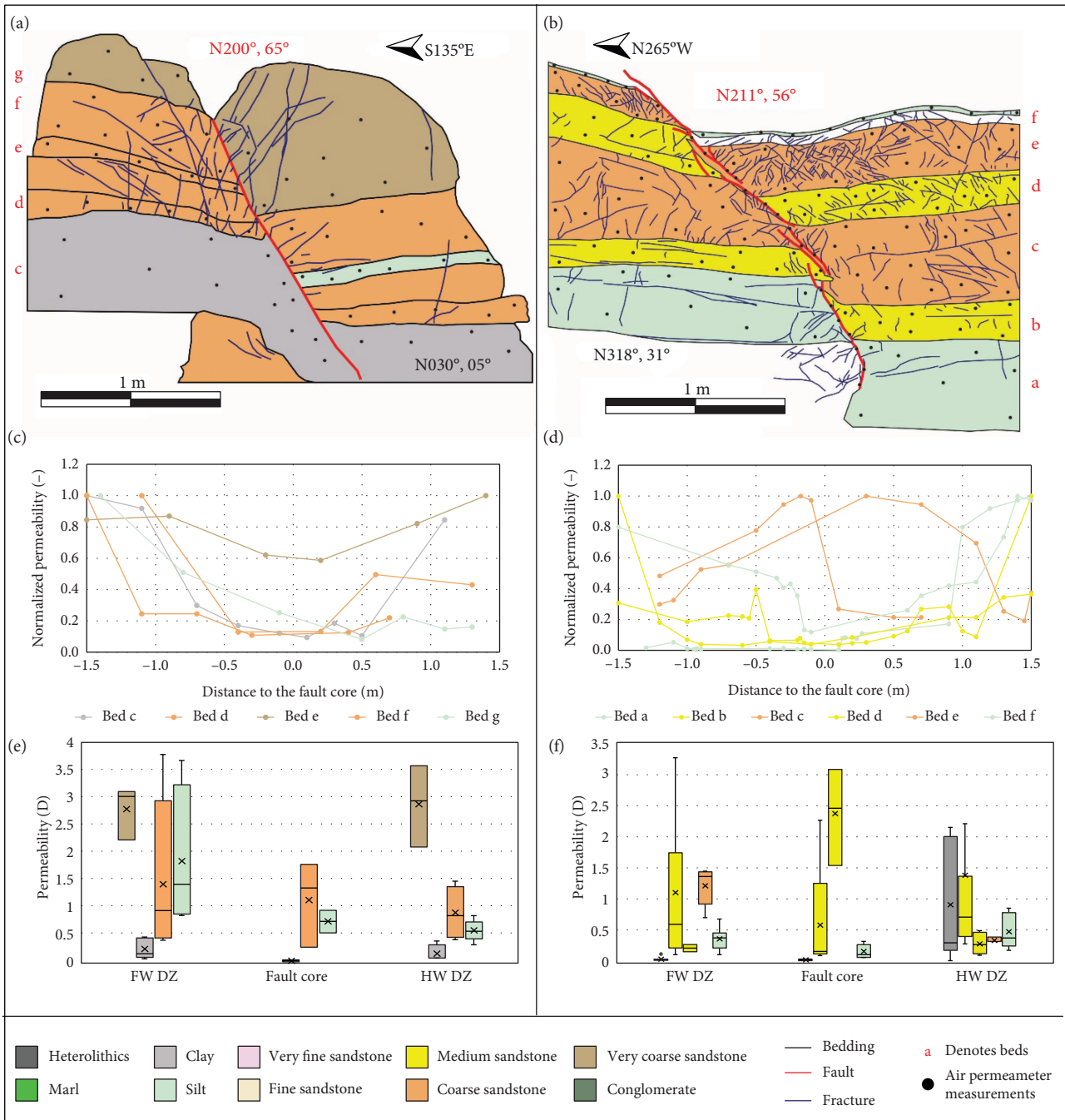


FIGURE 4: Permeability across incipient faults in different styles of multilayer package. Fault orientation is denoted in right hand rule with red text, whereas bed orientation is in black text: line drawings (a) of the FIE fault, which cuts through packages of evenly distributed clay layers and (b) the FIU fault, which cuts through packages with unevenly distributed clay layers. Fault orientation is denoted in right hand rule with red text, whereas bed orientation is in black text; permeability normalized for bed thickness for the (c) FIE fault and (d) FIU fault; variation of permeability measurements shown in a box and whisker plot, in order to show the high variability across the damage zone in the hanging wall (HW DZ), the fault core, and the damage zone of the footwall (FW DZ) in (e) the FIE fault and (f) the FIU fault. Color meaning is denoted in the legend below.

consist mostly of detrital quartz (generally monocrystalline), and feldspars (K-feldspars and plagioclase), as well as authigenic minor white mica (Figure 9(d)). Grains are subangular to subrounded and closely packed. Sorting is poor to moderate. Brownish limonite groundmass fills the intergranular

space. Coarse-grained sandstones consist of detrital quartz (both mono- and polycrystalline), feldspars, and rock fragments (Figure 9(e)). Conglomerate grains are subangular and closely packed with a poor sorting (Figure 9(f)). Brownish limonite groundmass fills the intergranular space.

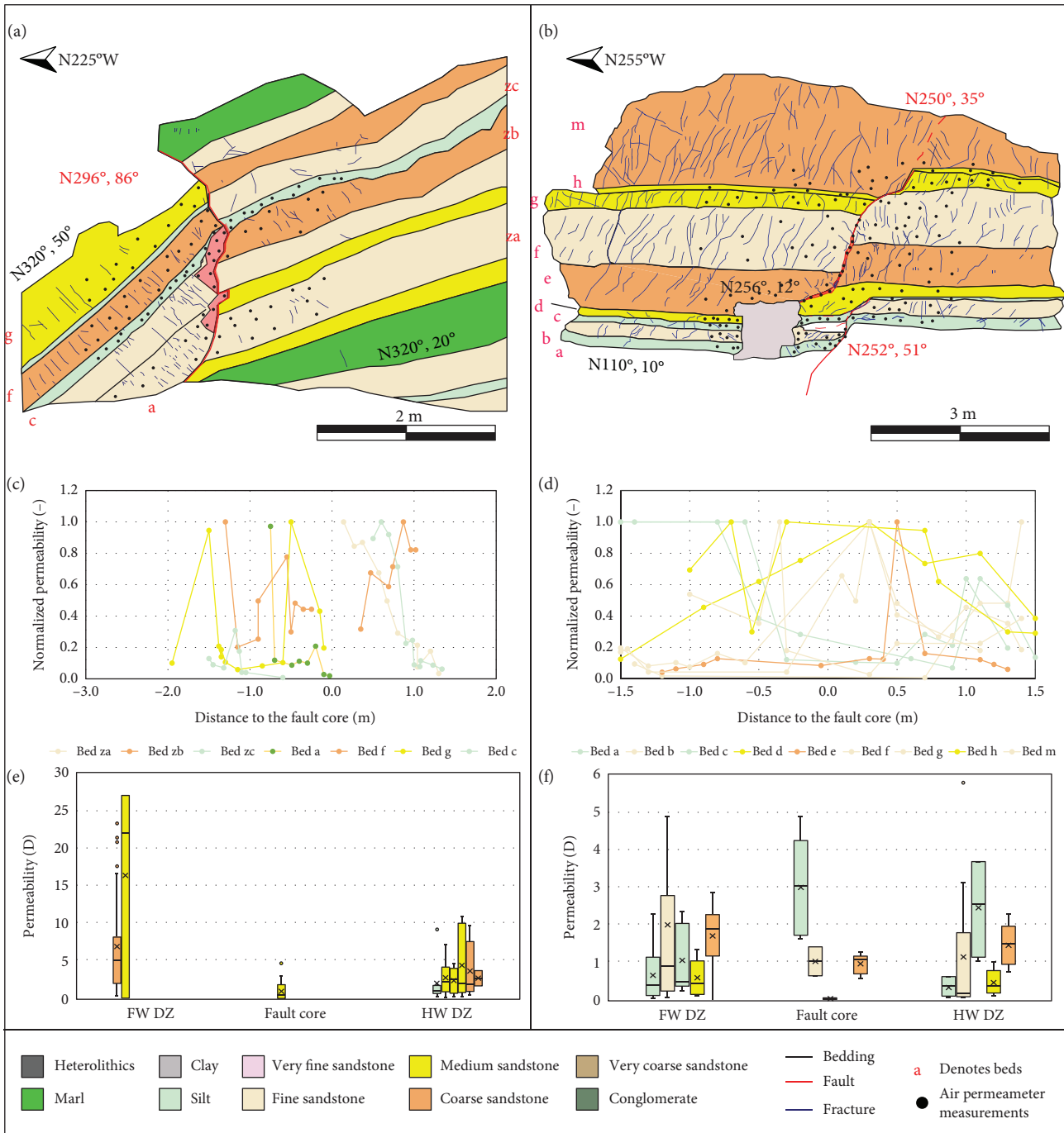


FIGURE 5: Permeability across well-developed faults in different styles of multilayer package. Fault orientation is denoted in right hand rule with red text, whereas bed orientation is in black text: line drawings of (a) the FWE fault, which cuts through packages of evenly distributed clay layers, and (b) the FWU fault, which cuts through packages with unevenly distributed clay layers. The grey block is representative of travertine deposit that covers the outcrop; permeability normalized for bed thickness for (c) the FWE fault and (d) the FWU fault; variation of permeability measurements shown in a box and whisker plot, in order to show the high variability across the damage zone in the hanging wall (HW DZ), the fault core, and the damage zone of the footwall (FW DZ) in (e) the FWE fault and (f) the FWU fault. Color meaning is denoted in the legend below.

consist of detrital quartz (both mono- and polycrystalline), feldspars, and rock fragments (mostly quartz-feldspar crystalline rocks), as well as authigenic rare white mica. Except for mica flakes, grains are subangular and closely packed,

and overall sorting is poor. There is evidence of intergranular pressure solution (microstylolites) on boundaries of some quartz grains. Brownish limonite groundmass fills the intergranular space.

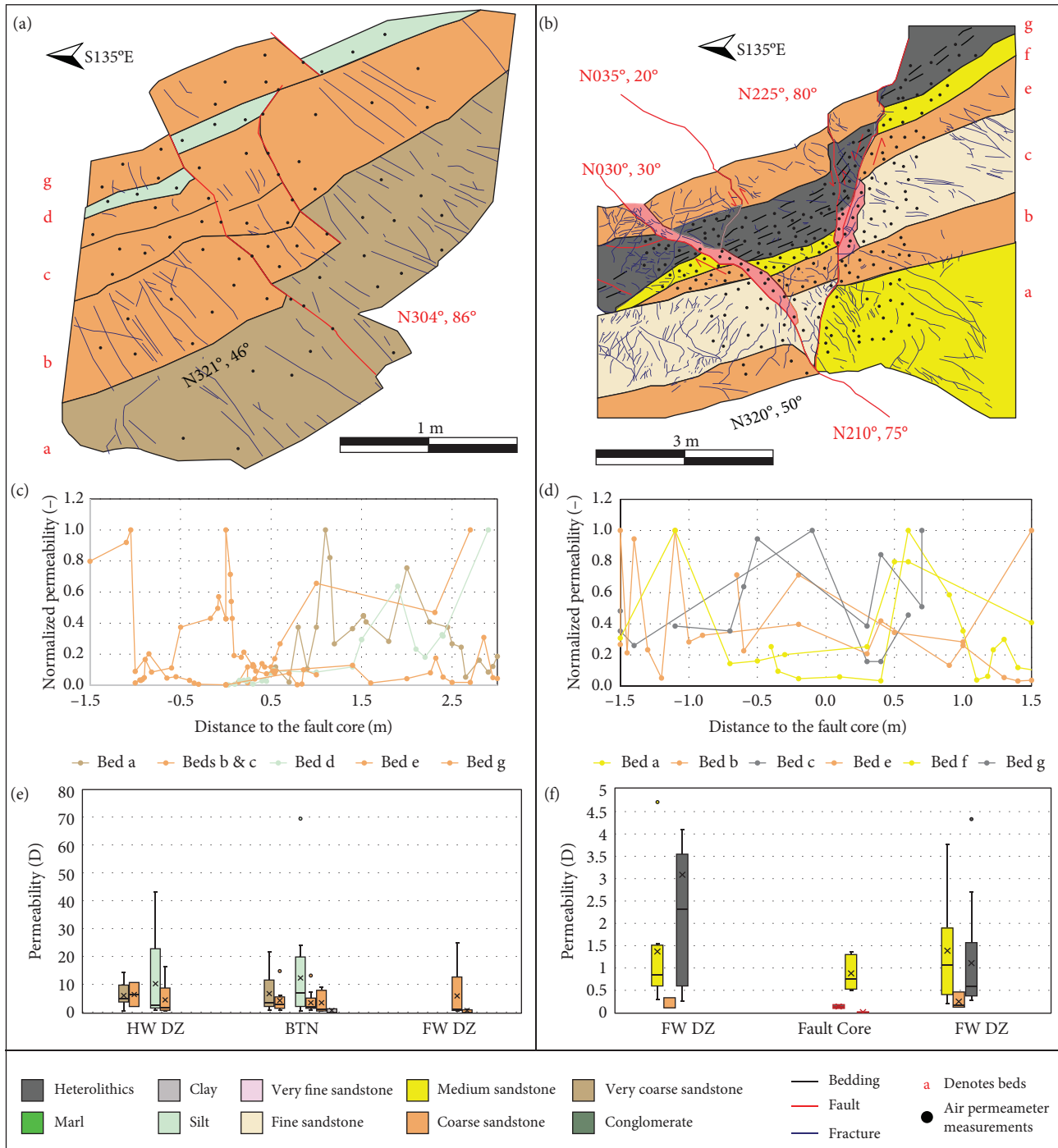


FIGURE 6: Permeability across complex faults in different styles of multilayer package. Fault orientation is denoted in right hand rule with red text, whereas bed orientation is in black text: line drawings of (a) the FCE faults, which cut through packages of evenly distributed clay layers, and (b) the FCU faults, which cut through packages with unevenly distributed clay layers; permeability normalized for bed thickness for (c) the FCE fault and (d) the FCU fault; variation of permeability measurements shown in a box and whisker plot, in order to show the high variability across the damage zone in the hanging wall (HW DZ), the fault core between the faults (BTN), and the damage zone of the footwall (FW DZ) in (e) the FCE fault and (f) the FCU fault. Color meaning is denoted in the legend below.

4.4. Microstructural and Mineralogical Analysis of Fault Rock. Thin section analysis of the fault core made up of shale gouge shows a clear initiation of smear along a microfault (offset < 1 cm) (Figure 10(a)). There is also evidence of shale

injection around the matrix surrounding coarser-grained material. In thin section analysis of crushed breccia, the boundaries between breccia clasts and interstitial limonite are quite sharp (Figure 10(b)). The angular clasts of

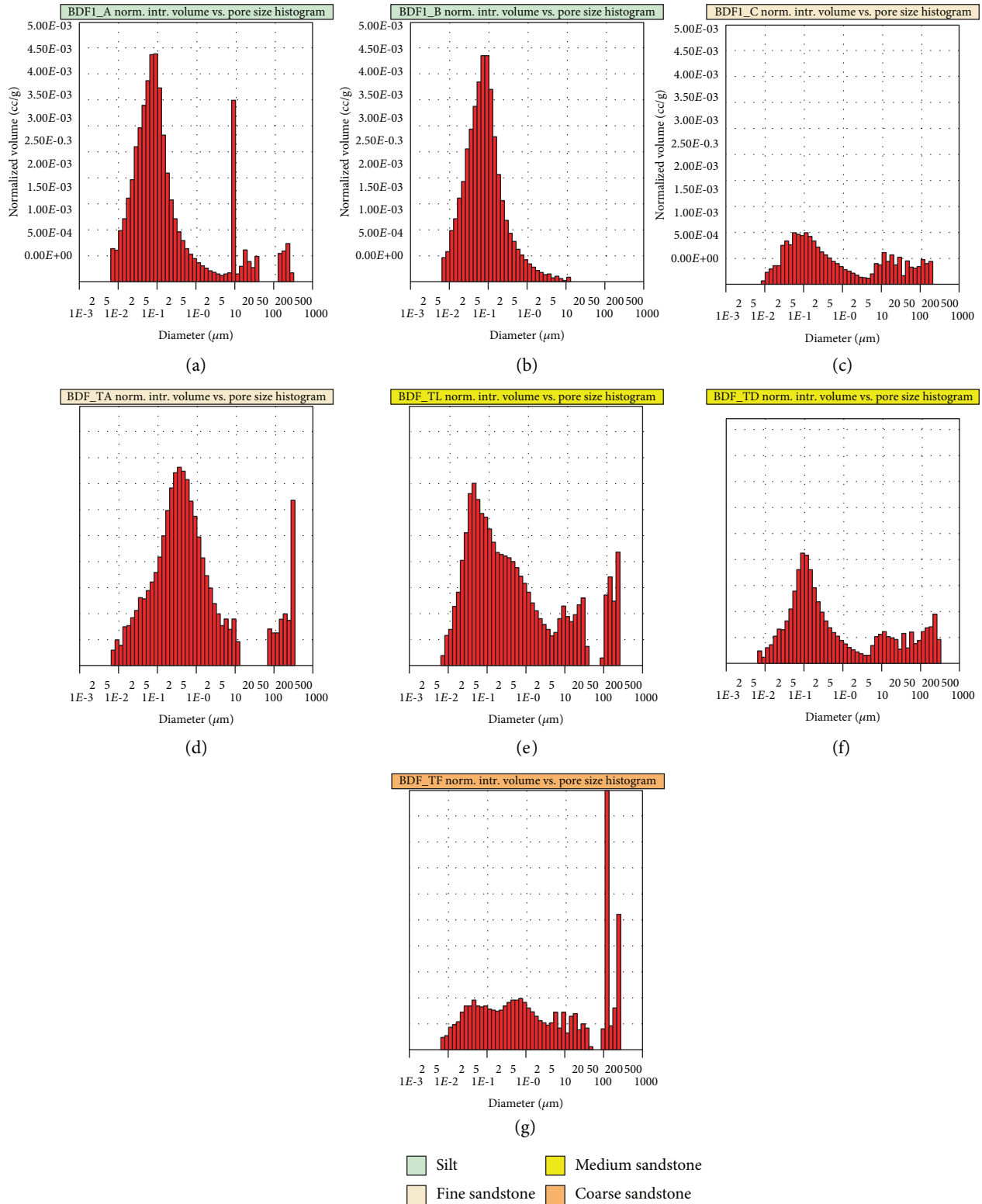


FIGURE 7: Results of Hg-intrusion pore size distribution analysis of host rock. Color in title denotes grain size.

sandstone are made of closely packed grains with intergranular limonite, which also coats/impregnates some grains. Calcite crystals are coarse, from bladed at the patch boundaries to equant in the patch center, indicating the progressive filling of preexisting large voids suddenly created by the

brecciation. Calcite crystals were later partly dissolved with formation of small equant vuggy pores.

In cataclasites, there are several samples with parent rock of differing material, which show different characteristics (Figures 10(c)–10(e)). In cataclaste stemming from

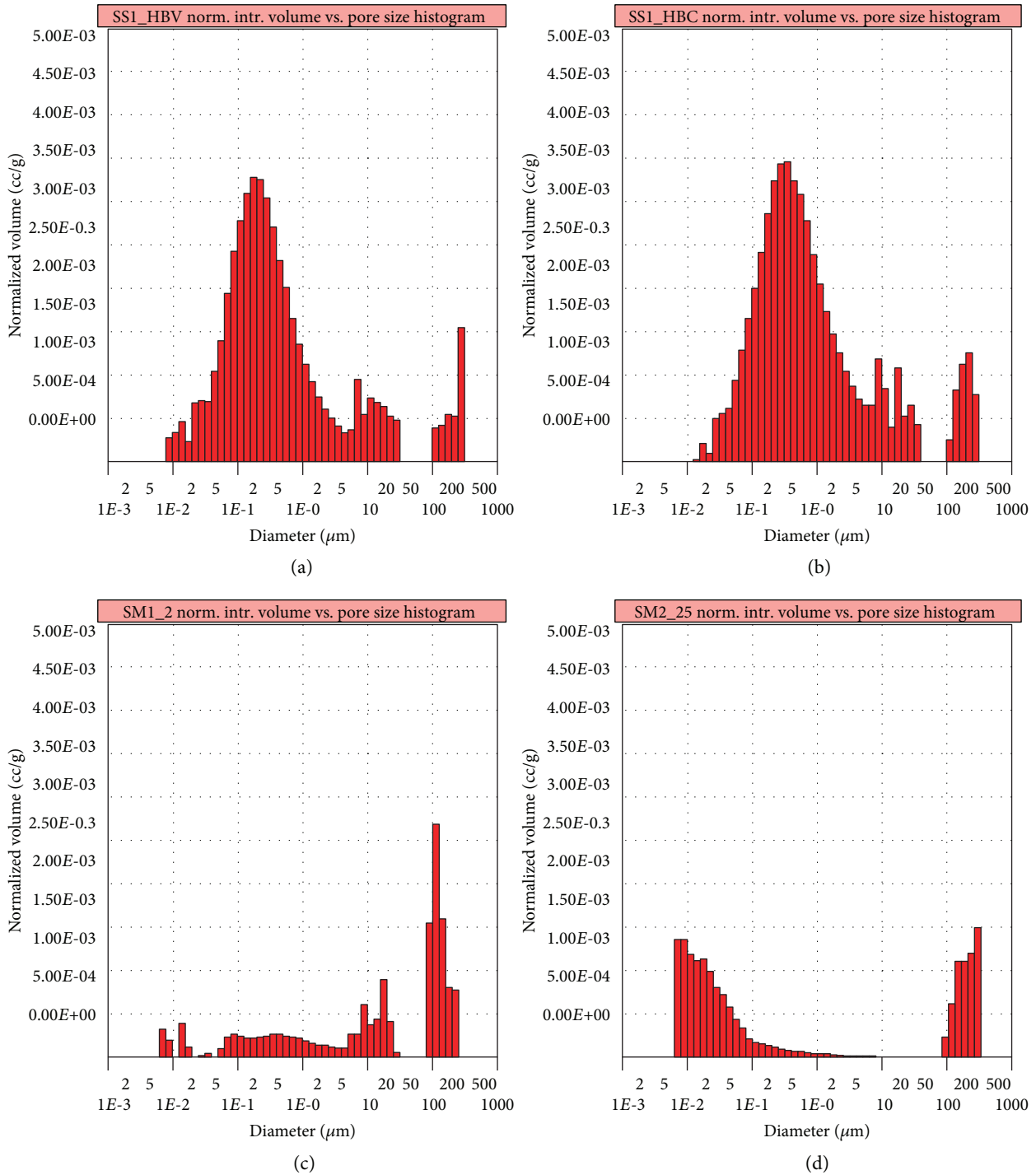


FIGURE 8: Results of Hg-intrusion pore size distribution analysis of fault rock.

heterolithic beds, cataclastic clasts can be distinguished by sharp changes in grain iso-orientation and zones richer in limonite between probable clasts. The rock is rich in white mica that is not iso-oriented parallel to the fault. Mica is mixed with both quartz and feldspar detrital grains (irregular “eroded” geometries and microfractures) and authigenic crystals of feldspar (euhedral, “rectangular shapes”) and quartz.

In cataclasites originating from sandstone, it is possible to distinguish sandstone clasts from interstitial sandstone (cataclastic matrix) (Figure 10(d)). Sandstone clasts are made of closely packed grains of detrital quartz (both poly- and monocrystalline) and feldspars, crystalline rock fragments, and rare mica flakes. The matrix also includes some grains made of limonite with floating detrital quartz and feldspar, suggesting multiple episodes of cataclasis and fault rock

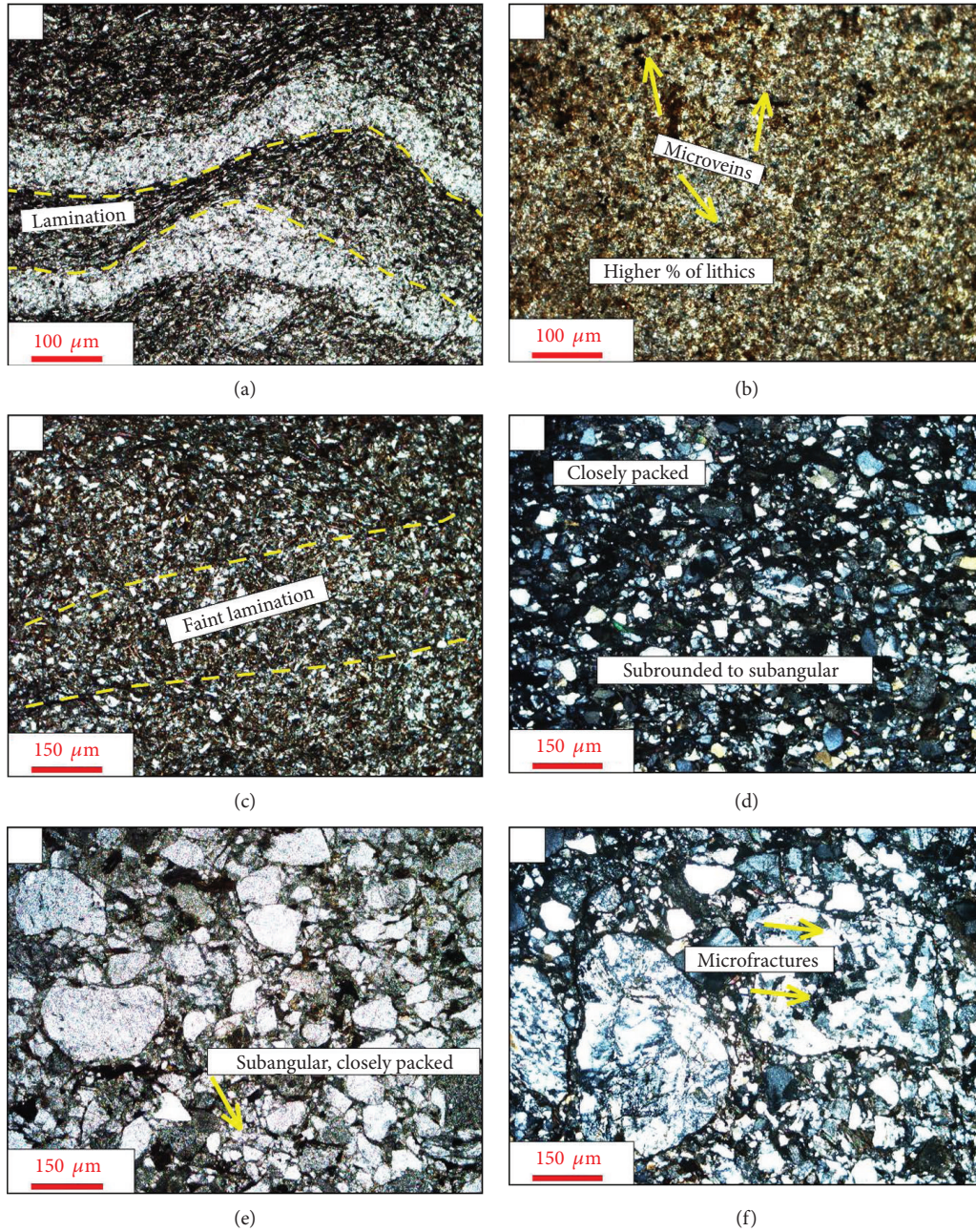


FIGURE 9: Thin sections of host rock found in the study area examples from: (a) claystone exhibiting plastic flow; fine sand; (b) siltstone with microfractures present; (c) fine sand with subtle layering iso-oriented; (d) medium sandstone; (e) coarse sandstone; (f) conglomerate.

mineralization. In another sample taken from a different cataclasite fault core, sandstone clasts made of closely packed grains are surrounded by interstitial sandstone made of relatively loosely packed grains of detrital quartz and feldspar with more intergranular brownish to rust red limonite than sandstone clasts (Figure 10(e)). In foliated cataclasite, loosely packed detrital quartz and feldspar grains are iso-oriented parallel to the fault and intergranular limonite is recognizable in the probable cataclasite matrix, although cataclasite clasts are not recognizable (Figure 10(f)). Large patches of dark brown to rust red limonite, mixed with later limpid equant calcite (mottled limonite/calcite texture), are

present in the probable cataclasite matrix, as well as small limonite veins.

4.5. *X-Ray MicroCT 3D Descriptive and Quantitative Analysis of Pore Network.* Synchrotron samples yield further insight into the microstructures developed within the fault core. The rock within the fault core can be highly variable due to the fact that they derive from different lithofacies and diagenesis processes (Table 4, Figures 11 and 12).

In order to evaluate the effect of both textural properties (Kozeny-Carman equation) and connectivity (Euler characteristic), both results have been plotted in a scatter graph

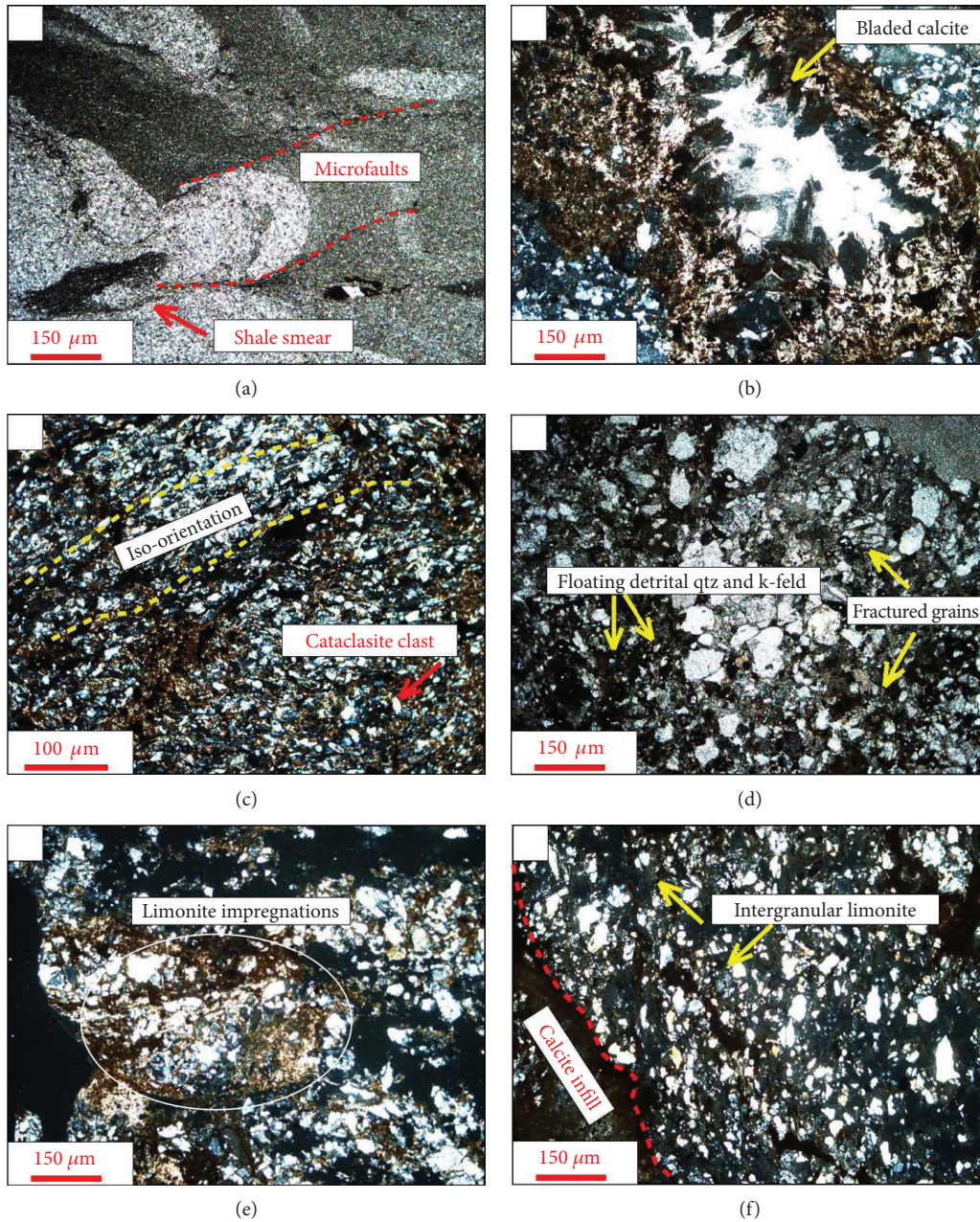


FIGURE 10: Thin sections cut from samples of fault core. (a) The darker parts are dominated by mica flakes and clay. Mica flakes have a tendency to iso-orientation and evidencing plastic flow within the lighter parts, which are made mainly of quartz and feldspar crystals and/or grains; (b) interstitial limonite between breccia clasts is rust red to dark brown (mottled color changes) and includes rare host rock-derived grains and patches of later calcite crystals in the middle of breccia clast interspaces; (c) cataclasite grains are barely distinguishable, both grains and crystals are fine sand to silt in size, and the interstitial spaces are filled by limonite that also coats/impregnates some grains and crystals; (d) interstitial sandstone is made of relatively loosely packed grains (detrital quartz and minor detrital feldspar, rock fragments, and mica) with more intergranular brownish to rust red limonite (also coating/impregnating some grains) than sandstone clasts; (e) fractured grains found in both clasts and matrix of the cataclasite; (f) grains iso-oriented parallel to the fault and with intergranular limonite are recognizable in the probable cataclasite matrix.

(Figure 11). In this graph, pervious rock samples, characterized by a higher porosity, wider pores (lower specific surface area), and better connectivity (lower Euler characteristic), are localized to the upper left area. Rock samples located to the right of the graph tend to have a poorly connected pore network (more impervious).

Sand-rich fault cores highly affected by dissolution tend to have the highest values of porosity, lowest of specific surface area, and lower Euler Characteristic (BDF_2a and SS_1a/b, Figures 12(a), 12(e), and 13(a)). Cementation is also present in some fault cores (Figure 12(d)), which drastically reduces the connectivity of the pore network. In the case of

TABLE 4: Results X-ray microCT 3D analysis of the pore network.

Name	ϕ_t (%)	S_v (mm^{-1})	Eu. ch. (mm^{-3})
BDF_1a	4.6	380.4	16003.4
BDF_1b	3.0	306.7	6532.2
BDF_2a	8.3	236.1	3831.9
BDF_2b	0.8	475.0	6486.8
BDF_6a	4.9	302.0	8823.6
BDF_6b	5.0	348.0	6988.5
BDF_7a	1.2	583.3	15308.2
BDF_7b	2.6	507.7	17519.1
BDF_9a	1.8	366.7	8067.4
BDF_11a	0.5	320.0	2502.4
BDF_11b	0.8	375.0	8797.2
BDF_12a	0.3	533.3	3679.1
BDF_12b	2.7	377.8	9949.3
BDF_12c	1.6	431.3	11936.7
SS_1a	8.7	287.4	2967.4
SS_1b	8.1	298.8	3953.8
SS_2a	2.2	381.8	10465.5
SS_2b	0.3	466.7	2181.9
SS_3a	1.9	431.6	13853.1
SS_3b	1.9	468.4	19135.4

Notes: ϕ_t : total porosity; S_v : specific surface area; Eu. Ch.: Euler characteristic.

silt- and clay-rich fault cores (Figures 12(f) and 13(b)), they are characterized by low porosity and very high values of Euler characteristics and specific surface area, indicating a pore network composed by isolated small pores (Figure 11).

In the samples from the Buca delle Fate (BDF) area, it was common to identify some microfractures. Protocataclastic material, characterized by microporosity, is also common and occasionally significant within the sample. Microfractures occasionally connect cataclastic zones. Samples BDF_1a and BDF_1b are characterized by a poorly connected pore network. Microfractures are present along with lithic material, like pyrites and mica. There are also microporosity areas related to diagenesis or protocataclasis. Sample BDF_2a has similar characteristics to BDF_1a and BDF_1b, but also contains evidence of a left-over vein after grain dissolution (Figure 12(a)). Some fractures present mineral precipitations connecting the opposite walls which validates the hypothesis of natural origin for most of the observed micro fractures. Sample BDF_2b is characterized by the presence of microfractures. There are some mineral growths within them, which can influence porosity. In some samples (BDF_6a and BDF_6b), possible shearing bands characterized by a higher porosity and connectivity (visually) were identified (Figure 12(b)). Some volumes characterized by microporosity are likely dissolution-related pore space. Samples BDF_7a and BDF_7b are characterized by grain size reduction. Most samples contain microfractures of varying intensity, along with grain size reduction and cataclasis (Figure 12(c)). A few samples show a high content of fine-grained material associated with cataclasis. Within the

volumes, dissolution of calcite also took place generating pores that are shaped like bladed calcite (sample BDF_9a) (Figure 12(d)). Some minerals like pyrites and/or other oxides are present within the samples. Sample BDF_11a, BDF_11b, and BDF_12a contain multiple microfractures with grain dissolution and minerals growing within the fractures, where oxidation is also present.

In the Sassoscritto (SS) samples, there are three prominent different textures and characteristics: (i) Samples SS_1a and SS_1b show well-defined grains and intergranular pore space, rare pore dissolution, and pyrites/oxides. Some grains present visible fractures (Figure 12(e)). (ii) Samples SS_2a and SS_2b show porous grains in sharp contact with clay material. (iii) Samples SS_3a and SS_3b are entirely composed of clay material (clay smeared material), characterized by isolated porosity (Figure 12(f)). Colored bands are present, possibly related to mineral alienation due to deformation.

5. Discussion

5.1. Permeability in the Damage Zone. The permeability in the damage zone may decrease or increase towards the main fault surface. This is likely due to the presence of microfractures, which is evidenced in thin section and synchrotron analysis. If microfractures are healed/sealed, matrix permeability decreases. These healed/sealed microfractures have been evidenced in thin sections, where microfractures may be filled by calcite and/or limonite. In some places, the limonite veins cut through calcite. There are also limonite halos in the intergranular space surrounding veins, with higher concentrations towards the vein as opposed to away from it, determined by the change in color from a dark red to light.

If microfractures are open, the matrix permeability may increase. This cannot be interpreted as a recent activity of the fault after exhumation as it is not general behavior and is normally associated with linkage areas. Therefore, it is interpreted that in certain areas of the fault zone, the differential stress allows the “recent” formation or opening of microfractures. Therefore, the cementation has not completely occluded the microfractures pore space. Fault architecture plays an important role in the distribution of these areas with higher matrix permeability. In an uneven distribution of the relative thickness, faults are normally composed by various segments and therefore more linkage areas. Of course, this behavior may vanish after the fault segments become totally connected. In the case of evenly thick packages, fault architecture is mainly characterized by a through-going plane; therefore, the permeability tends to decrease towards the main fault surface due to cementation.

5.2. Permeability in the Fault Core. While the composition of the fault cores in the study area can be highly variable, they are generally very immature and can be classified as protocataclastic. Therefore, the rocks within the fault core are highly related to the surrounding host rock in terms of composition, grain size, and hydraulic properties. Although clay smear is of common occurrence, sand size fault rock also occurs. In

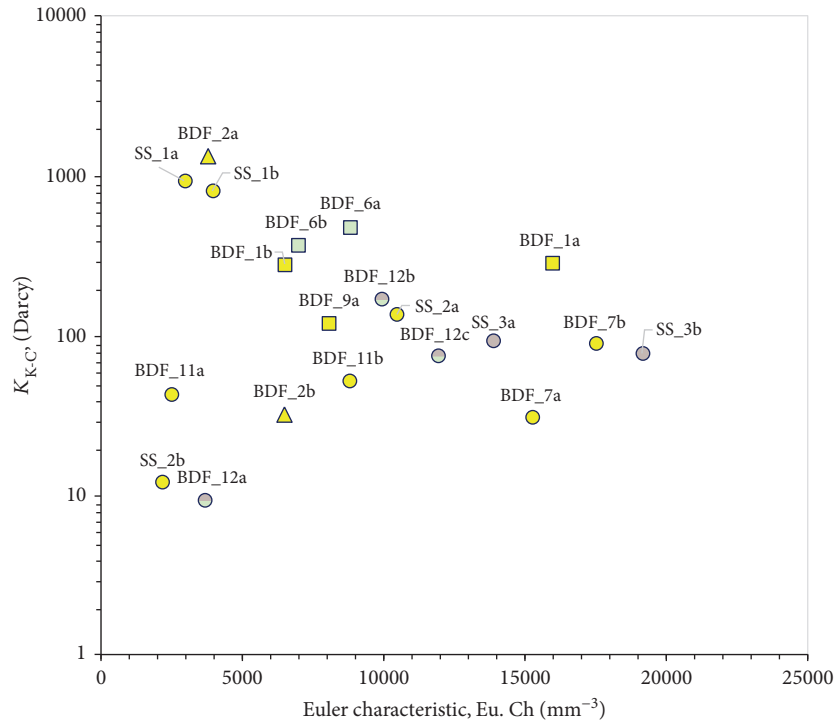


FIGURE 11: Scatter plot indicating the permeability estimates with the Kozeny-Carman equation (k_{K-C}) versus the Euler characteristic. For the Kozeny-Carman equation [92, 93], it was assumed that both the tortuosity (equal 1.5) and pore shape factor (equal 5) are constant. Rock samples with a higher permeability, wider pores, and better connectivity (more pervious) are localized to the upper left area. Rock samples located to the right of the graph tend to have a poorly connected pore network (more impervious). Description of the samples is located in Table 2. Detailed results in Table 4. Samples in bold can be observed in Figure 12.

general, sediments rich in clay are smeared roughly parallel to the fault plane, whereas sand sediments are deformed into blocks and patches. In consequence, fault core is variable in terms of porosity and permeability.

At the microscale, grain crushing, if present, might lead to an increment of the specific surface area and therefore a decrease in permeability [79]. However, the presence of microfractures may locally enhance the connectivity of the pore space and permeability. In general, samples are characterized by low connectivity (high values of Euler characteristic) due to a high degree of cementation (Figure 12(d)). However, it is expected that some micropores below the resolution of the images can connect the pore space and exert some minor contribution to permeability [79]. Clay-rich fault cores are less connected (highest values of Euler characteristic) and therefore less pervasive. Some samples (BDF_2a and SS_1a/b; Figures 12(a) and 12(e)) are characterized by an important dissolution that increases the porosity and reduces the specific surface area explaining some local enhancement of permeability.

Unevenly thick heterolithic beds, in general, have a relative increase of permeability at the fault core while those evenly thick show a decrease in permeability. This is likely due to the increased repetition of clay or silty clay layers. As more clay is introduced into the fault core, permeability decreases [11, 17, 95]. In evenly thick layers, permeability at the fault core was up to four orders of magnitude lower than permeability in the damage zone. In general, faults that cut

through clay layers with displacements larger than 4 m could experience a relative increase in permeability as smear continuity is lost, but in evenly thick layers of heterolithics, the influx of clay material “feeds” the smear and keeps permeability low [17, 96]. This factor is independent of fault offset, as faults with offsets lower than 2 m and as big as 30 m have the same results.

5.3. *Consequences to Fault Sealing.* In a fault zone, the damage zone is considered generally more permeable than the fault core due to the presence of fractures and fine-grained material, respectively. These interconnected fractures present in the damage zone facilitate fluid migration and storage and can also help the cementation process. The results of this study indicate that matrix permeability can decrease towards the main fault surface despite the expected increment of microfracture density. This may be attributed to the cementation of the microfractures near the once more permeable zone of the fault. Macrofractures observed in the outcrop were also cemented. Cementation may occur from different sources, as different kinds of cement (quartz, calcite, and limonite) are observed in the veins. Fault linkage zones can be characterized by a higher permeability possibly due to the presence of not cemented microfractures. These microfractures can be generated locally at low stress rates right after the last cementation event.

The fault core is shown to be variable in terms of the grain size of the fault rock and its thickness. Both elements

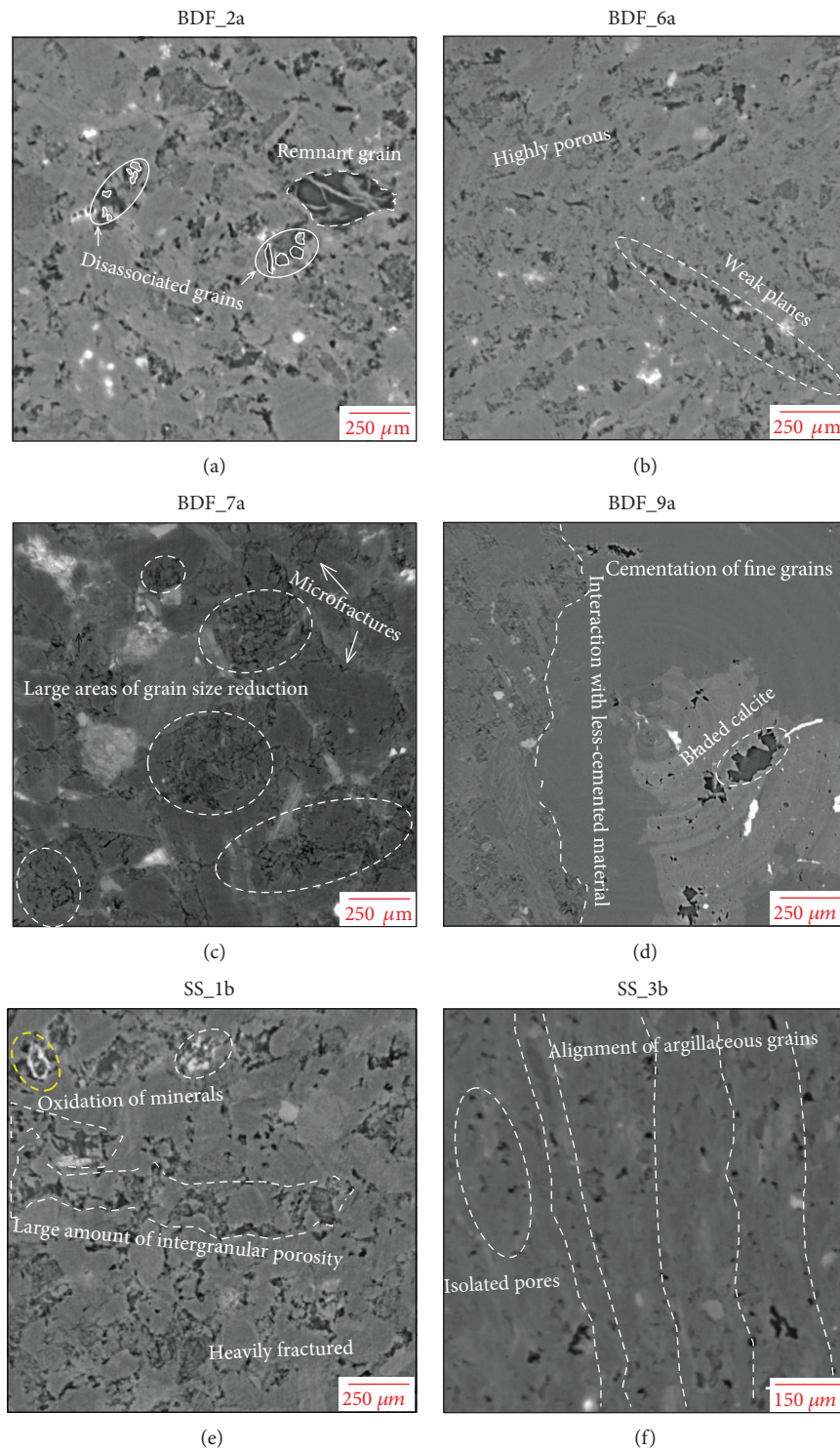


FIGURE 12: X-ray microCT images of some analyzed fault cores: (a) BDF_2a, sand-rich and affected by dissolution, (b) BDF_6a; silty sand fault core affected by both microfracturing and dissolution, (c) BDF_7a; sand-rich affected both microfracturing and dissolution, (d) BDF_9a; highly cemented sample, (e) SS_1b; sand-rich fault core highly affected by dissolution and microfracturing, and (f) SS_3b; clay-rich fault core with evidence of grain alignment. Description of the samples in Table 2.

have a significant impact on the final hydraulic behavior of the fault. The clay smear is perhaps the most important source of permeability reduction in the studied faults. The fine material in the smear is likely fed from the adjacent

shales and siltstones that form from the cataclasis process itself. These fault cores are composed sometimes entirely of lithic blocks of sandstones, which preserve or increase the original permeability. The sealing capacity of the faults

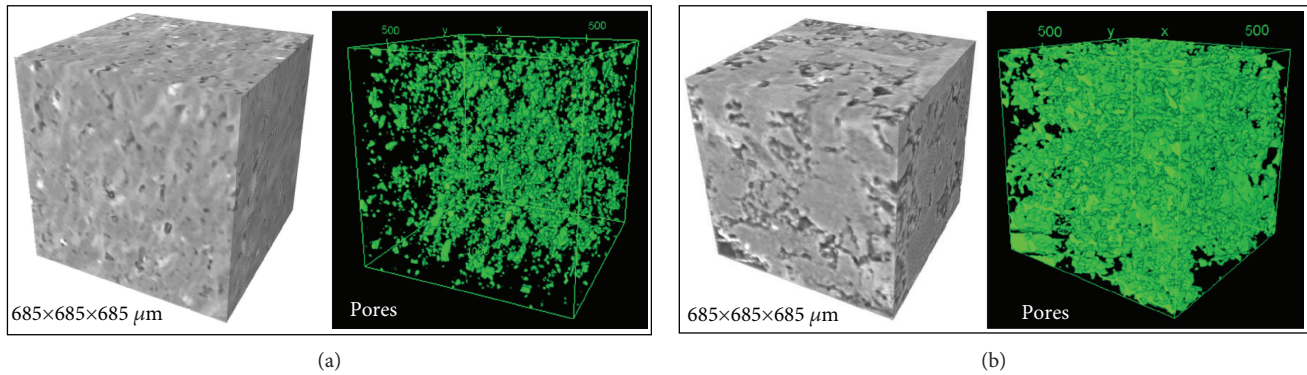


FIGURE 13: X-ray microCT 3D images of the main types of fault cores found in the study areas: (a) sand-rich fault core and (b) clay-rich fault core (characterized by clay smearing). The samples come from the same fault, which is located at the Sassoscritto area. The grey images correspond to the rendering of the 3D X-ray microCT images, whereas the green volumes to the right are the segmented pore space.

depends on whether the clay-rich fault core is present and the thickness of the fault core.

Although it is suggested that the width of the fault core is related to offset, at faults in the studied area, the fault core width was more associated with lithology [97, 98]. A change in the width of the fault core is usually accommodated for in the damage zone [99]; however, in faults studied at these locations, this is not necessarily true. Faults that passed through adjacent sandstone beds rarely exceeded a fault core width greater than 3 cm, regardless of offset and distribution of beds (evenly or unevenly thick beds). Faults that passed through heterolithic beds adjacent to sandstone created thicker fault cores, from 3 cm to 5 cm wide. Faults that passed through adjacent clay beds produced the widest fault cores, sometimes spanning up to 40 cm. At the studied sites, host rock competency influenced fault core width more than overall offset.

Considering all the elements, the faults with an ideal seal behavior (at least to the studied scale) correspond to faults within an evenly thick layer distribution. These faults are characterized by a clay-rich fault core and a cemented matrix near the main fault surface, which may guarantee a thick, low-permeability barrier zone. The fault with the worst sealing capacity corresponds to small-medium displacement hosted in unevenly thick layers. These faults present important linkage zones for fault segments characterized by relatively high permeability. Moreover, the existence of poorly deformed lithic block embeds in the fault core reduces its sealing efficiency.

6. Conclusions

In this paper, the sedimentological, stratigraphic, and structural controls on matrix permeability in a fault zone were analyzed. This study contributes to the better understanding of the petrophysical behaviors of natural reservoirs and how stratigraphic, sedimentological, and structural discontinuities in the rock may impact fluid flow across fault zones in different types of siliciclastic heterolithic packages.

In the studied faults, the damage zone is characterized by high cementation generally occluding both macrofractures

and microfractures (filled with quartz or calcite). The latter revealed a decrease in matrix permeability towards the main fault surface. In this case, a sort of cemented zone around the main fault surface may represent an important barrier for fluid flow. However, linkage zones, generally present in unevenly thick layers, may represent some increment of permeability in the matrix. This may be related to the presence of open microfractures in these zones.

Fault core permeability is mostly related to the rock feeding it. A higher amount of clay layers in evenly thick heterolithic packages increases the amount of clay material in the fault core, effectively lowering permeability. When the layers are evenly distributed, the clay particles feed the already present clay smear, extending its unbroken plane and creating a barrier to fluid flow. In unevenly thick packages, clay smear may still be present, but its connectivity is greatly decreased due to the larger influence of sand particles than clay. In unevenly thick layers, the damage zone remained the less efficient barrier to fluid flow. It is evident that the amount of clay layers and their distribution affect fluid flow across the fault, regardless of fault offset.

Data Availability

The data used to support the findings of this study are available from the corresponding author upon request.

Conflicts of Interest

The authors declare that they have no conflicts of interest.

Acknowledgments

This research was supported by the Reservoir Characterization Project (<http://www.rechproject.com>) and funded by Neptune Energy, Shell Italia E&P, and Total Italia E&P.

References

- [1] R. G. Walker, "Deep-water sandstone facies and ancient submarine fans: models for exploration for stratigraphic traps," *AAPG Bulletin*, vol. 62, no. 6, pp. 932–966, 1978.

- [2] L. Zhang, M. Pan, and H. Wang, "Deepwater turbidite lobe deposits: a review of the research frontiers," *Acta Geologica Sinica - English Edition*, vol. 91, no. 1, pp. 283–300, 2017.
- [3] P. Dromgoole, M. Bowman, A. Leonard, P. Weimer, and R. M. Slatt, "Developing and managing turbidite reservoirs – case histories and experiences: results of the 1998 EAGE/AAPG research conference," *Petroleum Geoscience*, vol. 6, no. 2, pp. 97–105, 2000.
- [4] M. Gainski, A. G. MacGregor, P. J. Freeman, and H. F. Nieuwland, "Turbidite reservoir compartmentalization and well targeting with 4D seismic and production data: Schiehallion Field, UK," *Geological Society, London, Special Publications*, vol. 347, no. 1, pp. 89–102, 2010.
- [5] R. H. Sibson, "Fault rocks and fault mechanisms," *Journal of the Geological Society*, vol. 133, no. 3, pp. 191–213, 1977.
- [6] R. J. Knipe, "Faulting processes and fault seal," in *Structural and Tectonic Modeling and its Application to Petroleum Geology*, R. M. Larsen, B. T. Larsen, H. Brekke, and E. Talleraas, Eds., pp. 325–342, Norwegian Petroleum Society Special Publications, 1992.
- [7] J. S. Caine, J. P. Evans, and C. B. Forster, "Fault zone architecture and permeability structure," *Geology*, vol. 24, no. 11, pp. 1025–1028, 1996.
- [8] C. Childs, T. Manzocchi, J. J. Walsh, C. G. Bonson, A. Nicol, and M. P. J. Schopfer, "A geometric model of fault zone and fault rock thickness variations," *Journal of Structural Geology*, vol. 31, no. 2, pp. 117–127, 2009.
- [9] D. R. Faulkner, C. A. L. Jackson, R. J. Lunn et al., "A review of recent developments concerning the structure, mechanics and fluid flow properties of fault zones," *Journal of Structural Geology*, vol. 32, no. 11, pp. 1557–1575, 2010.
- [10] Y. Pei, D. A. Paton, R. J. Knipe, and K. Wu, "A review of fault sealing behaviour and its evaluation in siliciclastic rocks," *Earth-Science Reviews*, vol. 150, pp. 121–138, 2015.
- [11] G. Yielding, P. Bretan, and B. Freeman, "Fault seal calibration: a brief review," *Geological Society, London, Special Publications*, vol. 347, no. 1, pp. 243–255, 2010.
- [12] M. Antonellini and A. Aydin, "Effect of faulting on fluid flow in porous sandstones: petrophysical properties," *AAPG Bulletin*, vol. 78, pp. 355–377, 1994.
- [13] A. Aydin, "Fractures, faults, and hydrocarbon entrapment, migration and flow," *Marine and Petroleum Geology*, vol. 17, no. 7, pp. 797–814, 2000.
- [14] R. G. Gibson, "Fault-zone seals in siliciclastic strata of the Columbus Basin, offshore Trinidad," *American Association of Petroleum Geologists Bulletin*, vol. 78, pp. 1372–1385, 1994.
- [15] J. R. Fulljames, L. J. J. Zijerveld, and R. C. M. W. Franssen, "Fault seal processes: systematic analysis of fault seals over geological and production time scales," *Norwegian Petroleum Society Special Publications*, vol. 7, pp. 51–59, 1997.
- [16] J. Schmatz, P. J. Vrolijk, and J. L. Urai, "Clay smear in normal fault zones – the effect of multilayers and clay cementation in water-saturated model experiments," *Journal of Structural Geology*, vol. 32, no. 11, pp. 1834–1849, 2010.
- [17] P. J. Vrolijk, J. L. Urai, and M. Kettermann, "Clay smear: review of mechanisms and applications," *Journal of Structural Geology*, vol. 86, pp. 95–152, 2016.
- [18] K. Corbett, M. Friedman, and J. Spang, "Fracture development and mechanical stratigraphy of Austin Chalk, Texas," *AAPG Bulletin*, vol. 71, pp. 17–28, 1987.
- [19] M. R. Gross, M. P. Fischer, T. Engelder, and R. J. Greenfield, "Factors controlling joint spacing in interbedded sedimentary rocks: integrating numerical models with field observations from the Monterey Formation, USA," *Geological Society, London, Special Publications*, vol. 92, no. 1, pp. 215–233, 1995.
- [20] W. Narr and J. Suppe, "Joint spacing in sedimentary rocks," *Journal of Structural Geology*, vol. 13, no. 9, pp. 1037–1048, 1991.
- [21] J. R. Shackleton, M. L. Cooke, and A. J. Sussman, "Evidence for temporally changing mechanical stratigraphy and effects on joint-network architecture," *Geology*, vol. 33, no. 2, pp. 101–104, 2005.
- [22] G. Strijker, G. Bertotti, and S. M. Luthi, "Multi-scale fracture network analysis from an outcrop analogue: a case study from the Cambro-Ordovician clastic succession in Petra, Jordan," *Marine and Petroleum Geology*, vol. 38, no. 1, pp. 104–116, 2012.
- [23] S. Tavani, F. Storti, F. Salvini, and C. Toscano, "Stratigraphic versus structural control on the deformation pattern associated with the evolution of the Mt. Catria anticline, Italy," *Journal of Structural Geology*, vol. 30, no. 5, pp. 664–681, 2008.
- [24] T. M. Mitchell and D. R. Faulkner, "The nature and origin of off-fault damage surrounding strike-slip fault zones with a wide range of displacements: a field study from the Atacama fault system, northern Chile," *Journal of Structural Geology*, vol. 31, no. 8, pp. 802–816, 2009.
- [25] H. M. Savage and E. E. Brodsky, "Collateral damage: evolution with displacement of fracture distribution and secondary fault strands in fault damage zones," *Journal of Geophysical Research*, vol. 116, no. B3, 2011.
- [26] J. E. Wilson, J. S. Chester, and F. M. Chester, "Microfracture analysis of fault growth and wear processes, Punchbowl Fault, San Andreas system, California," *Journal of Structural Geology*, vol. 25, no. 11, pp. 1855–1873, 2003.
- [27] I. Korneva, A. Ciloni, E. Tondi, F. Agosta, and M. Giorgioni, "Characterisation of the permeability anisotropy of Cretaceous platform carbonates by using 3D fracture modeling: the case study of Agri Valley fault zones (southern Italy)," *Italian Journal of Geosciences*, vol. 134, no. 3, pp. 396–408, 2015.
- [28] M. Zambrano, E. Tondi, I. Korneva et al., "Fracture properties analysis and discrete fracture network modelling of faulted tight limestones, Murge Plateau, Italy," *Italian Journal of Geosciences*, vol. 135, no. 1, pp. 55–67, 2016.
- [29] Z. K. Shipton, J. P. Evans, K. R. Robeson, C. B. Forster, and S. Snelgrove, "Structural heterogeneity and permeability in faulted eolian sandstone: implications for subsurface modeling of faults," *AAPG Bulletin*, vol. 86, pp. 863–883, 2002.
- [30] M. Antonellini, A. Ciloni, E. Tondi, M. Zambrano, and F. Agosta, "Fluid flow numerical experiments of faulted porous carbonates, Northwest Sicily (Italy)," *Marine and Petroleum Geology*, vol. 55, pp. 186–201, 2014.
- [31] H. Fossen, R. A. Schultz, Z. K. Shipton, and K. Mair, "Deformation bands in sandstone: a review," *Journal of the Geological Society*, vol. 164, no. 4, pp. 755–769, 2007.
- [32] E. Tondi, "Nucleation, development and petrophysical properties of faults in carbonate grainstones: evidence from the San Vito Lo Capo peninsula (Sicily, Italy)," *Journal of Structural Geology*, vol. 29, no. 4, pp. 614–628, 2007.
- [33] G. Ballas, H. Fossen, and R. Soliva, "Factors controlling permeability of cataclastic deformation bands and faults in porous

- sandstone reservoirs,” *Journal of Structural Geology*, vol. 76, pp. 1–21, 2015.
- [34] Q. J. Fisher and R. J. Knipe, “Fault sealing processes in siliciclastic sediments,” *Geological Society, London, Special Publications*, vol. 147, no. 1, pp. 117–134, 1998.
- [35] T. Ito and M. D. Zoback, “Fracture permeability and in situ stress to 7 km depth in the KTB scientific drillhole,” *Geophysical Research Letters*, vol. 27, no. 7, pp. 1045–1048, 2000.
- [36] K. Tadokoro and M. Ando, “Evidence for rapid fault healing derived from temporal changes in Swave splitting,” *Geophysical Research Letters*, vol. 29, no. 4, p. 6-1, 2002.
- [37] T. M. Mitchell and D. R. Faulkner, “Towards quantifying the matrix permeability of fault damage zones in low porosity rocks,” *Earth and Planetary Science Letters*, vol. 339–340, pp. 24–31, 2012.
- [38] Y. Nara, P. G. Meredith, T. Yoneda, and K. Kaneko, “Influence of macro-fractures and micro-fractures on permeability and elastic wave velocities in basalt at elevated pressure,” *Tectonophysics*, vol. 503, no. 1–2, pp. 52–59, 2011.
- [39] W. F. Brace, “Brittle fracture of rocks,” in *State of Stress in the Earth’s Crust*, W. R. Judd, Ed., pp. 110–178, Elsevier, New York, NY, USA, 1964.
- [40] C. H. Scholz, “Microfracturing and the inelastic deformation of rock in compression,” *Journal of Geophysical Research*, vol. 73, no. 4, pp. 1417–1432, 1968.
- [41] M. H. Anders, S. E. Laubach, and C. H. Scholz, “Microfractures: a review,” *Journal of Structural Geology*, vol. 69, pp. 377–394, 2014.
- [42] K. Mizoguchi and K. Ueta, “Microfractures within the fault damage zone record the history of fault activity,” *Geophysical Research Letters*, vol. 40, no. 10, pp. 2023–2027, 2013.
- [43] M. Boccaletti, F. Calamita, G. Deiana et al., “Migrating foredeep-thrust belt systems in the northern Apennines and Southern Alps,” *Palaeogeography, Palaeoclimatology, Palaeoecology*, vol. 77, no. 1, pp. 3–14, 1990.
- [44] G. Gandolfi and L. Paganelli, “Il “Macigno costiero” fra La Spezia e Grosseto,” *Giornali Geologiche*, vol. 54, no. 1, pp. 163–179, 1992.
- [45] F. Mostardini and S. Merlini, *Appennino Centro-Meridionale. Sezioni geologiche e proposta di modello strutturale*, vol. 24, Memorie della Società Italiana, 1986.
- [46] E. Patacca and P. Scandone, “Post-tortonian mountain building in the Apennines,” in *Advances in Earth Science Research*, A. Boriani, M. Bonafede, G. B. Piccardo, and G. B. Vai, Eds., vol. 80, pp. 157–176, Atti Conv. Accademia dei Lincei, 1989.
- [47] L. Carmignani, P. Conti, G. Cornamusini et al., “Geological map of Tuscany (Italy),” *Journal of Maps*, vol. 9, pp. 487–497, 2013.
- [48] Istituto Superiore per la Protezione e la Ricerca Ambientale, *Carta Geologica D’Italia, Agropoli Foglio 502, map, scale 1:10000*, Napoli, 1960.
- [49] G. Gasperi, “Geologia del promontorio di Piombino (Livorno),” *Memorie della Società Italiana*, vol. 7, pp. 11–28, 1968.
- [50] E. Mutti and F. Ricci Lucchi, “Le torbiditi dell’appennino settentrionale: Introduzione all’analisi di facies,” *Memorie Società Geologica Italiana*, vol. 11, pp. 161–199, 1972.
- [51] R. Catanzariti, D. Rio, S. Chicchi, and G. Plesi, *Eta’ e biostratigrafia a Nannofossili calcarei delle Arenarie di M. Modino e del Macigno nell’alto Appennino reggiano-modense*, vol. 56, Memorie Descrittive Carta Geologica d’Italia, 1991.
- [52] A. Brogi, “Bowl-shaped basin related to low-angle detachment during continental extension: the case of the controversial Neogene Siena Basin (central Italy, Northern Apennines),” *Tectonophysics*, vol. 499, no. 1–4, pp. 54–76, 2011.
- [53] G. Cornamusini, F. Elter, and F. Sandrelli, “The Corsica-Sardinia Massif as source area for the early northern Apennines foredeep system: evidence from debris flows in the “Macigno costiero” (Late Oligocene, Italy),” *International Journal of Earth Sciences*, vol. 91, no. 2, pp. 280–290, 2002.
- [54] F. Mazzarini, G. Corti, P. Manetti, and F. Innocenti, “Strain rate and bimodal volcanism in the continental rift: Debre Zeyt volcanic field, northern MER, Ethiopia,” *Journal of African Earth Sciences*, vol. 39, no. 3–5, pp. 415–420, 2004.
- [55] G. Cornamusini, *An Integrated Approach to the Study of a Foredeep Basin: Lithostratigraphy, Sedimentology, Petrography and Nannofossils Biostratigraphy of the Southern Tuscan Macigno Turbidites, Northern Apennines, Italy. Abstract 15*, I.A.S. Congress, Alicante, Spain, 1998.
- [56] P. Orlandi, G. Cortecchi, G. Protano, and F. Riccobono, “Mineral assemblages, stable isotopes and fluid inclusions in ore veins from the Macigno Formation at Calafuria (Livorno Mountains, northern Tuscany, Italy),” *Periodico di Mineralogia*, vol. 75, no. 1, pp. 73–84, 2006.
- [57] R. Di Giulio and R. Valloni, “Sabbie e areniti, analisi ottica e classificazione: Analisi microscopica delle areniti terrigene: Parametri metrologici e composizionali modelli,” *Acta Naturalia Ateneo Parmense*, vol. 28, pp. 55–101, 1992.
- [58] G. Cornamusini and A. Costantini, “Sedimentology of a Macigno turbidite section in the Piombino-Baratti area (northern Apennines, Italy),” *Giornali Geologi*, vol. 59, pp. 129–141, 1997.
- [59] F. O. Amore, G. Bonardi, G. Ciampo, P. De Capoa, V. Perrone, and L. Sgrosso, “Relazioni tra “Flysch interni” e domini appenninici: reinterpretazione delle formazioni di Pollica, San Mauro e Albidona nel quadro della evoluzione inframiocenica delle zone esterne appenniniche,” *Memorie della Società Geologica Italiana*, vol. 41, pp. 285–297, 1998.
- [60] R. W. H. Butler and W. D. McCaffrey, “Structural evolution and sediment entrainment in mass-transport complexes: outcrop studies from Italy,” *Journal of the Geological Society*, vol. 167, no. 3, pp. 617–631, 2010.
- [61] A. Cammarosano, G. Cavuoto, M. Danna et al., “Nuovi dati e nuove interpretazioni sui flysch terrigeni del Cilento (Appennino meridionale, Italia),” *Bollettino della Società Geologica Italiana*, vol. 119, pp. 395–405, 2004.
- [62] M. Fonesu, P. Haughton, F. Felletti, and W. McCaffrey, “Short length-scale variability of hybrid event beds and its applied significance,” *Marine and Petroleum Geology*, vol. 67, pp. 583–603, 2015.
- [63] G. Cavuoto, L. Martelli, G. Nardi, and A. Valente, “Depositional systems and architecture of Oligo-Miocene turbidite successions in Cilento (Southern Apennines),” *GeoActa*, vol. 3, pp. 129–147, 2005.
- [64] S. Vitale, S. Ciarcia, S. Mazzoli, A. Iannace, and M. Torre, “Structural analysis of the ‘Internal’ Units of Cilento, Italy: new constraints on the Miocene tectonic evolution of the southern Apennine accretionary wedge,” *Comptes Rendus Geoscience*, vol. 342, no. 6, pp. 475–482, 2010.

- [65] S. Critelli and E. Le Pera, "Detrital modes and provenance of Miocene sandstones and modern sands to the Southern Apennines thrust-top basins (Italy)," *Journal of Sedimentary Research*, vol. 64, no. 4a, pp. 824–835, 1994, A64.
- [66] G. Cavuoto, L. Martelli, G. Nardi, and A. Valente, "Turbidite depositional systems and architectures, Cilento, Italy," in *Atlas of Deep-Water Outcrops*, T. H. Nilsen, R. D. Shew, G. S. Steffens, and J. R. J. Studlick, Eds., vol. 56, AAPG Studies in Geology, 2007.
- [67] F. O. Amore, G. Ciampo, P. De Capoa, and E. Ruggero, "Problemi biostratigrafici dei sedimenti terrigeni nell'Appennino meridionale," *Memorie della Società Geologica Italiana*, vol. 41, pp. 621–625, 1998.
- [68] M. Russo, A. Zuppetta, and A. Guida, *Alcune precisazioni stratigrafiche sul Flysch del Cilento (Appennino meridionale)*, vol. 114, Bolletino della Società Geologica Italiana, 1995.
- [69] F. Balsamo, F. Storti, F. Salvini, A. T. Silva, and C. C. Lima, "Structural and petrophysical evolution of extensional fault zones in low-porosity, poorly lithified sandstones of the Barreiras Formation, NE Brazil," *Journal of Structural Geology*, vol. 32, no. 11, pp. 1806–1826, 2010.
- [70] E. Tondi, A. Rustichelli, A. Cilona et al., "Hydraulic properties of fault zones in porous carbonates, examples from central and southern Italy," *Italian Journal of Geosciences*, vol. 135, no. 1, pp. 68–79, 2016.
- [71] C. M. Filomena, J. Hornung, and H. Stollhofen, "Assessing accuracy of gas-driven permeability measurements: a comparative study of diverse Hassler-cell and probe permeameter devices," *Solid Earth*, vol. 5, no. 1, pp. 1–11, 2014, v.
- [72] C. A. Leon, "New perspectives in mercury porosimetry," *Advances in Colloid and Interface Science*, vol. 76-77, pp. 341–372, 1998.
- [73] A. Cilona, D. R. Faulkner, E. Tondi et al., "The effects of rock heterogeneity on compaction localization in porous carbonates," *Journal of Structural Geology*, vol. 67, pp. 75–93, 2014, v.
- [74] F. Arzilli, A. Cilona, L. Mancini, and E. Tondi, "Using synchrotron X-ray microtomography to characterize the pore network of reservoir rocks: a case study on carbonates," *Advances in Water Resources*, vol. 95, pp. 254–263, 2016.
- [75] M. Zambrano, E. Tondi, L. Mancini et al., "3D pore-network quantitative analysis in deformed carbonate grainstones," *Marine and Petroleum Geology*, vol. 82, pp. 251–264, 2017.
- [76] D. Zandomenighi, M. Voltolini, L. Mancini, F. Brun, D. Dreossi, and M. Polacci, "Quantitative analysis of X-ray microtomography images of geomaterials: application to volcanic rocks," *Geosphere*, vol. 6, no. 6, pp. 793–804, 2010.
- [77] O. Gharbi and M. J. Blunt, "The impact of wettability and connectivity on relative permeability in carbonates: a pore network modeling analysis," *Water Resources Research*, vol. 48, no. 12, 2012.
- [78] M. J. Blunt, B. Bijeljic, H. Dong et al., "Pore-scale imaging and modelling," *Advances in Water Resources*, vol. 51, pp. 197–216, 2013.
- [79] M. Zambrano, E. Tondi, L. Mancini et al., "Fluid flow simulation and permeability computation in deformed porous carbonate grainstones," *Advances in water resources*, vol. 115, pp. 95–111, 2018.
- [80] Í. B. da Silva, "X-ray computed microtomography technique applied for cementitious materials: a review," *Micron*, vol. 107, pp. 1–8, 2018.
- [81] A. Abrami, F. Arfelli, R. C. Barroso et al., "Medical applications of synchrotron radiation at the SYRMEP beamline of ELETTRA," *Nuclear Instruments and Methods in Physics Research*, vol. 548, no. 1-2, pp. 221–227, 2005.
- [82] G. Tromba, R. Longo, A. Abrami et al., "The SYRMEP beamline of elettra: clinical mammography and bio-medical applications," in *AIP Conference Proceedings*, vol. 1266, pp. 18–23, Melbourne, Australia, 2010.
- [83] P. Cloetens, R. Barrett, J. Baruchel, J. P. Guigay, and M. Schlenker, "Phase objects in synchrotron radiation hard X-ray imaging," *Journal of Physics D: Applied Physics*, vol. 29, no. 1, pp. 133–146, 1996.
- [84] D. R. Baker, L. Mancini, M. Polacci et al., "An introduction to the application of X-ray microtomography to the three-dimensional study of igneous rocks," *Lithos*, vol. 148, pp. 262–276, 2012.
- [85] F. Brun, S. Pacilè, A. Accardo et al., "Enhanced and flexible software tools for x-ray computed tomography at the Italian synchrotron radiation facility Elettra," *Fundamental Informaticae*, vol. 141, no. 2-3, pp. 233–243, 2015.
- [86] W. Palenstijn, K. Batenburg, and J. Sijbers, "Performance improvements for iterative electron tomography reconstruction using graphics processing units (GPUs)," *Journal of Structural Biology*, vol. 176, no. 2, pp. 250–253, 2011.
- [87] D. Gürsoy, F. De Carlo, X. Xiao, and C. Jacobsen, "TomoPy: a framework for the analysis of synchrotron tomographic data," *Journal of Synchrotron Radiation*, vol. 21, no. 5, pp. 1188–1193, 2014.
- [88] D. Paganin, S. C. Mayo, T. E. Gureyev, P. R. Miller, and S. W. Wilkins, "Simultaneous phase and amplitude extraction from a single defocused image of a homogeneous object," *Journal of Microscopy*, vol. 206, no. 1, pp. 33–40, 2002.
- [89] F. Brun, L. Mancini, P. Kasae, S. Favretto, D. Dreossi, and G. Tromba, "Pore3D: a software library for quantitative analysis of porous media," *Nuclear Instruments and Methods in Physics Research Section A: Accelerators, Spectrometers, Detectors and Associated Equipment*, vol. 615, no. 3, pp. 326–332, 2010.
- [90] C. Tomasi and R. Manduchi, "Bilateral filtering for gray and color images," in *Sixth International Conference on Computer Vision*, pp. 839–846, New Delhi, India, 1998.
- [91] J. A. Hartigan and M. A. Wong, "Algorithm AS 136: a K-means clustering algorithm," *Applied Statistics*, vol. 28, no. 1, pp. 100–108, 1979.
- [92] J. Kozeny, *Über Kapillare Leitung des Wassers im Boden, Sitzungsber.*, vol. 136, Akad. Wiss. Wien, Math. Naturw Klasse, 1927, Abt.II A.
- [93] P. C. Carman, "Fluid flow through granular beds," *Transactions of the American Institute of Chemical Engineers*, vol. 15, p. 150, 1937.
- [94] H. J. G. Gundersen, R. W. Boyce, J. R. Nyengaard, and A. Odgaard, "The Conneulor: unbiased estimation of connectivity using physical disectors under projection," *Bone*, vol. 14, no. 3, pp. 217–222, 1993.
- [95] B. R. Crawford, "Experimental fault sealing: shear band permeability dependency on cataclastic fault gouge characteristics," *Geological Society, London, Special Publications*, vol. 127, no. 1, pp. 27–47, 1998.
- [96] S. Uehara and M. Takahashi, "How rock mechanical properties affect fault permeability in Neogene mudstone?," *Energy Procedia*, vol. 37, pp. 5588–5595, 2013.

- [97] E. Scholz, *The Mechanics of Earthquakes and Faulting*, Cambridge University Press, Cambridge, New York, Port Chester, Melbourne, Sydney, 1990.
- [98] A. G. Hull, "A late Holocene marine terrace on the Kidnappers coast, North Island, New Zealand: some implications for shore platform development processes and uplift mechanism," *Quaternary Research*, vol. 28, no. 02, pp. 183–195, 1987.
- [99] M. R. Heynekamp, L. B. Goodwin, P. S. Mozley, and W. C. Haneberg, "Controls on fault-zone architecture in poorly lithified sediments, Rio Grande Rift, New Mexico: implications for fault-zone permeability and fluid flow," *Faults and Subsurface Fluid Flow in the Shallow Crust*, vol. 113, pp. 27–49, 1999.

Research Article

Mechanical Properties and Statistical Damage Constitutive Model of Rock under a Coupled Chemical-Mechanical Condition

Yun Lin ^{1,2,3} Feng Gao ^{1,2} Keping Zhou,² Rugao Gao ² and Hongquan Guo²

¹The State Key Laboratory of Safety and Health for Metal Mines of China, Maanshan, Anhui 243000, China

²School of Resource and Safety Engineering, Central South University, Changsha, Hunan 410083, China

³School of Civil, Environmental and Mining Engineering, University of Adelaide, Adelaide, SA 5005, Australia

Correspondence should be addressed to Feng Gao; csugaofeng@csu.edu.cn and Rugao Gao; gaorgcsu@163.com

Received 25 November 2018; Revised 18 January 2019; Accepted 16 April 2019; Published 14 May 2019

Academic Editor: Emanuele Tondi

Copyright © 2019 Yun Lin et al. This is an open access article distributed under the Creative Commons Attribution License, which permits unrestricted use, distribution, and reproduction in any medium, provided the original work is properly cited.

Chemical corrosion has a significant impact on the damage evolution behavior of rock. To investigate the mechanical damage evolution process of rock under a coupled chemical-mechanical (CM) condition, an improved statistical damage constitutive model was established using the Drucker-Prager (D-P) strength criterion and two-parameter Weibull distribution. The damage variable correction coefficient and chemical damage variable which was determined by porosity were also considered in the model. Moreover, a series of conventional triaxial compressive tests were carried out to investigate the mechanical properties of sandstone specimens under the effect of chemical corrosion. The relationship between rock mechanics properties and confining pressure was also explored to determine Weibull distribution parameters, including the shape parameter m and scale parameter F_0 . Then, the reliability of the damage constitutive model was verified based on experimental data. The results of this study are as follows: (i) the porosity of sandstone increased and the mechanical properties degraded after chemical corrosion; (ii) the relationships among the compressive strength, the peak axial strain, and confining pressures were linear, while the relationships among the elastic modulus, the residual strength, and confining pressures were exponential functions; and (iii) the improved statistical damage constitutive model was in good agreement with the testing curves with $R^2 > 0.98$. It is hoped that the study can provide an alternative method to analyze the damage constitutive behavior of rock under a coupled chemical-mechanical condition.

1. Introduction

The interaction between groundwater and rock has a significant influence on the deformation and strength of rock [1]. As known, underground water may lead to many hazards, for example, karst collapse of pillars [2]. In general, underground water is a complex aqueous solution with various ion components and pH values [3], and the stability of rock mass engineering, such as oil extraction, nuclear waste geological repository, energy underground reservoir, and carbon dioxide geological storage reservoir, is significantly affected by the corrosion of hydrochemical solutions [4–7]. Moreover, the influence of stress conditions on the mechanical behavior of rock is not negligible. Thus, it is of high importance to explore the mechanical behavior of rock under the coupled effects of hydrochemical environment and loading.

Due to the corrosion of chemical solutions, the pore structure would be changed and the physical and mechanical properties of rocks would deteriorate gradually with the increase in chemical damage. Many scholars have explored the effects of chemical corrosion on rock deformation and strength characteristics through theoretical and experimental methods [4, 8–18]. Ning et al. [16] studied the deterioration characteristics of mechanical properties of sandstone under acid corrosion and defined the chemical damage variable based on the change in the effective bearing area of sandstone specimens and then established the degradation equation of the strength and elasticity model. Feng et al. [9, 10] experimentally analyzed the evolution law of mechanical properties of rocks under the effect of chemical corrosion combined with neural network simulation and numerical analysis. Ding and Feng [19] studied the evolution laws of mechanical

properties of limestone under the corrosion effect of different chemical solutions. Feucht and Logan [20], Dieterich and Conrad [21], and Logan and Blackwell [22] experimentally analyzed the deformation of rock immersed in chemical solutions and then explored the relations among compressive strength, elastic modulus, and chemical corrosion. Han et al. [12, 13] explored the effects of chemical solutions on the deterioration characteristics of fracture toughness and compressive strength of sandstone under different freeze-thaw cycle conditions. Ni et al. [23] investigated the relationship between deterioration of mechanical properties of rock and damage variable of granite under different chemical solutions and freeze-thaw cycles based on experimental data. These researches mainly focus on the influence of chemical corrosion on the mechanical effect and the chemical damage variables of rock, and the results are of great significance.

A reasonable constitutive model is a useful method to investigate the damage evolution behavior of materials [24–26]. In recent years, many damage constitutive models have been established based on various strength theories or criteria, such as rock strain strength theory [27–29], Drucker-Prager (D-P) criterion [30–33], Mohr-Coulomb (M-C) criterion [34–37], and Hoek-Brown (H-B) criterion [38, 39]. However, the strength of microelements, which is affected by many factors, cannot be calculated accurately using the strain strength theory [39]. Meanwhile, the M-C criterion may cause great error at a high stress level, and the form of H-B criterion is too complex because it was developed from experimental results [40]. Though the D-P criterion is conservative in calculating the intensity of the microelement, it is still widely used due to its simple form. In the present work, the D-P criterion is used to describe the strength of microelements. So far, studies on the damage constitutive model of rocks treated with chemical corrosion are limited [41, 42]. Moreover, these studies mainly focused on the constitutive equations of rock under the chemical corrosion and uniaxial compression coupling. As known, the mechanical behaviors of rock under triaxial compression are different, but the chemical-mechanical (CM) coupling damage constitutive model of rock has not been well studied, especially the mechanical behavior in the post-peak stage of rock treated with chemical corrosion. So the results of published literatures are far from fully understanding the characteristics of deformation and destruction of rock affected by coupling chemical corrosion and load. All of these address a need to establish a chemical-mechanical coupling damage constitutive model to explore the mechanical response of rock.

As known, the model parameters in the constitutive models are highly affected by some mechanical properties, such as peak strength, peak axial strain, and elastic modulus [36, 37, 39]. In general, the values of these mechanical properties are obtained by conventional mechanical tests. Obviously, it is inconvenient to calculate the model parameters based on the data of conventional mechanical tests. The reason lies in the fact that the values of mechanical properties will change in response to various confining pressure values [36, 43, 44]. This also addresses a need to develop a more efficient method to obtain mechanics parameters of rocks.

Recently, some methods for quantitative estimation of rock mechanical parameters have been explored. For example, Li et al. [36] established the relationship between peak stress, peak strain, and confining pressure by M-C criterion and data fitting. Then they calculated the values of peak stress and peak strain of rock under different confining pressures and verified the applicability of these relationships by the constitutive model established. Yu et al. [45] explored the relationship between peak stress, peak strain, and elastic modulus and confining pressure of rock at different temperatures by data fitting. However, the mechanical behavior of rock after chemical corrosion is different, and further efforts are still needed to determine the model parameters for rock treated with chemical corrosion.

In this work, considering the chemical damage variable and damage variable correction coefficient, an improved statistical damage constitutive model of sandstone after chemical corrosion was established based on two-parameter Weibull distribution and D-P strength criterion. To verify the reliability of the constitutive model, a series of conventional triaxial compression tests of sandstone treated with chemical corrosion were carried out, and the relationships between mechanical properties of sandstone and confining pressures were explored. The Weibull parameters of the improved constitutive model, including the shape parameter m and scale parameter F_0 , were calculated based on these relationships, and then the theoretical curves were simulated and compared with the testing curves. The results showed that the improved model can well reflect the damage evolution behavior of sandstone treated with chemical corrosion.

2. Statistical Damage Constitutive Model

2.1. Damage Constitutive Model of Sandstone without Chemical Corrosion. In terms of damaged materials, it is usually difficult to analyze the pattern and damage mechanism of each microelement defect to determine the effective bearing area of the material. In order to measure the damage of materials through intermediate variables, Lemaitre [46] proposed an equivalent strain hypothesis. The hypothesis can be described as the following [47]: the strain generated by the effective stress on the intact materials is equivalent to the strain generated by the nominal stress on the damaged materials. The strain equivalence has been widely used in the establishment of the constitutive model of rock-like materials. Based on the assumption, the effective stress of rock can be represented by the nominal stress, that is,

$$\sigma_i^* = \frac{\sigma_i}{1 - D_m}, \quad (1)$$

where σ_i is the nominal stress, σ_i^* is the effective stress, and D_m is the material damage variable under load, which measures the degree of material damage. When $D_m = 0$, the material is in a nondestructive state. When $D_m = 1$, the material completely destroys, and $0 < D_m < 1$ corresponds to different degrees of damage.

Qian and Yin [48] believed that the residual strength of rock has high influence on the stability of geotechnical

systems. Based on experimental analysis, Xu et al. [39] found that the residual strength would become the main factor affecting the softening mechanical behavior in the post-peak stage of the stress-strain curves after macrocracks appear, and the damage variables should be improved in the post-peak stage. Gao et al. [32] improved the damage variable of rock by introducing a damage variable correction coefficient λ which was defined as the ratio of the residual strength and the peak strength and verified the reliability of the method using experimental results. In this study, the damage variable correction coefficient λ is also applied, $\lambda \in (0, 1)$. Then, equation (1) can be written as

$$\sigma_i^* = \frac{\sigma_i}{1 - \lambda D_m}. \quad (2)$$

Then, the strain can be written as equation (3) according to Hooke's law [49].

$$\varepsilon_1 = \frac{\sigma_1^* - \mu(\sigma_2^* + \sigma_3^*)}{E} = \frac{\sigma_1 - \mu(\sigma_2 + \sigma_3)}{E(1 - \lambda D_m)}, \quad (3)$$

where σ_1, σ_2 , and σ_3 are three principal stresses; ε_1 is the strain which corresponds to the stress of σ_1 ; E is the elastic modulus; and μ is Poisson's ratio.

Combining equations (2) and (3), the improved statistical damage constitutive model can be expressed as

$$\sigma_1 = (1 - \lambda D_m)E\varepsilon_1 + \mu(\sigma_2 + \sigma_3). \quad (4)$$

Under triaxial compression, the rock can be divided into a number of microelements with different defects and the damage of rock microelement is random. Then, we define N_t as the number of failed microelements and N is the total number of microelements. The ratio of N_t to N could be seen as the mechanical damage variable.

$$D_m = \frac{N_t}{N}. \quad (5)$$

The fracture of rock is caused by the failure of the weakest link according to the theory of fracture mechanics [50]. The Weibull distribution [51] was also proposed based on the weakest link theory and has applied to many groups of problems, for example, the size effect on failure in solids. Assuming that the strength level of the microelements of materials satisfies the Weibull distribution function, Krajcinovic and Silva [52] first proposed to calculate the damage variable of materials based on the Weibull distribution. Then, many scholars applied the distribution to establish various statistical constitutive models of rocks [27, 36, 42, 53–55].

On the other hand, the expression of the Weibull distribution can be divided into two kinds, i.e., three-parameter

Weibull distribution and two-parameter Weibull distribution. The expression of the three-parameter Weibull distribution is [32, 55]

$$P(F) = \frac{m}{F_0} \left(\frac{F - \gamma}{F_0} \right)^{m-1} e^{-(F-\gamma/F_0)^m}, \quad (6)$$

where $P(F)$ is the microelement strength distribution function, F is the parameter which indicates the strength level of the microelement, m is the shape parameter denoting the degree of homogeneity, F_0 is the scale parameter associated with the strength of microelements, and γ is the position parameter which represents the damage evolution threshold.

In most cases, the threshold γ is assumed to be zero [56]. Then, it becomes the two-parameter Weibull distribution and could be expressed as

$$P(F) = \frac{m}{F_0} \left(\frac{F}{F_0} \right)^{m-1} e^{-(F/F_0)^m}. \quad (7)$$

Quinn (Quinn and Quinn 2010) believed that it is very risky to assume that a finite threshold strength exists without careful screening or nondestructive evaluation, and the two-parameter Weibull function is the most commonly used for simplicity. Deng et al. [56] found that the two-parameter Weibull function is sufficient suitable for describing the statistical strength variation of materials. Moreover, the two-parameter Weibull distribution is the most widely accepted function in the treatment of rock properties, and the results of a large number of studies indicate that it is capable of describing the statistical strength of rock microelements [30, 36, 53, 54, 57, 58]. Therefore, it is appropriate to introduce the two-parameter Weibull distribution to calculate the damage variable of rocks.

Then, the damage variable D_m can be obtained based in equations (5) and (7).

$$D_m = \int_0^F P(F) dF = \int_0^F \frac{m}{F_0} \left(\frac{F}{F_0} \right)^{m-1} e^{-(F/F_0)^m} dx = 1 - e^{-(F/F_0)^m}. \quad (8)$$

Combining equation (8) and equation (4), the improved statistical damage constitutive model is

$$\sigma_1 = E\varepsilon_1 \left[1 - \lambda + \lambda e^{-(F/F_0)^m} \right] + \mu(\sigma_2 + \sigma_3). \quad (9)$$

2.2. Damage Constitutive Model of Sandstone under a Coupled CM Condition. Under the action of chemical corrosion and loading, the rocks show different damage characteristics. The chemical-mechanical coupling damage can be

obtained by the generalized damage variables derived from the equivalent strain principle, and the total damage variable can be expressed as [39]

$$D = D_c + D_m - D_c D_m, \quad (10)$$

where D is the total damage variable and D_c is the chemical damage variable.

Thus, the damage variable in equation (4) should be replaced by the total damage variable in equation (10). Then the damage constitutive model of sandstones after chemical corrosion is as follows:

$$\sigma_1 = E\varepsilon_1(1 - D_c)(1 - D_m) + 2\mu\sigma_3. \quad (11)$$

Combining equations (8) and (11), the improved damage constitutive model of rock treated with chemical corrosion can be expressed as

$$\sigma_1 = (1 - D_c)E\varepsilon_1 \left[1 - \lambda + \lambda e^{-(F/F_0)^m} \right] + \mu(\sigma_2 + \sigma_3). \quad (12)$$

2.3. Chemical Damage Variable. According to equation (12), the chemical damage variable has a significant influence on the mechanical evolution behavior of rock. Thus, the determination of the chemical damage variable should be identified firstly to establish the damage constitutive model of rock. Mechanical properties have been widely used to calculate the damage variable [28, 59], such as maximum strain, elastic modulus, and residual strain. However, it is not easy to obtain the value of mechanical property which depends on a large number of mechanical tests. Therefore, other simple, fast, and convenient methods have been explored by many scholars, such as the chemical damage variable based on CT number [60–62] and rock density [63–65]. Note that CT number, which can be expressed by the change rate of the attenuation coefficient of water, is often used to describe the attenuation coefficient of rock materials relative to the attenuation coefficient of water [60]. The change in porosity has also been widely used to define the damage variable of rock [12, 16, 23, 66]. Due to that, the porosity can be obtained by nuclear magnetic resonance (NMR) technique easily; the chemical damage variable characterized in terms of porosity is also used in this study, and it can be expressed as [67]

$$D_c = \frac{\varnothing_t - \varnothing_0}{1 - \varnothing_0}, \quad (13)$$

where \varnothing_t is the porosity of sandstone treated with chemical corrosion, and \varnothing_0 is the initial porosity.

Let E_0 be the elastic modulus of rock without chemical corrosion, then the elastic modulus and improved damage

constitutive model of rock treated with chemical corrosion can be expressed as

$$\begin{cases} E = \left(\frac{1 - \varnothing_t}{1 - \varnothing_0} \right) E_0, \\ \sigma_1 = E\varepsilon_1 \left[1 - \lambda + \lambda e^{-(F/F_0)^m} \right] + \mu(\sigma_2 + \sigma_3). \end{cases} \quad (14)$$

2.4. Determination of m and F_0 . A reasonable measurement of the strength level of microelements in rock is the key to establishing the damage evolution equation based on the theory of statistical damage. Li and Tang [29, 68, 69] preliminarily established a statistical damage evolution model of rocks using axial strain to measure the strength level of microelements. As known, the strength level of the rock microelement is not directly determined by the axial strain, but directly related to the stress state of the rock microelement. Therefore, it is unreasonable to adopt the axial strain to measure the strength level of the rock microelement. Some strength criterions have also been used to measure the strength of the microelement, where the Drucker-Prager yield criterion [70] is the most commonly used [30, 33, 71, 72]. In this study, the D-P criterion is proposed to measure the strength level of the rock microelement.

The D-P criterion is a generalized Mises yield criterion, which takes into account the effect of intermediate principal stress and hydrostatic pressure. It has a simple form and is widely used in geotechnical engineering. The expression is [73]

$$F = \partial_0 I_1 + \sqrt{J_2} = k_0, \quad (15)$$

where ∂_0 and k_0 are material parameters, I_1 and J_2 are the first invariant of the stress tensor and the second invariant of the stress deviator, respectively, and the parameters can be expressed as

$$\begin{cases} \partial_0 = \frac{\sin \varphi}{\sqrt{9 + 3 \sin^2 \varphi}}, \\ I_1 = \sigma_1^* + \sigma_2^* + \sigma_3^*, \\ J_2 = \frac{(\sigma_1^* - \sigma_2^*)^2 + (\sigma_2^* - \sigma_3^*)^2 + (\sigma_3^* - \sigma_1^*)^2}{6}, \end{cases} \quad (16)$$

where σ_1^* , σ_2^* , and σ_3^* are effective stresses and φ is the internal friction angle.

Combining equations (2), (4), (15), and (16), the strength level of microelement F can be calculated easily as

$$F = \frac{\partial_0 I_1' + \sqrt{J_2'}}{\sigma_1 - \mu(\sigma_2 + \sigma_3)} E\varepsilon_1, \quad (17)$$

where $I_1' = \sigma_1 + \sigma_2 + \sigma_3$ and $J_2' = 1/6[(\sigma_1 - \sigma_2)^2 + (\sigma_2 - \sigma_3)^2 + (\sigma_1 - \sigma_3)^2]$.

Under the condition of conventional triaxial compression testing, $\sigma_1 > \sigma_2 = \sigma_3$, then the strength of microelement F can be calculated as

$$F = \frac{\partial_0 I'_1 + \sqrt{J'_2}}{\sigma_1 - 2\mu\sigma_3} E\varepsilon_1. \quad (18)$$

Substituting equation (15) into equation (9), and then differentiating equation (9), the following expression can be obtained:

$$\begin{aligned} \frac{d\sigma_1}{d\varepsilon_1} = E & \left[1 - \lambda + \lambda e^{-(F/F_0)^m} \right] - \lambda m E \varepsilon_1 \frac{F^{m-1}}{F_0^m} e^{-(F/F_0)^m} \\ & \cdot \left\{ \partial_0 \left[\frac{E(\sigma_1 + 2\sigma_3)}{\sigma_1 - 2\mu\sigma_3} + \frac{E\varepsilon_1}{\sigma_1 - 2\mu\sigma_3} \frac{d\sigma_1}{d\varepsilon_1} - \frac{E\varepsilon_1(\sigma_1 + 2\sigma_3)}{(\sigma_1 - 2\mu\sigma_3)^2} \frac{d\sigma_1}{d\varepsilon_1} \right] \right. \\ & \left. + \frac{E(\sigma_1 - \sigma_3) + E\varepsilon_1(d\sigma_1/d\varepsilon_1)}{\sqrt{3}(\sigma_1 - 2\mu\sigma_3)} - \frac{E\varepsilon_1(\sigma_1 - \sigma_3)}{\sqrt{3}(\sigma_1 - 2\mu\sigma_3)^2} \frac{d\sigma_1}{d\varepsilon_1} \right\}. \end{aligned} \quad (19)$$

According to the characteristics of the curve of stress-strain of rocks, equation (9) satisfies the following geometrical conditions of the peak point P on the curve:

$$\begin{cases} \frac{d\sigma_1}{d\varepsilon_1} = 0, \\ \varepsilon_1 = \varepsilon_p, \\ \sigma_1 = \sigma_p, \end{cases} \quad (20)$$

where σ_p is the peak stress of rock and ε_p is the strain corresponding to the peak stress, which is called the peak strain in this study.

Then, we have

$$\begin{cases} \sigma_p = E\varepsilon_p \left[1 - \lambda + \lambda e^{-(F_p/F_0)^m} \right] + 2\mu\sigma_3, \\ \frac{mF_p^{m-1}}{F_0^m} = \frac{(\sigma_p - 2\mu\sigma_3)^2}{E\varepsilon_p [\sigma_p - 2\mu\sigma_3 + (\lambda - 1)E\varepsilon_p] \left[\partial_0(\sigma_p + 2\sigma_3) + 1/\sqrt{3}(\sigma_p - \sigma_3) \right]}, \end{cases} \quad (21)$$

where F_p is the strength of the microelement when the axial stress reaches the peak value.

Solving equation (21), the parameter m and F_0 can be calculated as

$$\begin{cases} m = \frac{\sigma_p - 2\mu\sigma_3}{[\sigma_p - 2\mu\sigma_3 + (\lambda - 1)E\varepsilon_p] \ln \left(\lambda E\varepsilon_p / \sigma_p - 2\mu\sigma_3 + (\lambda - 1)E\varepsilon_p \right)}, \\ F_0 = \frac{\partial_0(\sigma_p + 2\sigma_3) + 1/\sqrt{3}(\sigma_p - \sigma_3)}{(\sigma_p - 2\mu\sigma_3) \left[\ln \left(\lambda E\varepsilon_p / \sigma_p - 2\mu\sigma_3 + (\lambda - 1)E\varepsilon_p \right) \right]^{1/m}}. \end{cases} \quad (22)$$

Then the improved constitutive model of rock under chemical-loading conditions was established by combining

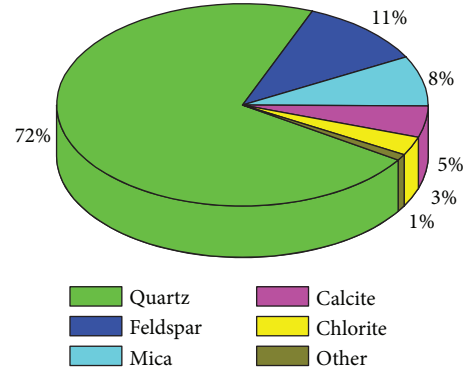


FIGURE 1: The average mineral composition content of sandstone specimen.

equations (14) and (22). To analyze the reliability and feasibility of the improved model, the damage constitutive model without the damage variable correction coefficient can be expressed as equation (23). In the model, the parameters m and F_0 can also be determined based on the above method, which is not described in this study.

$$\sigma_1 = E\varepsilon_1 e^{-(F/F_0)^m} + 2\mu\sigma_3. \quad (23)$$

3. Tests of Porosity and Triaxial Mechanical Properties

3.1. Materials and Experimental Methods. To analyze the change in porosity and the mechanical properties of rock treated with chemical corrosion and verify the reliability of the improved constitutive model established in this work, a series of conventional triaxial compression tests were conducted. The rock used in this study is fine-grained sandstone collected from Hunan Province, China. The selected rock samples belong to the same block to ensure the reliability of the test results. According to the standards of ISRM suggested [74, 75], these sandstones are cylinders with diameter of 50 ± 1 mm and height of 100 ± 1 mm. In addition, the specimens with larger discreteness were excluded by comparing the quality and longitudinal wave velocity (LWV) of specimens. The mean density and LWV of specimens retained are 2.41 g/cm^3 and 2310 m/s , respectively. The mineral components of the specimens were detected by X-ray detection, and the results are listed in Figure 1. It can be found that the mineral composition of sandstone is mainly quartz, feldspar, mica, calcite, etc.

Since the chemical corrosion of rock mass engineering is a long-term and slow process [4, 11, 76], chemical solutions with large concentration were selected to observe the effect of chemical solutions on rock in a laboratory environment. In the tests, three chemical solutions were prepared, i.e., an acidic solution with $0.01 \text{ mol/L H}_2\text{SO}_4$ ($\text{pH} = 2$), distilled water ($\text{pH} = 7$), and an alkaline solution with 0.01 mol/L NaOH ($\text{pH} = 12$). Specimens were divided into four sets, i.e., A, B, C, and D. Specimens of groups A, B, and C were immersed in H_2SO_4 solution, NaOH solution, and distilled

TABLE 1: Parameters of sandstone under the conditions of different chemical corrosions.

Chemical environment	Confining pressures (MPa)	σ_p (mPa)	ε_p	E (GPa)	Residual strength σ_r (MPa)	\varnothing_0 (%) [*]	\varnothing_t (%)	c (MPa)	φ (°)	μ
H ₂ SO ₄ solution	0	52.45	0.0102	9.19	28.26	5.06	10.76	14.90	30.55	0.28
	5	66.98	0.0108	10.52	38.63	5.12	10.63			
	10	83.17	0.0119	11.61	58.59	5.04	10.81			
	15	98.18	0.0124	12.15	65.07	5.09	10.77			
	20	113.59	0.0135	12.75	74.25	5.10	10.85			
	25	128.86	0.0143	12.93	82.78	5.13	10.82			
NaOH solution	0	55.74	0.0096	9.41	30.13	5.04	8.65	15.78	31.37	0.26
	5	72.97	0.0104	10.84	41.12	5.03	8.59			
	10	87.54	0.0117	11.93	61.49	5.12	8.66			
	15	103.75	0.0125	12.18	70.65	5.08	8.57			
	20	119.68	0.0134	12.86	82.23	5.14	8.62			
	25	135.48	0.0143	13.27	93.81	5.06	8.64			
Distilled water	0	63.13	0.0094	10.48	33.96	5.11	5.92	16.68	33.60	0.26
	5	78.95	0.0102	11.37	44.28	5.02	5.90			
	10	96.24	0.0122	12.24	64.29	5.09	5.87			
	15	114.32	0.0131	12.63	73.04	5.12	5.94			
	20	132.52	0.0138	12.95	85.75	4.96	5.84			
	25	149.11	0.0149	13.65	97.29	5.06	5.89			
Natural state	0	64.63	0.0092	10.83	39.56	5.12	5.12	17.13	34.07	0.25
	5	81.57	0.0101	11.41	65.31	5.06	5.06			
	10	100.95	0.0120	12.52	81.37	5.08	5.08			
	15	117.75	0.0129	12.94	93.91	5.07	5.07			
	20	135.28	0.0139	13.21	102.36	5.11	5.11			
	25	153.23	0.0151	13.81	107.93	5.10	5.10			

Note: c : cohesion of rocks.

water, and specimens of group D were in the natural state and used as references.

According to previous literatures [59, 77–84], the porosity could be tested by nuclear magnetic resonance (NMR). In this study, the AniMR-150 NMR imaging system of Central South University (China) was used to measure the porosity of sandstone treated with different chemical corrosions. Since the porosity increments of specimens from all groups are very small (almost 0) after 50 days of immersion, then the porosity with immersion time of 50 days is selected as the final porosity of sandstone specimens treated with chemical corrosion.

The conventional triaxial compression tests with various confining pressures (0, 5, 10, 15, 20, 25, and 30 MPa) were conducted on the MTS 815 material testing system with a maximum loading capability of 2600 kN. The experiment used the axial stress control, and the loading rate was a constant of 0.1 kN/s. During testing, the load and displacement were recorded directly by the system. In this study, the triaxial compressive strength was the peak load when the specimen failed, and the elastic modulus was the slope of the approximate line segment in the stress-strain curve. Note that there are three samples in each group, and the results are the average values of each group.

3.2. Experimental Results. Table 1 displays the average results of porosity and mechanical parameters of sandstone sample immersion in different chemical solutions. Note that the results of sandstone under the confining pressure of 30 MPa were used to verify the feasibility of the improved constitutive model, and the experimental data was not discussed in this section.

From Table 1, it can be seen that the porosity increases when sandstone specimens immersed in chemical solutions, and the porosity change of specimens immersed in H₂SO₄ solution is the largest, followed by that of specimens immersed in NaOH solution and distilled water, respectively. Thus, the order of the chemical damage variable of sandstone specimens treated with different chemical corrosion is $D_{\text{H}_2\text{SO}_4} > D_{\text{NaOH}} > D_{\text{water}}$. In terms of mechanical properties of sandstone in the same chemical environment, the peak strength, peak axial strain, elastic modulus, and residual strength increase with the increase in confining pressures. Under the condition of the same confining pressure, the peak strength, elastic modulus, and residual strength decrease with the chemical damage variable increasing, while the peak axial strain shows no apparent trend. Meanwhile, it can also be found that the internal friction angle and the cohesion decrease with the chemical damage variable increasing, while

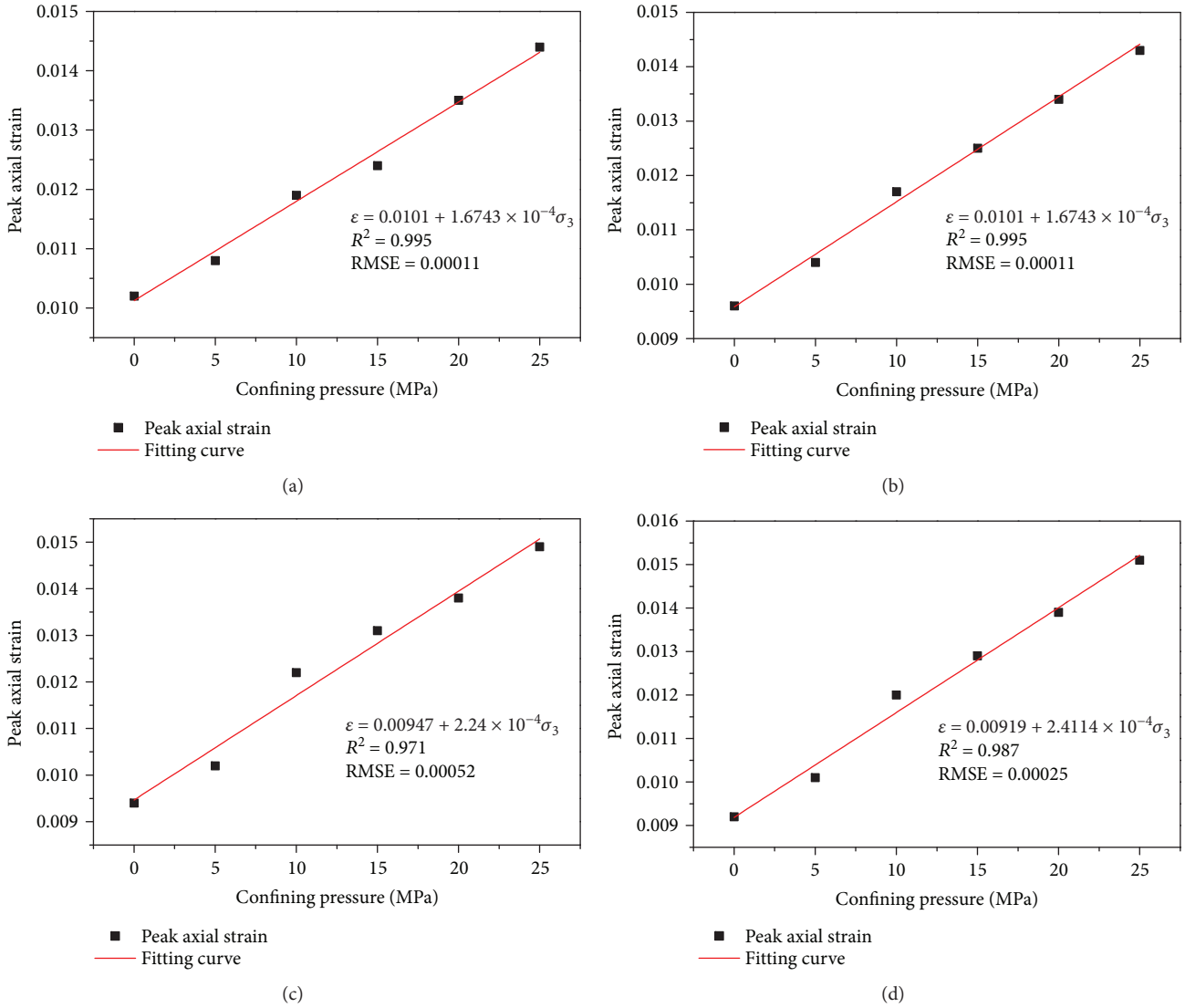


FIGURE 2: Peak axial strain at various confining pressures of sandstone specimens treated with different chemical corrosions. The chemical environment is (a) H_2SO_4 solution, (b) NaOH solution, (c) distilled water, and (d) natural state.

the evolution law of Poisson’s ratio is opposite. Overall, we can draw that the mechanical properties deteriorate under the condition of chemical corrosion, and the ascending order of the effect of chemical solution on mechanical properties is distilled water, NaOH solution, and H_2SO_4 solution, respectively.

3.3. Relationships between Mechanical Properties and Confining Pressures. From equation (22), it is obvious that the mechanical properties, such as σ_p , ϵ_p , E , and σ_r , contribute to the determination of m and F_0 . However, the values of the four mechanical parameters will change in response to various confining pressures, and they must be remeasured by a series of mechanical tests. This seems to be a rather awkward situation for the operation of the above method. Therefore, further efforts are still needed for the estimation of σ_p , ϵ_p , E , and σ_r .

According to the previous studies [36, 39, 85], the four mechanical properties have a certain relationship with confining pressures. Many studies suggested that it is a feasible method to obtain the mechanical parameters of rocks under different confining pressures by experimental fitting with small amounts of data. For example, Alam et al. (Alam et al. 2014) explored the relationship among triaxial strength, tangent modulus, and confining pressure using four points (different confining pressures). Li et al. [36] discussed the relationship among stress, peak axial strain, and confining pressure through six points and then verified the statistical damage constitutive model established in the literature. By fitting five sets of data, the relationship among stress, elastic modulus, and confining pressure was studied by Xu and Karakus [86]. Wang et al. [47] investigated the relationship among strain, elastic modulus, and confining pressure using six confining pressures. Golshani et al. (Golshani et al. 2006) established the relationship

TABLE 2: Regression results of peak axial strain versus confining pressures of sandstone treated with different chemical corrosions.

Chemical environment	a	b	Correlative coefficients R^2	RMSE
H ₂ SO ₄ solution	1.6743×10^{-4}	0.01010	0.995	1.1×10^{-4}
NaOH solution	1.9314×10^{-4}	0.00959	0.995	1.2×10^{-4}
Distilled water	2.24×10^{-4}	0.00947	0.971	5.2×10^{-4}
Natural state	2.4114×10^{-4}	0.00919	0.987	2.5×10^{-4}

between stress and confining pressure using six points. Based on six sets of data, Yoshinaka et al. (Yoshinaka et al. 2008) established the relationship between Young's modulus and confining pressure. Therefore, the method of experimental fitting is also used to determine the values of the four mechanical properties under different confining pressures in this study.

3.3.1. Peak Strength and Peak Axial Strain. The triaxial strength of rock under a confining pressure could be obtained by a certain strength criterion. The mostly widely used strength criterion is the Mohr-Coulomb strength criterion, and the criterion has been successfully used in many studies [36, 87–90] to obtain the peak axial stress of rocks. The M-C criterion is also adopted in this study, and then the peak axial stress of sandstone specimens can be expressed as

$$\sigma_p = \frac{1 + \sin \varphi}{1 - \sin \varphi} \sigma_3 + \frac{2c \cos \varphi}{1 - \sin \varphi}. \quad (24)$$

From equation (24), the value of the peak axial stress of sandstone under different confining pressures could be obtained based on the experimental data in Table 1.

The peak axial strain has a strong linear relationship (shown in equation (25)) with confining pressures [13, 36, 86]. Based on the experimental data in Table 1, the relationship between the peak axial strain and confining pressures of sandstone specimens treated with different chemical corrosion are regressed in Figure 2.

$$\varepsilon_p = a\sigma_3 + b, \quad (25)$$

where a and b are constants. It is obvious that ε_p is the peak axial strain of rock under uniaxial compression when the confining pressure is zero, then the parameter b is the strain of rock under uniaxial compression, and a represents the strain increasing rate with the increasing of confining pressure.

To evaluate the performance of the fitting curves, the root mean square error (RMSE) and coefficient of determination (R^2) were introduced [30, 91]. R^2 measures how well the association is between changes in two variables, and RMSE is used to find the sample standard deviation of the error

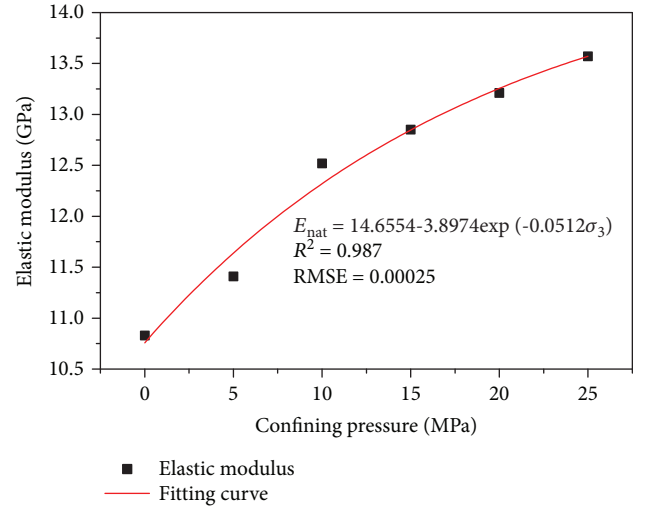


FIGURE 3: Elastic modulus of sandstone specimens under a natural state with various confining pressures.

between regressed and actual values. An ideal regression curve has $R^2 = 1$ and RMSE = 0.

$$R^2 = 1 - \frac{n-1}{n-2} \times \frac{\sum_{i=1}^n (y'_i - y_i)^2}{\sum_{i=1}^n (y'_i - y_a)^2}, \quad (26)$$

$$\text{RMSE} = \sqrt{\frac{1}{n} \times \sum_{i=1}^n (y'_i - y_i)^2},$$

where n is the number of data points, and y_i , y'_i and y_a are the fitting value, the actual value, and the average value of the stress at the i th data point.

The relationships between the peak axial strain and confining pressure are expressed in Table 2. It can be found that the linear relationship fits well the experimental data with $R^2 > 0.97$ and RMSE $< 6.0 \times 10^{-4}$. Then, the peak axial strain of sandstone specimens under different confining pressures can be calculated based on the fitting results.

3.3.2. Elastic Modulus. Figure 3 gives the elastic modulus of sandstone specimens with different confining pressures in the natural state. We can see that the increasing rate of elastic modulus decreases gradually with the confining pressure increasing, indicating that the relationship between elastic modulus and confining pressures could be fitted by an exponential equation shown in equation (27), which has been

TABLE 3: Elastic modulus of sandstone specimens treated with chemical corrosion at various confining pressures.

Chemical environment	Confining pressures (MPa)	Actual elastic modulus (GPa)	Predicted elastic modulus (GPa)	Error (%)
H ₂ SO ₄ solution	0	9.19	10.11	10.03
	5	10.52	10.96	4.21
	10	11.61	11.57	0.34
	15	12.15	12.08	0.59
	20	12.75	12.45	2.33
	25	12.93	12.76	1.33
NaOH solution	0	9.41	10.35	9.98
	5	10.84	11.20	3.34
	10	11.93	11.86	0.59
	15	12.18	12.37	1.60
	20	12.86	12.77	0.71
	25	13.27	13.06	1.58
Distilled water	0	10.48	10.67	1.78
	5	11.37	11.53	1.41
	10	12.24	12.22	0.18
	15	12.63	12.74	0.84
	20	12.95	13.13	1.41
	25	13.65	13.45	1.44

proposed and verified by Pourhosseini and Shabanimashcool [40] and Yang et al. [85].

$$E = a' + b' \exp(d\sigma_3), \quad (27)$$

where a' , b' , and d are constants which can be obtained by exponential fitting.

When the confining pressure is zero, then $E = a' + b'$ is the elastic modulus of rock under the uniaxial compressive state. So the parameter d is a fitting coefficient defining the increasing rate of elastic modulus with the increasing of confining pressures.

Using the method, the regression result of sandstone specimens under the natural state is shown in Figure 3 and the fitting equation is listed in equation (28). It can be seen that the exponential equation can fit the experimental data well with $R^2 = 0.971$ and $RMSE = 0.1411$.

$$E_{\text{nat}} = 14.6554 - 3.8974 \exp(-0.0512\sigma_3) (R^2 = 0.971), \quad (28)$$

where E_{nat} represents the elastic modulus of sandstone specimens under natural state.

As mentioned in Sections 2.2 and 2.3, the elastic modulus of sandstone specimens under the effect of loading and chemical corrosion could be described as

$$E = (1 - D_c)E_{\text{nat}} = \frac{1 - \varnothing_t}{1 - \varnothing_0} E_{\text{nat}}. \quad (29)$$

Combining equation (29) and the porosity of sandstone specimens under different states in Table 1, the elastic

modulus of sandstone specimens immersed in different chemical solutions are calculated and listed in Table 3. It is obvious that the error between the actual and predicted elastic modulus is less than 11%. Thus, it is feasible to calculate the elastic modulus of sandstone specimens under a coupled chemical-mechanical condition by using equations (28) and (29).

3.3.3. Residual Strength. Under the condition of different chemical corruptions, the testing results of the average residual strength with various confining pressures and the fitting curves are shown in Figure 4. The regression results listed in Table 4 reveal that the relationship between residual strength and confining pressures can be expressed by exponential equations ($R^2 > 0.97$, $RMSE < 2.5$), which is similar to the results of Xu et al. [39].

4. Verification of the Improved Damage Constitutive Model

In this study, the experiment results of conventional triaxial compression tests of sandstone treated with different chemical corruptions under a confining pressure of 30 MPa were used to verify the reliability of the improved damage constitutive model. The mechanical parameters of sandstone under the confining pressure of 30 MPa, which are used to simulate the mechanical behavior based on the improved damage constitutive model, can be calculated according to the relationships between mechanical properties and confining pressures in Section 3.3. The damage variable correction coefficient λ can be calculated based on the definition in Section 2.1. Then, the model parameters are obtained and listed in Table 5.

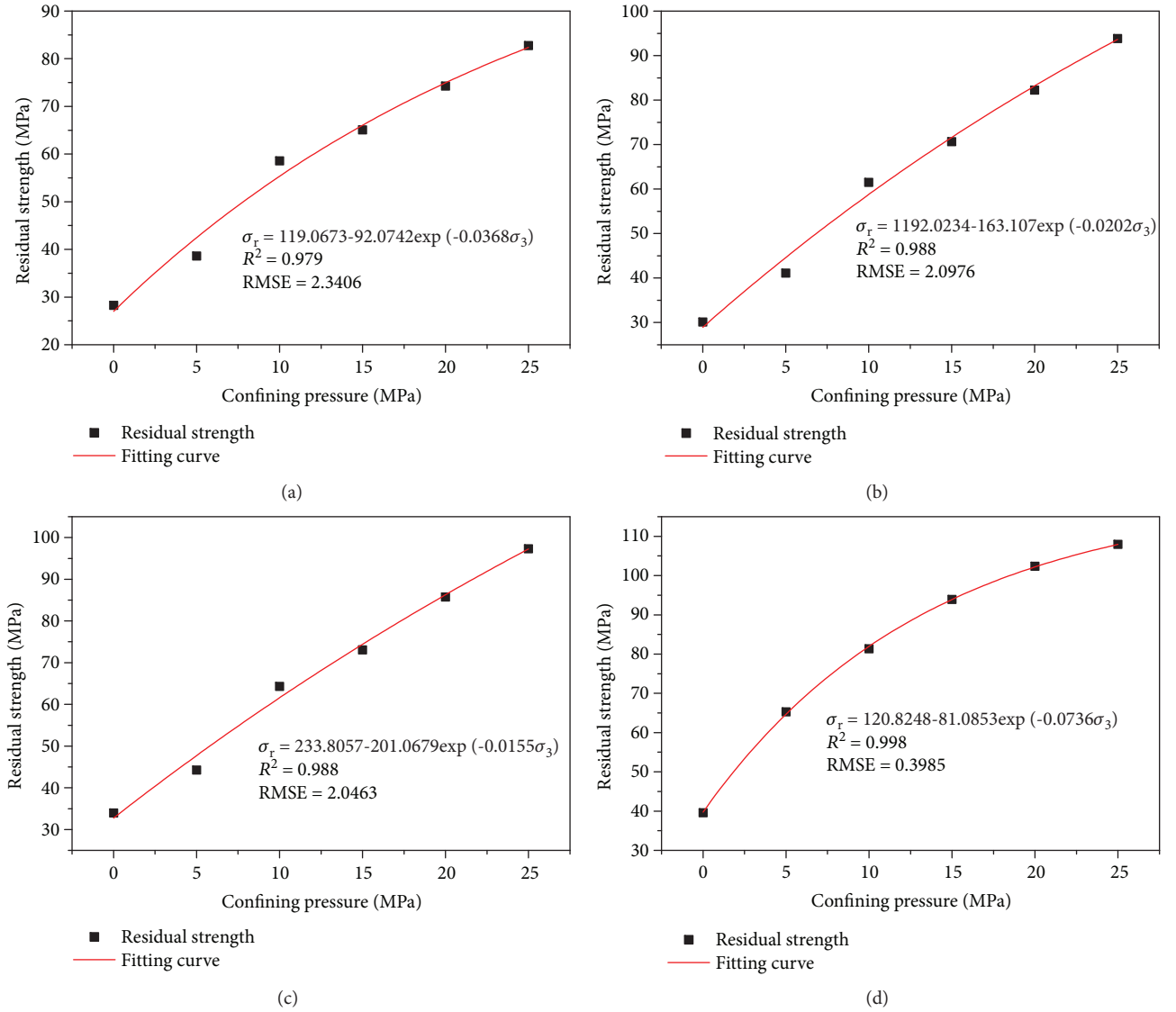


FIGURE 4: Residual strength at various confining pressures of sandstone specimens treated with different chemical corrossions. The chemical environment is (a) H_2SO_4 solution, (b) NaOH solution, (c) distilled water, and (d) natural state.

TABLE 4: Regression results of residual strength at various confining pressures.

Chemical environment	Regression equations
H_2SO_4 solution	$\sigma_r = 119.0673 - 92.0742 \exp(-0.0368\sigma_3) R^2 = 0.979, RMSE = 2.3406$
NaOH solution	$\sigma_r = 192.0234 - 163.1076 \exp(-0.0202\sigma_3) R^2 = 0.988, RMSE = 2.0976$
Distilled water	$\sigma_r = 233.8057 - 201.0679 \exp(-0.0155\sigma_3) R^2 = 0.988, RMSE = 2.0463$
Natural state	$\sigma_r = 120.8248 - 81.0853 \exp(-0.0736\sigma_3) R^2 = 0.998, RMSE = 0.3985$

TABLE 5: Parameters of sandstone treated with different chemical corrosion (30 MPa).

Chemical environment	σ_p (MPa)	ϵ_p	E (GPa)	m	F_0	\varnothing_0 (%)	\varnothing_t (%)	D_c	λ
H_2SO_4 solution	144.14	0.0151	12.99	2.4275	188.4859	5.08	10.76	0.0598	0.78
Distilled water	166.47	0.0162	13.70	2.7855	222.4475	5.14	5.94	0.0084	0.80
NaOH solution	151.27	0.0154	13.30	2.6737	201.4039	5.07	8.64	0.0376	0.82
Natural state	170.86	0.0165	13.81	2.8038	230.2525	5.11	5.11	0	0.81

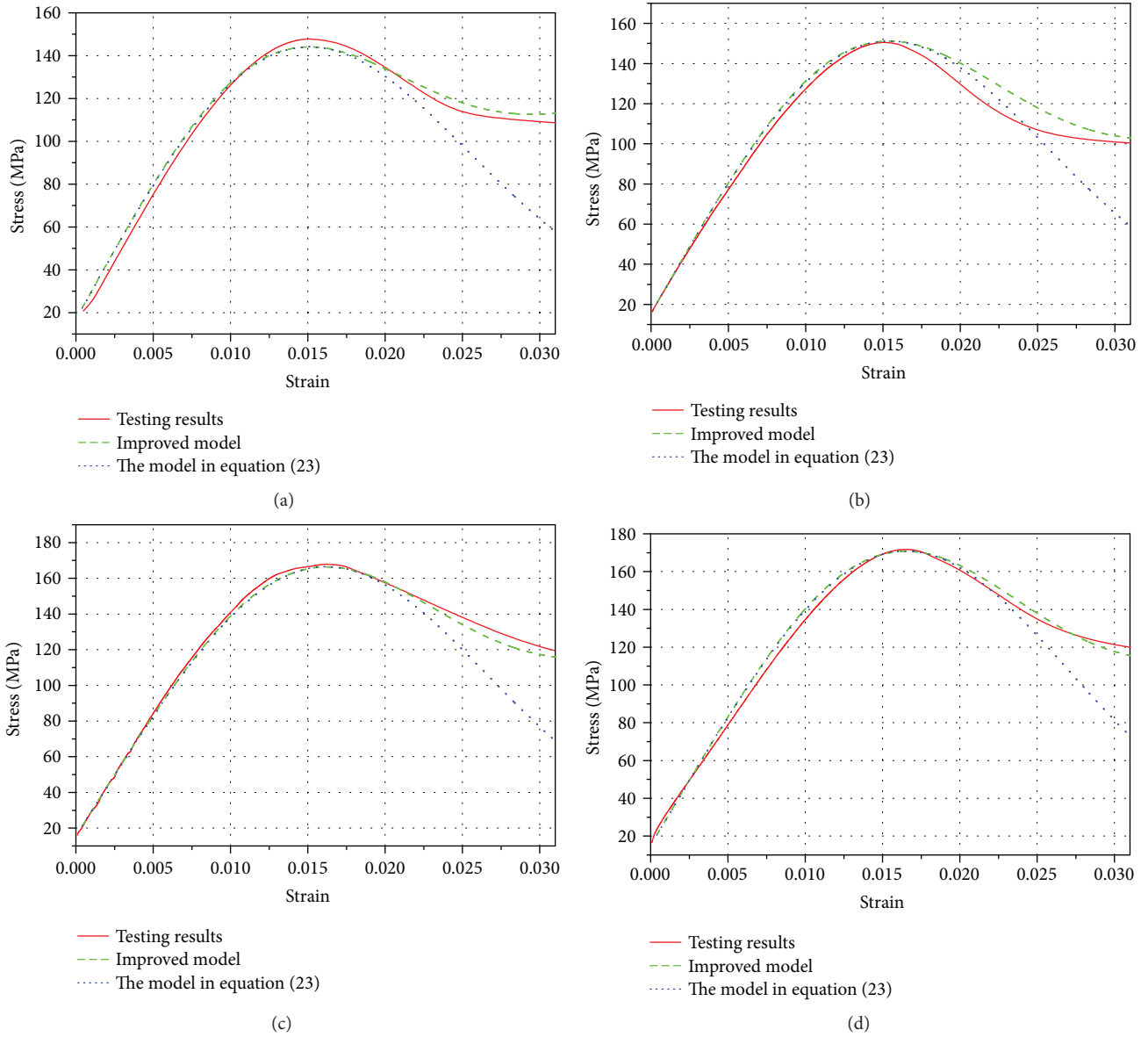


FIGURE 5: Theoretical curves and test curves of sandstone with different chemical corrosions under a confining pressure of 30 MPa. (a) H_2SO_4 solutions, (b) NaOH solution, (c) distilled water, and (d) natural state.

The statistical damage constitutive model established in equation (23) is also simulated to compare the fitting performance of the improved model established in this study. The fitting results of sandstone specimens simulated by the two damage constitutive models and the stress-strain curves of the testing results are shown in Figure 5. Figure 6 shows the coefficient of determination between the two models and experimental data.

From Figure 5, it is obvious that the fitting curves of the improved damage constitutive model proposed in this study are highly similar to the experimental results, and the improved model can well reflect the damage evolution behavior of sandstone treated with chemical corrosion. Compared with the simulation results of the improved model in this study, the fitting results of the model in equation (23)

agree well with the testing curves in the pre-peak stage, but the post-peak curves are greatly deviated from the testing curves, which may be caused by the reason that the damage variable correction coefficient is not considered in the model of equation (23).

In Figure 6, the coefficients between the improved model and experimental data are greater 0.98, indicating that the model is feasible and reliable to describe the mechanical behavior of rocks under a coupled chemical-mechanical condition. Both of the two damage constitutive models have good fitting performance with the coefficients greater than 0.9. It is worth noting that the coefficients of the improved model are larger than that of the model in equation (23), while the values of RMSE of the improved model are smaller, which reveals that the fitting performance of the improved

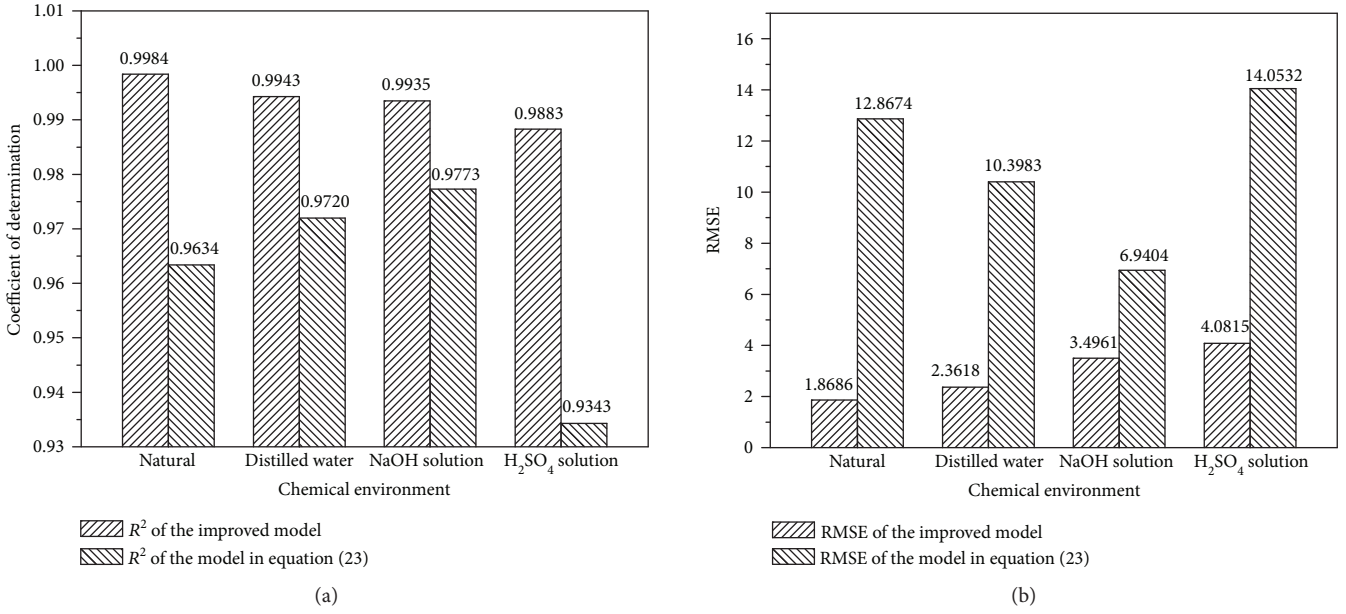


FIGURE 6: R^2 and RMSE between the two models and experimental data.

model proposed in this work is better. Figure 6 further reveals that chemical corrosion has influence on the fitting performance of the improved model, and the ascending order of the effect of different chemical corrosions is H_2SO_4 , NaOH, and distilled water, respectively. This may be caused by the error between the chemical damage variable calculated in this study and the actual chemical damage of rocks. The former is calculated based on the change of porosity and an approximation of the actual chemical damage variable, and the error increases with the increasing of chemical corrosion. Thus, the effect of H_2SO_4 solution and NaOH solution is larger.

Moreover, the improved curves have an increasing trend in the post-peak stage, which is not in accordance with the testing results. This may be due to that Lemaitre's strain-equivalent principle does not take into account that the partial compressive and shear stresses can continue to be propagated after the failure of the microelements of the rock [39]. Therefore, in order to establish a more reasonable statistic constitutive model for rock under the effect of chemical corrosion and loading, more factors should be considered in the future, such as the residual strain and post-peak elastic modulus.

5. Discussion

Figure 7 shows the relationships among m , F_0 , and the chemical damage variable of sandstone specimens. The regression results reveal that the relationships can be described by exponential equations shown in equation (30). Figure 7 further shows that m and F_0 are negatively correlated to the chemical damage variable, and both of them decrease with the chemical damage variable increasing. Based on the results of previous studies [39], m represents the brittleness of rocks and F_0 is the average macroscopic strength of rocks. As known, both

of the brittleness and macroscopic strength of rocks reduce as the chemical damage increases, which is consistent with the evolution law of the two parameters with the chemical damage variable. Thus, the parameter m can reflect the brittleness of sandstone, and F_0 can be used to describe the rock average strength. Moreover, we can obtain the deterioration characteristics of average strength and brittleness of rocks using the chemical damage variable. It may be a meaningful method to investigate the damage evolution behavior and establish the damage constitutive model of rock based on the relationships between m , F_0 , and chemical damage variable, and this will be the further study.

$$\begin{cases} m = -0.0324 \exp\left(\frac{D}{0.0327}\right) + 2.8340, R^2 = 0.999, \\ F_0 = 98.6574 \exp\left(-\frac{D}{0.1099}\right) + 131.4170, R^2 = 0.999. \end{cases} \quad (30)$$

In this study, the method of experimental fitting is used to determine the values of σ_p , ε_p , E , and σ_r . The result showed that the method is convenient and feasible to obtain the Weibull distribution parameters (m and F_0). Though it is only tested on sandstones under a coupled chemical-mechanical condition, it is expected to be suitable for other types of rocks in various environments. This claim needs verifications in future research.

The two-parameter Weibull distribution is the most widely used distribution function, and the results in this paper and other literatures [27, 42, 53, 54, 57, 58] also indicate that the distribution is capable of describing the strength level of the microelements of rock-like materials, while the three-parameter Weibull distribution is considered to be

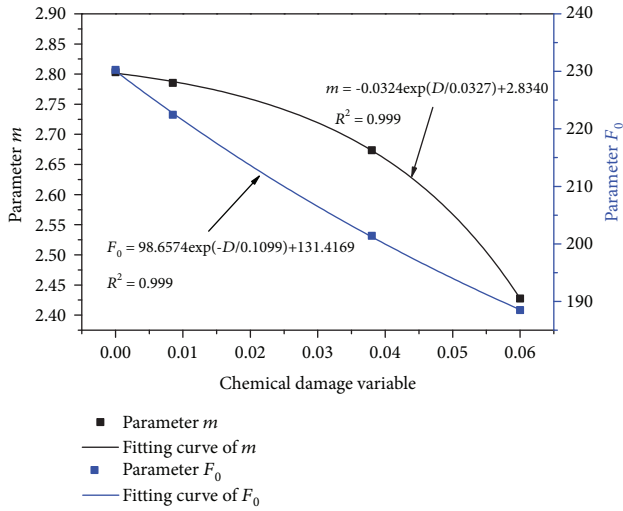


FIGURE 7: The variation of parameters m and F_0 with different chemical damage variables.

the most valuable statistical distribution and has been applied to establish constitutive models of rocks under a coupled thermal-mechanical condition [32, 86]. Therefore, it is necessary and meaningful to investigate the constitutive relationship of corroded rocks based on the three-parameter Weibull distribution, which will be carried out in the next work.

Moreover, the aim of this work is to provide an alternative method to describe the damage evolution process of rock under a coupled chemical-mechanical condition. However, it should be noted that it is still far from fully understanding the damage evolution characteristics of rocks. For example, the cumulative damage develops rapidly and the bearing capacity decay rapidly in the post-peak stage of the brittle materials [39, 55], then the model in this study would not be suitable.

6. Conclusions

In this work, an improved statistical damage constitutive model under a coupled chemical-mechanical condition is established and the following conclusions can be drawn:

- (1) An improved statistical damage constitutive model by combining Weibull distribution, chemical damage variable, and correction coefficient is proposed, which considers the chemical effects and residual strength of sandstone in post-peak stage
- (2) The chemical damage variable is defined in terms of porosity which can be obtained easily. The elastic modulus of sandstone treated with chemical corrosion can be calculated based on the chemical damage variable and initial elastic modulus of rock in the natural state. The fitting performance of the model would decrease with the chemical damage variable increasing
- (3) The relationships between mechanical parameters and confining pressures are determined. The physical

meaning of parameters in the damage constitutive model is discussed based on the correlations between the parameters and chemical damage variable, which enhanced the adoptability of the model

- (4) Based on testing results, the improved statistical damage constitutive model is verified. The fitting performance of the improved model in this study is better with $R^2 > 0.98$, indicating that the improved model is feasible to describe the damage evolution behavior of sandstone treated with different chemical corrosions. Though the proposed model is only tested on sandstones, the model is expected to be applicable to other types of rocks when the dominant damage mechanism due to chemical corrosion is the same

Symbols

σ_i :	Nominal stress (MPa)
σ_i^* :	Effective stress (MPa)
D_m :	Material damage variable under load
λ :	Damage variable correction coefficient
$\sigma_1, \sigma_2, \sigma_3$:	Three principal stresses (MPa)
ε_1 :	Strain correspond to the stress of σ_1
E :	Elastic modulus (GPa)
μ :	Poisson's ratio
N_i :	Number of failed microelements
N :	Total number of microelements.
$P(F)$:	Microelement strength distribution function
m, F_0 :	Shape parameter and scale parameter of Weibull distribution
F :	Parameter which indicates the strength level of the microelement
D :	Total damage variable
D_c :	Chemical damage variable
$\varnothing_0, \varnothing_t$:	Initial porosity of specimen, porosity of specimen after t days of immersion in chemical solutions (%)
E_0 :	Elastic modulus of rock without chemical corrosion (GPa)
∂_0, k_0 :	Material parameters
I_1, J_2 :	First invariant of the stress tensor and the second invariant of the stress deviator
$\sigma_1^*, \sigma_2^*, \sigma_3^*$:	Effective stresses of the three principal stresses (MPa)
φ :	Internal friction angle ($^\circ$)
σ_p :	Peak stress of rock (MPa)
ε_p :	Strain corresponding to the peak stress
F_p :	Strength of the microelement at peak point
σ_r :	Residual strength (MPa)
c :	Cohesion (MPa)
E_{nat} :	Elastic modulus of sandstone specimens under natural state (GPa)
RMSE:	Root mean square error
R^2 :	Coefficient of determination
n :	Number of data points
$\sigma_i, \sigma_p', \sigma_a'$:	Actual value, fitting value, and average value of the stress at the i th data point

Data Availability

Most of the data generated or analysed during this study are included in this manuscript, and all of the data are available from the corresponding author on reasonable request.

Conflicts of Interest

The authors declared no potential conflicts of interest with respect to the research, authorship, and/or publication of this article.

Authors' Contributions

The following are the authors' contributions in this study: Yun Lin—methodology, formal analysis, writing of original draft preparation, and review and editing; Feng Gao—formula derivation and paper revision; Keping Zhou—resources and supervision; Rugao Gao—mechanical testing, review, and editing; and Hongquan Guo—mechanical testing and paper revision.

Acknowledgments

The research presented in this paper was jointly supported by the National Natural Science Foundation of China (Grant No. 51474252 and No. 51774323), the Project of the State Key Laboratory of Safety and Health for Metal Mines of China (Grant No. 2016-JSKSSYS-02), and the Fundamental Research Funds Project of Central South University (Grant No. 2016zzts095). The first author would like to thank the Chinese Scholarship Council for the financial support to the joint PhD studies at the University of Adelaide.

References

- [1] Z. Zhou, X. Cai, W. Cao, X. Li, and C. Xiong, "Influence of water content on mechanical properties of rock in both saturation and drying processes," *Rock Mechanics and Rock Engineering*, vol. 49, no. 8, pp. 3009–3025, 2016.
- [2] H. Bai, D. Ma, and Z. Chen, "Mechanical behavior of groundwater seepage in karst collapse pillars," *Engineering Geology*, vol. 164, pp. 101–106, 2013.
- [3] É. Tóth, O. M. N. Dhubghail, G. Besson, L. Helm, and A. E. Merbach, "Coordination equilibrium—a clue for fast water exchange on potential magnetic resonance imaging contrast agents?," *Magnetic Resonance in Chemistry*, vol. 37, no. 10, pp. 701–708, 1999.
- [4] T. Han, J. Shi, Y. Chen, Z. Li, and C. Li, "Laboratory investigation on the mechanical properties of sandstone immersed in different chemical corrosion under freeze-thaw cycles," *Acta Mechanica Solida Sinica*, vol. 38, no. 6, pp. 503–520, 2017.
- [5] D. Hu, H. Zhou, Q. Hu, J. Shao, X. Feng, and H. Xiao, "A hydro-mechanical-chemical coupling model for geomaterial with both mechanical and chemical damages considered," *Acta Mechanica Solida Sinica*, vol. 25, no. 4, pp. 361–376, 2012.
- [6] D. W. Hu, H. Zhou, F. Zhang, and J. F. Shao, "Evolution of poroelastic properties and permeability in damaged sandstone," *International Journal of Rock Mechanics and Mining Sciences*, vol. 47, no. 6, pp. 962–973, 2010.
- [7] L. Tang, P. Zhang, and S. Wang, "Testing study on macroscopic mechanics effect of chemical action of water on rocks," *Chinese Journal of Rock Mechanics and Engineering*, vol. 21, pp. 526–531, 2002.
- [8] X. Fang, J. Xu, and P. Wang, "Compressive failure characteristics of yellow sandstone subjected to the coupling effects of chemical corrosion and repeated freezing and thawing," *Engineering Geology*, vol. 233, pp. 160–171, 2018.
- [9] X.-T. Feng, S. Chen, and S. Li, "Effects of water chemistry on microcracking and compressive strength of granite," *International Journal of Rock Mechanics and Mining Sciences*, vol. 38, no. 4, pp. 557–568, 2001.
- [10] X.-T. Feng, S. Chen, and H. Zhou, "Real-time computerized tomography (CT) experiments on sandstone damage evolution during triaxial compression with chemical corrosion," *International Journal of Rock Mechanics and Mining Sciences*, vol. 41, no. 2, pp. 181–192, 2004.
- [11] F. Gao, Q. Wang, H. Deng, J. Zhang, W. Tian, and B. Ke, "Coupled effects of chemical environments and freeze-thaw cycles on damage characteristics of red sandstone," *Bulletin of Engineering Geology and the Environment*, vol. 76, no. 4, pp. 1481–1490, 2017.
- [12] T. Han, J. Shi, and X. Cao, "Fracturing and damage to sandstone under coupling effects of chemical corrosion and freeze-thaw cycles," *Rock Mechanics and Rock Engineering*, vol. 49, no. 11, pp. 4245–4255, 2016.
- [13] T. Han, J. Shi, Y. Chen, and X. Cao, "Physical and mechanical properties of marble under the combined effects of chemical solutions and freeze-thaw cycles," *Geotechnical Testing Journal*, vol. 40, no. 6, article 20160225, 2017.
- [14] M. Kaczmarek and T. Hueckel, "Chemo-mechanical consolidation of clays: analytical solutions for a linearized one-dimensional problem," *Transport in Porous Media*, vol. 32, no. 1, pp. 49–74, 1998.
- [15] H. Li, D. Yang, Z. Zhong, Y. Sheng, and X. Liu, "Experimental investigation on the micro damage evolution of chemical corroded limestone subjected to cyclic loads," *International Journal of Fatigue*, vol. 113, pp. 23–32, 2018.
- [16] L. Ning, Z. Yunming, S. Bo, and S. Gunter, "A chemical damage model of sandstone in acid solution," *International Journal of Rock Mechanics and Mining Sciences*, vol. 40, no. 2, pp. 243–249, 2003.
- [17] S. Miao, M. Cai, Q. Guo, P. Wang, and M. Liang, "Damage effects and mechanisms in granite treated with acidic chemical solutions," *International Journal of Rock Mechanics and Mining Sciences*, vol. 88, pp. 77–86, 2016.
- [18] L. Qiao, Z. Wang, and A. Huang, "Alteration of mesoscopic properties and mechanical behavior of sandstone due to hydro-physical and hydro-chemical effects," *Rock Mechanics and Rock Engineering*, vol. 50, no. 2, pp. 255–267, 2017.
- [19] W. Ding and X. Feng, "Testing study on mechanical effect for limestone under chemical erosion," *Chinese Journal of Rock Mechanics and Engineering*, vol. 23, pp. 3571–3576, 2004.
- [20] L. J. Feucht and J. M. Logan, "Effects of chemically active solutions on shearing behavior of a sandstone," *Tectonophysics*, vol. 175, no. 1-3, pp. 159–176, 1990.
- [21] J. H. Dieterich and G. Conrad, "Effect of humidity on time- and velocity-dependent friction in rocks," *Journal of Geophysical Research: Solid Earth*, vol. 89, no. B6, pp. 4196–4202, 1984.
- [22] J. Logan and M. Blackwell, "The influence of chemically active fluids on the frictional behavior of sandstone," *EOS*

- Transactions of the American Geophysical Union*, vol. 64, pp. 835–837, 1983.
- [23] J. Ni, Y.-L. Chen, P. Wang, S.-R. Wang, B. Peng, and R. Azzam, “Effect of chemical erosion and freeze–thaw cycling on the physical and mechanical characteristics of granites,” *Bulletin of Engineering Geology and the Environment*, vol. 76, no. 1, pp. 169–179, 2017.
- [24] A. Chowdhury, “Constitutive modelling and Weibull statistical analysis for the porosity-mechanical property correlations in 3% yttria-stabilized zirconia system,” *International Journal of Refractory Metals and Hard Materials*, vol. 70, pp. 246–252, 2018.
- [25] K. Khaleedi, E. Mahmoudi, M. Datcheva, D. König, and T. Schanz, “Sensitivity analysis and parameter identification of a time dependent constitutive model for rock salt,” *Journal of Computational and Applied Mathematics*, vol. 293, pp. 128–138, 2016.
- [26] X. S. Liu, J. G. Ning, Y. L. Tan, and Q. H. Gu, “Damage constitutive model based on energy dissipation for intact rock subjected to cyclic loading,” *International Journal of Rock Mechanics and Mining Sciences*, vol. 85, pp. 27–32, 2016.
- [27] S. Chen, C. Qiao, Q. Ye, and M. U. Khan, “Comparative study on three-dimensional statistical damage constitutive modified model of rock based on power function and Weibull distribution,” *Environmental Earth Sciences*, vol. 77, no. 3, 2018.
- [28] S. Huang, Q. Liu, A. Cheng, and Y. Liu, “A statistical damage constitutive model under freeze-thaw and loading for rock and its engineering application,” *Cold Regions Science and Technology*, vol. 145, pp. 142–150, 2018.
- [29] G. Li and C.-A. Tang, “A statistical meso-damage mechanical method for modeling trans-scale progressive failure process of rock,” *International Journal of Rock Mechanics and Mining Sciences*, vol. 74, pp. 133–150, 2015.
- [30] J. Deng and D. Gu, “On a statistical damage constitutive model for rock materials,” *Computers & Geosciences*, vol. 37, no. 2, pp. 122–128, 2011.
- [31] C. Gao, L. Z. Xie, H. P. Xie et al., “Coupling between the statistical damage model and permeability variation in reservoir sandstone: theoretical analysis and verification,” *Journal of Natural Gas Science and Engineering*, vol. 37, pp. 375–385, 2017.
- [32] M. Gao, T. Li, T. Wei, and L. Meng, “A statistical constitutive model considering deterioration for brittle rocks under a coupled thermal-mechanical condition,” *Geofluids*, vol. 2018, 10 pages, 2018.
- [33] Z. Wang, Y. Li, and J. G. Wang, “A damage-softening statistical constitutive model considering rock residual strength,” *Computers & Geosciences*, vol. 33, no. 1, pp. 1–9, 2007.
- [34] H. Fu, J. Zhang, Z. Huang, Y. Shi, and W. Chen, “A statistical model for predicting the triaxial compressive strength of transversely isotropic rocks subjected to freeze–thaw cycling,” *Cold Regions Science and Technology*, vol. 145, pp. 237–248, 2018.
- [35] S. Li, Y. Lai, S. Zhang, and D. Liu, “An improved statistical damage constitutive model for warm frozen clay based on Mohr–Coulomb criterion,” *Cold Regions Science and Technology*, vol. 57, no. 2–3, pp. 154–159, 2009.
- [36] X. Li, W.-G. Cao, and Y.-H. Su, “A statistical damage constitutive model for softening behavior of rocks,” *Engineering Geology*, vol. 143–144, pp. 1–17, 2012.
- [37] H. Zhao, C. Zhang, W. Cao, and M. Zhao, “Statistical meso-damage model for quasi-brittle rocks to account for damage tolerance principle,” *Environmental Earth Sciences*, vol. 75, no. 10, 2016.
- [38] M. Ismael and H. Konietzky, “Constitutive model for inherent anisotropic rocks: ubiquitous joint model based on the Hoek–Brown failure criterion,” *Computers and Geotechnics*, vol. 105, pp. 99–109, 2019.
- [39] X. Xu, F. Gao, and Z. Zhang, “Thermo-mechanical coupling damage constitutive model of rock based on the Hoek–Brown strength criterion,” *International Journal of Damage Mechanics*, vol. 27, no. 8, pp. 1213–1230, 2017.
- [40] O. Pourhosseini and M. Shabanimashcool, “Development of an elasto-plastic constitutive model for intact rocks,” *International Journal of Rock Mechanics and Mining Sciences*, vol. 66, pp. 1–12, 2014.
- [41] L. Jiang and Y. Wen, “Damage constitutive model of sandstone during corrosion by AMD,” *Journal of Central South University (Science and Technology)*, vol. 42, no. 11, pp. 3502–3506, 2011.
- [42] S. Miao, H. Wang, M. Cai, Y. Song, and J. Ma, “Damage constitutive model and variables of cracked rock in a hydro-chemical environment,” *Arabian Journal of Geosciences*, vol. 11, no. 2, p. 19, 2018.
- [43] D. Fereidooni, G. R. Khanlari, M. Heidari, A. A. Sepahigero, and A. P. Kolahi-Azar, “Assessment of inherent anisotropy and confining pressure influences on mechanical behavior of anisotropic foliated rocks under triaxial compression,” *Rock Mechanics and Rock Engineering*, vol. 49, no. 6, pp. 2155–2163, 2016.
- [44] M. Hokka, J. Black, D. Tkalich et al., “Effects of strain rate and confining pressure on the compressive behavior of kuru granite,” *International Journal of Impact Engineering*, vol. 91, pp. 183–193, 2016.
- [45] S. Yu, H. Deng, and Y. Zhang, “The constitutive relationship of rock damage considering the effect of temperature and confining pressure,” *Journal of Railway Science and Engineering*, vol. 15, pp. 1–9, 2018.
- [46] J. Lemaitre, “A continuous damage mechanics model for ductile fracture,” *Journal of Engineering Materials and Technology*, vol. 107, no. 1, pp. 83–89, 1985.
- [47] B. Wang, F. Wang, and Q. Wang, “Damage constitutive models of concrete under the coupling action of freeze–thaw cycles and load based on Lemaitre assumption,” *Construction and Building Materials*, vol. 173, pp. 332–341, 2018.
- [48] J. Qian and Z. Yin, *Geotechnical Principles and Calculation*, China Water Resource and Hydropower Press, Beijing, China, 1994.
- [49] K. Dovstam, “Augmented Hooke’s Law in frequency domain. A three dimensional, material damping formulation,” *International Journal of Solids and Structures*, vol. 32, no. 19, pp. 2835–2852, 1995.
- [50] B. T. Brady, “A statistical theory of brittle fracture for rock materials part I—brittle failure under homogeneous axisymmetric states of stress,” *International Journal of Rock Mechanics and Mining Sciences & Geomechanics Abstracts*, vol. 6, no. 1, pp. 21–42, 1969.
- [51] W. Weibull, “A statistical distribution function of wide applicability,” *Journal of Applied Mechanics*, vol. 18, pp. 293–297, 1951.
- [52] D. Krajcinovic and M. A. G. Silva, “Statistical aspects of the continuous damage theory,” *International Journal of Solids and Structures*, vol. 18, no. 7, pp. 551–562, 1982.

- [53] M. R. M. Aliha and M. R. Ayatollahi, "Rock fracture toughness study using cracked chevron notched Brazilian disc specimen under pure modes I and II loading – a statistical approach," *Theoretical and Applied Fracture Mechanics*, vol. 69, pp. 17–25, 2014.
- [54] N. Erarslan, Z. Z. Liang, and D. J. Williams, "Experimental and numerical studies on determination of indirect tensile strength of rocks," *Rock Mechanics and Rock Engineering*, vol. 45, pp. 739–751, 2012.
- [55] X. Xu, M. Karakus, F. Gao, and Z. Zhang, "Thermal damage constitutive model for rock considering damage threshold and residual strength," *Journal of Central South University*, vol. 25, no. 10, pp. 2523–2536, 2018.
- [56] B. Deng, D. Jiang, and J. Gong, "Is a three-parameter Weibull function really necessary for the characterization of the statistical variation of the strength of brittle ceramics?," *Journal of the European Ceramic Society*, vol. 38, no. 4, pp. 2234–2242, 2018.
- [57] T. Saksala, "Damage-viscoplastic consistency model with a parabolic cap for rocks with brittle and ductile behavior under low-velocity impact loading," *International Journal for Numerical and Analytical Methods in Geomechanics*, vol. 34, no. 13, pp. 1362–1386, 2010.
- [58] M. Sari and C. Karpuz, "Rock variability and establishing confining pressure levels for triaxial tests on rocks," *International Journal of Rock Mechanics and Mining Sciences*, vol. 43, no. 2, pp. 328–335, 2006.
- [59] B. Ke, K. Zhou, C. Xu, H. Deng, J. Li, and F. Bin, "Dynamic mechanical property deterioration model of sandstone caused by freeze–thaw weathering," *Rock Mechanics and Rock Engineering*, vol. 51, no. 9, pp. 2791–2804, 2018.
- [60] R. Peng, Y. Yang, Y. Ju, L. Mao, and Y. Yang, "Computation of fractal dimension of rock pores based on gray CT images," *Chinese Science Bulletin*, vol. 56, no. 31, 2011.
- [61] J. Teng, J. Tang, Y. Zhang, and X. Li, "CT experimental study on the damage characteristics of anchored layered rocks," *KSCE Journal of Civil Engineering*, vol. 22, no. 9, pp. 3653–3662, 2018.
- [62] Y. Wang, X. Li, B. Zhang, and Y. Wu, "Meso-damage cracking characteristics analysis for rock and soil aggregate with CT test," *Science China Technological Sciences*, vol. 57, no. 7, pp. 1361–1371, 2014.
- [63] H. Chen, H. Tang, and S. Ye, "Damage model of control fissure in perilous rock," *Applied Mathematics and Mechanics*, vol. 27, no. 7, pp. 967–974, 2006.
- [64] J. Jin, X. Li, Z. Yin, and Y. Zou, "A method for defining rock damage variable by wave impedance under cyclic impact loadings," *Rock and Soil Mechanics*, vol. 32, pp. 1385–1393, 2011.
- [65] J.-Q. Xiao, D.-X. Ding, F.-L. Jiang, and G. Xu, "Fatigue damage variable and evolution of rock subjected to cyclic loading," *International Journal of Rock Mechanics and Mining Sciences*, vol. 47, no. 3, pp. 461–468, 2010.
- [66] G. Lu, E. Yan, X. Wang, L. Xie, and L. Gao, "Study of impact of fractal dimension of pore distribution on compressive strength of porous material," *Rock and Soil Mechanics*, vol. 35, pp. 2261–2269, 2014.
- [67] L. M. Kachanov, "Rupture time under creep conditions," *International Journal of Fracture*, vol. 97, no. 1/4, pp. 11–18, 1999.
- [68] G. Li, C.-A. Tang, and Z.-Z. Liang, "Development of a parallel FE simulator for modeling the whole trans-scale failure process of rock from meso- to engineering-scale," *Computers & Geosciences*, vol. 98, pp. 73–86, 2017.
- [69] L. C. Li, C. A. Tang, S. Y. Wang, and J. Yu, "A coupled thermo-hydrologic-mechanical damage model and associated application in a stability analysis on a rock pillar," *Tunnelling and Underground Space Technology*, vol. 34, pp. 38–53, 2013.
- [70] D. C. Drucker and W. Prager, "Soil mechanics and plastic analysis or limit design," *Quarterly of Applied Mathematics*, vol. 10, no. 2, pp. 157–165, 1952.
- [71] R. I. Borja, R. A. Regueiro, and T. Y. Lai, "FE modeling of strain localization in soft rock," *Journal of Geotechnical and Geoenvironmental Engineering*, vol. 126, no. 4, pp. 335–343, 2000.
- [72] B. Loret and J. H. Prevost, "Accurate numerical solutions for Drucker-Prager elastic-plastic models," *Computer Methods in Applied Mechanics and Engineering*, vol. 54, no. 3, pp. 259–277, 1986.
- [73] V. Mazel, H. Diarra, V. Busignies, and P. Tchoreloff, "Comparison of different failure tests for pharmaceutical tablets: applicability of the Drucker-Prager failure criterion," *International Journal of Pharmaceutics*, vol. 470, no. 1-2, pp. 63–69, 2014.
- [74] Z. T. Bieniawski and M. J. Bernede, "Suggested methods for determining the uniaxial compressive strength and deformability of rock materials," *International Journal of Rock Mechanics and Mining Sciences & Geomechanics Abstracts*, vol. 16, no. 2, pp. 138–140, 1979.
- [75] Z. Zhou, X. Cai, L. Chen, W. Cao, Y. Zhao, and C. Xiong, "Influence of cyclic wetting and drying on physical and dynamic compressive properties of sandstone," *Engineering Geology*, vol. 220, pp. 1–12, 2017.
- [76] W. Rùhaak, C.-D. Heldmann, L. Pei, and I. Sass, "Thermo-hydro-mechanical-chemical coupled modeling of a geothermally used fractured limestone," *International Journal of Rock Mechanics and Mining Sciences*, vol. 100, pp. 40–47, 2017.
- [77] A. R. Adebayo, M. E. Kandil, T. M. Okasha, and M. L. Sanni, "Measurements of electrical resistivity, NMR pore size and distribution, and x-ray CT-scan for performance evaluation of CO₂ injection in carbonate rocks: a pilot study," *International Journal of Greenhouse Gas Control*, vol. 63, pp. 1–11, 2017.
- [78] A. Z. Al-Yaseri, M. Lebedev, S. J. Vogt, M. L. Johns, A. Barifcani, and S. Iglauer, "Pore-scale analysis of formation damage in Bentheimer sandstone with in-situ NMR and micro-computed tomography experiments," *Journal of Petroleum Science and Engineering*, vol. 129, pp. 48–57, 2015.
- [79] J. Li, K. Zhou, W. Liu, and H. Deng, "NMR research on deterioration characteristics of microscopic structure of sandstones in freeze–thaw cycles," *Transactions of Nonferrous Metals Society of China*, vol. 26, no. 11, pp. 2997–3003, 2016.
- [80] C. Liu, H. Deng, Y. Wang, Y. Lin, and H. Zhao, "Time-varying characteristics of granite microstructures after cyclic dynamic disturbance using nuclear magnetic resonance," *Crystals*, vol. 7, no. 10, pp. 306–317, 2017.
- [81] H. Liu, L. Xiao, F. Deng, W. Chen, and P. Galvosas, "Emerging NMR approaches for characterizing rock heterogeneity," *Microporous and Mesoporous Materials*, vol. 269, pp. 118–121, 2018.
- [82] X. Yang, L. Weng, and Z. Hu, "Damage evolution of rocks under triaxial compressions: an NMR investigation," *KSCE Journal of Civil Engineering*, vol. 22, no. 8, pp. 2856–2863, 2018.
- [83] Y. Zhao, G. Zhu, Y. Dong, N. N. Danesh, Z. Chen, and T. Zhang, "Comparison of low-field NMR and microfocus

- X-ray computed tomography in fractal characterization of pores in artificial cores,” *Fuel*, vol. 210, pp. 217–226, 2017.
- [84] K.-p. Zhou, B. Li, J. L. Li, H. W. Deng, and F. Bin, “Microscopic damage and dynamic mechanical properties of rock under freeze–thaw environment,” *Transactions of Nonferrous Metals Society of China*, vol. 25, no. 4, pp. 1254–1261, 2015.
- [85] S.-Q. Yang, P. Xu, and P. G. Ranjith, “Damage model of coal under creep and triaxial compression,” *International Journal of Rock Mechanics and Mining Sciences*, vol. 80, pp. 337–345, 2015.
- [86] X. L. Xu and M. Karakus, “A coupled thermo-mechanical damage model for granite,” *International Journal of Rock Mechanics and Mining Sciences*, vol. 103, pp. 195–204, 2018.
- [87] H. Jiang, “Simple three-dimensional Mohr–Coulomb criteria for intact rocks,” *International Journal of Rock Mechanics and Mining Sciences*, vol. 105, pp. 145–159, 2018.
- [88] J. Shen, S. D. Priest, and M. Karakus, “Determination of Mohr–Coulomb shear strength parameters from generalized Hoek–Brown criterion for slope stability analysis,” *Rock Mechanics and Rock Engineering*, vol. 45, no. 1, pp. 123–129, 2012.
- [89] M. Singh, A. Raj, and B. Singh, “Modified Mohr–Coulomb criterion for non-linear triaxial and polyaxial strength of intact rocks,” *International Journal of Rock Mechanics and Mining Sciences*, vol. 48, no. 4, pp. 546–555, 2011.
- [90] A. I. Sofianos and P. P. Nomikos, “Equivalent Mohr–Coulomb and generalized Hoek–Brown strength parameters for supported axisymmetric tunnels in plastic or brittle rock,” *International Journal of Rock Mechanics and Mining Sciences*, vol. 43, no. 5, pp. 683–704, 2006.
- [91] N. N. Sirdesai, A. Singh, L. K. Sharma, R. Singh, and T. N. Singh, “Determination of thermal damage in rock specimen using intelligent techniques,” *Engineering Geology*, vol. 239, pp. 179–194, 2018.

Research Article

Investigation of the Velocities of Coals of Diverse Rank under Water- or Gas-Saturated Conditions for Application in Coalbed Methane Recovery

Jizhao Xu,^{1,2,3,4} Cheng Zhai ,^{1,2,3} Pathegama Gamage Ranjith,⁴ Yong Sun,^{1,2,3} Jisheng Guo,^{1,2,3} Zheng Ma,^{1,2,3} Huiteng Ma,^{1,2,3} and Lei Qin⁵

¹Key Laboratory of Coal Methane and Fire Control, Ministry of Education, China University of Mining and Technology, Xuzhou, Jiangsu 221116, China

²State Key Laboratory of Coal Resources and Safe Mining, Xuzhou, Jiangsu 221116, China

³School of Safety Engineering, China University of Mining and Technology, 221116 Xuzhou, China

⁴Department of Civil Engineering, Building 60, Monash University, Clayton, VIC 3800, Australia

⁵College of Safety Science and Engineering, Xi'an University of Science and Technology, 710054 Xi'an, China

Correspondence should be addressed to Cheng Zhai; greatzc@cumt.edu.cn

Received 30 November 2018; Revised 29 January 2019; Accepted 27 March 2019; Published 2 May 2019

Guest Editor: Giorgio Minelli

Copyright © 2019 Jizhao Xu et al. This is an open access article distributed under the Creative Commons Attribution License, which permits unrestricted use, distribution, and reproduction in any medium, provided the original work is properly cited.

Coalbed methane recovery enhanced by hydraulic or nonaqueous fracturing methods has been studied for decades, and it is of significance to evaluate fracturing results and scope for field applications. Monitoring variation in velocity is one way to explain fracturing effects. However, the existence of residual water or gas within cracks or pores may affect velocity measurements, and the correlation between velocity and inherent coal attributes (such as density and porosity) has not been studied comprehensively. In this paper, coal of different ranks (lignite, bituminite, and anthracite) was prepared under water and gas saturation to approximately simulate the residual water and gas in cracks under field applications. Correlations between the velocity and coal attributes were studied. For both water- and gas-saturated cores, the diverse velocity distributions were highly correlated to rank and saturation media. The longitudinal ultrasonic pulse velocity (UPV_p) and transverse ultrasonic pulse velocity (UPVs) of different cores were distributed differently. For coal saturated with water or gas, the UPV_p values of lignite, bituminite, and anthracite had positive linear correlations with the corresponding UPVs values. The discrete velocity ratio data were fit as negative linear correlations with UPVs, and different coals had different declining degrees, the difference of which might be attributed to the characteristics of structural cracks and the inherent properties of the coal, such as grain size and pore shape, which result in decreasing coal integrity and strength. Moreover, the difference in acoustic resistance between coal and fluids might have an inverse impact on the acoustic energy, and a larger difference might cause a large amount of energy to dissipate and finally cause the velocity to decrease. Under water and gas saturation conditions, the UPV_p showed a positive linear correlation with density and a negative linear correlation with porosity. Finally, a potential field application was designed on the relations between the velocity and the elastic parameters to estimate fracturing effects by monitoring the petrophysical parameters of coal lithologies.

1. Introduction

Effective coalbed methane (CBM) drainage is a topical research issue around the world. CBM also occupies an increasing proportion of the resource structure in China, and its efficient use is likely to ease the pressure on other

diminishing fossil fuel reserves [1–4]. CBM reserves in China typically have properties that constrain their extractability, such as great depth, great density, or low permeability [5–7]. Some technologies, such as hydraulic and nonaqueous fracturing, have been proposed to improve fracture connection and thus enhance the permeability of the CBM reserves

[8–11]. Meanwhile, the inherent properties of coal also play an important role in controlling fracturing [12–14]. For example, bulk density and strength (bulk modulus and shear modulus) provide information about integrity under different pressure-temperature states, as well as mineral constituents and their distribution influence homogeneity. Coal rank correlates with the degree of anisotropy in some respects, such as anisotropic ultrasonic velocity, porosity, and fracture orientation. It is of significance to evaluate fracturing results and scope for field applications. The ultrasonic pulse velocity (UPV) method is commonly used to obtain various information on material properties and rock quality because it is convenient, nondestructive, and highly efficient [15, 16]. The UPV method can be used to detect microscopic cracks within the matrix [17, 18] and to evaluate the efficacy of consolidation in concrete [19, 20].

The UPV testing method in a laboratory setting uses a pair of transducers (one transducer as a signal emitter and another transducer as a receiver) to quantify ultrasonic pulse transmission through a sample using an oscilloscope. There are two main parameters of interest: longitudinal ultrasonic pulse velocity (UPVp) and transverse ultrasonic pulse velocity (UPVs), as shown in Figure 1. The velocity is calculated as follows [21]:

$$V = \frac{L}{t_2 - t_1}, \quad (1)$$

where L is the length of the sample, t_1 and t_2 are the docking time of the transducers and the first arrival time of the wave signal by the receiver sensor, respectively, and $t_2 - t_1$ is the travel time.

Vilhelm et al. [22] studied velocity dispersion in fractured rocks over a wide frequency range (~ 1 kHz, ~ 40 kHz, and ~ 1 MHz) and successfully used a displacement discontinuity approach in a theoretical model to conclude that the first arrivals of seismic waves can be used to evaluate P -wave velocity. Nakahata et al. [23] proposed a time domain simulation tool based on finite integration and an image-based modeling approach to better understand the characteristics of ultrasonic wave propagation in concrete. Pulse wave velocities are thought to reflect the mechanical properties of rocks [24–27], which were evaluated using the UPV method by Vasaneli et al. [28], in terms of the physical and mechanical properties of a highly porous building limestone. Statistical information on the correlation between compressional and shear wave velocities and the corresponding Poisson's ratios of different lithologies at different pressure-temperature conditions has also been found [29–33]. Lokajčićek et al. [34] studied the influence of thermal heating on elastic wave velocity within granulite samples under different stress levels using a three-dimensional P -wave elastic anisotropy method.

UPV testing has also been used to evaluate coal properties and various influencing factors such as confining stress, temperature, moisture content, and porosity. The ultrasonic wave velocity of coal under lower confining stress increases with rank because of fracture closure [35, 36]. Liu et al. [37] divided the effects of water saturation on P -wave propagation

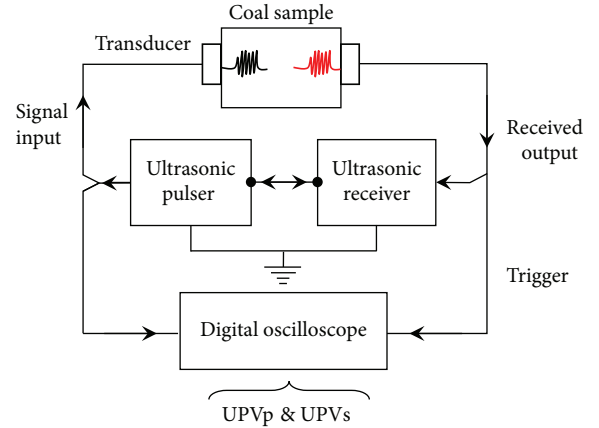


FIGURE 1: Schematic diagram of the UPV device used in this study.

in fractured coal into three types. Pulse wave velocity and anisotropy of tectonically deformed coal have been used to show that the V_p/V_s ratio, Poisson's ratio, and anisotropy are all sensitive to deformation type and extent [21]. Additionally, structural fractures were found to have a significant impact on the elastic properties of coal samples from different deformation environments [21]. Lwin [38] studied the effect of different gases (He , N_2 , CH_4 , and CO_2) on the ultrasonic response of coal and revealed a significant difference in density, P -wave modulus, and impedance for CO_2 saturation compared with CH_4 saturation. Yu et al. [39] studied pore variations and changes in P -wave velocity of coal affected by ultrasonic excitation and found that the P -wave velocity decreased with increasingly affected cycles.

The velocity monitoring method has been applied to fracturing estimation; however, residual water or gas occupies pores and cracks after fracturing. The impact of residual water or gas on the accurate evaluation of velocity and the correlations between inherent attributes (porosity, density, and rank) have not been studied comprehensively. In this paper, three different ranks of coals, including 24 lignites, 26 bituminites, and 26 anthracites, are tested (UPVp and UPVs) under both water and gas (air) saturation. The correlations among velocity, density, and porosity are described, and the statistical results can provide reference parameters for further field monitoring in coal physics in terms of CBM reservoir fracturing processes.

2. Materials and Methods

2.1. Coal Preparation. Lignite, bituminite, and anthracite samples were collected from the Shengli Coal Mine, Inner Mongolia; the Datong Coal Mine, Shanxi; and the Yangzhuang Coal Mine, Huaibei; respectively. The large coal blocks were wrapped with preservative film and transferred to the State Key Laboratory of Coal Resources and Safe Mining in Xuzhou, Jiangsu, before being cored to produce 5 cm diameter cylinders with 10 cm height (Figures 2(a) and 2(b)). To conveniently measure the pulse velocity of the cores, the tops and bottoms of the cylinders were ground flat to ensure a parallelism error of ≤ 0.005 mm [40]. The detailed properties of the 24 lignite cores ($R_{o,max}$ of 0.32), 26 bituminite cores

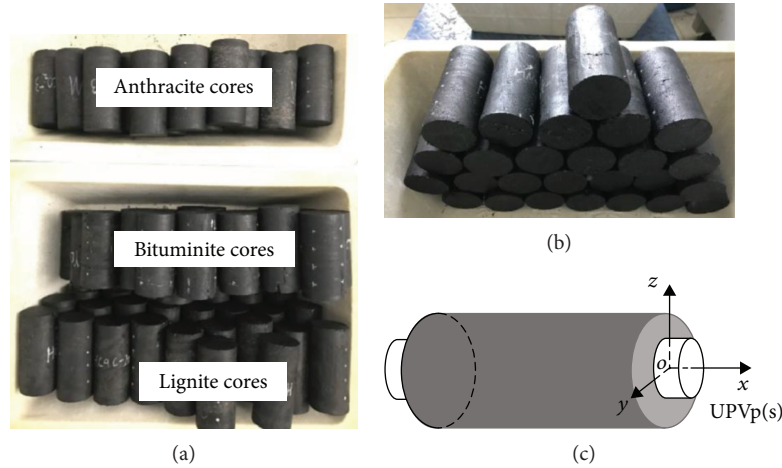


FIGURE 2: Images of 76 coals with different ranks. (a) Overall view of the 76 coal cores, (b) lateral display of lignite cores, and (c) sketch image of UPV test method.

($R_{o,max}$ of 1.13), and 26 anthracite cores ($R_{o,max}$ of 3.05) [41] are listed in Table 1. The density of the lignite, bituminite, and anthracite cores was measured to be 1.28 g/cm^3 to 1.55 g/cm^3 , 1.23 g/cm^3 to 1.42 g/cm^3 , and 1.29 g/cm^3 to 1.61 g/cm^3 , respectively. The porosity of the cores was measured to be in the ranges of 1.07% to 3.17%, 0.3% to 4.0% and 0.3% to 2.9%, respectively. The core samples were preserved in a curing box to maintain their original structure and moisture content.

2.2. Experimental Equipment and Procedures. The UPV test equipment used to record the UPVp and UPVs values of the cores under water and gas saturation (the gas during the experiment and referred to in the paper is air) was an HS-YS4A Sonic wave parameter tester (Tianhong Electronics, Xiangtan, China). This apparatus operates with a high signal-to-noise ratio and has low temperature excursions and high repeatability with low failure rate. The instrument has two emitter options, 160 V or 1000 V, and the amplifier can be regulated with multistage attenuation processes.

Gas saturation was carried out in an autoclave with a pressure of 1.5 MPa to ensure that air occupied the internal pores or cracks in the cores, and water saturation was undertaken using a vacuum pump (ZN-BSJ, Suzhou Niumag Analytical Instrument Corporation, Suzhou, China) by depressurizing the cores to approximately -1.0 MPa, thus allowing water ingress into the pore spaces of the core.

The ambient temperature during the experiments was 25°C , and to eliminate the high-frequency effect on fluid-saturated samples when measuring velocity, the 160 V emitter was chosen with a frequency of 50 kHz. The experimental procedure was carried out in the following steps:

- (i) All the cores were placed in a vacuum drying oven at 60°C for 72 h to remove the original gas and water from the cores, and their masses were tested using an electronic balance and were recorded as M_{pre}
- (ii) The cores were placed in the autoclave at a pressure of 1.5 MPa for 72 h to achieve gas saturation, the

velocity parameters were tested using the velocity apparatus by connecting the core surface and the transducers, and the values were recorded as $UPVp_{-gas}$ and $UPVs_{-gas}$

- (iii) The cores were then immersed in the water saturator, and all the air was exhausted to ensure that water occupied the pores, at a pressure of -0.95 MPa for 72 h. The mass of water-saturated cores was recorded as M_{water} ; then, the velocities were measured as $UPVp_{-water}$ and $UPVs_{-water}$

3. Results

Figure 3 shows box plots of velocity recorded in different cores. There are significant differences in terms of velocity distribution and discrete degree according to coal rank and saturation media. For example, the box plot ranges (from lower to upper quartile) of UPVp are larger than those of UPVs for both water-saturated and gas-saturated cores. The UPVp(s) box plot ranges of water-saturated cores exceed those of gas-saturated cores. Water saturation in microcracks improves the continuity of wave propagation with less discrete velocity than gas saturation conditions. Statistically, the width of the UPVp box plots is smaller than the corresponding UPVs box plots under water saturation conditions, which indicates that UPVp has less data dispersion than UPVs. Thus, UPVp is more accurate or reliable for characterizing the existence of micro- or macrocracks with the assistance of adsorbed water. Anthracite cores have a smaller UPVp box plot width than the other plots, which means that the greater rank has less porosity and higher homogeneity, resulting in greater velocity concentration.

UPVp and UPVs velocity ranges and mean values for the three types of coal are listed in Table 2. The largest values in the velocity ranges were recorded in anthracite cores ($UPVp_{-water}$ 1.63 km/s to 2.25 km/s, $UPVs_{-water}$ 1.26 km/s to 1.87 km/s, $UPVp_{-gas}$ 1.12 km/s to 1.94 km/s, and $UPVs_{-gas}$ 0.74 km/s to 1.69 km/s). The lowest velocity ranges were recorded in lignite cores, with intermediate values recorded

TABLE 1: Detail properties of the coals with different ranks.

Type	Density (g/cm ³)	Porosity (%)	Proximate analysis (%)					Maceral analysis (%)			
			M_{ad}	A_{ad}	V_{daf}	FC_{ad}	$R_{o,max}$ (%)	V	I	E	M
Lignite	1.28-1.55	1.07-3.17	11.37	14.63	53.41	20.59	0.32	79.5	15.5	3.6	1.4
Bituminite	1.23-1.42	0.3-4.0	8.83	3.30	29.64	58.23	1.13	58.7	32.6	3.4	5.3
Anthracite	1.29-1.61	0.3- 2.9	2.10	7.73	6.48	83.69	3.05	86.4	10.5	1.5	1.6

M_{ad} : water content; A_{ad} : ash content; V_{daf} : volatile component; FC_{ad} : fixed carbon content; V : vitrinite; I : inertinite; E : exinite; M : mineral content; $R_{o,max}$: the maximum reflectance of vitrinite.

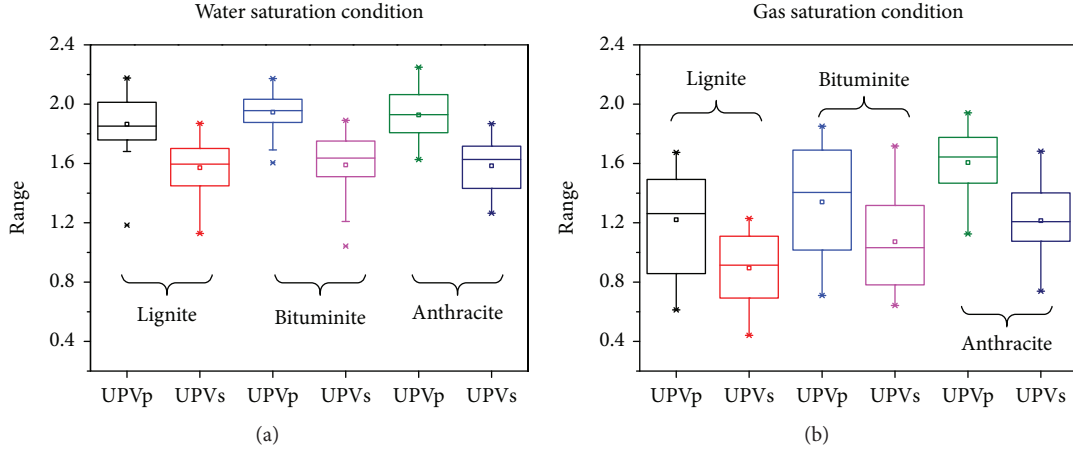


FIGURE 3: Box plots of different coal rank samples at (a) water saturation and (b) gas saturation condition.

TABLE 2: UPVp and UPVs velocity ranges and the mean values of three ranks of coals.

	Water saturation condition (km/s)				Gas saturation condition (km/s)			
	UPVp	UPVp _{mean}	UPVs	UPVs _{mean}	UPVp	UPVp _{mean}	UPVs	UPVs _{mean}
Lignite	[1.18, 2.17]	1.86	[1.13, 1.87]	1.57	[0.61, 1.67]	1.22	[0.44, 1.23]	0.90
Bituminite	[1.61, 2.17]	1.95	[1.04, 1.89]	1.59	[0.71, 1.85]	1.34	[0.64, 1.72]	1.07
Anthracite	[1.63, 2.25]	1.93	[1.26, 1.87]	1.58	[1.12, 1.94]	1.61	[0.74, 1.69]	1.21

in bituminite cores. In addition, the anthracite cores had the largest UPVp_{mean} value of 1.93 km/s and UPVs_{mean} value of 1.58 km/s under water saturation, with UPVp_{mean} and UPVs_{mean} values of 1.61 km/s and 1.21 km/s, respectively, under gas saturation. The mean velocity values of other sample types followed a trend similar to the measured velocities, and it is posited that coal rank is largely responsible for the variation in recorded ultrasonic velocity.

4. Discussion

4.1. Correlation between UPVp and UPVs. Given the different velocity distributions of the three ranks of coal, it is necessary to analyze correlations between the UPVp and UPVs under the two different conditions. The scatter of velocity data and correlations of fit are shown in Figure 4. The UPVp and UPVs values of the cores differed for both conditions, and they might depend on the coal rank and components within the coal matrix. Velocity values of cores from the same

coal blocks were not consistent, because of the various orientations and distributions of microcracks. When an elastic wave transfers to existing defects, such as cleats, cracks, or pores, some reflection, refraction, and diffraction of waves and friction at the crack surface and the grain boundaries might be generated, causing amplitude attenuation and energy decrease [21, 40, 42]. The crack number and distribution might be the main factors influencing velocity decrease. The larger the number of existing cracks is, the greater the energy decrease, and the smaller the velocity is. Under water and gas saturation, the UPVp values generally exceed the UPVs values, and the UPVp and UPVs values of the same cores under water saturation exceed those under gas saturation, indicating that the discrete degree of velocity might occur more frequently under gas saturation due to the large dispersion of air molecules. The scatter in velocity data values is well fit and listed in Table 3.

Dependent on Figure 4, the UPVp values of lignite, bituminite, and anthracite coal showed positive linear correlations

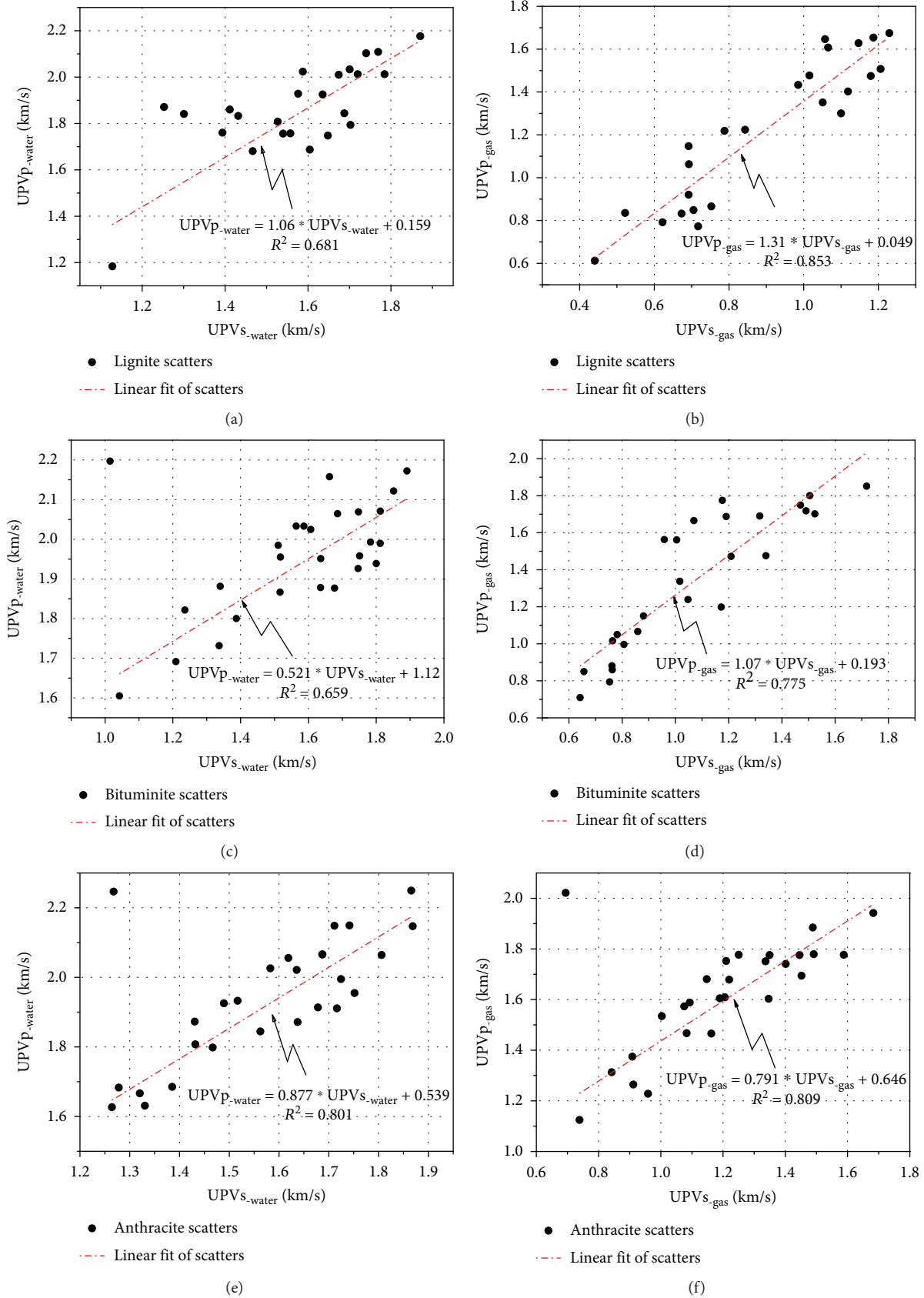


FIGURE 4: Scatterplot of velocity data and goodness-of-fit correlations between UPVs and UPVp of lignite, bituminite, and anthracite cores under water and gas saturation.

TABLE 3: Correlations between UPVp and UPVs for lignite, bituminite, and anthracite under water or gas saturation.

	Condition	Equation	R^2
Lignite	Water saturation	$UPVp_{-water} = 1.06 * UPVs_{-water} + 0.159$	0.681
	Gas saturation	$UPVp_{-gas} = 1.31 * UPVs_{-gas} + 0.049$	0.853
Bituminite	Water saturation	$UPVp_{-water} = 0.521 * UPVs_{-water} + 1.12$	0.659
	Gas saturation	$UPVp_{-gas} = 1.07 * UPVs_{-gas} + 0.193$	0.775
Anthracite	Water saturation	$UPVp_{-water} = 0.877 * UPVs_{-water} + 0.539$	0.801
	Gas saturation	$UPVp_{-gas} = 0.791 * UPVs_{-gas} + 0.646$	0.809

with their corresponding UPVs values, under water and gas saturation, similar to the results reported by Kahraman [16], Sayed et al. [43], and Kassab and Weller [44] that UPVp scatter had a strong linear correlation with the corresponding UPVs scatter of dry rock or wet rock samples. When the UPVs-water value was 2.0 km/s, the potential UPVp-water values of lignite, bituminite, and anthracite were 2.279 km/s, 2.162 km/s, and 2.293 km/s, respectively. This difference appears to be dependent on porosity and moisture content, given that the lower the porosity and the higher the moisture content is, the larger the UPVp value is [45].

4.2. Analysis of Velocity Ratio vs. UPVs. Because the different cores have various UPVp and UPVs values, a parameter V_r , namely, velocity ratio, is introduced to eliminate the impact of coal volume and density [21, 37] (seen in equation (2)) and to explore potential correlations between the ratio and the corresponding UPVs values for lignite, bituminite, and anthracite.

$$\begin{cases} V_{r_water} = \frac{UPVp_{-water(i)}}{UPVs_{-water(i)}}, \\ V_{r_gas} = \frac{UPVp_{-gas(i)}}{UPVs_{-gas(i)}}, \end{cases} \quad (2)$$

where V_{r_water} and V_{r_gas} are the velocity ratios of coal under water and gas saturation, respectively, and i is the number of one kind of coal; specifically, i equals to 24 for lignite and 26 for bituminite and anthracite. As seen in Figure 5, V_r correlates linearly with the corresponding UPVs values. The linear fitting equations are listed in Table 4. These discrete V_r data are fitted as negative linear relationships with UPVs, and different coals have different declining degrees. The difference in the velocity ratio might be attributed to the characteristics of structural cracks and inherent properties of the coal, such as grain size and pore shape, which result in the decrease of the coal integrity and strength.

For one particular coal with certain porosity, elastic waves show different responses to different fluids occupying the cracks; for example, the UPVp has higher sensitivity with a small amount of gas compared to the UPVs, and the UPVp value might decrease by a larger degree than the UPVs value [46, 47]. As shown in Figure 5, the declining tendency of the correlations between V_r and UPVs indicates that the degree

of increase in the UPVp is smaller than that in the UPVs, when the elastic wave propagates via cracks occupied by fluids. According to Kuster and Toksoz [40], different media had different acoustic resistance (AR) values; for example, the AR value of gas was $0.0043 \times 10^4 \text{ g}/(\text{m}^2 \cdot \text{s})$, whereas that of water was $(0.29 - 0.66) \times 10^4 \text{ g}/(\text{m}^2 \cdot \text{s})$, and coal had a smaller AR difference with water. It seemed that the difference in declining tendency might be attributed to coal rank, and the coal with a lower rank had a large amount of fissures. When the fissures were filled with water or gas, the larger AR difference between the coal and gas caused a large amount of energy to dissipate by means of wave reflection or refraction, and the V_r value changes were greater. Thus, the existence of cracks or pores had a significant inverse effect on wave velocity, considering the occupying fluids and coal rank.

Moreover, under water saturation conditions, the V_r scatter of lignite, bituminite, and anthracite had good linear fits with the corresponding UPVs, whereas the velocity ratio scatter of lignite and bituminite was more discrete under gas saturation, and those of anthracite had good linear correlation with the UPVs gas. The difference was expected that the adsorbed water improved the matrix homogeneity, given that the density of water exceeds that of air used in the experiments. Lignite had a mean V_r value of 1.19 when water-saturated and 1.36 when gas-saturated. Bituminite and anthracite had mean V_r values of 1.24 and 1.22, respectively, when they were under water saturation, and they had mean values of 1.26 and 1.34, respectively, under gas saturation. According to the linear fitting, when the $UPVs_{-water}$ value was 1.4 km/s, the potential V_{r_water} values of lignite, bituminite, and anthracite were 1.285, 1.335, and 1.259, respectively, and when the $UPVs_{-gas}$ value was 1.0 km/s, the potential V_{r_gas} values of lignite, bituminite, and anthracite were 1.418, 1.239, and 1.443, respectively. The parameter V_r value of coal might provide evidence to locate the cracks after fracturing by measuring the velocity ratio using the measure media.

4.3. Correlations between UPVp and Density. Figure 6 shows the distributions and relationships between UPVp and density for lignite, bituminite, and anthracite cores under water- and gas-saturated conditions, by considering the acoustic signal travel time along the coal sample. There were positive linear correlations between the UPVp and the density for lignite, bituminite, and anthracite under the two

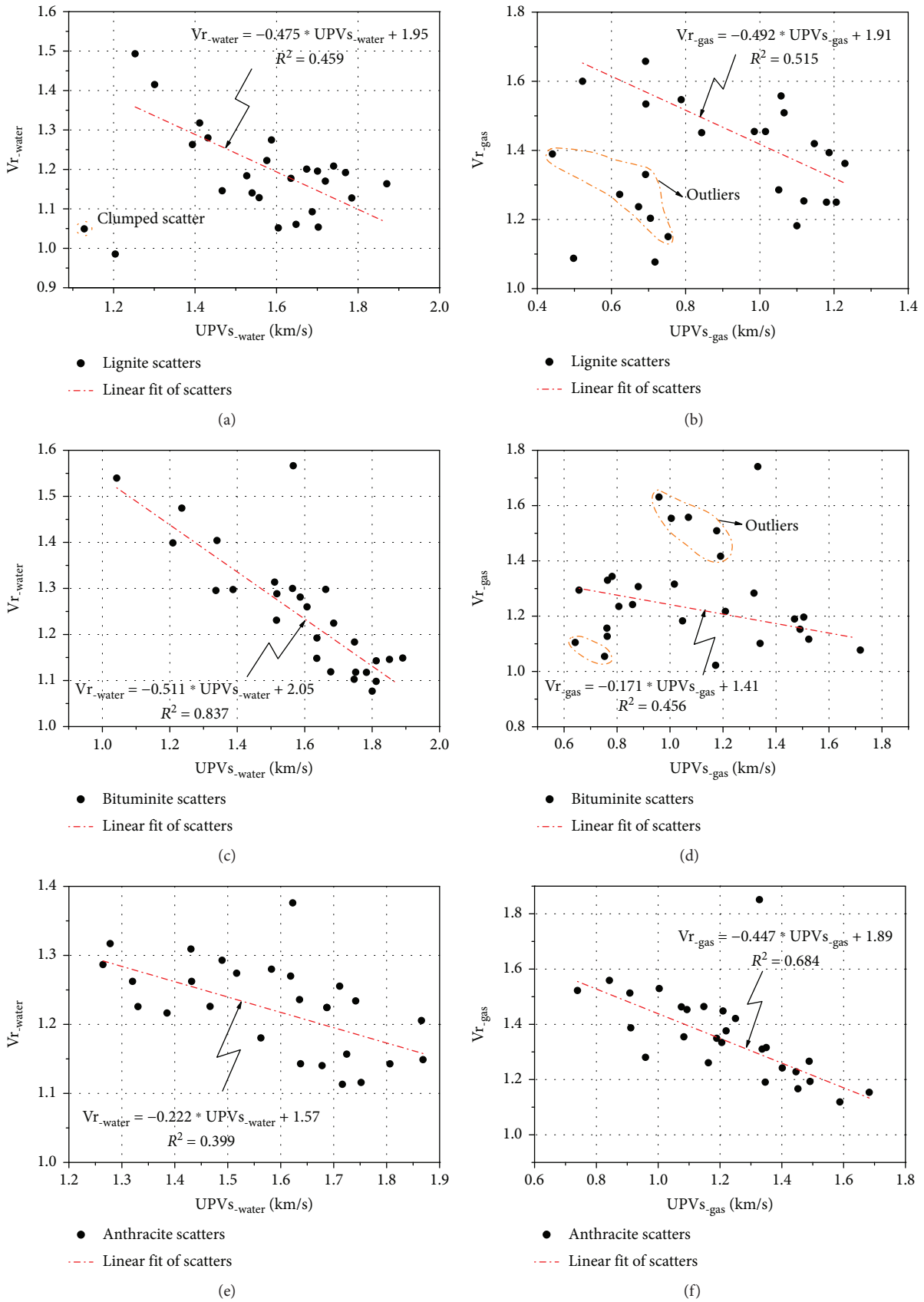


FIGURE 5: Correlations between V_{r_water} and $UPVs_water$ and between V_{r_gas} and $UPVs_gas$ for (a, b) lignite, (c, d) bituminite, and (e, f) anthracite.

TABLE 4: Linear fit equations of Vr for lignite, bituminite, and anthracite under water and gas saturation.

	Condition	Equation	R^2
Lignite	Water saturation	$Vr_{-water} = -0.475 * UPVs_{-water} + 1.95$	0.459
	Gas saturation	$Vr_{-gas} = -0.492 * UPVs_{-gas} + 1.91$	0.515
Bituminite	Water saturation	$Vr_{-water} = -0.511 * UPVs_{-water} + 2.05$	0.837
	Gas saturation	$Vr_{-gas} = -0.171 * UPVs_{-gas} + 1.41$	0.456
Anthracite	Water saturation	$Vr_{-water} = -0.222 * UPVs_{-water} + 1.57$	0.399
	Gas saturation	$Vr_{-gas} = -0.447 * UPVs_{-gas} + 1.89$	0.684

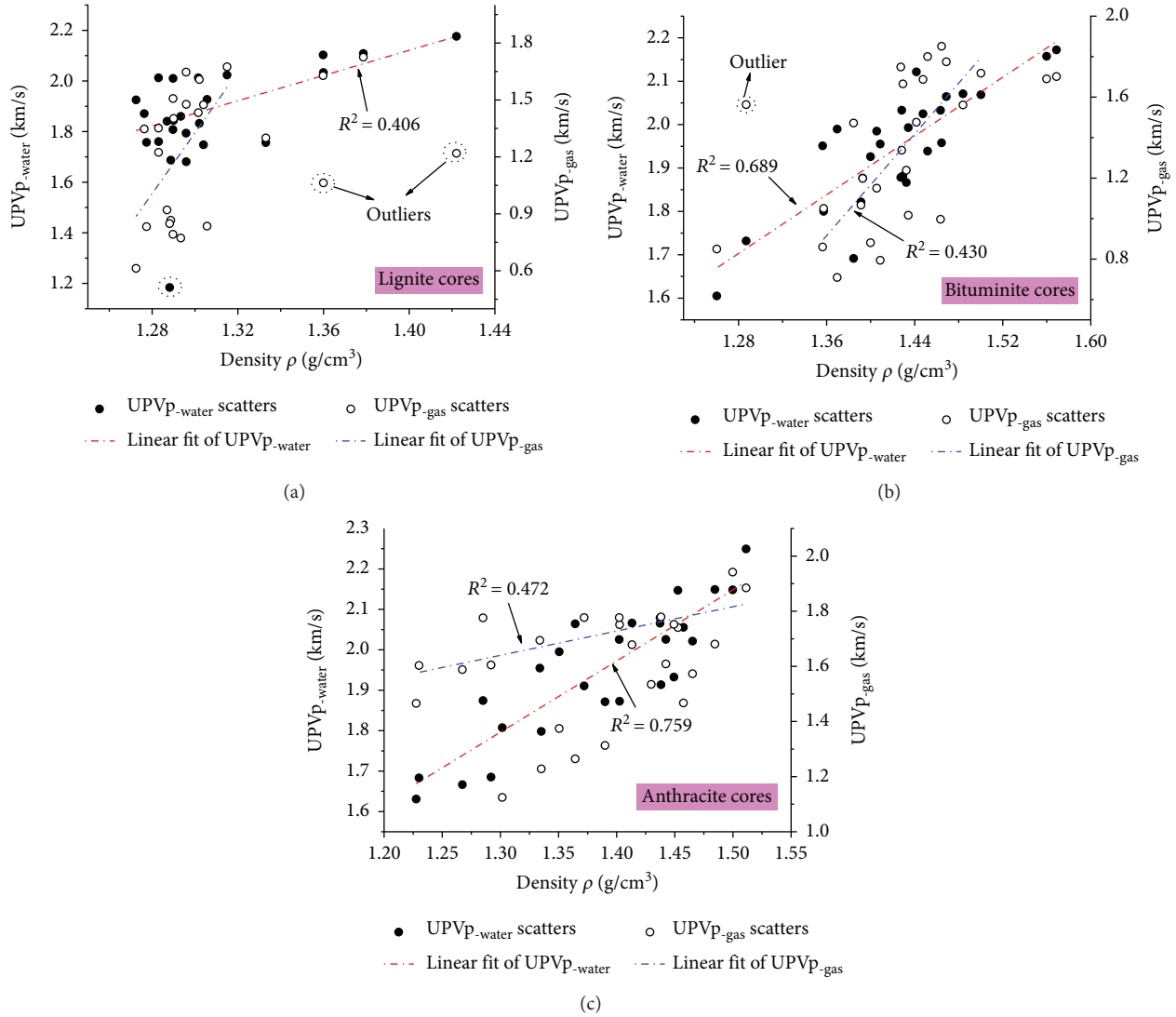


FIGURE 6: Scatterplot and distribution of velocity data and the corresponding trends between UPVp and density for (a) lignite, (b) bituminite, and (c) anthracite at water/gas-saturated conditions.

conditions, and as coal density increases, the UPVp velocity is different but generally trends upward. The values are listed in Table 5. The linear correlation coefficients for the anthracite UPVp values were 0.759 and 0.472, respectively, under

water- and gas-saturated conditions, whereas the corresponding coefficients for bituminite coal were 0.689 and 0.430, respectively. For water-saturated lignite coal, the linear fitting coefficient was 0.406, and its UPVp_{-gas} scatter had

TABLE 5: Correlations between UPVp and porosity under water and gas saturation.

	Condition	Equation	R^2
Lignite	Water saturation	$UPVp_{-water} = 2.49^* \rho - 1.36$	0.406
	Gas saturation	\	\
Bituminite	Water saturation	$UPVp_{-water} = 1.69^* \rho - 0.46$	0.689
	Gas saturation	$UPVp_{-gas} = 6.28^* \rho - 7.62$	0.430
Anthracite	Water saturation	$UPVp_{-water} = 1.76^* \rho - 0.49$	0.759
	Gas saturation	$UPVp_{-gas} = 0.88^* \rho + 0.49$	0.472

poor correlation with density (R^2 less than 0.20), which might be attributed to the low rank and complex crack properties due to the large anisotropy, causing high possibility of discrete velocity distribution.

It should be noticed that there were several outliers of UPVp scatter for lignite and bituminite due to their high dispersion, and these outliers were labeled using the dotted cycles. The fitting difference might be explained from three aspects: (a) the presence of complex components, such as grains with different sizes, mineral distribution, or incomplete evolution of the plant material in the coal, leads to greater anisotropy in the lignite coal matrix, resulting in random distributions of density and wave velocity [24, 36]. (b) Fluids may occupy the void space, increasing the whole saturated coal density. Given that the water density is larger than gas density, the water-saturated coal had larger UPV values than the gas-saturated coal [37, 38]. Different coals have various UPVp values, which are mostly affected by physicochemical properties and coal rank. (c) Different coals have various pore structures and distributions. For example, anthracite has a large volume of micropores, whereas lignite and bituminite have numerous macropores or cracks [48]. The occupied water in the smaller volume pores is more likely to promote an increase in velocity with increasing density.

4.4. Correlations between the UPVp Values and Porosity. The presence of fissures always has a significant impact on pulse wave transmission, and wave velocity increases parallel to the bedding planes, but decreases in the perpendicular direction [49–51]. In this paper, coal porosity ϕ was calculated using a weighing method described as follows:

$$\phi = \frac{V_{crack}}{V_{core}} = \frac{\Delta M}{\rho_w V_{core}} = \frac{M_{water} - M_{pre}}{\rho_w V_{core}} = \frac{4(M_{water} - M_{pre})}{\rho_w \pi D^2 h}, \quad (3)$$

where V_{crack} and V_{core} are the volumes (cm^3) of cracks and coal cores, respectively; ρ_w is the density of water and equals to 1.0 g/cm^3 ; ΔM is the mass difference between M_{water} and M_{pre} , (g); M_{water} and M_{pre} are the coal mass at completely saturated and dry conditions, respectively (g); and D and h are the diameter and height of the coal cores, respectively, (cm).

The porosity calculated in equation (3) only considers connected cracks, and closed pores are excluded for simplification. Figure 7 shows the scatterplot of data and the correlations between the UPVp and ϕ under water and gas saturation. The lignite cores had a mean ϕ value of 3.06, the bituminite cores had a mean ϕ value of 2.09, and the anthracite cores had a mean ϕ value of 1.21. This finding indicates that coal rank is inversely related to porosity; the coal with a lower rank had a larger porosity. For each kind of coal, the small porosity difference might be related to the number of connected cracks and the fact that some internal closed pores were not filled with water. However, the trend did not have disadvantageous impacts on the final results. The existence of fissures or cracks caused some reflection and refraction of waves at the crack surface, and some friction at grain boundaries, directly causing amplitude attenuation and a large energy decrease and delaying the first arrival time of the wave, finally resulting in a velocity decrease, which was coincident with the conclusion by Kohlhauser and Hellmich [51] and Li et al. [52].

As shown in Figure 7 and Table 6, the declining trends of lignite and bituminite under gas saturation were higher than under water saturation, whereas for anthracite, correlations between $UPVp_{-water}$ and ϕ had a larger decline compared to correlations between $UPVp_{-gas}$ and ϕ . The decline difference might be related to water sensitivity of the coals. That is, micropores within anthracite generally account for 50% of the total pores [53, 54], and water exhibits various modes of infiltration, such as seepage in macropores as well as diffusion and adsorption in micropores. Due to the larger adsorption capacity of anthracite, the adsorbed water molecules could squeeze into voids and increase the distance between grains, which might have some inverse impacts on the velocity. Meanwhile, the velocity of water-saturated cores decreased with increasing ϕ , which indicated that very large numbers of unconnected pores existed in addition to the pores filled with water. Crack properties such as surface physicochemistry, fracture roughness, and connectivity, should also be considered in the evaluation of velocity transmission.

4.5. Potential Applications. Based on the above results and the reported results from Kahraman [16], Vasaneli et al. [28], and Liu et al. [37], it is evident that wave velocity has some correlations with the rock properties, such as density and porosity. According to Chen et al. [21], Sansalone and Streett [55], and Bogas et al. [56], the coal regarded as a homogenous material simply might have some relations between velocity and the related mechanical parameters, shown in the following equation:

$$UPV = \sqrt{\frac{E_d}{\rho} \cdot \frac{(1 - v_d)}{(1 + v_d) \cdot (1 - 2v_d)}}, \quad (4)$$

$$v_d = \frac{1/2(UPVp/UPVs)^2 - 1}{(UPVp/UPVs)^2 - 1}, \quad (5)$$

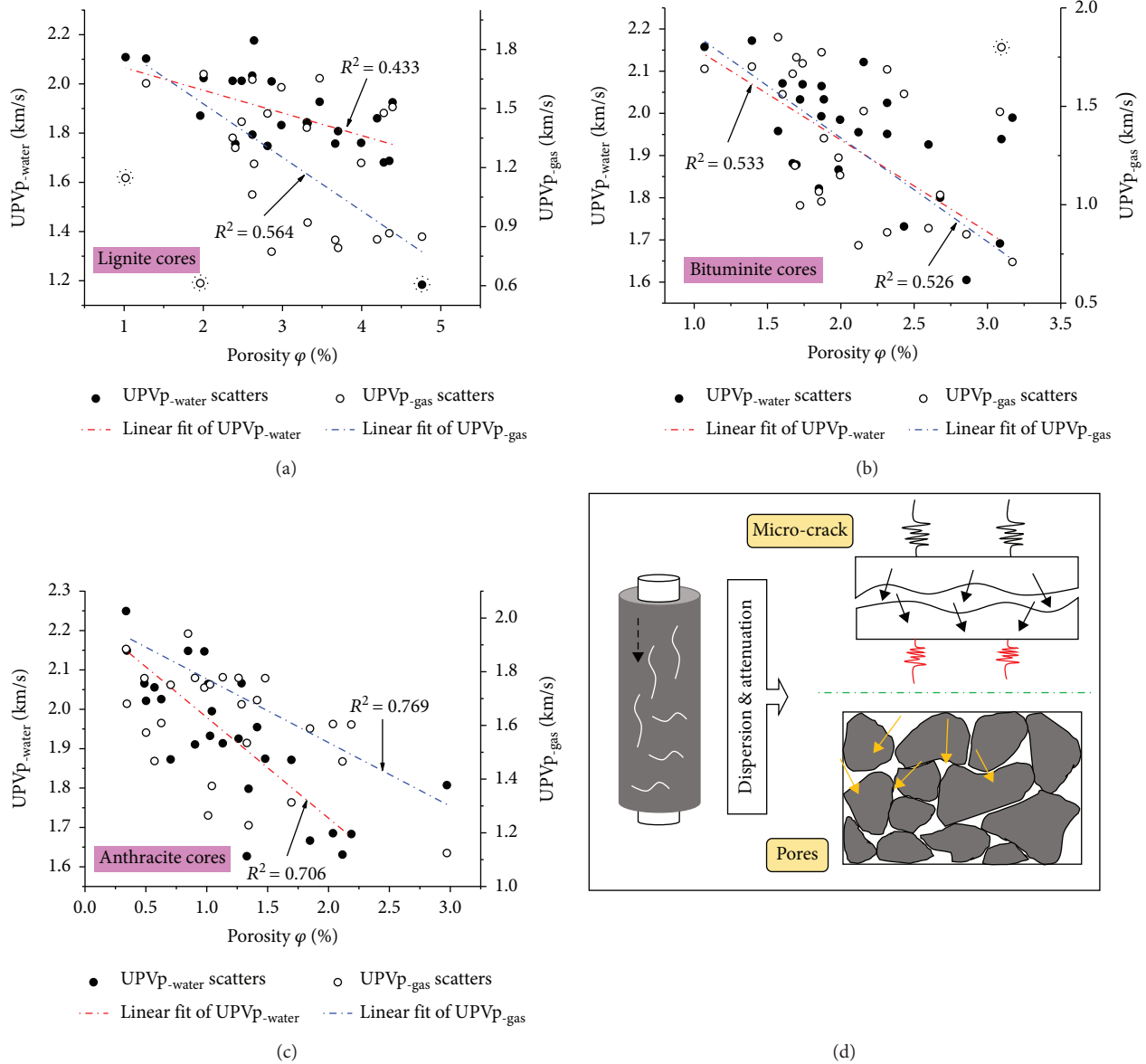


FIGURE 7: Scatterplot and linear correlations between UPV and porosity under water and gas saturation for (a) lignite, (b) bituminite, and (c) anthracite (d) showing a sketch of wave transmission within the coal matrix.

TABLE 6: Linear fit equations between UPV and porosity at water and gas saturation.

	Condition	Equation	R^2
Lignite	Water saturation	$UPVp_{-water} = -0.092^* \varphi + 2.16$	0.433
	Gas saturation	$UPVp_{-gas} = -0.272^* \varphi + 2.07$	0.564
Bituminite	Water saturation	$UPVp_{-water} = -0.218^* \varphi + 2.37$	0.533
	Gas saturation	$UPVp_{-gas} = -0.527^* \varphi + 2.39$	0.526
Anthracite	Water saturation	$UPVp_{-water} = -0.256^* \varphi + 2.24$	0.706
	Gas saturation	$UPVp_{-gas} = -0.237^* \varphi + 2.01$	0.769

where ν_d is the dynamic Poisson's ratio, E_d is the elastic modulus, and ρ is the density. Based on the above equation, the P -wave velocity is directly proportional to the square root

of the dynamic modulus of elasticity and inversely proportional to the square root of its density, and the Poisson's ratio ν_d is proportional to the square of velocity ratio. Based on

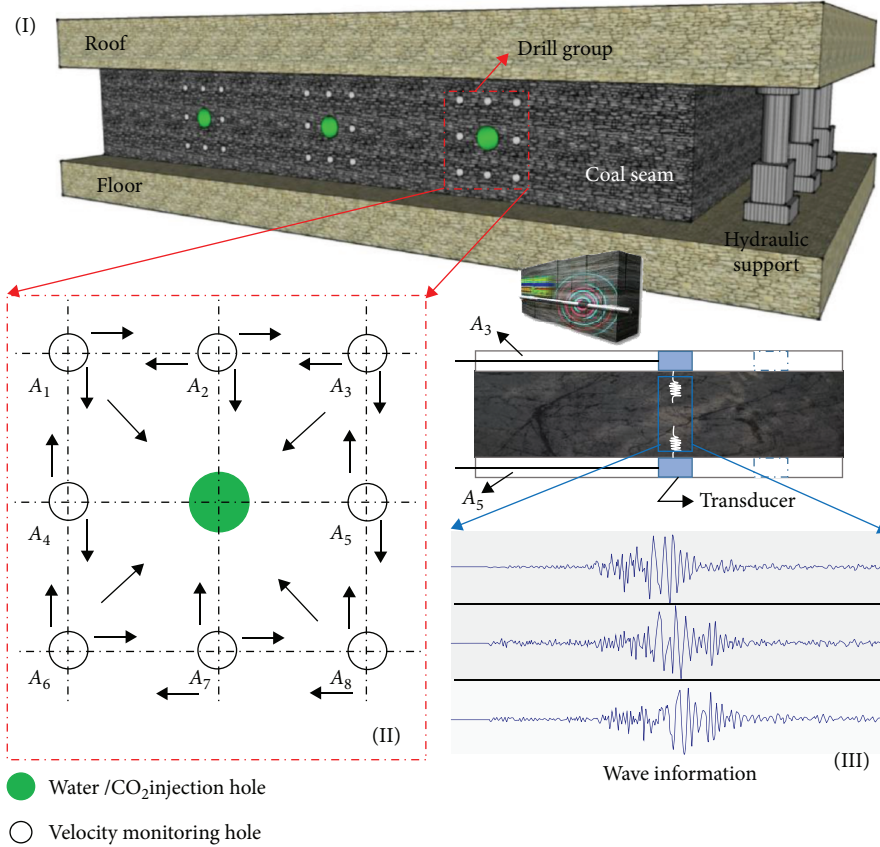


FIGURE 8: Potential application of velocity measurements by hydraulic fracturing or CO₂ fracturing during enhanced CBM recovery.

equations (4) and (5), the determined UPVp and UPVs could approximately deduce the elastic parameters, and the relevant intensity region of specified coal layers could be plotted, from which the potential fracture-generating region could be drawn. The UPV test method has application in enhanced CBM recovery by hydraulic fracturing or aqueous fracturing methods (such as CO₂ fracturing), as shown in Figure 8.

A number of drill groups are advanced into a coal seam with each group containing a single fracturing fluid (water or LCO₂) injection hole and eight monitoring holes (A_1, A_2, \dots, A_8) around the injection hole (hole depth of J), as shown in parts (I) and (II) in Figure 8. Taking the example of monitoring holes A_3 and A_5 , two transducers are initially placed at the bottom of the monitoring holes and simultaneously moved by the same distance (l) from the hole bottom in sequence to measure the velocity distributions of the region between hole A_3 and hole A_5 , and velocity values are recorded as $V_{A_3-A_5(i)}$ ($i = 0, 1, 2, \dots, J/l$). When the fracturing process is finished, the posttest velocity of the specific region is recorded as $V'_{A_3-A_5(i)}$ ($i = 0, 1, 2, \dots, J/l$). By comparing the pre- and posttest velocities, the relationship between velocity and cracks can be deduced:

$$\begin{cases} V'_{A_3-A_5(i)} < V_{A_3-A_5(i)} ; \text{ some cracks are generated,} \\ V'_{A_3-A_5(i)} = V_{A_3-A_5(i)} ; \text{ no cracks are generated.} \end{cases} \quad (6)$$

Thus, it is possible to locate petrological changes caused by the mechanical effects of water or CO₂ injection, rapidly identify the effective fracture zone, and deduce fracture orientations. Depending on the collected velocity data, it is possible to forecast changes in physical parameters when subjected to crustal stress. This potential application could save a significant amount of core drilling work and help to obtain useful information about coal at depth in real time.

Although correlations among velocity, density, and porosity of water and gas-saturated coal cores have been identified, there is still a need for further study. For example, velocities recorded in different cores with various fluid media and fluid contents should be further investigated and velocity anisotropy should be quantified in future research. Additionally, correlations between velocities of different coal types under fluid saturation and the relevant elastic properties should be tested.

5. Conclusions

Based on this study, the following major conclusions can be drawn:

- (i) The velocities recorded in the three different coal ranks displayed various distributions and discrete degrees, likely related to rank and saturation media. By comparing the range of the UPVp and UPVs box plots, it is evident that the UPVp is more accurate or

reliable for characterizing the existence of micro- or macrocracks with the assistance of adsorbed water

- (ii) The UPVp values of lignite, bituminite, and anthracite coals showed positive linear correlations with their corresponding UPVs values, under water and gas saturation. The UPVp values correlated positively with the density of water/gas-saturated cores and correlated negatively with the porosity of both prepared cores
- (iii) The ratio of UPVp/UPVs had a negative linear correlation with the UPVs values for lignite, bituminite, and anthracite, and the different decline trends might be attributed to coal rank. The coals with lower rank had large amounts of fissures. The larger difference of acoustic resistance between coal and gas dissipated a large amount of energy by means of wave reflection or refraction

Data Availability

The data used to support the findings of this study are available from the corresponding author upon request.

Conflicts of Interest

The authors declare that they have no conflicts of interest.

Acknowledgments

This work was financially supported by the National Key Technologies Research & Development program (2018YFC0808403), the National Natural Science Foundation of China (51774278), the Natural Science Foundation of Jiangsu Province (BK20170001), and the Jiangsu Province Fifth 333 High-Level Talents Training Project (BRA2018032).

Supplementary Materials

The total data in the paper are listed as the following table: parameter data of lignite cores under water/gas-saturated conditions, parameter data of bituminite cores under water/gas-saturated conditions, and parameter data of anthracite cores under water/gas-saturated conditions. (*Supplementary Materials*)

References

- [1] I. Palmer, "Coalbed methane completions: a world view," *International Journal of Coal Geology*, vol. 82, no. 3-4, pp. 184-195, 2010.
- [2] N. Vedachalam, S. Srinivasalu, G. Rajendran, G. A. Ramadass, and M. A. Atmanand, "Review of unconventional hydrocarbon resources in major energy consuming countries and efforts in realizing natural gas hydrates as a future source of energy," *Journal of Natural Gas Science and Engineering*, vol. 26, pp. 163-175, 2015.
- [3] P. Booth, H. Brown, J. Nemeik, and R. Ting, "Spatial context in the calculation of gas emissions for underground coal mines," *International Journal of Mining Science and Technology*, vol. 27, no. 5, pp. 787-794, 2017.
- [4] J. Xu, C. Zhai, L. Qin, S. Wu, Y. Sun, and R. Dong, "Characteristics of pores under the influence of cyclic cryogenic liquid carbon dioxide using low-field nuclear magnetic resonance," *Geofluids*, vol. 2018, Article ID 1682125, 14 pages, 2018.
- [5] Q. Zou and B. Lin, "Fluid-solid coupling characteristics of gas-bearing coal subjected to hydraulic slotting: an experimental investigation," *Energy & Fuels*, vol. 32, no. 2, pp. 1047-1060, 2018.
- [6] G. Ni, Z. Li, and H. Xie, "The mechanism and relief method of the coal seam water blocking effect (WBE) based on the surfactants," *Powder Technology*, vol. 323, pp. 60-68, 2018.
- [7] T. A. Moore, "Coalbed methane: a review," *International Journal of Coal Geology*, vol. 101, pp. 36-81, 2012.
- [8] J. Xu, C. Zhai, and L. Qin, "Mechanism and application of pulse hydraulic fracturing in improving drainage of coalbed methane," *Journal of Natural Gas Science and Engineering*, vol. 40, pp. 79-90, 2017.
- [9] T. Liu, B. Lin, Q. Zou, C. Zhu, and F. Yan, "Mechanical behaviors and failure processes of precracked specimens under uniaxial compression: a perspective from microscopic displacement patterns," *Tectonophysics*, vol. 672-673, pp. 104-120, 2016.
- [10] Q. Li, B. Lin, and C. Zhai, "The effect of pulse frequency on the fracture extension during hydraulic fracturing," *Journal of Natural Gas Science and Engineering*, vol. 21, pp. 296-303, 2014.
- [11] C. Zhai, J. Xu, S. Liu, and L. Qin, "Fracturing mechanism of coal-like rock specimens under the effect of non-explosive expansion," *International Journal of Rock Mechanics and Mining Sciences*, vol. 103, pp. 145-154, 2018.
- [12] E. A. Novikov, R. O. Oshkin, V. L. Shkuratnik, S. A. Epshtein, and N. N. Dobryakova, "Application of thermally stimulated acoustic emission method to assess the thermal resistance and related properties of coals," *International Journal of Mining Science and Technology*, vol. 28, no. 2, pp. 243-249, 2018.
- [13] J. Lazar, T. Kanduč, S. Jamnikar, F. Grassa, and S. Zavšek, "Distribution, composition and origin of coalbed gases in excavation fields from the Preloge and Pesje mining areas, Velenje Basin, Slovenia," *International Journal of Coal Geology*, vol. 131, pp. 363-377, 2014.
- [14] L. D. Connell, S. Mazumder, R. Sander, M. Camilleri, Z. Pan, and D. Heryanto, "Laboratory characterisation of coal matrix shrinkage, cleat compressibility and the geomechanical properties determining reservoir permeability," *Fuel*, vol. 165, pp. 499-512, 2016.
- [15] Q. Lyu, X. Long, P. G. Ranjith, J. Tan, Y. Kang, and W. Luo, "A damage constitutive model for the effects of CO₂-brine-rock interactions on the brittleness of a low-clay shale," *Geofluids*, vol. 2018, Article ID 7321961, 14 pages, 2018.
- [16] S. Kahraman, "The correlations between the saturated and dry P-wave velocity of rocks," *Ultrasonics*, vol. 46, no. 4, pp. 341-348, 2007.
- [17] O. Kılıç, "The influence of high temperatures on limestone P-wave velocity and Schmidt hammer strength," *International Journal of Rock Mechanics and Mining Sciences*, vol. 43, no. 6, pp. 980-986, 2006.
- [18] R. Fort, M. Alvarez de Buergo, and E. M. Perez-Monserrat, "Non-destructive testing for the assessment of granite decay in heritage structures compared to quarry stone,"

- International Journal of Rock Mechanics and Mining Sciences*, vol. 61, pp. 296–305, 2013.
- [19] M. Favaro, R. Mendichi, F. Ossola et al., “Evaluation of polymers for conservation treatments of outdoor exposed stone monuments. Part I: photo-oxidative weathering,” *Polymer Degradation and Stability*, vol. 91, no. 12, pp. 3083–3096, 2006.
- [20] M. Myrin and K. A. Malaga, “A case study on the evaluation of consolidation treatments of Gotland sandstone by use of ultrasound pulse velocity measurements,” in *Heritage, Weathering and Conservation*, vol. 2, R. Fort, M. Alvarez de Buergo, M. Gomez-Heras, and C. Vazquez-Calvo, Eds., pp. 749–755, Taylor and Francis, London, UK, 2010.
- [21] H. Chen, B. Jiang, T. Chen, S. Xu, and G. Zhu, “Experimental study on ultrasonic velocity and anisotropy of tectonically deformed coal,” *International Journal of Coal Geology*, vol. 179, pp. 242–252, 2017.
- [22] J. Vilhelm, V. Rudajev, T. Lokajiček, and R. Živor, “Velocity dispersion in fractured rocks in a wide frequency range,” *Journal of Applied Geophysics*, vol. 90, pp. 138–146, 2013.
- [23] K. Nakahata, G. Kawamura, T. Yano, and S. Hirose, “Three-dimensional numerical modeling of ultrasonic wave propagation in concrete and its experimental validation,” *Construction and Building Materials*, vol. 78, pp. 217–223, 2015.
- [24] E. Yasar and Y. Erdogan, “Correlating sound velocity with the density, compressive strength and Young’s modulus of carbonate rocks,” *International Journal of Rock Mechanics and Mining Sciences*, vol. 41, no. 5, pp. 871–875, 2004.
- [25] S. Kahraman, “Evaluation of simple methods for assessing the uniaxial compressive strength of rock,” *International Journal of Rock Mechanics and Mining Sciences*, vol. 38, no. 7, pp. 981–994, 2001.
- [26] G. Vasconcelos, P. B. Lourenço, C. A. S. Alves, and J. Pamplona, “Ultrasonic evaluation of the physical and mechanical properties of granites,” *Ultrasonics*, vol. 48, no. 5, pp. 453–466, 2008.
- [27] A. A. E. Aliabdo and A. E. M. A. Elmoaty, “Reliability of using nondestructive tests to estimate compressive strength of building stones and bricks,” *Alexandria Engineering Journal*, vol. 51, no. 3, pp. 193–203, 2012.
- [28] E. Vasanelli, D. Colangiuli, A. Calia, M. Sileo, and M. A. Aiello, “Ultrasonic pulse velocity for the evaluation of physical and mechanical properties of a highly porous building limestone,” *Ultrasonics*, vol. 60, pp. 33–40, 2015.
- [29] G. Zandt and C. J. Ammon, “Continental crust composition constrained by measurements of crustal Poisson’s ratio,” *Nature*, vol. 374, no. 6518, pp. 152–154, 1995.
- [30] N. I. Christensen, “Poisson’s ratio and crustal seismology,” *Journal of Geophysical Research: Solid Earth*, vol. 101, no. B2, pp. 3139–3156, 1996.
- [31] S. Chevrot and R. D. Van der Hilst, “The Poisson ratio of the Australian crust: geological and geophysical implications,” *Earth and Planetary Science Letters*, vol. 183, no. 1–2, pp. 121–132, 2000.
- [32] S. Ji, Q. Wang, and M. H. Salisbury, “Composition and tectonic evolution of the Chinese continental crust constrained by Poisson’s ratio,” *Tectonophysics*, vol. 463, no. 1–4, pp. 15–30, 2009.
- [33] Q. Wang, S. Ji, S. Sun, and D. Marcotte, “Correlations between compressional and shear wave velocities and corresponding Poisson’s ratios for some common rocks and sulfide ores,” *Tectonophysics*, vol. 469, no. 1–4, pp. 61–72, 2009.
- [34] T. Lokajiček, V. Rudajev, R. D. Dwivedi, R. K. Goel, and A. Swarup, “Influence of thermal heating on elastic wave velocities in granulite,” *International Journal of Rock Mechanics and Mining Sciences*, vol. 54, pp. 1–8, 2012.
- [35] A. Morcote, G. Mavko, and M. Prasad, “Dynamic elastic properties of coal,” *Geophysics*, vol. 75, no. 6, pp. E227–E234, 2010.
- [36] F. Dirgantara, L. M. Batzle, and B. J. Curtis, “Maturity characterization and ultrasonic velocities of coals,” in *SEG Technical Program Expanded Abstracts 2011*, p. 4424, San Antonio, TX, USA, 2011.
- [37] J. Liu, D. Liu, Y. Cai, Q. Gan, and Y. Yao, “Effects of water saturation on P-wave propagation in fractured coals: an experimental perspective,” *Journal of Applied Geophysics*, vol. 144, pp. 94–103, 2017.
- [38] M. J. Lwin, “The effect of different gases on the ultrasonic response of coal,” *Geophysics*, vol. 76, no. 5, pp. E155–E163, 2011.
- [39] G. Q. Yu, C. Zhai, L. Qin, Z. Q. Tang, S. L. Wu, and J. Z. Xu, “Changes to coal pores by ultrasonic wave excitation of different powers,” *Journal of China University of Mining & Technology*, vol. 47, pp. 264–270, 2018.
- [40] G. T. Kuster and M. N. Toksoz, “Velocity and attenuation of seismic waves in two-phase media: part I. theoretical formulations,” *Geophysics*, vol. 39, no. 5, pp. 587–606, 1974.
- [41] J. Xu, C. Zhai, S. Liu, L. Qin, and S. Wu, “Pore variation of three different metamorphic coals by multiple freezing-thawing cycles of liquid CO₂ injection for coalbed methane recovery,” *Fuel*, vol. 208, pp. 41–51, 2017.
- [42] T. Mandal, J. M. Tinjum, and T. B. Edil, “Non-destructive testing of cementitious stabilized materials using ultrasonic pulse velocity test,” *Transportation Geotechnics*, vol. 6, pp. 97–107, 2016.
- [43] N. A. el Sayed, H. Abuseda, and M. A. Kassab, “Acoustic wave velocity behavior for some Jurassic carbonate samples, north Sinai, Egypt,” *Journal of African Earth Sciences*, vol. 111, pp. 14–25, 2015.
- [44] M. A. Kassab and A. Weller, “Study on P-wave and S-wave velocity in dry and wet sandstones of Tushka region, Egypt,” *Egyptian Journal of Petroleum*, vol. 24, no. 1, pp. 1–11, 2015.
- [45] Y. M. Wang, Y. K. Miao, X. J. Meng, G. Q. Shen, and Y. C. Dong, “The calculation technique of physical transverse wave velocity curve for rock,” *Petroleum Geology and Recovery Efficiency*, vol. 13, pp. 58–61, 2006.
- [46] J. Wang, S. Wu, J. Geng, and P. Jaiswal, “Acoustic wave attenuation in the gas hydrate-bearing sediments of Well GC955H, Gulf of Mexico,” *Marine Geophysical Research*, vol. 39, no. 4, pp. 509–522, 2018.
- [47] B. Das and R. Chatterjee, “Well log data analysis for lithology and fluid identification in Krishna-Godavari Basin, India,” *Arabian Journal of Geosciences*, vol. 11, no. 10, 2018.
- [48] X. J. Xu, J. Liu, and L. Wang, “Influence of pore size distribution of different metamorphic grade of coal on adsorption constant,” *Journal of China Coal Society*, vol. 38, pp. 294–300, 2013.
- [49] W. Li and Y. Cho, “Combination of nonlinear ultrasonics and guided wave tomography for imaging the micro-defects,” *Ultrasonics*, vol. 65, pp. 87–95, 2016.
- [50] C. S. Vishnu, M. A. Mamtani, and A. Basu, “AMS, ultrasonic P-wave velocity and rock strength analysis in quartzites devoid of mesoscopic foliations – implications for rock mechanics studies,” *Tectonophysics*, vol. 494, no. 3–4, pp. 191–200, 2010.

- [51] C. Kohlhauser and C. Hellmich, "Ultrasonic contact pulse transmission for elastic wave velocity and stiffness determination: influence of specimen geometry and porosity," *Engineering Structures*, vol. 47, pp. 115–133, 2013.
- [52] H. Li, B. Q. Lin, Y. D. Hong et al., "Effect of microwave irradiation on pore and fracture evolutions of coal," *Journal of China University of Mining & Technology*, vol. 46, pp. 1194–1201, 2017.
- [53] Y. G. Wang, M. G. Li, B. B. Chen, and S. H. Dai, "Experimental study on ultrasonic wave characteristics of coal samples under dry and water saturated conditions," *Journal of China Coal Society*, vol. 40, pp. 2445–2450, 2015.
- [54] J. Xu, C. Zhai, S. Liu, L. Qin, and R. Dong, "Investigation of temperature effects from LCO₂ with different cycle parameters on the coal pore variation based on infrared thermal imagery and low-field nuclear magnetic resonance," *Fuel*, vol. 215, pp. 528–540, 2018.
- [55] M. Sansalone and W. B. Streett, *Impact-Echo Nondestructive Evaluation of Concrete and Masonry*, Bullbrier Press, Ithaca, NY, USA, 1997.
- [56] J. A. Bogas, M. G. Gomes, and A. Gomes, "Compressive strength evaluation of structural lightweight concrete by non-destructive ultrasonic pulse velocity method," *Ultrasonics*, vol. 53, no. 5, pp. 962–972, 2013.

Research Article

Structural and Mineralogical Characterization of a Fossil Hydrothermal System Located at the Outermost Front of the Southern Apennines Fold-and-Thrust Belt

Paolo Fulignati ¹, Fabrizio Agosta ², Claudia Belviso ^{3,4}, Giacomo Prosser ²,
Antonio Lettino ^{3,4}, Angela Vita Petruolo ², and Francesco Cavalcante ^{3,4}

¹Dipartimento di Scienze della Terra, Università di Pisa, Pisa 56126, Italy

²Dipartimento di Scienze, University of Basilicata, Potenza 85100, Italy

³Istituto di Metodologie per l'Analisi Ambientale-CNR, Tito Scalo 85050, Italy

⁴Istituto di Struttura della Materia-CNR, Area di Tito Scalo, PZ 85050, Italy

Correspondence should be addressed to Francesco Cavalcante; francesco.cavalcante@imaa.cnr.it

Received 12 November 2018; Accepted 30 January 2019; Published 28 April 2019

Academic Editor: Fabien Magri

Copyright © 2019 Paolo Fulignati et al. This is an open access article distributed under the Creative Commons Attribution License, which permits unrestricted use, distribution, and reproduction in any medium, provided the original work is properly cited.

Aiming at investigating the hydrothermal circulation along the eastern flank of the Vulture volcano, along the outermost edge of the southern Apennine fold-and-thrust belt (ftb), we studied the fossil hydrothermal alteration that mineralized a transtensional fault that crosscuts volcanoclastic rocks in the Rapolla area. On the basis of structural, mineralogical, and fluid inclusion data, three main stages of activity of the hydrothermal system are documented. Stage 1 was produced by the circulation of fluids having low-pH conditions ($\text{pH} \approx 3\text{-}4$) and relatively high- SO_4^{2-} activity, as testified by the hydrothermal alteration mainly carried out by the alunite group minerals (particularly jarosite), which is typical of an advanced argillic alteration facies. Hydrothermal fluids were characterized by a high temperature of about $200^\circ\text{-}210^\circ\text{C}$. These hot fluids altered and mineralized the matrices of pyroclastic rocks and sealed both burial-related and fault-related fracture networks. Later hydrothermal circulation (Stage 2) was recorded by opal A-rich veins present both within and outside the fault zone. The fluids responsible of opal A precipitation were characterized by lower temperature conditions, probably lower than 100°C . Current goethite mineralization takes place along the main slip surfaces of the study high-angle fault zone due to low temperature ($<30^\circ\text{C}$) underground water circulation. This study highlights that a high-temperature hydrothermal system developed in the past within the transtensional fault zone of the Rapolla area when a high thermal anomaly was present. If we take into account that this area is still affected by a heat flux positive anomaly (90 mW/m^2), we may infer that it has the potentiality to be considered an interesting site for future exploration devoted to the finding of medium-enthalpy geothermal resources at depth.

1. Introduction

Hydrothermal systems cause the redistribution of both energy and mass in response to circulating H_2O fluids and form in response to thermal perturbations among which the magma-induced thermal anomalies are the most frequent [1]. A hydrothermal system is comprised of the following components: a heat source, a permeable reservoir in which fluids can flush and trigger an active convective circulation, a recharge system, and an impermeable cover, respectively.

The rocks affected by a hydrothermal fluid circulation undergo to a variety of alteration processes due to the instability of the primary mineralogical assemblages, which tend to reequilibrate by forming new minerals stable under the new conditions [2]. As a consequence, the different alteration mineralogical assemblages are primarily controlled by the physical-chemical conditions of the hydrothermal fluids.

High-temperature geothermal systems are quite common in areas characterized by active extensional tectonic environments [3–5]. In the Central Mediterranean region, a very

pronounced regional heat flow anomaly ($>150 \text{ mW/m}^2$) characterizes both the central and southern sectors of the Tyrrhenian Sea and the thinned and stretched fold-and-thrust belt exposed along the Tyrrhenian side of the central and southern Apennines, Italy. There, thinning of the lithosphere due to extensional tectonics is accompanied by igneous processes; large-scale intrusion and extrusion phenomena cause the formation of a positive regional anomaly, which is locally greater than 400 mW/m^2 [3, 6]. Such a significant positive heat flow anomaly is associated with both active and fossil hydrothermal systems, which localize in the high- and medium-enthalpy geothermal fields of the Tuscany, Latium, and Campania regions of Italy. Some of them, the Larderello and Mt. Amiata geothermal fields, for instance, have been exploited for power production since the beginning of the 20th century.

In contrast, the eastern sector of both central and southern Apennines is made up of several tectonostratigraphic units characterized by low values of heat flux ($\sim 30 \text{ mW/m}^2$). There, the estimated temperature varies from ca. 30°C , at 1000 m below the earth surface, to ca. 60°C , at depth of 3000 m [6]. As a consequence, the occurrence of hydrothermal activity in the eastern portion is rarely reported and just limited to some low-temperature thermal springs. The only significant thermal anomaly localizes in the Vulture area, a Middle-Upper Pleistocene volcano whose last episodes of activity took place about 130 kyr [7], with values of heat flux up to 90 mW/m^2 [6]. In this work, we report for the first time evidences of a fossil high-temperature hydrothermal system located along the eastern flanks of the Vulture volcano. The study site, positioned in the vicinity of the Rapolla village of the Basilicata Region, lies along the outermost edge of the southern Apennines. It provides a unique opportunity to investigate the interplay between shallow-rooted faulting, which was associated with very recent thrusting episodes, and high-temperature hydrothermal fluid circulations. The results might help to improve our understanding of the modalities of fluid migration through the upper crust at the frontal portion of active fold-and-thrust belts, and it might represent a key knowledge for a successful exploration and exploitation of geothermal and mineral resources. In fact, integrated geological, structural, mineralogical, and geochemical investigations of either active or fossil hydrothermal systems could be pivotal for the assessment of the relationship between crustal structures and potential geothermal resources [8–12].

2. Geological Setting

The study area is located along the outer front of the southern Apennines fold-and-thrust (ftb), at the western margin of the southernmost part of the Pliocene-Pleistocene in age, Bradano Trough foredeep basin [13]. The southern Apennines ftb is made up of NE-verging, rootless tectonic nappes of Mesozoic-Tertiary sedimentary successions, which were originally pertaining to the African-Adriatic margin, and synorogenic top-thrust deposits [14–19]. During the Upper Miocene-Early Pliocene times, the entire pile of tectonic nappes overthrust the Apulian Platform, which was

crosscut already by NW-SE to NNW-SSE and minor NE-SW trending extensional faults associated with Cretaceous tectonics and Plio-Quaternary foreland bulging and foreland basin system development [20–25]. Contractional deformation of the whole southern Apennines orogenic wedge ended during the Early Pleistocene and was followed by uplift and exhumation [26–28]. During the Middle Pleistocene, the alkaline potassic to ultrapotassic Vulture stratovolcano formed at the outermost edge of the southern Apennines ftb ([7, 29–32] and reference therein; [33]). Activity of the Vulture volcano was likely controlled by a $\text{N}40^\circ\text{--}50^\circ\text{E}$ trending lithospheric discontinuity, which formed in response of the velocity variations that characterized the subduction-related rollback of the Apulian Platform. In detail, the Vulture volcano is made up of lavas and pyroclastics of tephra-phonolitic, phonofoiditic, and foiditic compositions, whereas melilitites and carbonatites are subordinate. Genesis of the Vulture volcano is still unclear, even though an OIB-type mantle source is inferred [7].

At the peripheral sectors of the Vulture volcano, pre-, syn-, and postvolcanic fluviolacustrine sedimentary deposits of the Pliocene and Pleistocene age crop out. Among these, the Venosa basin is located along the northeastern edge of the Vulture volcano [34], and it includes the fluviolacustrine deposits of the Middle Pleistocene age (Figure 1). High-angle fractures often form orthogonal sets with a varying attitude all around the flanks of the Vulture volcano (Figure 1) and were interpreted as due to local stress fields associated with the Vulture-related bulging [35–37]. However, main WNW-ESE to NW-SE striking fracture sets are documented throughout the whole volcanic edifice (cf. rose diagrams in Figure 1) and quite subparallel to the present regional $\sigma_{\text{h,max}}$ of southern Italy [38].

The stratigraphic setting of the eastern Vulture area is reported by Petrullo et al. [24], who documented pronounced lateral variations of the Cenozoic mixed carbonate-terrigenous formations topping the Mesozoic carbonates of the Apulian Platform. Such a geological setting was interpreted as due to Eocene-to-Miocene in age, strike-slip, and extensional tectonics, which caused the formation of NW-SE, N-S, and NE-SW striking high-angle fault sets. The tectonic setting of the study area was inferred from well logs and seismic profiles downloaded from the VIDEPI website (Figures 2 and 3). Well data were reinterpreted adopting a consistent stratigraphic scheme based on fossil content and lithology. The original seismic profiles, downloaded from the VIDEPI website in raster format, were also reinterpreted and then converted into SEG Y files, imported into the MoveTM software, and then digitized (cf. [24]).

Focusing on the Plio-Quaternary tectonic evolution of the eastern Vulture area, NE-verging thrusting of a tertiary allochthonous complex on the topmost infill of the Bradano Trough occurred by means of a sole thrust that localized on top of the Pliocene clay units (Figure 2(b)). Low-angle splay thrust faults departing from this sole thrust were documented by Sinisi et al. [37]. The allochthonous complex was not profoundly affected by the latest stages of activity of the NW-SE high-angle faults (Figure 2(b)), whereas both

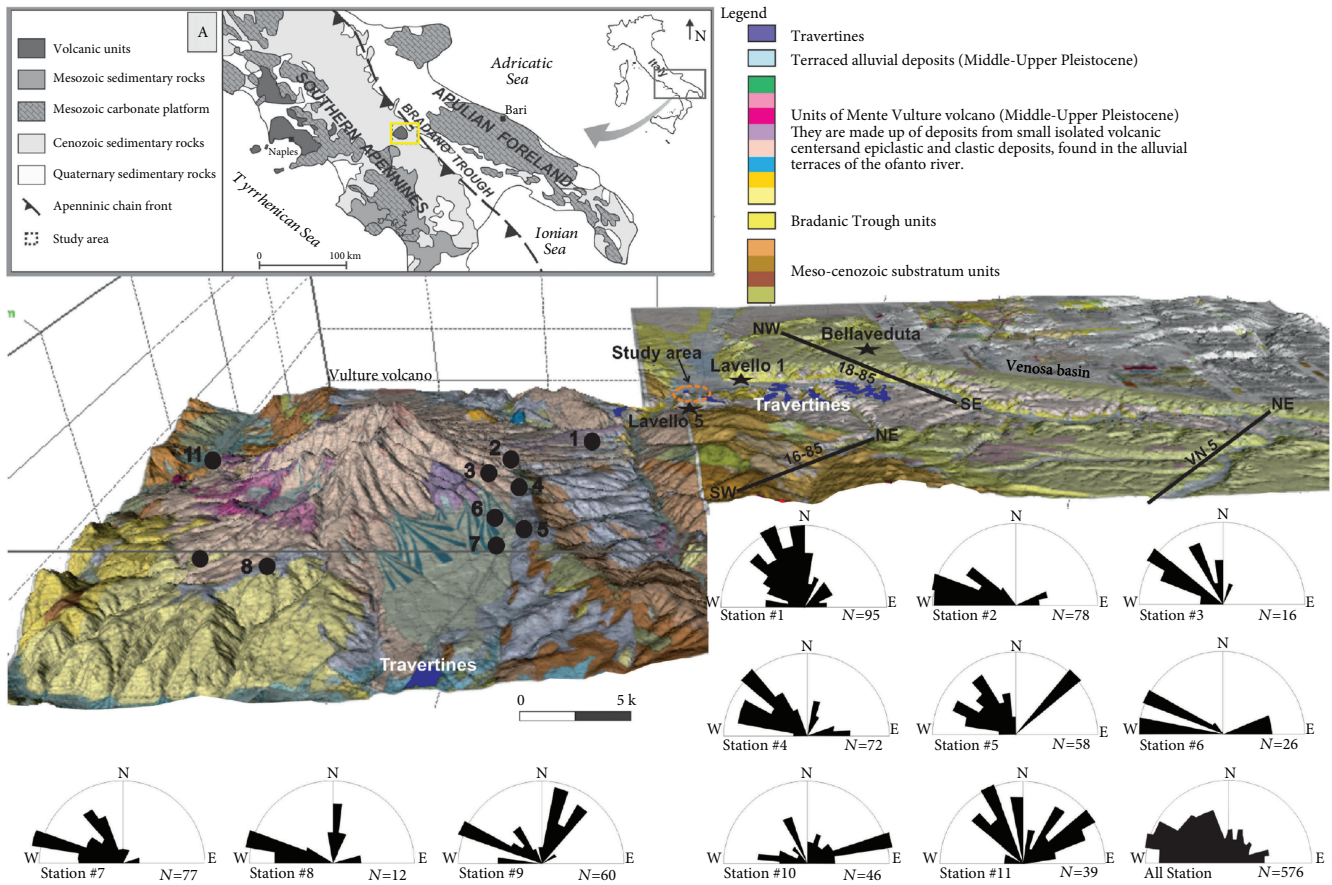


FIGURE 1: 3D geological map, constructed using Move™ software, of the Vulture volcano area (modified after [54]). Location of measurement stations (# 1 to 11) and rose diagrams (bin size 10°, the outer circle corresponds to the 20% of cumulative data) of the high-angle fractures crosscutting the fluviolacustrine deposits and volcanic rocks are reported (modified after [36]). The Lavello 5, Lavello 1, and Bellaveduta wells and the 16-85, VN 5, and 18-85 seismic lines are located in the map.

NE-SW and N-S fault sets were mainly active prior to the formation of the Bradano Trough (Figure 2(c)). The eastward lateral termination of the allochthonous complex is nicely shown by the well log correlation reported in Figure 3.

3. Sampling and Methods

Selected key outcrops were studied in detail by means of integrated field and laboratory analyses. The field survey was aimed at deciphering the geological setting and fault architecture exposed along the artificial outcrops of the Toppo D’Aguzzo Quarry, which occurs in the vicinity of the Rapolla village of Basilicata (Italy). In particular, field structural analyses focused on the nature, distribution, and relative timing of the formation of the structural elements exposed along the walls and pavements of the aforementioned quarry.

To determine the mineralogical composition of veins and pipe fluid conduit infill, 44 samples were collected at 3 different stations (cf. Figure 4) and then analyzed by X-ray diffraction (XRD) analysis using a Rigaku Miniflex powder diffractometer equipped with a sample spinner, with Cu-K α radiation, 30 kV, and 15 mA. Since most of the samples showed a zonation with different colors, each of them was investigated to define the order and the evolution of the

different mineral phases over time. With this aim, selected samples were also analyzed by optical microscopy (OM) using an optical polarizing microscope. Scanning electron microscopy (SEM) investigation was also performed using a PHILIPS XL30 ESEM operating at a beam current of 1 μ A and an accelerating voltage of 15 kV.

Doubly polished thin sections (100-300 μ m thick) were prepared for petrography and microthermometric determinations of fluid inclusions. Measurements on fluid inclusions were made using a Linkam THMS 600 heating-freezing stage. The accuracy of measurements is estimated at $\pm 2^\circ\text{C}$ at 398°C controlled by the melting point of $\text{K}_2\text{Cr}_2\text{O}_7$ and $\pm 0.1^\circ\text{C}$ at 0°C and $\pm 0.2^\circ\text{C}$ at -56.6°C controlled by using certified pure water and CO_2 -bearing synthetic fluid inclusions (Synthetic Fluid Inclusion Reference Set, Bubbles Inc., USA).

4. Results

4.1. Geological and Structural Analyses. In the Rapolla area, the structural grain is provided by NE-SW high-angle faults (Figure 4). The NE-striking faults crosscut both gravel and coeval tuff deposits and were interpreted as tear faults of the NE-verging splay thrust faults displacing the allochthonous complex on the foredeep deposits [37]. The NE-SW

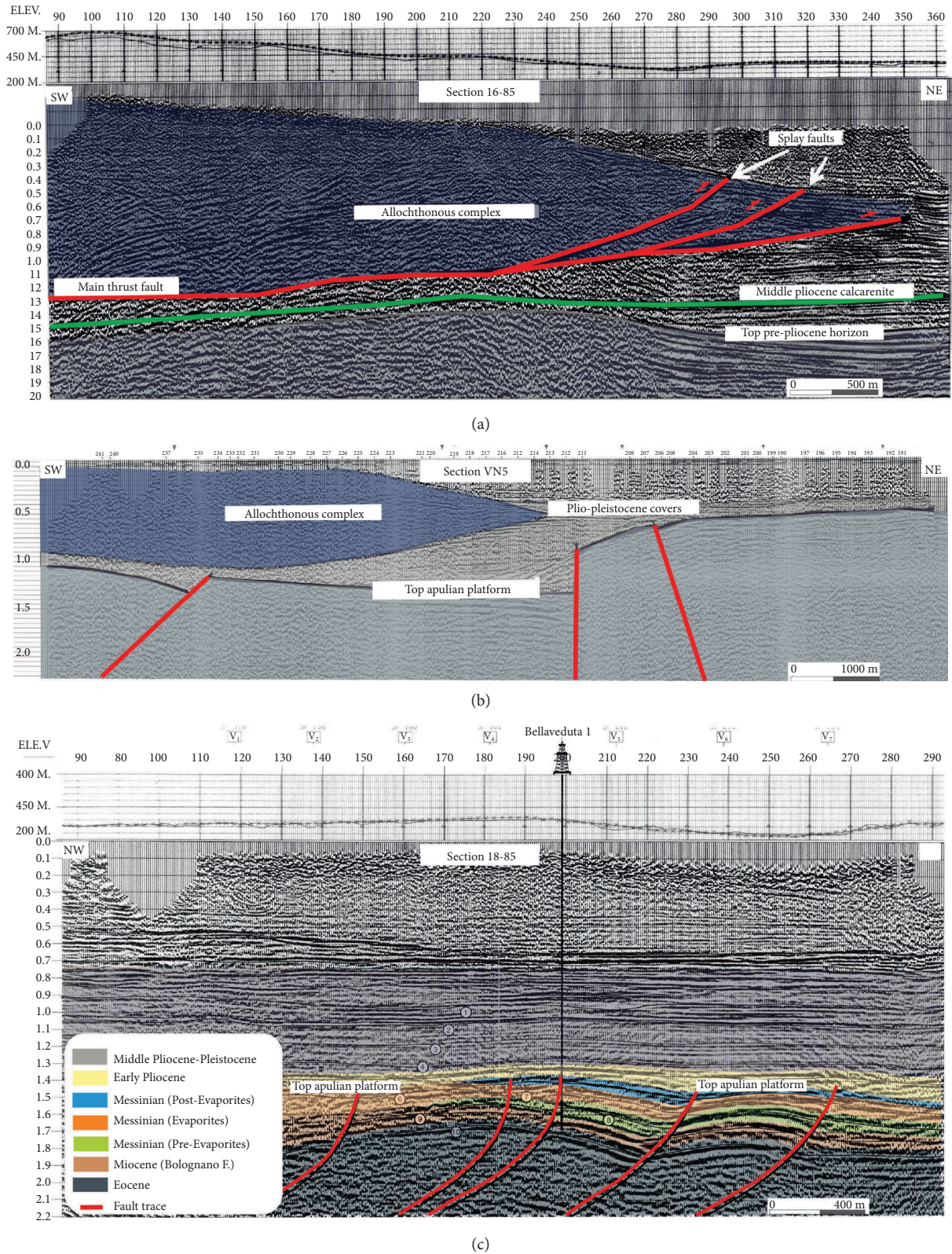


FIGURE 2: (a) Interpreted NE-SW-oriented seismic reflection profiles 16-85 in which the main decollement and the splay thrust faults displacing the Pleistocene sedimentary succession are highlighted; (b) interpreted NE-SW-oriented seismic reflection profiles VN5 across the south-eastern sector of the study area, showing the allochthonous complex overlying the Plio-Pleistocene covers and NW-SE-directed faults displacing the Apulian Platform; (c) interpreted NW-SE-oriented seismic 18-85 across the north-western sector of the study area, showing the listric geometry of the N-S-directed fault zone that displaces gently folded Eocene-Miocene succession. See Figure 1 for location.

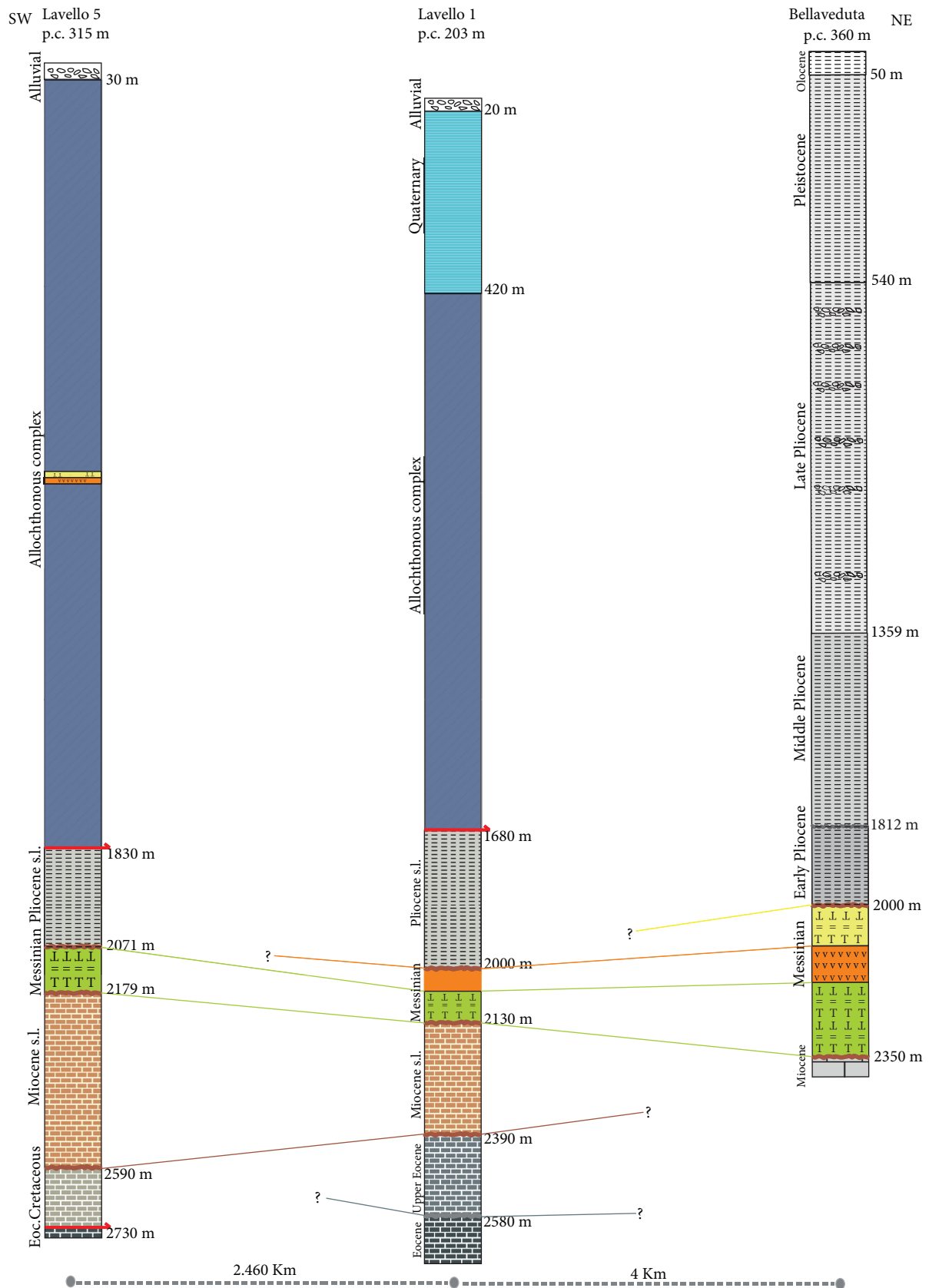


FIGURE 3: Schematic stratigraphic profile, NW-SE oriented, derived from the correlation of Lavello 5, Lavello 1, and Bellaveduta exploration wells. See Figure 1 for the location of the wells.

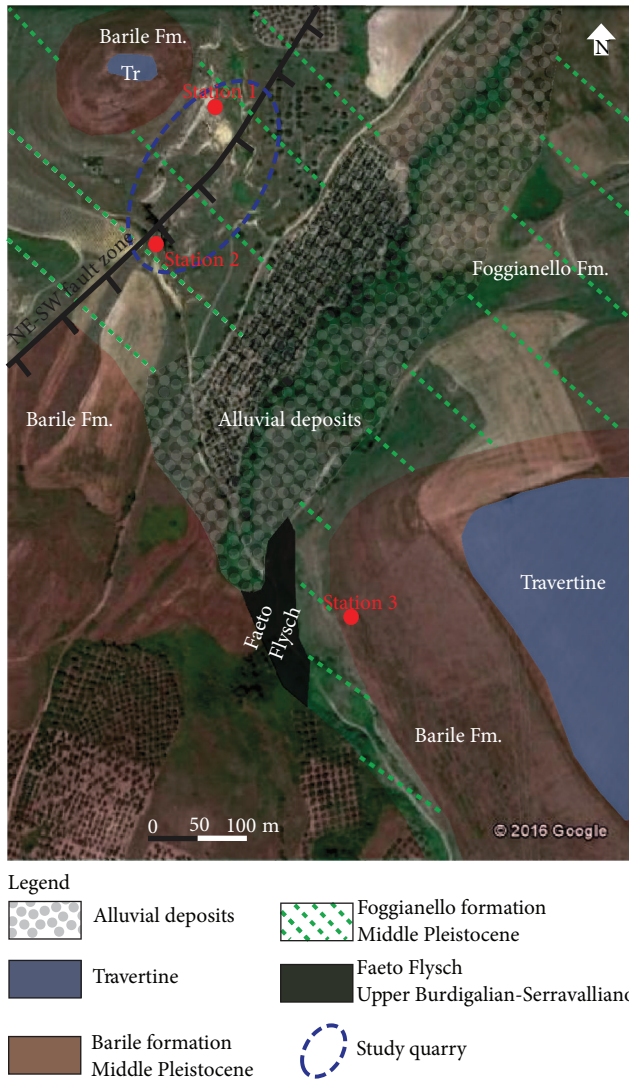


FIGURE 4: Geological map based on Google earth image of the Rapolla area, in which the location of the sampling sites and the investigated outcrops for structural analysis are reported.

trending, SE dipping normal fault zone exposed at the Toppo D'Aguzzo Quarry in the vicinity of the Rapolla village of Basilicata, is characterized by an average throw of 25 m. It includes multiple slip surfaces coated with kinematic markers such as calcite fibers, calcite steps, and abrasive striae, which are all consistent with pure extensional kinematics. The fault core, as thick as several cm, consists of grain- and matrix-supported poorly cohesive cataclasites and major slip surfaces (Figure 5(a)). Many subsidiary synthetic and antithetic slip surfaces localize in the vicinity of the fault core (inset of Figure 5(a)). Away from the main slip surfaces, the weakly fractured footwall fault damage zone is crosscut by N-S and NE-SW striking, subvertical veins (Figure 5(b)), and minor E-W veins (Figure 5(c)). Subsidiary NE-SW normal faults are also present throughout the whole footwall fault damage zone and are characterized by small vertical fractures that mainly localize at their mode-II extensional quadrants (Figure 5(d)). Such a structural architecture

is hence consistent with predominant opening-mode mechanisms and dilation of the whole high angle, NE-SW trending fault zone (cf. [37]), similar to other normal fault zones in carbonates [39, 40] and siliciclastic rocks [41]. Late NW-SE joints abutting all the aforementioned fracture sets are also documented within the footwall fault damage zone (Figure 5(e)).

4.2. Mineralogical and Petrographic Analyses. The mineralogical analyses were performed only on the samples collected from site 1 to 3 represented by pyroclastics of the Foggianello and Barile synthem, respectively, within and outside the study NE-SW trending, high-angle fault zone. Figure 6 shows the OM and SEM images and the XRD patterns of a representative sample collected from site 3 (cf. Figure 4), within the volcanoclastic rocks of the Barile synthem. In detail, a dark host rock (Figure 6(a)) reveals the presence of abundant clinopyroxene and feldspars (plagioclase and k-feldspars) by means of optical microscopy analysis (Figure 6(b)). This host rock is crosscut by a 1 cm thick, whitish, N-S trending silica-rich vein that includes some lithic fragments derived from the flanking microconglomerates (Figure 6(c)). SEM and EDX data (Figure 6(d)) support the aforementioned interpretation. XRD data performed on the dark host rock also indicates the presence of micas, pyroxene, and feldspars, whereas the whitish vein is almost exclusively made up of opal A (Figure 6(e)).

A representative hand specimen collected from site 1 (cf. Figure 4) is shown in Figure 7. There, the weakly fractured yellowish host rock, which pertains to the Foggianello synthem, is crosscut by a whitish NE-SW trending vein (Figure 7(a)). Optical microscopy analyses are consistent with the presence of quartz, feldspars, and strongly altered phenocrysts of pyroxenes in the host rock (Figure 7(b)). Results of SEM analyses point out to crystals of quartz characterized by a rim of pervasive jarosite and opal, which are dominant in the whitish vein (Figure 7(c)). Goethite is also present along the vein margin. X-ray profiles confirm that host rock is characterized by both jarosite and quartz minerals besides a large amount of opal A (Figure 7(d)).

Figure 8(a) displays a representative hand specimen collected from site 2 (cf. Figure 4), within the highly fractured pyroclastic rocks of the fault damage zone, pertaining to the Foggianello synthem. Results of optical microscopy analysis indicate the presence of quartz, feldspars, and rare clinopyroxenes in the host rock. The brown veins, ca. NE-SW trending, are characterized by iron oxide-hydroxide (Figure 8(b)), which is consistent with the presence of goethite within the host rock, together with both jarosite and opal A (Figure 8(c)). Isolated feldspar grains are also identified within the host rock. In detail, the SEM image (Figure 8(d)) shows a crystal of quartz with a rim of jarosite (EDX spectrum) and pervasive opal A. XRD performed on both host rocks and veins confirms the aforementioned results (Figure 8(e)). In fact, X-ray patterns of the host rock delineate of a large amount of jarosite and, subordinately quartz. The veins show a broad band from 15 to 32° 2θ indicating the presence of opal A.

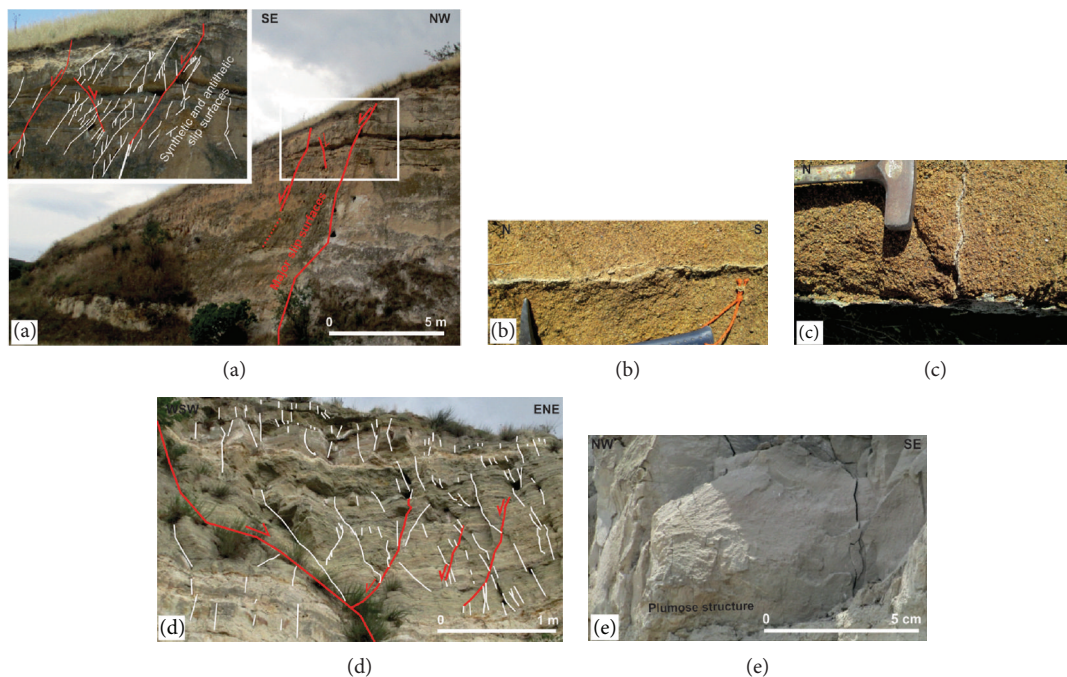


FIGURE 5: Main structural elements present along the NE-SE fault zone exposed at the Toppo D'Aguzzo quarry. (a) Cross-sectional view of the fault zone. Both synthetic and antithetic slip surfaces located at the hanging wall of the main slip surface are reported in the inset. (b) Subvertical N-S striking veins forming an eye structure. (c) High-angle E-W striking vein abutting against a N-S vein. (d) The pyroclastic rocks exposed within the footwall damage zone are crosscut by NE-SW striking fractures localized at the dilational quadrants of sheared parental slip surfaces. See text for further details. (e) Plumose structure displayed along a NW-SE joint.

4.3. Fluid Inclusion Analysis. Fluid inclusions hosted within quartz crystals were classified according to phase types at room temperature. All descriptions refer to fluid inclusion assemblages (FIAs), which were strictly defined as fluid inclusion vacuoles along the same growth zone in a single crystal or along a single healed fracture that formed at about the same time or during the same set of P-T conditions [42]. The observed inclusions occur as trails that crosscut the quartz crystals (Figures 9(a) and 9(b)) and were assigned to a probable secondary origin according to the criteria of Roedder [43] and Goldstein [44]. These are small in size ($<15\ \mu\text{m}$, most of them $<10\ \mu\text{m}$), and part of them shows an ellipsoidal morphology whereas the others have an irregular shape (Figures 9(a) and 9(b)). Two types of inclusions were identified in the examined samples by microscopic observation at room temperature: Type 1 two-phase (liquid + vapor) inclusions (L + V), liquid-rich at room temperature; Type 2 liquid only (L) inclusions.

Type 1 (L + V) inclusions comprise about 80% of the fluid inclusion population. They are characterized by a scarce variability in the vapor/liquid ratio, with the vapor bubble that occupies around 10-20% of the total volume at room temperatures (Figure 9(a)). Vapor bubble often vibrates. Type 2 (L) inclusions mainly occur in the planar groups along variably healed fracture planes (Figure 9(b)). They are very small in size ($<5\ \mu\text{m}$ in diameter). Due to the small size of the inclusions, the petrographic relationships between the two populations of fluid inclusions are not clear; as a consequence, we cannot make an unequivocal interpretation of

the timing of entrapment only based on microscopic observation at room temperature.

Microthermometric analyses were conducted on Type 1 (L + V) fluid inclusions. Results of this investigation are reported in Figure 9(c). Upon heating, total homogenization (T_h) of these inclusions was observed through the disappearance of vapor in the liquid phase at temperatures ranging between 167 and 261°C with a mode around 200°C (Figure 9(c)). The small size of the inclusions hindered the observation of initial ice melting, and also final ice melting (T_{mi}) was possible to be observed only in very few inclusions. The T_{mi} values are around -1.5°C, corresponding to salinity of about 2.6 NaCl wt.%_{equiv.} calculated according to Bodnar [45]. However, the scarce statistics does not allow having great confidence concerning this value of salinity.

5. Discussion

The results of integrated geological, structural, mineralogical, and fluid inclusion analyses of a hydrothermally altered high-angle fault zone exposed in the vicinity of the Rapolla village, along the eastern flank of the Vulture volcano, are consistent with the occurrence of a relatively high-temperature, fossil, hydrothermal system whose temperature and composition varied with time. The alteration mineralogical paragenesis associated with the hydrothermal veins and fluid inclusion data suggest that the earliest fluids that circulated in the system (Stage 1) were characterized by temperature around 200°-210°C and low-pH conditions (pH < 4). Individual

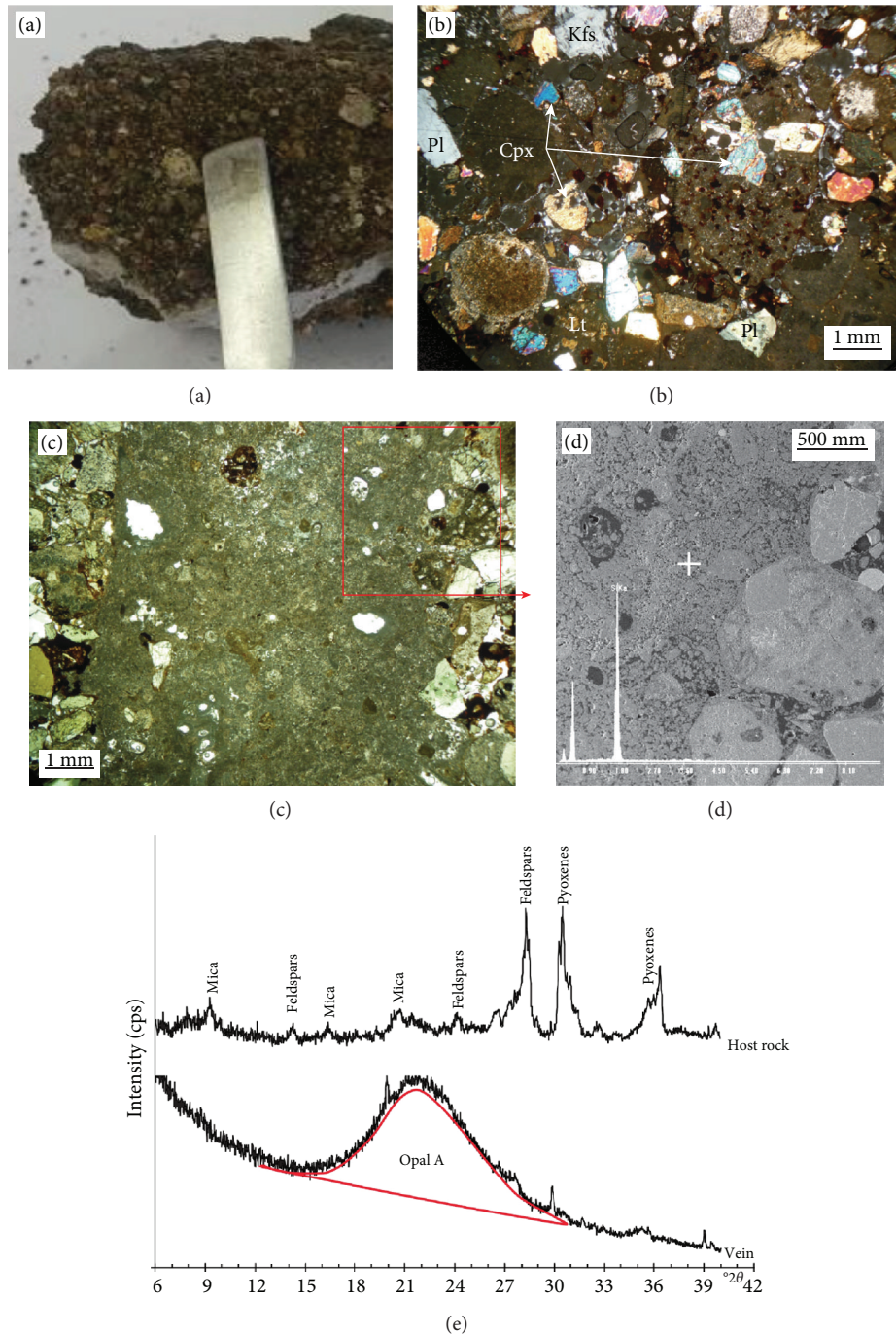


FIGURE 6: (a) Picture of representative sample (dark host rock and white vein); (b) OM observation of host rock. Kfs: k-feldspar; Cpx: clinopyroxene; Pl: plagioclase; Lt: lithic fragments. (c) OM observation vein; (d) SEM image and EDX spectra of opal; (e) XRD diffraction profiles of the host rock and vein.

hand specimens collected from the pyroclastics pertaining to the Foggianello synthem (cf. Sections 4.1 and 4.2) point out to the formation of an advanced argillic mineralogical assemblage. The alteration mineralogical assemblage is dominated by the alunite group minerals (mainly jarosite), which are stable under low-pH conditions ($\text{pH} < 4$) and high- SO_4^{2-} ion activity [46]. Jarosite also precipitated within the cross-orthogonal N-S and E-W striking fracture sets, and in the fault-related NE-SW striking fracture. Development of this

high-temperature hydrothermal system required that a significant thermal anomaly, able to efficiently supply heat to the overlying pyroclastic rocks, was established in the area at the time of jarosite precipitation. The heat source could be envisaged in a shallow magma chamber connected to the development of the Vulture volcano. The occurrence of a relatively shallow magma chamber during emplacement of the Fara d'Olivo ignimbrite, during the Middle Pleistocene, is strongly suggested by the fact that an impressive caldera

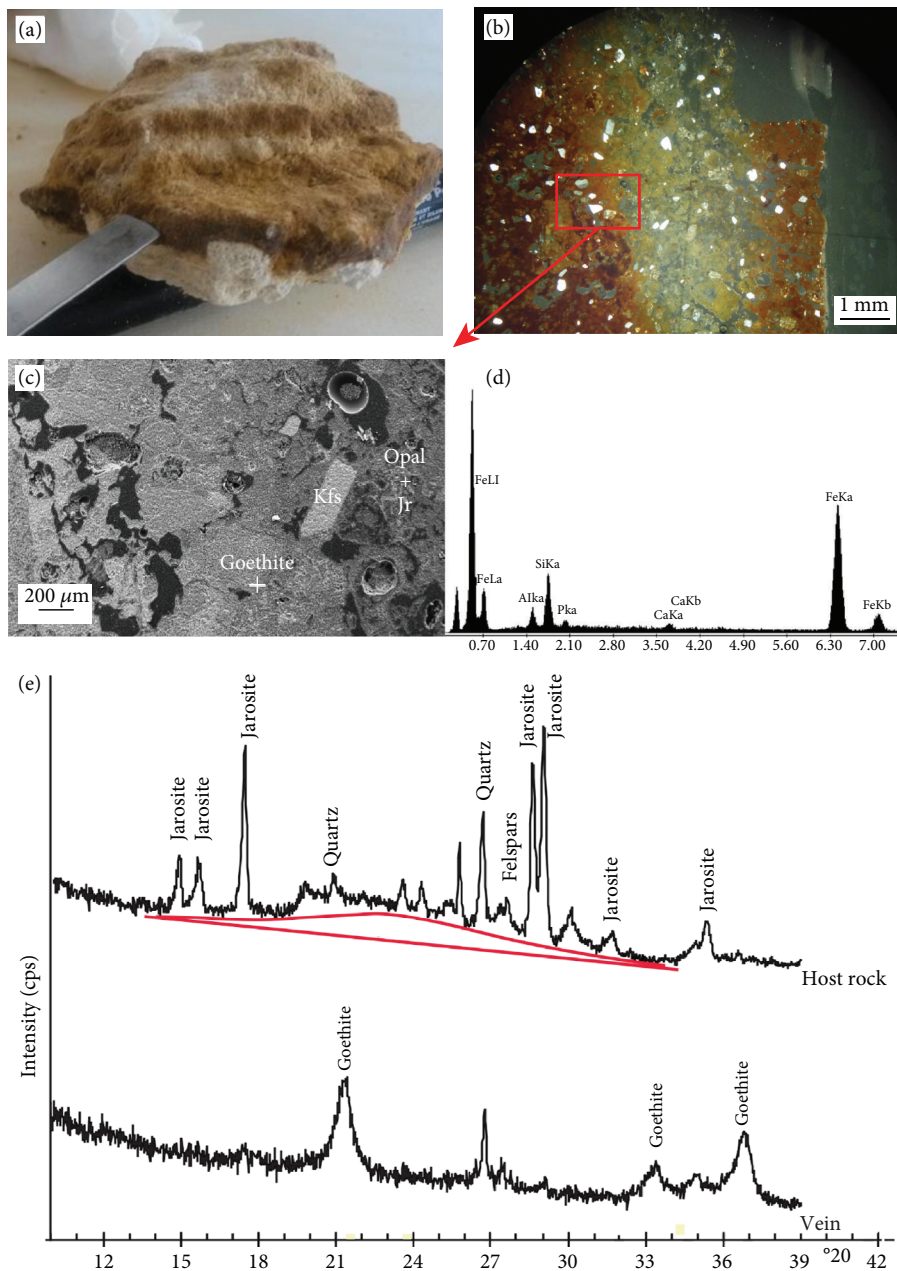


FIGURE 7: (a) Picture of the representative sample (yellow host rock and white vein); (b) OM observations (crossed polars); (c, d) SEM image and EDX spectra of goethite. Jr: jarosite; Qtz: quartz. (e) XRD diffraction profiles of the host rock and vein.

depression formed in response to the big explosive eruption that spread over a large area of ignimbritic deposits and emptied the magma chamber ([34] and references therein). It is known that calderas are the result of the collapse of rocks that overlies shallow magma chambers, which takes place after the sudden withdrawal of magma due to an explosive eruption [47, 48].

Both acidic conditions of the early hydrothermal fluids and the inferred high-SO₄²⁻ ion activity were likely related to the input of deep H₂S from organic substances entrapped within the Apulian Platform and/or from degassing from the Vulture magma chamber. H₂S condensed in oxygenated hydrothermal fluids producing H₂SO₄ (equation 1), which

lowered the pH conditions and gave rise to the advanced argillic mineralogical assemblage.



A drop of temperature and acidity of the fluids, with opal A precipitation (Stage 2) both outside and within the NE-SW trending high-angle fault zone, followed the aforementioned high-temperature and low-pH hydrothermal activity stage (Stage 1). Outside the fault zone, within the volcanoclastic rocks of the Barile synthem, opal A precipitated within both N-S and E-W cross-orthogonal joint sets (cf. Figure 5). Differently, within the Fara d’Olivio pyroclastics of the

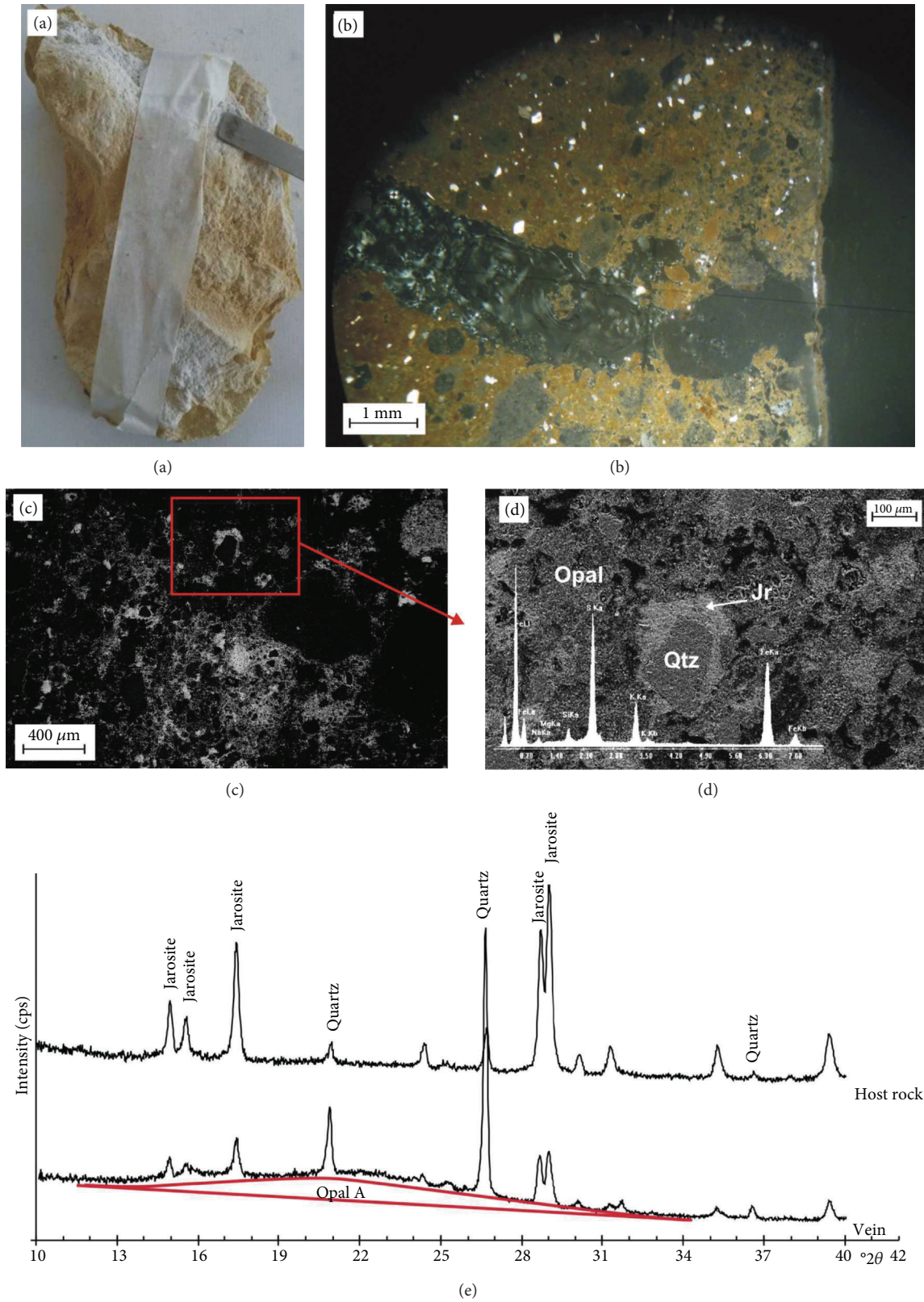


FIGURE 8: (a) Picture of representative sample (host rock white and brown vein); (b) OM observations; (d) SEM image and EDX spectra goethite. Jr: jarosite, Kfs: k-feldspar. (e) XRD diffraction profiles of the host rock and vein.

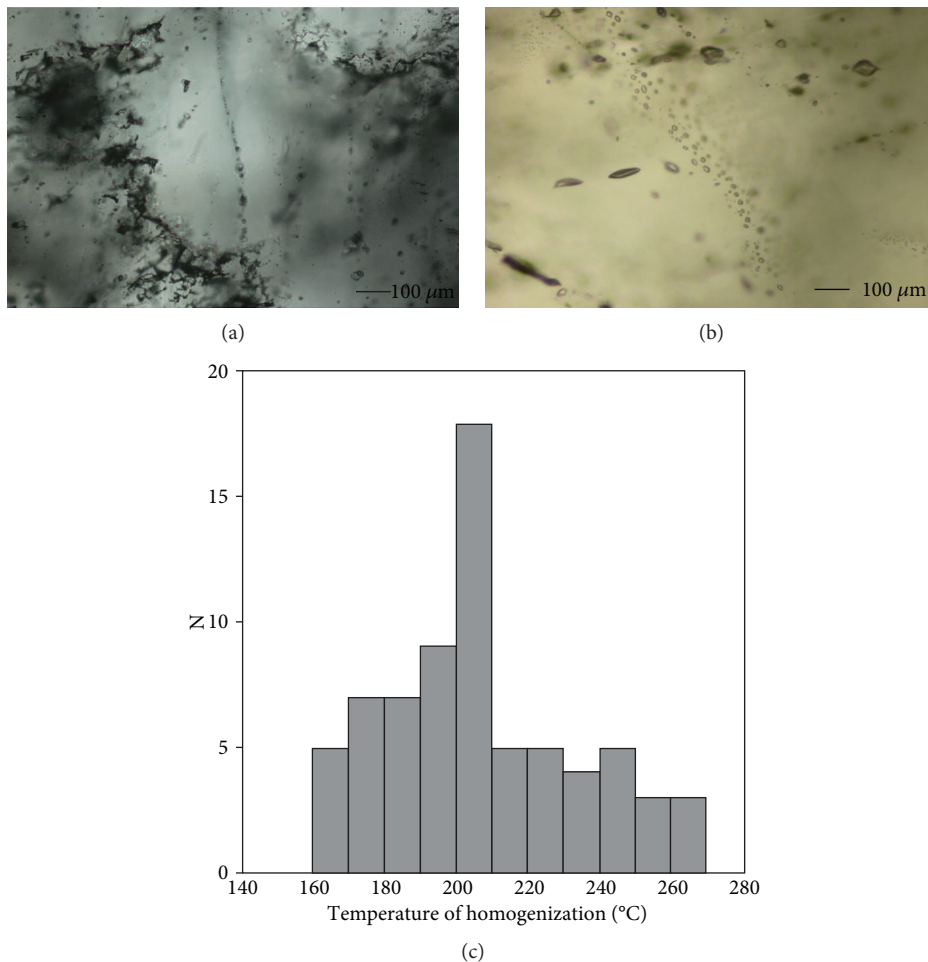


FIGURE 9: (a) Microphotograph of secondary trails of Type 1 two-phase liquid-rich (L + V) fluid inclusions; (b) microphotograph of secondary trails of Type 2 liquid only (L) fluid inclusions; (c) histogram of the homogenization temperatures of the studied Type 1 fluid inclusions. *N* = number of measurements.

Foggianello synthem forming the footwall damage zone of the study fault zone, opal A precipitated within N-S, E-W, and NE-SW trending high-angle joints and sheared joints (cf. Figure 5). Opal A precipitated as a consequence of a drop of temperature of the hydrothermal fluids, which likely reduced the solubility of silica in solution. Hence, opal A precipitation during Stage 2 postdated crystallization of jarosite both within the fault-related joint and sheared joint sets (cf. Figure 5). We may hypothesize that the observed secondary fluid inclusion assemblage, which is made up of very small monophasic inclusions (Type 2, Figure 9(b)), is representative of the hydrothermal fluids that circulated during Stage 2 and hence consistent with temperatures lower than 100°C. If so, the drop of temperature that characterized the hydrothermal fluids between Stage 1 and Stage 2 is in the order of about 100°C. Such a significant drop of temperature could be therefore related to the cooling of a shallow magma chamber of the Vulture volcano ([34] and references therein) and to the progressive deepening of the magma source [36] within an evolved, deeply rooted, NE-SW trending, high-angle trans-tensional fault zone [37].

The latest evolution of the aforementioned hydrothermal system was characterized by the goethite mineralization

along the main slip surface (Stage 3). This mineralization partly developed as supergene alteration of jarosite and was related to the circulation of CO₂-bearing meteoric water at low temperatures (< 30°C) through the main structural discontinuities under neutral to weakly acidic conditions (pH = 6-7). Occurrence of travertine deposits in the Rapolla area [37] can represent the surficial expression of the circulation of these low-temperature fluids, which could be considered, to some extent, analogous to those present in the local Fe-rich aquifer of the Vulture volcano [49].

High-temperature hydrothermal systems in the frontal sector of recently active fold-and-thrust belts are rarely observed, because a low amount of heat flow characterizes these regions [50, 51]. The particular conditions that led to the development of a high-temperature hydrothermal system in the Rapolla area, where the lithosphere thickness is around 90–100 km [28], must just be sought in the occurrence of the Vulture volcano, which formed in the frontal sector of the Apennines chain, not far from the western margin of the Apulia foreland. The origin of the Vulture volcano is related to the unusual mantle dynamic that has occurred after cessation of collision between the Adria–Africa and Europe plates [52]. This unusual feature allows considering the Rapolla

area as a very rare case of a high-temperature hydrothermal system developed at the very front of an orogen.

Presently, the only evidence of a geothermal system in the area is represented by saline waters at temperatures of 35°C that have been discovered during drilling of some wells in the Bradano foredeep (Forestella and Montemilone wells) at a depth of about 600 m [53]. Waters circulate within a horst formed by fractured Cretaceous carbonates of the Apulian Platform, located about 15 km East of the study area, sealed by Pleistocene clay. This finding, together with the heat flux anomaly reported for the Vulture area [6], point out the possible presence of a low- to medium-enthalpy geothermal system.

6. Conclusions

The results of this integrated geostructural, mineralogical, and fluid inclusion study take in evidences that high-temperature (ca. 200–210°C) hydrothermal circulation occurred at quite shallow depths during burial diagenesis of pyroclasts pertaining to the Middle Pleistocene Foggianello and Barile synthems, Vulture volcano, southern Italy. There, at the outermost edge of the southern Apennine fth, the hydrothermal system was due to a short-time living, high positive thermal anomaly that localized along the eastern flanks of the Vulture volcano. Three main stages of activity of the hydrothermal system were documented. Stage 1 produced the circulation of fluids having low-pH conditions (pH < 3–4) and relatively high-SO₄²⁻ activity, as testified by the main hydrothermal mineralogical assemblage formed by jarosite and minor silica, typical of advanced argillic alteration facies. Hydrothermal fluids were characterized by high temperature around 200°–210°C. These hot fluids altered and mineralized the matrices of pyroclastic rocks and sealed both burial-related (N-S and E-W striking) and fault-related (NE-SW striking) fracture networks. Later hydrothermal circulation (Stage 2) was recorded by opal A-rich veins, which are present both inside and outside the transtensional fault zone. The fluids responsible of the second stage of development of the Rapolla area hydrothermal system were characterized by temperature conditions probably lower than 100°C. Currently, goethite mineralization occurs along the main slip surfaces of the study high-angle fault zone, which is due to the circulation of meteoric-derived fluids pertaining to the local aquifer. This study highlights that a high-temperature hydrothermal system developed in the past in the Rapolla area within the transtensional fault zone, when a high thermal anomaly was present. If we take into account that this area is still affected by a heat flux positive anomaly (90 mW/m²), we may infer that it has the potentiality to be considered an interesting site for future exploration devoted to the finding of medium-enthalpy geothermal resources at depth.

Data Availability

The data used to support the findings of this study are available from the corresponding author upon request.

Conflicts of Interest

The authors declare that they have no conflicts of interest.

Acknowledgments

The present work was supported by the Italian Ministry of Education and Research (RIL 2015–2017 grants to FA and GP), the Reservoir Characterization Project (FA and AVP), and the University of Pisa “Fondi d’Ateneo 2017” MIUR (PF). Alessandro Laurita (Microscopy Laboratory–University of Basilicata) is kindly acknowledged for his assistance in the SEM investigations. The authors also acknowledge the contribution of Francesco Colucci during the field and laboratory analyses.

References

- [1] D. L. Norton, “Theory of hydrothermal systems,” *Annual Review of Earth and Planetary Sciences*, vol. 12, no. 1, pp. 155–177, 1984.
- [2] F. Pirajno, *Hydrothermal Mineral Deposits. Principles and Fundamental Concepts for the Exploration Geologist*, Springer-Verlag, Berlin, Heidelberg, 1992.
- [3] S. Bellani, A. Brogi, A. Lazzarotto, D. Liotta, and G. Ranalli, “Heat flow, deep temperatures and extensional structures in the Larderello geothermal field (Italy): constraints on geothermal fluid flow,” *Journal of Volcanology and Geothermal Research*, vol. 132, no. 1, pp. 15–29, 2004.
- [4] J. P. Brun, M. A. Gutscher, and DEKORP-ECORS teams, “Deep crustal structure of the Rhine Graben from DEKORP-ECORS seismic reflection data: a summary,” *Tectonophysics*, vol. 208, no. 1–3, pp. 139–147, 1992.
- [5] I. Lucchitta, “Role of heat and detachment in continental extension as viewed from the eastern Basin and Range Province in Arizona,” *Tectonophysics*, vol. 174, no. 1–2, pp. 77–114, 1990.
- [6] R. Cataldi, F. Mongelli, P. Squarci, L. Taffi, G. Zito, and C. Calore, “Geothermal ranking of Italian territory,” *Geothermics*, vol. 24, no. 1, pp. 115–129, 1995.
- [7] L. Beccaluva, M. Coltorti, P. Di Girolamo et al., “Petrogenesis and evolution of Mt. Vulture alkaline volcanism (southern Italy),” *Mineralogy and Petrology*, vol. 74, no. 2–4, pp. 277–297, 2002.
- [8] A. Brogi and P. Fulignati, “Tectonic control on hydrothermal circulation and fluid evolution in the Pietratonda-Poggio Peloso (southern Tuscany, Italy) carbonate-hosted Sb-mineralization,” *Ore Geology Reviews*, vol. 44, pp. 158–171, 2012.
- [9] A. Brogi, L. Fabbrini, and D. Liotta, “Sb-Hg ore deposit distribution controlled by brittle structures: the case of the Selvena mining district (Monte Amiata, Tuscany, Italy),” *Ore Geology Reviews*, vol. 41, no. 1, pp. 35–48, 2011.
- [10] M. Gasparrini, G. Ruggieri, and A. Brogi, “Diagenesis versus hydrothermalism and fluid–rock interaction within the Tuscan Nappe of the Monte Amiata CO₂-rich geothermal area (Italy),” *Geofluids*, vol. 13, no. 2, 179 pages, 2013.
- [11] D. Liotta, G. Ruggieri, A. Brogi, P. Fulignati, A. Dini, and I. Nardini, “Migration of geothermal fluids in extensional terrains: the ore deposits of the Boccheggiano-Montieri area (southern Tuscany, Italy),” *International Journal of Earth Sciences*, vol. 99, no. 3, pp. 623–644, 2010.

- [12] D. Liotta, A. Brogi, M. Meccheri, A. Dini, C. Bianco, and G. Ruggieri, "Coexistence of low-angle normal and high-angle strike- to oblique-slip faults during Late Miocene mineralization in eastern Elba Island (Italy)," *Tectonophysics*, vol. 660, pp. 17–34, 2015.
- [13] E. Patacca and P. Scandone, "The 1627 Gargano earthquake (southern Italy): identification and characterization of the causative fault," *Journal of Seismology*, vol. 8, no. 2, pp. 259–273, 2004.
- [14] M. Boccaletti, F. Calamita, G. Deiana et al., "Migrating foredeep-thrust belt systems in the northern Apennines and southern Alps," *Palaeogeography, Palaeoclimatology, Palaeoecology*, vol. 77, no. 1, pp. 3–14, 1990.
- [15] P. Casero, F. Roure, I. Moretti, L. Sage, and R. Vially, "Evoluzione geodinamica neogenica dell'Appennino meridionale," *Memorie della Societa Geologica Italiana*, vol. 41, pp. 109–120, 1988.
- [16] E. Patacca and P. Scandone, "Post-Tortonian mountain building in the Apennines. The role of the passive sinking of a relic lithospheric slab," in *The Lithosphere in Italy: Advances in Earth Science Research : a Mid-term Conference Convened by the Italian National Committee for the International Lithosphere Program, Volume 80 of Atti dei convegni Lincei*, A. Boriani, M. Bonafede, G. B. Piccardo, and G. B. Vai, Eds., pp. 157–176, Accademia Nazionale dei Lincei, 1989.
- [17] E. Patacca and P. Scandone, "Late trust propagation and sedimentary response in the thrust belt-foredeep system of the southern Apennines (Pliocene-Pleistocene)," in *Anatomy of an Orogen: The Apennines and Adjacent Mediterranean Basins*, G. B. Vai and I. P. Martini, Eds., pp. 401–440, Kluwer Academic Publishers, Great Britain, 2001.
- [18] E. Patacca, R. Sartori, and P. Scandone, "Tyrrhenian basin and Apenninic arcs: kinematic relations since late Tortonian times," *Memorie della Societa Geologica Italiana*, vol. 45, pp. 425–451, 1990.
- [19] S. Piedilato and G. Prosser, "Thrust sequences and evolution of the external sector of a fold and thrust belt: an example from the southern Apennines (Italy)," *Journal of Geodynamics*, vol. 39, no. 4, pp. 386–402, 2005.
- [20] V. Del Gaudio, P. Pierri, A. Frepoli, G. Calcagnile, N. Venisti, and G. B. Cimini, "A critical revision of the seismicity of Northern Apulia (Adriatic microplate — Southern Italy) and implications for the identification of seismogenic structures," *Tectonophysics*, vol. 436, no. 1–4, pp. 9–35, 2007.
- [21] P. Favali, G. Mele, and G. Mattiotti, "Contribution to the study of the Apulian microplate geodynamics," *Memorie della Societa Geologica Italiana*, vol. 44, pp. 71–80, 1990.
- [22] I. Korneva, E. Tondi, F. Agosta et al., "Structural properties of fractured and faulted Cretaceous platform carbonates, Murge plateau (southern Italy)," *Marine and Petroleum Geology*, vol. 57, pp. 312–326, 2014.
- [23] V. La Bruna, F. Agosta, J. Lamarche, S. Viseur, and G. Prosser, "Fault growth mechanisms and scaling properties in foreland basin system: the case study of Monte Alpi, southern Apennines, Italy," *Journal of Structural Geology*, vol. 116, pp. 94–113, 2018.
- [24] A. V. Petrullo, F. Agosta, G. Prosser, and E. Rizzo, "Cenozoic tectonic evolution of the northern Apulian carbonate platform (southern Italy)," *Italian Journal of Geosciences*, vol. 136, no. 2, pp. 296–311, 2017.
- [25] M. Sella, C. Turci, and A. Riva, "Petroleum geology of the 'Fossa Bradanica' (foredeep of the southern Apennine thrust belt)," in *Classic Petroleum Provinces*, J. Brooks, Ed., vol. 50, no. 1, pp. 369–378, Geological Society of London Special Publications, 1990.
- [26] N. Ciaranfi, P. Pieri, and G. Ricchetti, "Note alla carta geologica delle Murge e del Salento (Puglia centro-meridionale)," *Memorie della Societa Geologica Italiana*, vol. 41, pp. 449–460, 1992.
- [27] C. Doglioni, F. Mongelli, and P. Pieri, "The Puglia uplift (SE Italy): an anomaly in the foreland of the Apenninic subduction due to buckling of a thick continental lithosphere," *Tectonics*, vol. 13, no. 5, pp. 1309–1321, 1994.
- [28] C. Doglioni, P. Harabaglia, G. Martinelli, F. Mongelli, and G. Zito, "A geodynamic model of the southern Apennines accretionary prism," *Terra Nova*, vol. 8, no. 6, pp. 540–547, 1996.
- [29] C. Doglioni, F. Innocenti, and G. Mariotti, "Why Mt. Etna?," *Terra Nova*, vol. 13, no. 1, pp. 25–31, 2001.
- [30] J. E. Guest, A. M. Duncan, and D. K. Chester, "Monte Vulture volcano (Basilicata, Italy): an analysis of morphology and volcanoclastic facies," *Bulletin of Volcanology*, vol. 50, no. 4, pp. 244–257, 1988.
- [31] L. La Volpe and C. Principe, "Comments on 'Monte Vulture Volcano (Basilicata, Italy): an analysis of morphology and volcanoclastic facies' by J. E. Guest, A. M. Duncan and D. K. Chester," *Bulletin of Volcanology*, vol. 53, no. 3, pp. 222–227, 1991.
- [32] F. Stoppa and C. Principe, "Erratum to 'Eruption style and petrology of a new carbonatitic suite from the Mt. Vulture Southern Italy: the Monticchio Lakes formation'," *Journal of Volcanology and Geothermal Research*, vol. 78, pp. 251–265, 1998.
- [33] D. Scrocca, C. Doglioni, and F. Innocenti, "Constraints for an interpretation of the Italian geodynamics: a review," *Memorie Descrittive della Carta Geologica d'Italia*, vol. 62, pp. 15–46, 2003.
- [34] P. Giannandrea, L. La Volpe, C. Principe, and M. Schiattarella, "Unità stratigrafiche a limiti inconformi e storia evolutiva del vulcano medio-pleistocenico di Monte Vulture (Appennino meridionale, Italia)," *Bollettino - Societa Geologica Italiana*, vol. 125, pp. 67–92, 2006.
- [35] P. Beneduce and S. I. Giano, "Osservazioni preliminari sull'assetto morfostrutturale dell'edificio vulcanico del Monte vulture (Basilicata)," *Il Quaternario Italian Journal of Quaternary Sciences*, vol. 9, pp. 325–330, 1996.
- [36] M. Schiattarella, P. Beneduce, P. Di Leo, S. I. Giano, P. Giannandrea, and C. Principe, "Assetto strutturale ed evoluzione morfotettonica quaternaria del vulcano del Monte Vulture (Appennino lucano)," *Bollettino- Societa Geologica Italiana*, vol. 124, pp. 543–562, 2005.
- [37] R. Sinisi, A. V. Petrullo, F. Agosta, M. Paternoster, C. Belviso, and F. Grassa, "Contrasting fault fluids along high-angle faults: a case study from southern Apennines (Italy)," *Tectonophysics*, vol. 690, pp. 206–218, 2016.
- [38] P. Montone, M. T. Mariucci, S. Pondrelli, and A. Amato, "An improved stress map for Italy and surrounding regions (Central Mediterranean)," *Journal of Geophysical Research*, vol. 109, no. B10, 2004.
- [39] F. Agosta, P. Ruano, A. Rustichelli, E. Tondi, J. Galindo-Zaldívar, and C. Sanz de Galdeano, "Inner structure and deformation mechanisms of normal faults in conglomerates and carbonate grainstones (Granada Basin, Betic cordillera, Spain):

- inferences on fault permeability,” *Journal of Structural Geology*, vol. 45, pp. 4–20, 2012.
- [40] F. Agosta, C. Wilson, and A. Aydin, “The role of mechanical stratigraphy on normal fault growth across a cretaceous carbonate multi-layer, Central Texas (USA),” *Italian Journal of Geosciences*, vol. 134, no. 3, pp. 423–441, 2015.
- [41] N. C. Davatzes and A. Aydin, “The formation of conjugate normal fault systems in folded sandstone by sequential jointing and shearing, Waterpocket monocline, Utah,” *Journal of Geophysical Research*, vol. 108, no. B10, 2003.
- [42] R. H. Goldstein and T. J. Reynolds, “Systematics of fluid inclusions in diagenetic minerals,” *Society for Sedimentary Geology Short Course*, vol. 31, pp. 1–199, 1994.
- [43] E. Roedder, “Fluid inclusions,” *Reviews in Mineralogy*, vol. 12, pp. 1–644, 1984.
- [44] R. H. Goldstein, “Petrographic analysis of fluid inclusions,” in *Fluid Inclusions Analysis and Interpretation*, I. Samson, A. Anderson, and D. Marshall, Eds., vol. 32, pp. 9–53, Mineralogical Association of Canada, Short Course, 2003.
- [45] R. J. Bodnar, “Revised equation and table for determining the freezing point depression of H₂O-NaCl solutions,” *Geochimica et Cosmochimica Acta*, vol. 57, no. 3, pp. 683–684, 1993.
- [46] R. E. Stoffregen, “Genesis of acid-sulfate alteration and Au-Cu-Ag mineralization at Summitville, Colorado,” *Economic Geology*, vol. 82, no. 6, pp. 1575–1591, 1987.
- [47] M. Branney and V. Acocella, “Chapter 16 - Calderas,” in *Encyclopedia of Volcanoes*, H. Sigurdsson, Ed., 299–315, 2015.
- [48] K. Wohletz and G. Heiken, *Volcanology and Geothermal Energy*, University Of California Press Berkeley, 1992.
- [49] M. Paternoster, S. Parisi, A. Caracausi, R. Favara, and G. Mongelli, “Groundwaters of Mt. Vulture volcano, southern Italy: chemistry and sulfur isotope composition of dissolved sulfate,” *Geochemical Journal*, vol. 44, no. 2, pp. 125–135, 2010.
- [50] N. McQuarrie and T. A. Ehlers, “Techniques for understanding fold-and-thrust belt kinematics and thermal evolution,” in *Linkages and feedbacks in orogenic systems*, R. D. Law, J. R. Thigpen, A. J. Mershat, and H. D. Stowell, Eds., vol. 213, pp. 25–54, Geological Society of America, 2017.
- [51] H. N. Pollack, S. J. Hurter, and J. R. Johnson, “Heat flow from the Earth’s interior: analysis of the global data set,” *Reviews of Geophysics*, vol. 31, no. 3, pp. 267–280, 1993.
- [52] G. De Astis, P. D. Kempton, A. Peccerillo, and T. W. Wu, “Trace element and isotopic variations from Mt. Vulture to Campanian volcanoes: constraints for slab detachment and mantle inflow beneath southern Italy,” *Contributions to Mineralogy and Petrology*, vol. 151, no. 3, pp. 331–351, 2006.
- [53] G. Tamburriello, M. Balasco, E. Rizzo, P. Harabaglia, V. Lapenna, and A. Siniscalchi, “Deep electrical resistivity tomography and geothermal analysis of Bradano foredeep deposits in Venosa area (Southern Italy): preliminary results,” *Annals of Geophysics*, vol. 51, no. 1, 2008.
- [54] P. Giannandrea, L. La Volpe, C. Principe, and M. Schiattarella, “Carta Geologica del Monte Vulture alla scala 1:25.000,” in *Litografia Artistica Cartografica*, Firenze, 2004.

Research Article

Analysis of Fracture Roughness Control on Permeability Using SfM and Fluid Flow Simulations: Implications for Carbonate Reservoir Characterization

Miller Zambrano ^{1,2,3} Alan D. Pitts,^{1,3} Ali Salama,¹ Tiziano Volatili,^{1,2,3} Maurizio Giorgioni,⁴ and Emanuele Tondi^{1,2,3}

¹School of Science and Technology-Geology Division, University of Camerino, Italy

²GeoMORE s.r.l, Camerino, Italy

³Reservoir Characterization Project, Italy

⁴Shell Italia Exploration and Production, Italy

Correspondence should be addressed to Miller Zambrano; miller.zambrano@unicam.it

Received 30 November 2018; Accepted 14 February 2019; Published 23 April 2019

Academic Editor: Jaewon Jang

Copyright © 2019 Miller Zambrano et al. This is an open access article distributed under the Creative Commons Attribution License, which permits unrestricted use, distribution, and reproduction in any medium, provided the original work is properly cited.

Fluid flow through a single fracture is traditionally described by the cubic law, which is derived from the Navier-Stokes equation for the flow of an incompressible fluid between two smooth-parallel plates. Thus, the permeability of a single fracture depends only on the so-called hydraulic aperture which differs from the mechanical aperture (separation between the two fracture wall surfaces). This difference is mainly related to the roughness of the fracture walls, which has been evaluated in previous works by including a friction factor in the permeability equation or directly deriving the hydraulic aperture. However, these methodologies may lack adequate precision to provide valid results. This work presents a complete protocol for fracture surface mapping, roughness evaluation, fracture modeling, fluid flow simulation, and permeability estimation of individual fracture (open or sheared joint/pressure solution seam). The methodology includes laboratory-based high-resolution structure from motion (SfM) photogrammetry of fracture surfaces, power spectral density (PSD) surface evaluation, synthetic fracture modeling, and fluid flow simulation using the Lattice-Boltzmann method. This work evaluates the respective controls on permeability exerted by the fracture displacement (perpendicular and parallel to the fracture walls), surface roughness, and surface pair mismatch. The results may contribute to defining a more accurate equation of hydraulic aperture and permeability of single fractures, which represents a pillar for the modeling and upscaling of the hydraulic properties of a geofluid reservoir.

1. Introduction

Fractures exert a vital contribution on determining the migration and storage for geofluids, such as groundwater, and hydrocarbons. Thus, the analysis and modeling of fractures are imperative for characterizing reservoirs and simulating their behavior during the production stage. Fluid flow through fractures is traditionally described by the cubic law, derived from the Navier-Stokes equation for the flow of an incompressible fluid between two smooth-parallel plates

[1]. Thus, the permeability (intrinsic permeability) of a single fracture may be represented by the equation

$$k = \frac{e^2}{12}, \quad (1)$$

where e corresponds to the hydraulic aperture. Since fractures are normally rough, the hydraulic aperture differs from the mechanical aperture (separation between the two

fracture wall surfaces). The hydraulic aperture is in fact an equivalent value which can be derived from field analysis like tracer tests and hydraulic tests [2] and laboratory fluid flow experiments (e.g., [3]).

Several authors have studied the effect of roughness of the walls on fracture permeability working with various materials, such as glass [4], rocks [5], and concrete [6]. These authors included a correction term, a so-called friction factor (f), on the permeability of rough fractures:

$$k = \frac{e^2}{12f}, \quad (2)$$

where the friction factor is defined by the common base equation

$$f = \left[1 + c_1 \left(\frac{r_a}{2e} \right)^{c_2} \right], \quad (3)$$

where r_a is the difference between the highest peak and the lowest valley of the physical roughness, and both terms c_1 and c_2 are constants with slightly different values depending on the author. Thus, the friction factor depends only on the relative hydraulic roughness ($r_a/2e$) ignoring the frequency (or wavelength) of the asperities.

Another widely used methodology derives the hydraulic aperture from the mechanical aperture, E , and the joint roughness coefficient (JRC) as proposed by Barton et al. [7]:

$$e = \frac{E^2}{\text{JRC}^{2.5}}, \quad (4)$$

where JRC is derived by comparing the fracture profile obtained with the Barton Comb with the standard tables provided by Barton and Choubey [8]. This methodology is perhaps the simplest and cheapest way to obtain fracture surface roughness values and has been widely used in outcrop studies [9–13]. The disadvantages of this method are related to the moderate resolution (about 1 mm) and the inaccuracy of equation (4) at relatively wide apertures (with respect to the JRC value). For instance, considering a fracture with 100 μm mechanical aperture and a JRC equal to 2, equation (4) gives a hydraulic aperture equal to 1767 μm .

Considering the previous arguments, the main objective of this work is to find empirical equations that describe the effect of fracture roughness on permeability at different apertures. In order to reach this goal, some problems which should be overcome are (i) to develop a protocol for mapping the fracture surface, (ii) to evaluate the fracture roughness as a function of the wavelength of the asperities, and (iii) to validate the relationships using a significant number of samples, roughness values, and aperture scenarios.

Various approaches have been reported in the literature for mapping the surface of fractures and faults in the field or laboratory involving the use of Lidar [14, 15], laboratory profilometers [16–18], and SfM photogrammetry (e.g., [12, 19]). Corradetti et al. [19] applied SfM photogrammetry for mapping fracture surfaces obtaining 3D reconstructions with point-cloud densities of equal quality to

Lidar-derived data. Among these methods, SfM photogrammetry shows great promise as it is inexpensive (photo-camera and processing software) and extremely flexible regarding the scales and conditions (applicable in the field and laboratory). For example, SfM photogrammetry has been successfully used as an analytical tool to gather geologic data from outcrop studies [20–23], as well as at smaller scales on fault surfaces [19] and fossilized human footprints [24].

Evaluation of fracture roughness is achieved by implementing the power spectral density (PSD), which provides a more objective description based on the frequency distribution of the asperities in the Fourier domain. This approach has been successfully applied by previous authors for describing the roughness of fractures (e.g., [25]) and fault surfaces [14, 15, 18, 19]. To increase the statistical significance of the results, approximately 2000 fractures were modeled using the software SYNFRAC [25–27] creating computer-generated synthetic fractures, using input parameters of the fractal dimension, fracture roughness (an output of the PSD analysis of real fractures), and the standard deviation of the asperities height.

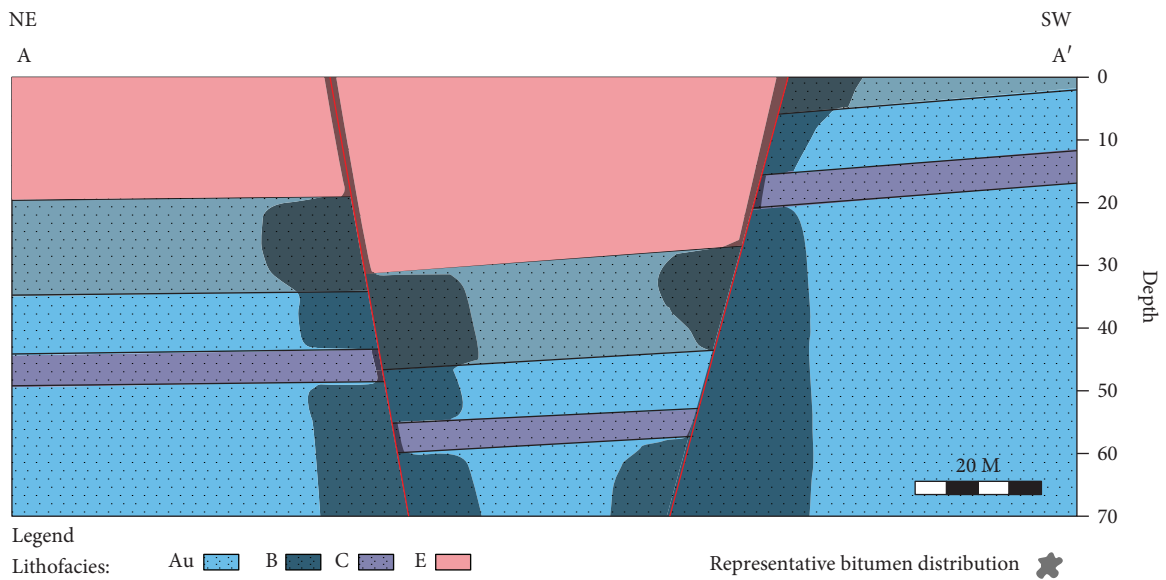
A key benefit of incorporating computer-generated synthetic fractures is the capability to work with a large amount of fracture data to perform direct fluid flow simulations, such as (i) the finite difference method (e.g., [28]), (ii) the finite element method (e.g., [29, 30]), (iii) the finite volume method (e.g., [31]), and the lattice-Boltzmann method (e.g., [32]). The lattice-Boltzmann method (LBM) describes the flow of many particles interacting with a medium and among themselves following the Navier-Stokes equation at the macroscopic scale (e.g., [33]). The LBM has been implemented to compute permeability using 3D images of rocks and soft sediments obtained by micro-CT imaging techniques [34–38] and from reconstructed models [39–41] generating results consistent with laboratory measurements [40, 42]. The simplest LBM is based on the Bhatnagar-Gross-Krook (BGK) collision operator, which consists of a single relaxation time approximation [43]. Despite its widespread use, the BGK-LBM brings some issues, for example, the computed permeability values may be viscosity-dependent [44]. An alternative approach involves the use of multiple relaxation times (MRT) methods, which solve the drawbacks of the BGK method and are characterized by more stability [45–47].

In this study, the permeability values of single isolated fractures (synthetic and natural) were calculated via LBM, using the PALABOS open source library [48]. The method and the code have been previously implemented by Zambrano et al. [38] for quantifying the permeability in deformed porous carbonates using X-ray microtomography synchrotron-based images [49]. Following these authors, rather than the BGK method (e.g., [34]), the MRT approach has been adopted in the present study to assure that permeability values are viscosity-independent.

The selected study area, the Roman Valley Quarry (Figure 1(a)), is an inactive quarry located at the northern termination of the Majella Mountain (Abruzzo region, Italy). The Majella Mountain is the orogenic expression of a thrust-



(a)



(b)

FIGURE 1: (a) Structural map of the Roman Valley Quarry (modified after Volatili et al. [13]). Notes: red lines = faults, white dashed lines = lithofacies boundaries (see Table 1 for details). (b) Stratigraphic and structural scheme of the study area; oil distribution is arbitrarily representative considering field observations (see Volatili et al. [13] for more details).

related anticline, with internal deformation characterized by high-angle normal, strike-slip and oblique-slip normal faults, small folds, multiple sets of opening-mode fractures, pressure solution seams, and deformation bands [50–57].

The Roman Valley quarry has been heavily studied by previous authors focusing on the structural, sedimentological, and diagenetic properties [54, 56], and the fluid flow behavior of the fractured carbonates at the macroscale [13].

Here, the bitumen distribution suggests that the main hydrocarbon flow occurred through the damage zones of the principle NW-SE-oriented oblique slip faults [54] (Figure 1(b)). The distribution of major lithofacies at the Roman Valley Quarry is another element influencing the presence of bitumen which has been previously described by Rustichelli et al. [56] (see Table 1). Concerning the fractures, the most pervasive ones are represented by both

TABLE 1: Characteristics of lithofacies exposed in the Roman Valley Quarry.

Lithofacies		Thickness	Φ_m (%)	k_m (mD)	Bitumen distribution
Au:	Alternation of medium- to coarse-grained bioclastic grainstones (Au1) and medium-grained bioclastic grainstones (Au2).	40 to 60 m	~27.5	83.13 (V) 160.09 (H)	Abundant in both matrix and fractures near faults
B:	Medium-grained grainstones.	10-to 15-m	~26.4	444.82 (V) 530.94 (H)	Abundant in both matrix and fractures near to faults
C:	Alternations of two echinoid plates and spines rich facies: fine-grained bioclastic grainstones (C1) and fine- to very fine-grained bioclastic packstones (C2). Argillaceous to marly beds (<3 cm thick) are common.	10 to 15 m	~10.9	~0.30 (V) ~2.51 (H)	Absent in matrix and oil stain in fractures
E:	Alternation of two planktonic foraminifera facies: marly wackestones (E1) and marly mudstones (E2).	60-65-m	~28.8	~0.085 (V) ~0.081 (H)	Absent in both matrix and fractures

Notes: lithofacies description from Rustichelli et al. [56], matrix porosity (Φ_m) obtained with helium pycnometer and gas permeability (k_m) measurements (performed in both horizontal, H, and vertical, V, direction) were reported by Volatili et al. [13]. Bitumen distribution from field observations [13, 54, 56].

pressure solution seams (often sheared with sliding/tearing mode displacement) and joints (opening mode fractures).

Considering the significance of these fractures, this work focused on investigating both cases of open mode and sheared fractures with a small sliding/tearing mode displacement, in the order of millimeters, allowing the assumption of a negligible wall wearing. For this last case, the mismatch between opposite walls was also computed due to its importance as a mechanism for maintaining fracture openings even at reservoir depths.

2. Methodology

In this work, we present a multiphase integrated methodology for characterizing fracture surfaces and their effect on permeability. This approach combines fracture surface scanning using structure from motion photogrammetry, a statistical and spectral description of individual natural fracture surfaces, modeling of synthetic fractures, and computational calculation of permeability by fluid flow simulation.

2.1. Sample Collection. During the summer of 2018, a suite of oriented hand samples was collected from the study site comprising three (i.e., Au, B, and C) of the four major lithofacies of the Bolognano Formation present in the quarry (Figure 2, Table 1). The field sampling procedure involved manually removing blocks containing fracture surfaces that showed minimal signs of physical and chemical weathering. Sampling targeted these specific lithofacies based on accessibility, quality of well-developed fracture surfaces, and the fact that they have been well documented in previous studies focused on fracture distribution and mechanical properties [13, 54, 56]. After removal from the outcrop but prior to analysis, the rock samples were cleaned using a soft-bristled brush to remove debris and other obstructions but without abrading the surface.

2.2. Mapping Surface Topography. The workflow for mapping surface topography involves the following key stages: (1) fracture surface image set acquisition and (2) image alignment and three-dimensional digital rock model creation using SfM.

2.2.1. Image Set Acquisition. SfM photo scanning was performed at the University of Camerino photogrammetry laboratory (Figure 3(a)). We used a tripod-mounted Canon EOS 100D with the standard kit lens fixed at 55 mm. Images of samples were recorded inside a photo-lightbox to maintain full control of camera positions and ambient lighting and to reduce shadows and glare ensuring high image quality. To achieve the desired >70% inter-photo overlap, fracture samples were placed on a 360-degree rotating stage and manually rotated at 10-degree angular increments between photos. After completing a full orbit of the object, the camera was reset at a new vertical position, and the next orbit was conducted adhering to the same 10-degree increments but offset one position from the initial starting point. This procedure was repeated along three horizontal rotations from different vertical positions followed by 2-3 photos directly above the object oriented normal to the fracture surface.

2.2.2. Image Alignment and Three-Dimensional Model Creation. Fracture surface models were aligned and processed using Agisoft PhotoScan Pro (<http://www.agisoft.com>). For each fracture surface, approximately 63 photos were used as input images to create the digital point cloud model. We follow the procedure described by Carrivick et al. [58] and Zimmer et al. [24] for camera settings and photo procedure, and Pitts et al. [22] for image alignment and point cloud generation.

Agisoft-generated coded targets were placed inside the scene to aid in the imagery processing; these coded targets are automatically recognized by the software and help build connection points between the image sets (Figure 3(b)). Additionally, a 5-centimeter scale was placed on the sample surface to calibrate the spatial reference.

As a measure to define the error of the model, we follow the methodology established by Corradetti et al. [19]. This calls for modeling a piece of graph paper under the same condition as fracture imaging (same light, relative distance, and number of photos). Under the assumption that the graph paper is perfectly planar, the standard deviation of the height of the scanned asperities is considered as the error of the model [19]. In our case, this value is approximately 20 μm , whereas the point density (points/area) is 34 points/mm.



(a)



(b)



(d)



(c)

FIGURE 2: Sample location sites. (a) Sampling locations inside the Roman Valley Quarry. (b) Sample site 1 from lithofacies (b) with scale card showing centimeter increments. (c) Sample site 2 from lithofacies Au. (d) Sample site 3 from lithofacies (c). Rock hammer for scale, 22 cm in length.

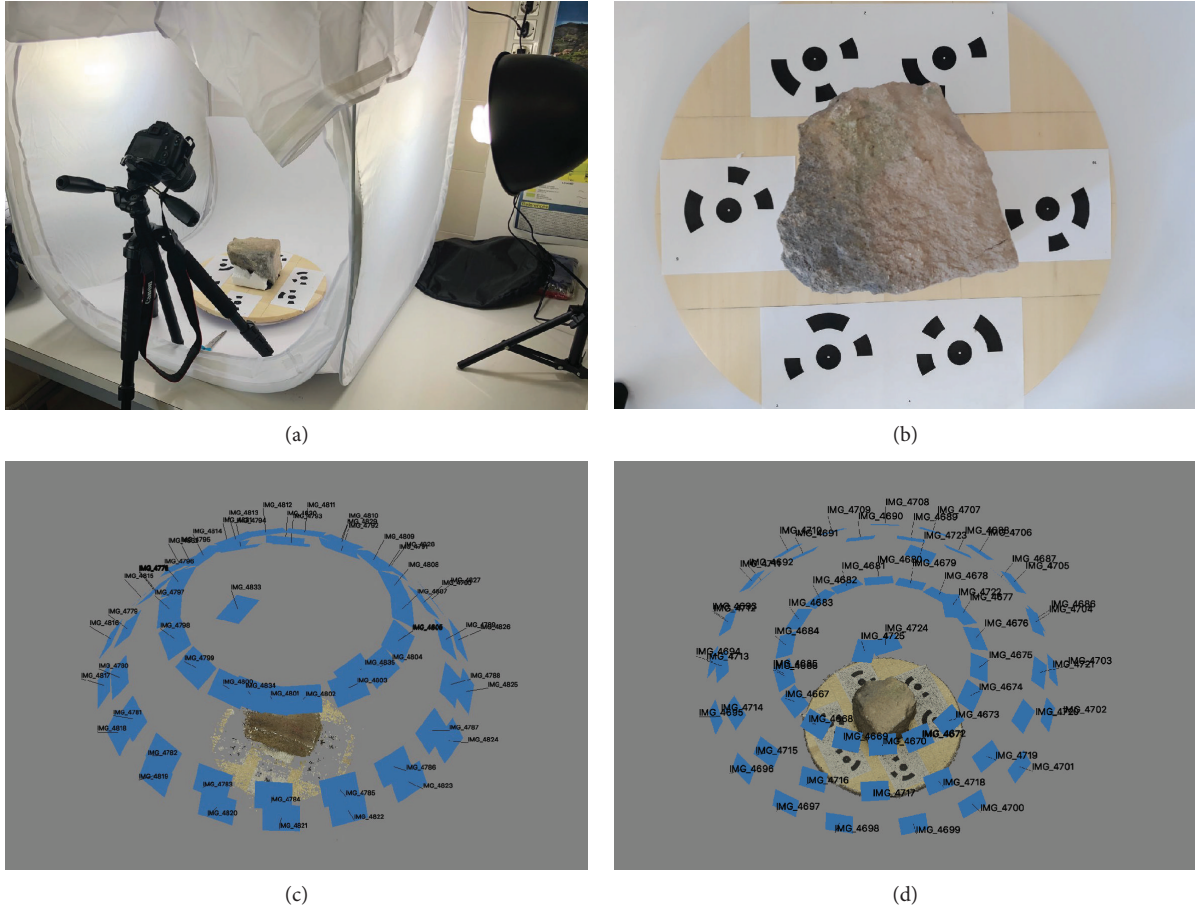


FIGURE 3: Photogrammetry setup and three-dimensional SfM procedure. (a) Photo light box used in the photogrammetry lab. (b) The collected sample placed on the rotating stage with unique photo-targets generated by Agisoft PhotoScan. (c) Sparse point cloud generated during the photo alignment phase of the SfM procedure. (d) Fully rendered photo-realistic 3D model showing camera positions.

2.3. Fracture Surface Processing and Analysis

2.3.1. Extraction and Processing of 3D Fracture Surface Model.

Trimmed 3D point clouds were exported from Agisoft as “.xyz” text files. Then, a rectangular subregion of each fracture surface of interest was extracted from the point cloud and processed to remove undesirable trend and eventual noise (Figure 4). This technique, previously documented by Corradetti et al. [19], consists of (i) removing the artificial trend of the surface, (ii) surface interpolation, and (ii) sampling in a regular grid.

2.3.2. Fracture Roughness Assessment. A complete description of the fracture roughness is given by the specification of two functions: the probability density function (depending on the media and standard deviation) for heights and the PSD [59] (Figure 5).

The Fourier power spectrum, $P(k)$, is defined as the square of the modulus of the Fourier transform [60]. Considering a cross section of the rock, this profile can be represented as a summation of sinusoidal components, each with its own amplitude, wavelength, and phase. The squared amplitude of each sinusoid component is referred to as its “power” (Figure 5(b)). The power spectrum regulated in an

appropriate manner is referred to as the PSD, $G(k)$, and it provides a valuable definition of surface roughness. The PSD as a function of k in a bi-logarithmic scale graph of a self-affine function exhibits an apparent linear slope, which is defined from the following power law equation:

$$G(k) \propto k^{-\alpha}, \quad (5)$$

where the exponent of the power law α is related with the fractal dimension, D [59], as follows:

$$D = \frac{(7 - \alpha)}{2}. \quad (6)$$

From a physical aspect, the fractal dimension shows the proportion of high-frequency to low-frequency sinusoid components (roughness). High D values are related to greater surface roughness. By stacking and normalizing the power spectra, it is possible to reduce the noise associated with a single profile and create a single spectrum which represents the entire rough surface in each direction (e.g., [15, 19]). The MATLAB script used to perform the procedures described above is partially modified from Corradetti et al. [19].

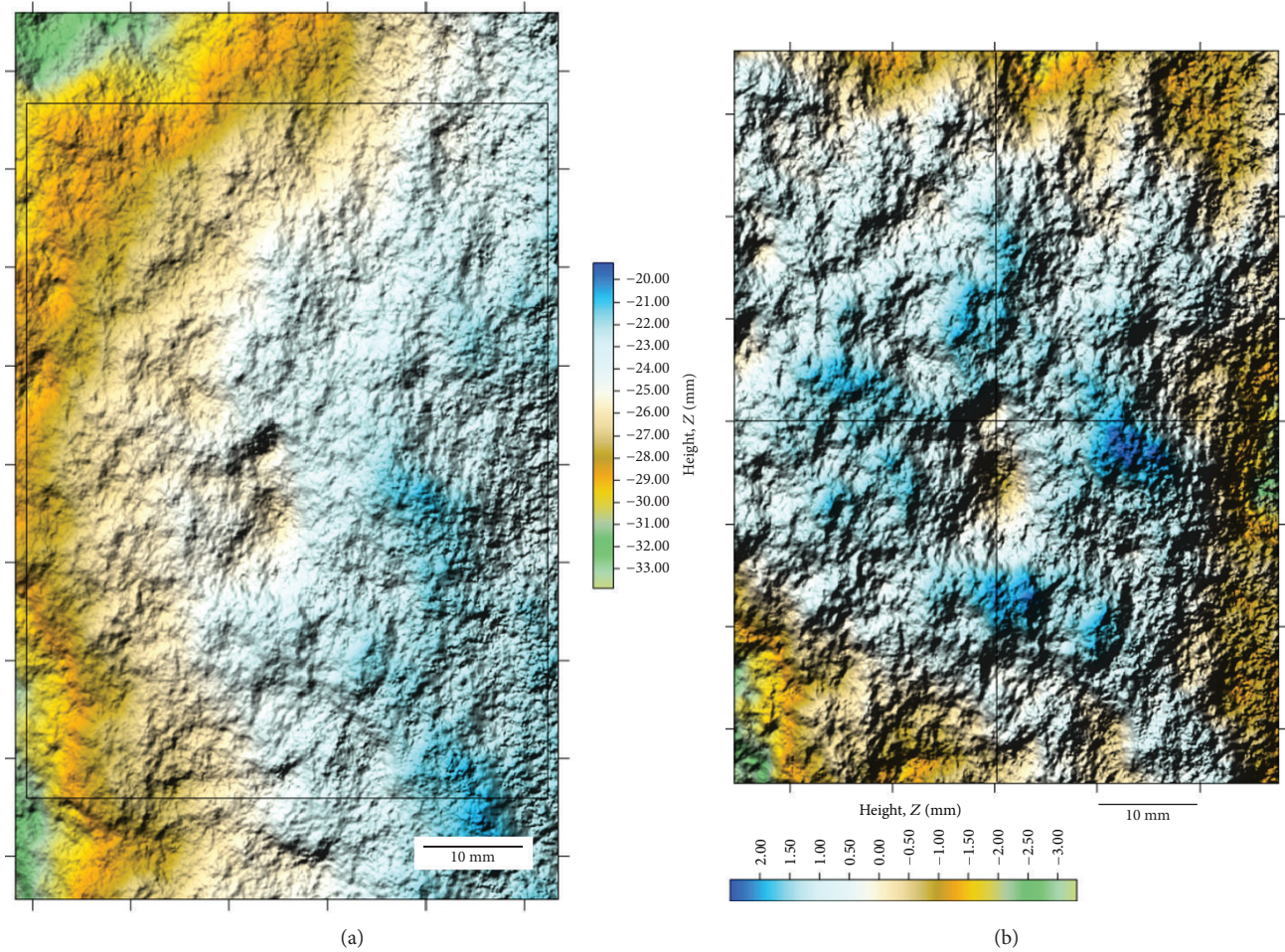


FIGURE 4: Fracture surface processing. (a) Original exported fracture surface containing an artificial trend. (b) Resulting image after removing the artificial trend and assigning a new reference grid according to a millimeter scale.

2.4. Single Fracture Modeling. Since a limited number of natural fracture surfaces were available, additional synthetic fracture surfaces were used to strengthen the statistical significance of the results. Following the procedure described by Ogilvie et al. [25], more than 2000 computer-generated synthetic fractures were created using the software SYNFRAC [25–27]. SYNFRAC is based on a mathematical model of a rough surface reported by Brown [59]. The software can model open fractures by introducing mismatch values with the spatial and spectral roughness parameters. For the scope of the present study, the mismatch values were not considered for surface modeling, but were measured after the fracture modeling (see Section 2.5.1).

The individual fracture surfaces (natural and synthetic) were used to model dilation associated with (Figure 6): (i) opening mode displacement (joint and/or opened pressure solution seam), various ranges of aperture, and (ii) sliding/tearing mode displacement (sheared joint and/or sheared pressure solution seam). In both cases, it is assumed that both walls are identical. In the second case, because the shear process is minimum, and the displacement is in the order of mm, it is assumed that no physical wearing of the fracture surfaces has occurred. To illustrate different

scenarios, a wide range of displacements (opening and sliding/tearing mode) were considered (the PYTHON code for fracture modeling is available at <https://github.com/superrostom/synthetic-fracture>).

2.5. Lattice-Boltzmann Method and Permeability Computation. Lattice-Boltzmann simulations were performed using the open-source computational fluid dynamics software PALABOS [48] following the methodology described by Zambrano et al. [38].

This procedure consists of imposing a single-phase fluid flow through a 3D porous media maintaining a fixed pressure gradient between the inlet and outlet opposing faces of the model; the rest of the faces were padded (Figure 7). A bounce-back boundary condition was assigned to the fracture surfaces. An MRT collisional operator [45, 46], with a D3Q19 lattice, is used instead of the popular BGK [43] as in Degruyter et al. [34]. Moreover, the geometry of the media is obtained by the SfM photogrammetry outputs and modeling differently than Degruyter et al. [34] and Zambrano et al. [38] who used X-ray micro CT images.

The simulation ended once the imposed steady-state condition was reached (standard deviation of the average

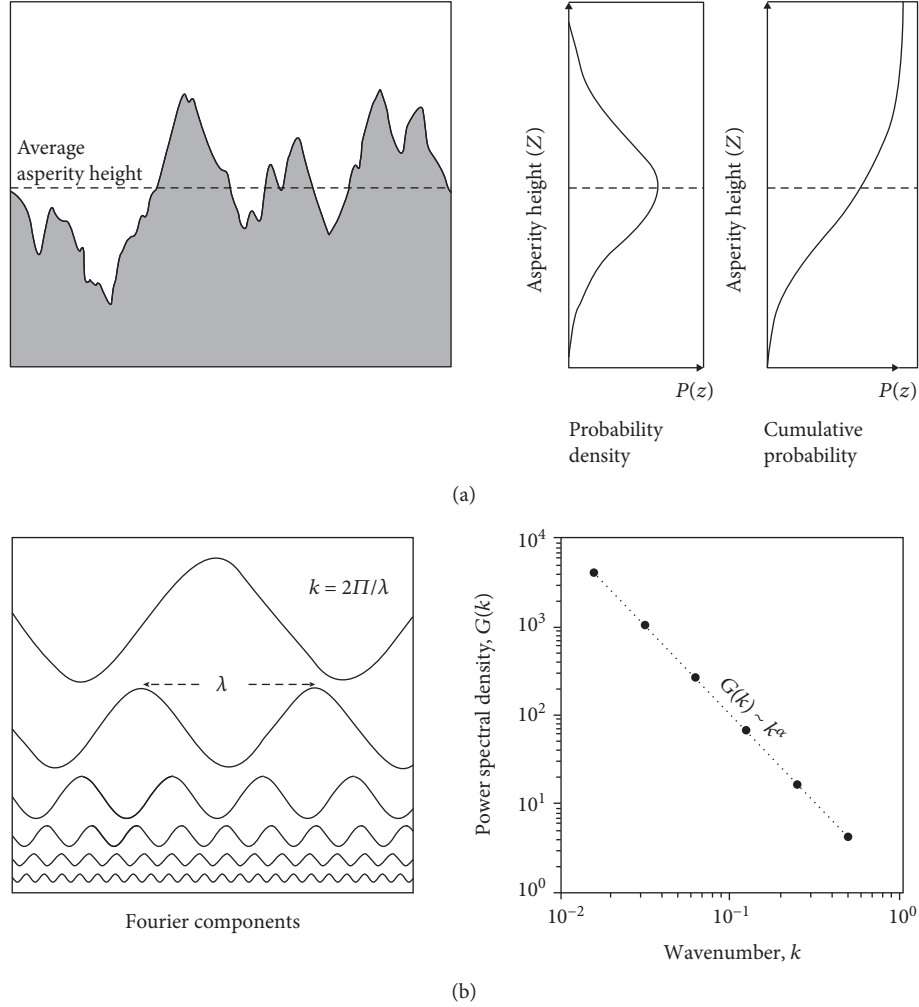


FIGURE 5: Illustration of a complete description of surface roughness: (a) in terms of statistical height distribution, probability density and (b) in terms of frequencies distribution, Fourier power spectrum (modified from Brown [59]).

energy $< 10^{-4}$ after 1000 steps). Then, the permeability component parallel to the imposed flow was calculated applying Darcy's law,

$$\frac{\delta P}{\delta x} = \frac{\mu}{k} U, \quad (7)$$

where $\delta P/\delta x$ is the pressure gradient, μ is the fluid kinematic viscosity, and U is the average fluid velocity per unit of area. The permeability was calculated, using the same procedure, in two orthogonal directions: along strike and along dip (k_x and k_y , respectively). In the case of sliding/tearing mode displacement, the x -direction corresponds to the slip direction. All the variables are handled in lattice units prior to permeability calculation. For convenience, permeability values were converted to millidarcy which is the most commonly used permeability unit in the oil industry. All the provided values of permeability correspond to a volume of $1.25 \times 10^{-4} \text{ m}^3$ ($50 \times 50 \times 50 \text{ mm}^3$).

2.5.1. Mismatch Evaluation. The mismatch between the opposite fracture walls is of extreme importance since this

factor may keep fractures open even at reservoir depths. Since the mismatch was not imposed during fracture modeling, it was measured after the generation of the synthetic fractures. The mismatch was evaluated only for the sliding/tearing mode fractures, whereas it was unnecessary in the case of opening mode fractures since the aperture is constant. For the evaluation of the mismatch value, the methodology of the power spectral density ratio (PSDr), introduced by Ogilvie et al. [25], was followed. The methodology consists of obtaining a relationship between the PSD of the aperture and both surfaces of the fracture, as follows:

$$\text{PSDr} = \frac{\text{PSD}_{\text{aperture}}}{(\text{PSD}_{\text{upper_wall}} + \text{PSD}_{\text{lower_wall}})}. \quad (8)$$

The results of this calculation can be represented in a graph where the parameters associated with the mismatch and the degree of mismatch between the surfaces at different wavelengths can be obtained (Figure 8).

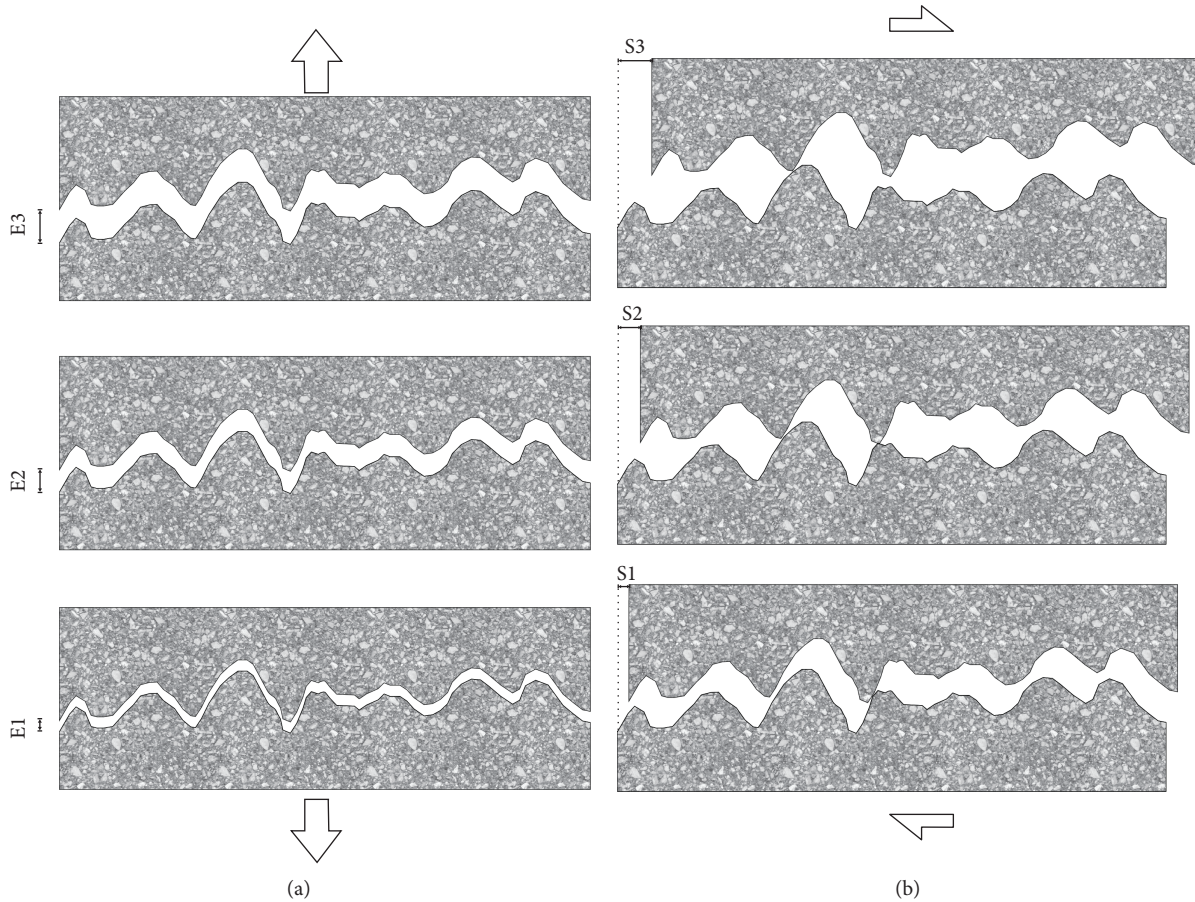


FIGURE 6: Mechanisms considered for possible fracture aperture generation in the study area. (a) Opening mode displacement, E, (joint and/or opened pressure solution seam) and (b) sliding/tearing mode displacement, S, (sheared joint and/or sheared pressure solution seam).

Following the definition of Ogilvie et al. [25], these parameters are the following:

- (i) Minimum mismatch length (ML_{min}): wavelength at which the fractures start to match, indicated by the wavelength where the PSD ratio values fall below its maximum value ($PSDr_{max}$)
- (ii) Maximum mismatch length (ML_{max}): wavelength at which the fracture opposing surfaces reach the maximum matching, thus the minimum value of PSD ratio ($PSDr_{min}$)

The calculation of these parameters was made using a MATLAB code. In this case, (ML_{min}) is considered as the only reliable indicator of the mismatch since (ML_{max}) often falls outside the scale of the study (Figure 8).

3. Results

The results of this work consist of an analysis of surface topography performed on fracture samples from three lithofacies (Au, B, and C), and the computed permeability in function of the fracture properties, including fractal dimension, opening and sliding/tearing displacement, and minimum mismatch length.

3.1. Fracture Surface Properties. In Table 2, the values correspond to the fractal dimension (D), the average height of asperities, and their standard deviation. The traditional roughness measurement, JRC, was added to compare both techniques and the results with previous works in the same outcrop. For the fracture description, we followed Agosta et al. [54]. The set PS2a corresponds to pressure solution seams (generated during background deformation) often sheared, with normal or left lateral kinematics, often impregnated by tar. The set PS2b corresponds to pressure solution seams (generated during background deformation) which are generally un-sheared.

3.2. Permeability Results. The results of the work are presented in Figures 9–14. In each graph, the different surface roughness values (expressed in fractal dimension) are illustrated. When pertinent, error bars are added to show the variability of the results.

In the case of opening mode displacement, the results indicate that the permeability increased proportionally to the mechanical aperture following a positive power-law relationship (Figure 9(a)). Similarly, the hydraulic aperture (derived from equation (1)) is related with the mechanical aperture by means of a positive power law with exponents varying from 1.6 to 1.8 for fractal dimension (D) values between 1.6 and 2.5, respectively (Figure 9(b)).

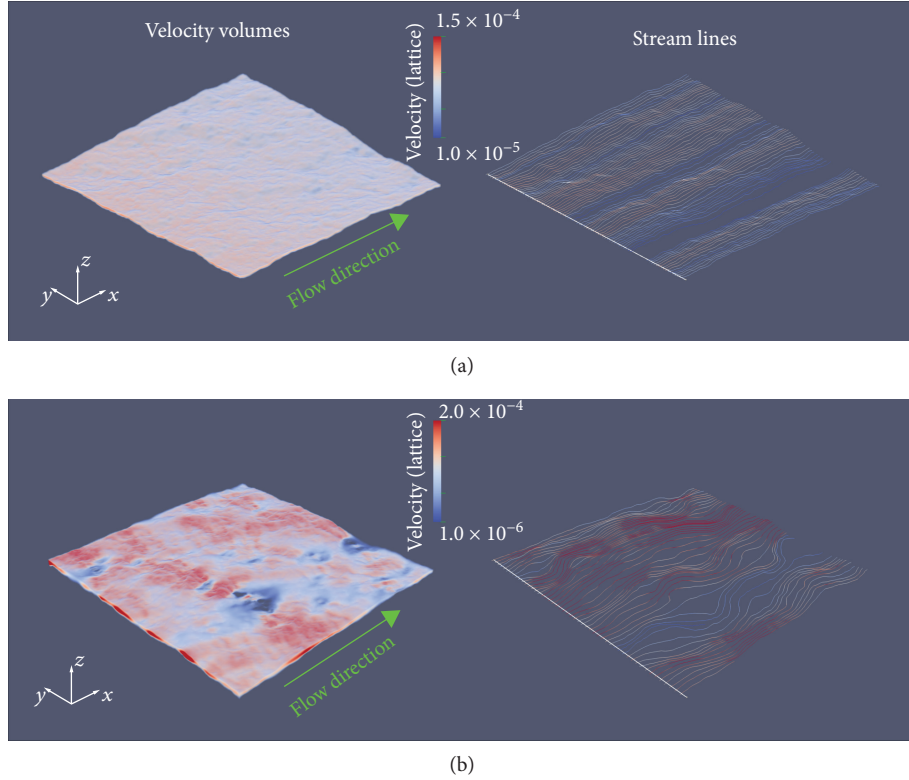


FIGURE 7: Examples of lattice velocity field volumes with the corresponding streamlines. (a) Fracture with opening mode displacement equals to 1 mm. (b) Fracture with sliding/tearing mode displacement equals to 50 mm. Both fractures have a considerable roughness ($D = 2.5$; Std. dev. = 4 mm). The size of the samples is about 50×50 mm. Images are rendered using PARAVIEW software [63].

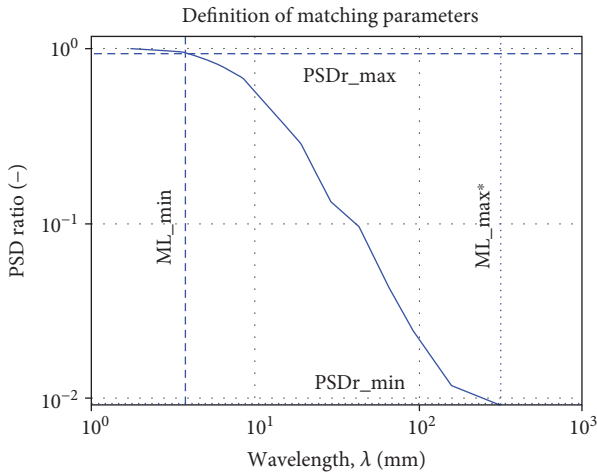


FIGURE 8: A typical PSD ratio graph used for defining the mismatching parameters. *The maximum mismatch length (ML_{max}) often falls at the limit or outside the studied wavelength range.

With respect to the case of sliding/tearing displacement, the results indicate that the permeability component parallel to the displacement (k_x) increases proportionally to the sliding/tearing displacement (S_x) following a positive power-law relationship (Figure 10(a)). The permeability component perpendicular to the displacement (k_y) is also related by a power law with the sliding/tearing displacement

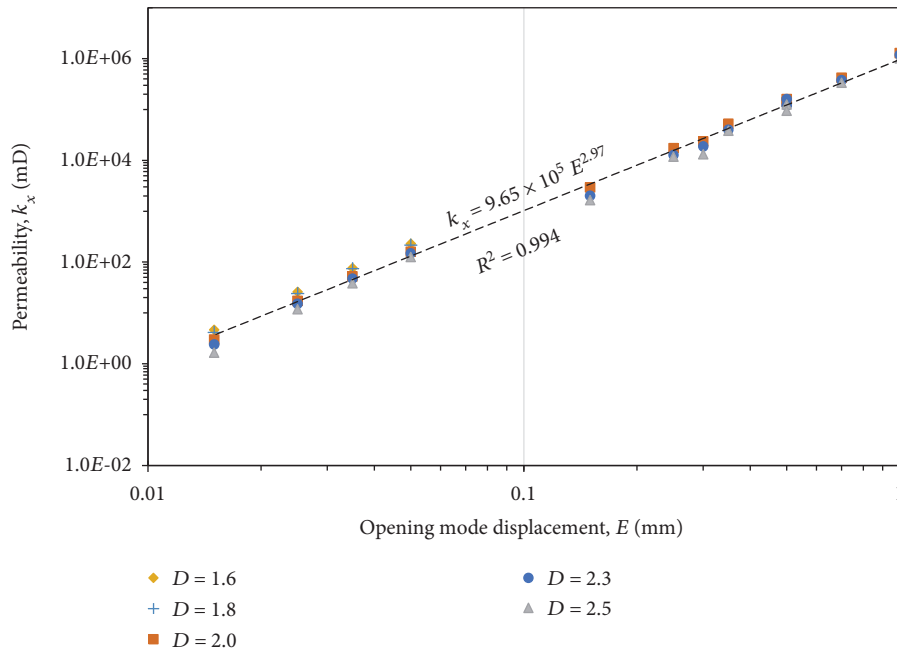
TABLE 2: Results of the surface analysis.

ID	Field description			Surface Analysis			
	Orientation	Set	Lithofacies	JRC	SD	D_x	D_y
F-1	200/72	PS2a	Au	10	1.22	1.89	1.91
F-2	285/85	PS2b	Au	12	2.85	1.85	1.93
F-3	195/80	PS2a	B	9	1.49	1.90	1.78
F-4	210/V	PS2a	C-2	8	1.97	1.90	1.67
F-5	200/80	PS2a	C-1	10	1.66	1.85	1.96
F-6	120/85	PS2b	C-1	11	0.82	1.96	1.95

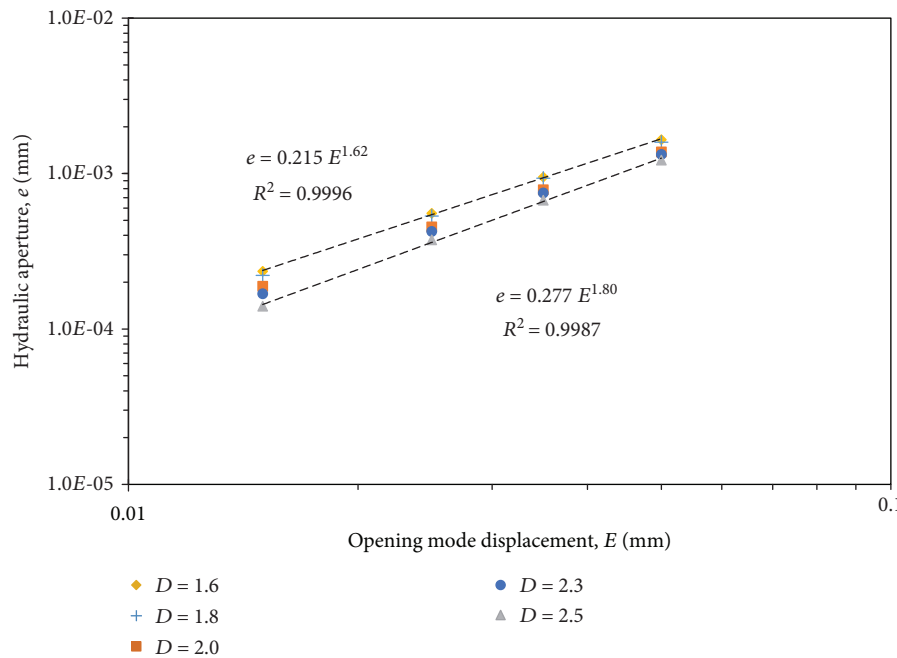
Notes: orientation noted as dip direction/dip angle. SD: standard deviation of asperity height. D_x and D_y are the fractal dimensions in the strike and dip directions, respectively.

(S_x). The anisotropy ratio, k_y/k_x , is generally higher for low values of fractal dimension (Figure 10(b)). The anisotropy ratio value tends to decrease as a function of the sliding/tearing displacement (S_x) following a negative power-law relationship. The highest value of anisotropy was near 2.6 for fractal dimension (D) equal to 2.0 and sliding/tearing displacement (S_x) equal to 0.5 mm.

The fracture roughness, expressed in terms of fractal dimension (D), showed a different influence in the permeability on single fractures depending on their kinematic: opening or sliding/tearing mode. For the opening mode displacement case, the permeability is inversely proportional to the fractal dimension (Figure 11(a)). This relationship



(a)



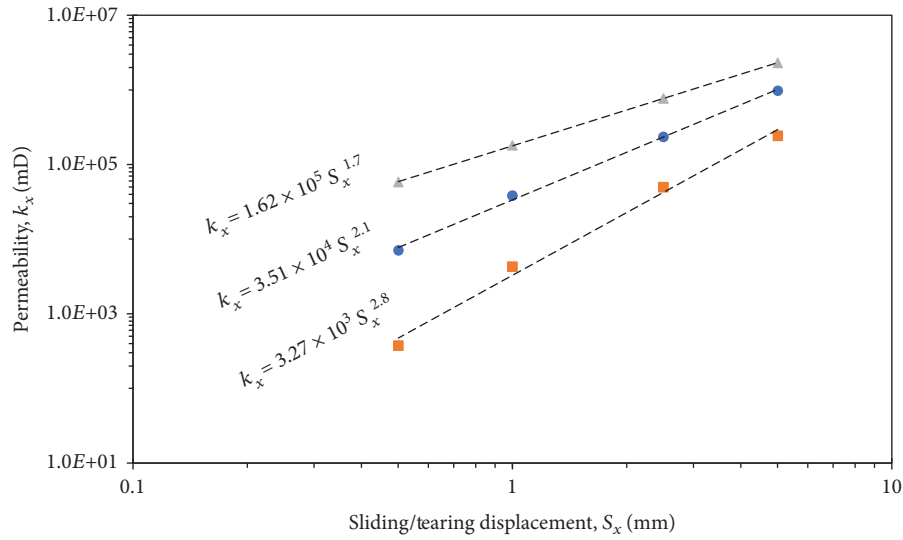
(b)

FIGURE 9: (a) Single-fracture permeability versus opening mode displacement; results indicate a positive power-law relationship (nearly cubic). (b) Hydraulic aperture (computed with the equation (1)) versus the opening mode displacement (mechanical aperture); the relationship follows a positive power law with exponent between 1.6 and 1.8. Axes are in logarithmic scale, and the dashed lines correspond to the best-fitting power laws.

follows a negative power law with the slope depending on the opening mode displacement values. A higher roughness (fractal dimension) implies a decrease in permeability. For the simulated scenarios, rough fractures ($D = 2.5$) showed permeability values between 45% and 65% lower than smooth fractures ($D = 1.6$). For fractures with the sliding/tearing displacement, the permeability is proportional to

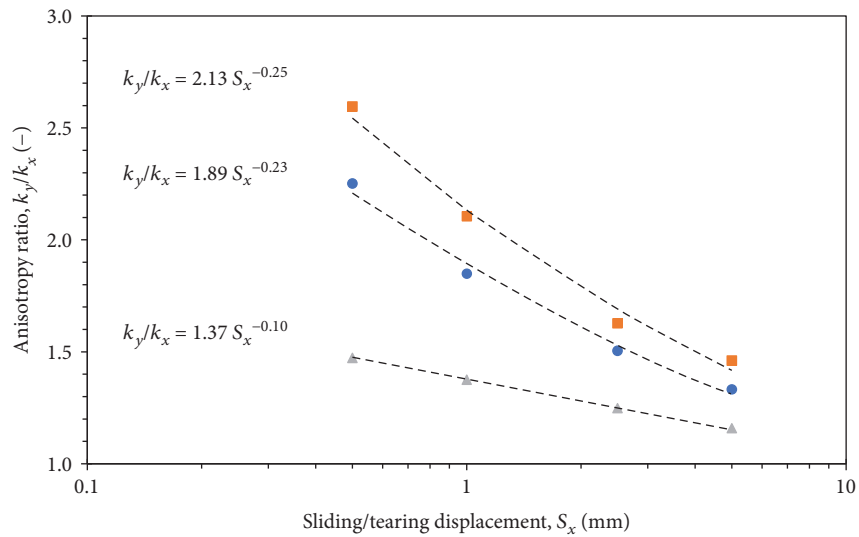
the fractal dimension following a positive power law (Figure 11(b)). In this case, an increment of the fractal dimension (roughness) from 2.0 to 2.5 represents an enhancement of the permeability of approximately one order of magnitude.

It is expected that this positive relationship between displacement and permeability should stabilize at a certain



- $D = 2.0$
- $D = 2.3$
- ▲ $D = 2.5$

(a)



- $D = 2.0$
- $D = 2.3$
- ▲ $D = 2.5$

(b)

FIGURE 10: Single fracture permeability versus sliding/tearing displacement. (a) Permeability along the shear direction. (b) Anisotropy permeability ratio, k_y/k_x , as a function of sliding/tearing displacement. Axes are in logarithmic scale, and the dashed lines correspond to the best-fitting power laws.

point, as the permeability and porosity cannot increase indefinitely. This behavior is observed when the porosity is evaluated at higher displacement values (Figure 11). In this case, thanks to the simplified calculation of porosity in comparison with permeability, a large volume of data was considered (more than 2000 fractures). The porosity is proportional to the sliding/tearing displacement following a nonlinear

relationship with variable slope. The most significant change of slope occurs near 10 mm and after approximately 30 mm of sliding/tearing displacement, where the porosity seems to stabilize at values between 3% and 4%. The fractures with higher fractal dimension (roughness) tend to have higher porosity, which agrees with the permeability results. As previously mentioned, these results do not consider the possible

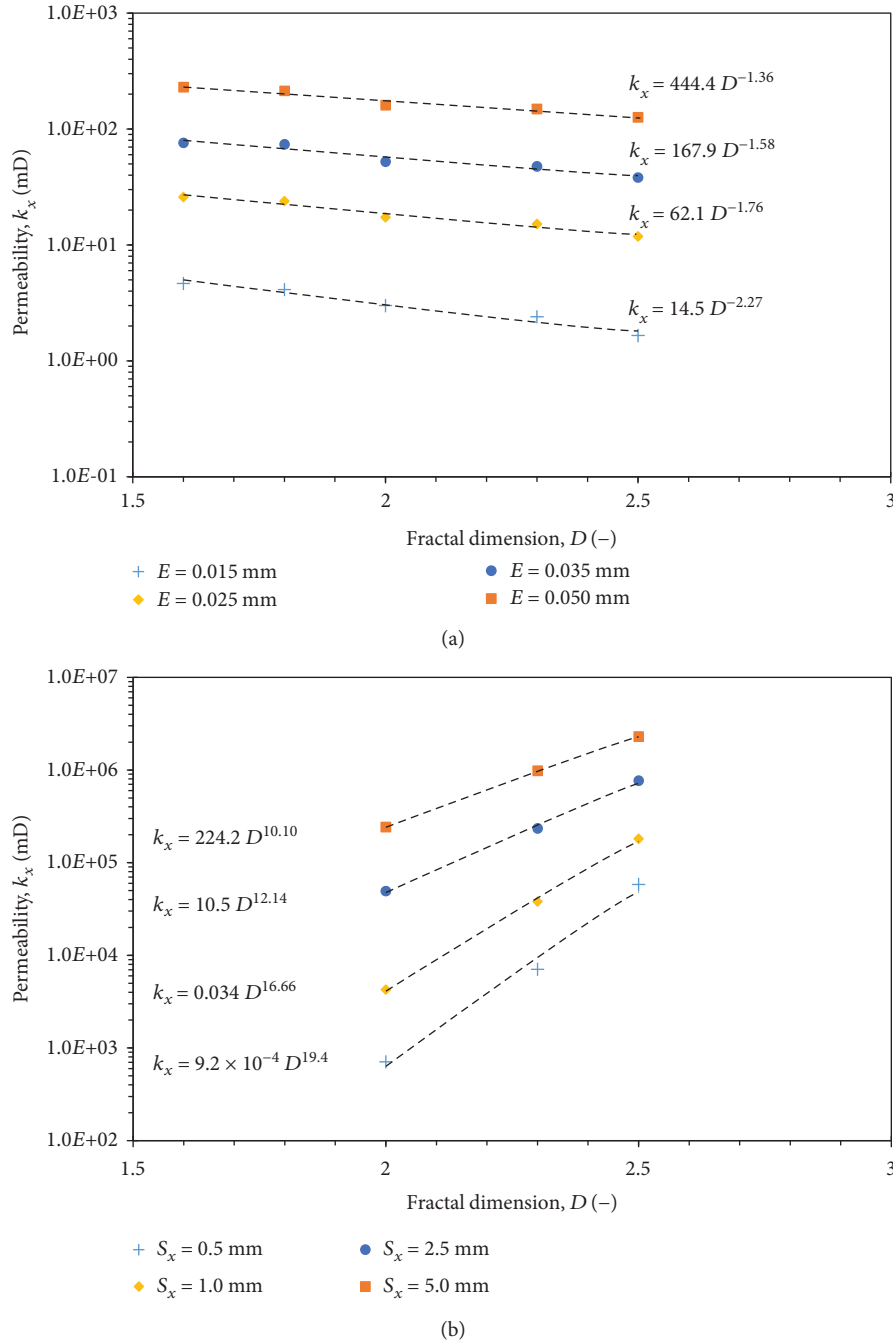


FIGURE 11: Permeability as a function of fractal dimension. (a) Permeability versus open mode displacement. Note the inversely proportional control of the fractal dimension on permeability. (b) Permeability versus sliding/tearing displacement. Note the proportional control of the fractal dimension on permeability. Axes are in logarithmic scale, and the dashed lines correspond to the best-fitting power laws.

physical wearing of the surfaces due to shearing particularly at high sliding/tearing displacement.

The fracture permeability is related to the porosity following a power law (Figure 13), which differs from the theoretical relationship based on the smooth parallel-plate equation; here, we also assumed smooth parallel plates for the porosity. The power-law relationship seems to be unaffected by the roughness (fractal dimension). Similar behaviors were obtained for both permeability components k_x and k_y .

The minimum mismatch length, ML_{min} , was evaluated as a function of the displacement (Figure 14(a)). Results indicate that within the evaluated range (a maximum displacement of 5 mm), the minimum mismatch is linearly proportional to the displacement. The permeability is proportional to the minimum mismatch length following a power-law relationship (depending on the fractal dimension). In other words, higher values of fractal dimension imply a higher permeability for similar mismatch values.

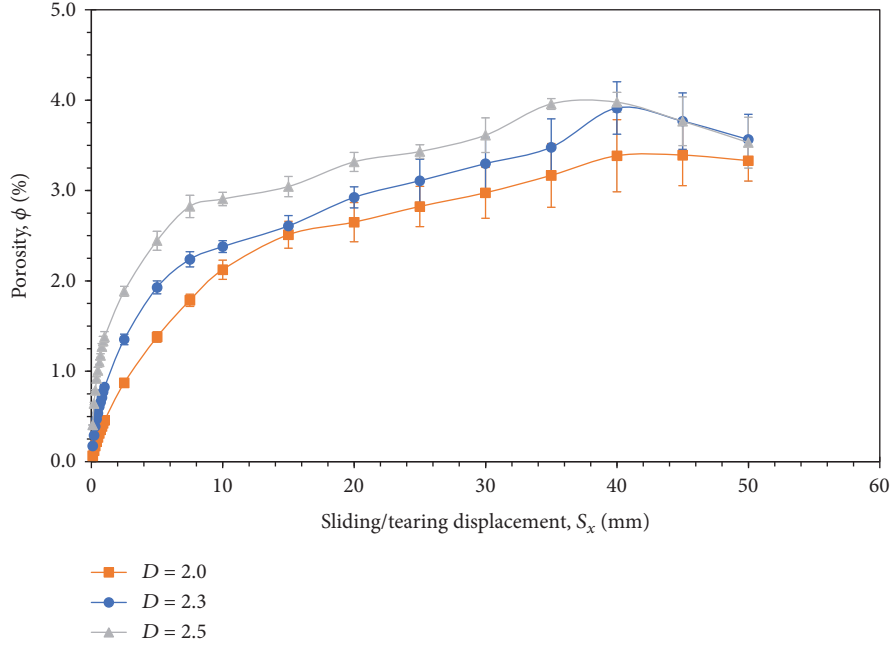


FIGURE 12: Porosity versus sliding/tearing displacement. Error bars indicate the standard error.

4. Discussion

The present work evaluates the effect of fracture surface features such as roughness, aperture, and mismatch on permeability using fracture surface scanning by SfM photogrammetry, numerical modeling, and lattice-Boltzmann fluid flow simulation.

4.1. SfM Photogrammetry Surface Scanning. The results of this study demonstrate the versatility of the SfM procedure as an analytical tool which can be applied at a wide range of scales including millimeter-scale features such as fracture surfaces. The controlled conditions in the photogrammetry laboratory allowed a highly detailed scan and extraction of the micro surface topography of samples sized $30 \times 30 \times 30$ cm producing a point cloud with a density of 34 points/mm and an estimated error of $20 \mu\text{m}$. This method produces more realistic and applicable results than the traditional Barton Comb, with results comparable to those reported by Candela et al. [14], Renard et al. [18], and Corradetti et al. [19] using both Lidar or laser profilometers. However, the SfM methodology is several orders of magnitude more cost-effective and is readily accessible. A future implementation of this study could include developing a workflow suitable for in situ field studies. However, more variables need to be controlled and results yielding lower accuracy are expected.

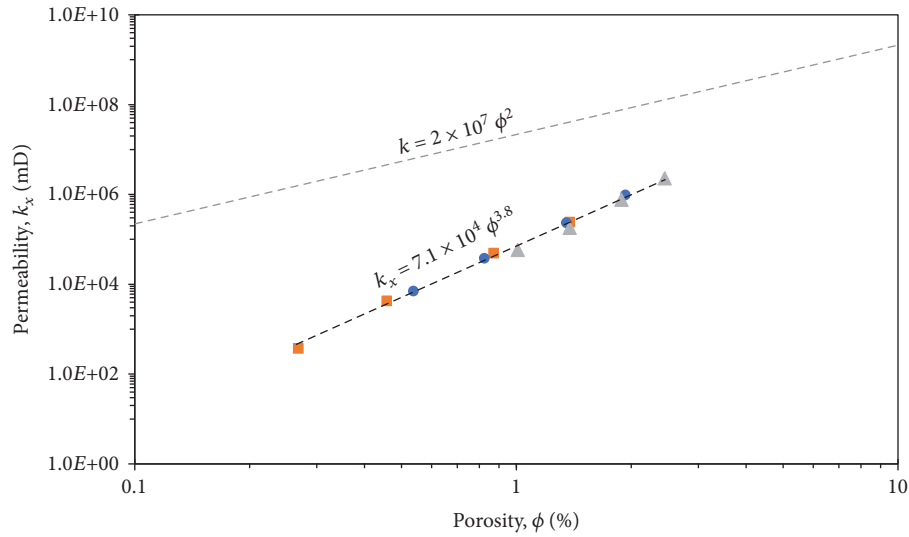
4.2. Fracture Roughness Characterization. This methodology proved to be highly efficient in expressing the fracture roughness allowing a more accurate and representative measure with respect to the relative hydraulic roughness [4–6] or the JRC [7, 8]. However, more data is necessary for evaluating control of the lithofacies in the fracture roughness, as it is

observed for other properties such as distribution and spacing (e.g., [61]).

Another important aspect of these results is the reproducibility of synthetic fractures with similar characteristics. This step was important to increase the data volumes leading to a greater statistical significance of the results and validity of the inferred relationships. The lattice-Boltzmann procedure also played a key role in this study as it allows the estimation of permeability values for controlled scenarios with different imposed properties (i.e., roughness, opening mode, and sliding/tearing displacement). This permits evaluation of the relationship between permeability, porosity, mismatch, and other imposed properties. The computed permeability may present some inaccuracy in low-resolution models as previously reported by Zambrano et al. [38]. Therefore, permeability results may be considered not as the real values but only as approximations.

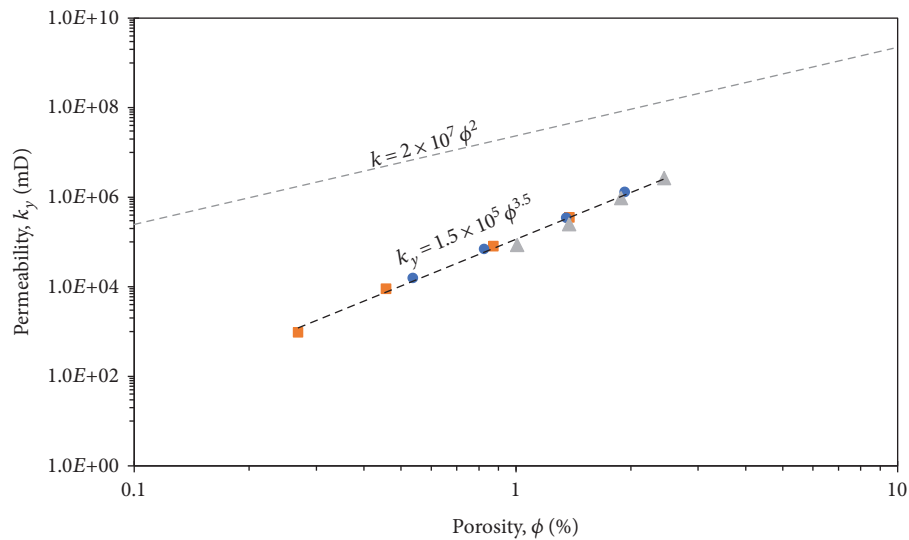
4.3. Permeability in Function of Fracture Properties. Two situations were considered to explain the presence of open fractures: (i) dilation due to opening mode displacement (joint or opened pressure solution seam) and (ii) dilation due to mismatch caused by shearing and sliding/tearing displacement.

In the first case, the results followed the expectation and confirmed previous interpretations: (i) permeability tends to increase with opening following a nonlinear relationship, (ii) a higher fractal dimension (greater roughness) correlates to lower permeability, and (iii) the effect of roughness is less significant at greater opening values. It is expected that higher roughness (higher frequencies of asperities) may expose a wider area in contact with the migrating fluid, diminishing its velocity due to friction. Evidently, at higher opening values, this effect should be less evident because it



- $D = 2.0$
- $D = 2.3$
- ▲ $D = 2.5$

(a)



- $D = 2.0$
- $D = 2.3$
- ▲ $D = 2.5$

(b)

FIGURE 13: Permeability components—(a) parallel to shear, k_x , and (b) perpendicular to shear, k_y —versus porosity of a single fracture after sliding/tearing displacement. Dashed line represents the relationship permeability-porosity for ideal smooth fractures, whereas the dotted line (best-fitting power law) indicates the same relationship when roughness is included.

is the specific area (area/volume) which has a control on the permeability, as has been previously reported by Zambrano et al. [38] for porous media.

The second case (sliding/tearing displacement) creates an aperture due to the mismatch between the opposite walls of the fracture. We found significant differences between these two cases concerning the effect of the roughness of the permeability. In fact, the effect of roughness on permeability is inverse. Given the same displacement, fractures with

higher roughness values permit the creation of larger voids and therefore enhance the fluid flow. So, the effect of friction exerted by the roughness on fluid flow has a secondary role in the case of mismatch due to sliding/tearing displacement. The continuous dilatancy of the fracture due to sliding/tearing displacement should cease at a certain value depending on the asperity frequencies present in the fracture. Nevertheless, it is difficult to verify this behavior for real fractures, where a 20 mm sliding/tearing displacement likely leads to

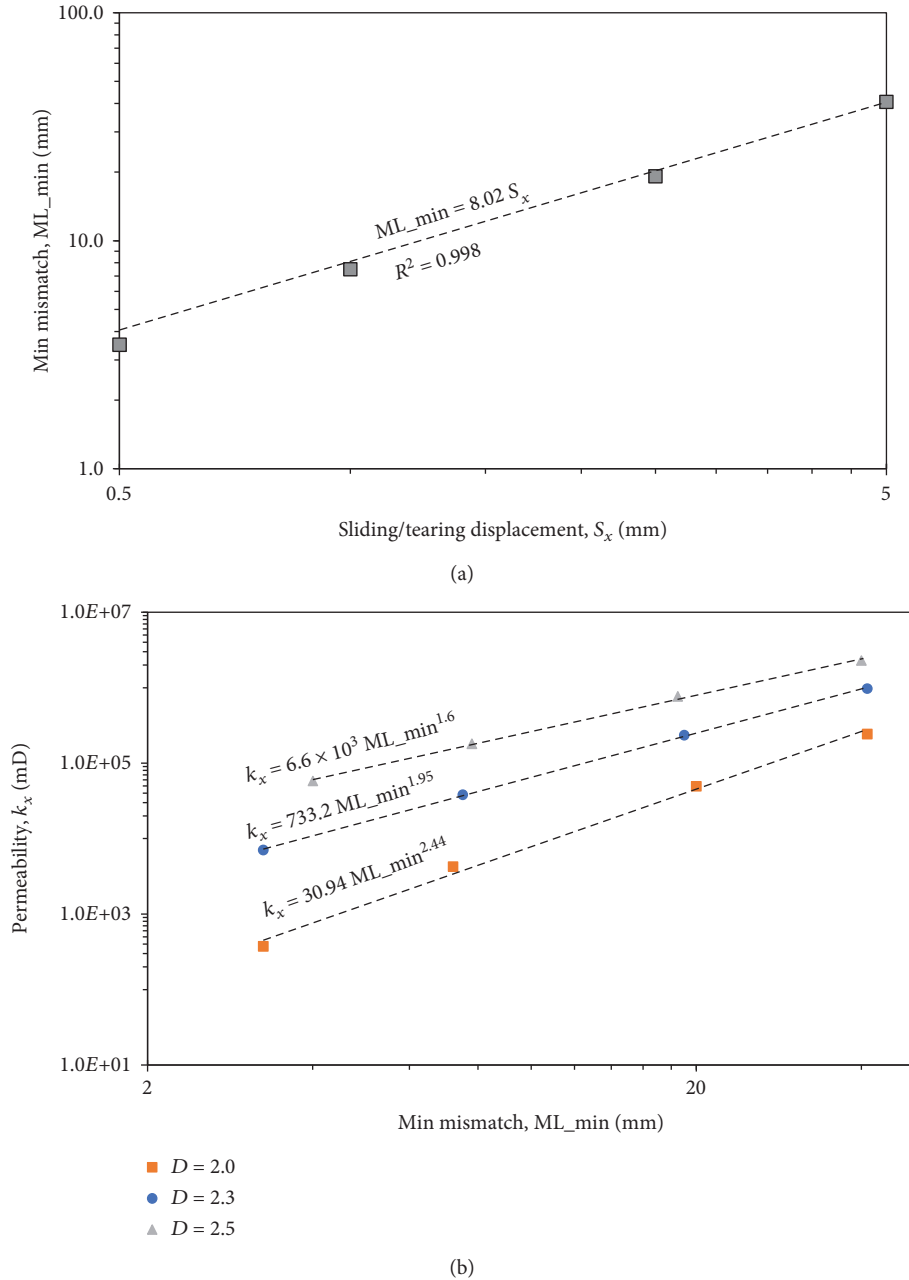


FIGURE 14: (a) Minimum mismatch length versus sliding/tearing displacement. (b) Permeability versus minimum mismatch length. Permeability is directly proportional to the minimum mismatch length, which is related to the shear displacement.

fracture wall wearing and the generation of cataclastic material [54], eventually reducing permeability. However, our model has greater applicability to small displacements where the damage of the fracture walls is negligible.

The permeability anisotropy in fractures with sliding/tearing displacement is significant and dependent on the roughness (fractal dimension). For low displacement (0.5 mm), the anisotropy can reach values up to 2.6 for fractures with a fractal dimension of 2.0. For the same displacement, fractures with high roughness ($D = 2.5$) showed lower values of permeability anisotropy near 1.5. For higher sliding/tearing displacement, the permeability anisotropy decreases approaching the value 1.

The mismatch itself has a positive control on the permeability. The importance of this result is that the mismatch could also be produced by diagenetic processes (e.g., cementation, dissolution) and shearing. Zambrano et al. [38], using X-ray microtomographic images in shear compactive bands hosted in porous carbonates, showed the existence of complex channelized porous networks along the shear surface within these structures.

4.4. Consequences to Reservoir Modeling. The results agree with the macroscale observations of previous authors in the study area, where both opened/sheared pressure solution seams and fault-related joints present the greatest

values of aperture and the most important bitumen impregnation [13, 54, 56].

The relationship between permeability and porosity for rough fractures clearly deviates from the ideal smooth parallel plate case (for the studied scenarios). Fracture permeability is lower for the same porosity range (<0.2%) in comparison to the theoretical values. Instead, the power-law slope is higher, indicating a more important control of porosity as it was expected. The equation itself may be useful to estimate the permeability of fractures if the fracture porosity is known.

After their formation, both closing and opening mode fractures are often subjected to a shear process, and even with a small imperceptible sliding/tearing displacement, they cannot be modeled as simple opening mode fracture. At reservoir depth, preexisting fractures (joints and pressure solution seams) that are favorably oriented to be sheared (accordingly to the orientations of the stress field which affected the area) may be characterized by a mismatch between the fracture walls enhancing the fracture opening. Therefore, the findings of this work may have a significant impact on fracture modeling workflows for subresolution faults (e.g., [62]). In fractures with small shear displacement, contrary to the open mode case, the roughness may influence positively the permeability. Sliding/tearing displacement also may enhance the fracture permeability eventually decelerating when the cataclasis process starts. If the shear displacement is small ($S_x < 1$ mm), the permeability anisotropy is significant enough to be considered in the fracture modeling workflow.

5. Conclusions

We presented a new multifaceted approach to characterize surface fracture roughness by SfM photogrammetry, numerical modeling, and computational fluid dynamics simulation. This methodology provides a better quantification of surface parameters that are not possible to obtain using former surface roughness measurement and analysis tools.

In addition, this study illustrates the crucial relationships between permeability and other fracture properties, such as roughness, porosity, opening mode-sliding/tearing displacement, and mismatch. The obtained relationships pointed out the following statements:

- (i) In joints (opening mode fractures) and/or opened pressure solution seams, the roughness tends to reduce the permeability. Thus, the permeability is inversely proportional to the fractal dimension
- (ii) In sheared joints and/or pressure solution seams (assuming an insignificant surface wearing), the sliding/tearing mode displacement may cause mismatch and therefore enhance the porosity and permeability. The validity of this behavior may depend on the point that displacement starts to produce cataclastic material. Small shear displacements and mismatch may be extremely important to guarantee storage and migration of geofluid at depth

thanks to asperities-supported aperture. Permeability anisotropy is very significant for small shear displacements, characterized by higher values of permeability component perpendicular to the shear displacement

- (iii) Porosity exerts a more important control on permeability in rough fractures (higher power-law slope). The empiric relationship may result in greater utility for estimating the fracture permeability if the fracture porosity is known

Data Availability

The data used to support the findings of this study are available from the corresponding author upon request.

Conflicts of Interest

The authors declare that they have no conflicts of interest.

Acknowledgments

This research was supported by the FAR Project 2014 “Characterization and modeling of natural reservoirs of geofluids in fractured carbonate rocks,” funded by the University of Camerino, Principal investigator Emanuele Tondi, and the Reservoir Characterization Project (<http://www.rechproject.com>). We also acknowledge and thank Amerigo Corradetti for generously sharing his code for power spectral density (PSD) analysis of surfaces and thoughtful conversations that helped move this work forward.

References

- [1] D. Snow, *A parallel Plate Model of Fractured Permeable Media*, [Ph.D. Thesis], University of California, Berkeley, 1965.
- [2] Y. W. Tsang, “Usage of “equivalent apertures” for rock fractures as derived from hydraulic and tracer tests,” *Water Resources Research*, vol. 28, no. 5, pp. 1451–1455, 1992.
- [3] P. A. Witherspoon, J. S. Y. Wang, K. Iwai, and J. E. Gale, “Validity of cubic law for fluid flow in a deformable rock fracture,” *Water Resources Research*, vol. 16, no. 6, pp. 1016–1024, 1980.
- [4] G. M. Lomize, *Flow in Fractured Rocks*, Gosenergoizdat, Moscow, 1951.
- [5] C. Louis, “A study of ground water flow in jointed rock and its influence on the stability of rock masses,” in *Rock Mechanics Research Report*, Imperial College, London, 1969, Rock Mechanics Research Report 10.
- [6] E. F. de Quadros, *Determinação das características do fluxo de água em fraturas de rochas*, Department of Civil Construction Engineering, Polytechnic School, University of Sao Paulo, 1982.
- [7] N. Barton, S. Bandis, and K. Bakhtar, “Strength, deformation and conductivity coupling of rock joints,” *International Journal of Rock Mechanics and Mining Sciences & Geomechanics Abstracts*, vol. 22, no. 3, pp. 121–140, 1985.
- [8] N. Barton and V. Choubey, “The shear strength of rock joints in theory and practice,” *Rock Mechanics*, vol. 10, no. 1-2, pp. 1–54, 1977.

- [9] M. Zambrano, E. Tondi, I. Korneva et al., “Fracture properties analysis and discrete fracture network modelling of faulted tight limestones, Murge Plateau, Italy,” *Italian Journal of Geosciences*, vol. 135, no. 1, pp. 55–67, 2016.
- [10] E. Panza, F. Agosta, M. Zambrano et al., “Structural architecture and discrete fracture network modelling of layered fractured carbonates (Altamura Fm., Italy),” *Italian Journal of Geosciences*, vol. 134, no. 3, pp. 409–422, 2015.
- [11] E. Panza, F. Agosta, A. Rustichelli et al., “Fracture stratigraphy and fluid flow properties of shallow-water, tight carbonates: the case study of the Murge Plateau (southern Italy),” *Marine and Petroleum Geology*, vol. 73, pp. 350–370, 2016.
- [12] D. H. Kim, I. Gratchev, and A. Balasubramaniam, “Determination of joint roughness coefficient (JRC) for slope stability analysis: a case study from the Gold Coast area, Australia,” *Landslides*, vol. 10, no. 5, pp. 657–664, 2013.
- [13] T. Volatili, M. Zambrano, A. Cilona et al., “From fracture analysis to flow simulations in fractured carbonates: the case study of the Roman Valley Quarry (Majella Mountain, Italy),” *Marine and Petroleum Geology*, vol. 100, pp. 95–110, 2019.
- [14] T. Candela, F. Renard, M. Bouchon et al., “Characterization of fault roughness at various scales: implications of three-dimensional high resolution topography measurements,” *Pure and Applied Geophysics*, vol. 166, no. 10–11, pp. 1817–1851, 2009.
- [15] T. Candela, F. Renard, Y. Klinger, K. Mair, J. Schmittbuhl, and E. E. Brodsky, “Roughness of fault surfaces over nine decades of length scales,” *Journal of Geophysical Research*, vol. 117, no. B8, article B08409, 2012.
- [16] F. Renard, C. Voisin, D. Marsan, and J. Schmittbuhl, “High resolution 3D laser scanner measurements of a strike-slip fault quantify its morphological anisotropy at all scales,” *Geophysical Research Letters*, vol. 33, no. 4, article L04305, 2006.
- [17] F. Renard, K. Mair, and O. Gundersen, “Surface roughness evolution on experimentally simulated faults,” *Journal of Structural Geology*, vol. 45, pp. 101–112, 2012.
- [18] F. Renard, T. Candela, and E. Bouchaud, “Constant dimensionality of fault roughness from the scale of micro-fractures to the scale of continents,” *Geophysical Research Letters*, vol. 40, no. 1, pp. 83–87, 2013.
- [19] A. Corradetti, K. McCaffrey, N. De Paola, and S. Tavani, “Evaluating roughness scaling properties of natural active fault surfaces by means of multi-view photogrammetry,” *Tectonophysics*, vol. 717, pp. 599–606, 2017.
- [20] S. P. Bemis, S. Micklethwaite, D. Turner et al., “Ground-based and UAV-based photogrammetry: a multi-scale, high-resolution mapping tool for structural geology and paleoseismology,” *Journal of Structural Geology*, vol. 69, pp. 163–178, 2014.
- [21] K. J. W. McCaffrey, R. R. Jones, R. E. Holdsworth et al., “Unlocking the spatial dimension: digital technologies and the future of geoscience fieldwork,” *Journal of the Geological Society of London*, vol. 162, no. 6, pp. 927–938, 2005.
- [22] A. D. Pitts, C. I. Casciano, M. Patacci, S. G. Longhitano, C. Di Celma, and W. D. McCaffrey, “Integrating traditional field methods with emerging digital techniques for enhanced outcrop analysis of deep water channel-fill deposits,” *Marine and Petroleum Geology*, vol. 87, pp. 2–13, 2017.
- [23] P. R. Nesbit, P. R. Durkin, C. H. Hugenholtz, S. M. Hubbard, and M. Kucharczyk, “3-D stratigraphic mapping using a digital outcrop model derived from UAV images and structure-from-motion photogrammetry,” *Geosphere*, vol. 14, no. 6, pp. 2469–2486, 2018.
- [24] B. Zimmer, C. Liutkus-Pierce, S. T. Marshall, K. G. Hatala, A. Metallo, and V. Rossi, “Using differential structure-from-motion photogrammetry to quantify erosion at the Engare Sero footprint site, Tanzania,” *Quaternary Science Reviews*, vol. 198, pp. 226–241, 2018.
- [25] S. R. Ogilvie, E. Isakov, and P. W. Glover, “Fluid flow through rough fractures in rocks. II: a new matching model for rough rock fractures,” *Earth and Planetary Science Letters*, vol. 241, no. 3–4, pp. 454–465, 2006.
- [26] E. Isakov, S. R. Ogilvie, C. W. Taylor, and P. W. Glover, “Fluid flow through rough fractures in rocks I: high resolution aperture determinations,” *Earth and Planetary Science Letters*, vol. 191, no. 3–4, pp. 267–282, 2001.
- [27] S. R. Ogilvie, E. Isakov, C. W. Taylor, and P. W. J. Glover, “Characterization of rough-walled fractures in crystalline rocks,” *Geological Society, London, Special Publications*, vol. 214, no. 1, pp. 125–141, 2003.
- [28] M. J. Blunt, B. Bijeljic, H. Dong et al., “Pore-scale imaging and modelling,” *Advances in Water Resources*, vol. 51, pp. 197–216, 2013.
- [29] M. B. Cardenas, “Three-dimensional vortices in single pores and their effects on transport,” *Geophysical Research Letters*, vol. 35, no. 18, article L18402, 2008.
- [30] M. B. Cardenas, “Direct simulation of pore level Fickian dispersion scale for transport through dense cubic packed spheres with vortices,” *Geochemistry, Geophysics, Geosystems*, vol. 10, no. 12, article Q12014, 2009.
- [31] B. Bijeljic, A. Raeini, P. Mostaghimi, and M. J. Blunt, “Predictions of non-Fickian solute transport in different classes of porous media using direct simulation on pore-scale images,” *Physical Review E*, vol. 87, no. 1, article 013011, 2013.
- [32] M. C. Sukop, H. Huang, C. L. Lin, M. D. Deo, K. Oh, and J. D. Miller, “Distribution of multiphase fluids in porous media: comparison between lattice Boltzmann modeling and micro-x-ray tomography,” *Physical Review E*, vol. 77, no. 2, article 026710, 2008.
- [33] A. J. C. Ladd, “Numerical simulations of particulate suspensions via a discretized Boltzmann equation: part 2. Numerical results,” *Journal of Fluid Mechanics*, vol. 271, pp. 311–339, 1994.
- [34] W. Degruyter, A. Burgisser, O. Bachmann, and O. Malaspinas, “Synchrotron X-ray microtomography and lattice Boltzmann simulations of gas flow through volcanic pumices,” *Geosphere*, vol. 6, no. 5, pp. 470–481, 2010.
- [35] F. Khan, F. Enzmann, M. Kersten, A. Wiegmann, and K. Steiner, “3D simulation of the permeability tensor in a soil aggregate on basis of nanotomographic imaging and LBE solver,” *Journal of Soils and Sediments*, vol. 12, no. 1, pp. 86–96, 2012.
- [36] H. Andrä, N. Combaret, J. Dvorkin et al., “Digital rock physics benchmarks—part II: computing effective properties,” *Computational Geosciences*, vol. 50, pp. 33–43, 2013.
- [37] S. M. Shah, F. Gray, J. P. Crawshaw, and E. S. Boek, “Micro-computed tomography pore-scale study of flow in porous media: effect of voxel resolution,” *Advances in Water Resources*, vol. 95, pp. 276–287, 2015.
- [38] M. Zambrano, E. Tondi, L. Mancini et al., “Fluid flow simulation and permeability computation in deformed porous

- carbonate grainstones,” *Advances in Water Resources*, vol. 115, pp. 95–111, 2018.
- [39] G. Jin, T. W. Patzek, and D. B. Silin, “Direct prediction of the absolute permeability of unconsolidated consolidated reservoir rock,” *Proceedings of SPE Annual Technical Conference and Exhibition*, 2004, pp. 1–15, Houston, TX, USA, September 2004.
- [40] Y. Keehm, T. Mukerji, and A. Nur, “Permeability prediction from thin sections: 3D reconstruction and lattice-Boltzmann flow simulation,” *Geophysical Research Letters*, vol. 31, no. 4, article L04606, 2004.
- [41] K. Wu, M. I. J. Dijke, G. D. Couples et al., “3D stochastic modelling of heterogeneous porous media – applications to reservoir rocks,” *Transport in Porous Media*, vol. 65, no. 3, pp. 443–467, 2006.
- [42] Y. Keehm, *Computational Rock Physics: Transport Properties in Porous Media and Applications*, [Ph.D. Thesis], Stanford University, Stanford, CA, USA, 2003.
- [43] P. L. Bhatnagar, E. P. Gross, and M. Krook, “A model for collision processes in gases. I. Small amplitude processes in charged and neutral one-component systems,” *Physics Review*, vol. 94, no. 3, pp. 511–525, 1954.
- [44] A. Narvaez, T. Zauner, F. Raischel, R. Hilfer, and J. Harting, “Quantitative analysis of numerical estimates for the permeability of porous media from lattice-Boltzmann simulations,” *Journal of Statistical Mechanics: Theory and Experiment*, vol. 2010, no. 11, article P11026, 2010.
- [45] D. d’Humières, “Generalized lattice-Boltzmann equations,” in *Rarefied Gas Dynamics: Theory and Simulations, Progress in Astronautics and Aeronautics*, B. D. Shizgal and D. P. Weave, Eds., vol. 159, pp. 450–458, AIAA, Washington, D. C, USA, 1992.
- [46] D. d’Humières, I. Ginzburg, M. Krafczyk, P. Lallemand, and L.-S. Luo, “Multiple-relaxation-time lattice Boltzmann models in three dimensions,” *Philosophical Transactions of the Royal Society A*, vol. 360, no. 1792, pp. 437–451, 2002.
- [47] C. Pan, L. S. Luo, and C. T. Miller, “An evaluation of lattice Boltzmann schemes for porous medium flow simulation,” *Computers & Fluids*, vol. 35, no. 8-9, pp. 898–909, 2006.
- [48] J. Latt, *Palabos, Parallel Lattice Boltzmann Solver*, FlowKit, Lausanne, Switzerland, 2009, <http://www.palabos.org/>.
- [49] M. Zambrano, E. Tondi, L. Mancini et al., “3D pore-network quantitative analysis in deformed carbonate grainstones,” *Marine and Petroleum Geology*, vol. 82, pp. 251–264, 2017.
- [50] F. Ghisetti and L. Vezzani, “Normal faulting, extension and uplift in the outer thrust belt of the central Apennines (Italy): role of the Caramanico fault,” *Basin Research*, vol. 14, no. 2, pp. 225–236, 2002.
- [51] V. Scisciani, E. Tavarnelli, and F. Calamita, “The interaction of extensional and contractional deformations in the outer zones of the Central Apennines, Italy,” *Journal of Structural Geology*, vol. 24, no. 10, pp. 1647–1658, 2002.
- [52] E. Tondi, M. Antonellini, A. Aydin, L. Marchegiani, and G. Cello, “The role of deformation bands, stylolites and sheared stylolites in fault development in carbonate grainstones of Majella Mountain, Italy,” *Journal of Structural Geology*, vol. 28, no. 3, pp. 376–391, 2006.
- [53] A. P. Lavenue, J. Lamarche, R. Salardon, A. Gallois, L. Marié, and B. D. Gauthier, “Relating background fractures to diagenesis and rock physical properties in a platform-slope transect. Example of the Maiella Mountain (central Italy),” *Marine and Petroleum Geology*, vol. 51, pp. 2–19, 2014.
- [54] F. Agosta, M. Alessandrini, E. Tondi, and A. Aydin, “Oblique normal faulting along the northern edge of the Majella Anticline, central Italy: inferences on hydrocarbon migration and accumulation,” *Journal of Structural Geology*, vol. 31, no. 7, pp. 674–690, 2009.
- [55] A. Aydin, M. Antonellini, E. Tondi, and F. Agosta, “Deformation along the leading edge of the Maiella thrust sheet in central Italy,” *Journal of Structural Geology*, vol. 32, no. 9, pp. 1291–1304, 2010.
- [56] A. Rustichelli, E. Tondi, F. Agosta, C. Di Celma, and M. Giorgioni, “Sedimentologic and diagenetic controls on pore-network characteristics of Oligocene–Miocene ramp carbonates (Majella Mountain, central Italy),” *AAPG Bulletin*, vol. 97, no. 3, pp. 487–524, 2013.
- [57] A. Iadanza, G. Sampalmieri, and P. Cipollari, “Deep-seated hydrocarbons in the seep “brecciated limestones” of the Maiella area (Adriatic foreland basin): evaporitic sealing and oil re-mobilization effects linked to the drawdown of the Messinian salinity crisis,” *Marine and Petroleum Geology*, vol. 66, pp. 177–191, 2015.
- [58] J. L. Carrivick, M. W. Smith, and D. J. Quincey, *Structure from Motion in the Geosciences*, John Wiley & Sons, 2016.
- [59] S. R. Brown, “Simple mathematical model of a rough fracture,” *Journal of Geophysical Research: Solid Earth*, vol. 100, no. B4, pp. 5941–5952, 1995.
- [60] A. Schuster, “On the investigation of hidden periodicities with application to a supposed 26 day period of meteorological phenomena,” *Journal of Geophysical Research*, vol. 3, no. 1, p. 13, 1898.
- [61] A. Rustichelli, F. Agosta, E. Tondi, and V. Spina, “Spacing and distribution of bed-perpendicular joints throughout layered, shallow-marine carbonates (Granada Basin, southern Spain),” *Tectonophysics*, vol. 582, pp. 188–204, 2013.
- [62] M. Antonellini, A. Cilona, E. Tondi, M. Zambrano, and F. Agosta, “Fluid flow numerical experiments of faulted porous carbonates, northwest Sicily (Italy),” *Marine and Petroleum Geology*, vol. 55, pp. 186–201, 2014.
- [63] J. Ahrens, B. Geveci, and C. Law, *ParaView: an End-User Tool for Large Data Visualization*, *Visualization Handbook*, Elsevier, 2005.

Research Article

History Matching of a Channelized Reservoir Using a Serial Denoising Autoencoder Integrated with ES-MDA

Sungil Kim,^{1,2} Baehyun Min ,^{1,3} Seoyoon Kwon,^{1,3} and Min-gon Chu¹

¹Center for Climate/Environment Change Prediction Research, Ewha Womans University, 52 Ewhayeodae-gil, Seodaemun-gu, Seoul 03760, Republic of Korea

²Petroleum and Marine Research Division, Korea Institute of Geoscience and Mineral Resources, 124 Gwahak-ro, Yuseong-gu, Daejeon 34132, Republic of Korea

³Department of Climate and Energy Systems Engineering, Ewha Womans University, 52 Ewhayeodae-gil, Seodaemun-gu, Seoul 03760, Republic of Korea

Correspondence should be addressed to Baehyun Min; bhmin01@ewha.ac.kr

Received 31 October 2018; Accepted 17 January 2019; Published 16 April 2019

Guest Editor: Sergio Longhitano

Copyright © 2019 Sungil Kim et al. This is an open access article distributed under the Creative Commons Attribution License, which permits unrestricted use, distribution, and reproduction in any medium, provided the original work is properly cited.

For an ensemble-based history matching of a channelized reservoir, loss of geological plausibility is challenging because of pixel-based manipulation of channel shape and connectivity despite sufficient conditioning to dynamic observations. Regarding the loss as artificial noise, this study designs a serial denoising autoencoder (SDAE) composed of two neural network filters, utilizes this machine learning algorithm for relieving noise effects in the process of ensemble smoother with multiple data assimilation (ES-MDA), and improves the overall history matching performance. As a training dataset of the SDAE, the static reservoir models are realized based on multipoint geostatistics and contaminated with two types of noise: salt and pepper noise and Gaussian noise. The SDAE learns how to eliminate the noise and restore the clean reservoir models. It does this through encoding and decoding processes using the noise realizations as inputs and the original realizations as outputs of the SDAE. The trained SDAE is embedded in the ES-MDA. The posterior reservoir models updated using Kalman gain are imported to the SDAE which then exports the purified prior models of the next assimilation. In this manner, a clear contrast among rock facies parameters during multiple data assimilations is maintained. A case study at a gas reservoir indicates that ES-MDA coupled with the noise remover outperforms a conventional ES-MDA. Improvement in the history matching performance resulting from denoising is also observed for ES-MDA algorithms combined with dimension reduction approaches such as discrete cosine transform, K-singular vector decomposition, and a stacked autoencoder. The results of this study imply that a well-trained SDAE has the potential to be a reliable auxiliary method for enhancing the performance of data assimilation algorithms if the computational cost required for machine learning is affordable.

1. Introduction

In the petroleum industry, history matching is an essential process to calibrate reservoir properties (e.g., facies, permeability, and PVT parameters) by conditioning one or more reservoir models to field observations such as production and seismic data [1]. Ensemble-based data assimilation methods based on Bayes theorem [2–4] have been applied to solve a variety of petroleum engineering problems since the early 2000's [5]. Specifically, ensemble Kalman filter

(EnKF) [2], ensemble smoother (ES) [6], and ensemble smoother with multiple data assimilation (ES-MDA) [7] have been utilized for history matching of geological features such as channels (the subject of this study). Loss of geological characteristics due to pixel-based manipulation of channel features (such as shape and connectivity) is challenging for an ensemble-based history matching of a channelized reservoir. Note, the loss is regarded as noise in this study. Despite sufficient conditioning to field observations during ensemble updates, increase in noise often

causes failure to deliver the geologically plausible reservoir models. This decreases the reliability of history matching results [8]. For this reason, a relevant problem is how to update the reservoir models with consideration for geological plausibility in a practical manner.

Previous studies have improved the performance of ensemble-based history matching by adopting data transformation [9–13]. In general, transformation methods have a substantial energy compaction property that is useful for feature extraction and dimension reduction of parameters and helping to save computational cost in data processing. If essential features are adequately acquired, updating the features can also yield an improved history matching performance over calibrating original parameters. For these reasons, discrete cosine transform (DCT) [14, 15], discrete wavelet transform [1], K-singular value decomposition (K-SVD) [16, 17], and autoencoder (AE) [18] have been employed as ancillary parameterizations of ensemble-based methods. For history matching of channelized reservoirs, DCT has been utilized to preserve channel properties because DCT figures out overall trends and main patterns of channels by using only essential DCT coefficients [19–22]. Updating essential DCT coefficients implies the importance of determining the optimal number of DCT coefficients for preserving channel connectivity and continuity [22]. K-SVD has an advantage of sparse representations of data as weighted linear combinations of prototype realizations. However, it takes preprocessing time to construct a set of prototype realizations called a dictionary. As a remedy, a combination of DCT and iterative K-SVD was proposed to complement the limitations of both methods [23]. Canchumuni et al. [18] coupled AE with ES-MDA for an efficient parameterization and compared its performance with that of ES-MDA coupled with principal component analysis.

Recent advances in machine learning have offered opportunities for using complex meta-heuristic tools based on artificial neural networks (if the tools are well trained at affordable computational cost). In petroleum engineering, examples include production optimization [24–26] and history matching [18, 27–29]. As investigated in [18, 27], AE is a multilayer neural network that learns efficient data coding in an unsupervised manner. This is useful for representation (encoding) of a given dataset followed by reconstruction of the encoded dataset [30, 31]. In image processing and recognition, AE has a capability of denoising through encoding and decoding processes if noise data is input and purified data is output [32]. This type of AE is called denoising autoencoder (DAE) [33, 34].

Taking this capability of DAE into consideration, this study designs a serial denoising autoencoder (SDAE) and integrates the algorithm in the ensemble update of ES-MDA to improve the performance of ensemble-based history matching. The SDAE learns how to eliminate the noise and restore the clean reservoir models through encoding and decoding processes using the noise realizations as inputs and the original realizations as outputs of the SDAE. The trained SDAE imports the posterior reservoir models derived using Kalman gain of ES-MDA for purifying the models and exports the purified models as prior models

for the subsequent assimilation of ES-MDA. The ES-MDA coupled with SDAE is applied to history matching of a channelized gas reservoir. Its performance is compared with that of the conventional ES-MDA. Also, denoising effects are investigated for ES-MDA coupled with dimension reduction methods such as DCT and K-SVD.

2. Methodology

In this study, ES-MDA is the platform to calibrate the reservoir models for history matching. A procedure of ES-MDA is mainly composed of two steps: numerical simulation for the reservoir models and update of reservoir parameters. A brief description of ES-MDA is given in Section 2.1. SDAE purifies noise in the updated reservoir models (Section 2.2). AE (Section 2.2), DCT (Section 2.3), and K-SVD (Section 2.4) are introduced as parameterization techniques. Section 2.5 proposes the ES-MDA algorithm coupled with the SDAE and the parameterization methods.

2.1. ES-MDA. Ensemble-based history matching methods update parameters of the target models using observed data such as production rate and 4D seismic data. For model updates, EnKF utilizes observed data one-time step by one-time step in time sequence. The principle of EnKF might cause inconsistency between the updated static models and dynamic behaviors due to sequential updates without returning to an initial time step [7, 35]. ES updates models using observed data measured at all time steps at once to solve the inconsistency issue [6]. However, history matching performance obtained using ES was often less satisfactory due to the one-time calibration of the reservoir models. ES-MDA is a variant of ES. ES-MDA repeats ES with inflation coefficients for the covariance matrix of observed data measurement error. Therefore, it has advantages in not only history matching performance but also the consistency between static data and dynamic data [35].

For ensemble-based history matching, the equation of model update is as follows:

$$m_i = m_i^b + C_{md}(C_{dd} + \alpha_p C_D)^{-1}(d_i^{\text{unc}} - d_i), \quad \text{for } i = 1, \dots, N_{\text{ens}}, \quad (1)$$

where m is the state vector consisting of reservoir parameters (e.g., facies and permeability), the subscript i means the i th ensemble member, the superscript b means before update in this study, C_{md} is the cross-covariance matrix of m and d , C_{dd} is the autocovariance matrix of d , α_p is the inflation coefficients for C_D (which is the covariance matrix of the observed data measurement error [7]), d is the simulated responses obtained by running a forward simulation, d^{unc} is the observation data perturbed by inflated observed data measurement error, and N_{ens} is the number of ensemble members (i.e., the reservoir models in the ensemble). In equation (1), $C_{md}(C_{dd} + \alpha_p C_D)^{-1}$ is the Kalman gain that is computed with regularization by singular value decomposition (SVD) using 99.9% of the total energy in singular values [7].

Definitions of C_{md} and C_{dd} are as follows:

$$C_{md} = \frac{1}{N_{\text{ens}} - 1} \sum_{i=1}^{N_{\text{ens}}} (m_i - \bar{m})(d_i - \bar{d})^T, \quad (2)$$

$$C_{dd} = \frac{1}{N_{\text{ens}} - 1} \sum_{i=1}^{N_{\text{ens}}} (d_i - \bar{d})(d_i - \bar{d})^T, \quad (3)$$

where \bar{m} is the mean of state vectors and \bar{d} is the mean of dynamic vectors.

The condition for α_p is as follows:

$$\sum_{p=1}^{N^a} \frac{1}{\alpha_p} = 1, \quad (4)$$

where N^a is the number of assimilations in ES-MDA. ES-MDA updates all state vectors N^a times using an inflated covariance matrix of measurement error compared to the single assimilation of ES [7, 35]. In other words, ES has $N^a = 1$ and $\alpha_{p=1} = 1$ because of the single assimilation.

In equation (1), the perturbed observation d^{unc} is computed as follows:

$$d_i^{\text{unc}} = d_i^{\text{obs}} + \sqrt{a_p} C_D^{1/2} z_{d,i}, \quad \text{for } i = 1, \dots, N_{\text{ens}}, \quad (5)$$

where d^{obs} means the original observed data. On the right-hand side of equation (5), the second term is the perturbation term quantifying reservoir uncertainty caused by data measurement, processing, and interpretation. The stochastic feature of C_D is realized by $z_d \sim N(0, I_{N_d})$, where z_d is the random error matrix of observations generated with a mean of zero and a standard deviation of I_{N_d} , where N_d is the number of time steps of observation data.

2.2. Autoencoder, Denoising Autoencoder, and Serial Denoising Autoencoder

2.2.1. Autoencoder.

AE is an unsupervised learning neural network that enables encoding given data compactly on a manifold and then decoding the encoded data into the original data space [36]. Here, the manifold refers to the dimension that represents essential features of the original data [33, 37]. As a well-designed manifold is useful for data compression and restoration, AE has been recently utilized as a preprocessing tool for feature extraction of the reservoir models [18, 38]. Figure 1(a) is a schematic diagram of AE that shows compression and reconstruction of a channelized reservoir model composed of two facies: sand channels with high permeability and shale background with low permeability. Throughout this paper, indicators for shale and sand facies are 0 and 1, respectively (see the original reservoir model in Figure 1(a)). As a multilayer neural network, AE typically consists of three types of layers: one input layer, one or more hidden layers, and one output layer. Each layer is composed of interconnected units called neurons or nodes [39]. In Figure 1, orange and peach

circles indicate original and reconstructed data. Dark blue diamonds and purple squares represent encoded and double-encoded coefficients, respectively. Light blue diamonds are reconstructed double-encoded coefficients.

If an original reservoir model m is imported to the input layer, the encoded model h is as follows:

$$h = f_{\text{AE}}(m) = W_{\text{enc}} m + b_{\text{enc}}, \quad (6)$$

where $f_{\text{AE}}(\bullet)$ is the encoder of AE, W_{enc} and b_{enc} are the weight matrix and bias vector for $f_{\text{AE}}(\bullet)$, respectively. The subscript enc refers to encoding. For example, in Figure 1(a), m composed of facies indexes in 5,625 gridblocks is compressed into 2,500 coefficients denoted as h_1 in the hidden layer.

The above encoding process is followed by the decoding process as follows:

$$\hat{m} = g_{\text{AE}}(h) = W_{\text{dec}} h + b_{\text{dec}}, \quad (7)$$

where \hat{m} is the reconstructed reservoir model, $g_{\text{AE}}(\bullet)$ is the decoder of AE, W_{dec} is the weight matrix for $g_{\text{AE}}(\bullet)$, and b_{dec} is the bias vector for $g_{\text{AE}}(\bullet)$. The subscript dec refers to decoding. In Figure 1(a), the encoded coefficients h_1 are reconstructed as \hat{m} in the output layer. In Figure 1(b), the encoded h_1 is encoded again into h_2 . For feature extraction, the number of nodes in hidden layers is smaller than that of the input layer. For data reconstruction, the number of nodes in the output layer is the same as that in the input layer.

Training AE indicates tuning W_{enc} , b_{enc} , W_{dec} , and b_{dec} in the direction of minimizing the dissimilarity between the original model m and the reconstructed model \hat{m} . The dissimilarity is quantified as the loss function E given as follows:

$$E = \frac{1}{N_{\text{train}}} \sum_{i=1}^{N_{\text{train}}} \sum_{j=1}^{N_{\text{para}}} (m_{ij} - \hat{m}_{ij})^2 + \lambda \Omega_W + \beta \Omega_s, \quad (8)$$

where N_{train} is the number of the reservoir models used for AE training, N_{para} is the number of parameters in each reservoir realization, m_{ij} is the j th model parameter value for the i th model, λ is the coefficient for the L2 regularization, Ω_W is the sum of squared weights, β is the coefficient for the sparsity regularization, and Ω_s is the sparsity of network links between nodes of adjacent layers. Ω_W and Ω_s are given as follows:

$$\Omega_W = \frac{1}{2} \sum_{i=1}^{N_{\text{train}}} \sum_{j=1}^{N_{\text{para}}} w_{ij}^2, \quad (9)$$

$$\Omega_s = \sum_{k=1}^{N_{\text{node}}} \rho \log \left(\frac{\rho}{\hat{\rho}_k} \right) + (1 - \rho) \log \left(\frac{1 - \rho}{1 - \hat{\rho}_k} \right), \quad (10)$$

$$\hat{\rho}_k = \frac{1}{N_{\text{train}}} \sum_{i=1}^{N_{\text{train}}} h_k(m_i), \quad (11)$$

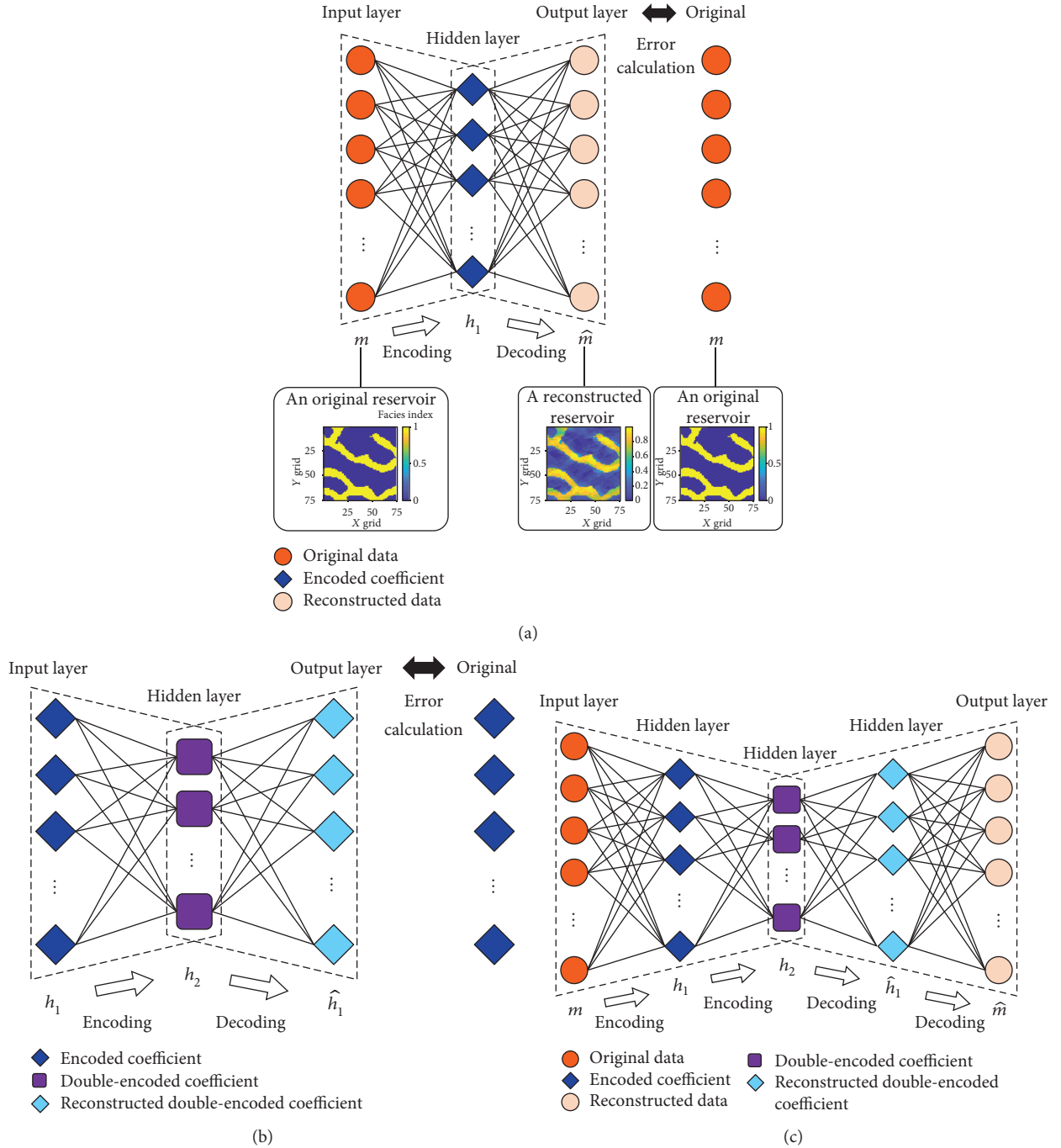


FIGURE 1: Two autoencoders (a) and (b) used to construct a stacked autoencoder (c).

where w_{ij} is the weight for a node of the j th parameter of the i th model, N_{node} is the number of nodes in a hidden layer, ρ is a desired value for the average output activation measure, $\hat{\rho}_k$ is the average output activation measure of the k th node in a hidden layer, and $h_k(m_i)$ is an assigned value in that k th node [40].

For further feature extraction, an AE (Figure 1(b)) can be nested in another AE, as shown in Figure 1(c). This nested AE is called a stacked AE (SAE) [33]. In Figure 1(b), the encoded model h_1 composed of 2,500

coefficients is compressed into another encoded model h_2 composed of 465 coefficients. Figure 1(c) is a combination of Figures 1(a) and 1(b). In Figure 1(c), h_2 is expanded and becomes the reconstructed model \hat{m} composed of 5,625 gridblocks via the reconstructed encoded model \hat{h}_1 composed of 2,500 coefficients.

2.2.2. Denoising Autoencoder. DAE is an AE trained with noise data as inputs and clean data as outputs. A well-trained DAE is expected to be able to refine reservoir

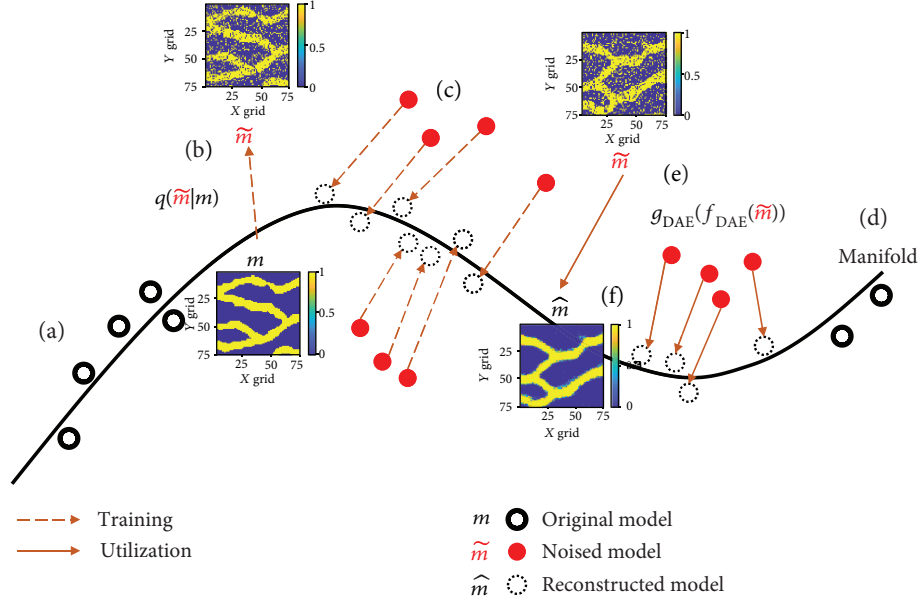


FIGURE 2: Schematic diagram of manifold learning using a denoising autoencoder (DAE) for geomodels: (a) generating the original models as training outputs; (b) noising the original models stochastically as training inputs; (c) learning of purification from the noise models to the original models; (d) building of a manifold dimension; (e) applying DAE to the noise models obtained from ES-MDA for obtaining the purified models; (f) delivering the purified models to ES-MDA.

realizations updated at each data assimilation and make the realizations preserve clean channel features in terms of shape and connectivity. This denoising process is also called purification in this study. Figure 2 shows a procedure of DAE applied to the purification of a channelized reservoir. For obtaining training data of DAE in this study, the clean original models are generated using a multipoint statistics modelling technique called single normal equation simulation (SNESIM) [41] (Figure 2(a)). Black solid circles in Figure 2(a) and m of Figure 2(b) are the original models which are corrupted stochastically with artificial noise using the conditional probability, $q(\tilde{m}|m)$ (Figure 2(b)). The noise models including \tilde{m} are presented with red balls. All the noise models are marked with red colors. In Figure 2(c), black dotted circles and dashed lines indicate the reconstructed models and training the DAE, respectively. The training of DAE is a process to grasp out a manifold and is displayed as a black curve (Figure 2(d)). The main dimension is reflected to represent the original models and purified reservoir models derived from the corresponding noise models. The reconstructed models of Figure 2(c) would be located nearby the manifold if the training is well designed. Once a trained DAE is obtained, Figures 2(e) and 2(f) show the purification of models by regarding the updated models at each assimilation of ES-MDA as the noise models. A noise model \tilde{m} is reconstructed as \hat{m} through the following process:

$$\hat{m} = g_{\text{DAE}}(f_{\text{DAE}}(\tilde{m})), \quad (12)$$

where $f_{\text{DAE}}(\bullet)$ and $g_{\text{DAE}}(\bullet)$ are the encoder and decoder of DAE, respectively. Note that \hat{m} becomes the prior model m_i^b in equation (1).

2.2.3. *Types of Noise.* Two noise types are considered artificial noises that might occur unexpectedly during data assimilation: salt and pepper noise (SPN) [42] and Gaussian noise (GN) [43]. SPN can be caused by sharp and sudden disturbances in the image signal. GN is statistical noise having a probability density function equal to that of the Gaussian distribution [43]. Both SPN and GN are typical noise types in digital image recognition and so have been used for DAEs [33].

Figure 3 compares a clean reservoir model, the model corrupted with SPN, and the model corrupted with GN. In Figure 3(a), the clean model consists of two facies values: 0 (shale) and 1 (sand). Because the facies value of a grid cell blurred with SPN is converted either from 0 to 1 or from 1 to 0, SPN makes mosaic effects that might break and disconnect sand channels in the shale background while inducing sparse sand facies in the shale background (Figure 3(b)). Grid cells to be perturbed are randomly selected using a specific ratio over the reservoir domain. The range of GN values is $[-1, 1]$. For preserving the range $[0, 1]$ of given data, the facies value at a grid cell is set as 0 if the value is negative after GN is added. The value is 1 if any facies value added with GN is greater than 1 (Figure 3(c)). In brief, the need to remove two noise types necessitates the design of serial DAEs as an auxiliary module embedded in an ensemble-based data assimilation algorithm.

Figure 4 shows how trained SPN and GN filters denoise a channelized reservoir model updated using ES-MDA. This study executes SPN and GN filters sequentially. Grid cells of the updated model have facies values following the Gaussian distribution, as seen in the histogram of Figure 4(a). Recall that the ideal facies models follow the discrete bimodal distribution (not the Gaussian) before import to the simulator.

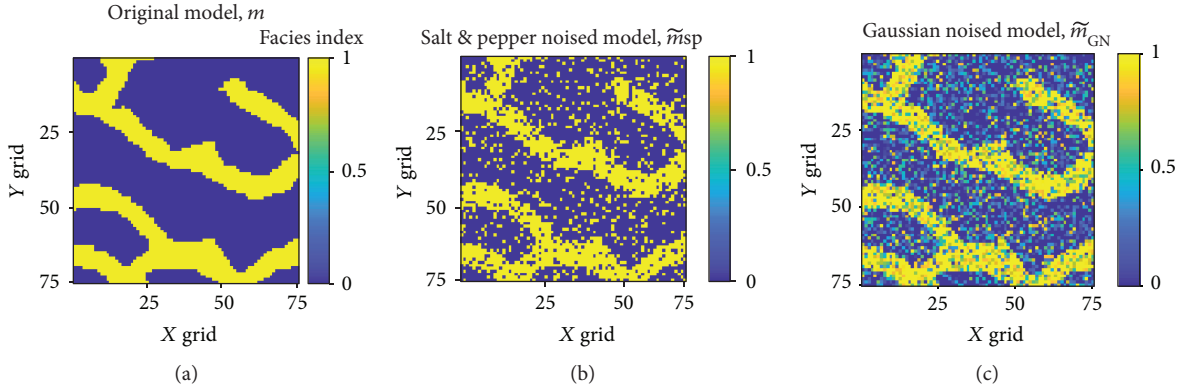


FIGURE 3: Three realizations of the (a) original, (b) salt and pepper noise, and (c) Gaussian noise reservoir models.

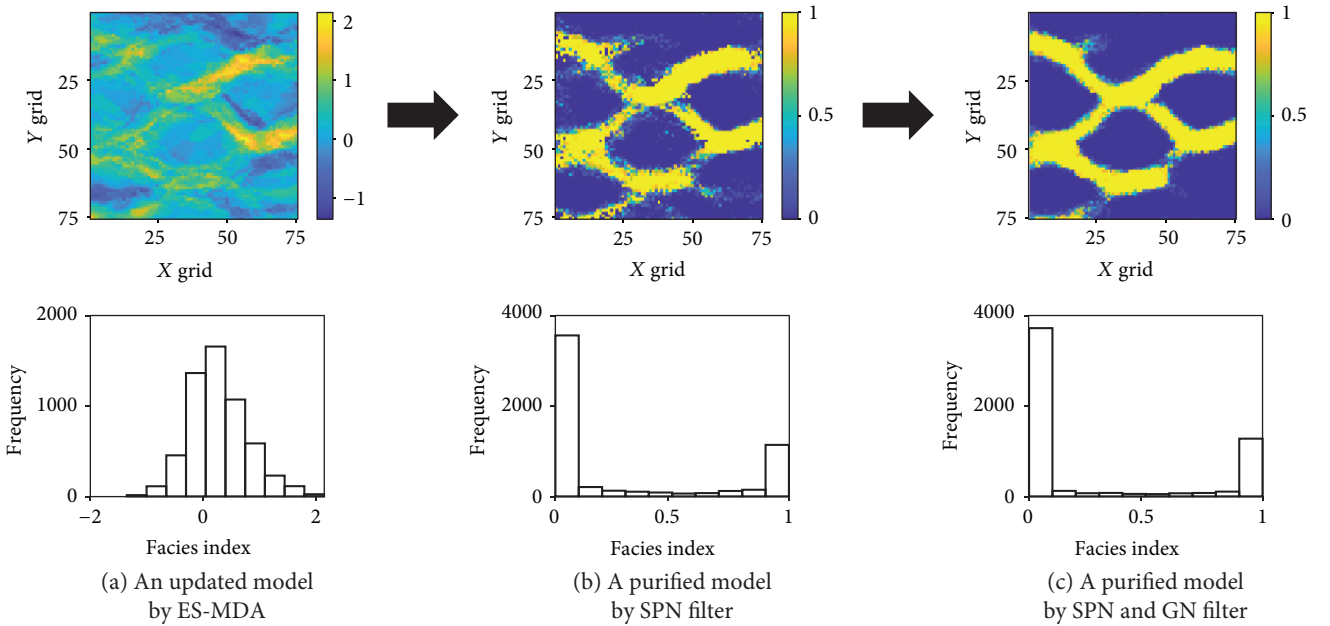


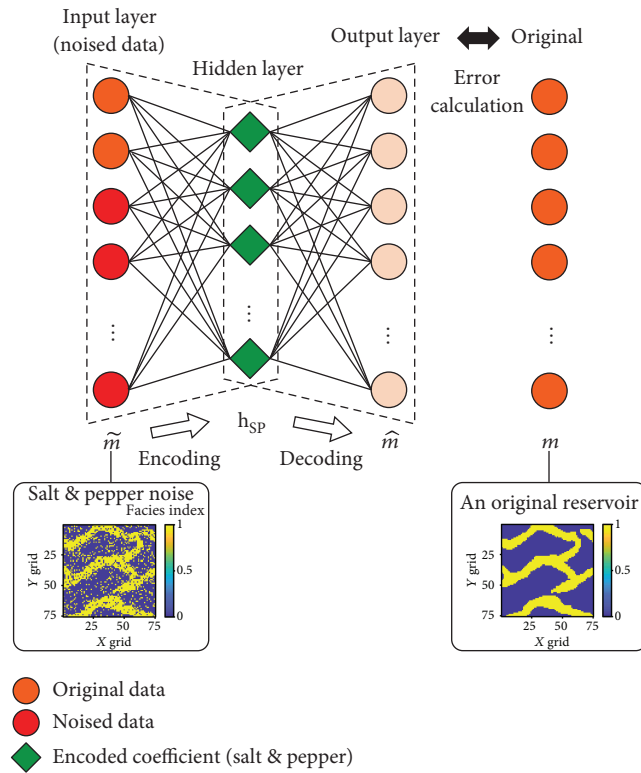
FIGURE 4: (a) A reservoir realization updated using ES-MDA. (b) A purified model using a salt and pepper noise (SPN) filter. (c) A further purified model using a Gaussian noise (GN) filter on (b).

Using the SPN filter (Figure 4(b)), a purified model yields the histogram following the bimodal distribution. However, it still reveals blurred channel borders. Some grid values are neither 0 (shale) nor 1 (sand). To obtain more distinct channel traits, the GN filter is applied to Figure 4(b) which yields Figure 4(c). After the GN filtering, a cutoff method is carried out to keep every facies value as either 0 or 1 for reservoir simulation [23].

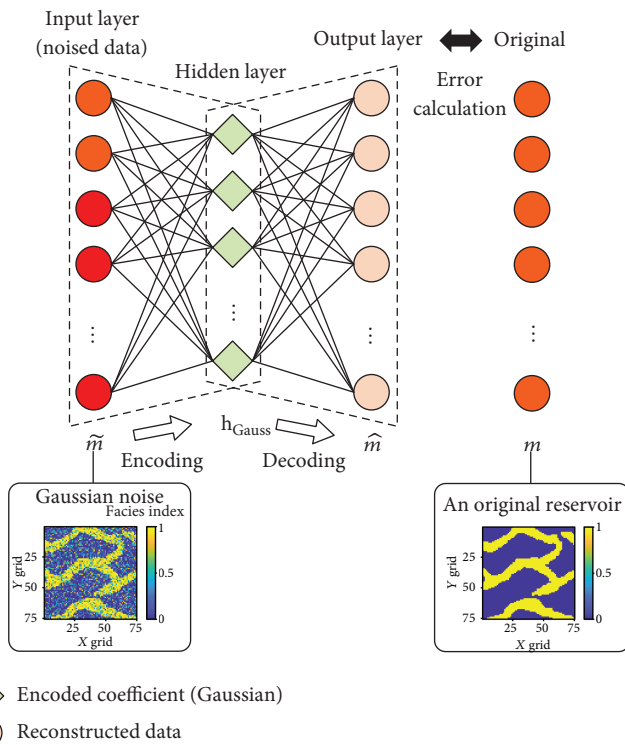
2.2.4. Serial Denoising Autoencoder. This research proposes a serial denoising autoencoder (SDAE) with consideration of the two noise types. Figure 5 describes the operating procedure of the SDAE denoising a channelized reservoir model. Figure 5(a) shows a DAE trained with the reservoir models corrupted with SPN. Figure 5(b) is a trained DAE with GN. The two neural networks are herein called the SPN filter and the GN filter. Orange circles are original data. Red circles correspond to data noise with SPN or

GN. Dark and light green diamonds indicate encoded coefficients in the hidden layers of SPN and GN filters, respectively. Peach colored circles indicate reconstructed data. m , \tilde{m} , and \hat{m} represent the original, noise, and reconstructed models, respectively. In Figure 5(c), \tilde{m} is imported to the input layer of the SDAE. The quality of \tilde{m} is improved (in terms of geological plausibility such as channel pattern and connectivity) using the SPN and GN filters. It is expected that the output of the SDAE \hat{m}_{GN} will be similar to the corresponding original model m during training the SDAE. During data assimilation, \hat{m}_{GN} becomes m_i^b in equation (1) after passing the cutoff method.

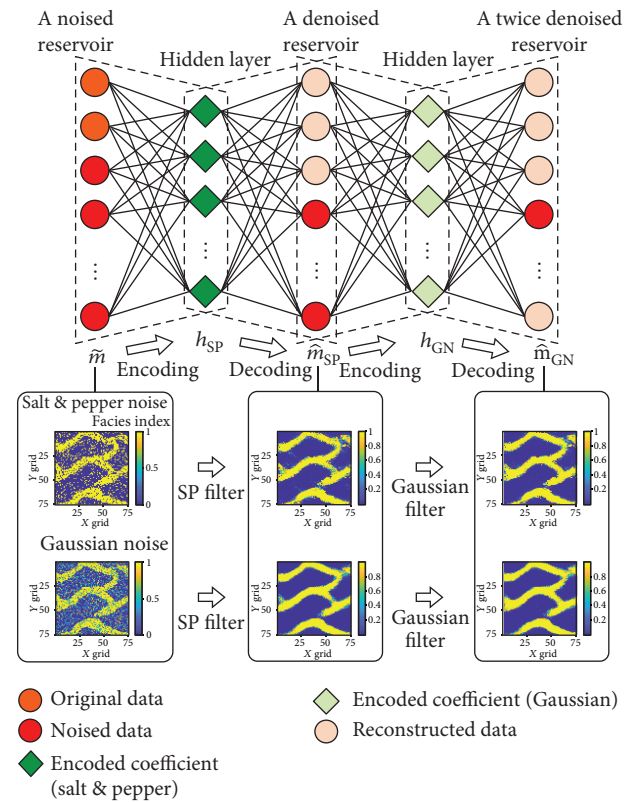
2.3. Extraction of Geologic Features Using Discrete Cosine Transform. An efficient reduction of the number of parameters can contribute to improving the history matching performance [1, 15, 17]. Discrete cosine transform (DCT) presents finite data points in a sum of coefficients of cosine functions at different frequencies [44]. Figure 6 depicts



(a)



(b)



(c)

FIGURE 5: (a) A denoising autoencoder eliminating salt and pepper noise. (b) A denoising autoencoder eliminating Gaussian noise. (c) A serial denoising autoencoder with the original, noise, and purified reservoir models.

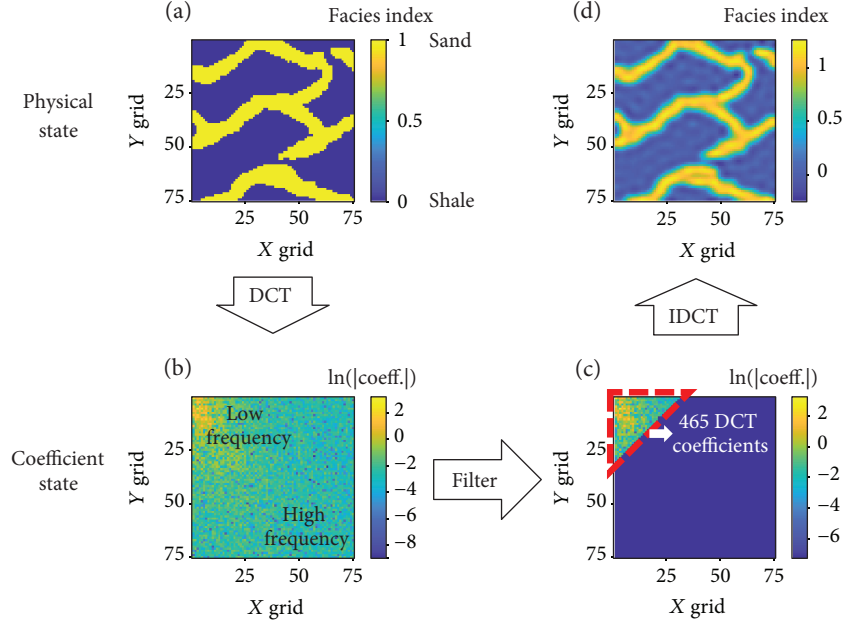


FIGURE 6: Example of discrete cosine transform (DCT) and inverse DCT (IDCT) applied to the reproduction of shale and sand facies of a channelized reservoir.

an example that applies DCT for extracting features of a channelized reservoir model. Figure 6(a) shows an image of physical parameters (e.g., facies) for a channel reservoir. The DCT application to Figure 6(a) yields Figure 6(b) which shows a distribution of DCT coefficients. In Figure 6(b), DCT coefficients are arranged following an order of cosine frequencies: the upper left part is filled with lower (i.e., more essential) frequencies of cosine functions, and the lower right part is filled with higher frequencies of the functions. DCT coefficients in the lower-frequency region (regarded as essential) have higher energy (for representing the channel image) than those in the higher-frequency region. The total number of DCT coefficients is the same as the number of gridblocks: $75 \times 75 = 5,625$. The number of the upper left coefficients is 465 which is equal to the sum $\sum_{i=1}^{30} i$: from 30 DCT coefficients on the 1st row to 1 DCT coefficient on the 30th row. Throughout this study, the number of essential rows is constant at 30. Hence, the number of essential DCT coefficients N_{DCT} becomes 465 if any data assimilation algorithm is combined with DCT. Thus, the data compression ratio is approximately 12.1 ($\approx 5,625/465$). In Figure 6(c), the coefficients in the upper left part within the red dotted triangle are preserved while the other coefficients are assumed as zero (corresponding to the negative infinity in the color scale). Figure 6(d) shows that a channel image reconstructed using the 465 DCT coefficients is similar to the original image shown in Figure 6(a). This reconstruction is referred to as inverse DCT (IDCT). Due to the data compression, the channel borders get blurred in Figure 6(d). Nevertheless, it seems that Figure 6(d) reliably restores the main channel trend of Figure 6(a).

2.4. Construction of Geologic Dictionaries. Sparse coding is the process used to calculate representative coefficients for

the prototype models composing a geologic dictionary [45–47]. The premise of sparse coding is that geomodels are presented with a weighted linear combination of the prototype models [48, 49]. Once a library Y is built with a large number of sample geomodels, K-SVD extracts essential features from Y and then constructs both the dictionary matrix D and its weight matrix X : $Y \cong DX$ [16]. Orthogonal matching pursuit (OMP) aids the decomposition of Y [50, 51].

Figure 7 compares sparse coding to construct geologic dictionaries using K-SVD and OMP in the original facies domain and in the DCT domain. The procedure starts with constructing the library matrix Y (a N_{para} by N_{lib} matrix in Figure 7(c)) which consists of a variety of channel reservoir realizations generated by SNESIM (Figure 7(b)) with a given training image (Figure 7(a)). Herein, N_{para} is the number of parameters in each reservoir realization and N_{lib} is the number of reservoir realizations in Y . In Figure 7(c), N_{para} equals N_{grid} . Applying OMP and K-SVD decomposes Y into D and X (Figure 7(d)). Strictly speaking, the multiplication of D and X produces Y' , which is the reconstructed Y (see the right-hand side of Figure 7(d)). D is a N_{grid} by N_{dict} matrix and X is a N_{dict} by N_{lib} matrix. D and Y' are visualized in Figures 8(a) and 8(b), respectively.

The above procedure to construct D and X can be carried out in the DCT domain as well if each reservoir realization is transformed into DCT coefficients (Figure 7(e)). For this modified sparse coding, Figure 7(f) shows that applying K-SVD and OMP builds D_{DCT} (Figure 8(c)) and Y'_{DCT} (Figure 8(d)) of which the dimensions are N_{DCT} by N_{dict} and N_{dict} by N_{lib} , respectively. It appears that both procedures sufficiently capture the channel connectivity and pattern of the original realizations (compare Figures 8(b) and 8(d) with Figure 7(b)). Also, N_{DCT} is typically smaller than N_{grid} for dimensionality reduction. For this reason, the

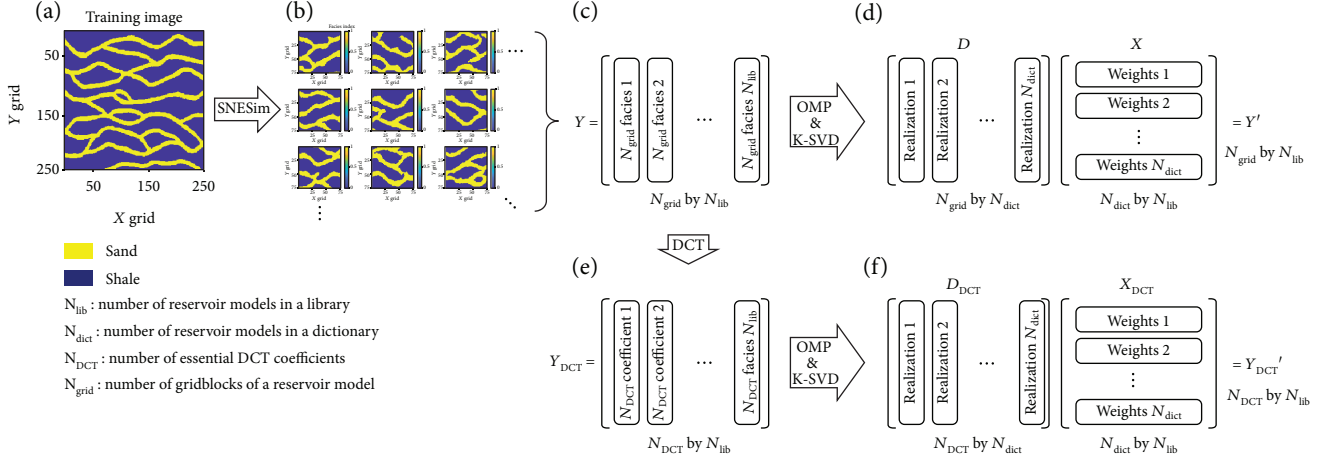


FIGURE 7: Construction of sparse geologic dictionaries using K-SVD without and with DCT: (a) training image, (b) generation of the initial channel models (Y) using SNESIM, (c) organization of the models in a matrix, (e) transformation of Y into DCT coefficients, and construction of D and X from Y using K-SVD in (d) facies domain and (f) in DCT domain.

computational cost of sparse coding is reduced more in the DCT domain than in the original grid domain [16, 23]. Furthermore, the previous work by the authors [23] claimed that iterating the modified sparse coding has the potential to improve the overall history matching performance of a channelized reservoir by updating the geologic dictionary in every assimilation of ES-MDA. N_{qual} qualified ensemble members are selected for the efficient update of the geologic dictionary. More details on iterative update of sparse geologic dictionaries can be found in [23].

2.5. Integration of DCT, K-SVD, and SAE in ES-MDA with SDAE. In this study, ten variants of ES-MDA are investigated to analyze the effects of SDAE on history matching performance of a channelized reservoir. Table 1 summarizes state vectors and postprocesses of the ten ES-MDA algorithms. Note, some algorithms are integrated with one or more of the transformation techniques addressed in Section 2. The first to fifth ES-MDA algorithms update the reservoir models without the SDAE. The sixth to tenth ES-MDA algorithms (which correspond to the first to fifth algorithms in numerical order) apply the SDAE as a noise remover to the ensemble update addressed in equation (1).

Figure 9 shows the flowchart of the ten algorithms. First, the N_{lib} (thousands of) reservoir models are realized using SNESIM (Figure 9(a)) for considering various geological scenarios [17, 18, 23]. For the parameterization techniques, the K-SVD uses the whole realization pool for constructing the geologic dictionary (see the left box of Figure 9(a)). The SAE and SDAE utilize some realizations as their training data. The initial ensemble is composed of randomly selected N_{ens} realizations from the pool (see the right box of Figure 9(a)). As shown in Figure 9(b), forward reservoir simulation is run for the initial ensemble and the initial parameters are imported to the ten algorithms (depending on their transformation techniques). For each ES-MDA algorithm, the transformed parameters are updated using the Kalman gain (Figure 9(c)). For example, for the first algorithm, the facies indexes (i.e., 0 for shale and 1 for

sand) are the target parameters of the reservoir models updated using the conventional ES-MDA without any transformation. These original coefficients are transformed into the DCT domain for the second algorithm. The third algorithm updates weight coefficients of K-SVD [23]. The fourth algorithm adjusts weight coefficients of K-SVD in the DCT domain with an iterative update of the dictionary matrix [23]. The fifth algorithm updates coefficients encoded using SAE (as described in Section 2.2.1). It should be clarified that the SAE and SDAE have different purposes. Similar to the DCT, the SAE is used to represent the facies distribution of a reservoir model in a lower dimension. The number of nodes in the hidden layer of the SAE equals the number of representatives. Meanwhile, the SDAE introduced in Section 2.2.4 aims at purifying the reservoir models in each data assimilation.

The updated reservoir parameters are retransformed into the facies domain to figure out the updated reservoir realizations in the physical state (see the left box in Figure 9(d)). Neither 0 nor 1 facies values are changed as 0 or 1 using the cut-off (see the right box in Figure 9(d)). In this study, 0.5 is the threshold facies value distinguishing sand from shale. The ensemble update is repeated until the assimilation count p reaches the number of assimilations N^a (Figure 9(e)). After the final assimilation is complete, well behaviors are predicted through forward simulation for the updated reservoir models (Figure 9(f)).

3. Results and Discussion

The ten ES-MDA algorithms addressed in Table 1 were applied to history matching and production forecasts of a channelized gas reservoir to investigate the efficacy of denoising using the proposed SDAE on ensemble-based reservoir model calibration. Section 3.1 provides the field description and experimental settings for the algorithms. Section 3.2 describes experimental settings for SAE and SDAE. The simulation results of the ten algorithms are compared

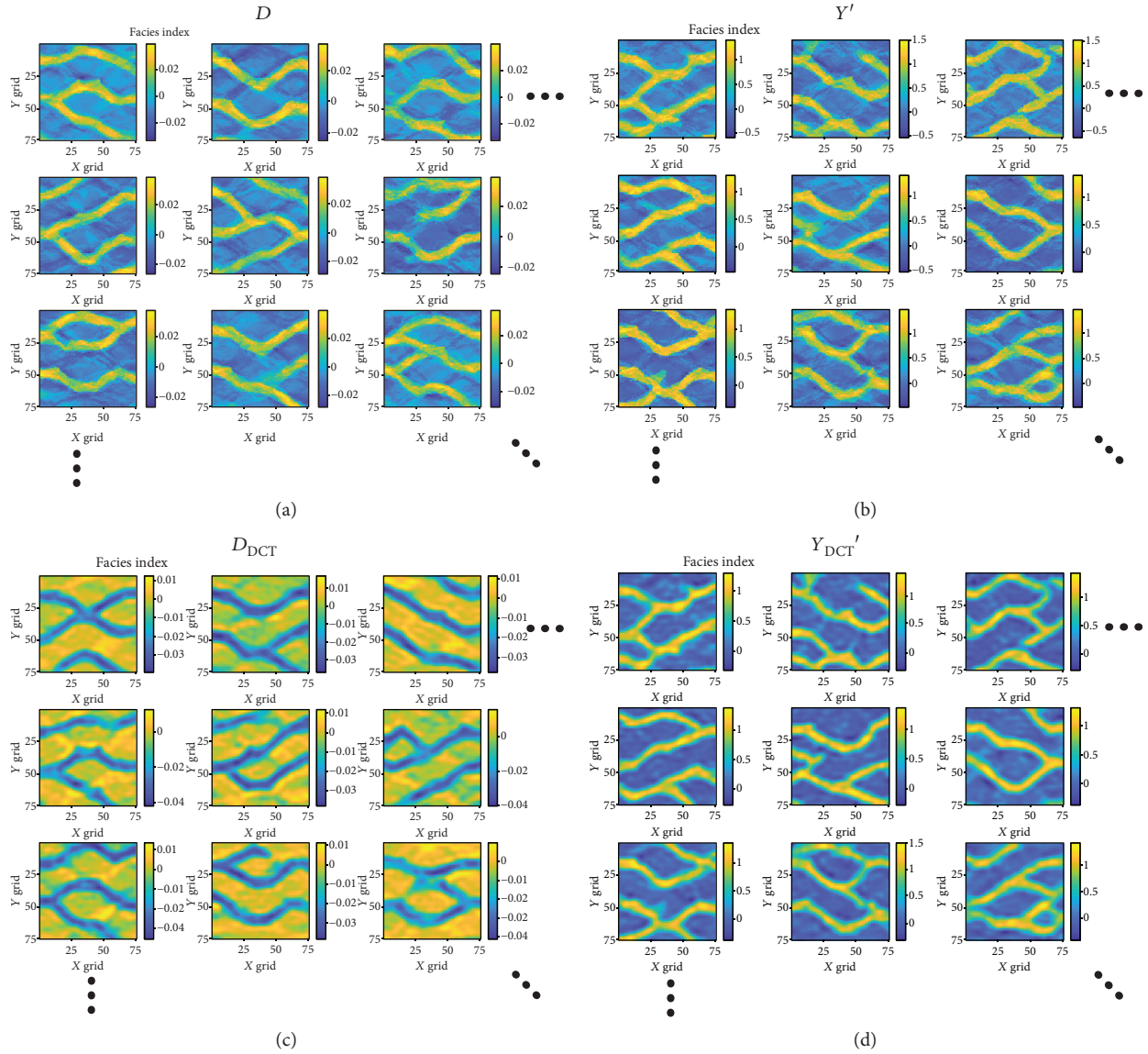


FIGURE 8: Reservoir realizations of dictionaries and reconstructed libraries from Figure 7. (a, b) D and Y' of Figure 7(d), respectively. (c, d) D_{DCT} and Y_{DCT}' of Figure 7(f), respectively.

TABLE 1: Comparison of state vectors and postprocesses after each assimilation for ten ES-MDA algorithms investigated in this study.

	State vector m	Postprocess after every assimilation
Algorithm w/o denoising		
ES-MDA	Facies index	
ES-MDA-DCT	DCT coefficients in facies domain	
ES-MDA-K-SVD	Weight matrix X in facies domain	Cutoff
ES-MDA-DCT-i-K-SVD	X in DCT domain	
ES-MDA-SAE	Encoded coefficients in facies domain	
Algorithm w/ denoising		
ES-MDA	Facies index	SPN filter
ES-MDA-DCT	DCT coefficients in facies domain	↓
ES-MDA-K-SVD	Weight matrix X in facies domain	GN filter
ES-MDA-DCT-i-K-SVD	X in DCT domain	↓
ES-MDA-SAE	Encoded coefficients in facies domain	Cutoff

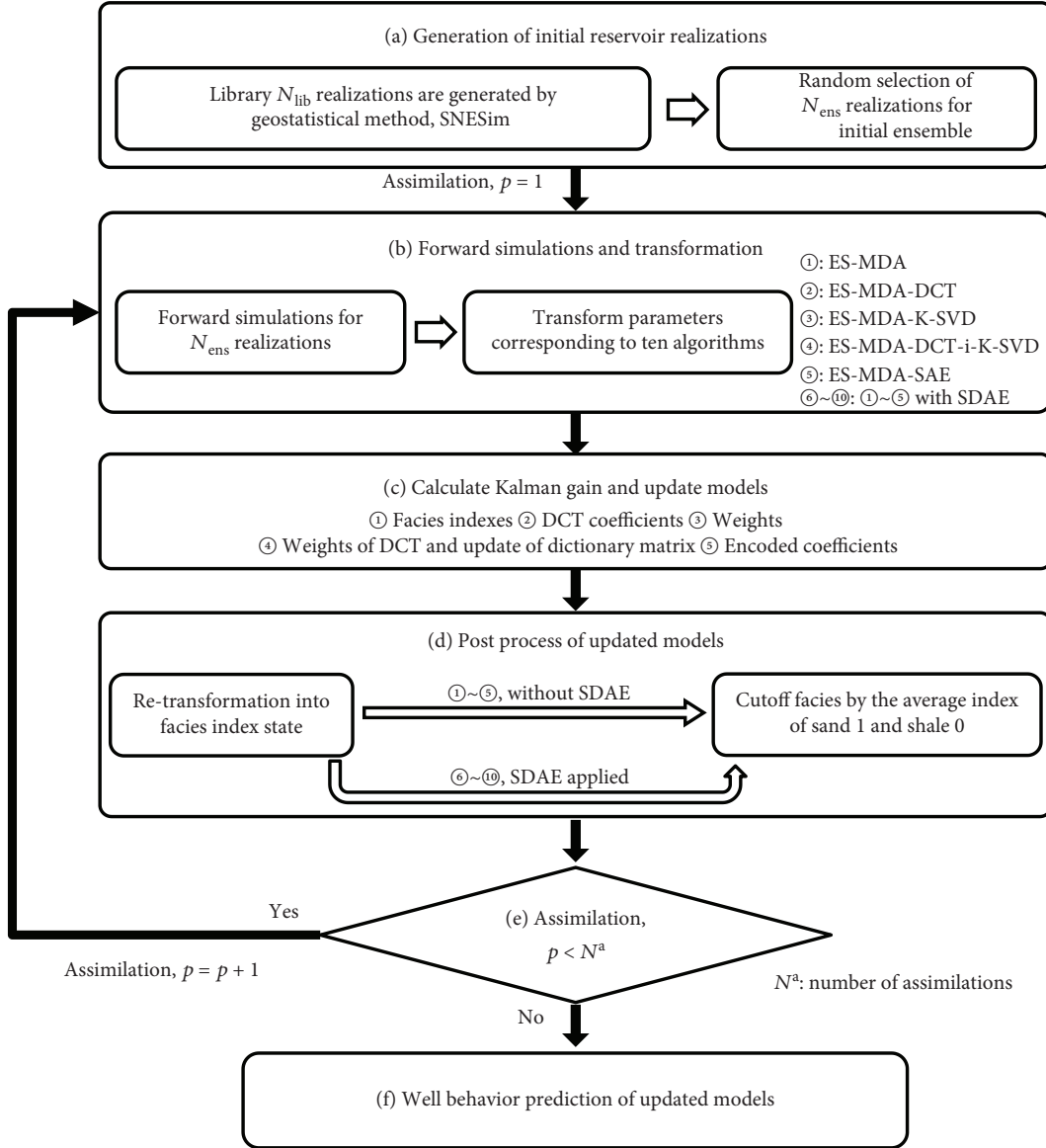


FIGURE 9: Flowchart of ten ES-MDA algorithms conducted in this study.

regarding history-matched and history-predicted production rates (Section 3.3), updated facies distribution (Section 3.4), and error estimation (Section 3.5).

3.1. Field Description. Table 2 summarizes properties of a channelized gas reservoir model applied to the ES-MDA algorithms. This gas reservoir is composed of two facies: sand and shale. Boundaries of the gas reservoir are attached to a numerical aquifer modelled by pore volume multiplication.

Figure 10 shows the training image (Figure 10(a)) and reference model (Figure 10(b)) employed for the ten algorithms. Sixteen vertical gas production wells are set up: eight wells (P1, P4, P6, P7, P9, P12, P14, and P15) are drilled in the sand formation while the other eight wells (P2, P3, P5, P8, P10, P11, P13, and P16) are drilled in the shale formation. Facies information at the well locations

are used as hard data of SNESIM that realizes the reference model and N_{lib} reservoir realizations.

Table 3 describes well coordinates, operating conditions, and simulation period for history matching and forecast. The total simulation period was 7,000 days: 3,500 days for history matching was followed by production forecasts for 3,500 days. Target parameters of history matching were gas production rate and bottomhole pressure (BHP). Water production rate was regarded as the watch parameter (thus excluded from the matching targets).

Table 4 presents the number of the reservoir models and parameters used for the ten algorithms. $N^a = 4$ and $\alpha_p = 4$ according to equation (4) for all the ES-MDA algorithms.

3.2. Experimental Settings for SAE and SDAE. Recall that the SDAE was designed for denoising updated ensemble members, while the SAE was adopted as a feature extraction tool

TABLE 2: Reservoir properties of the channelized gas reservoir.

Parameter	Value
Number of gridblocks in the x -direction (dimensionless)	75
Number of gridblocks in the y -direction (dimensionless)	75
Number of gridblocks in the z -direction (dimensionless)	1
Grid size (ft ³)	200 × 200 × 100
Initial gas saturation (fraction)	0.75
Initial water saturation (fraction)	0.25
Initial reservoir pressure (psia)	3,000
Index of sand facies (dimensionless)	1
Index of shale facies (dimensionless)	0
Permeability of sand facies (md)	300
Permeability of shale facies (md)	0.1

(such as the DCT). All autoencoders were developed using the *trainAutoencoder* toolbox in MATLAB [40].

Table 5 describes experimental settings for the SDAE. As the SDAE was the sequence of SPN and GN filters (Figure 5(c)), the number of hidden nodes in each filter was the same. With the 15% visiting probability, SPN altered the rock facies values of the visited gridblocks either from 0 to 1 or vice versa for each training the reservoir model. The SPN filter was trained with 2,100 noise reservoir models: 700 clean reservoir models were equiprobably noise three times. The number of the reservoir models used for training the GN filter was 2,000. All the training models originated from one clean model. For each training model, GN contaminated all gridblocks with the mean of 0 and standard deviation of 0.35. If a contaminated value of a gridblock was smaller than the minimum facies index of 0, the minimum was assigned to that gridblock. Also, the maximum of 1 was assigned if a value exceeded the maximum.

Table 6 describes hyperparameters used for the SAE. 5,625 gridblocks were represented by 465 node values in the second hidden layer via 2,500 node values in the first hidden layers. Note, the number of SAE coefficients in the second hidden layer is kept equal to the number of DCT coefficients for a fair comparison throughout the study.

3.3. History Matching and Forecasts of Dynamic Data.

Figure 11 presents profiles of gas production rate during the 10-year history matching and the following 10-year prediction periods. Figures 11(a)–11(e) are the profiles obtained using the five ES-MDA algorithms uncoupled with SDAE. Figures 11(f)–11(j) are those obtained using the algorithms coupled with SDAE. In each subfigure, the solid grey and light blue lines represent the production behaviors of the initial and final updated ensembles, respectively. The dark blue line corresponds to the mean of the final ensemble. The red line indicates the production profile from the reference model (Figure 10(b)) regarded as actual data. The profiles at the production wells (P1, P4, P9, and P15) located

on the sand formation were presented because these wells near the reservoir boundary were sensitive to the aquifer water influx in this case study.

For all ten ES-MDA algorithms, the updated ensembles decreased the discrepancies between the reference and updated ensemble models compared to the initial ensembles. Furthermore, the comparison of the subfigures indicates the denoising using the SDAE was effective to improve both matching and prediction accuracy during data assimilation. The five ES-MDA algorithms with SDAE yielded better performance (Figures 11(f)–11(j)) than the uncoupled algorithms (Figures 11(a)–11(e)) after the assimilations were complete. For the updated ensembles, reservoir uncertainty was somewhat left at well P15 during the prediction period. This was because the decrease in gas rate due to water breakthrough was hardly observed at this well during the history matching period. As shown in the reference model, the inflow from the numerical aquifer could arrive at well P15 after breaking through wells P12 or P14. This late water breakthrough caused the remaining uncertainty at well P15 despite the satisfactory assimilation results at the other wells. Figure 12 shows well BHP profiles during both periods. Every final ensemble got conditioned to the reference data sufficiently. This yielded the narrow bandwidth of the simulation results including the reference data at most wells. Also, denoising effects caused by the use of the SDAE were captured at well P15.

Figure 13 compares matched and predicted water production rate at the four production wells. Discrepancies between the updated ensemble mean profiles (dark blue lines) and the reference profiles (red lines) remained in the results of the ES-MDA algorithms without SDAE. For example, simulation results were somewhat unmatched to observations at well P1 in Figure 13(a) and at well P4 in Figure 13(b). The SDAE was effective in correcting these discrepancies. When comparing Figures 13(a)–13(e) and corresponding Figures 13(f)–13(j), both matching and prediction accuracy improved due to the coupling of SDAE and ES-MDA. In particular, remarkable improvements due to denoising were captured in prediction at wells P4 and P9. At wells P9 and P15, discrepancies were observed but acceptable considering water rate was used as the watch parameter and not used for history matching.

3.4. Distribution of Facies and Permeability after History Matching.

Figure 14 presents the evolution of an ensemble member obtained using the ES-MDA coupled with the SDAE method over four assimilations. The row number indicates the assimilation sequence. The first column presents the ensemble member obtained using ES-MDA (Figure 14(a)). The second column shows the member denoise using the SPN filter (Figure 14(b)). The denoise model was purified again using the GN filter, as shown in the third column (Figure 14(c)). Channel features blurred in Figure 14(a) improved significantly by passing the two filters in sequence. The filtering functionality of the trained SDAE refined the facies value of each gridblock in the ensemble member similar to 0 (i.e., shale) or 1 (i.e., sand). Finally, applying the cutoff

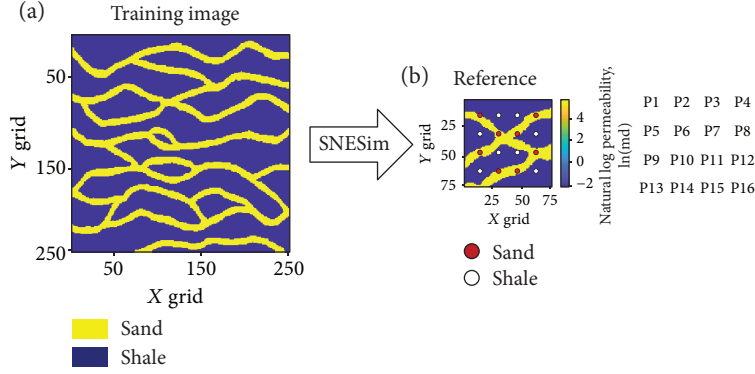


FIGURE 10: Training images and the reference model used for history matching. P1 to P16 indicate well numbers.

TABLE 3: Experimental settings for reservoir simulation.

Parameter	Value
Observed well data	Gas rate and BHP
Maximum well gas production rate (Mscf/day)	15,000
Minimum well BHP (psia)	1,000
Total simulation period (days)	7,000
History matching period (days)	3,500
Prediction period (days)	3,500
Coordinates of well locations in sand facies (dimensionless)	(14, 14), (62, 14), (30, 30), (46, 30), (14, 46), (62, 46), (30, 62), (46, 62)
Coordinates of well locations in shale facies (dimensionless)	(30, 14), (46, 14), (14, 30), (62, 30), (30, 46), (46, 46), (14, 62), (62, 62)

TABLE 4: Number of parameters used for the ten ES-MDA algorithms.

Parameter	Symbol	Value
Number of the static reservoir models used for constructing an initial library matrix Y	N_{lib}	3,000
Number of the static reservoir models used for constructing an initial dictionary matrix D	N_{dict}	1,000
Number of gridblocks in each reservoir model	N_{grid}	5,625
Number of filtered DCT coefficients in each reservoir model	N_{DCT}	465
Number of ensemble members	N_{ens}	100
Number of qualified ensemble members	N_{qual}	20

to the filtered model yielded the prior model of the next assimilation (Figure 14(d)). The cutoff delivered the models only composed of sand and shale facies.

Figure 15 compares the updated permeability distributions obtained using the ten ES-MDA algorithms. The first row of Figure 15 deploys the reference field and the mean of the initial ensemble members. The initial ensemble mean reveals high dissimilarity to the reference in terms of channel

TABLE 5: Experimental settings for the SDAE.

Parameter	Value or function	
Transfer function	Logistic sigmoid function	
Backpropagation algorithm	Levenberg-Marquardt	
	SPN filter	GN filter
Number of nodes in the hidden layer	5,000	5,000
Number of the reservoir models used for training the filter	2,100	2,000

TABLE 6: Experimental settings for the SAE.

Parameter	Value or function
Transfer function	Logistic sigmoid function
Backpropagation algorithm	Levenberg-Marquardt
Number of nodes in the first hidden layer	2,500
Number of nodes in the second hidden layer	465
Number of nodes in the third hidden layer	2,500
Number of the models used for training the SAE	100

connectivity and pattern. The average maps of the updated ensemble members obtained using the ten algorithms are arrayed in the second and third rows. The conventional ES-MDA without SDAE had broken and thus had geologically less plausible channels due to the direct perturbation of gridblock pixels (i.e., facies) (Figure 15(a)). Though coupling DCT with ES-MDA reduced the pixel heterogeneity, the quality of the ensemble mean was less satisfactory. ES-MDA-K-SVD showed better results than the two previous algorithms. However, there was a room for improvement regarding connectivity between wells P9 and P14 (Figure 15(c)). For the ES-MDA-DCT-i-K-SVD, inconsistent channel widths and broken connectivity between wells P1 and P6 were observed (Figure 15(d)). Similar to the ES-MDA-K-SVD, ES-MDA-SAE suffered from the connectivity issue (Figure 15(e)).

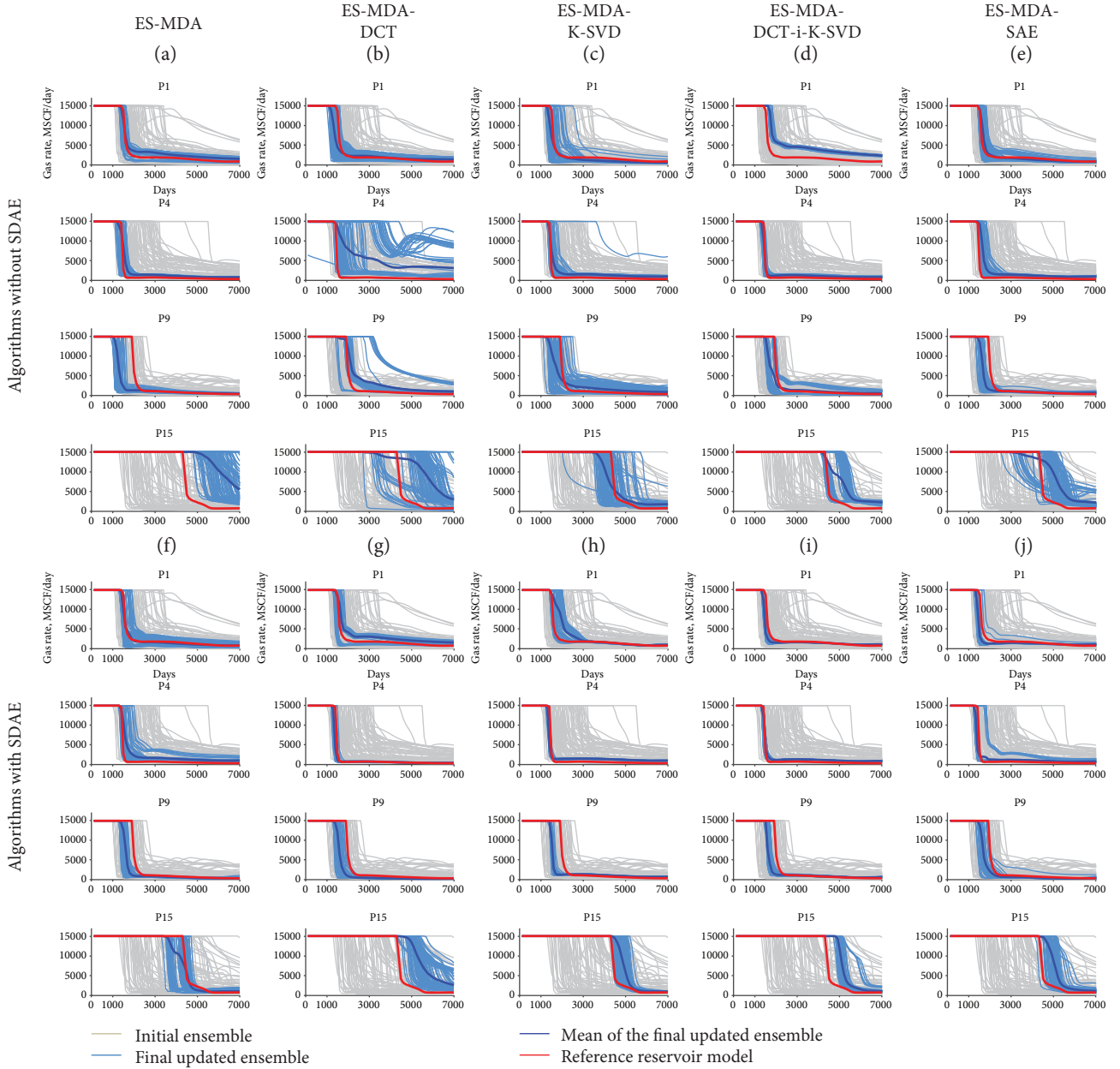


FIGURE 11: Profiles of gas production rate at the four wells (P1, P4, P9, and P15) obtained by executing the ten ES-MDA algorithms. The latter five algorithms from (f) to (j) are the algorithms coupled with SDAE.

When comparing the plots on the second and third rows in the same column, the results obtained using the five ES-MDA algorithms with SDAE (Figures 15(f)–15(j)) preserved the main X-shaped channel patterns with consistent channel width, though Figures 15(g)–15(j) had unexpected channel connectivity between wells P9 and P14. In the case of Figures 15(b) and 15(g), it seems that coupling feature extraction techniques (such as DCT and SAE) might deteriorate history matching performance due to data compression of a reservoir realization. The same issue was seen in Figures 15(e) and 15(j). An improvement in the results is expected if an optimal number of essential coefficients and hyperparameters are used for the transformation. In

summary, the above results imply a well-trained machine learning-based noise remover has the potential to preserve geological plausibility of a target reservoir model during ensemble-based history matching.

Figure 16 displays error histograms of facies distributions for the final ensembles. The error equals $N_m/N_{\text{grid}} \times 100(\%)$, where N_m is the number of facies-unmatched gridblocks where the updated facies are different from the facies in the reference model. Histograms are scaled 0 to 50 for the y -axis to make the results more readable. Note, the sum of the frequencies for ensemble members is 100 in each histogram. For the initial ensemble, the range of errors is between 17 and 37% (see the first row of Figure 16). All

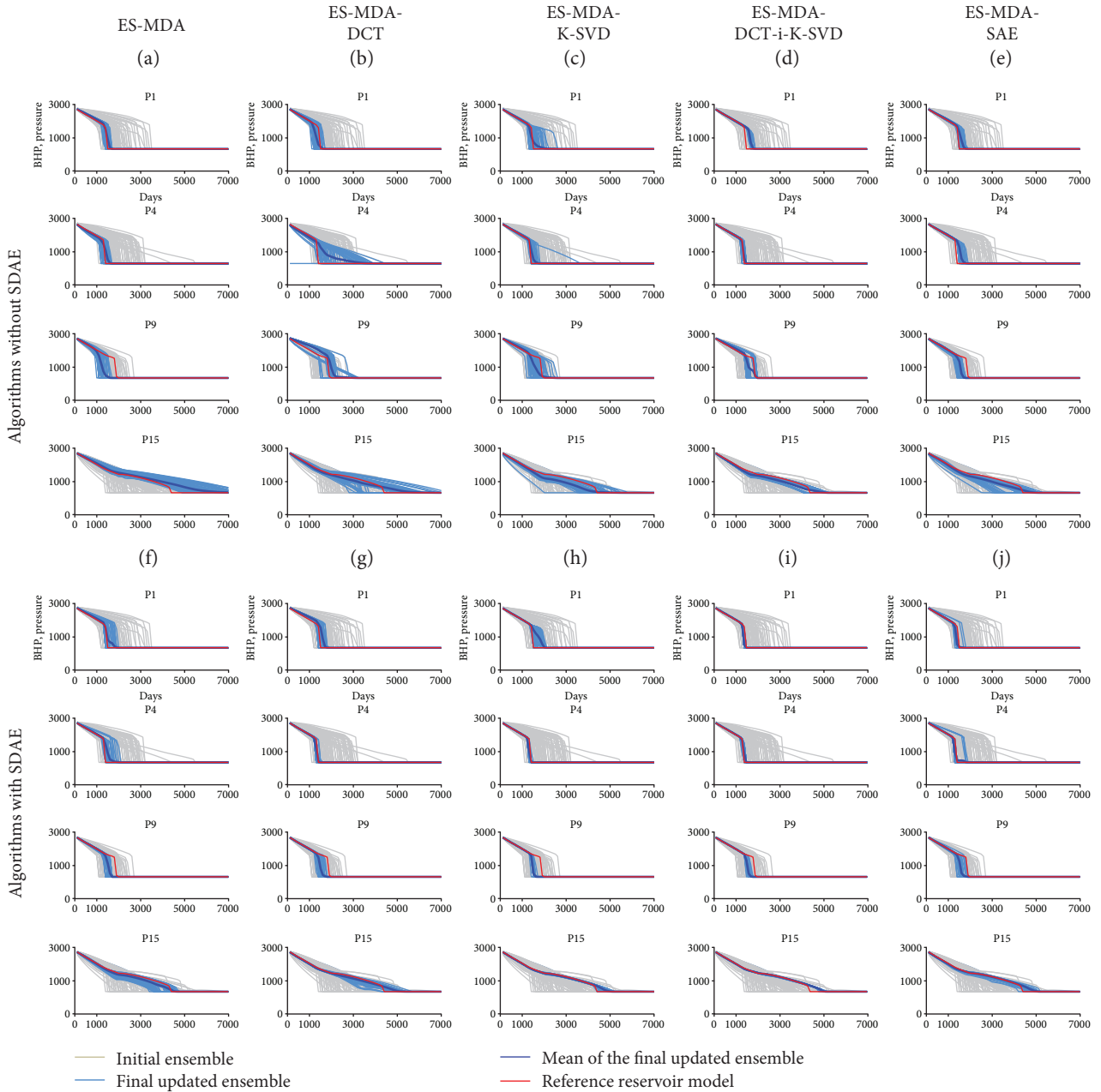


FIGURE 12: Profiles of BHP at the four wells (P1, P4, P9, and P15) obtained by executing the ten ES-MDA algorithms. The latter five algorithms from (f) to (j) are the algorithms coupled with SDAE.

ten algorithms decreased errors compared to the initial ensemble. The ES-MDA-SAE had a smaller error range (Figures 16(e) and 16(j)) than the other algorithms uncoupled (Figures 16(a)–16(d)) or coupled with the SDAE (Figures 16(f)–16(i)). In Figures 16(e) and 16(j), histogram bars are cut because of the scale. Embedding the SDAE in the ES-MDA contributed to reducing errors regardless of which transformation technique was combined with the ensemble-based data assimilation algorithm. Note, the results of the quantitative error analysis addressed in Figure 16 do not often correspond to the qualitative analysis

of geological plausibility shown in Figure 15. For example, it appears Figure 15(i) has more similar geological patterns to the reference model in comparison with Figure 15(j). Also, Figure 16(i) had higher error values than Figure 16(j). This incompatibility emphasizes the importance of a multisource data interpretation.

Tables 7 and 8 summarize the discrepancies between observation and simulation results for dynamic data (gas rate, water rate, and BHP) during the history matching and prediction periods, respectively. The discrepancies were calculated for the wells located on the sand channel as the

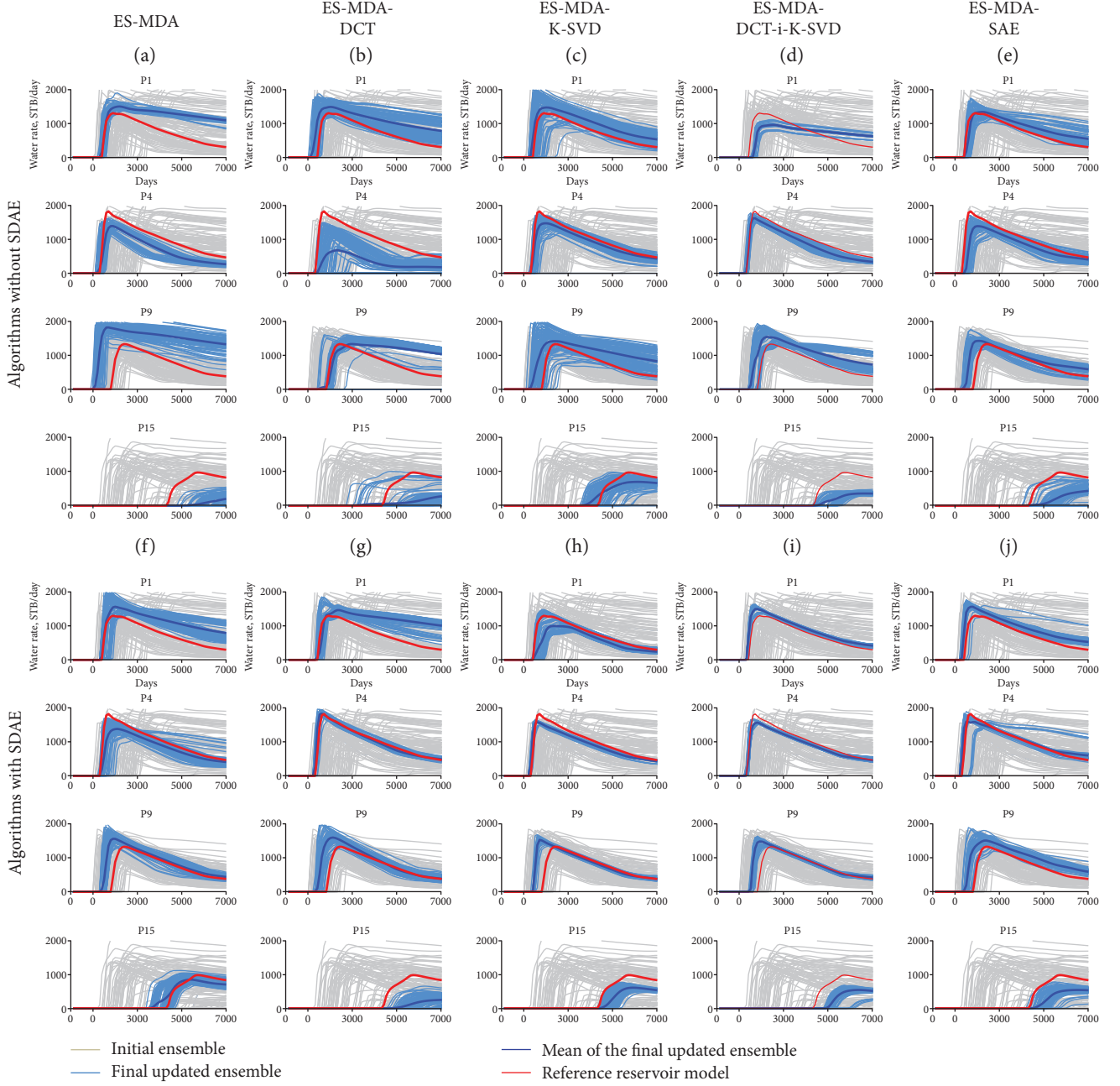


FIGURE 13: Profiles of water production rate at the four wells (P1, P4, P9, and P15) obtained by executing the ten ES-MDA algorithms. The latter five algorithms from (f) to (j) are the algorithms coupled with SDAE.

cumulative gas production was insignificant at the wells on the shale background.

The quality of the updated ensemble was quantified using the equations as follows:

$$\varepsilon_i = \frac{1}{N_d} \sum_{j=1}^{N_d} \left(\frac{d_j - d_j^{\text{obs}}}{d_j^{\text{obs}}} \right)^2, \quad \text{for } i = 1, \dots, N_{\text{ens}}, \quad (13)$$

$$\mu_\varepsilon = \frac{(1/N_{\text{ens}}) \sum_{i=1}^{N_{\text{ens}}} \varepsilon_i^{\text{upd}}}{(1/N_{\text{ens}}) \sum_{i=1}^{N_{\text{ens}}} \varepsilon_i^{\text{init}}} \times 100(\%), \quad (14)$$

$$\sigma_\varepsilon = \frac{\sqrt{(1/N_{\text{ens}} - 1) \sum_{i=1}^{N_{\text{ens}}} (\varepsilon_i^{\text{upd}} - \overline{\varepsilon_i^{\text{upd}}})^2}}{\sqrt{(1/N_{\text{ens}} - 1) \sum_{i=1}^{N_{\text{ens}}} (\varepsilon_i^{\text{init}} - \overline{\varepsilon_i^{\text{init}}})^2}} \times 100(\%), \quad (15)$$

where $\varepsilon_{i,\text{type}}$ is the error of the i th ensemble member in terms of each dynamic data type, μ_ε is the normalized mean of ε , and σ_ε is the normalized standard deviation of ε . The superscripts upd and init indicate the updated and initial ensemble members, respectively.

The overall ensemble quality was improved using the SDAE as the errors were significantly reduced after SDAE

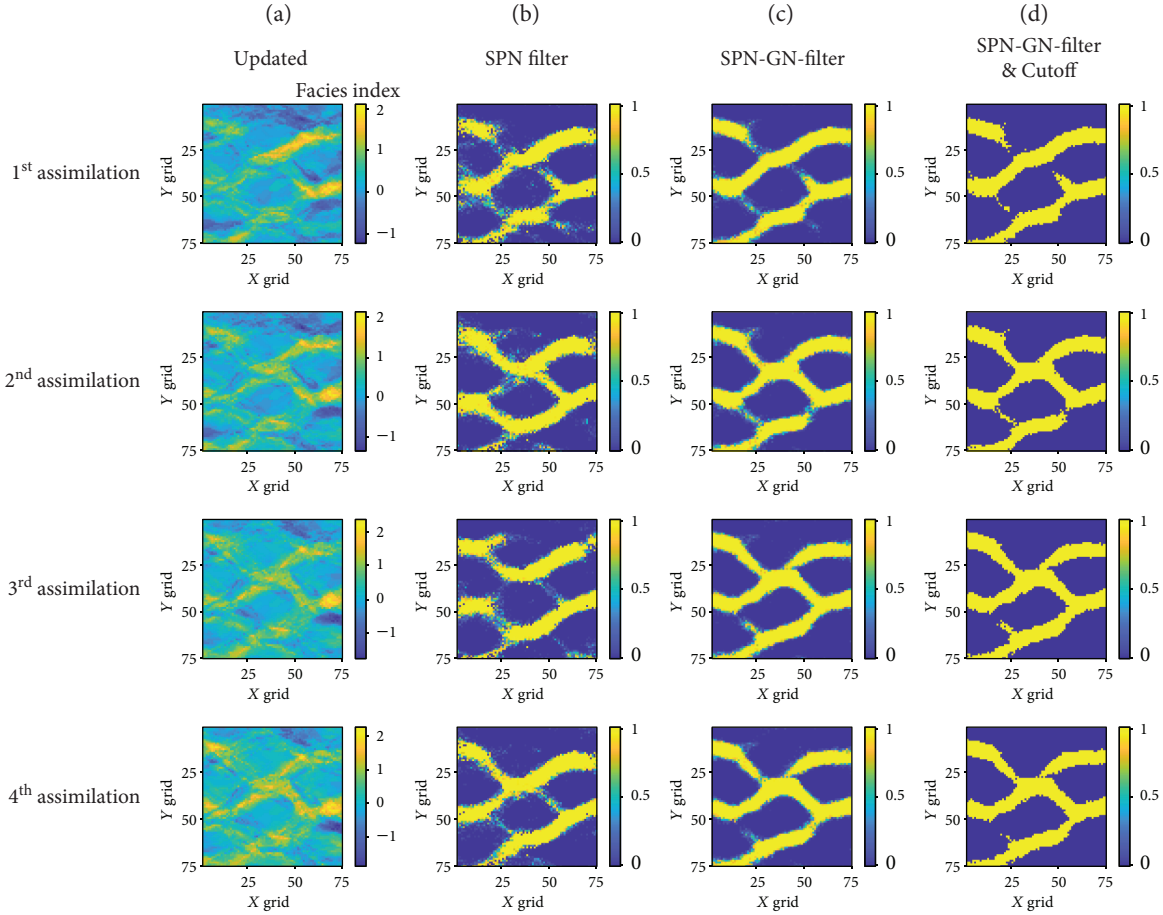


FIGURE 14: Updated facies distribution results of the first ensemble member in every assimilation by the ES-MDA with SDAE.

activation. The SDAE helped any ES-MDA algorithm reduce μ_ϵ and σ_ϵ . For example, μ_ϵ for the matched gas rate obtained using ES-MDA without and with the SDAE were 20.98% and 5.17%, respectively. σ_ϵ was also reduced from 40.23% to 8.27%. Furthermore, the average values of μ_ϵ and σ_ϵ for the ES-MDA algorithms were decreased for all data types after coupling the SDAE. For the history matching, the average error values of gas rate, water rate, and BHP were improved from 13.44% to 4.95%, from 76.85% to 37.65%, and from 21.04% to 13.14%, respectively. For the prediction, the average error values went from 35.29% to 5.39%, from 6.29% to 6.78%, and from 53.03% to 18.18%, respectively. The ES-MDA-DCT yielded ϵ values greater than 100% for the prediction, which indicated the degradation of the ensemble. This phenomenon claims any less- or unoptimized feature extraction might cause the deterioration of the ensemble quality.

3.5. Computational Costs for the Denoising Process. Table 9 summarizes the computational cost required for executing the transformation and denoising methods embedded in the ES-MDA. The specification of the computer used in this study was Intel (R) Core (TM) i7-8700 CPU at 3.2 GHz with 16 GB RAM. The cost for reservoir simulation was excluded

from Table 9 because each ES-MDA algorithm expended the same cost for the ensemble update. The total number of reservoir simulation runs was 400, which was the product of the ensemble size (100) and the number of assimilations (4). The machine learning-based methods were more expensive than the transformation methods. It took a few seconds for the activation of the DCT to transform and reconstruct reservoir facies in each assimilation. It took approximately 3.6 hours for the K-SVD to construct the library and weight matrices, as addressed in [23]. In contrast, the ES-MDA-DCT-i-K-SVD needed only about one-ninth of the time for the ES-MDA-K-SVD due to the dimension reduction of reservoir parameters by DCT. It took approximately 8.7 hours to train the SAE. The SDAE was the most computationally expensive method. It took 17.9 hours to train the two filters: 7.2 hours for the SPN filter and 10.7 hours for the GN filter. Nonetheless, the overall results addressed in this study highlight the efficacy of the proposed SDAE as a supplementary tool to the data assimilation algorithm for improving the ensemble quality. Once developed, the noise remover could be easily applied to other algorithms without additional learnings. It is also anticipated that the development of computer hardware will enhance the efficacy of soft computing for big data machine learning.

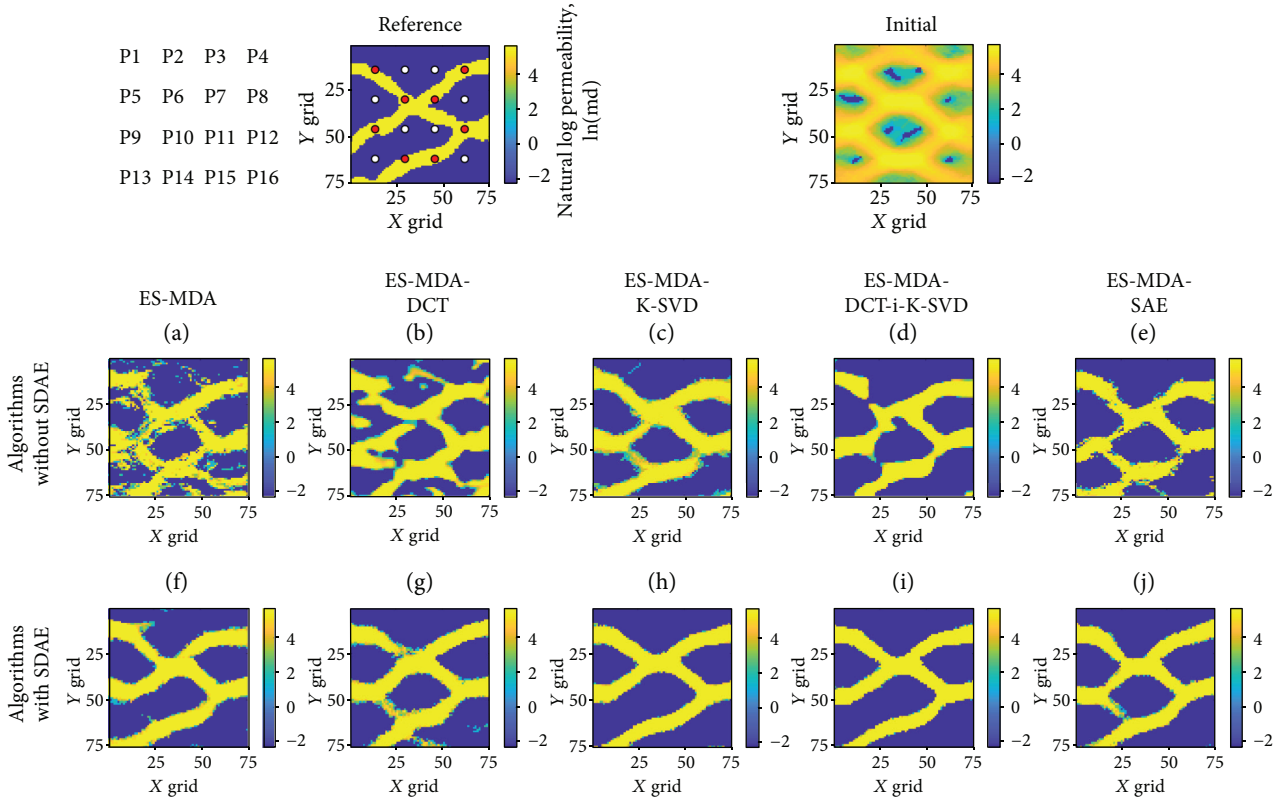


FIGURE 15: Permeability distributions of the ensemble mean maps obtained using the ten ES-MDA algorithms.

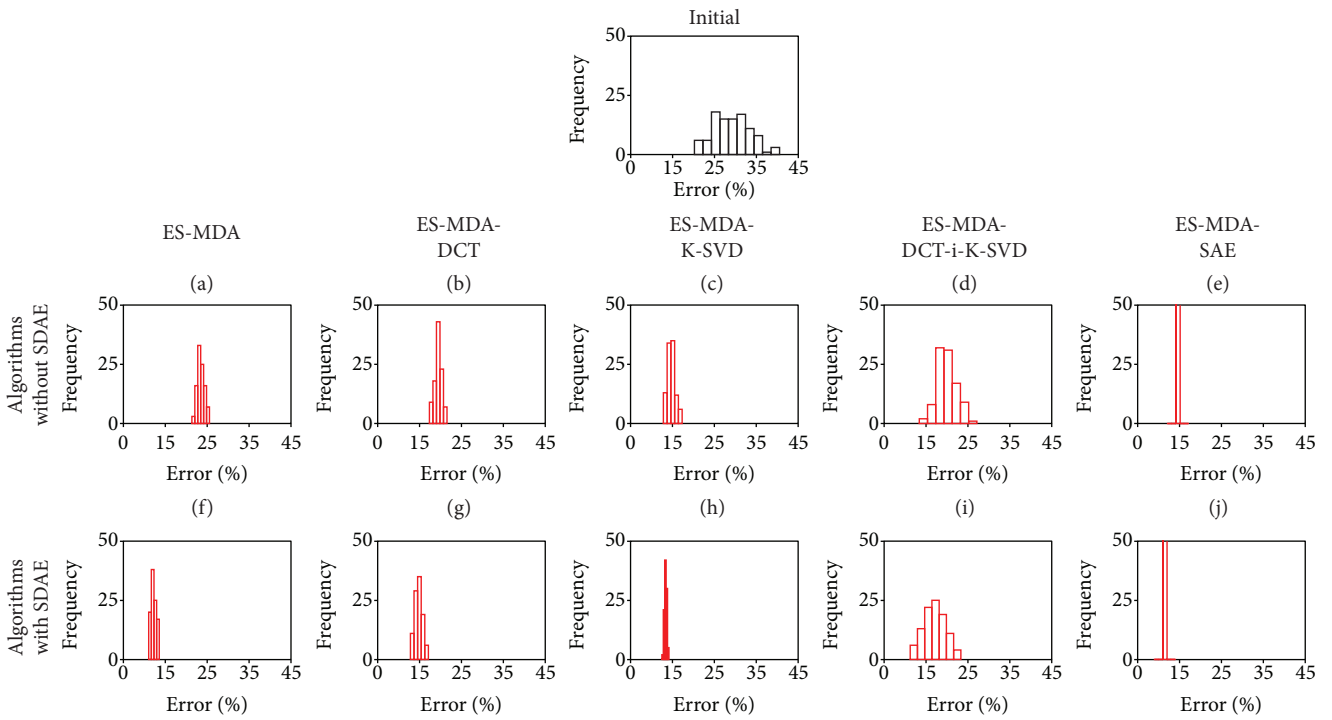


FIGURE 16: Error histograms for facies distribution of the final ensembles obtained using the ten ES-MDA algorithms.

TABLE 7: Statistical parameters of history matching errors for gas rate, water rate, and BHP (only for the wells installed in the sand formation). μ_ε and σ_ε refer to the mean and standard deviation of errors, respectively.

	Gas rate		Water rate		BHP	
	μ_ε (%)	σ_ε (%)	μ_ε (%)	σ_ε (%)	μ_ε (%)	σ_ε (%)
ES-MDA without SDAE						
ES-MDA	20.98	40.23	223.13	91.10	24.17	31.73
ES-MDA-DCT	27.74	43.94	41.66	25.55	31.08	32.64
ES-MDA-K-SVD	5.49	13.40	46.73	52.59	13.72	17.32
ES-MDA-DCT-i-K-SVD	2.08	3.66	41.00	19.63	14.96	8.62
ES-MDA-SAE	10.89	12.80	31.70	18.67	21.27	10.69
Average	13.44	22.80	76.85	41.51	21.04	20.20
ES-MDA with SDAE						
ES-MDA	5.17	8.27	39.99	30.40	16.48	21.51
ES-MDA-DCT	4.55	10.08	41.22	31.27	15.37	13.85
ES-MDA-K-SVD	4.60	6.91	53.49	12.48	15.48	12.85
ES-MDA-DCT-i-K-SVD	6.92	8.29	29.34	12.55	9.69	4.82
ES-MDA-SAE	3.50	6.78	24.22	19.82	8.66	15.74
Average	4.95	8.07	37.65	21.30	13.14	13.75

TABLE 8: Statistical parameters of prediction errors for gas rate, water rate, and BHP (only for the wells installed in the sand formation). μ_ε and σ_ε refer to the mean and standard deviation of errors, respectively.

	Gas rate		Water rate		BHP	
	μ_ε (%)	σ_ε (%)	μ_ε (%)	σ_ε (%)	μ_ε (%)	σ_ε (%)
ES-MDA without SDAE						
ES-MDA	48.00	35.27	0.56	0.88	97.46	135.43
ES-MDA-DCT	105.83	136.65	16.03	16.40	88.58	57.90
ES-MDA-K-SVD	6.61	17.23	6.97	8.44	24.93	21.78
ES-MDA-DCT-i-K-SVD	6.44	2.23	2.61	1.92	37.27	37.20
ES-MDA-SAE	9.57	12.58	5.19	2.16	16.90	23.16
Average	35.29	40.79	6.27	5.96	53.03	55.09
ES-MDA with SDAE						
ES-MDA	2.48	3.12	10.28	12.38	19.16	35.29
ES-MDA-DCT	12.98	12.57	1.72	1.66	31.59	14.63
ES-MDA-K-SVD	4.20	1.10	3.77	1.56	13.35	5.15
ES-MDA-DCT-i-K-SVD	4.24	4.19	8.24	3.14	11.22	1.84
ES-MDA-SAE	3.06	2.10	9.89	4.24	15.59	22.39
Average	5.39	4.62	6.78	4.60	18.18	15.86

TABLE 9: Comparison of the computational cost required for executing an auxiliary module embedded in ES-MDA.

Algorithm	Auxiliary module	Computational cost (hour)
ES-MDA	N/A	0.0
ES-MDA-DCT	DCT	Less than 0.1
ES-MDA-K-SVD	K-SVD	3.6
ES-MDA-DCT-i-K-SVD	Iterative K-SVD in DCT domain	0.4
ES-MDA-SAE	SAE	8.7
SDAE	SPN filter + GN filter	$7.2 + 10.7 = 17.9$

4. Conclusions

The SDAE was implemented as the postprocessor of ES-MDA for enhancing the preservation of geological plausibility during ensemble-based history matching. The SDAE is composed of SPN and GN filters facilitating and purifying the updated reservoir models resulting from the smoothing effects. The denoising effects were investigated by comparing the results of the five ES-MDA algorithms coupled with the SDAE and those uncoupled. The application was to history matching of the channelized gas reservoir. The results obtained using ten different algorithms showed the performance difference between the cases with and without the

SDAE in terms of production data matching and geological plausibility. The SDAE showed excellent accuracy in history matching and prediction for gas rate, water rate, and BHP. Executing the SDAE decreased the average matching error by 75% in the ES-MDA results. The SDAE was also efficient for improving the performance of the ES-MDA algorithms combined with the data transformation methods. The improvement in the matching and prediction accuracy of dynamic data resulted from the conservation of geological plausibility achieved using the SDAE. Consequently, the purified models followed the discrete bimodal distribution for mimicking the channelized reservoir while maintaining channel width and connectivity consistently. These results highlight the potential of the machine learning-based noise remover as an efficient auxiliary method that enhances the performance of ensemble-based history matching if the proxy is designed properly at affordable computational cost.

Nomenclature

b_{enc} :	Bias vector of the neural network in an encoder
b_{dec} :	Bias vector of the neural network in a decoder
C_D :	Covariance matrix of observed measurement error
C_{dd} :	Autocovariance matrix of simulation data d
C_{md} :	Cross-covariance matrix of state vector m and simulation data d
d :	Simulation data
d^{obs} :	Observation data
d^{unc} :	Perturbed observation data
\bar{d} :	Mean of simulation data
D :	Dictionary matrix
E :	Loss function
$f_{\text{AE}}(\bullet)$:	Encoder function of autoencoder
$f_{\text{DAE}}(\bullet)$:	Encoder function of denoising autoencoder
$g_{\text{AE}}(\bullet)$:	Decoder function of autoencoder
$g_{\text{DAE}}(\bullet)$:	Decoder function of denoising autoencoder
h :	Encoded coefficient
m :	State vector of a reservoir model
\bar{m} :	Mean of state vectors
\tilde{m} :	Noise reservoir model
\hat{m} :	Reconstructed reservoir model
m^{b} :	State vector of a reservoir model before an update
I_{N_d} :	Identity matrix
K :	Number of parameters in a model for training
N :	Number of models for training
N^{a} :	Number of assimilations
N_d :	Number of time steps in observations
N_{DCT} :	Number of essential DCT coefficients
N_{dict} :	Number of reservoir models in the dictionary matrix D
N_{ens} :	Number of ensemble members
N_{grid} :	Number of gridblocks in a reservoir model
N_{lib} :	Number of reservoir models in the library matrix Y
N_{node} :	Number of nodes in a hidden layer
N_{train} :	Number of reservoir models used for AE training
N_{para} :	Number of parameters in a reservoir model
w :	Weight coefficients of a node in a hidden layer
W_{dec} :	Weight matrix of the neural network in a decoder

W_{enc} :	Weight matrix of the neural network in an encoder
x_{kn} :	Each value of model parameters for autoencoder training
X :	Weight matrix
Y :	Library matrix
Y' :	Reconstructed library matrix
z_d :	Random error to observations
α_p :	Inflation coefficients of C_D
β :	Sparsity regularization term in the loss function
ε :	Error
λ :	Coefficient for L2 regularization term
ρ :	Desire average output activation measure
$\hat{\rho}$:	Average output activation measure of a node in a hidden layer
μ :	Mean
Ω_W :	Sum of squared weights in the loss function
Ω_s :	Sparsity of network links between nodes of two layers
σ :	Standard deviation.

Subscripts

AE:	Autoencoder
DAE:	Denoising autoencoder
DCT:	Discrete cosine transform
dec:	Decoder
dict:	Dictionary
enc:	Encoder
ens:	Ensemble
lib:	Library
para:	Parameter
s:	Sparsity
train:	Training
type:	Dynamic data type
W :	Weight.

Superscripts

a:	Assimilation
b:	Before update
dec:	Decoding
enc:	Encoding
init:	Initial
obs:	Observation
upd:	Update.

Data Availability

The data used to support the findings of this study are available from the corresponding author upon request.

Disclosure

Part of this study was presented at the 2018 AGU Fall Meeting.

Conflicts of Interest

The authors declare no conflict of interest.

Acknowledgments

The authors acknowledge Schlumberger for providing reservoir simulation software. This research was supported by the Basic Science Research Program through the National Research Foundation of Korea (NRF) funded by the Ministry of Education (NRF-2018R1A6A1A08025520) and Global Infrastructure Program through the NRF funded by the Ministry of Science and ICT (NRF-2017K1A3A1A05069660). Dr. Sungil Kim was partially supported by the Basic Research Project of the Korea Institute of Geoscience and Mineral Resources (Project No. GP2017-024).

References

- [1] X. Luo, T. Bhakta, M. Jakobsen, and G. Nævdal, "An ensemble 4D-seismic history-matching framework with sparse representation based on wavelet multiresolution analysis," *SPE Journal*, vol. 22, no. 3, pp. 985–1010, 2017.
- [2] G. Evensen, "Sequential data assimilation with a nonlinear quasi-geostrophic model using Monte Carlo methods to forecast error statistics," *Journal of Geophysical Research*, vol. 99, no. C5, pp. 10143–10162, 1994.
- [3] G. Nævdal, T. Manneseth, and E. H. Vefring, "Near-well reservoir monitoring through ensemble Kalman filter," in *SPE/DOE Improved Oil Recovery Symposium*, Tulsa, OK, USA, April 2002, SPE-75235-MS.
- [4] F. Bouttier and P. Courtier, *Data Assimilation Concepts and Methods*, Meteorological Training Course Lecture Series, European Centre for Medium-Range Weather Forecasts, 2002.
- [5] D. S. Oliver and Y. Chen, "Recent progress on reservoir history matching: a review," *Computational Geosciences*, vol. 15, no. 1, pp. 185–221, 2011.
- [6] P. J. Van Leeuwen and G. Evensen, "Data assimilation and inverse methods in terms of a probabilistic formulation," *Monthly Weather Review*, vol. 124, no. 12, pp. 2898–2913, 1996.
- [7] A. A. Emerick and A. C. Reynolds, "History matching time-lapse seismic data using the ensemble Kalman filter with multiple data assimilations," *Computational Geosciences*, vol. 16, no. 3, pp. 639–659, 2012.
- [8] K. Park and J. Choe, "Use of ensemble Kalman filter with 3-dimensional reservoir characterization during waterflooding," in *SPE Europec/EAGE Annual Conference and Exhibition*, Vienna, Austria, June 2006, Paper No. 100178.
- [9] R. J. Lorentzen, G. Nævdal, and A. Shafieirad, "Estimating facies fields by use of the ensemble Kalman filter and distance functions—applied to shallow-marine environments," *SPE Journal*, vol. 3, no. 1, pp. 146–158, 2012.
- [10] Y. Shin, H. Jeong, and J. Choe, "Reservoir characterization using an EnKF and a non-parametric approach for highly non-Gaussian permeability fields," *Energy Sources, Part A: Recovery, Utilization, and Environmental Effects*, vol. 32, no. 16, pp. 1569–1578, 2010.
- [11] K. Lee, S. Jung, and J. Choe, "Ensemble smoother with clustered covariance for 3D channelized reservoirs with geological uncertainty," *Journal of Petroleum Science and Engineering*, vol. 145, pp. 423–435, 2016.
- [12] X. Luo, A. S. Stordal, R. J. Lorentzen, and G. Nævdal, "Iterative ensemble smoother as an approximate solution to a regularized minimum-average-cost problem: theory and applications," *SPE Journal*, vol. 20, no. 5, pp. 962–982, 2015.
- [13] H. Zhou, L. Li, and J. J. Gómez-Hernández, "Characterizing curvilinear features using the localized normal-score ensemble Kalman filter," *Abstract and Applied Analysis*, vol. 2012, Article ID 805707, 18 pages, 2012.
- [14] S. Kim, C. Lee, K. Lee, and J. Choe, "Aquifer characterization of gas reservoirs using ensemble Kalman filter and covariance localization," *Journal of Petroleum Science and Engineering*, vol. 146, pp. 446–456, 2016.
- [15] Y. Zhao, F. Forouzanfar, and A. C. Reynolds, "History matching of multi-facies channelized reservoirs using ES-MDA with common basis DCT," *Computational Geosciences*, vol. 21, no. 5-6, pp. 1343–1364, 2017.
- [16] M. Aharon, M. Elad, and A. Bruckstein, "K-SVD: an algorithm for designing overcomplete dictionaries for sparse representation," *IEEE Transactions on Signal Processing*, vol. 54, no. 11, pp. 4311–4322, 2006.
- [17] F. Sana, K. Katterbauer, T. Y. Al-Naffouri, and I. Hoteit, "Orthogonal matching pursuit for enhanced recovery of sparse geological structures with the ensemble Kalman filter," *IEEE Journal of Selected Topics in Applied Earth Observations and Remote Sensing*, vol. 9, no. 4, pp. 1710–1724, 2016.
- [18] S. A. Canchumuni, A. A. Emerick, and M. A. Pacheco, "Integration of ensemble data assimilation and deep learning for history matching facies models," in *Offshore Technology Conference*, Rio de Janeiro, Brazil, October 2017, OTC-28015-MS.
- [19] B. Jafarpour and D. B. McLaughlin, "Estimating channelized-reservoir permeabilities with the ensemble Kalman filter: the importance of ensemble design," *SPE Journal*, vol. 14, no. 2, pp. 374–388, 2013.
- [20] S. Kim, C. Lee, K. Lee, and J. Choe, "Characterization of channelized gas reservoirs using ensemble Kalman filter with application of discrete cosine transformation," *Energy Exploration & Exploitation*, vol. 34, no. 2, pp. 319–336, 2016.
- [21] S. Kim, C. Lee, K. Lee, and J. Choe, "Characterization of channel oil reservoirs with an aquifer using EnKF, DCT, and PFR," *Energy Exploration & Exploitation*, vol. 34, no. 6, pp. 828–843, 2016.
- [22] S. Kim, H. Jung, K. Lee, and J. Choe, "Initial ensemble design scheme for effective characterization of three-dimensional channel gas reservoirs with an aquifer," *Journal of Energy Resources Technology*, vol. 139, no. 2, article 022911, 2017.
- [23] S. Kim, B. Min, K. Lee, and H. Jeong, "Integration of an iterative update of sparse geologic dictionaries with ES-MDA for history matching of channelized reservoirs," *Geofluids*, vol. 2018, Article ID 1532868, 21 pages, 2018.
- [24] B. H. Min, C. Park, J. M. Kang, H. J. Park, and I. S. Jang, "Optimal well placement based on artificial neural network incorporating the productivity potential," *Energy Sources, Part A: Recovery, Utilization, and Environmental Effects*, vol. 33, no. 18, pp. 1726–1738, 2011.
- [25] Z. Ma, J. Y. Leung, and S. Zanon, "Integration of artificial intelligence and production data analysis for shale heterogeneity characterization in steam-assisted gravity-drainage reservoirs," *Journal of Petroleum Science and Engineering*, vol. 163, pp. 139–155, 2018.
- [26] I. Jang, S. Oh, Y. Kim, C. Park, and H. Kang, "Well-placement optimisation using sequential artificial neural networks," *Energy Exploration & Exploitation*, vol. 36, no. 3, pp. 433–449, 2017.

- [27] S. Ahn, C. Park, J. Kim, and J. M. Kang, "Data-driven inverse modeling with a pre-trained neural network at heterogeneous channel reservoirs," *Journal of Petroleum Science and Engineering*, vol. 170, pp. 785–796, 2018.
- [28] H. Jeong, A. Y. Sun, J. Lee, and B. Min, "A learning-based data-driven forecast approach for predicting future reservoir performance," *Advances in Water Resources*, vol. 118, pp. 95–109, 2018.
- [29] Y. Liu, W. Sun, and L. J. Durlofsky, "A deep-learning-based geological parameterization for history matching complex models," <https://arxiv.org/abs/1807.02716>.
- [30] M. A. Ranzato, C. Poultney, S. Chopra, and Y. LeCun, "Efficient learning of sparse representations with an energy-based model," in *Advances in Neural Information Processing Systems 19*, pp. 1137–1144, The MIT Press, 2007.
- [31] D. Erhan, Y. Bengio, A. Courville, P. A. Manzagol, and P. Vincent, "Why does unsupervised pre-training help deep learning," *Journal of Machine Learning Research*, vol. 11, pp. 625–660, 2010.
- [32] S. S. Roy, S. I. Hossain, M. A. H. Akhand, and K. Murase, "A robust system for noisy image classification combining denoising autoencoder and convolutional neural network," *International Journal of Advanced Computer Science and Applications*, vol. 9, no. 1, pp. 224–235, 2018.
- [33] P. Vincent, H. Larochelle, I. Lajoie, Y. Bengio, and P. A. Manzagol, "Stacked denoising autoencoders: learning useful representations in a deep network with a local denoising criterion," *Journal of Machine Learning Research*, vol. 11, pp. 3371–3408, 2010.
- [34] L. Chen and W. Y. Deng, "Instance-wise denoising autoencoder for high dimensional data," *Geofluids*, vol. 2016, Article ID 4365372, 13 pages, 2016.
- [35] A. A. Emerick and A. C. Reynolds, "Ensemble smoother with multiple data assimilation," *Computers & Geosciences*, vol. 55, pp. 3–15, 2013.
- [36] Y. Bengio, "Learning deep architectures for AI," *Foundations and Trends® in Machine Learning*, vol. 2, no. 1, pp. 1–127, 2009.
- [37] O. Chapelle, B. Schölkopf, and A. Zien, *Semi-Supervised Learning*, MIT Press, Cambridge, MA, USA, 2006.
- [38] K. Lee, J. Lim, S. Ahn, and J. Kim, "Feature extraction using a deep learning algorithm for uncertainty quantification of channelized reservoirs," *Journal of Petroleum Science and Engineering*, vol. 171, pp. 1007–1022, 2018.
- [39] S. Mohaghegh, "Virtual-intelligence applications in petroleum engineering: part 1—artificial neural networks," *Journal of Petroleum Technology*, vol. 52, no. 9, pp. 64–73, 2013.
- [40] M. H. Beale, M. T. Hagan, and H. B. Demuth, *Deep Learning Toolbox™ Reference*, The MathWorks, Natick, MA, USA, 2018.
- [41] S. Strebelle, "Conditional simulation of complex geological structures using multiple-point statistics," *Mathematical Geology*, vol. 34, no. 1, pp. 1–21, 2002.
- [42] S. Deivalakshmi, S. Sarath, and P. Palanisamy, "Detection and removal of salt and pepper noise in images by improved median filter," in *2011 IEEE Recent Advances in Intelligent Computational Systems*, pp. 363–368, Trivandrum, India, September 2011.
- [43] M. Wang, S. Zheng, X. Li, and X. Qin, "A new image denoising method based on Gaussian filter," in *2014 International Conference on Information Science, Electronics and Electrical Engineering*, pp. 163–167, Sapporo, Japan, April 2014.
- [44] N. Ahmed, T. Natarajan, and K. R. Rao, "Discrete cosine transform," *IEEE Transactions on Computers*, vol. C-23, no. 1, pp. 90–93, 1974.
- [45] K. Kreutz-Delgado, J. F. Murray, B. D. Rao, K. Engan, T. W. Lee, and T. J. Sejnowski, "Dictionary learning algorithms for sparse representation," *Neural Computation*, vol. 15, no. 2, pp. 349–396, 2003.
- [46] M. M. Khaninezhad, B. Jafarpour, and L. Li, "Sparse geologic dictionaries for subsurface flow model calibration: part I. Inversion formulation," *Advances in Water Resources*, vol. 39, pp. 106–121, 2012.
- [47] M. R. Khaninezhad and B. Jafarpour, "Sparse geologic dictionaries for field-scale history matching application," in *SPE Reservoir Simulation Symposium*, Houston, TX, USA, February 2015, SPE-173275-MS.
- [48] L. Li and B. Jafarpour, "Effective solution of nonlinear subsurface flow inverse problems in sparse bases," *Inverse Problems*, vol. 26, no. 10, article 105016, 2010.
- [49] E. Liu and B. Jafarpour, "Learning sparse geologic dictionaries from low-rank representations of facies connectivity for flow model calibration," *Water Resources Research*, vol. 49, no. 10, pp. 7088–7101, 2013.
- [50] T. T. Cai and L. Wang, "Orthogonal matching pursuit for sparse signal recovery with noise," *IEEE Transactions on Information Theory*, vol. 57, no. 7, pp. 4680–4688, 2011.
- [51] J. A. Tropp and A. C. Gilbert, "Signal recovery from random measurements via orthogonal matching pursuit," *IEEE Transactions on Information Theory*, vol. 53, no. 12, pp. 4655–4666, 2007.

Review Article

Recent Advance of Microbial Enhanced Oil Recovery (MEOR) in China

Haicheng She ¹, Debin Kong ², Yiqiang Li ², Zaiqiang Hu, ¹ and Hu Guo ^{2,3}

¹School of Civil Engineering and Architecture, Xi'an University of Technology, Xi'an, 710048 Shaanxi, China

²State Key Laboratory of Petroleum Resources and Prospecting, China University of Petroleum-Beijing, Beijing 102249, China

³School of Petroleum Engineering and Environment Engineering, Yan'an University, Yan'an, 716000 Shaanxi, China

Correspondence should be addressed to Debin Kong; mrdebin@163.com and Hu Guo; truetutors@126.com

Haicheng She and Debin Kong contributed equally to this work.

Received 13 May 2018; Revised 10 August 2018; Accepted 30 October 2018; Published 9 April 2019

Guest Editor: Giorgio Minelli

Copyright © 2019 Haicheng She et al. This is an open access article distributed under the Creative Commons Attribution License, which permits unrestricted use, distribution, and reproduction in any medium, provided the original work is properly cited.

Compared with other enhanced oil recovery (EOR) techniques like gas flooding, chemical flooding, and thermal production, the prominent advantages of microbial enhanced oil recovery (MEOR) include environment-friendliness and lowest cost. Recent progress of MEOR in laboratory studies and microbial flooding recovery (MFR) field tests in China are reviewed. High biotechnology is being used to investigate MFR mechanisms on the molecular level. Emulsification and wettability alternation due to microbial effects are the main interests at present. Application of a high-resolution mass spectrum (HRMS) on MEOR mechanism has revealed the change of polar compound structures before and after oil degradation by the microbial on the molecular level. MEOR could be divided into indigenous microorganism and exogenous microorganism flooding. The key of exogenous microorganism flooding was to develop effective production strains, and difficulty lies in the compatibility of the microorganism, performance degradation, and high cost. Indigenous microorganism flooding has good adaptation but no follow-up process on production strain development; thus, it represents the main development direction of MEOR in China. More than 4600 wells have been conducted for MEOR field tests in China, and about 500 wells are involved in MFR. 47 MFR field tests have been carried out in China, and 12 field tests are conducted in Daqing Oilfield. MFR field test's incremental oil recovery is as high as 4.95% OOIP, with a typical slug size less than 0.1 PV. The input-output ratio can be 1 : 6. All field tests have shown positive results in oil production increase and water cut reduction. MEOR screening criteria for reservoirs in China need to be improved. Reservoir fluid, temperature, and salinity were the most important three parameters. Microbial flooding technology is mature in reservoirs with temperature lower than 80°C, salinity less than 100,000 ppm, and permeability above 5 mD. MFR in China is very close to commercial application, while MFR as quaternary recovery like those in post-polymer flooding reservoirs needs further study.

1. Introduction

Oil and gas remain the main primary energies in the world. Enhanced oil recovery involves how to recover as most original oil in place (OOIP) as possible economically. According to the development stage, it can be divided into primary recovery (natural energy development), secondary recovery (water injection or gas injection to main reservoir pressure), and tertiary recovery [1]. Tertiary recovery is also known as

enhanced oil recovery (EOR), which includes polymer flooding, surfactant flooding, gas flooding, thermal production, and microbial enhanced oil recovery (MEOR). The EOR process has two basic features: (a) effectiveness of recovery of more oil and (b) relatively low cost. MEOR is believed to be the cheapest EOR process. To get the goal of highest economical recovery, sound understanding of the basic mechanisms of enhancing oil recovery is necessary, which is sometimes not available to nonpetroleum engineers. Thus,

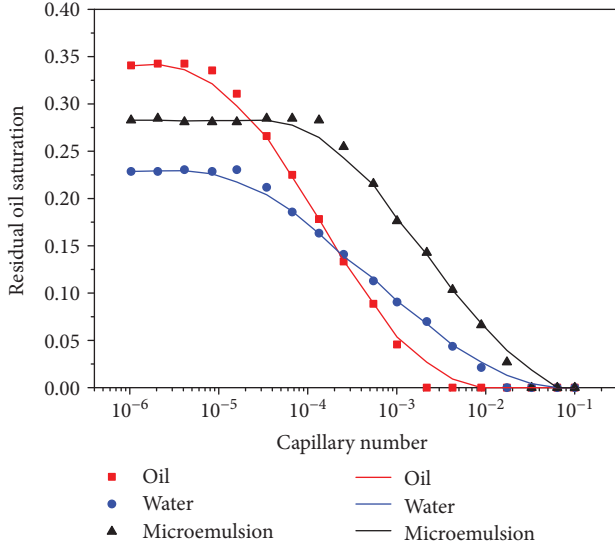


FIGURE 1: Example of a capillary desaturation curve (CDC) [2].

a brief introduction about the basic mechanisms of oil recovery is necessary.

The overall displacement efficiency of any oil recovery displacement process can be considered conveniently as the product of microscopic and macroscopic displacement efficiencies [1]. In equation form,

$$E = E_D \cdot E_V, \quad (1)$$

where E = the overall displacement efficiency (oil recovered by process/oil in place at start of process), E_D = the microscopic displacement efficiency expressed as a fraction, and E_V = the macroscopic (volumetric) displacement efficiency expressed as a fraction. Many factors affect microscopic displacement efficiency, like pore structure and distribution, microscopic heterogeneity, wettability, and interfacial tension. E_D is reflected in the magnitude of residual oil saturation (S_{or}) in the region contacted by the displacing fluid [1]. Factors affecting S_{or} significantly determine E_D . The most significant parameter to affect or determine S_{or} is the capillary number, which is defined as the ratio of viscous force to capillary force. The capillary number has many expressions, and the following is the most frequently used one.

$$N_c = \frac{v\mu}{\sigma}, \quad (2)$$

where N_c = capillary number, σ = interfacial tension (IFT) between displaced and displacing fluid, in mN/m, v = velocity of displacing fluid, in m/s, and μ = viscosity of displacing fluid, in mPa·s.

Many laboratory tests investigated the relationship between N_c and S_{or} and gave well-correlated curves between N_c and S_{or} , which are called capillary desaturation curves (CDC). An example of CDC is shown in Figure 1 [2]. Obviously, the larger the capillary number, the lower the residual oil saturation. From the CDC perspective, the highest

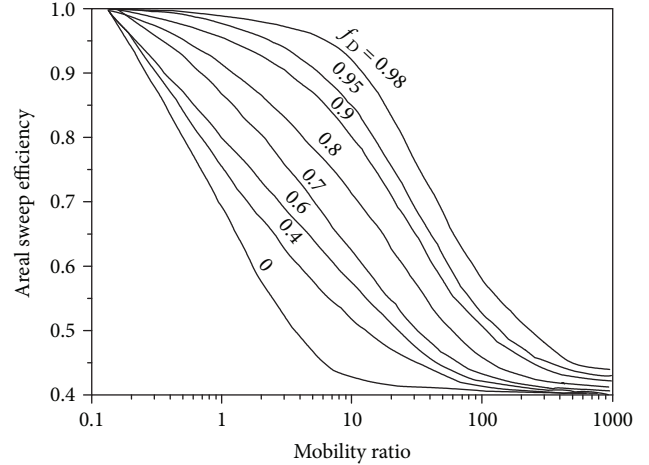


FIGURE 2: Areal sweep efficiency affected by the mobility ratio [1].

displacing viscosity and the lowest IFT are beneficial to the reduction of S_{or} and thus to the increase in displacement efficiency. A higher velocity resulting from a great pressure gradient can also contribute to S_{or} reduction. This is the most basic mechanism of chemical flooding EOR techniques and other techniques.

Macroscopic (volumetric) displacement efficiency (E_V) is also known as sweep efficiency. It can be further expressed as the product of areal sweep efficiency (E_A) and vertical sweep efficiency (E_I).

$$E_V = E_A \cdot E_I, \quad (3)$$

where E_A = area sweep efficiency and E_I = vertical sweep efficiency. Sweep efficiency is determined by reservoir heterogeneity, formation property, and fluid property. For a given reservoir, sweep efficiency is significantly, if not completely, determined by mobility ratio M , which is defined as follows:

$$M = \frac{\lambda_w}{\lambda_o} = \frac{k_w/\mu_w}{k_o/\mu_o} = \frac{k_{rw}}{k_{ro}} \cdot \frac{\mu_o}{\mu_w}, \quad (4)$$

where λ_w = water phase mobility; λ_o = oil phase mobility; k_w and k_o refer to water and oil phase effective permeability, respectively, in D; μ_w and μ_o refer to water viscosity and oil viscosity, in mPa·s; k_{rw} and k_{ro} refer to water and oil phase relative permeability, respectively. Areal sweep efficiency and vertical sweep efficiency affected by the mobility ratio is shown in Figures 2 and 3 [1], respectively. Obviously, as reflected in these two figures, the smaller the mobility ratio, the larger the sweep efficiency, especially when $M < 1$. When $M > 1$, flow becomes unstable and sweep efficiency decreased as M increased. Typically, the mobility ratio M is larger than unity due to the large contrast of oil and water viscosity, especially for heavy oil. To increase the sweep efficiency, the most important way is to reduce the mobility ratio, which can be attained by increasing the water phase viscosity, or reducing the oil viscosity, or improving the relative permeability. This is the key idea of mobility control, which is of vital importance in all EOR techniques.

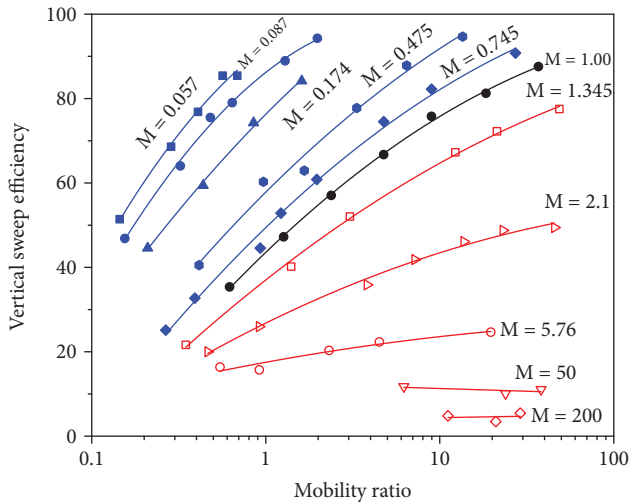


FIGURE 3: Vertical sweep efficiency affected by the mobility ratio [1].

Microbial enhanced oil recovery (MEOR) is a main topic of interest in energy researches as an environment-friendly and low operating-cost treatment technology [3, 4]. MEOR is a general designation of a series of technologies to increase oil production by propagation and metabolites of microbes [5]. The MEOR diagram can be seen in Figure 4 [6]. MEOR also follows the basic EOR principle of enlarging the sweep efficiency and increasing the capillary number. In the current situation of low oil price, MEOR is very promising, especially for the marginal reservoir and/or uneconomical reservoir, and microbial flooding was a potential alternative to other EOR/IOR methods, since it has high success ratio (as high 90% positive effects) according to a worldwide field test survey [4]. MEOR is very environmentally friendly and has no negative environmental impact [7, 8]. Since the implementation of the revised China Environment Protection Law in 2015, environment protection in petroleum exploration and development has never been given more emphasis than ever, which obviously adds to the total cost. Compared with thermal flooding and gas flooding, the preeminent advantages of microbial flooding were environmentally friendly characteristics and the lowest cost for increasing oil production [5, 9]. Compared with other technologies of EOR, the distinct features of microbial flooding include the low energy consumed by microorganisms, the combination of multiple mechanisms, and the reduced loss caused by degradation by some of the endogenous microorganisms [9]. Figure 5 shows different EOR cost estimations [10]. Table 1 [5] also summarizes the cost of different EOR techniques reported in 2002. These data show the relative cost advantages of MEOR compared with other EOR techniques. Although MEOR progress is well reviewed [4, 8], due to the language barrier, much MEOR progress in China is not included. MEOR progress in China is reviewed from both theoretical and practical aspects.

Microbial flooding was used in a wide range, including high water cut, heavy oil [11], marginal reservoir, and post-polymer flooding reservoir [12–16]. It could be applied to sandstone [17], carbonate [18, 19], light oil, heavy oil [11, 20, 21], and medium/high-permeability and low-permeability reservoirs [20, 22, 23].

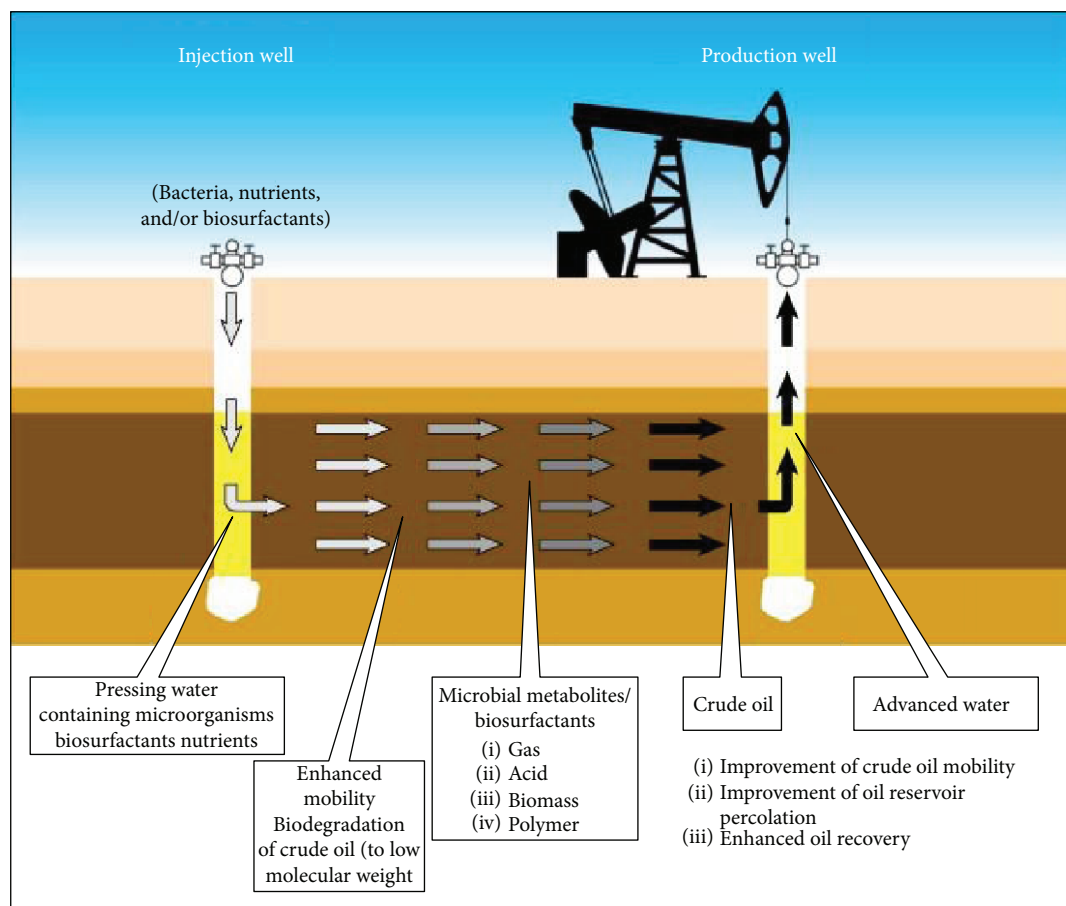
2. Fundamentals of MEOR

2.1. MEOR Types. According to application, MEOR processes can be classified into four types [4]: microbial flooding recovery (MFR), cycle microbial recovery (CMR), microbial selective plugging recovery (MSPR), and others. According to a worldwide implemented field trial survey [4], MFR ranks first in the world among all MEOR trials judged from trial types, as can be seen in Figure 6 [4]. However, the MEOR application in China is quite different. MEOR in China can be divided into microbial flooding recovery (MFR), cycle microbial recovery (CMR), microbial selective plugging recovery (MSPR), and microbial wax removal (MWR). According to our survey of previous MEOR field tests and application in China, if judged from the application of well numbers, the total MEOR well number in China is more than 4600, while there are more than 3000 wells (producers and injectors) for MWR, accounting for about 65%, as can be seen in Figure 7. This figure is a summary of various field tests in China, and it is the first figure to describe MEOR types according to field test well numbers. Up to present, about 500 wells have been involved in MFR in China. These processes often involve more than one mechanism; thus, this classification is general. Since some MEOR data is not public or fully public, our survey involves most but not all MEOR field tests in China.

According to the source of the strains, microbial flooding could also be divided into indigenous microbial flooding and exogenous microbial flooding [9]. Exogenous microorganism indicated that the suitable microbes screened on a similar condition but not in the reservoirs were injected underground and increased oil production by using its propagation and metabolites. Indigenous microorganism means microbes were developed by remaining/residual oil as the carbon source on the basis of the active matter existing in formations and introducing the air and the inorganic salt with phosphorus source and nitrogen source when injecting water [5]. Indigenous microorganism flooding was the development trend with the advantages of good adaptability and avoiding of microbes' culture development and production process.

As introduced before, oil recovery was mainly determined by the displacement efficiency and sweep efficiency. MEOR had a double mechanism of improving the displacement efficiency and sweep oil efficiency [5, 9]. In the laboratory experiments, oil recovery could be increased by 10% by microorganism in a tertiary model [24] and increased by 5% by using microbial flooding and by 16% by combined microbial-chemical flooding in post-polymer flood reservoirs [25]. In another high-permeability (1400 mD) test, oil recovery could be increased by 18.4% [26]. A lot of experiments about microbial flooding and field had been studied in China [27]. The experience of field was not only beneficial to deeply understand microbial flooding mechanisms but also would provide evidence and guideline for industrial application to microbial flooding [5].

2.2. Microbial Community. The study on microbial community in the oil reservoir, especially the accurate analysis of the complex structure of the microbial community and



TRENDS in Biotechnology

FIGURE 4: MEOR diagram [6].

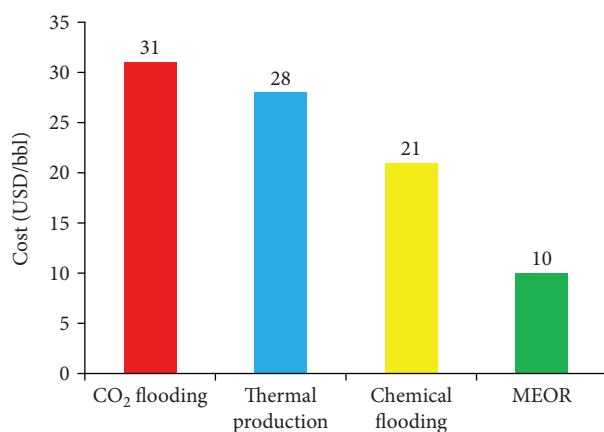


FIGURE 5: Different EOR technique cost estimation [10].

changes in monitoring, had significant importance for microbial flooding [28]. Different methods may be used to classify microbes according to research area or purpose. According to the growth dependence on oxygen, there are aerobic bacteria, facultative bacteria, and anaerobic bacteria in formations [29]. According to influence on oil production, some microbes in the oil reservoir were favorable for oil

production, while others were not. Detecting microbes involves complex high-tech biotechnology, such as terminal restriction fragment length polymorphism (T-RFLP) [11, 16, 23, 30], gene bank [31], denaturing gradient gel electrophoresis (DGGE) [30], and most probable number (MPN) [32], which are beyond the scope of this paper. Microbial community structures and diversity characterization in Shengli Oilfield by such technologies are well documented [30, 33]. Figure 8 [33] shows microbe diversity in the second largest oil production reservoir in China. DGGE application in analyzing microbial diversity and community structure is explained elsewhere [30]. A new way of relating microbes that could not be cultured in extreme environments was provided by the molecular fingerprint technology with 16S rDNA as the main aspect [15, 34], which is important but beyond the understanding of petroleum engineers. Thus, MEOR requires close collaboration of different disciplines like petroleum engineering, chemistry, biology, and physics. The concrete microbes' names and characterization ways in MEOR are available elsewhere [4].

In studies of indigenous microorganism for improved oil recovery, the DGGE method was valuable for analyzing microbial community structures and monitoring community dynamics at the molecular level [35]. The analysis of microbial colony with T-RFLP technology in the pilot tests [36]

TABLE 1: Cost per incremental oil for different EOR techniques [5].

EOR techniques	Steam flooding	Combustion in situ	Gas flooding	Chemical flooding	MEOR
Cost (USD/bbl)	3-6	5-10	2-8	8-12	1-4

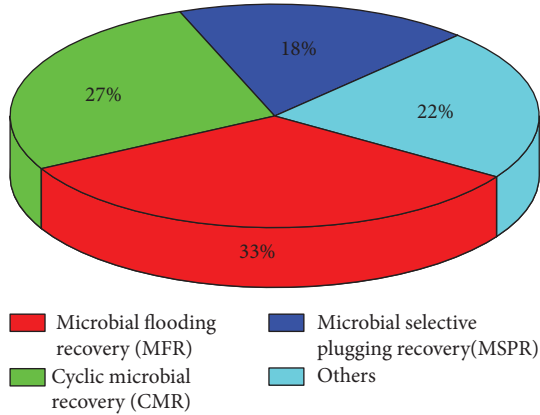


FIGURE 6: Worldwide MEOR trials [4].

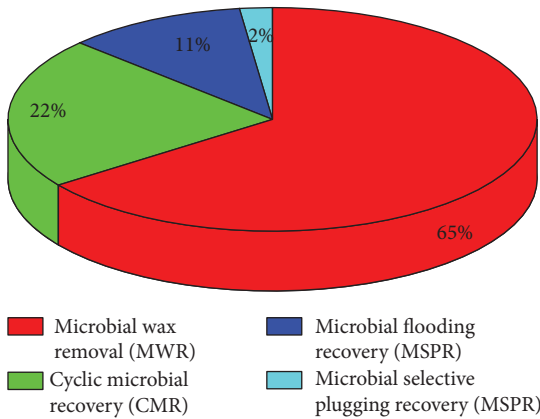


FIGURE 7: MEOR applications in China.

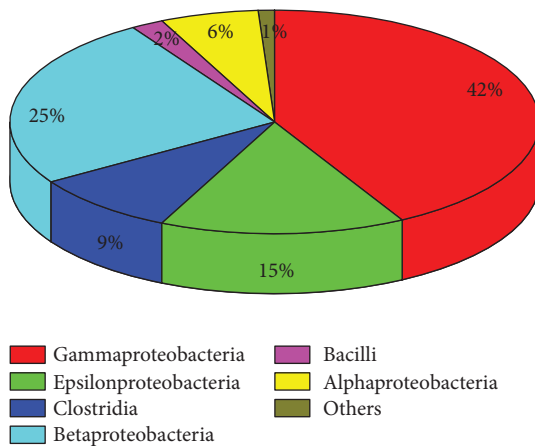


FIGURE 8: The diversity of bacteria in oil reservoirs [33].

in Shengli Oilfield showed the real situation changes of microorganisms in reservoirs, and the changes of diversity of indigenous microbial colony were promoted by the

microbial flooding technology, which are verified by the fact that the diversity of the microorganism in the reservoir was negatively correlated with oil production in general. The core flooding tests [37] showed that the different distribution of crude oil and other metabolites in the core was the key factor affecting the microbial diversity in the reservoir. Studies on Daqing Oilfield [38] showed the number of microorganisms in water after polymer flooding was two orders of magnitude lower than that after water flooding. The field tests also proved that the substrates could be offered from metabolites of aerobic organisms in the formations after being activated by oxygen [29, 34].

2.3. *Exogenous Microorganism and Indigenous Microorganism.* According to the source of the strains, microorganisms can be divided into exogenous microorganisms (EM) and indigenous microorganisms (IM). Thus, microbial flooding recovery could be divided into indigenous microbial flooding recovery (IMFR) and exogenous microbial flooding recovery (EMFR) [9]. Exogenous microorganism indicated that the suitable microbes screened on a similar condition as the reservoir condition but not in the reservoirs were injected underground, increasing oil production by using its propagation and metabolites. Indigenous microorganism meant microbes were developed by using the remaining oil as the carbon source on the basis of the active matter existing in formations and introducing the air and the inorganic salt with phosphorus source and nitrogen source when injecting water [5]. Indigenous microorganism flooding was the development trend with the advantages of good adaptability and avoiding of microbes' culture development and production process. In recent years, the studies in China were generally about indigenous microorganisms [12, 16, 29, 37–40]. As for the carbon source of indigenous microorganisms, many scholars worked on microorganisms that took hydrocarbon in crude oils as the only carbon source [13, 24, 41], while some studied the microorganisms that took both polyacrylamide and hydrocarbon as the carbon source in post-polymer flooding reservoirs [12, 16, 25, 42]. It is worth mentioning that polymer flooding is very mature in China and has the largest commercial scale and production in the world [43].

Some microbes had significant influence on polymer which reduced the viscosity and molecular weight of polymer [12, 44]. The viscosity of polymer decreased by 52.1% in 7 days when microbes were cultured for 7 days without additional nutrition. After sucrose was added, the viscosity reduction of polymer reached 92% [12, 25]. Microbes also had influence on the polymer molecules, hydrolyzing the amide group into carboxylic acid [12, 44]. NMR tests showed that the polymer amide group content decreased from 74.6% to 60.8%, while the carboxylic group had an evident increase [12].

3. EOR Mechanisms

3.1. Oil Degradation by Microorganisms. Reducing oil viscosity is one of the main mechanisms in MEOR [8]. In macroscopic view, oil viscosity reduction is related with oil degradation, while in microscopic view, it is caused by the oil composition change, which are often detected by gas chromatography [5]. Laboratory experiments in Daqing Oilfield showed that the content of long-chain hydrocarbon content in crude oil was relatively decreased after microbial effect, and short- and medium-chain hydrocarbon content was relatively increased, which led to the light component of crude oil increasing by more than 30% [24]. Organic acid was produced to reduce the pH value from 7 to 6 to 5.5, and active material was produced to decrease the viscosity by more than 36% and interfacial tension was reduced from 35.67 mN/m to 8.1 mN/m. Further study [25] showed that after different microbes took effect with Daqing crude oil, the composition of crude oil was changed obviously and the wax and gum chicle content was decreased by 48% and 9.68%, respectively. The average acid value of Daqing crude was 10 times higher than that before and after the effect of suitable microbes [42], which indicated that bioproducts like acids are produced with significant amount.

The application of the high-resolution mass spectrum (HRMS) on the MEOR mechanism has revealed the change of polar compound structures before and after oil degradation by the microbe on the molecular level [45]. The study shows that this degradation mainly involves polar heteroatomic compounds changing from a high-molecular-weight compound into a small compound, and the alkyl chains of nitrogen compounds are easy to be degraded. This degradation produces small-molecular-weight organic acid dissolved in water, and some of this organic acid contains nitrogen, sulfur impurity atoms, and many aromatic rings. The number of organic acids even increases by one or two orders of magnitude [45].

Almost all the microbial laboratory and filed experiments had proved that microorganisms could be used to reduce the viscosity of crude oil, but the viscosity reduction content varied [41]. The viscosity and interfacial tension respectively decreased by 40% and 50% when *Bacillus* sp. was adopted [42]. The offshore heavy oil viscosity could be reduced by 66% by using one microbe. With the compound use of two microbes, the viscosity was decreased from 1146 cp to 5.11 cp, decreasing by 99% [12]. A study also showed that after a 14-hour reaction between streptococcus and crude oil, the oil viscosity decreased from 4000 mPa.s to 500 mPa.s, which are caused by both microbes and metabolites, with metabolites playing a major role [46]. As for viscosity-reducing causes, in addition to pectin degradation and biological emulsion, CO₂ produced by microbes in a supercritical state (high temperature and high pressure in reservoir) resolved in crude oil and thus reduced oil viscosity [41]. A field test in Dagang indicated that wax and gel contents respectively decrease by 2.2% and 3.7% [42]. Samples from five well groups in Daqing Oilfield also showed that the content of saturated hydrocarbon increased, while that of nonhydrocarbon decreased, which was consistent with the results of

laboratory experiments [16]. Oil degradation by microorganisms accounts for MWR and MFR.

3.2. Biosurfactants in Microbial Metabolism. The microbial surfactant could be metabolized [5]. Surfactants included biosurfactants [41, 47], organic solvent [42], acids [41], and gas [41]. Gas was mainly CO₂, CH₄, and a small quantity of ethane [47]. The composition of biosurfactants mainly consisted of rhamnolipid [46, 48], as well as a mixture of paraffin ester and glyceride [46] which did not belong to sugar ester but phospholipid and polyketones. The main composition of acids was fatty acid [41, 49], acetic acid, propionic [41], and butyrate [42]. The mass fraction of fatty acid increased from 1% to more than 60% after the microbial effect [42]. Dagang Oilfield MEOR field tests showed that the content of low fatty acid increased notably with formic acid and acetic acid increasing 10 times and isobutyric acid increasing 7 times after nutrient solution was injected one year [35]. Organic solvent included alcohol, such as ethane [42]. It is notable that although biosurfactants are produced in MOER to reduce IFT, only few were reported to reduce IFT to an ultra-low level (10^{-3} mN/m).

3.3. Emulsification. Emulsification was one of the main mechanisms of MEOR [4, 7, 50, 51]. However, there is no satisfactory criterion to characterize the capacity of microbes on crude oil emulsification in China. At present, the simplest way to study and apply microbial flooding is the five-level classification method involving the direct observation of oil-water emulsion [5]. This method is simple and practical, but the disadvantage includes lack of quantitative characterization, which is well included in other much more complex ways of emulsion coefficient EI24 and the Tub-scan emulsion stability parameter measurement method [5]. The microscopic model flooding experiments used by the oil-water emulsion visual observation method found that crude oil was emulsified by microorganisms [24]. Microtransparent simulation models showed that the degraded crude oil was emulsified in different degrees in the form of various oil droplet sizes, and the oil droplets were tensile and deformed and had seepage flows [52]. The biogas produced was beneficial for emulsifying crude oil [5]. The degree of crude oil emulsion was seen with high correspondence to the growth rate of microorganisms [41]. The emulsification effectiveness for heavy oil was obviously improved by the effect of complex formulation of two types of microorganisms, as supported by the fact that as the emulsion stability increased, the average particle size decreased by 67.3% with notably reduced heavy oil viscosity [11]. The composition and structure of organic acid change lead to wettability alternation, and it also makes water-in-oil emulsion into oil-in-water, thus reducing the viscosity of oil, which in turn improves the flow rheological property [45]. This accounts for the common phenomenon of emulsification in MEOR on the molecular level and is considered to have notable progress on MEOR mechanism [45].

3.4. Altering Reservoir Physical Properties. Physical properties of the reservoir could be changed by the metabolism product of microbes, and the porosity was likely to be increased.

According to one laboratory test, the permeability was reduced from 284 mD to 24 mD, and the viscosity might be reduced by as large as 10 times due to the effects of acid [9]. The ability of reducing reservoir permeability is the main mechanism in MSPR as well as MFR. Two microbes were selected for cultivation from more than one hundred bacteria in post-polymer flooding reservoirs in Daqing Oilfield, and laboratory experiment indicated that the plugging rate of the profile of control bacteria was over 70% [13]. The field test in Daqing also indicated that reservoir permeability was decreased after profile control and the water injection profile was significantly improved. Microbes can produce biosurfactants through metabolism and change its wettability, and much attention has been given to this mechanism. The surfactants produced by microbes were adsorbed on the surface of porous media; the wetting state of the surface of porous media was thus changed due to the effects of the amphiprotic group in surfactants [40]. Microbes could make the reservoir wettability change from oil-wet to water-wet [9]. Most researches in China focused on the surfactant produced by microbes, while quantitative characterization of the wettability index after microbial mediation, contact angle, and other methods was seldom used. The most frequently used method is to test IFT by using the spinning drop method.

3.5. Microscopic Mechanism. Microscopic mechanisms of microbes contacting with crude oil and changing the pore surface as well as crude oil properties to enhance oil recovery help to clarify MEOR mechanisms. An experiment with a microscopic visible physical model [3, 13] indicated that microorganisms consuming crude oil could migrate directionally to crude oil and contact directly with crude oil and make the microbe colony highly concentrated towards carbon source and crude oil. The basis for microorganisms consuming crude oil to enhance oil recovery was its ability to automatically search for carbon source and directionally migrate. Microbes automatically migrate to crude oil, concentrate, and multiply constantly. The distribution regularity of the concentration of the surfactant as well as the acid in its metabolites was exactly the same with that of bacteria. The automatic directional migration of microbes was attributed to its chemotaxis. The microscopic mechanism of peeling off oil film and oil droplets by microbes could be seen in Figures 9(a)–9(c) [13]. Although hydrophilic, the bacteria could be hydrophobic at one end. Due to the synergistic effect with its metabolites, the bacteria entered into the space between pore surface and oil film or oil droplets, grew and reproduced massively, and entered deeply inward, and finally the oil film was peeled off. Their experiments also indicated that a proper time was required for the migration and concentration of microbes and metabolites, and it would be better to adopt huff and puff or intermittent methods during field MEOR. A microscopic photoetching physical model [3, 40] also indicated that due to the growth and metabolism of microbes attached to the oil-water interface, the oil-water IFT was reduced, the interface was softened, and the flow ability of the remaining oil was enhanced. This is because the surfactant produced by the microbial metabolism concentration of the surfactant at the interface was increased,

generating a surface tension gradient. Once the gradient exceeded the viscous force, spontaneous interface deformation and movement, namely, Marangoni convection, would appear, and together with migration behavior of microbes and disturbance action of high pressure, positions of droplets in pores would be changed.

4. Microbial Flooding Recovery Designing

The system of microbial flooding involves activation of material composition in the system, injection of slugs, nutrition concentration, and the size of nutrition-injecting slug. Lots of studies had been conducted about the activation system. The feasibility of using corn starch as the activation system was studied [32]. The ultimate recovery increase could be significantly influenced by the cultivation time of injecting slugs, nutrition concentration, and the size of nutrition-injecting slug. It had been proved that injecting 0.4 PV slugs with a corn starch concentration at 10–20 mL/L and cultivating for 15–20 d was optimum for the condition. However, in many actual field tests of microbial flooding in China, slug size was no larger than 0.1 PV [44]. In view of the extra-low permeability reservoir in Dingbian, Changqing Oilfield, bacteria concentration of 10% and slug size of 0.5 PV were selected according to the laboratory core flooding test experiment with a tertiary recovery of 8% OOIP [53]. Actual MEOR design parameters in Daqing Oilfield in China were well summarized [54].

4.1. Reservoir Screening Criteria. Screening criteria for a reservoir varied greatly [9]. Different criteria existed due to different reservoir conditions and research progress. Safdel et al. [4] made a critical review on different MEOR screen criteria in different countries, although the data used for China are not latest. When microbial flooding was conducted, factors that must be taken into account [9] involved remaining oil saturation, hydrocarbon compositional analysis, fluid chemistry and composition, depth of reservoir, salinity of formation water, formation water sample analysis, estimated net oil increment, and economic aspects. According to laboratory research and field tests in China and with consideration of researches abroad, 8 major parameters were selected for reservoir screening and evaluation in microbial flooding could be seen in Table 2 [5]. Screening criteria by Shengli Oilfield in China could be seen in Table 3 [14]. Considering the MEOR research history and field test scale and number, as well as being the largest branch company of Sinopect, Shengli Oilfield screen criteria represent the standard of Sinopec. Major oil companies and their production share in China are available in a publication [43].

Temperature has direct influence on the growth of microorganisms [41]. There is optimum temperature for the growth of microorganisms, which could be largely affected when the optimum temperature was exceeded. Previous studies [41] also showed that 8 facultative anaerobes could grow well at 45–60°C, while they cannot grow when the temperature is higher than 75°C. Laboratory tests showed that for the same microorganism, when the temperature increased from 37°C to 73°C, the bacterial concentration

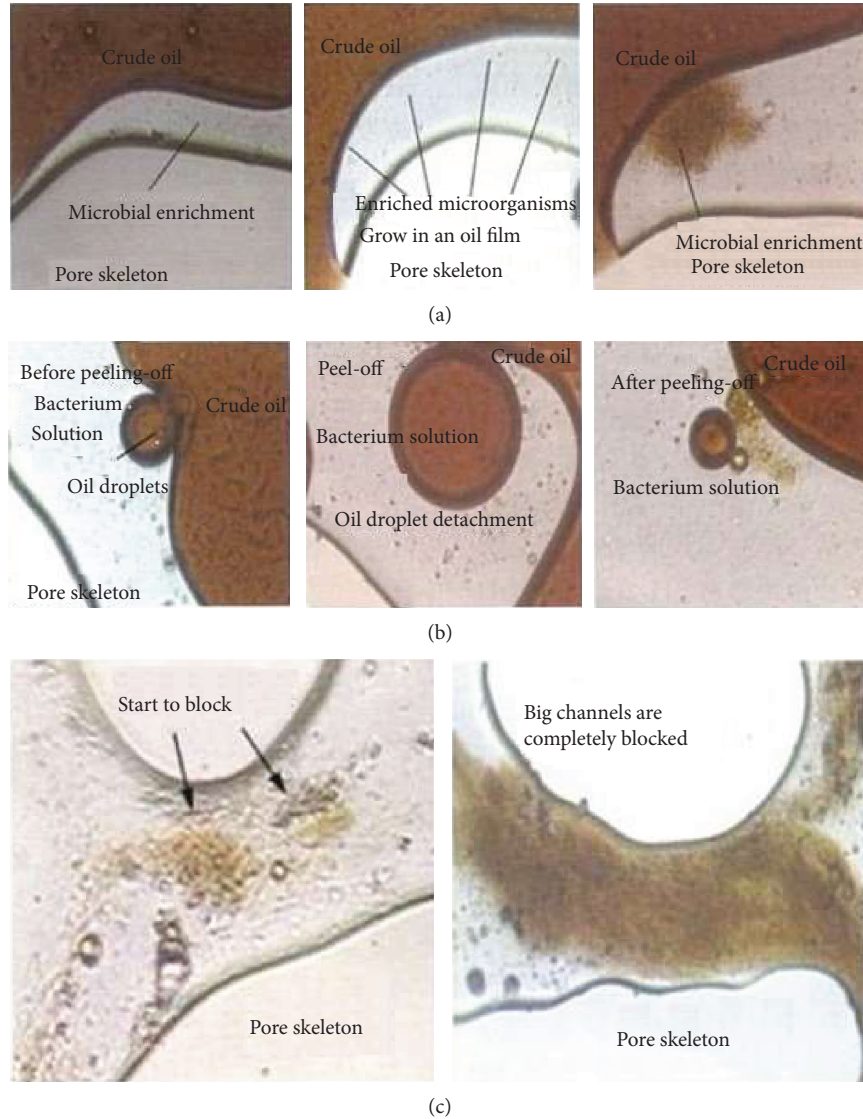


FIGURE 9: (a) The microbial growth and peeling-off oil film [13]. (b) The peeling-off course of oil droplet [13]. (c) A large amount of modular/floss stopping big orifices [13].

TABLE 2: CNPC MEOR reservoir screening parameter [5].

Parameter	Value range	Optimum
Formation temperature ($^{\circ}\text{C}$)	20-80	30-60
Crude viscosity (mPa·s)	10-500	30-150
Permeability (mD)	≥ 50	≥ 150
Porosity (%)	12-25	17-25
Brine salinity (g/L)	≥ 300	≥ 100
Wax content (%)	≥ 4	≥ 7
Water cut (%)	40-95	60-85
Total bacterial concentration in produced fluid (number/mL)	≥ 100	≥ 1000

dropped remarkably [20]. 80°C was the critical reservoir temperature for MEOR, and if the temperature exceeded 80°C , the microorganism's growth rate was very slow [14]. One

TABLE 3: MEOR reservoir screen parameter in Shengli oilfield [14].

Formation temperature ($^{\circ}\text{C}$)	Permeability (mD)	Formation brine (pH)	Formation brine salinity (mg/L)	Dead oil viscosity at 50°C
≤ 80	≥ 50	6~8	≤ 150000	≤ 3000

pilot in the HKL-801 block (reservoir temperature 80°C) in Shengli Oilfield was effective while the one in the BNL-32 block showed no obvious effects because the temperature was 91°C [14]. In addition to reservoir temperature, reservoir heterogeneity also affected microbial flooding recovery significantly [14]. However, there were no reservoir heterogeneity criteria for MEOR yet. Although Jiangnan Oilfield in central China reported cultivated thermophilic bacteria (*Geobacillus kaustophilus*) that could grow at 100°C and

TABLE 4: Chao 50 block microbial flooding field test in Daqing Oilfield [61–63].

Area of block (km ²)	2.43
OOIP (tons)	1667000
Reservoir depth (m)	989
Reservoir thickness (m)	7.9-9.5
Reservoir temperature (°C)	55
Injectors/producers	2/10
Formation brine salinity (ppm)	4450
Formation brine divalent (ppm)	14
Average permeability (mD)	25
Average porosity (%)	17
Dead oil viscosity (cP)	20.2
Formation oil viscosity (cP)	9.7
Original oil saturation (%)	57
Water cut	95%
Implementation time	June 2004-Sep 2005
Injection slug (PV)	0.005
Microbe concentration	5% (first slug), 2% (second slug)
Effective well ratio	74.2%
EOR (% OOIP)	3%
Water cut reduction (%)	30.3
Input-output ratio	1 : 6
Effective duration time	3 years
Expansion test	Yes

salinity of 350000 ppm and the paraffin removal pilot test in a well with 117°C temperature and 250000 ppm salinity verified satisfied paraffin and plug removal effects [55–57], the MEOR reservoir temperature criteria in China remains at 80°C, the highest reservoir temperature with use of MEOR 155°C for Norwegian fields [4].

Salinity was another key screen parameter affecting microbial flooding [5, 14]. High-salinity and high calcium concentration formation water was not suitable to the application of the microbial flooding technology [55]. It was reported that two microorganisms separated from produced fluid grew well in the salinity range of 100000-200000 ppm, while when the salinity was higher than 200000 ppm, the growth rate of these two microorganisms got slower [58]. By using 16S rDNA technology, these two microorganisms were proved to be *Pseudomonas aeruginosa* and *Bacillus subtilis* [58]. A pilot test [55–57] indicated that microorganisms cultivated at a salinity of 350000 ppm could remove paraffin in a well of 250000 ppm salinity with good performance.

4.2. Typical Field Tests. Field tests are a necessary stage for any EOR technology going from laboratory to real application; this is especially crucial for MEOR. The physical simulation methods learned from chemical flooding practice have some limitations, such as the impossibility of simulating oxygen-free and endogenous environments like real reservoir condition, and the short length of cores resulted in the exclusion of microorganisms without full growth and propagation [32, 59]. Shengli Oilfield MEOR tests showed that results

between laboratory experiments and field tests varied greatly, which may be attributed to the complex reservoir conditions and/or physical simulation method limitations. Therefore, it was necessary to improve the evaluation method like choosing the low injection rate and the suitable core length to keep microorganisms staying in the core for at least 14 days [32]. More importantly, it is necessary to conduct field tests to check the technique effect and avoid risk and to learn from previous field tests to reduce costs in the low oil price era. Field trial data on global microbial flooding is available online [4, 54, 60]. Only a few typical MEOR field tests in China are selected to provide more operational information, such as cycle microbial recovery (CMR) and microbial flooding recovery (MFR), which are not available in the previous publication [60]. According to our own survey, up to present, there have been more than 47 MFR field tests in China, involving more than 500 wells (injectors and producers) and 15 oilfields in China. Different from previous studies focused on microbial huff and puff, or CMR, which are not real microbial flooding tests, this paper focuses on real MFR to show what progress and experience have been made in China. Below are some typical MFR projects based on latest references available. To better help possible reservoir screening and field application in similar reservoirs, the key parameters of incremental oil recovery and economic parameters are given. It is, to the best of our knowledge, the most detailed operational learning in view of the EOR scope from previous field tests in China.

4.2.1. Daqing Oilfield. Up to present, more than 12 MFR field tests have been conducted in Daqing Oilfield. Some MFR tests are available in reference [54]. Among these field tests, Chao 50 in Chaoyanggou Oilfield is very prominent. Two microorganisms (*Brevibacillus brevis* and *Bacillus cereus*) were selected from indigenous microorganisms to conduct field tests of single well simulation and microbial flooding in ultra-low-permeability reservoirs in Daqing Oilfield [22, 61, 62]. From 2002 to 2003, 60 wells were put into CMR tests. The average formation permeability was 10 mD, and the formation temperature was 55°C. Among the 60 wells, formation permeability of 28 wells was 15-25 mD, and that of 22 wells was 5-15 mD, and formation permeability of 10 wells was below 5 mD. 71.7% wells were seen as having positive results, and the input-output ratio was 1 : 8. Based on previous single-well MEOR success, microbial flooding recovery (MFR) tests were carried out in 50 blocks with 2 injection wells and 10 production wells [61]. The reservoir data and field test performance are given in Table 4 [61–63]. Well patterns and field test performance are given in Figure 10 [63] and Figure 11 [63], respectively. The liquid-producing capacity increased from 43.6 to 79.6 tons, daily oil production increased from 24.7 t to 40.8 t, and water cut decreased by 30% and the incremental oil recovery was 3% OOIP with an effective duration of three years. Considering the low injection slug (0.005 PV) compared to chemical flooding slug, the incremental oil recovery is very prominent. Another very successful microbial flooding field test was reported to have an incremental oil recovery of 4.45% OOIP by 0.05

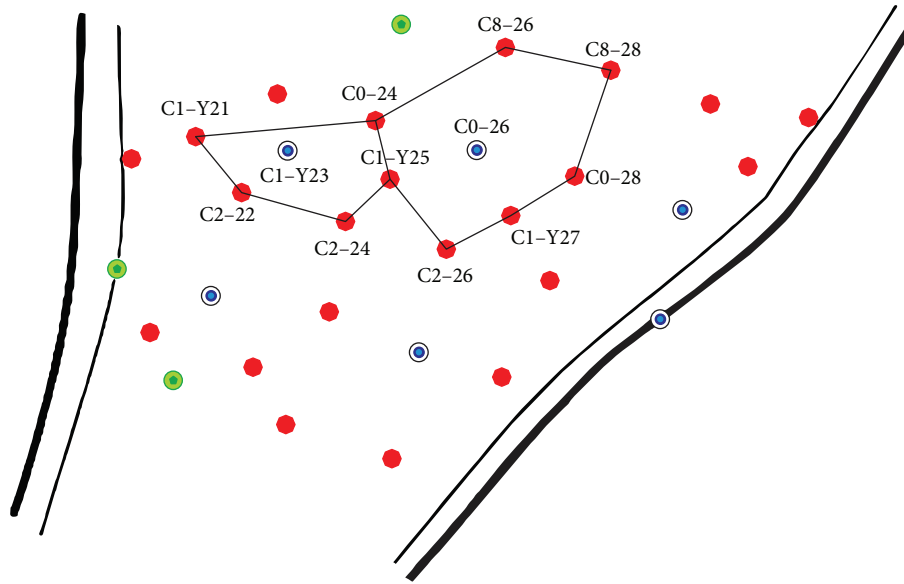


FIGURE 10: Chao 50 MFR field test well pattern in Daqing Oilfield [54].

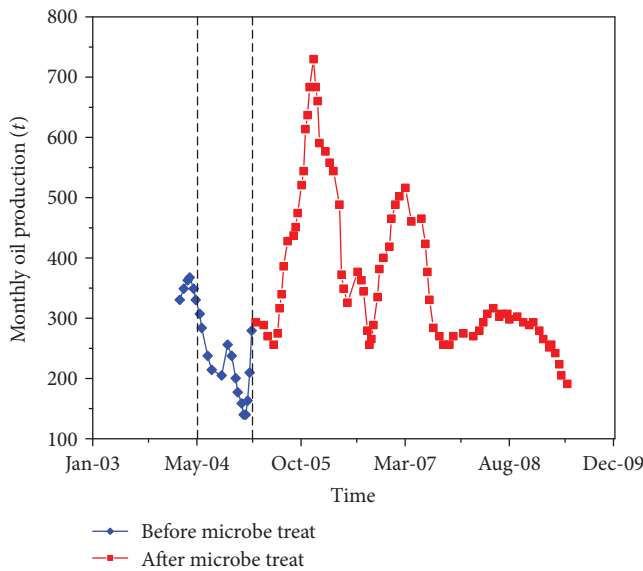


FIGURE 11: Chao 50 MFR field test production performance [54].

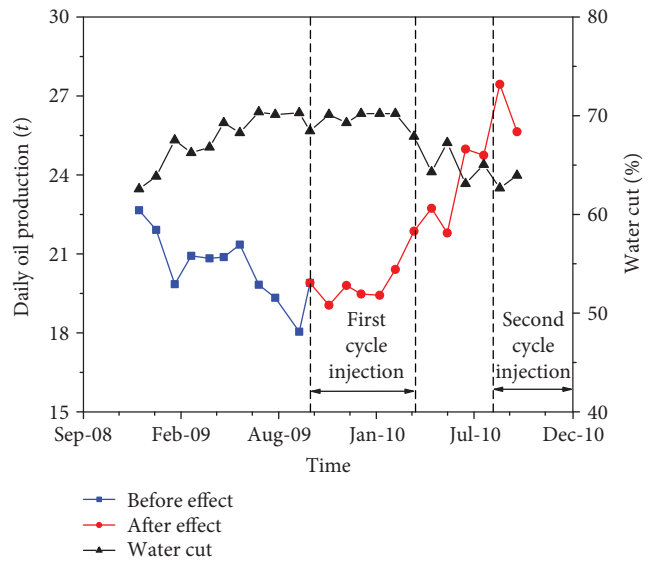


FIGURE 12: Chao 50 expansion MRF field test production performance [54].

PV bacteria slug [54]. The Chao 50 input/output ratio was 1 : 6. This successful pilot test indicated that MFR can succeed in the reservoir with permeability lower than present criteria at 50 mD, seen in Table 2 and Table 3. This test also showed that microbial flooding could set an effective displacement system which made the dead oil well remobilized. This field test verified that the injection-production relationship significantly affected microbial flooding effects. Based on the success of MRF in Chao 50, expansion microbial flooding tests with 9 injectors and 24 producers were conducted in 2009 [54]. The production performance of the expansion test can be seen in Figure 12 [54]. Detailed information of the expansion field test is not made public yet, but it is reported that microbial flooding makes the block production turn from decreasing to increasing.

4.2.2. *Shengli Oilfield.* Since Shengli Oilfield has been the second largest oil producer for a long time, MEOR in Shengli provides for the industry a valuable experience. MEOR research in Shengli Oilfield started since 1995, and MEOR field tests have been conducted since 1997 [14]. Although more than one thousand wells have been used in MWR and CMR in Shengli Oilfield, only 9 blocks have been conducted for MFR. Table 5 [14, 36, 64, 65] is a summary of 7 microbial flooding field tests in Shengli. The MRF test in Shan 12 is well introduced in a previous publication [30]. Among these field tests, only Guan 3 Block is not of fault block type, while the other 6 are all fault block reservoirs. And these 6 blocks are water flood reservoirs, while Guan 3 block is a post-polymer flood reservoir. In other words, the first 6 tests in Table 5 are all in tertiary recovery stage, while the last is in

TABLE 5: Recent microbial flooding recovery field tests in Shengli Oilfield.

Case	Block	Implement time	T (°C)	Perm (mD)	Salinity (ppm)	Dead oil viscosity at 50°C (mPa·s)	Inj./Pro	Area (km ²)	Type	Incremental oil (ton)	Water cut ¹ ↓	EOR ² ↑ (%)
1	ZNXQ	1998.3-1999.09	54	477	1100	48	3/8	0.9	EMFR	5090	5	
2	Li 32	1998.06-2002.2	91	525	4600	88	4/7	1.8	EMFR	2001	slight	
3	Pan2-33	2000.08-2002.11	67	436	43900	1100	4/11	0.9	EMFR	7800	1.3	
4	Luo 801	1999.07-now	80	231	7790	353	5/13	1.25	Air EMFR	122800	7.3	4.95
5	Shan 12	2005.08-2008.06	66	263	20000	38	1/7	0.31	Air IMFR	8520	2	
6	Zhan 32	2011.11-now	63	682	9000	1885	3/12	0.69	Air IMFR	22855	5.5	5.5
7	Guan 3	2008.11-2012.12	69	2500	5920	1000	6/17	0.84	Air IMFR	21000	0.7	1.27

Note: T = reservoir temperature; Perm = permeability; Inj. = injectors; Pro = producers. ¹↓ means water cut reduction; ²↑ means incremental oil recovery.

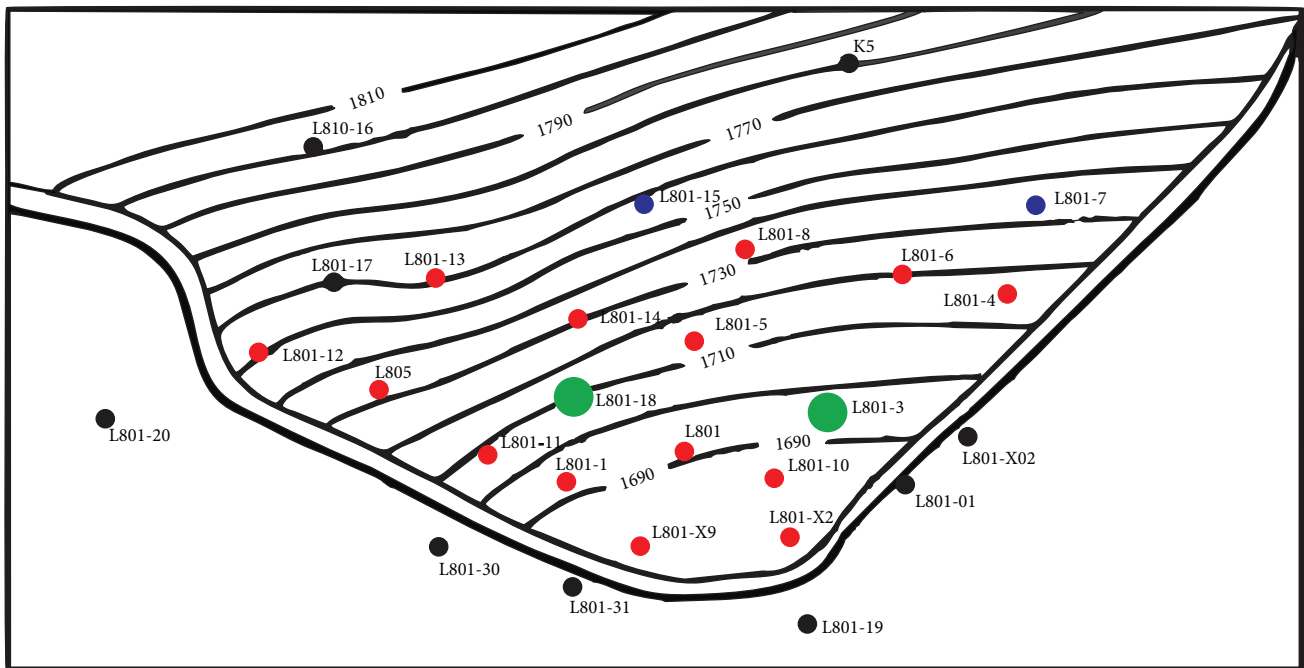


FIGURE 13: Luo 801 Block in Shengli Oilfield MEOR field test [65].

quaternary recovery stage. Since Shengli Oilfield has the second largest polymer flooding commercial use in China, the MFR test in Guan 3 is worthy of special attention. Polymer flooding in this block started in December 1994 and entered into the post-water flooding stage in April 1997 [14]. MFR started in November 2008. Although profile control measures have been taken before bacteria injection, injected bacteria broke through 4 days after injection in the latter stage. This test indicated the difficulty of MEOR in the post-polymer flooding reservoir with high heterogeneity. Among the 7 MFR field tests in Table 5, only three were reported with obvious enhanced oil recovery. In this block, MFR field tests have been enlarged from five wells (1 injector, 4 producers) in 2011 to 15 wells (3 injectors, 12 producers) in 2014 [14, 64]. In 2015, the field test has been enlarged, but the data has not been made public. Incremental oil recovery in

Zhan 32 is a predicted recovery. Among all the blocks that are conducted for MEOR, Luo 801 deserves the most attention for several reasons. First, it has the longest MEOR application lasting time in China, probably in the world. Second, it has currently the highest field proven enhanced oil recovery in MEOR. The staged actual enhanced oil recovery is 4.95% OOIP, higher than the best one in Daqing Oilfield [54]. Finally, two kinds of microbial flooding (IMFR, EMFR) are both tested in the same block. The production history of Luo 801 is well introduced in reference [64, 65]. Figure 13 [65] shows the well pattern of MFR field tests. In Figure 13, green represents the two injectors from 2002 to 2011, while blue represents 3 injectors operated from July 1999 to August 2002, and red represents producers operated from 1999 to present [65]. The production performance of Luo 801 is shown in Figure 14 [65]. This data shows that microbial

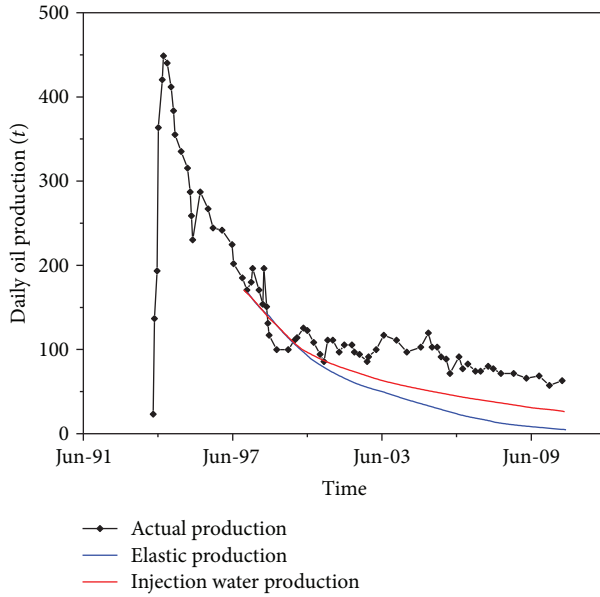


FIGURE 14: Luo 801 production curve and decline forecast [65].

flooding indeed improved oil recovery. For potential reservoir screening consideration, reservoir parameters and MFR field test performance are summarized in Table 6 from various references [30, 33, 60, 64, 65]. After air-assisted MFR, the annual water cut increase rate changed from 9% to 0.53%, and it has been maintained lower than 1.5% for 8 years [14]. The input/output ratio was not reported and is estimated to be 1:4 according to a comparison with some similar MRF projects in Shan 12. MFR success in Luo 801 paved a way towards enlarging MEOT tests in other blocks like Zhan 32 in Table 5. The cost for incremental oil from Luo 801 microbial flooding blocks is as low as 7 USD/bbl (339.56 yuan/ton) [65]. Some latest MEOR projects in Shengli Oilfield have not been made public.

4.2.3. Changqing Oilfield. Changqing Oilfield is the largest oilfield if judged by production oil equivalent. Almost all reserves of Changqing Oilfield are from low-permeability reservoirs, and more than half are of ultra-low-permeability formation. Since the reservoir permeability bound given by CNPC and Sinopec is 50 mD, whether ultra-low-permeability reservoirs are suitable to use MOER draws attention. A pilot in an ultra-low-permeability reservoir was conducted in 2009 in Ansai in Changqing Oilfield [31, 66–68]. The average permeability of Ansai Oilfield is 1.29 mD, and the average porosity is 12.4%. The pilot was conducted to check the microbial flooding effect, which contains one well group with 1 injector and 6 producers. Oil production in this block started from March 1990, and the daily oil production per well before MFR is 1.48 tons [31]. The well pattern is shown in Figure 15 [31, 68]. Oil production before and after MFR is given in Table 7 [31, 68] while reservoir parameters are given in Table 8 [31, 66–68]. Oil production indicates that microbial flooding can reduce water cut and increase oil production. The water cut increase rate was reduced from 10.86% to 4.42%, and the comprehensive production decline rate was changed from 2.34% to -2.58%,

TABLE 6: Luo 801 block microbial flooding field test in Shengli Oilfield.

Area of block (km ²)	1.25
OOIP (tons)	2910000
Reservoir depth (m)	1680-1800
Reservoir thickness (m)	15.5
Reservoir temperature (°C)	75-80
Injectors/producers	5/13
Formation brine salinity (ppm)	9794
Formation brine divalent (ppm)	NA
Average permeability (mD)	218
Average porosity (%)	23.4
Dead oil viscosity (cP)	221.7
Formation oil viscosity (cP)	12.8
Original oil saturation (%)	60
Water cut	86.5
Implementation time	July 1999-
Injection slug (PV)	0.25
Microbe concentration	NA
Effective wells ratio	NA
EOR (% OOIP)	4.95
Water cut reduction (%)	7.3
Input-output ratio	≈1:4
Effective duration time	>15 years
Expansion test	Yes

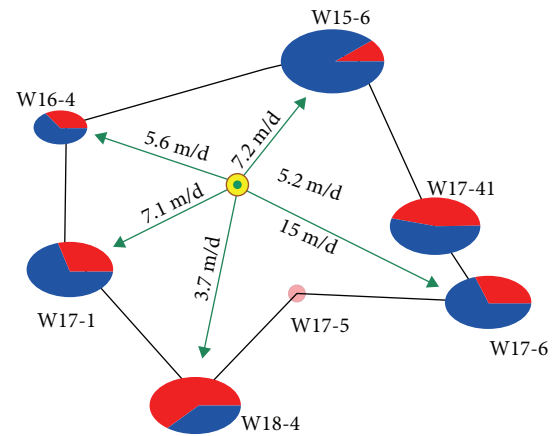


FIGURE 15: MRF pilot well pattern and bacteria flow velocity [31, 68].

which means oil production was significantly increased [68]. This pilot also shows that production performance has a positive relation with microbe movement. This is in agreement with other field tests in Daqing and Shengli. MEOR is a water-enhanced improved oil technique. Only when an effective injection-production relationship is formed can effective oil production be attained. In other words, if water injection is difficult, MEOR is likely ineffective. The economic performance is very good, with an input-output ratio of 1:5.9. This indicated that the permeability ground should be lower.

TABLE 7: Well performance of Ansai MFR pilot [31, 68].

No	Before MFR			After MFR (December 18, 2009)				
	Daily fluid (m ³)	Daily oil (ton)	Watercut (%)	Daily fluid (m ³)	Daily oil (tons)	Watercut (%)	Daily oil increase (tons)	Cumulative incremental oil (tons)
1	2.13	0.67	62.7	4.02	2.2	34.9	1	169.7
2	5.37	1.43	68.2	4.28	1.86	48.4	0.45	57.93
3	5.73	1.59	67	5.19	12.17	50.2	0.46	34.37
4	5.01	1.04	75.6	4.65	0.52	86.6	0.5	33.56
5	7.54	1.1	82.6	5.45	0.92	80	0.07	2.09
6	5.36	3.04	32.6	3.53	2	32.5	0	0
Total	31.14	8.87	66.1	27.12	19.67	57.6	0.66	297.65

TABLE 8: Ansai MFR pilot in Changqing Oilfield [31, 67, 68].

Area of block (km ²)	NA
OOIP (tons)	NA
Reservoir depth (m)	1220-1241
Reservoir thickness (m)	15.8
Reservoir temperature (°C)	45
Injectors/producers	1/6
Formation brine salinity (ppm)	92600
Formation brine divalent (ppm)	NA
Average permeability (mD)	5.22
Average porosity (%)	14
Dead oil viscosity (cP)	10.5 at 20°C
Oil saturation (%)	60
Water cut before test (%)	67.1
Implementation time	June 28-August 21, 2009
Injection slug (PV)	0.003
Microbe concentration	3%
Effective well ratio	67
EOR (% OOIP)	NA
Water cut reduction (%)	8.5
Input-output ratio	1 : 5.9
Effective duration time	1 year
Expansion test	Yes

5. Conclusions

Compared with thermal production, gas flooding, and other enhanced oil recovery methods, the prominent advantages of MEOR are much lower costs and more environment friendliness compared to other EOR techniques. Field tests show that the input-output ratio of microbial flooding recovery is as high as 1 : 6, with a much lower total cost than all the other EOR techniques like polymer flooding, gas flooding, and thermal production.

Indigenous microorganism flooding is the development trend with the advantages of good adaptability and avoiding of microbes' culture development and production process compared with exogenous microbial flooding.

Both laboratory and field tests have verified that the crude oil composition changed remarkably as the saturated hydrocarbon proportion increased; aromatics, nonhydrocarbon,

and asphaltene proportion decreased; and the acid value increased while wax and pectin proportion decreased.

The microbial metabolism produced surface active compounds including biosurfactants, alcohol, acid, and biogases. The most common and desired biosurfactant was rhamnolipid which could reduce interfacial tension. Biogases were mostly carbon dioxide and methane, and little ethane. The acid was mainly fatty acid like methanolic acid, acetic acid, and propanoic acid.

The crude became emulsified with different extents due to effects of microbes.

Microbial products could change the wettability toward more water being wet and also reduce formation permeability remarkably. The microbial profile control mechanism could be accounted into one or all the mechanisms including microbes forming a reticular biofilm in porous media, precipitation of the colony, and formation of a bridge plug due to absorption of other microbes, the biogas block effects.

The basis for microorganisms consuming crude oil to enhance oil recovery was its ability to automatically search for carbon source and directionally migrate. Microbial effects on remaining oil could be ordered ranked in a descending order as island remaining oil, membranaceous remaining oil, columnar remaining oil, blind end remaining oil, and cluster remaining oil.

Application of a high-resolution mass spectrum (HRMS) on MEOR mechanism has revealed the change of polar compound structures before and after oil degradation by the microbe on the molecular level.

The reservoir screening parameters include temperature, salinity, oil viscosity, permeability, porosity, wax content, water cut, and microorganism concentration in which production fluid, temperature, and salinity were the three most important parameters. It is possible to use MFR in a reservoir with permeability as low as 5 mD.

Microbial flooding recovery field tests in China show that MRF is close to commercial application, since a high incremental oil recovery of 4.95% OOIP was attained with a typical 0.1 PV slug. Three typical reservoirs with detailed MFR field tests data were reviewed for possible guide for similar reservoirs.

Conflicts of Interest

The authors declare no conflict of interest.

Acknowledgments

The authors wish to express their appreciation for the funding provided by the National Natural Science Foundation of China (No. 51874320, 51604285), National Science and Technology Major Project of China (No. 2016ZX05010-003-001 and No. 2016ZX05025-003-010), Shaanxi Provincial Key Laboratory of Technology and Innovation Engineering (2014SZ15-Z02), Yan'an University Doctor Scientific Research Initialization Foundation (No. YDBK2018-52), and the China Scholarship Council (201706440109).

References

- [1] D. W. Green and G. P. Willhite, *Enhanced Oil Recovery*, Society of Petroleum Engineers Richardson, Texas, TX, USA, 2018.
- [2] J. Sheng, *Modern Chemical Enhanced Oil Recovery: Theory and Practice*, Gulf Professional Publishing, 2011.
- [3] H. Guo, Y. Li, Y. Zhao et al., "Progress of microbial enhanced oil recovery in China," in *Proceedings of SPE Asia Pacific Enhanced Oil Recovery Conference, Society of Petroleum Engineers*, pp. 1–16, Kuala Lumpur, Malaysia, 2015.
- [4] M. Safdel, M. A. Anbaz, A. Daryasafar, and M. Jamialahmadi, "Microbial enhanced oil recovery, a critical review on worldwide implemented field trials in different countries," *Renewable and Sustainable Energy Reviews*, vol. 74, pp. 159–172, 2017.
- [5] J. He, Y. Wang, and G. Liang, *Emerging Strategic Technology of the Oilfield Development*, Petroleum Industry Press, 2018.
- [6] R. Marchant and I. M. Banat, "Microbial biosurfactants: challenges and opportunities for future exploitation," *Trends in Biotechnology*, vol. 30, no. 11, pp. 558–565, 2012.
- [7] C. Ke, G. Lu, Y. Li, W. Sun, Q. Zhang, and X. Zhang, "A pilot study on large-scale microbial enhanced oil recovery (MEOR) in Baolige Oilfield," *International Biodeterioration & Biodegradation*, vol. 127, pp. 247–253, 2018.
- [8] J. Patel, S. Borgohain, M. Kumar, V. Rangarajan, P. Somasundaran, and R. Sen, "Recent developments in microbial enhanced oil recovery," *Renewable and Sustainable Energy Reviews*, vol. 52, pp. 1539–1558, 2015.
- [9] S. Zahid and H. A. Khan, "A review on microbial EOR with special reference to its use in marginal and/or mature assets," in *Proceedings of International Oil Conference and Exhibition in Mexico*, pp. 1–9, Veracruz, Mexico, 2007.
- [10] Q. Cui, "Recent progress in MEOR technology in low-medium permeability reservoirs," in *Proceedings of 7th Chemical Flooding Enhanced Oil Recovery Conference, Chinese Petroleum Society*, pp. 1–9, Dalian, Liaoning Province, China, 2017.
- [11] Y. Qi, D. Wang, M. Wang, G. Li, X. Lyu, and T. Ma, "Effects of resin degradation and biological emulsification on the viscosity break of heavy oils," *Acta Petrolei Sinica*, vol. 33, no. 4, pp. 670–675, 2012.
- [12] Y. Liu, C. Hao, S. Hu, F. Zhao, S. Wen, and D. Wang, "Capability and mechanism of microbe action in polymer-flooding reservoir," *Acta Petrolei Sinica*, vol. 29, no. 5, pp. 717–722, 2008.
- [13] G. Jing, S. Guo, and L. Yu, "Mechanism of enhanced oil recovery using microorganisms consuming crude oil," *Acta Petrolei Sinica*, vol. 27, no. 6, pp. 84–92, 2006.
- [14] S. Sun, "Field practice and analysis of MEOR in Shengli oil-field," *Journal of Oil and Gas Technology*, vol. 36, no. 2, pp. 149–152, 2014.
- [15] H. Dong, Y. She, Z. Wang, F. Shu, F. Zhang, and L. Chai, "The diversities and functions of polysaccharide microbial produced in the reservoirs after polymer flooding," *Journal of Oil & Gas Technology*, vol. 34, no. 5, pp. 112–115, 2012.
- [16] J. Le, F. Liu, J. Zhang et al., "A field test of activation indigenous microorganism for microbial enhanced oil recovery in reservoir after polymer flooding," *Acta Petrolei Sinica*, vol. 35, no. 1, pp. 99–106, 2014.
- [17] R. S. Bryant, A. K. Stepp, K. M. Bertus, T. E. Burchfield, and M. Dennis, "Microbial enhanced waterflooding field tests," in *Proceedings of SPE/DOE Improved Oil Recovery Symposium*, pp. 1–12, Tulsa, OK, USA, 1994.
- [18] A. Zekri, M. Ghannam, and R. Almehaideb, "Carbonate rocks wettability changes induced by microbial solution," in *Proceedings of SPE Asia Pacific Oil and Gas Conference and Exhibition*, pp. 1–10, Jakarta, Indonesia, 2003.
- [19] R. Almehaideb and A. Y. Zekri, "Optimization of microbial flooding in carbonate reservoirs," in *Proceedings of SPE Asia Pacific Oil and Gas Conference and Exhibition*, pp. 1–10, Melbourne, Australia, 2002.
- [20] Q. Feng and Z. Chen, "Study and application of enduring high temperature bacteria," *Petroleum Exploration and Development*, vol. 27, no. 3, pp. 50–54, 2000.
- [21] Y. Li, Y. Yang, X. Sun et al., "The application of laser confocal method in microscopic oil analysis," *Journal of Petroleum Science and Engineering*, vol. 120, pp. 52–60, 2014.
- [22] W. Guo, Z. Hou, M. Shi, and X. Wu, "The recovery mechanism and application of *Brevibacillus brevis* and *Bacillus cereus* in extra-low permeability reservoir of Daqing," *Petroleum Exploration & Development*, vol. 34, no. 1, pp. 73–78, 2007.
- [23] Y. Long, W. Wang, Y. Xu et al., "The research on bio-chemical combination drive and its application in Y9 reservoir in block ZJ2 of Jing'an oilfield," *Journal of Oil and Gas Technology*, vol. 35, no. 9, pp. 142–145, 2013.
- [24] J. Sui, M. Shi, F. Sun, Z. Yang, P. Han, and X. Wu, "Microbial EOR studies on the microorganisms using petroleum hydrocarbons as sole carbon source," *Acta Petrolei Sinica*, vol. 22, no. 5, pp. 53–57, 2001.
- [25] G. Liao, M. Shi, W. Li, Z. Hou, P. Han, and Z. Yang, "Selection and evaluation of microorganisms taking partially hydrolyzed polyacrylamide and crude oil as nutritional source," *Acta Petrolei Sinica*, vol. 24, no. 6, pp. 59–63, 2003.
- [26] Y. Li, J. Zhang, Q. Huang, and K. Ma, "Establishment of microbial oil displacement system for offshore oilfield and its effect evaluation," *Journal of Oil and Gas Technology*, vol. 36, no. 4, pp. 157–160, 2014.
- [27] W. Guo, C. Shi, X. Wan, W. Li, and M. Shi, "Study on pilot test of microbial profile modification after polymer flooding in Daqing Oilfield," *Acta Petrolei Sinica*, vol. 27, Supplement 1, 2006.
- [28] H. Wang, Z. Song, B. Hao et al., "Relationship between structures of microbial colony in produced fluids and oil production performance in microbial flooding oil field," *Acta Petrolei Sinica*, vol. 34, no. 3, pp. 535–539, 2013.
- [29] T. Xiang, Q. Feng, N. T. Nazina, Y. She, F. Ni, and J. Zhou, "Mechanism of indigenous microbial enhancement of oil recovery and pilot test," *Acta Petrolei Sinica*, vol. 25, no. 6, pp. 63–67, 2004.

- [30] X. Wang, Y. Xue, S. Yuan, Z. Huang, and Y. Ma, "Influences of microbial community structures and diversity changes by nutrients injection in Shengli oilfield, China," *Journal of Petroleum Science and Engineering*, vol. 133, pp. 421–430, 2015.
- [31] J. Liu, K. Shen, Z. Huang, H. Huai, and F. Chen, "A pilot study on MEOR in Ansai extra-low permeability oil field," *Xinjiang Petroleum Geology*, vol. 31, no. 6, pp. 634–636, 2010.
- [32] H. Cheng, X. Wang, D. Xu, G. Ma, and W. Wang, "Experiments on EOR employing indigenous microorganisms," *Petroleum Exploration & Development*, vol. 33, no. 1, pp. 91–94, 2006.
- [33] J. Lin, B. Hao, G. Cao et al., "A study on the microbial community structure in oil reservoirs developed by water flooding," *Journal of Petroleum Science and Engineering*, vol. 122, pp. 354–359, 2014.
- [34] X. Wang, Z. Chen, X. Li et al., "Microbial flooding in Guan 69 block, Dagang Oilfield," *Petroleum Exploration and Development*, vol. 32, no. 2, pp. 107–109, 2005.
- [35] H. Cheng, S. Xiao, W. Wang, H. Zhang, and X. Wang, "Application of denaturing gradient gel electrophoresis method to study of oil recovery using indigenous microorganism," *Acta Petrolei Sinica*, vol. 26, no. 6, pp. 82–85 and 89, 2005.
- [36] G. Cao, T. Liu, Y. Ba et al., "Microbial flooding after polymer flooding pilot test in Ng3 of Zhong 1 area, Gudao oil field," *Petroleum Geology and Recovery Efficiency*, vol. 20, no. 6, pp. 94–96, 2013.
- [37] Z. Song, L. Guo, S. Yuan, B. Hao, and X. Wu, "Microbial plugging and community distribution of indigenous thermophilic microbes in high-temperature oil reservoirs," *Acta Petrolei Sinica*, vol. 31, no. 6, pp. 975–979, 2010.
- [38] Z. Yang, M. Shi, D. Wang, J. Chang, and X. Dou, "Study on authigenous microorganism community distribution and oil recovery mechanism in Daqing Oilfield," *Acta Petrolei Sinica*, vol. 27, Supplement 1, pp. 95–100 and 105, 2006.
- [39] J. Xiu, L. Yu, and Y. Guo, "A mathematical coupling model of seepage field and microbial field in the indigenous microbe enhancing oil recovery," *Acta Petrolei Sinica*, vol. 31, no. 6, pp. 988–989, 2010.
- [40] W. Zhu, X. Xia, S. Guo, J. Li, Z. Song, and G. Qu, "Microscopic oil displacement mechanism of indigenous microorganisms under high-temperature and high-pressure conditions in reservoirs," *Acta Petrolei Sinica*, vol. 35, no. 3, pp. 528–535, 2014.
- [41] Z. Chen, Q. Feng, R. Liu, J. Chen, and F. Ni, "Development and application of thermophilic microorganism species in oil recover y," *Acta Petrolei Sinica*, vol. 22, no. 6, pp. 59–62, 2001.
- [42] X. Wu, Z. Hou, M. Shi, and Y. Wang, "Research on using microorganism to improve chemical-flooding effect," *Acta Petrolei Sinica*, vol. 27, Supplement 1, pp. 91–94, 2006.
- [43] H. Guo, J. Dong, Z. Wang et al., "2018 EOR Survey in China-part 1," in *Proceedings of SPE Improved Oil Recovery Conference*, pp. 1–22, Tulsa, OK, USA, 2018.
- [44] G. Liao, D. Ma, and Z. Wang, *Practice and Theory of Industrial & Pilot Test in Oilfield Development*, Petroleum Industry Press, 2018.
- [45] Y. She, *Study on Mechanism of Enhanced Oil Recovery Using Petroleum Reservoir Microbiology Resources*, [Ph.D. thesis], Wuhan University, 2010.
- [46] W. Zhang, C. Lin, M. Zhou, and H. Wang, "Application of geological model dynamic updating method in Guanjiapu oilfield, Dagang," *Petroleum Exploration and Development*, vol. 37, no. 2, pp. 220–225, 2010.
- [47] H. Cheng, M. Liu, J. Hu, Q. Feng, H. Li, and J. Liang, "Study on novel nutrient system based on starch-cellulose for microbial flooding," *Acta Petrolei Sinica*, vol. 31, no. 1, pp. 105–109, 2010.
- [48] L.-N. Yi, Z.-P. Li, L. Liu, Y.-Q. Bi, X.-T. Wang, and J.-P. Yi, "Functional microbial stimulation for oil recovery enhancement based on microbial community analysis," *Biotechnology & Biotechnological Equipment*, pp. 1–9, 2018.
- [49] L. Li, G. Wu, Q. Ye, W. Deng, and B. Xu, "Electrochemical modification of Pt/C catalyst by silicomolybdic acid," *Acta Physico-Chimica Sinica*, vol. 22, no. 4, pp. 419–423, 2006.
- [50] C. Ke, W. Sun, Y. Li, G. Lu, Q. Zhang, and X. Zhang, "Microbial enhanced oil recovery in Baolige Oilfield using an indigenous facultative anaerobic strain *Luteimonas huabeiensis* sp. nov.," *Journal of Petroleum Science and Engineering*, vol. 167, pp. 160–167, 2018.
- [51] S. J. Geetha, I. M. Banat, and S. J. Joshi, "Biosurfactants: production and potential applications in microbial enhanced oil recovery (MEOR)," *Biocatalysis and Agricultural Biotechnology*, vol. 14, pp. 23–32, 2018.
- [52] Q. Feng, H. Yang, T. N. Nazina, J. Wang, Y. She, and F. Ni, "Pilot test of indigenous microorganism flooding in Kongdian Oilfield," *Petroleum Exploration and Development*, vol. 32, no. 5, pp. 125–129, 2005.
- [53] K. Wang, J. Wang, S. Li, and L. Zhao, "Development of microbial enhanced oil recovery in Dingbian block," *Science Technology and Engineering*, vol. 11, no. 23, pp. 5529–5532, 2011.
- [54] J. Le, X. Wu, R. Wang, J. Zhang, L. Bai, and Z. Hou, "Progress in pilot testing of microbial-enhanced oil recovery in the Daqing oilfield of North China," *International Biodeterioration & Biodegradation*, vol. 97, pp. 188–194, 2015.
- [55] H. Zhang, L. Huang, L. Yu et al., "The technology of microbe flooding in hypersaline and high temperature reservoir," *Acta Palaeontologica Sinica*, vol. 47, no. 4, pp. 493–497, 2008.
- [56] S. Yi, K. Hu, B. Li, J. Yang, and W. Zhang, "Field application of the technology of microbial paraffin cleaning and preventing in well of high temperature and hyperhaline of Jiangnan Oilfield," *Journal of Oil & Gas Technology*, vol. 31, no. 4, pp. 146–148 and 427, 2009.
- [57] L. Fu, W. Zhou, J. Wang, Y. Zeng, P. Xiong, and H. Wang, "Isolation, identification and performance studies of a thermophilic oil-degrading strain YBW1," *Journal of Hubei University of Technology*, vol. 6, no. 2, pp. 84–87, 2011.
- [58] S. Jia, Q. Zhang, L. Zhang, F. Hu, and F. Chen, "Experimental study on MEOR in Huatugou Oilfield," *Journal of Xian Shiyou University*, vol. 29, no. 4, pp. 64–68, 2014.
- [59] W. Wang, B. Wei, Y. Tan, and X. Wang, "Problems confronted in microbial enhanced oil recovery," *Petroleum Exploration & Development*, vol. 31, no. 6, pp. 88–91, 2004.
- [60] C. Gao, "Experiences of microbial enhanced oil recovery in Chinese oil fields," *Journal of Petroleum Science and Engineering*, vol. 166, pp. 55–62, 2018.
- [61] F. Wang, Z. Wang, and X. Wang, "MEOR pilot effect and prehension on block 50 of Chaoyanggou oil field," *Petroleum Geology & Oilfield Development in Daqing*, vol. 27, no. 3, pp. 102–105, 2008.
- [62] J. Tan, *Water Flooding Adjustment Technical Evaluation and Application in Chaoyanggou Oilfield*, [M.S. Thesis], Northeast Petroleum University, 2016.

- [63] Z. Hou, X. Dou, R. Jin et al., "The application of MEOR in Daqing oilfields," in *Proceedings of SPE Enhanced Oil Recovery Conference*, pp. 1–5, Kuala Lumpur, Malaysia, 2011.
- [64] C. F. Li, Y. Li, X. M. Li, Y. B. Cao, and Y. T. Song, "The application of microbial enhanced oil recovery technology in Shengli Oilfield," *Petroleum Science and Technology*, vol. 33, no. 5, pp. 556–560, 2015.
- [65] W. Weidong, L. Junzhang, G. Xueli et al., "MEOR field test at block Luo 801 of Shengli oil field in China," *Petroleum Science and Technology*, vol. 32, no. 6, pp. 673–679, 2014.
- [66] Q. Liu and D. Qian, "Modulated amplitude waves with non-zero phases in Bose-Einstein condensates," *Journal of Mathematical Physics*, vol. 52, no. 8, pp. 1–12, 2011.
- [67] K. Shen, *MEOR Pilot in Ansai Oilfield*, [M.S. Thesis], Northwest University, 2013.
- [68] J. Liu, H. Zhang, J. Hou, B. Zhang, S. Dong, and H. Huai, "Field test on microbial flooding of ultra-low permeability reservoir in Ansai oilfield," *Petroleum Geology and Engineering*, vol. 25, no. 1, pp. 115–117 and 121, 2011.

Research Article

Variable Pore Structure and Gas Permeability of Coal Cores after Microwave Irradiation

Yi-du Hong,¹ Bai-quan Lin,² Hua Xiang,³ Chuan-jie Zhu,² Zheng Wang,² and Wen Nie¹ 

¹Quanzhou Institute of Equipment Manufacturing, Haixi Institutes, Chinese Academy of Sciences, Quanzhou, Fujian 362000, China

²School of Safety Engineering, China University of Mining and Technology, Xuzhou, Jiangsu 221116, China

³Department of Offshore Oil and Gas Field Development, Faculty of Oil and Gas Field Development, Gubkin Russian State University of Oil and Gas, Moscow 119991, Russia

Correspondence should be addressed to Wen Nie; wen.nie@fjirms.ac.cn

Received 18 May 2018; Revised 25 July 2018; Accepted 18 September 2018; Published 6 December 2018

Academic Editor: Emanuele Tondi

Copyright © 2018 Yi-du Hong et al. This is an open access article distributed under the Creative Commons Attribution License, which permits unrestricted use, distribution, and reproduction in any medium, provided the original work is properly cited.

The experimental work in this paper investigated the effect of microwave energy on pore structure and gas permeability of coal cores. Fifteen coal samples were irradiated under the condition of 2.45 GHz with 6 kW. The effect of microwave irradiation on the pore structure of coal samples was evaluated by nuclear magnetic resonance (NMR). The water saturation degree has little influence on transverse relaxation time (T_2) distribution before the microwave treatment. By contrast, water saturation degree obviously affects the T_2 distribution after the microwave energy treatment. Coal permeability increased after microwave energy treatment. But fractal dimension decreased after microwave energy treatment. The results show that microwave energy has a potential for degassing coal seams.

1. Introduction

Gas permeability is an important parameter for coalbed methane (CBM) production which could be affected by fracture and cleat apertures [1]. Currently, low permeability of coalbed limits the production and utilization of CBM, especially in China [2]. Furthermore, with mining depth in China increasing 10–25 m annually, the poor permeability and high CBM content phenomena become common [3]. Coal seams can be artificially fractured by several measures, such as hydraulic fracturing, hydraulic slotting, CO₂ injection, and N₂ injection, which can increase connectivity of fractures in coal seams for facilitating CBM extraction [4–9]. However, these methods may be not always effective when the coal seam has faults, caves, or large cracks penetrating the ground [10]. As a new degassing coal seam technology, formation microwave heating treatment (FMHT) is few limited by formation geology and is capable to distribute heat over a large reservoir volume thanks to the propagation of electromagnetic energy through the medium [11].

Selective heating nature of microwave would induce thermal stress at the interface between different materials with various dielectric constants [12]. Furthermore, poor thermal conductivity of coal matrix exacerbates the uneven temperature distribution resulting in thermal stress [13]. Thus, microwave energy would induce fractures and increase cleat apertures in the coal matrix [14]. In other words, the microwave energy treatment would influence the pore structure. Sahoo et al. confirmed micro cracks and fissures developed along grain boundaries under microwave irradiation [15]. Ruisanchez et al. found that thermal shock from microwave irradiation produces small cracks and microfissures in coke particle by microphotographs [16]. Liu et al. found that the surface of raw coal was complete and its structure was free of visible microfractures according to several SEM images [17]. Zhao et al. found that a large number of volatiles were released during microwave pyrolysis, which results in an increase in pore volume and specific surface area of lignite [18]. Ge et al. also indicate pore volume and surface area of low-rank coal increased after microwave irradiation treatment [19]. Wang et al. found that the specific surface area

of lignite samples increases, average pore diameter and total pore volume decrease when microwave power increases from 400 W to 800 W, and irradiation time increases from 4 to 16 min [20]. In our previous work, coal cores were collected from underground mines of Shenmu coalfield, China (the coal rank is gas coal), and were used to evaluate the effect of microwave irradiation on pore structure [21, 22]. The porosity, pore size, and pore number increased, but fractal dimensions decreased after microwave energy treatment. However, the effect of microwave energy treatment on gas permeability is still unclear. The permeability is physically significant for coalbed methane development. Therefore, it needs to pay more attention to research the microwave energy on gas permeability of coal.

Perera et al. found that there is a clear increase in gas permeability of naturally fractured black coal with increasing temperature for any confining pressure at high injection pressure (more than 10 MPa) [23]. And temperature does not affect permeability for injection pressure less than 9 MPa. Zhao et al. found gas permeability of coal cores changes a little during 20 to 300°C heating process but increases sharply during 300 to 600°C [24]. Li et al. found that gas permeability increased with temperature when thermal stress was greater than effective stress [25]. Feng et al. found that gas permeability of anthracite decreased at first then increased and finally decreased again with temperature increasing [26]. Wu et al. found that the increased temperature can induce a series of results, such as promoting gas desorption, enhancing gas slippage effect, and inducing coal matrix thermal swelling, resulting in decomposition [27]. And all of those can affect the gas permeability of coal further.

However, investigations of effect of microwave energy on coal gas permeability are not sufficient to provide guidance for FMHT application in field [28, 29]. The main objective of this study is to investigate the effect of microwave energy on the pore structure and gas permeability of coal cores by experiments. Nuclear magnetic resonance (NMR) measurement and permeability test was carried out to evaluate the effect of microwave energy processing on pore structure and gas permeability. In addition, the effect of water saturation degree on transverse relaxation time (T_2) distribution was investigated.

2. Experimental Methodology

2.1. Coal Samples. Fifteen natural coal cores (25 mm in diameter and 60 mm in height) were collected from Yuanzhuang coal mine, Huaibei, China (the coal rank is 1/3 coking coal, which is different with the coal in [21, 22]). Several lump coals were obtained from the working face and immediately sent to the laboratory for experiments. Proximate analysis of coal was accomplished according to the Chinese Coal Proximate Analysis Standard GB/T 212-2008. Maximum vitrinite reflectance of the three coal samples in oil (room temperature, 23°C) was measured. Coal maceral compositions are as shown in Table 1. The coal cores were treated by a microwave heating system (Figure 1). Pore structure of coal cores was measured by an NMR

TABLE 1: Proximate analysis and maximum vitrinite reflectance of coal samples.

Coal	$R_{\text{omax}}/\%$	$M_{\text{ad}}/\%$	$A_{\text{ad}}/\%$	$V_{\text{ad}}/\%$	$F_{\text{c,ad}}/\%$
HY	0.9190	2.56	12.10	32.75	52.59

Notes: R_{omax} is the maximum vitrinite reflectance; M is the moisture; A is the ash; V is the volatile matter; Fc is the fixed carbon; ad is the air-dry basis.



FIGURE 1: Microwave heating system.



FIGURE 2: Low-field nuclear magnet resonance.

instrument (Figure 2). And the coal porosity was carried out by a gravimetric method.

2.2. Microwave Heating System. A novel microwave heating system (Figure 1) was carried out to heat coal cores. Microwave frequency is 2450 ± 25 MHz and microwave power is 6 kW in this study. In general, thermal decomposition does not occur when the temperature is lower than 200°C [30]. Thus, the processing temperature varies from 50 to 200°C. The basic parameter and processing temperature of coal cores are as shown in Table 2.

2.3. NMR Measurements. A nondestructive approach, nuclear magnetic resonance (NMR) measurement, was carried out to evaluate the effect of microwave energy on the pore structure

TABLE 2: Basic parameters and processing temperature of coal samples.

Sample ID	d/mm	h/mm	$T/^\circ C$	Sample ID	d/mm	h/mm	$T/^\circ C$
HY-01	24.2	63.0	50	HY-09 [#]	24.3	62.1	50
HY-02	24.4	62.4	100	HY-10	24.1	61.1	50
HY-03	24.2	62.6	150	HY-11	24.2	59.7	100
HY-04	24.3	61.3	200	HY-12	24.1	61.1	150
HY-05	24.4	62.1	50	HY-13	24.2	60.4	200
HY-06	24.3	60.4	100	HY-14*	24.2	60.7	—
HY-07	25.0	61.0	150	HY-15*	24.2	61.6	—
HY-08	24.3	62.2	200				

Notes: d is diameter of coal cores; h is height of coal cores; T is the processing temperature; [#] this sample was broken into three pieces after microwave treatment; *these two samples are not treated by microwave irradiation.

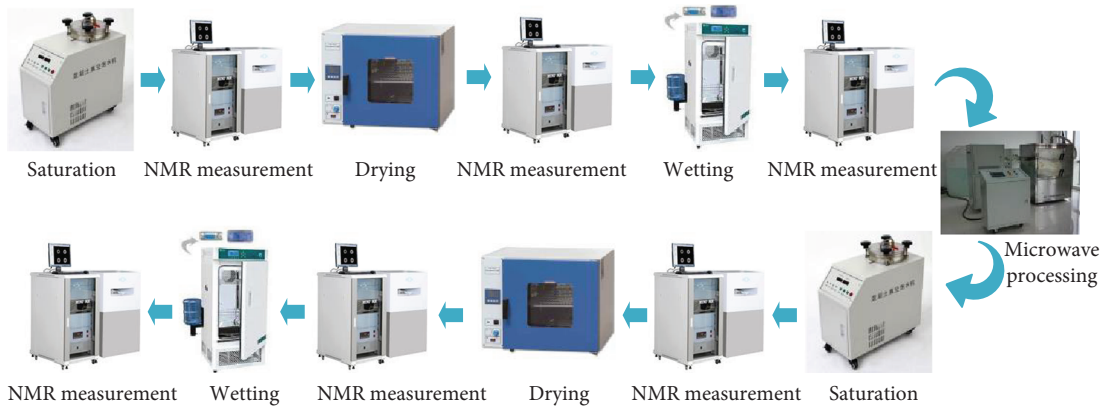


FIGURE 3: Experimental procedure for NMR measurement.

of coal cores. NMR utilizes an external magnetic field to align hydrogenous fluid component of the sample and presents number of hydrogen atoms by the amplitude of the dipole moment [31]. Therefore, it is a measurement of the water volume in the pore structure. NMR has been widely used for the characterization of complex porous media, such as the petroleum reservoir rocks and coal [32–36]. For example, a recent research by Zhang et al. demonstrated that the successful use of the NMR to obtain pore size distribution of mudrock and fine-grained sandstone samples [37]. When the magnetic field is small, few paramagnetic minerals within the coal could influence the measured results and the magnetic information on solid state proton (^{13}C and 1H) can be shielded [31, 38]. The longitudinal (T_1) and transverse (T_2) relaxation time can be used to characterize the pore distribution. T_2 is the preferred measurement method because the measurement of T_2 is fast and usually provides similar results with respect to T_1 [39]. The T_2 relaxation time can be interpreted as follows [40]:

$$\frac{1}{T_2} = \frac{1}{T_{2B}} + \rho \left(\frac{S}{V} \right) + \frac{D(\gamma G T_E)^2}{12}, \quad (1)$$

where T_{2B} is the free relaxation time, ms; ρ is a constant representing the transverse relaxation strength, $\mu m/ms$; S/V is the specific surface area which relates to the pore size;

D is the diffusion coefficient, $\mu m^2/ms$; γ is the gyromagnetic ratio, MHz/T; and G is the field-strength gradient, Gs/cm; T_E is the interecho spacing, ms.

Since the value of T_{2B} is always much larger than T_2 , i.e., $(1/T_2) \gg (1/T_{2B})$, and the values of D and T_E are always small, (1) can be simplified as shown below [33, 41]:

$$\frac{1}{T_2} = \rho \left(\frac{S}{V} \right). \quad (2)$$

T_2 distribution in smaller pores relaxes faster than that in larger pores [40]. Therefore, T_2 distribution is similar to the pore size distribution. Larger pores mean longer relaxation time while smaller pores produce shorter relaxation time.

A MINI MR instrument manufactured by the Shanghai Niumag Corporation (China) (Figure 2) was used to carry out the NMR measurements. Constant magnetic field strength of this instrument is 0.53 T, while resonance frequency is 23 MHz and constant temperature is 32°C. The measurement parameters include the following: interecho spacing, 0.23 ms; the number of scans, 32; and sampling frequency, 333.33 KHz. Then, transverse relaxation time (T_2) distributions were computed by the simultaneous iterative reconstruction technique with 100,000 iterations [42].

NMR measurement procedures were carried out according to Figure 3. “Saturation” means that coal samples were

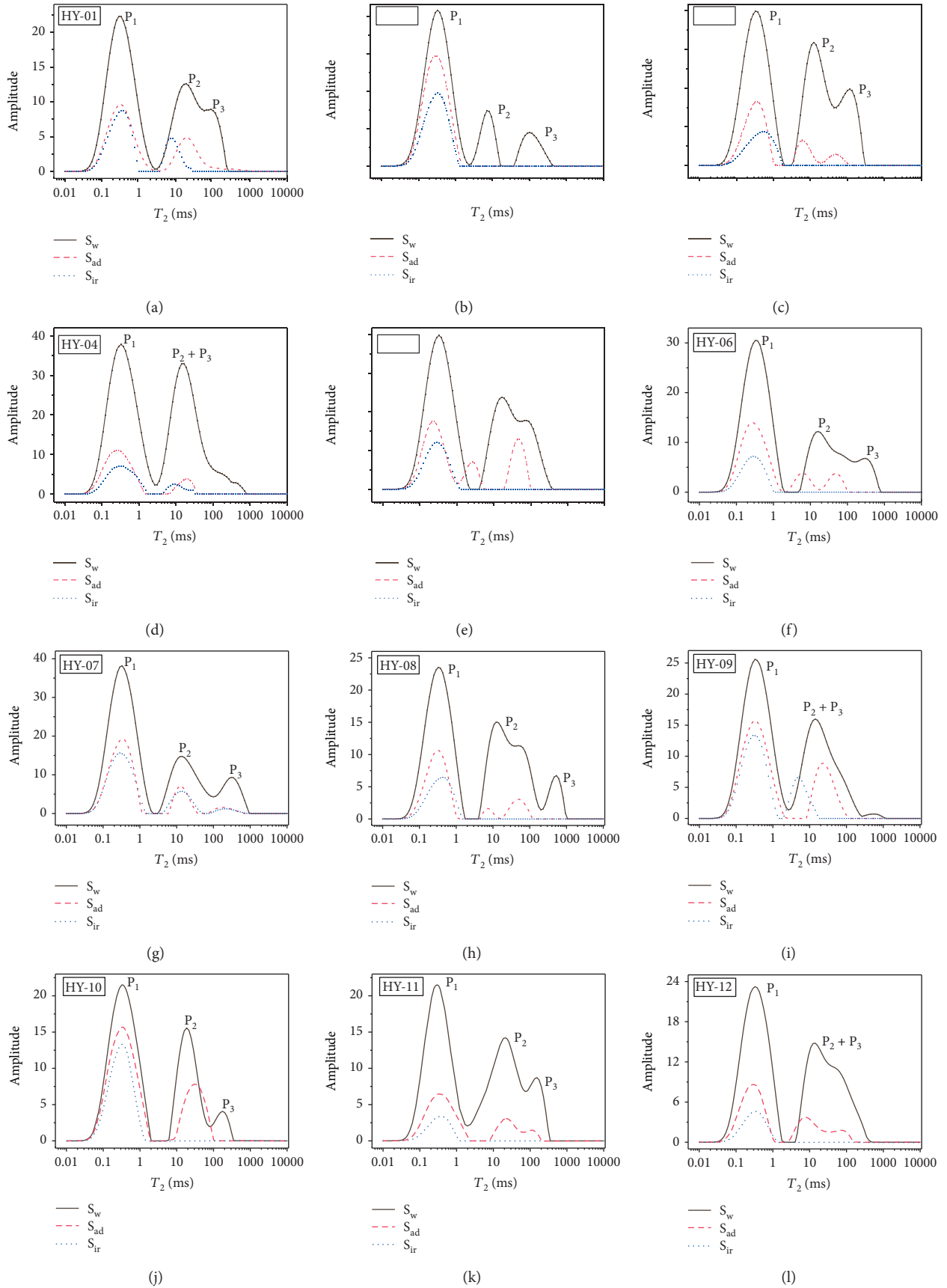


FIGURE 4: Continued.

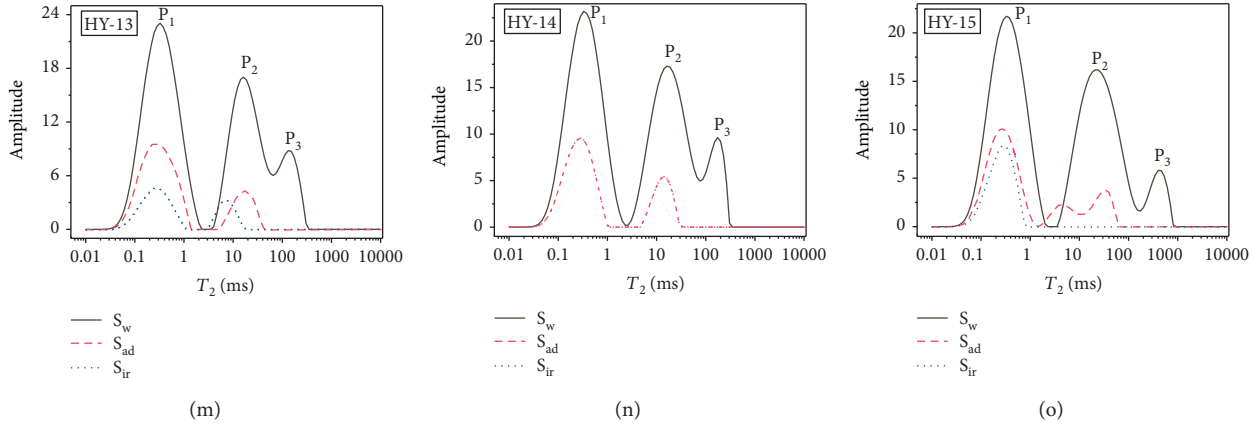


FIGURE 4: NMR T_2 distribution before microwave treatment with various water saturation.

saturated with 100% distilled water for at least 72 hours. The T_2 spectrum at “drying” shows that coal samples were dried for 24 hours in a vacuum furnace at 40°C with absolute pressure ~ 8 kpa. “Wetting” means that coal samples were processing with $\sim 20^\circ\text{C}$ and 100% humidity for 24 hours. “NMR measurement” shows that coal samples were measured by the NMR instrument. “Microwave processing” is that coal samples are heated by the microwave heating system. The NMR measurements were carried out after “saturation” (S_w), “drying” (S_{ir}), and “wetting” (S_{ad}) processing.

In addition, the permeability test was carried out after all NMR measurement. Anhydrous copper sulphate dried coal cores under ambient temperature $\sim 25^\circ\text{C}$ for 24 hours before the permeability test. The test gas is nitrogen and the lateral confining pressures are 3 MPa and 10 MPa for gas permeability measurement, respectively. In this test, the temperature is ambient temperature ($\sim 25^\circ\text{C}$). And the permeability test carried out under an initial lateral confining pressure 3 MPa.

3. Experiment Results

NMR measurements of fifteen coal cores with various water saturation degrees were performed before microwave treatment (Figure 4). Black solid lines are T_2 spectra at S_w , while red dash lines are T_2 spectra at S_{ad} and blue dash lines are T_2 spectra at S_{ir} . Wave trough can be used to separate the peaks. So distribution of the T_2 spectra at S_w is commonly three peaks, p_1 at 0.03–3 ms, p_2 at 3–100 ms, and p_3 at >100 ms (Figure 4). The two peaks will be regarded as a new peak if without clear wave trough [21]. For example, in sample HY-04 (Figure 4(d)), the wave trough between p_2 and p_3 is not clear. So the two peaks can be considered as a new peak ($p_2 + p_3$). For multiple peaks, the amplitude of the wave trough between peaks can be used to identify the connection among pores [31]. Take HY-011 as example (Figure 4(g)), the amplitude of wave troughs between three peaks is much larger than zero, which suggests well-connected multipores exist in this coal sample. However, in HY-02 (Figure 4(b)), the amplitude of wave troughs between three peaks is equal to zero. This indicates that the pore connection is bad.

S_w means coal core processing by “saturation,” S_{ir} means processing by “drying,” and S_{ad} means processing by “wetting.”

The effect of water saturation degree on T_2 distribution is obviously after the microwave energy treatment (Figure 5). Taking HY-01 as an example, the second peak (from left to right) of T_2 distribution at S_{ir} locates at the left hand of the T_2 distributions at S_{ad} (Figure 5(a)). This is consistent with our previous work [21, 22].

Permeability of twelve coal samples (HY-04, HY-09, and HY-13 deformed after microwave energy treatment) was measured (Figure 6(a)). HY-14 and HY-15 represent the coal permeability without microwave energy treatment. Ambient temperature is 25°C in this study, and therefore, the temperature of untreated coal samples is marked as 25°C . The coal permeability increases with increased processing temperature (Figure 6(a)). This indicates that microwave energy treatment improved pore connectivity of coal. The connectivity of pore is main factor which affects the permeability of coal [43]. In general, permeability of coal sample decrease exponentially with the increase of effective stress [44]. In this study, with lateral confining pressure increase from 3 MPa to 10 MPa, the permeability decreases. But the permeability of coal samples treated is still higher than that of coal samples untreated under 10 MPa confining pressure.

4. Discussions

4.1. T_2 Distribution of Coal Cores. Moisture in pore structure always can be divided into four types: free moisture, capillary moisture, chemically bound moisture, and water of hydration [45]. Chemically bound moisture and water of hydration are difficult to remove. Free moisture would not completely evaporate until 110°C , and capillary moisture would completely evaporate when temperature exceeds to 180°C with atmospheric pressure [46, 47]. The water boiling temperature is 40°C at absolute pressure ~ 8 kpa. Thus, the free moisture can mostly be removed after “drying” processing. The T_2 spectra at S_{ir} may only indicate capillary moisture, chemically bound moisture, water of hydration, and a little part of free moisture in the pore structure. And the water saturation degree at S_{ir} is lower than that of S_{ad} . Therefore, the

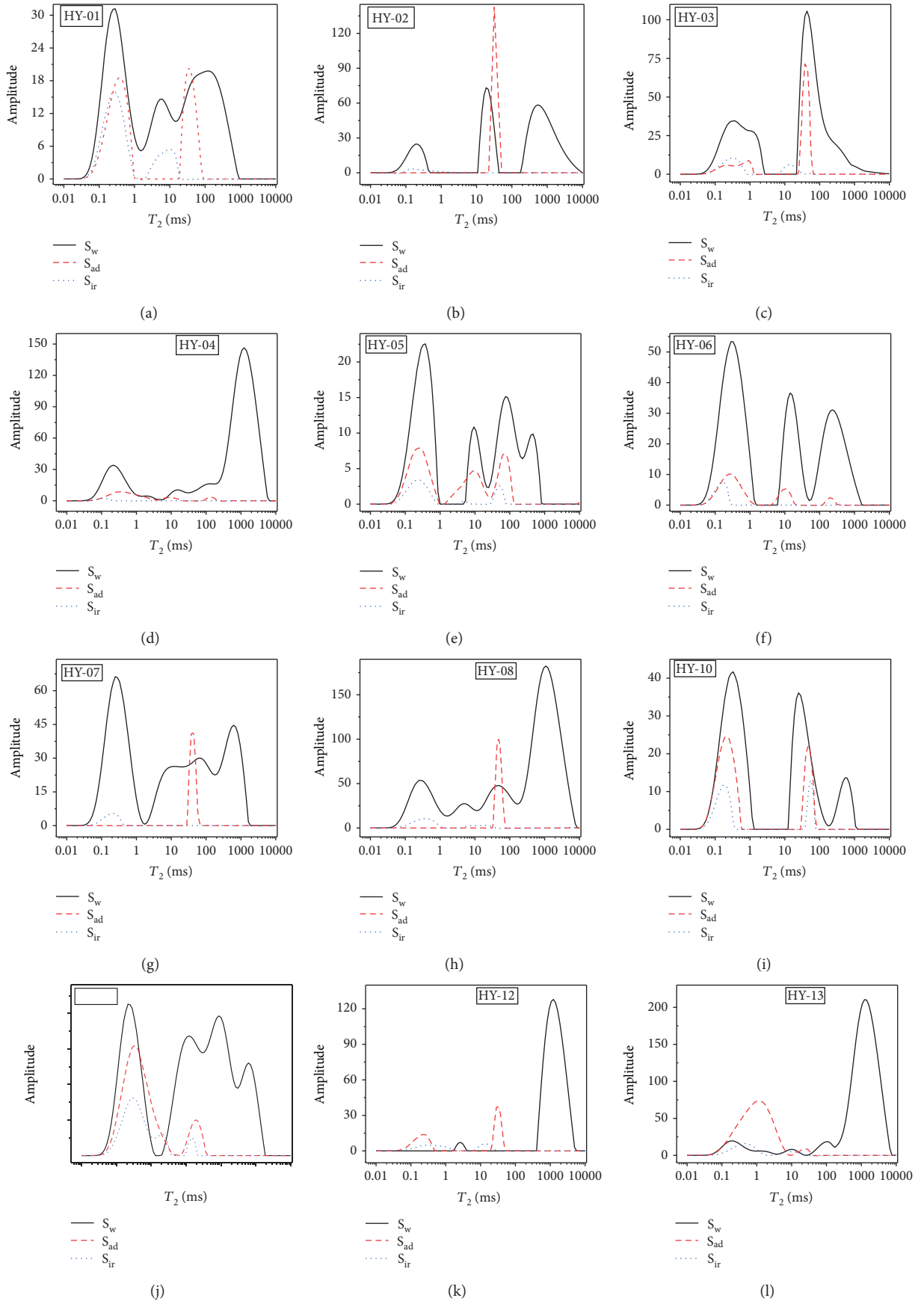


FIGURE 5: NMR T_2 distribution after microwave treatment with various water saturation.

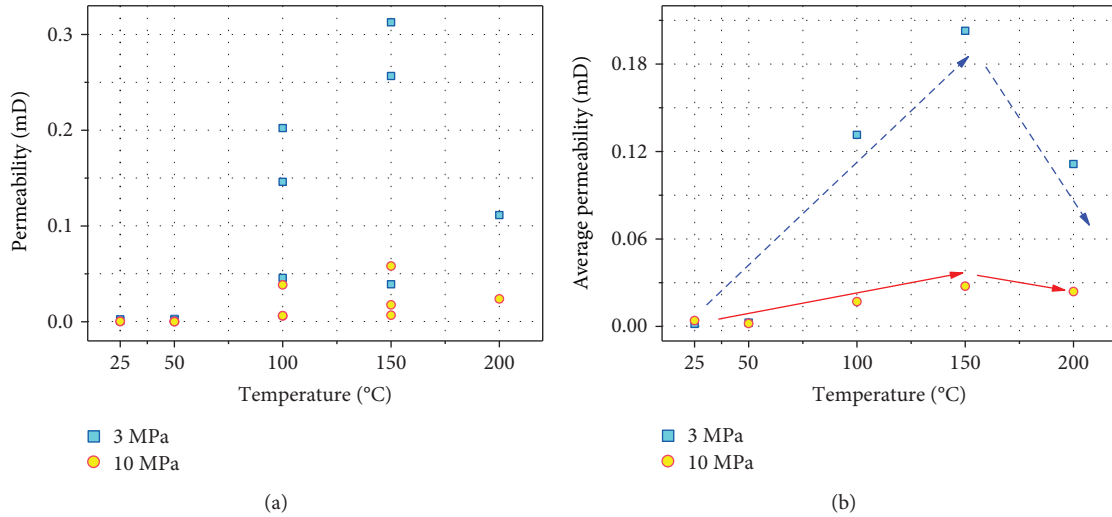


FIGURE 6: Effect of microwave treatment on coal permeability.

number and amplitude of peaks of T_2 spectra at S_{ad} is larger than that of S_{ir} (Figure 4).

Although the amplitude of T_2 distribution decreases with decreasing water saturation degree, the water saturation degree has little influence on T_2 distribution location (before microwave treatment) (Figure 4). This is different to our previous work that the T_2 distributions at S_{ir} and S_{ad} were located at the left-hand side of the T_2 distributions at S_w [21, 22]. The reason could be the differences of the pore structure and wettability of coal. The pore structure (including volume, specific surface area, and pore connectivity) relates to coal ranks [31, 48, 49]. The rank of coal used in this study differs from that in our previous work. Thus, the water distribution in pore structure of the coal used in this study is different. Furthermore, the composition of mineral and functional groups relates to coal ranks [50], which affects the wettability and hydrophobicity of coal surface [51]. And the pores in coal are not simple geometrical shapes such as cylinders or shapes. The pore walls may be rough and the pore may contain many tiny irregularities. And the wettability of coal decreases with the increase of surface roughness [21]. Thus, the microporosity on the pore walls containing water depends on the wettability of coal pore surface. In NMR measurement, all pore space of the water molecules of the pore fluid diffuse before relaxing by interacting with the pore walls would be regarded as a single pore. Thus, the microporosity contained in the rough pore surface and in the irregularities will often be included by NMR measurement as part of the total volume of the large pore [40]. Therefore, the microporosity may appear in larger relaxation time of the T_2 distribution at S_w . Moreover, the microporosity contained in the rough surface may not contain water caused by high surface roughness or low wettability. The pore structure and wettability of coal would affect the T_2 distribution.

The area under the T_2 distribution curve is proportional to the number of hydrogen protons in the pore fluids within the pore structure [40]. Therefore, the area of T_2 distribution can be calibrated to give a porosity value. The area under the

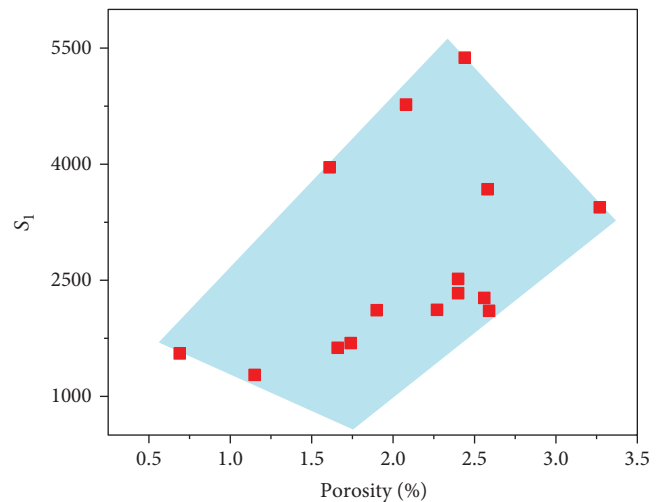


FIGURE 7: Relation between S_1 and porosity. S_1 is the area under the T_2 distribution curve of coal cores without microwave processing.

T_2 distribution curve (S_1) increases with increased porosity (Figure 7). It should be noted that the porosity here is the porosity of coal sample without microwave energy treatment. The linear relation between the area of T_2 distribution and porosity is not obvious. The reason may be the heterogeneity of coal samples. The extraction of lump coal is usually extremely sparse compared to the volume of coal seams. Moreover, cores are more easily taken from well-consolidated part in lump coal.

4.2. Effect of Microwave Energy on T_2 Distributions. This suggests that the pore structure and wettability of coal is influenced by microwave energy treatment. In general, thermal decomposition does not occur when the temperature is lower than 200°C [30]. In this study, the maximum processing temperature is 200°C. Thus, there is no thermal

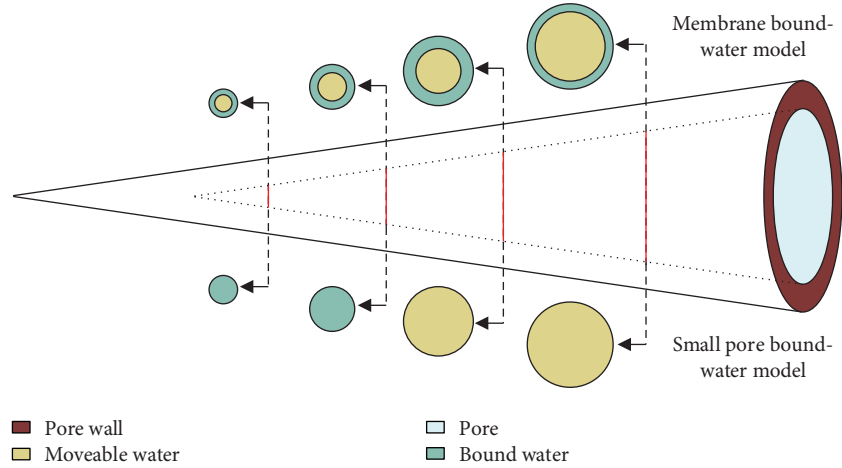


FIGURE 8: NMR bound-water model.

decomposition in the coal cores, which means the coal rank would not change after microwave energy treatment. The thermal fracture results from the different microwave-absorbing properties or a different dielectric permittivity and loss factor of each phase [12]. Moreover, the microwave energy treatment would influence the pore surface roughness of coal, which may affect the wettability [21]. Therefore, the effect of water saturation degree on T_2 distribution is different pre- and postmicrowave.

Small pore bound-water (SPBW) model and membrane bound-water (MBW) model are always used to describe the state of bound water in pore structure (Figure 8) [22]. SPBW is based on the assumption that the free fluids reside in large pores and the bound fluids reside in small pores, while MBW believes that a given pore can contain both free and bound fluids [22]. As Figure 5 shows, the water saturation degree can influence T_2 distribution. This suggests that MBW model may be more suitable to describe the state of bound water. This is consistent with our previous work [21, 22].

T_2 distribution at S_w changes after microwave processing (Figure 9). According to the amplitude changing, these spectra can be divided into several cases. First, the amplitude of T_2 distribution at S_w of treated samples is larger than that of untreated samples at all spectra (such as Figure 9(a), 9(g), and 9(h)). Second, not all amplitude of the spectra becomes larger after microwave treatment (such as Figure 9(d) and 9(l)). In this case, the amplitude of the spectra decreases after microwave treatment when T_2 is less than 100 ms. Microwave energy treatment can induce fractures and increase pore sizes. Moreover, the microporosity contained in the rough pore surface and in the irregularities will often be regarded as part of the total volume of the large pore in NMR measurement [40]. Thus, a majority of microporosity cannot appear in T_2 distribution at S_w of treated coal samples. This confirmed the MBW model is more suitable to describe the state of bound water in coal. According (2), the changing of T_2 distribution at S_w also suggests that the specific surface area of the coal sample changed after microwave treatment.

The surface integral of T_2 distribution at S_w can be used to characterize the pore system because of the abscissa of the T_2 distribution representing the pore size and the ordinate representing the pore number [21, 30, 38]. A dimensionless parameter (R_s) was used to evaluate the effect of microwave energy treatment on coal samples, which can be defined as

$$R_s = \frac{S_2 - S_1}{S_1}, \quad (3)$$

where S_1 is a curved surface integral of the T_2 distribution at S_w before microwave energy treatment and S_2 is a curved surface integral of the T_2 distribution at S_w after microwave energy treatment.

R_s increases with increasing processing temperature (Figure 10). This suggests that the pore volume increases with processing temperature. This also confirmed that microwave energy treatment would induce fractures. This is consistent with our previous work that the porosity increases after microwave heating [21].

4.3. Gas Permeability of Coal Cores Pre- and Postmicrowave.

The influence of processing temperature on average permeability is evaluated (Figure 6(a)). HY-04 and HY-13 deformed after microwave energy treatment and cannot be carried out in the gas permeability test. Thus, permeability of HY-08 was used to present the average permeability of coal samples at 200°C. The average permeability increases at first then decreases with incremental processing temperature (the turning point is 150°C). This is different from the work by Li, who found that the permeability decreases at first then increases and finally decreases again with temperature increasing (25–180°C) under lateral confining pressure 6 MPa [52]. The coal matrix would produce thermal expansion resulting in pore space shrink, which would induce permeability decreasing. But with the processing temperature increasing, the thermal expansion may induce coal matrix fracturing. Thus, pore space increased would result in the permeability increasing. Furthermore, fractures in coal matrix

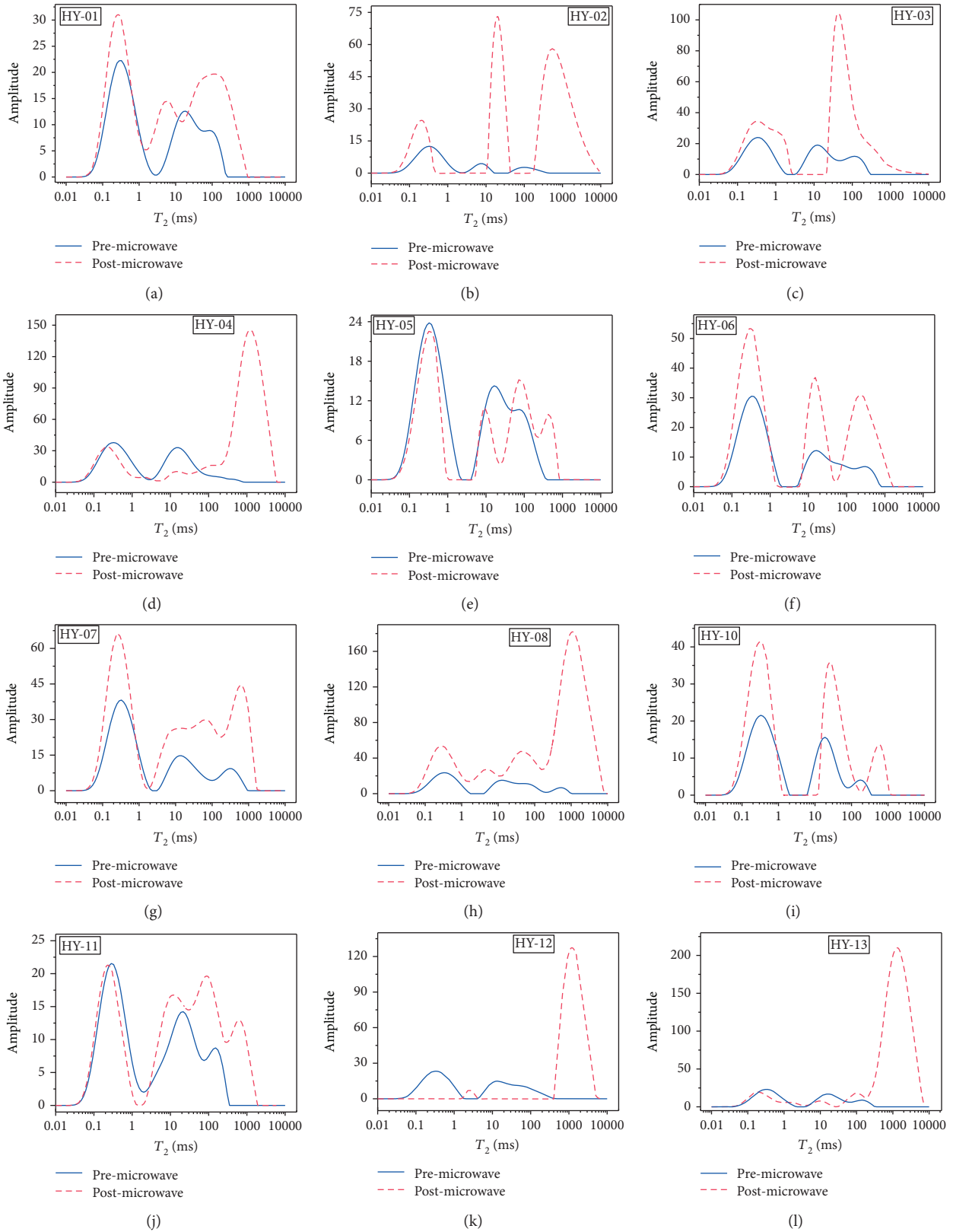


FIGURE 9: Effect of microwave treatment on NMR T_2 distribution at S_w .

would result in coal mechanical strength (such as elasticity modulus) decreasing [53]. Therefore, gas permeability would decrease again with more and more induced fracture. In

theory, the microwave energy treatment cannot only induce fractures and increase cleat apertures by thermal expansion but also facilitate coal fracturing by selective heating nature.

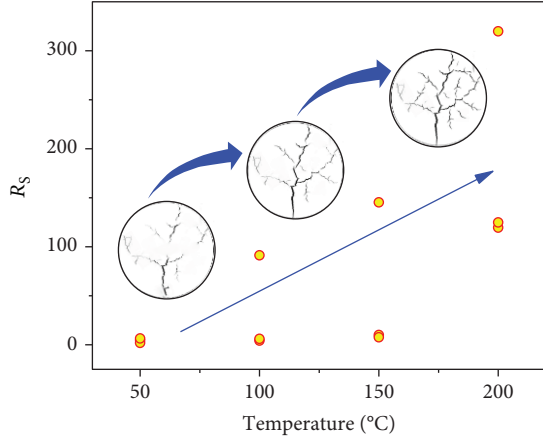


FIGURE 10: Effect of processing temperature on R_s .

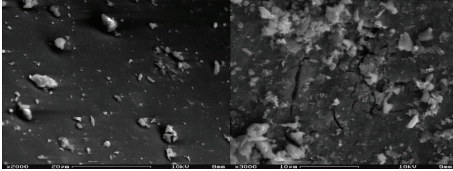


FIGURE 11: Microphotographs of an untreated coke particle (a) and a coke particle subjected to microwave treatment (b) [16].

This is confirmed by Ruisanchez's work [16]. SEM micrographs of the particle microstructure show that the coke particle is more cracked after microwave treatment (Figure 11). Kumar et al. also found the fracture volume of coal increased from 1.8% to 16.1% after microwave exposure via micro-focused X-ray computed tomography [12]. The coal samples used in this work would maintain pore structure well, which decreases the effect of lateral confining pressure on the pore structure. As discussed in Section 4.2, the specific surface area changed after microwave energy treatment. And the specific surface area influences the gas permeability [54, 55]. All of these factors induced gas permeability increasing at first and then decreasing with processing temperature increased in this study. This may also suggest that 150°C is the optimal processing temperature for improving coal permeability under lateral confining pressure (3 MPa and 10 MPa) in this study.

Fractal dimension, a nonlinear mathematics method initially proposed by Mandelbrot [56], has been extensively employed for quantifying the complexity of structure and physical properties of coal [57, 58]. Fractal dimension D can be calculated as [22]

$$D = 3 - \frac{\ln V_p}{\ln T_2 - \ln T_{2\max}}, \quad (4)$$

where $T_{2\max}$ is transverse relaxation time of the T_2 spectrum corresponding to maximum pore size; T_2 is the transverse relaxation time of the T_2 spectrum corresponding to pore size r ; V_p is the ratio between the whole pore volume that

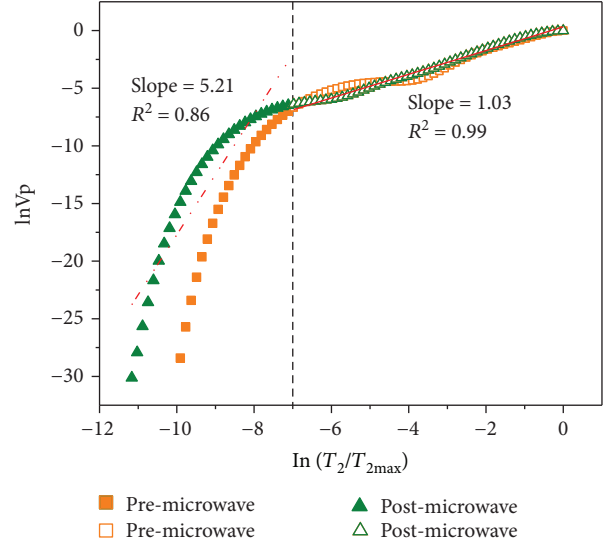


FIGURE 12: Curve of $\ln(V_p)$ versus $\ln(T_2/T_{2\max})$.

pore size not exceeding r and total pore volume. The prerequisite for the formula is that transverse relaxation time is directly proportional to pore size [59]. The other prerequisite is that maximum T_2 value is much larger than the minimum T_2 value exhibited by the medium [59]. In this study, the maximum T_2 value is fourth orders of magnitude larger than the minimum T_2 value. The curve of $\ln(V_p)$ versus $\ln(T_2/T_{2\max})$ of the coal core is as shown in Figure 12. And the slope between $\ln(V_p)$ versus $\ln(T_2/T_{2\max})$ is used to calculate the fractal dimension. The value of $\ln(V_p)$ increased rapidly at first then increased slowly with $\ln(T_2/T_{2\max})$ increasing. This turning point is about -7 . So the curve is divided into two parts for linear fitting. It found that the slope of the left part is larger than 3. The fractal dimension calculated from this will be negative. This suggests that the calculated fractal dimension according to the left part curve has less physical meaning. For this reason, the fractal dimension is calculated when $\ln(T_2/T_{2\max})$ is larger than -7 in this study.

Fractal dimension decreased after microwave energy treatment (Figure 13(a)). On one hand, the microwave energy treatment would induce fractures in the coal matrix, which would increase the complexity of the pore surface. On the other hand, the microwave treatment may crack pore surface and induce debris. The debris would be taken out during water saturating process. And the pore surface would become smooth. In this study, the second factor may be more obvious. The permeability increased after microwave treatment (Figure 6(a)), and the fractal dimension decreased after microwave treatment (Figure 13(a)). In general, permeability decreases with fractal dimension increasing [60]. However, fractal dimension shows a poor correlation with permeability in this study (Figure 13(b)). This may be due to the following three reasons: (1) the limited number of coal cores brings the inevitable samples errors. (2) The error in the estimated fractal dimension may relate to the assumption T_2 is directly proportional to pore size. The pore structure of coal is

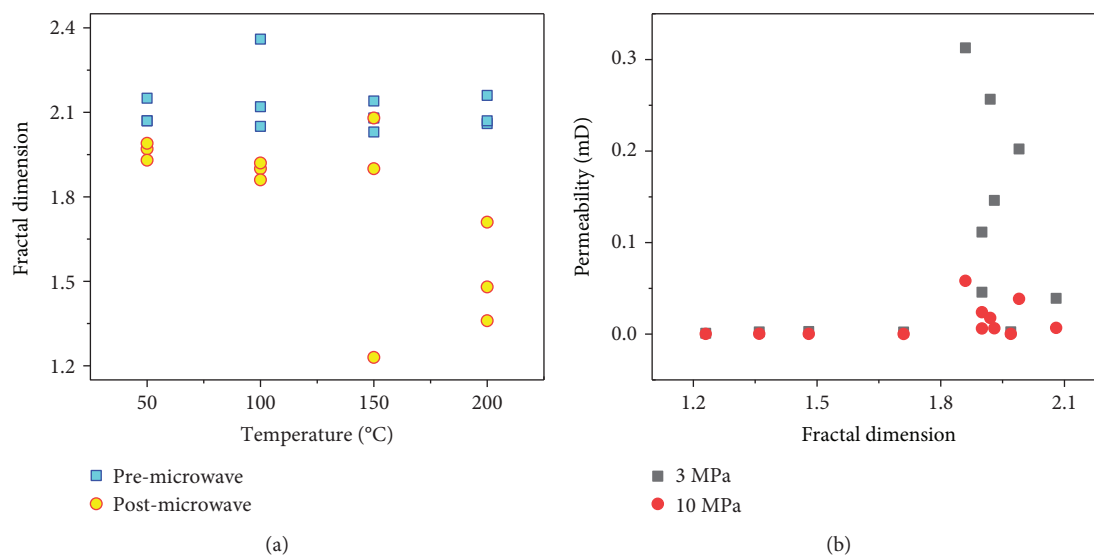


FIGURE 13: (a) Fractal dimension vs. processing temperature and (b) fractal dimension vs. permeability.

complex and may not fully meet this assumption. (3) The gas permeability is measured by nitrogen; by contrast, the NMR measurement is based on the water in the pore structure. Firstly, molecules size can affect gas transport in coal [61]. Secondly, water may react with clay mineral in pore structure, which would influence the water transport [62]. Thirdly, coal swelling/shrinkage during gas adsorption/desorption would influence the gas permeability [63]. Therefore, the nitrogen transport in coal is different to the water.

5. Conclusions

This study presents the potential use of microwave energy for inducing fractures and increasing cleat apertures in coal cores, which would change pore structure and gas permeability. The coal samples were irradiated with microwave frequency 2.45 GHz and power 6 kW. The nuclear magnetic resonance (NMR) measurements were carried out for evaluating the changing of transverse relaxation time (T_2) distribution of various water saturation degree ($S_w > S_{ad} > S_{ir}$). The fractal dimension is calculated according to T_2 distribution. The gas permeability of coal samples was also measured. Major findings are summarized as follows:

- (1) The amplitude of T_2 distribution has a positive relation with water saturation degree, and the water saturation degree has little influence on T_2 distribution location before microwave treatment. And the area of T_2 distribution positively relates to the porosity
- (2) The location and amplitude of T_2 distribution has a noticeable relation with water saturation degree after the microwave energy treatment. And MBW model is more suitable to describe the state of bound water in the pore structure
- (3) The permeability of coal samples increased after microwave treatment. The gas permeability of coal cores increased at first and then decreased with

processing temperature increasing. And the turning point is about 150°C. In addition, the fractal dimension decreased after microwave energy treatment. However, fractal dimension shows a poor correlation with permeability in this study

Data Availability

The data used to support the findings of this study are available from the corresponding author upon request.

Conflicts of Interest

The authors declare that they have no conflicts of interest.

Acknowledgments

The research is supported by CAS Pioneer Hundred Talents Program (2017-120) and the Open Fund (PLN1502) of the State Key Laboratory of the Oil and Gas Reservoir Geology and Exploitation, Southwest Petroleum University.

References

- [1] T. A. Moore, "Coalbed methane: a review," *International Journal of Coal Geology*, vol. 101, pp. 36–81, 2012.
- [2] H. Dai, Q. Zhao, B. Lin et al., "Premixed combustion of low-concentration coal mine methane with water vapor addition in a two-section porous media burner," *Fuel*, vol. 213, pp. 72–82, 2018.
- [3] H. Xie, J. Wang, B. Shen et al., "New idea of coal mining: scientific mining and sustainable mining capacity," *Journal of China Coal Society*, vol. 37, pp. 1069–1079, 2012.
- [4] Q. Li, B. Lin, and C. Zhai, "The effect of pulse frequency on the fracture extension during hydraulic fracturing," *Journal of Natural Gas Science and Engineering*, vol. 21, pp. 296–303, 2014.

- [5] N. Guanhua, L. Baiquan, and Z. Cheng, "Impact of the geological structure on pulsating hydraulic fracturing," *Arabian Journal of Geosciences*, vol. 8, no. 12, pp. 10381–10388, 2015.
- [6] L. B. Colmenares and M. D. Zoback, "Hydraulic fracturing and wellbore completion of coalbed methane wells in the Powder River Basin, Wyoming: implications for water and gas production," *AAPG Bulletin*, vol. 91, no. 1, pp. 51–67, 2007.
- [7] Q. Zou and B. Lin, "Fluid–solid coupling characteristics of gas-bearing coal subjected to hydraulic slotting: an experimental investigation," *Energy & Fuels*, vol. 32, no. 2, pp. 1047–1060, 2018.
- [8] L. Qin, C. Zhai, S. Liu, and J. Xu, "Factors controlling the mechanical properties degradation and permeability of coal subjected to liquid nitrogen freeze-thaw," *Scientific Reports*, vol. 7, no. 1, p. 3675, 2017.
- [9] A. S. Ranathunga, M. S. A. Perera, P. G. Ranjith, Y. Ju, V. Vishal, and P. N. K. de Silva, "A macro-scale experimental study of sub- and super-critical CO₂ flow behaviour in Victorian brown coal," *Fuel*, vol. 158, pp. 864–873, 2015.
- [10] A. S. Ranathunga, M. S. A. Perera, and P. G. Ranjith, "Deep coal seams as a greener energy source: a review," *Journal of Geophysics and Engineering*, vol. 11, no. 6, p. 063001, 2014.
- [11] M. Bientinesi, L. Petarca, A. Cerutti et al., "A radiofrequency/microwave heating method for thermal heavy oil recovery based on a novel tight-shell conceptual design," *Journal of Petroleum Science and Engineering*, vol. 107, pp. 18–30, 2013.
- [12] H. Kumar, E. Lester, S. Kingman et al., "Inducing fractures and increasing cleat apertures in a bituminous coal under isotropic stress via application of microwave energy," *International Journal of Coal Geology*, vol. 88, no. 1, pp. 75–82, 2011.
- [13] W. Zhao, J. Chen, X. D. Chang et al., "Effect of microwave irradiation on selective heating behavior and magnetic separation characteristics of Panzhihua ilmenite," *Applied Surface Science*, vol. 300, pp. 171–177, 2014.
- [14] E. Lester, S. Kingman, and C. Dodds, "Increased coal grindability as a result of microwave pretreatment at economic energy inputs," *Fuel*, vol. 84, no. 4, pp. 423–427, 2005.
- [15] B. K. Sahoo, S. De, and B. C. Meikap, "Improvement of grinding characteristics of Indian coal by microwave pretreatment," *Fuel Processing Technology*, vol. 92, no. 10, pp. 1920–1928, 2011.
- [16] E. Ruisanchez, A. Arenillas, E. J. Juarez-Perez, and J. A. Menendez, "Pulses of microwave radiation to improve coke grindability," *Fuel*, vol. 102, pp. 65–71, 2012.
- [17] J.-Z. Liu, J.-F. Zhu, J. Cheng, J.-H. Zhou, and K.-F. Cen, "Pore structure and fractal analysis of Ximeng lignite under microwave irradiation," *Fuel*, vol. 146, pp. 41–50, 2015.
- [18] X. Q. Zhao, B. W. Guo, W. L. Wang et al., "Experimental study on microwave pyrolysis of three Chinese lignite," *Journal of Analytical and Applied Pyrolysis*, vol. 124, pp. 303–309, 2017.
- [19] L. C. Ge, Y. W. Zhang, Z. H. Wang, J. H. Zhou, and K. F. Cen, "Effects of microwave irradiation treatment on physicochemical characteristics of Chinese low-rank coals," *Energy Conversion and Management*, vol. 71, pp. 84–91, 2013.
- [20] W. Wang, F. Xin, Y. Tu, and Z. Wang, "Pore structure development in Xilingol lignite under microwave irradiation," *Journal of the Energy Institute*, vol. 91, no. 1, pp. 75–86, 2018.
- [21] Y. D. Hong, B. Q. Lin, C. J. Zhu, and H. Li, "Effect of microwave irradiation on petrophysical characterization of coals," *Applied Thermal Engineering*, vol. 102, pp. 1109–1125, 2016.
- [22] Y. D. Hong, B. Q. Lin, C. J. Zhu, and H. Li, "Influence of microwave energy on fractal dimension of coal cores: implications from nuclear magnetic resonance," *Energy & Fuels*, vol. 30, no. 12, pp. 10253–10259, 2016.
- [23] M. S. A. Perera, P. G. Ranjith, S. K. Choi, and D. Airey, "Investigation of temperature effect on permeability of naturally fractured black coal for carbon dioxide movement: an experimental and numerical study," *Fuel*, vol. 94, pp. 596–605, 2012.
- [24] Z. Yangsheng, Q. Fang, W. Zhijun, Z. Yuan, L. Weiguo, and M. Qiaorong, "Experimental investigation on correlation between permeability variation and pore structure during coal pyrolysis," *Transport in Porous Media*, vol. 82, no. 2, pp. 401–412, 2010.
- [25] Z. Li, X. Xian, and Q. Long, "Experiment study of coal permeability under different temperature and stress," *Journal of China University of Mining and Technology*, vol. 38, pp. 523–527, 2009.
- [26] Z. Feng, Z. Wan, Y. Zhao et al., "Experimental study of permeability of anthracite and gas coal masses under high temperature and triaxial stress," *Chinese Journal of Rock Mechanics and Engineering*, vol. 29, pp. 689–696, 2010.
- [27] S. Wu, D. Tang, S. Li, H. Wu, X. Hu, and X. Zhu, "Effects of geological pressure and temperature on permeability behaviors of middle-low volatile bituminous coals in eastern Ordos Basin, China," *Journal of Petroleum Science and Engineering*, vol. 153, pp. 372–384, 2017.
- [28] H. Li, B. Lin, W. Yang, Y. Hong, and Z. Wang, "A fully coupled electromagnetic-thermal-mechanical model for coalbed methane extraction with microwave heating," *Journal of Natural Gas Science and Engineering*, vol. 46, pp. 830–844, 2017.
- [29] B. Lin, H. Li, Z. Chen, C. Zheng, Y. Hong, and Z. Wang, "Sensitivity analysis on the microwave heating of coal: a coupled electromagnetic and heat transfer model," *Applied Thermal Engineering*, vol. 126, pp. 949–962, 2017.
- [30] Y. D. Cai, D. M. Liu, Y. B. Yao, Z. T. Li, and Z. J. Pan, "Partial coal pyrolysis and its implication to enhance coalbed methane recovery, part I: an experimental investigation," *Fuel*, vol. 132, pp. 12–19, 2014.
- [31] Y. Yao, D. Liu, Y. Che, D. Tang, S. Tang, and W. Huang, "Petrophysical characterization of coals by low-field nuclear magnetic resonance (NMR)," *Fuel*, vol. 89, no. 7, pp. 1371–1380, 2010.
- [32] D. Xuan, S. Fu, and R. Xie, "Study on NMR logging bulk volume of irreducible water model," *Nuclear Electronics & Detection Technology*, vol. 27, no. 3, pp. 578–582, 2007.
- [33] Y. He, Z. Mao, L. Xiao, and X. Ren, "An improved method of using NMR T₂ distribution to evaluate pore size distribution," *Chinese Journal of Geophysics*, vol. 48, pp. 373–378, 2005.
- [34] N. Golsanami, J. Sun, and Z. Zhang, "A review on the applications of the nuclear magnetic resonance (NMR) technology for investigating fractures," *Journal of Applied Geophysics*, vol. 133, pp. 30–38, 2016.
- [35] A. S. Khorshidi, J. Storsley, L. N. Malunga, S. J. Thandapilly, and N. Ames, "Advancing the science of wheat quality evaluation using nuclear magnetic resonance (NMR) and ultrasound-based techniques," *Cereal Chemistry*, vol. 95, no. 3, pp. 347–364, 2018.
- [36] M. F. Marccone, S. Wang, W. Albabish, S. Nie, D. Somnarain, and A. Hill, "Diverse food-based applications of nuclear

- magnetic resonance (NMR) technology,” *Food Research International*, vol. 51, no. 2, pp. 729–747, 2013.
- [37] N. Zhang, F. Zhao, P. Guo et al., “Nanoscale pore structure characterization and permeability of mudrocks and fine-grained sandstones in coal reservoirs by scanning electron microscopy, mercury intrusion porosimetry, and low-field nuclear magnetic resonance,” *Geofluids*, vol. 2018, 20 pages, 2018.
- [38] S. Li, D. Tang, Z. Pan, H. Xu, and W. Huang, “Characterization of the stress sensitivity of pores for different rank coals by nuclear magnetic resonance,” *Fuel*, vol. 111, pp. 746–754, 2013.
- [39] R. L. Kleinberg, C. Straley, W. E. Kenyon, R. Akkurt, and S. A. Farooqui, “Nuclear magnetic resonance of rocks: T_1 vs. T_2 ,” in *SPE Annual Technical Conference and Exhibition*, p. 11, Houston, TX, USA, 1993.
- [40] G. R. Coates, L. Xiao, and M. G. Prammer, *NMR Logging Principles and Applications*, Halliburton Energy Services, Houston, TX, USA, 1999.
- [41] R. L. Kleinberg, “Utility of NMR T_2 distributions, connection with capillary pressure, clay effect, and determination of the surface relaxivity parameter ρ_2 ,” *Magnetic Resonance Imaging*, vol. 14, no. 7-8, pp. 761–767, 1996.
- [42] C. Han, *Study on Simultaneous Iterative Reconstruction Technique Inversion Method of NMR Relaxation Signal*, Jilin University, 2014.
- [43] Z. Lv, “Study on the connectivity of pore structure of coal in three-dimensional space,” in *Proceedings 2011 International Conference on Computer Distributed Control and Intelligent Environmental Monitoring (CDCIEM 2011)*, pp. 1797–1799, Changsha, China, (2011).
- [44] Y. Meng, Z. Li, and F. Lai, “Experimental study on porosity and permeability of anthracite coal under different stresses,” *Journal of Petroleum Science and Engineering*, vol. 133, pp. 810–817, 2015.
- [45] Y. Yao, D. Liu, J. Liu, and S. Xie, “Assessing the water migration and permeability of large intact bituminous and anthracite coals using NMR relaxation spectrometry,” *Transport in Porous Media*, vol. 107, no. 2, pp. 527–542, 2015.
- [46] S. Marland, B. Han, A. Merchant, and N. Rowson, “The effect of microwave radiation on coal grindability,” *Fuel*, vol. 79, no. 11, pp. 1283–1288, 2000.
- [47] M. S. Seehra, A. Kalra, and A. Manivannan, “Dewatering of fine coal slurries by selective heating with microwaves,” *Fuel*, vol. 86, no. 5-6, pp. 829–834, 2007.
- [48] J. Pan, Y. Zhao, Q. Hou, and Y. Jin, “Nanoscale pores in coal related to coal rank and deformation structures,” *Transport in Porous Media*, vol. 107, no. 2, pp. 543–554, 2015.
- [49] H. Li, B. Lin, W. Yang et al., “Experimental study on the petrophysical variation of different rank coals with microwave treatment,” *International Journal of Coal Geology*, vol. 154-155, pp. 82–91, 2016.
- [50] D. Prinz, W. Pyckhout-Hintzen, and R. Littke, “Development of the meso- and macroporous structure of coals with rank as analysed with small angle neutron scattering and adsorption experiments,” *Fuel*, vol. 83, no. 4-5, pp. 547–556, 2004.
- [51] T. T. Chau, “A review of techniques for measurement of contact angles and their applicability on mineral surfaces,” *Minerals Engineering*, vol. 22, no. 3, pp. 213–219, 2009.
- [52] M. Li, *The Research on Pyrolysis-Penetration and Microstructure of Lignite*, Taiyuan University of Technology, Taiyuan, China, 2012.
- [53] Y. Wang, M. Li, B. Chen, and S. Dai, “Experimental study on ultrasonic wave characteristics of coal samples under dry and water saturated conditions,” *Journal of China Coal Society*, vol. 40, pp. 2445–2450, 2015.
- [54] M. Zambrano, E. Tondi, L. Mancini et al., “Fluid flow simulation and permeability computation in deformed porous carbonate grainstones,” *Advances in Water Resources*, vol. 115, pp. 95–111, 2018.
- [55] M. Zambrano, E. Tondi, L. Mancini et al., “3D Pore-network quantitative analysis in deformed carbonate grainstones,” *Marine and Petroleum Geology*, vol. 82, pp. 251–264, 2017.
- [56] B. B. Mandelbrot, *The Fractal Geometry of Nature*, Macmillan, 1983.
- [57] W. I. Friesen and R. J. Mikula, “Fractal dimensions of coal particles,” *Journal of Colloid and Interface Science*, vol. 120, no. 1, pp. 263–271, 1987.
- [58] W. Chengyang, H. Shixiong, S. Wenjing, and C. Wei, “Fractal dimension of coal particles and their CH_4 adsorption,” *International Journal of Mining Science and Technology*, vol. 22, no. 6, pp. 855–858, 2012.
- [59] H. Daigle, A. Johnson, and B. Thomas, “Determining fractal dimension from nuclear magnetic resonance data in rocks with internal magnetic field gradients,” *Geophysics*, vol. 79, no. 6, pp. D425–D431, 2014.
- [60] Y. B. Yao, D. M. Liu, D. Z. Tang et al., “Fractal characterization of seepage-pores of coals from China: an investigation on permeability of coals,” *Computers & Geosciences*, vol. 35, no. 6, pp. 1159–1166, 2009.
- [61] X. J. Cui, R. M. Bustin, and G. Dipple, “Selective transport of CO_2 , CH_4 , and N_2 in coals: insights from modeling of experimental gas adsorption data,” *Fuel*, vol. 83, no. 3, pp. 293–303, 2004.
- [62] J. Sun, Z. Yang, H. Guo, Q. Xiao, M. Hao, and X. Xu, “Comparative study of tight reservoir permeability using steady-state and unsteady-state methods,” *Rock and Soil Mechanics*, vol. 34, pp. 1009–1016, 2013.
- [63] Z. Pan and L. D. Connell, “Modelling of anisotropic coal swelling and its impact on permeability behaviour for primary and enhanced coalbed methane recovery,” *International Journal of Coal Geology*, vol. 85, no. 3-4, pp. 257–267, 2011.